# TECTONOMETAMORPHIC EVOLUTION OF THE KIOSK DOMAIN, CENTRAL GNEISS BELT, GRENVILLE PROVINCE, ONTARIO: CONSTRAINTS FROM GEOCHRONOLOGY AND THERMOBAROMETRY

by

John Gordon Joseph Foster

Submitted in partial fulfillment of the requirements
for the degree of Master of Science

at

Dalhousie University
Halifax, Nova Scotia
July 2012

DALHOUSIE UNIVERSITY

DEPARTMENT OF EARTH SCIENCES

The undersigned hereby certify that they have read and recommend to the Faculty of Graduate Studies for acceptance a thesis entitled "TECTONOMETAMORPHIC EVOLUTION OF THE KIOSK DOMAIN, CENTRAL GNEISS BELT, GRENVILLE PROVINCE, ONTARIO: CONSTRAINTS FROM GEOCHRONOLOGY AND THERMOBAROMETRY" by John Gordon Joseph Foster in partial fulfillment of the requirements for the degree of Master of Science.

Dated: July 20, 2012

External Examiner: _____

Co-supervisors: _____

_____

Readers: _____

_____

_____

DALHOUSIE UNIVERSITY

DATE: July 20, 2012

AUTHOR: John Gordon Joseph Foster

TITLE: TECTONOMETAMORPHIC EVOLUTION OF THE KIOSK DOMAIN, CENTRAL GNEISS BELT, GRENVILLE PROVINCE, ONTARIO: CONSTRAINTS FROM GEOCHRONOLOGY AND THERMOBAROMETRY

DEPARTMENT OR SCHOOL: Department of Earth Sciences

DEGREE: M.Sc. CONVOCATION: October YEAR: 2012



Signature of Author

*For The Skipper and Nan*

*"Time and tide waits for no man"*

# TABLE OF CONTENTS

**List of Tables** . . . . . **viii**

**List of Figures** . . . . . **x**

**Abstract** . . . . . **xiv**

**List of abbreviations used** . . . . . **xv**

**Acknowledgements** . . . . . **xvi**

**Chapter 1 Introduction** . . . . . **1**

1.1 The Grenville Orogen . . . . . 1
1.1.1 The Grenville Province . . . . . 2
1.1.2 Subdivisions of the Grenville Province . . . . . 4
1.1.3 The Allochthon Boundary Thrust . . . . . 7
1.1.4 Numerical models for the tectonic evolution of the southwest Grenville Province . . . . . 11

1.2 Objectives . . . . . 14

1.3 Thesis structure and organization . . . . . 15

**Chapter 2 Geological setting** . . . . . **17**

2.1 Introduction . . . . . 17

2.2 The Central Gneiss Belt . . . . . 19

2.3 The Bonfield domain . . . . . 20

2.4 The Kiosk domain . . . . . 21

2.5 The Algonquin domain . . . . . 29

2.6 Summary . . . . . 34

**Chapter 3 Zircon Geochronology** . . . . . **37**

3.1 Introduction . . . . . 37

3.2 Method . . . . . 38

3.3 Sample description . . . . . 40
3.3.1 Bonfield Batholith . . . . . 40
3.3.2 Kiosk domain . . . . . 42

3.3.3 McLintock subdomain . . . 43

3.4 Zircon morphology and analytical results . . . 48
3.4.1 Bonfield domain . . . 49
3.4.2 Kiosk domain . . . 51
3.4.3 McLintock subdomain . . . 63

3.5 Discussion . . . 63
3.5.1 Zircon morphology . . . 63
3.5.2 Trace-element data . . . 66
3.5.3 Synthesis . . . 68

3.6 Conclusions . . . 73

**Chapter 4 Monazite Geochronology . . . 74**

4.1 Introduction . . . 74

4.2 Method . . . 75

4.3 Sample description . . . 78
4.3.1 CA108b . . . 80
4.3.2 PS08-101a . . . 81

4.4 Monazite chemical zoning and analytical results . . . 84
4.4.1 CA108b . . . 87
4.4.2 PS08-101a . . . 88

4.5 Discussion . . . 92
4.5.1 ca. 1480-1450 Ma ages . . . 92
4.5.2 ca. 1200-1135 Ma ages . . . 96
4.5.3 ca. 1080-1060 Ma ages . . . 96

4.6 Conclusions . . . 97

**Chapter 5 $^{40}$Ar/$^{39}$Ar Thermochronology . . . 98**

5.1 Introduction . . . 98

5.2 Method . . . 99

5.3 Sample description . . . 101
5.3.1 JF10-39 . . . 101
5.3.2 JF10-35 . . . 102

5.4 Hornblende analytical results . . . 104
5.4.1 JF10-39 . . . 105
5.4.2 JF10-35 . . . 105
5.4.3 LR10-3.3 . . . 105

5.5 Discussion . . . 107

5.6 Conclusions . . . 115

**Chapter 6 Thermobarometry . . . 116**

6.1 Introduction . . . 116
6.1.1 Summary of relevant thermobarometry data . . . 117

6.2 Method . . . 119
6.2.1 Data acquisition . . . 119
6.2.2 Pressure-temperature calculation . . . 124

6.3 Sample descriptions and analytical results . . . 125
6.3.1 JF10-12 . . . 128
6.3.2 JF10-88 . . . 128
6.3.3 CA108b . . . 132
6.3.4 Orthogneiss samples . . . 135

6.4 Discussion . . . 138
6.4.1 Interpretation of results . . . 138

6.5 Conclusions . . . 144

**Chapter 7 Discussion and conclusions . . . 145**

7.1 Tectonic history of the study area . . . 145
7.1.1 Pre-Grenvillian development . . . 146
7.1.2 Grenvillian orogeny . . . 149

7.2 Regional implications . . . 150

7.3 Future work . . . 158

7.4 Conclusions . . . 158

**Appendix A Zircon Analytical Data . . . 160**

**Appendix B Monazite Analytical Data . . . 189**

**Appendix C Thermochronology hornblende analytical data . . . 197**

**Appendix D Mineral abbreviations used . . . 200**

**Appendix E Thermobarometry analytical data . . . 202**

**References . . . 234**

# LIST OF TABLES


Table 3.1 Summary of zircon ages. . . . . 49

Table 4.1 Instrument analytical conditions for major-element analysis. . . . . 78

Table 4.2 Instrument analytical conditions for minor-element analysis. . . . . 79

Table 4.3 Summary table of monazite weighted mean ages. . . . . 87

Table 5.1 Summary of plateau and weighted mean ages. . . . . 105

Table 5.2 Average amphibole compositions. . . . . 106

Table 5.3 Amphibole $^{40}Ar/^{39}Ar$ data for sample JF10-39. Analyses used in weighted-mean age calculation are denoted by an asterisk. . . . . 108

Table 5.4 Amphibole $^{40}Ar/^{39}Ar$ data for sample JF10-35. . . . . 110

Table 5.5 Amphibole $^{40}Ar/^{39}Ar$ data for sample LR10-3.3. Analyses used in weighted-mean age calculation are denoted by an asterisk. . . . . 112

Table 6.1 Comparison of thermobarometry results for samples from McLeish (2008) that were re-evaluated in this study. . . . . 120

Table 6.2 Major-element electron-microprobe analytical conditions . . . . . 122

Table 6.3 Average pressure-temperature results for the six samples evaluated. 126

Table 6.4 Average mineral compositions for sample JF10-12. . . . . 130

Table 6.5 Average mineral compositions for sample JF10-88. . . . . 133

Table 6.6 Average mineral compositions for sample CA108b. . . . . 136

Table 6.7 Average mineral compositions for sample NA023a (after McLeish, 2008) . . . . . 139

Table 6.8 Average mineral compositions for sample NA046 (after McLeish, 2008) . . . . . 140

Table 6.9 Average mineral compositions for sample NA061e (after McLeish, 2008) . . . . . 141

Table A.1 Table of Zircon U-Pb Analytical Data . . . . . 184

Table A.2 Table of Zircon Trace-Element Analytical Data . . . . . 187

Table B.1 Monazite major-element data . . . . . 190
Table B.2 Monazite trace-element data and analytical results . . . . . 195
Table B.3 Monazite trace-element data and analytical results (continued) . . . 196

Table C.1 JF10-35 amphibole analyses . . . . . 198
Table C.2 JF10-39 amphibole analyses . . . . . 199

Table E.1 CA108b biotite analyses . . . . . 205
Table E.2 CA108b garnet analyses . . . . . 206
Table E.3 CA108b garnet analyses (continued) . . . . . 207
Table E.4 CA108b garnet analyses (continued) . . . . . 208
Table E.5 CA108b ilmenite analyses . . . . . 209
Table E.6 CA108b biotite analyses . . . . . 210
Table E.7 CA108b plagioclase analyses . . . . . 211
Table E.8 JF10-12 amphibole analyses . . . . . 213
Table E.9 JF10-12 clinopyroxene analyses . . . . . 214
Table E.10 JF10-12 clinopyroxene analyses (continued) . . . . . 215
Table E.11 JF10-12 garnet analyses . . . . . 216
Table E.12 JF10-12 garnet analyses (continued) . . . . . 217
Table E.13 JF10-12 ilmenite analyses . . . . . 218
Table E.14 JF10-12 plagioclase analyses . . . . . 219
Table E.15 JF10-88 amphibole analyses . . . . . 225
Table E.16 JF10-88 amphibole analyses . . . . . 226
Table E.17 JF10-88 biotite analyses . . . . . 227
Table E.18 JF10-88 garnet analyses . . . . . 228
Table E.19 JF10-88 garnet analyses (continued) . . . . . 229
Table E.20 JF10-88 garnet analyses (continued) . . . . . 230
Table E.21 JF10-88 K-feldspar analyses . . . . . 231
Table E.22 JF10-88 orthopyroxene analyses . . . . . 232
Table E.23 JF10-88 plagioclase analyses . . . . . 233

# LIST OF FIGURES


Figure 1.1 Generalized map of Archean and Perterozoic Orogens in North America . . . . . 3

Figure 1.2 Comparison of time intervals and tectonic nomenclature for the time period 1550-950 Ma within the Grenville Province (modified from Foster, 2005) . . . . . 5

Figure 1.3 Comparison of lithotectonic domain subdivisions of the southwest Grenville Province. . . . . 6

Figure 1.4 Subdivisions of the Grenville Province of Rivers et al. (1989) (from Slagstad, 2003) . . . . . 8

Figure 1.5 Subdivisions of the southwestern CGB of Culshaw et al. (1997) . . 9

Figure 1.6 Subdivisions of the southwestern Grenville Province of Carr et al. (2000) . . . . . 10

Figure 1.7 Map of the western Grenville Province . . . . . 12

Figure 1.8 Comparison of numerical models for the southwest Grenville Province. 14

Figure 2.1 Geological map of the study area . . . . . 18

Figure 2.2 Outcrop photos of the Bonfield domain metaplutonic gneiss . . . . 22

Figure 2.3 Lower-hemisphere Schmidt nets for the Kiosk and Algonquin domains . . . . . 25

Figure 2.4 Map of the first vertical derivative of the HRAM data for the study area and surrounding lithotectonic domains . . . . . 26

Figure 2.5 Map of the horizontal gradient of the airborne gravity data for the study area and surrounding lithotectonic domains . . . . . 27

Figure 2.6 Outcrop photos of the representative Kiosk domain orthogneisses . 30

Figure 2.7 Outcrop photos of Kiosk domain migmatites . . . . . 31

Figure 2.8 Outcrop photos of representative morphologies of mafic bodies in the Kiosk domain . . . . . 32

Figure 2.9 Outcrop photos of previously unmapped large coronitic metagabbro from the hangingwall of the BBLSZ . . . . . 33

Figure 2.10 Outcrop photos of representative gneisses from the McLintock subdomain . . . . . 35

Figure 3.1 Location map of geochronology, thermochronology, and thermobarometry samples evaluated in this study . . . . . 41
Figure 3.2 Outcrop picture and photomicrographs for sample JF10-48 . . . . 44
Figure 3.3 Outcrop picture and photomicrographs of typical Kiosk domain meta-quartz-monzonite orthogneiss . . . . . 45
Figure 3.4 Outcrop picture and photomicrographs of Kiosk domain amphibolite enclave sample . . . . . 46
Figure 3.5 Outcrop picture and photomicrographs of McLintock subdomain amphibolite dyke sample . . . . . 47
Figure 3.6 Representative CL images of zircons from the study area . . . . . 50
Figure 3.7 Tera-Wasserburg concordia diagram and weighted mean plot for JF10-48 . . . . . 51
Figure 3.8 Trace element plots for JF10-48 . . . . . 52
Figure 3.9 Tera-Wasserburg concordia diagram and weighted mean plot for JF10-16 . . . . . 53
Figure 3.10 Trace element plots for JF10-16 . . . . . 54
Figure 3.11 Tera-Wasserburg concordia diagram and weighted mean plot for JF10-17 . . . . . 55
Figure 3.12 Trace element plots for JF10-17 . . . . . 56
Figure 3.13 Tera-Wasserburg concordia diagram and weighted mean plot for JF10-30 . . . . . 58
Figure 3.14 Trace element plots for JF10-30 . . . . . 59
Figure 3.15 Tera-Wasserburg concordia diagram and weighted mean plot for JF10-71 . . . . . 60
Figure 3.16 Trace element plots for JF10-71 . . . . . 61
Figure 3.17 Tera-Wasserburg concordia diagram and weighted mean plot for CA109 . . . . . 62
Figure 3.18 Tera-Wasserburg concordia diagram and weighted mean plot for CA17 . . . . . 64
Figure 3.19 Ideal igneous and metamorphic chondrite normalized REE profiles 67
Figure 3.20 Compilation of probability density curves for all data evaluated in this study . . . . . 70

Figure 4.1 Example of background selection procedure for high and low background positions on the Th M$\alpha$ peak from WDS scan of monazite. 79

Figure 4.2 Outcrop pictures and photomicrographs for sample CA108b . . . . 82

Figure 4.3 BSE images of the two grains analysed in sample CA108b . . . . 83

Figure 4.4 Hand-sample pictures and photomicrographs for sample PS08-101a 85

Figure 4.5 BSE images of the two grains analysed in sample PS08-101a . . . 86

Figure 4.6 WDS chemical maps for two grains analysed in CA108b . . . . . 89

Figure 4.7 Geochronology results for the large grain in sample CA108b . . . 90

Figure 4.8 Geochronology results for the small grain in sample CA108b . . . 91

Figure 4.9 WDS chemical maps for two grains analysed in PS08-101a . . . . 93

Figure 4.10 Geochronology results for the Ksp-Qtz ribbon grain in sample PS08-101a . . . . . 94

Figure 4.11 Geochronology results for the matrix grain in sample PS08-101a . 95

Figure 5.1 Amphibole $^{40}Ar/^{39}Ar$ age spectra reported in Cosca et al. (1991) . 100

Figure 5.2 Outcrop and photomicrographs of sample JF10-39 . . . . . 103

Figure 5.3 Outcrop and photimicrographs of sample JF10-35 . . . . . 104

Figure 5.4 Amphibole $^{40}Ar/^{39}Ar$ weighted mean age plot for sample JF10-39 107

Figure 5.5 Amphibole $^{40}Ar/^{39}Ar$ plateau age plot for sample JF10-35 . . . . . 109

Figure 5.6 Amphibole $^{40}Ar/^{39}Ar$ weighted mean age plot for sample LR10-3.3 111

Figure 5.7 Example amphibole $^{40}Ar/^{39}Ar$ age spectra (sample JF10-39) showing the argon degassing domains discussed in text. . . . . 114

Figure 6.1 Map showing regional isotherms and isobars for the CGB . . . . . 118

Figure 6.2 Pressure-temperature plot of the six samples evaluated . . . . . 127

Figure 6.3 Outcrop pictures and photomicrographs for sample JF10-12 . . . . 129

Figure 6.4 High-resolution WDS maps and analytical traverse of a selected garnet in sample JF10-12 . . . . . 131

Figure 6.5 Outcrop pictures and photomicrographs for sample JF10-88 . . . . 132

Figure 6.6 High-resolution WDS maps and analytical traverse of a selected garnet in sample JF10-88 . . . . . 134

Figure 6.7 High-resolution WDS maps and analytical traverse of a selected garnet in sample CA108b . . . . . 137

Figure 6.8 Summary of thermobarometry and P-T paths for the Algonquin domain . . . . . 142

Figure 7.1 Conceptual tectonic model of the development of the study area in the southwest Grenville Province . . . . . 147

Figure 7.2 Summary of major tectonic events and lithologies for select domains in the CGB . . . . . 151

Figure 7.3 Structural cross-section through the study area . . . . . 154

Figure 7.4 The stop-convergence numerical model for the southwest Grenville Province. . . . . 157

Figure A.1 Grain Mount (GB6). Numbered boxes correspond to close up CL and BSE images, red boxes are those in the following sections. . . 161

Figure A.2 Grain Mount (GB5). Numbered boxes correspond to close up CL and BSE images, red boxes are those in the following sections. . . 170

Figure B.1 CA108b large matrix monazite grain trace-element analyses locations. . . . . 191

Figure B.2 CA108b small matrix monazite grain trace-element analyses locations. . . . . 192

Figure B.3 PS08-101a K-feldspar-quartz ribbon monazite grain trace-element analyses locations. . . . . 193

Figure B.4 PS08-101a matrix monazite grain trace-element analyses locations. 194

Figure E.1 CA108b analysis locations (i) . . . . . 203

Figure E.2 CA108b analysis locations (ii) . . . . . 204

Figure E.3 JF10-12 analysis locations . . . . . 212

Figure E.4 JF10-88 analysis locations (i) . . . . . 220

Figure E.5 JF10-88 analysis locations (ii) . . . . . 221

Figure E.6 JF10-88 analysis locations (iii) . . . . . 222

Figure E.7 JF10-88 analysis locations (iv) . . . . . 223

Figure E.8 JF10-88 analysis locations (v) . . . . . 224

# ABSTRACT

The Kiosk domain in the Central Gneiss Belt, southwestern Grenville Province, Ontario comprises ca.1655 Ma orthogneisses and volumetrically minor ca. 1480-1460 Ma paragneisses that were affected by granulite-facies metamorphism between ca. 1480 and ca. 1000 Ma. The objectives of this study are: (i) to determine the protolith ages from the Kiosk domain and the underlying southern Bonfield Batholith; (ii) to determine the timing of major tectonic episodes; (iii) to determine the pressure-temperature conditions of peak metamorphism; and (iv) to use these data to constrain the position of the Allochthon Boundary Thrust in the southwestern Grenville Province.

Geochronological data show that the orthogneiss that dominates the Kiosk domain crystallized at ca. 1655 Ma. Inherited zircon cores have characteristic igneous crystal morphologies and trace element geochemistry suggesting magmatic crystallization. Zircon data from the southern Bonfield Batholith also exhibit crystal morphological and trace-element geochemical signatures characteristic of igneous crystallization at ca. 1240 Ma. Metamorphic monazites in paragneisses, and overgrowths of zircon cores in orthogneisses and mafic bodies in the Kiosk and northern Algonquin domains reveal a polymetamorphic history. Widespread metamorphism at ca. 1460 Ma that produced volumetrically significant migmatites in the Kiosk domain are age-equivalent to plutons in the Algonquin domain, and was responsible for growth of early metamorphic monazite. Monazite also locally preserves evidence of early-Grenvillian metamorphism (ca. 1200-1130 Ma). Metamorphic rims on monazite and zircon record Grenvillian metamorphism at ca. 1080-1060 Ma reflecting crustal thickening and cratonward propagation of the Grenville Orogen. Zircon rims also yield a less constrained ca. 1000 Ma age.

Kiosk domain gneisses preserve granulite-facies mineral assemblages with variable degrees of retrogression. Protracted high-temperature conditions led to diffusive homogenisation of most metamorphic minerals, obliterating evidence of the prograde metamorphic history. Multi-equilibrium thermobarometry based on average compositions of matrix minerals records P-T conditions of ca. 10 kbar and 800°C, consistent with other estimates of peak metamorphic conditions in the southwest Grenville Province.

Field and geochronological data produced in this study call into question previous interpretations of the location of the Allochthon Boundary Thrust in the southwest Grenville Province. In the study area, the data suggest that the Allochthon Boundary Thrust is also different in structural character from its expression to the east and west, potentially reflecting an imbricated shear zone. In light of recent ductile crustal flow models of orogen development, the study area could represent intercalation of Allochthonous and Parautochthonous domains in a ductile, heterogeneous, mid- to lower-crustal flow regime.

# LIST OF ABBREVIATIONS USED

| | |
|---|---|
| A | Ahmic domain |
| AD | Algonquin domain |
| B | Britt domain |
| BBLSZ | Big Bob Lake shear zone |
| CAB | Composite Arc Belt |
| CABBZ | Composite Arc Belt Boundary Zone |
| CGB | Central Gneiss Belt |
| CMB | Central Metasedimentary Belt |
| CMBBZ | Central Metasedimentary Belt Boundary Zone |
| GFTZ | Grenville Front Tectonic Zone |
| GH | Go Home domain |
| H | Huntsville subdomain |
| M | Muskoka domain |
| MC | McCraney subdomain |
| MCL | McLintock subdomain |
| MCR | Mid-Continent Rift |
| MR | Moon River subdomain |
| N | Novar subdomain |
| NTLMZ | North Tea Lake mylonite zone |
| NTLSZ | North Tea Lake shear zone |
| P | Powassan domain |
| PS | Parry Sound domain |
| PSSZ | Parry Sound shear zone |
| R | Rosseau domain |
| S | Seguin subdomain |
| SD | Shawanaga Domain |
| SoP | Southern Province |
| SSZ | Shawanaga shear zone |
| TL | Tilden Lake domain |
| TTSZ | Tom Thomson shear zone |
| $X^3Y^1n$ | late-Paleoproterozoic to early-Mesoproterozoic gneiss |
| $X^3Y^1sn$ | late-Paleoproterozoic to early-Mesoproterozoic paragneiss |
| $X^3Y^1g$ | late-Paleoproterozoic to early-Mesoproterozoic granitoid |
| $X^3Y^1mn$ | late-Paleoproterozoic to early-Mesoproterozoic gabbro-norite |
| $Y^1g$ | early-Mesoproterozoic granitoid |

# ACKNOWLEDGEMENTS

I would like to take a moment to thank the people who have helped me during the course of my graduate research.

I cannot thank my supervisors, Dr. Nick Culshaw, Dr. Rebecca Jamieson, and Dr. Christopher Gerbi, enough for the opportunity to pursue research in the Grenville, and for graciously funding this study from their respective NSERC and NSF research grants. Their vigilance, guidance and constructive feedback helped immensely throughout the course of this study. In particular, I'd like to thank Nick for his constant encouragement, for stimulating discussions of Grenville tectonics, and for the delightful and innumerable conversations of topics from the physical to the spiritual, and everything in between. My sincerest thanks.

Special thanks to Dr. Brendan Murphy, Dr. Djordje Grujic, and Dr. Richard Cox for their participation on the examination committee, and for providing critical and helpful reviews that improved this thesis.

I would like to recognise and thank several others whose contributions were instrumental during the course of this study. Dr. Jeffrey Marsh provided crucial zircon data, guidance, assistance with zircon analysis, and crucial edits of geochronology work. Dr. Carl Guilmette provided invaluable instruction in metamorphic petrology, mineral chemistry, thermobarometry, and critical edits of thermobarometry work. Holly Steenkamp was absolutely indispensable during monazite analysis and data processing. Keith Taylor ran the argon analysis, helped in sample preparation, and was always available for meaningful discussions of argon data. Matt Kliffer trained me to use the crystal isolation facilities and helped with every step of zircon sample preparation.

I would like to thank the administrative and technical staff at the Department of Earth Sciences for all their help great and small, in particular Thomas Duffet, Darlene van de Rijt, and Norma Keeping.

I would like to thank all my friends for their constant encouragement and for making my time in Halifax a happy one, especially Carl Guilmette, Mike Giles, Meghan Penney, Rich Holden, Holly Steenkamp, and Mark Merrimen. A warm thank you to my family for their unwavering support, especially my Mother and Grandmother, who always knew when to say just the right little thing.

Last, but certainly not least, I would like express my most heartfelt gratitude to Sam Anderson for her love, encouragement, and patience. Without her, completion of this research simply would not have been possible.

# CHAPTER 1

# INTRODUCTION

The Kiosk domain in the Central Gneiss Belt of the southwest Grenville Province of Canada has remained largely unstudied in detail. Study beyond reconnaissance-level field mapping completed in the mid- to late-1980's has not been conducted. As a result, the Kiosk domain represents a "gap" in the geological knowledge base for the southwest Grenville Province. This thesis represents a concerted attempt to bridge that gap, and elucidate the geochronological and metamorphic history of the Kiosk domain in particular, with special reference to the nearby Bonfield and Algonquin domains.

## 1.1 The Grenville Orogen

The preserved parts of the Grenville Orogen indicate that it was a large, hot orogen that was active during the Mesoproterozoic. It extends from Mexico through eastern North America and Greenland, with inliers exposed in the Paleozoic Appalachian and Caledonian Orogens (Fig. 1.1). It is also continuous through Scandinavia as the Sveconorwegian Province, and through Central America, Antarctica, and Australia (Hoffman, 1988, 1989, 1991; Moores, 1991; Borg and DePaolo, 1994; Weil et al., 1998). The Grenville Orogen, along with other similar aged orogens, are part of a worldwide orogenic system that formed during the assembly of the late-Mesoproterozoic to early-Neoproterozoic supercontinent Rodinia (McMenamin and McMenamin, 1990). The present erosional surface of the Grenville Orogen exposes the mid-crustal levels of a deeply eroded orogenic belt,

in North America it is inferred to have formed as a result of a continental collision between Proterozoic Laurentia and a continent (Amazonia) or continents to the southeast at ca. 1200-1000 Ma (Hoffman, 1989; Rivers, 1997; Culshaw et al., 1997; Tohver et al., 2006; Hynes and Rivers, 2010). The term "Grenville Orogen" is used here to denote the entire orogenic system, whereas the term "Grenville Province" is used here to denote the deeply eroded portion of the Grenville Orogen that is exposed in Canada.

### *1.1.1 The Grenville Province*

The Grenville Province forms the youngest portion of the Canadian Shield, and is exposed almost uninterrupted for over 2000 km from the Labrador coast to the Great Lakes (Wilson, 1918). The Grenville Front represents the northern margin of the Grenville Province, and truncates the Archean Superior Province, and the Paleoproterozoic Penokean, New Quebec, Torngat, and Makkovik Orogens. (Fig. 1.1) (Wynne-Edwards, 1972; Gower et al., 1990; Rivers, 1997; Davidson, 1998; Rivers and Corrigan, 2000; Gower and Krogh, 2002). The Grenville Province comprises reworked polycyclic Archean and Paleo- to Mesoproterozoic rocks derived from the ancient basement of Laurentia and its shelf cover sequences and accreted domains, as well as monocyclic rocks accreted just prior to Grenvillian orogenesis (Rivers et al., 1989; Rivers, 1997) The orogen as a whole is characterized by high-grade metamorphic rocks at the present erosion level, predominantly at amphibolite- to granulite-facies in the western Grenville Province (Jamieson et al., 1992), with eclogite-facies rocks intercalated with granulite-facies rocks forming a wide belt in the eastern Grenville Province (Indares and Rivers, 1995; Indares, 1997; Rivers et al., 2002). Greenschist-facies rocks are found locally in the eastern and western Grenville Province (Rivers, 1983b,a; van Gool, 1992).

Several phases of metamorphism have been recognized in the Grenville Province. Following the works of Wynne-Edwards (1972) and Moore and Thompson (1980), several authors have suggested temporal divisions for major tectonic events in the Grenville Province (e.g. McLelland et al., 1996; Rivers, 1997; Rivers and Corrigan, 2000; Gower and Krogh, 2002). The pre-Grenvillian Pinwarian orogeny refers to a high-grade metamorphic and magmatic event at ca. 1495-1445 Ma that is associated with orogen-scale domain accretion Krogh et al. (1996); Rivers (1997); Rivers and Corrigan (2000). Rivers

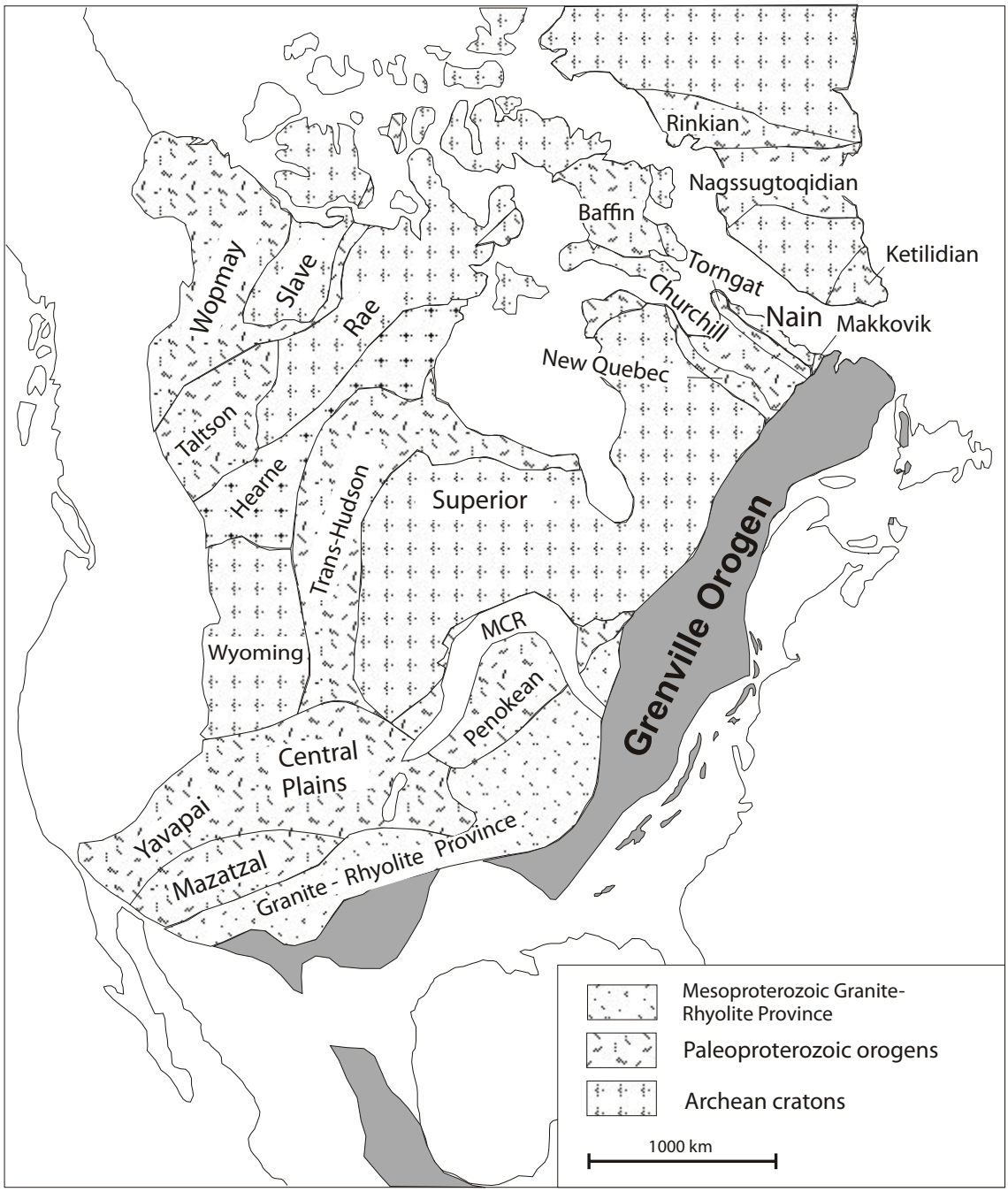


Figure 1.1: Generalized map showing the location of the Grenville Orogen in North America, including its subsurface extensions, exposed outliers in the Appalachians, and continuation into Texas and Mexico. Abbreviation: MCR Mid-Continent Rift (modified from Tollo et al., 2004).

(1997) divided the timing of thrusting and metamorphism in the Grenville Orogeny into three pulses, that were subsequently reclassified by Rivers and Corrigan (2000). There include the Shawinigan orogenic pulse (ca. 1190-1140 Ma), the Ottawan orogenic pulse (ca. 1080-1020 Ma), and the Rigolet orogenic pulse (ca. 1000-980 Ma) (Fig. 1.2). For the purpose of this study the temporal classification of Rivers and Corrigan (2000) is followed. The overall high metamorphic grade of rocks exposed suggests that the low-grade upper-crustal regime has been removed, exposing the mid- to lower-crustal regime at surface (Culshaw et al., 1997).

### *1.1.2 Subdivisions of the Grenville Province*

Many studies have proposed different subdivisions of the Grenville Province at varying scales. Whilst there are certain common features in these subdivision schemes, they differ in detail. It is important to choose the most appropriate subdivisions for the scale of the study area. The subdivisions of Wynne-Edwards (1972); Rivers et al. (1989); Culshaw et al. (1997); Carr et al. (2000) pertain to the study area, and are summarized below (Fig. 1.3).

**Wynne-Edwards (1972)** The subdivisions of Wynne-Edwards (1972) are the most commonly employed by workers in the southwest Grenville Province. He proposed a three-part subdivision: i) the Grenville Front Tectonic Zone (GFTZ), an orogen-scale shear zone(s) marking the northwestern boundary of the Grenville Province that experienced active thrusting at ca. 990 Ma (Haggart et al., 1993; Krogh, 1994); ii) the structurally overlying Central Gneiss Belt (CGB), which comprises rocks of Laurentia (pre-1400 Ma) and the associated supracrustal continental margin sequences and plutonic rocks, reworked during Grenvillian orogenesis and; iii) the structurally overlying Central Metasedimentary Belt (CMB), which comprises post-1400 Ma continental arc terranes and marginal basin sequences that were accreted to Laurentia during the Grenville orogeny. The Central Metasedimentary Belt Boundary Zone (CMBBZ) separates the CGB from the CMB in the southwest Grenville Province (Culshaw et al., 1983; Hanmer and McEachern, 1992).

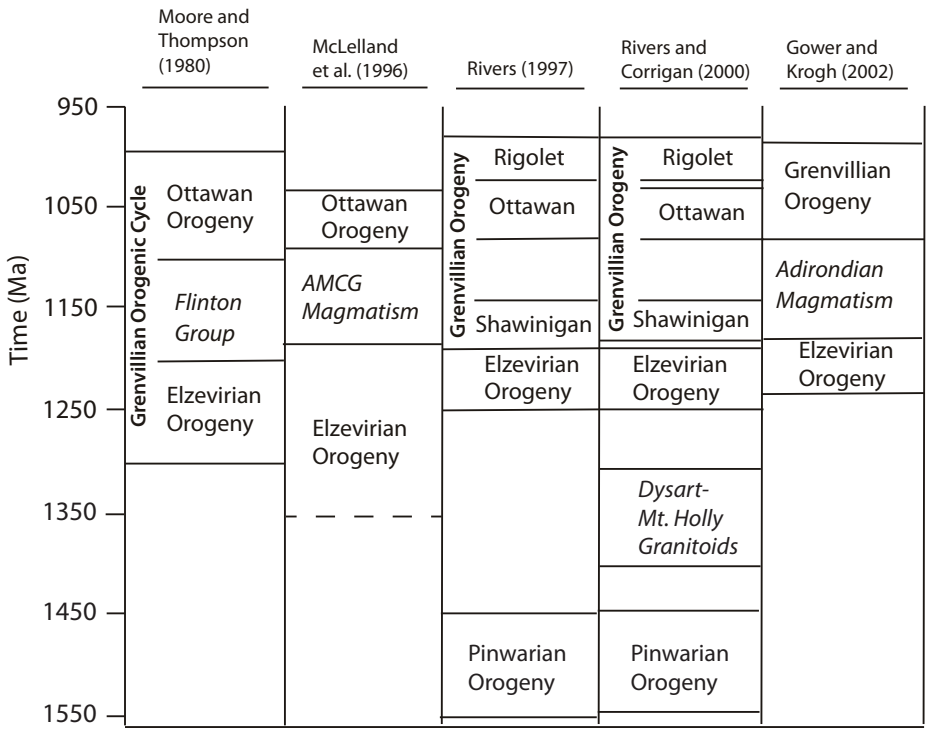


Figure 1.2: Comparison of time intervals and tectonic nomenclature for the time period 1550-950 Ma within the Grenville Province (modified from Foster, 2005)

**Rivers et al. (1989)** Rivers et al. (1989) subdivided the Grenville Province into three major units (Fig. 1.4): (i) the Parautochthonous Belt, which is a wide belt of reworked lithologies correlative with Archean and Paleoproterozoic rocks in the Grenville Province foreland; (ii) the Allochthonous Polycyclic Belt, which is a belt of rocks that preserve a pre-Grenvillian history of deformation, metamorphism, and plutonism, that cannot be correlated with rocks in the parautochthon; and (iii) the Allochthonous Monocyclic Belt, which is a belt of dominantly supracrustal rocks that experienced only Grenvillian deformation, metamorphism, and plutonism.

**Culshaw et al. (1997)** Culshaw et al. (1997) proposed a detailed lithotectonic subdivision of the CGB based on systematic field mapping along the shores of Georgian Bay (Fig. 1.5) . They proposed five structural levels: *Level 1* is the lowermost structural level, is roughly equivalent to the Parautochthonous Belt of Rivers et al. (1989), and comprises reworked Archean and Paleo- to Mesoproterozoic rocks with pre-Grenvillian

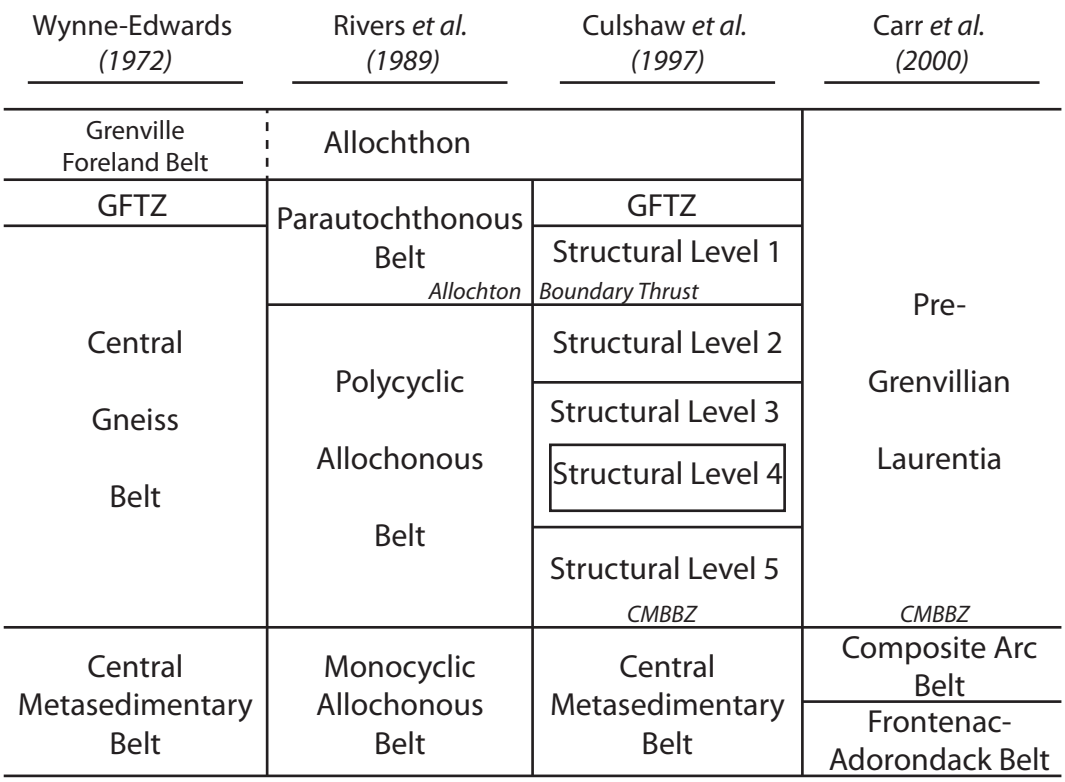


Figure 1.3: Comparison of lithotectonic domain subdivisions of the southwest Grenville Province.

deformation and metamorphism. *Level 2* is the lowermost allochthonous level and forms the hangingwall of the ABT (Ketchum and Davidson, 2000), including the Algonquin, Lower Rosseau, and Lower Go Home domains. Structural level 2 lacks Archean deformation and metamorphism. *Level 3* is a suite of Laurentian rocks that lack pre-Grenvillian metamorphic history, and forms the hangingwall of the ABT along Georgian Bay. The domains included in this level are the Shawanaga, Upper Rosseau, and Upper Go Home. Unique to structural level 3 are enclaves of retrogressed eclogite and anorthosite that are contained within migmatites and the upper- and lower-bounding shear zones. *Level 4* is the Parry Sound domain, which comprises granulites and anorthosites dated at ca. 1425-1315 Ma and ca. 1163 Ma, with a high-grade metamorphic overprint at ca. 1160-1120 Ma (van Breemen et al., 1986; Wodicka, 1994; Wodicka et al., 1996). The Parry Sound domain is anomalous with respect to age and lithology, and it is interpreted to be a far travelled allochthonous klippe that is related to the CMBBZ or the Adirondack Highlands (Wodicka et al., 1996). *Level 5* is the footwall of the CMBBZ and is the uppermost structural level of the CGB. This level lacks Paleoproterozoic lithologies or evidence of a

pre-Grenvillian metamorphic and deformation history. The domains included in this level are the Muskoka domain, and the Seguin and Moon River subdomains.

**Carr et al. (2000)** Carr et al. (2000) proposed a three-part subdivision of the southwestern Grenville Province focussing on protolith affinity (Fig. 1.6): (i) pre-Grenvillian Laurentia, which comprises ca. 1740 and ca. 1450 Ma plutonic rocks and associated supracrustal continental margin sequences, and corresponds to the Grenville foreland, GFTZ, and CMB of Wynne-Edwards (1972); (ii) the Composite Arc Belt, which comprises ca. 1300-1250 Ma continental arcs and associated supracrustal rocks corresponding to the CMB of Wynne-Edwards (1972); and (iii) the Frontenac-Adirondack Belt, which comprises supracrustal rocks and granitoid plutons and anorthosites, corresponding to the Central Granulite Terrane of Wynne-Edwards (1972).

The subdivision schemes outlined above are useful when discussing aspects of the geological history of the southwestern Grenville Province at different scales. Wynne-Edwards (1972) and Rivers et al. (1989) are most appropriate when referring to large-scale tectonics or assemblages of lithotectonic domains, and Culshaw et al. (1997) is especially useful when discussing lithotectonic domains in detail. This thesis uses these classification schemes as appropriate for the level of observation.

### *1.1.3 The Allochthon Boundary Thrust*

A model for the movement of a ductile thrust-wedge over a basal detachment in foreland fold-and-thrust belts was proposed by Platt (1986). He showed that ductile thrust wedges have an overall similar architecture to those that formed above the brittle-ductile transition, in that they are also governed by critical wedge processes, determined by the rheological properties of the wedge. This result provides a basis for treating mid-crustal fold-and-thrust belts as wedge-shaped systems with similar properties to upper-crustal belts, with the exception that they have smaller critical angles, although problems of section balancing and obtaining accurate estimates of shortening still persist. Early-workers interpreted the Grenville Province in the tectonic framework of a ductile foreland fold-and-thrust belt consisting of several first-order, orogen-scale belts separated by large thrust-sense shear

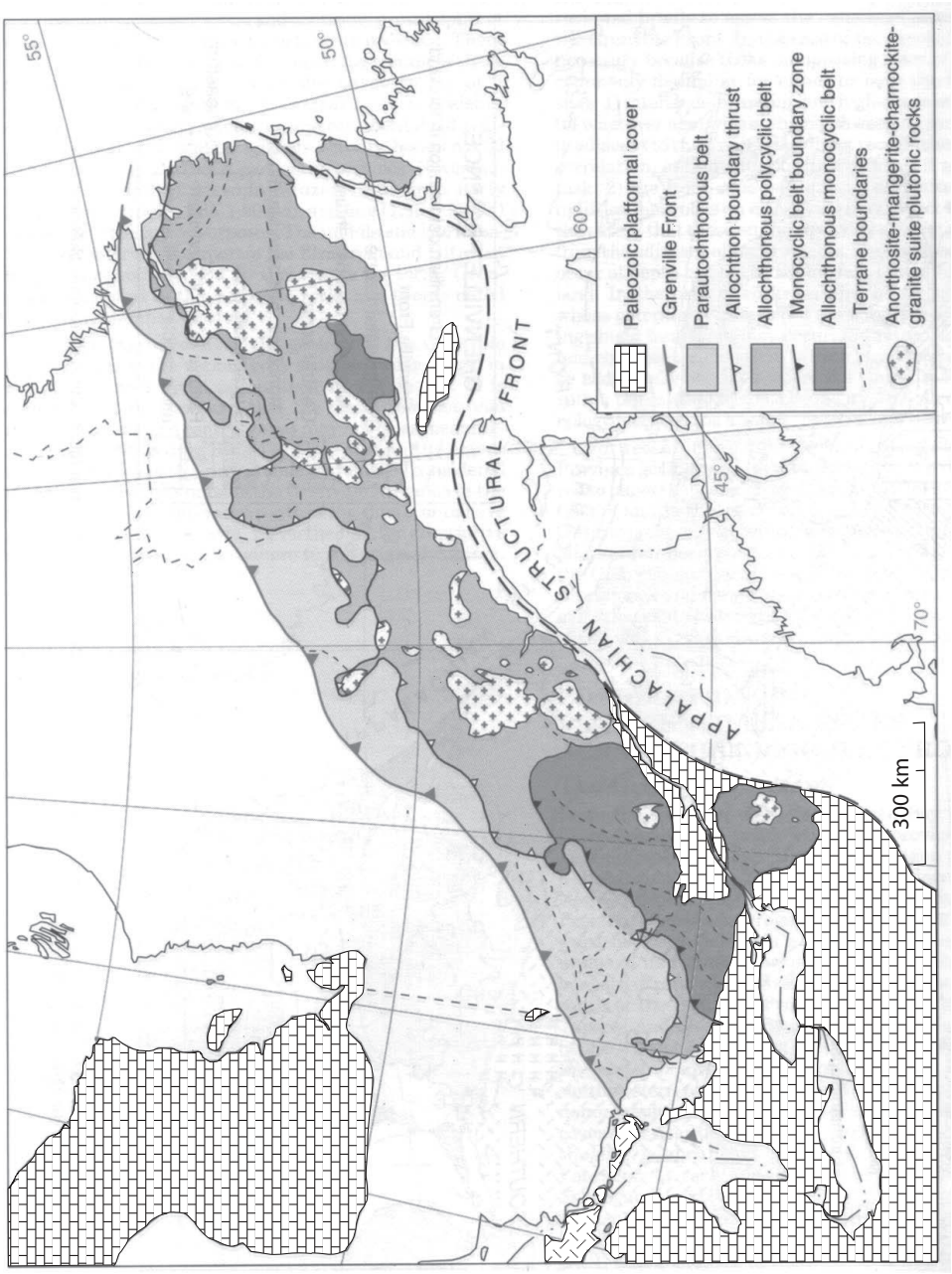


Figure 1.4: Subdivisions of the Grenville Province of Rivers et al. (1989) (from Slagstad, 2003)

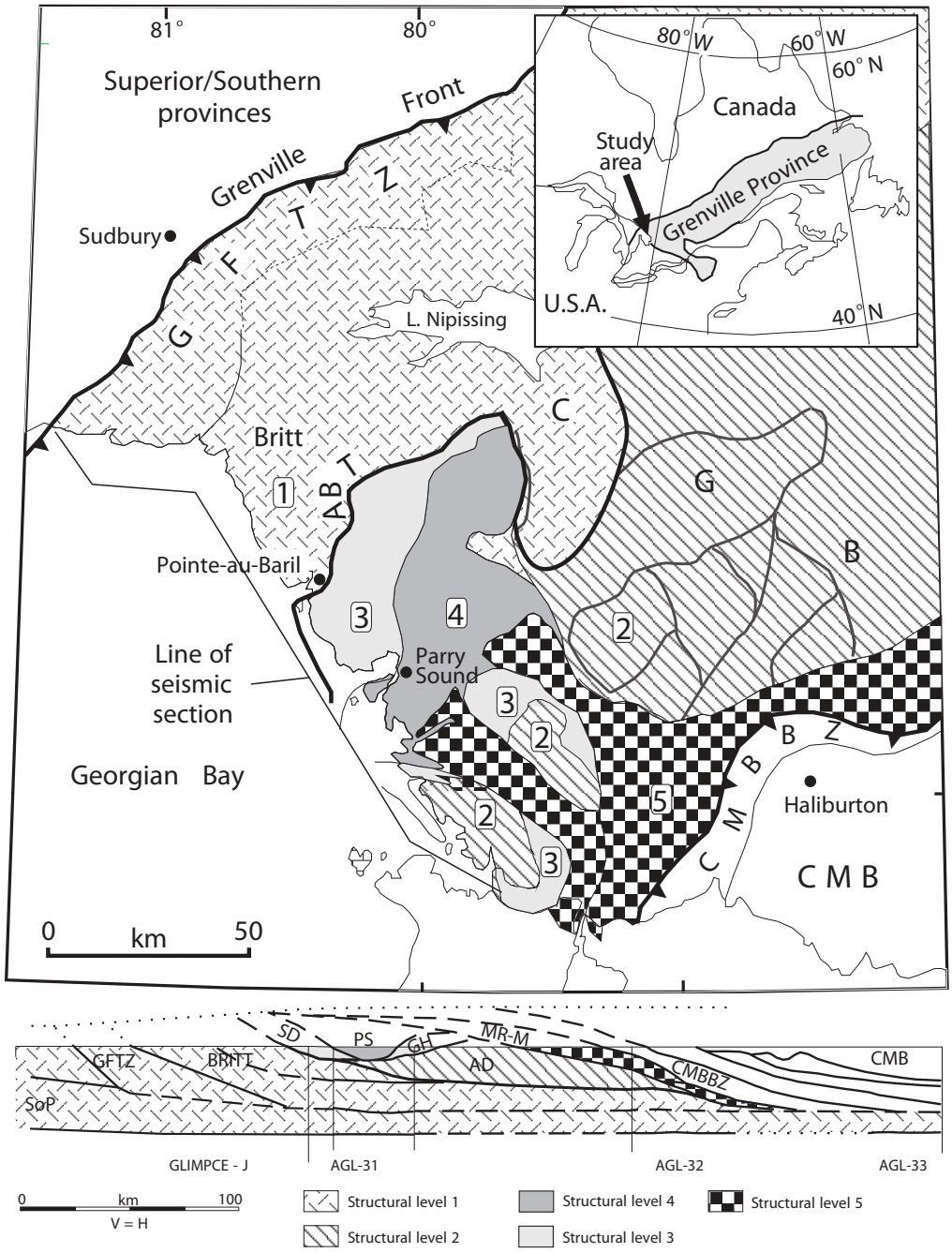


Figure 1.5: Subdivisions of the southwestern CGB into five structural levels (Culshaw et al., 1997). ABT modified from Ketchum and Davidson (2000). Seismic interpretation (after White et al., 2000). Structural level 1: Britt and Nepewassi domains. Structural level 2: Algonquin, Lower Rosseau, and Lower Go Home domains. Structural level 3: Shawanaga, Ahmic, Upper Rosseau, and Upper Go Home domains. Structural level 4: Parry Sound domain. Structural level 5: Muskoka domain, Seguin and Moon River subdomains (modified from Slagstad, 2003). For abbreviations see List of abbreviations used.

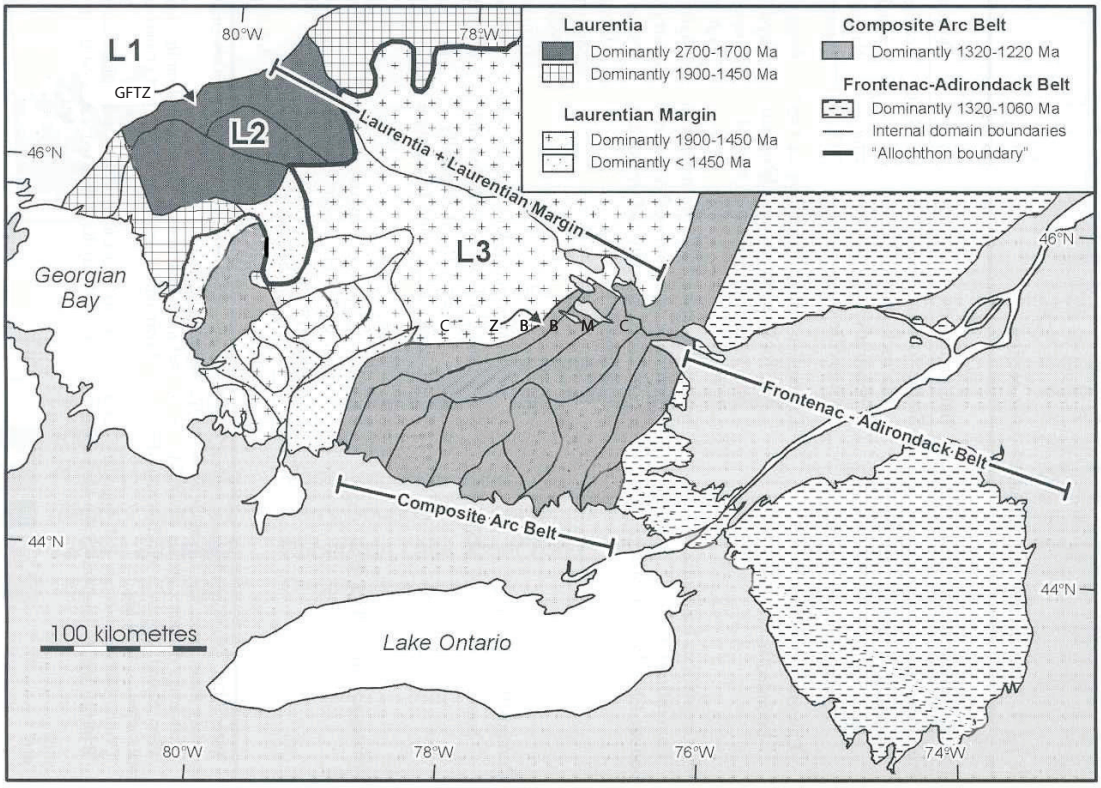


Figure 1.6: Subdivisions of the southwestern Grenville Province of (Carr et al., 2000). L1: Laurentian foreland northwest of the Grenville Front; L2: Archean crust with ca. 1740 and ca. 1450 Ma plutons; L3: ca. 1800-1680 Ma supracrustal rocks with ca. 1450 Ma continental arc granitoids. Abbreviations are: CMBBZ, Central Metasedimentary Belt boundary thrust zone; GFTZ, Grenville Front tectonic zone.

zones (e.g. Wynne-Edwards, 1972; Rivers et al., 1989).

The Allochthon Boundary Thrust is the broadly northeast-striking décollement separating the Parautochthonous and Allochthonous Belts (Rivers et al., 1989) (Fig. 1.7). The structural position of the ABT is well constrained in the eastern Grenville Province and in the westernmost portion of the CGB. In the southwestern CGB the Shawanaga shear zone, separating the Britt and Shawanaga domains, is interpreted to be the ABT. This portion of the ABT originated as a thrust-sense shear zone with an overall northwest-directed tectonic transport direction, but was reactivated as a normal-sense shear zone with southeast-directed displacement (Jamieson et al., 1992; Culshaw et al., 1994; Ketchum, 1994; Culshaw et al., 1997). In western Quebec, the ABT coincides with the Watson Lake Shear zone, along which granulite-facies gneisses overlie amphibolite-facies granitoid rocks and paragneisses (Davidson, 1996; Indares, 1997; Ketchum and Davidson, 2000). Between these two locations, however; the position of the ABT is not as well constrained, and has been the subject of several re-interpretations (c.f. Rivers et al., 1989; Davidson, 1996; Ketchum and Davidson, 2000; Dickin and McNutt, 2003).

Ketchum and Davidson (2000) proposed a set of three lithological criteria to constrain the position of the ABT in the southwest Grenville Province: (i) olivine metadiabase bodies of the ca. 1240 Ma Sudbury dyke swarm is restricted to the footwall; (ii) regionally extensive ca. 1170-1150 Ma coronitic olivine metagabbro is restricted to the hangingwall; and (iii) retrogressed eclogite associated with metamorphosed anorthosite and ultramafic rocks are restricted to the hangingwall (Ketchum et al., 1994; Davidson, 1986b; Grant, 1987). Using these lithostratigraphic criteria requires the ABT to be placed north of the Bonfield and Kiosk domains, implying they are both completely allochthonous.

### *1.1.4 Numerical models for the tectonic evolution of the southwest Grenville Province*

Rivers (1994) proposed first-order comparisons of the tectonic development of the Mesozoic Himalayan Orogen and the Mesoproterozoic Grenville Orogen. Corrigan (1995) refined this conceptual model suggesting an ”Andean” type configuration from ca. 1450 to 1200 Ma changing to a “Himalayan” type continent-continent collision from ca. 1190

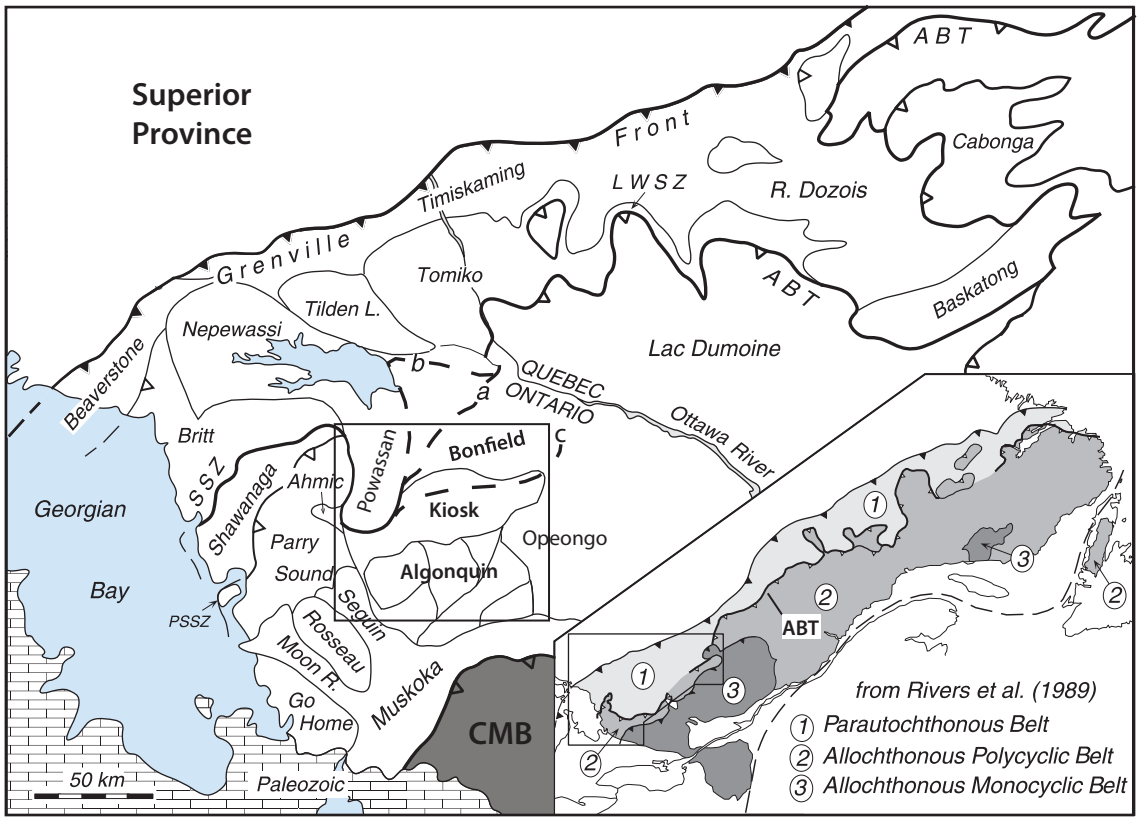


Figure 1.7: Map of the western Grenville Province. Major boundary thrust zones are shown with a heavy black line, and the Allochthon Boundary Thrust is indicated. Three interpretations of the position of the ABT in the central portion of the map are indicated in heavy dashed line segments. The interpretations are: a, Davidson (1986b); b, Ketchum and Davidson (2000); c, Dickin and McNutt (2003). The position of the ABT of Rivers et al. (1989) is shown in the inset map. The black box shows the location of the study area. Abbreviations are: LWSZ, Watson Lake shear zone; for other abbreviations see List of abbreviations used (modified from Ketchum and Davidson, 2000).

to 980 Ma (cf. Rivers, 1997). Recently, several studies have postulated that the tectonic development of the Himalayan Orogen can be explained by mid-crustal channel flow, and workers have built on this hypothesis to propose heterogeneous, ductile, mid- and lower-crustal flow model of the Grenville Orogen (Beaumont et al., 2001, 2004; Jamieson et al., 2004; Carr and Simony, 2006; Beaumont et al., 2006; Godin et al., 2006; Hodges, 2006; St-Onge et al., 2006; Jamieson et al., 2007, 2010). Jamieson et al. (2007, 2010) compared orogen-scale structure and thermal histories with numerical models in which the thermo-mechanical properties were specified, and the orogen structure was modelled. Their models were run over a ca. 100 My-emt (Millions of years-elapsed model time), modelling the convergent Grenville orogeny. Two fundamental model types were run: (i) *constant-convergence* models where orogenic convergence continues to transport material to the orogen foreland; and (ii) *stop-convergence* models, where convergence is halted, and gravity-driven mid-crustal flow sustains foreland-directed tectonic transport. The latter model very closely approximated the crustal structure and pressure-temperature characteristics of the CGB along Georgian Bay, leading to the conclusion that the interior CGB was the site of ductile flow under an orogenic plateau (Fig. 1.8). Allochthonous blocks of lower crust underwent several hundred kilometres of tectonic displacement in the mid-crustal flow zone prior to final exhumation at the orogenic margin. The variable mid- to lower-crustal rheology of the final crustal architecture of the models. In particular, if relatively weak lower-crustal blocks enter the model in the early stages of convergence they can become partially exhumed into the mid-crustal flow zone and transported toward the orogenic margin. In contrast, a competent lower-crustal indentor remained attached to the mantle lithosphere and was continually overthrust by the weaker mid- and lower-crust. This can provide a framework for the thrust emplacement of the lithotectonic domains of the CGB in the southwestern Grenville Province.

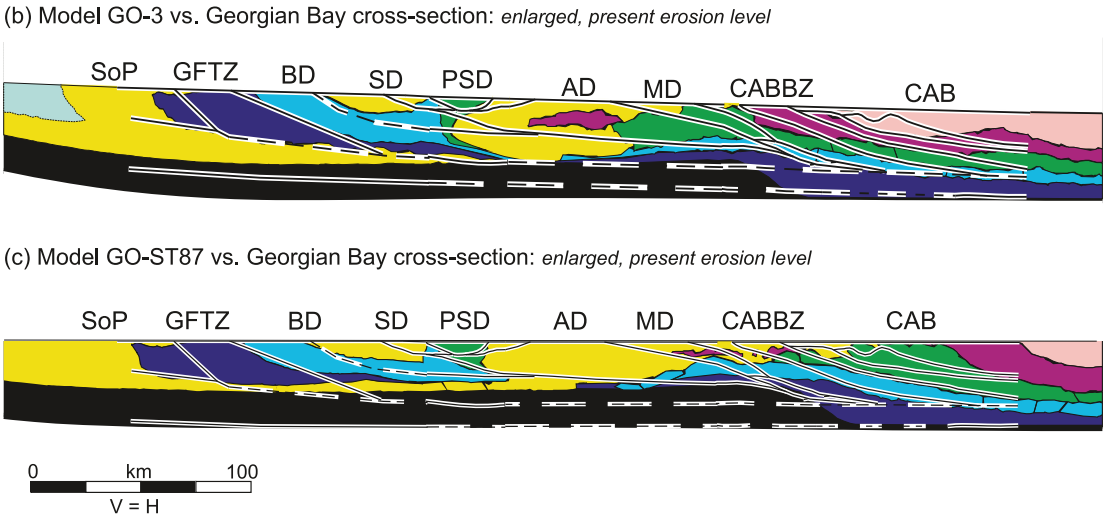


Figure 1.8: Comparison of numerical models for the southwest Grenville Province, truncated at present erosion level and overlain with geological cross-sections (from Jamieson et al., 2010). There is a general agreement of the model result with geological cross-section. Model GO-3 (b) is a constant-convergence model, and GO-ST87 (c) is a stop-convergence model. Abbreviations are: BD, Britt domain; MD, Muskoka domain, other abbreviations after List of abbreviations used.

## 1.2 Objectives

This thesis investigates the Kiosk domain in the southwestern Grenville Province (Fig. 1.7). Regional thermobarometric studies in the southwest Grenville Province have demonstrated pervasive metamorphism at granulite- and locally amphibolite-grade facies conditions during Grenvillian orogenesis, however; there has been little direct thermobarometry work conducted on the Kiosk domain. Practically no geochronology data exist for the Kiosk domain, in contrast, to the south in the Algonquin domain the protolith ages and timing of deformation and metamorphism is relatively well known. The analytical techniques employed, in addition to field work, are electron microprobe (EMP) analysis of silicate minerals for thermobarometry, EMP monazite geochronology, SHRIMP-RG zircon geochronology and trace-element geochemistry, and amphibole $^{39}Ar/^{40}Ar$ thermochronology.

The main objectives of this study are:

- To use U-Pb geochronology of orthogneisses, paragneisses, and cross-cutting mafic dykes to constrain the timing of major tectonic events experienced by the Kiosk domain, in particular, the timing of Grenvillian deformation along the northern boundary shear zone and an internal through-going shear zone.
- To use U-Pb geochronology of granitic plutonic rocks of the southern Bonfield Batholith to constrain the timing of plutonism in the southern Bonfield domain.
- To use amphibole $^{39}Ar/^{40}Ar$ thermochronology to constrain the timing of cooling of rocks above and below the boundary shear zone between the southern Bonfield and Kiosk domains.
- To use multi-equilibria thermobarometry techniques to assess the peak Grenvillian pressure-temperature conditions experienced by the Kiosk domain.
- To use these data to test the hypothesis that the boundary shear zone between the southern Bonfield and Kiosk domains represents the ABT.

To satisfy these objectives, field work for this thesis was carried out at selected locations in the Kiosk and southern Bonfield domain to target the geochronological and metamorphic history of the major, through-going shear zones. In addition, other data were incorporated from previous field seasons to produce a larger data set using a consistent methodology, to provide a wider understanding of the geochronology and thermobarometry of the Kiosk domain, and to relate that data to nearby lithotectonic domains. Field and laboratory efforts focussed on major shear zone rocks in an attempt to test if the northern boundary of the Kiosk domain represents the ABT.

## 1.3 Thesis structure and organization

The chapters in this thesis are written as a collection of "technical reports," each focussing on a different technique that was applied during the course of this study.

The individual chapters are: *Chapter 2* , which discusses the geological setting of

the study area, highlighting the lithologies and pertinent field relations observed during targeted field work carried out for this study. *Chapter 3* , which presents U-Pb zircon geochronology for the study area. Zircon geochronology was the main geochronology technique employed along a transect from the Bonfield domain, structurally below the Kiosk domain, to the Algonquin domain, structurally above. *Chapter 4* , presents reconnaissance-level U-Pb monazite geochronology completed in this study. Monazite work was two-fold: (i) proof of concept of monazite as a viable chronometer for Kiosk domain paragneisses; and (ii) to elucidate the geochronology of rocks from an internal shear zone in the Kiosk domain versus rocks from outside in the shear zone in the domain interior. *Chapter 5* , discusses reconnaissance-level thermochronology along the NTLSZ to elucidate the cooling history of the northern boundary shear zone of the Kiosk domain. *Chapter 6* discusses multi-equilibria thermobarometry of orthogneisses, paragneisses and cross-cutting dykes from the Kiosk domain and northern Algonquin domain. *Chapter 7* synthesises contributions from individual chapters into an integrated conceptual model for the tectonometamorphic development of the Kiosk domain, with special reference to the under- and over-lying Bonfield and Algonquin domains. The data are then discussed in terms of the classic thrust-mechanics model of development of the Grenville Province, with particular reference to the impact that new data have on the interpreted position of the ABT. The data are also presented in the framework of modern numerical models for heterogeneous mid- and lower-crustal ductile flow in the Grenville Province.

# CHAPTER 2

# GEOLOGICAL SETTING

## 2.1 Introduction

The Kiosk and Algonquin domains in the CGB of eastern Ontario consist of Mesoproterozoic orthogneisses and paragneisses that overlie the metaplutonic rocks of the Bonfield domain. Lithotectonic domains in the study area are characterised by distinctive lithological, structural, and geophysical signatures, and are separated by boundary shear zones often consisting of mylonitic gneisses. The lowest structural unit of the Allochthonous Polycyclic Belt in the study area is the Bonfield domain. This is a poorly studied domain of granitic gneisses and migmatites that is mostly underlain by the Bonfield Batholith (Lumbers, 1971; Lumbers et al., 1991). Overlying the Bonfield domain are the Kiosk and Algonquin domains. These domains are characterised by the "puzzle-like" assemblage of smaller subdomains with distinctive lithologies and structural trends separated by ductile, high-strain shear zones (Davidson et al., 1982; Culshaw et al., 1983; Davidson, 1984, 1986c,b; Culshaw et al., 1988; Davidson and van Breemen, 1988; Culshaw et al., 1989, 1990).

In this chapter, the lithologies and field relations of the main units in the Kiosk domain, and other units of interest in the underlying Bonfield and overlying Algonquin domains are discussed. Figure 2.1 is a geological map for the study area, highlighting pertinent structural elements and the location of samples discussed in later chapters of this thesis.

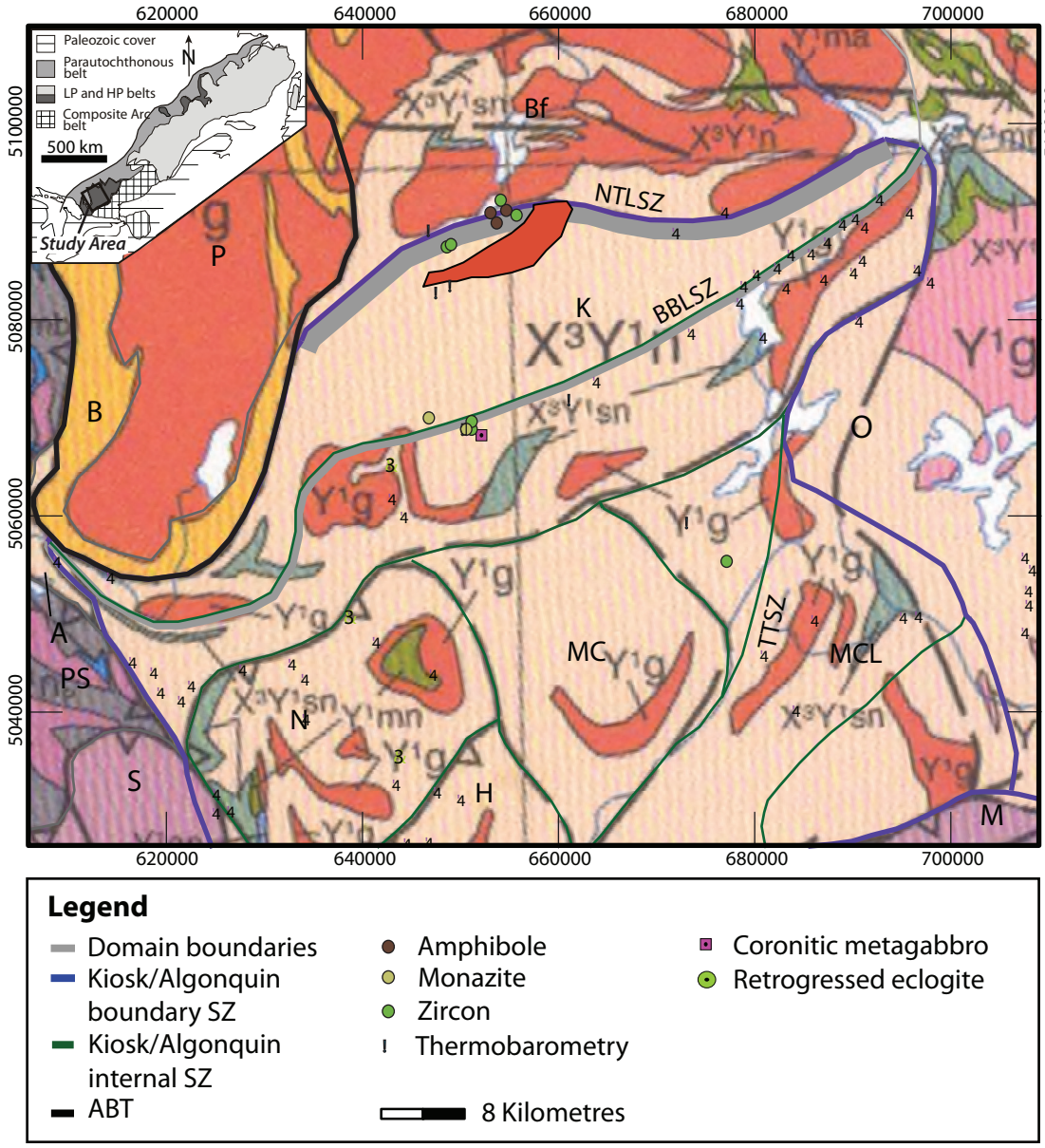


Figure 2.1: Geological map of the study area. Geology from Davidson (1998), except where discussed in text. ABT from Ketchum and Davidson (2000). Domain boundaries from Culshaw et al. (1983); Davidson (1986c). Locations of amphibole thermochronology, zircon and monazite geochronology, and thermobarometry samples discussed elsewhere in this thesis are shown. Thick grey lines of the NTLSZ and BBLSZ schematically indicate the width of the shear zone. Inset map modified from Foster (2005). For abbreviations see List of abbreviations used.

## 2.2 The Central Gneiss Belt

The Central Gneiss Belt comprises most of the Grenville Province in southwestern Ontario and western Quebec (Figs. 1.5 and 1.7). Most of the CGB is composed of variably southeast-dipping, upper-amphibolite- to granulite-facies orthogneisses and paragneisses. Igneous protolith ages range from ca. 2680 Ma for trondhjemite gneiss near the GFTZ (Chen et al., 1995) to ca. 1340 Ma granitoid rocks found in many localities throughout the CGB (Corrigan et al., 1994; Chen et al., 1995; Ketchum et al., 1998; Slagstad, 2003; Slagstad et al., 2004a,c). Most igneous protoliths formed during two major magmatic episodes on the Laurentian margin at ca. 1750-1600 Ma and ca. 1470-1340 Ma (Rivers, 1997; Ketchum and Davidson, 2000), with other localized events at >1700 Ma and ca. 1450-1350 Ma (van Breemen and Davidson, 1988; Tuccillo et al., 1992; Corrigan et al., 1994; Dudas et al., 1994; Ketchum et al., 1994; Jamieson et al., 2001).

Tectonic development of the CGB is the result of protracted, northwest-directed tectonic transport and thrust emplacement of discrete, shear-zone bound lithotectonic domains (e.g. Davidson and Morgan, 1981; Davidson et al., 1982; Culshaw et al., 1983; Davidson, 1984). Lithotectonic domains are characterized by distinct lithological, structural, geochronological, and metamorphic histories, and are separated by boundary zones of Grenvillian age. Reconnaissance mapping in the 1980's underpins the current subdivisions of the CGB (Davidson et al., 1982; Culshaw et al., 1983; Davidson, 1984). Early workers interpreted the CGB as a broadly coaxial, imbricated thrust sequence formed during northwest-directed tectonic transport of the Grenville Orogen (e.g. Jamieson et al., 1992; Wodicka, 1994; Wodicka et al., 1996; Culshaw et al., 1997). Some studies in the southwestern and eastern Grenville Province have proposed out-of-sequence thrust models for sub-horizontal northwest-vergent structures and emplacement of lithotectonic domains in the Allochthonous and Parautochthonous belts (e.g. Nadeau and Hanmer, 1992; Culshaw et al., 1997; Rivers et al., 2002; Foster, 2005). Culshaw et al. (1997) proposed a model of ductile lower- to mid-crustal flow during synorogenic thrusting and extension to explain the emplacement of shear zone bound lithotectonic domains in the southwest Grenville Province (cf. Culshaw et al., 1994). Their model also interpreted the reactivation of thrust-sense shear zones as extensional shear zones consistent with thermally activated

extension related to a weak lower crust. Recently, workers have created numerical models of heterogeneous, ductile, mid- and lower-crustal flow which address incompatibilities and inconsistencies with applying brittle-regime thrust-mechanics to ductile, mid-crustal levels of orogens (e.g. Culshaw et al., 2006; Jamieson et al., 2007, 2010).

## 2.3 The Bonfield domain

The Bonfield domain lies east of the Powassan Batholith, and south of the Mulock Pluton in the southwest Grenville Province (Fig. 1.7). The Bonfield domain (Fig. 2.1) comprises the northern portion of structural level 2 of Culshaw et al. (1997), or the base of the Allochthonous Polycyclic Belt of Rivers et al. (1989) (Fig. 1.5). This region of the CGB was mapped by Lumbers (1971, 1975), but has not been the focus of further detailed study. The lithotectonic position of this zone remains poorly constrained, which has led to several different interpretations. Easton (1992) assigned this zone to the Powassan domain in the Allochthonous Belt in the hangingwall of the ABT. Davidson (1996) reinterpreted the position of the ABT in the CGB, drawing a segment of the ABT on a northwest trend through this zone, placing the northwest Bonfield domain in the Parautochthonous Belt and the southeast portion in the Allochthonous Belt. Ketchum and Davidson (2000) repositioned the ABT and placed it on the northern margin of this zone, at the boundary with the Nepewassi, Tilden Lake, and Tomiko domains. Though not explicitly stated, they imply a linkage of the Bonfield domain with the Kiosk domain in the Allochthonous Belt.

Most of the Bonfield domain is underlain by granitic metaplutonic rocks of the Bonfield Batholith and smaller satellite plutons, quartzofeldspathic orthogneisses derived from these plutonic rocks, and undifferentiated intermediate-composition orthogneiss and migmatitic orthogneiss that host the metaplutonic rocks (Lumbers et al., 1991). Three rock types have been documented in the study area: (i) pink to creamy-pink quartzofeldspathic plutonic rocks of syeno- to monzo-granitic composition that preserve primary igneous textures; (ii) creamy-brown/green, moderately- to well-foliated gneiss with upper-amphibolite-facies mineral assemblages, representing the deformed equivalents of these plutonic rocks. These lithologies show signs of recrystallization and metamorphism and only rarely preserve relict igneous textures; and (iii) pale-cream undifferentiated host

metagranodiorite orthogneiss of unknown affinity, with thick mafic bands (Lumbers et al., 1991; McLeish, 2008).

During field work for this study, only the deformed equivalents of Bonfield Batholith plutonic rocks were observed in the immediate footwall of the NTLSZ. These rocks are creamy-brown amphibole-biotite metagranodiorite gneisses that have a very consistent amphibolite-facies meta-monzo-granite mineralogy in the study area. These rocks become increasingly well foliated with proximity to the NTLSZ, where Bonfield domain fabrics are reworked parallel to the northeast-striking structural trend of the shear zone. These rocks preserve a dominantly flattening strain (S>L), with a moderately defined stretching lineation.

A reconnaissance-level study of the geology of Algonquin Provincial Park by McLeish (2008) introduced the informal name, "Bonfield terrane" for to this zone, however; *domain* is preferred over *terrane* as the latter implies specific tectonic conditions that do not apply to this area. For example, CGB gneissic domains are not bounded by crustal-scale suture zones, and on most palinspastic restorations of the orogen they restore as a single unit (Culshaw and Dostal, 1997). This study will use the name "Bonfield domain" *sensu lato*.

## 2.4 The Kiosk domain

The Kiosk domain was recognised during reconnaissance mapping by the Geological Survey of Canada in the southwestern Grenville Province (e.g. Davidson and Morgan, 1981; Culshaw et al., 1983; Davidson, 1986b,c). Reconnaissance-level mapping in the Kiosk domain conducted inside the boundaries of Algonquin Provincial Park was completed by Davidson (1986c), in a study that focussed primarily on coronitic metagabbros in the eastern and central Kiosk domain. The Kiosk domain was mapped mainly as undifferentiated orthogneiss and associated paragneiss with consistent northeast-striking gneissosity defined by compositional layering, and lacking large-scale, through-going structures. Since the time of this study, relatively little work has been completed in the Kiosk domain. The sparseness of data in the Kiosk domain is a function of the limited access of the area, both

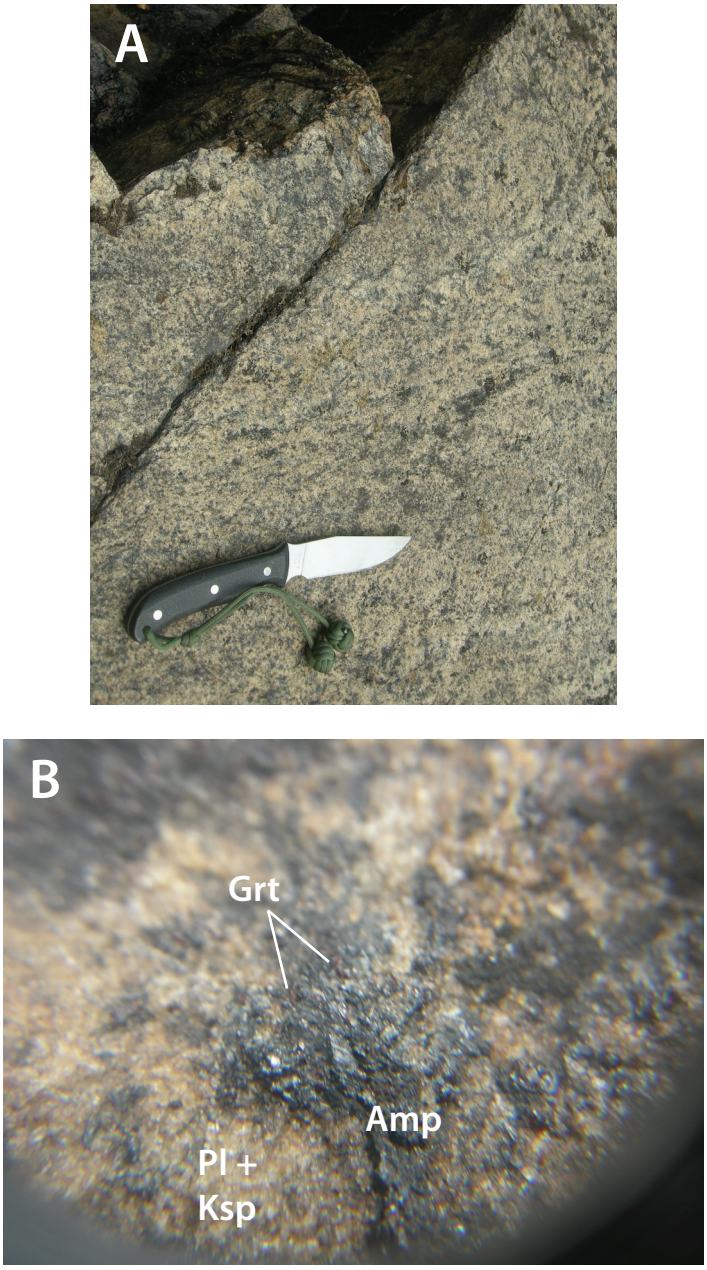


Figure 2.2: Outcrop photos of the Bonfield domain metaplutonic gneiss. A) Moderately foliated metagranodiorite; note elongate disconnected amphibole- and K-feldspar-rich layers (knife for scale). B) Close-up photo of large amphibole aggregate in plagioclase-quartz-K-feldspar matrix (view through 16x hand-lens) (UTM x: 0654145, y: 0654145).

in physiographic access to remote wooded terrain, and regulatory access, as most of the area lies within the bounds of Algonquin Provincial Park.

The Kiosk domain (Fig. 2.1), first recognised by Davidson and Morgan (1981), comprises the middle portion of structural level 2 of Culshaw et al. (1997) (Fig. 1.5). The Kiosk domain preserves a pervasive straight northeast-striking, gently southeast-dipping gneissic foliation which is not observed elsewhere is the Central Gneiss Belt on a domain-scale. There is a well developed down-dip stretching lineation expressed as quartz or feldspar rods in quartzofeldspathic rocks (Fig. 2.3). High-resolution aeromagnetic (HRAM) geophysical surveys demonstrate that the Kiosk domain has distinctive geophysical properties with respect to the surrounding lithotectonic domains. This domain preserves regionally straight northeast-trending geophysical lineaments. This HRAM geophysical signature contrasts sharply to the chaotic geophysical signatures of the surrounding domains. First vertical derivatives of reduced-to-pole HRAM data are designed to produce maximum signal from the edges of geobodies, and the penetrative structural grain of the Kiosk domain can be observed in the first vertical derivative map (Fig. 2.4). This map shows the domain-wide extent of the distinctive northeast-trending fabric that characterises the Kiosk domain. This fabric is consistent with northwest-directed thrust imbrication of the CGB and tectonic transport of the Grenville Orogen toward its foreland. In contrast to the Kiosk domain, the surrounding lithotectonic domains do not preserve such a regionally extensive northeast-striking fabric, and have more chaotic HRAM patterns suggesting more locally variable structures (Fig. 2.4).

The North Tea Lake Shear Zone (NTLSZ) is a wide zone of high-grade, ductile, high-strain deformation separating the Kiosk domain from the underlying Bonfield domain (Davidson, 1986c). Structures within this shear zone follow the northeast-striking, gently southeast-dipping structural trend characteristic of the Kiosk domain. The principal lithology associated with this shear zone is a highly sheared meta-quartz-monzonite straight gneiss that contain straight mafic layers reworked parallel to foliation, and preserved migmatites. Within the NTLSZ, the North Tea Lake Mylonite Zone (NTLMZ),

is a narrow, relatively low-grade, brittle-ductile zone of normal-sense shear and upper-greenschist-facies mineral assemblages. This zone is characterised by black cryptocrystalline mylonites with K-feldspar porphyroclasts. These rocks are associated with amphibole-blastic migmatites and meta-quartz-monzonite straight gneisses interpreted as the protoliths of the NTLMZ (Ratcliffe, 2011).

The Kiosk domain was previously considered a relatively homogeneous block of gneisses and meta-plutonic rocks with no large-scale internal shear zones (e.g. Davidson and Morgan, 1981; Culshaw et al., 1983; Grant, 1987, 1988; Easton, 1992). Davidson (1986c) first proposed subdividing the Kiosk domain into informal north and south "belts" based on the presence of coronitic metagabbro. Dickin and McNutt (2003) proposed a roughly coincident division of the Kiosk domain along the ABT based on contrasting ca. 1400-1800 Ma Sm-Nd model ages to the south, and ca. 1800-2000 Ma model ages to the north. During field work for this study, a relatively narrow high-strain shear zone was discovered in the central Kiosk domain that coincides with both the lithological division of Davidson (1986c) and the proposed ABT of Dickin and McNutt (2003). This shear zone was termed the "Big Bob Lake shear zone" (Fig. 2.1). The horizontal gradient of the Bouguer-corrected airborne gravity residual anomaly data, designed to highlight lateral density changes of geobodies, highlights the domain-wide scale of this shear zone (Fig. 2.5). In the western side of the Kiosk domain, the BBLSZ separates grey meta-quartz-monzonite orthogneisses separated by pink and dark grey layered paragneisses in the hangingwall from similar rocks in the footwall.

The Kiosk domain is underlain by undifferentiated and interlayered pink to cream meta-quartz-monzonite straight gneisses, which range from monzo-granite, quartz-monzodiorite, and mafic orthogneisses that form layers or enclaves in quartzofeldspathic orthogneiss. In the western Kiosk domain, orthogneiss is interlayered with pink K-feldspar-sillimanite paragneisses, garnet-K-feldspar straight paragneiss with or without abundant sillimanite, and quartzites. Orthogneisses typically have granulite-facies mineral assemblages that are variably retrogressed to upper-amphibolite-facies assemblages. Granulite-facies assemblages in mafic layers in monzonite orthogneiss have been retrogressed to amphibole-biotite amphibolite-facies assemblages in parts of the northern Kiosk domain. In larger

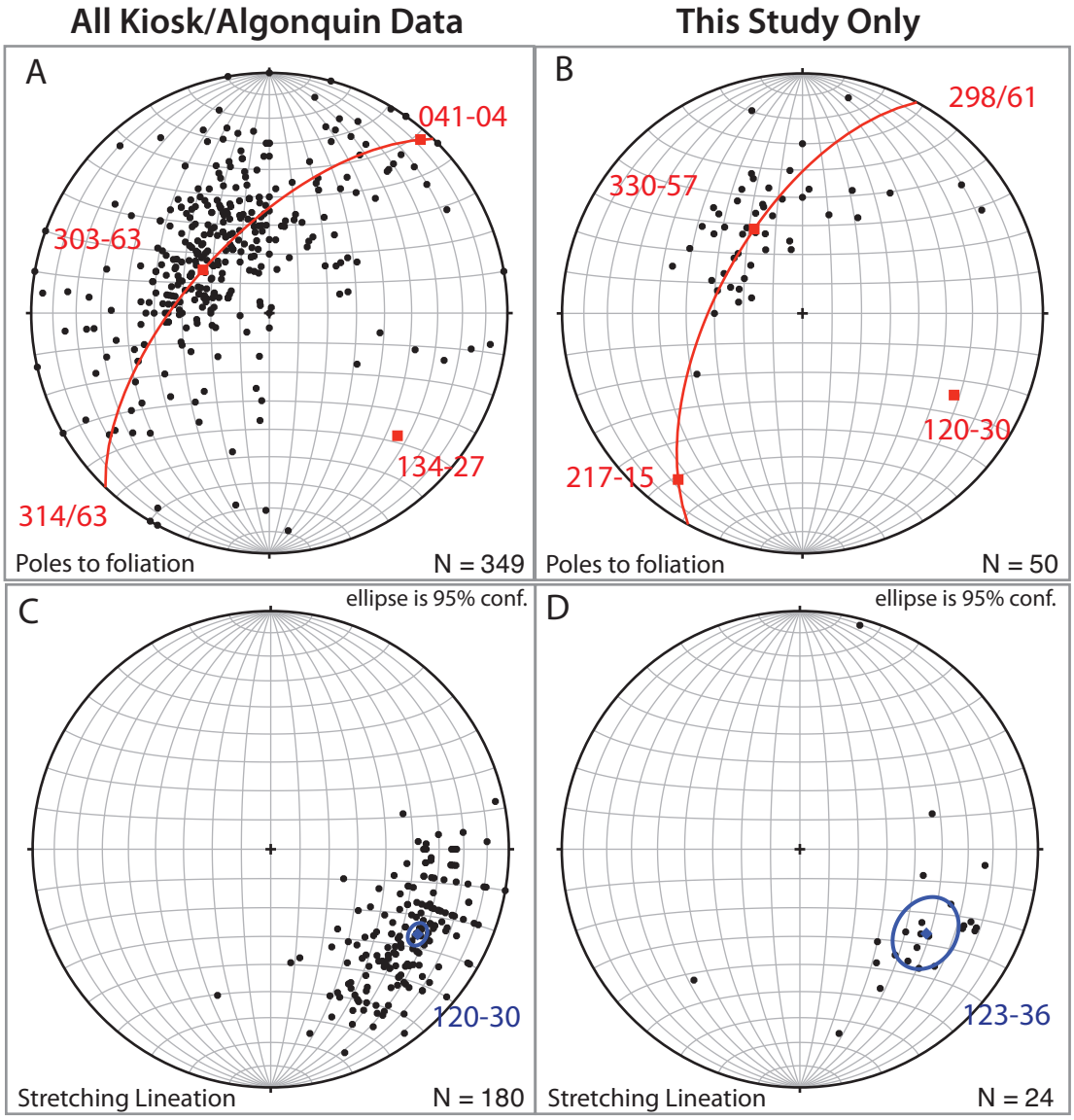


Figure 2.3: Lower-hemisphere Schmidt nets for the Kiosk and Algonquin domains. A) Poles to foliation for all data from the Kiosk and Algonquin domains from 2007, 2008, 2009, and 2010 field seasons (*Courtesy N. Culshaw*). Red values are the conical best-fit eigenvectors (±7°at 95% confidence). Note that though data in this plot are somewhat scattered, there is a central cluster around the 300-63 axis. B) Poles to foliation in the Kiosk domain collected during this study. Red values are the conical best-fit eigenvectors (±15°at 95% confidence). C) Lineations for all data through the Kiosk and Algonquin domains from 2007, 2008, 2009, and 2010 field seasons. Blue point is the mean vector, and blue ellipse is ±4°at 95% confidence. D) Lineation data from the Kiosk domain collected during this study. Blue point is the mean vector, and blue ellipse is ±12°at 95% confidence. There is a strong correlation between the regional data compilation from Algonquin and Kiosk domains and those of this study, particularly the lineation direction mean vector. Note that throughout this thesis planar orientations are given as dip-direction/dip.

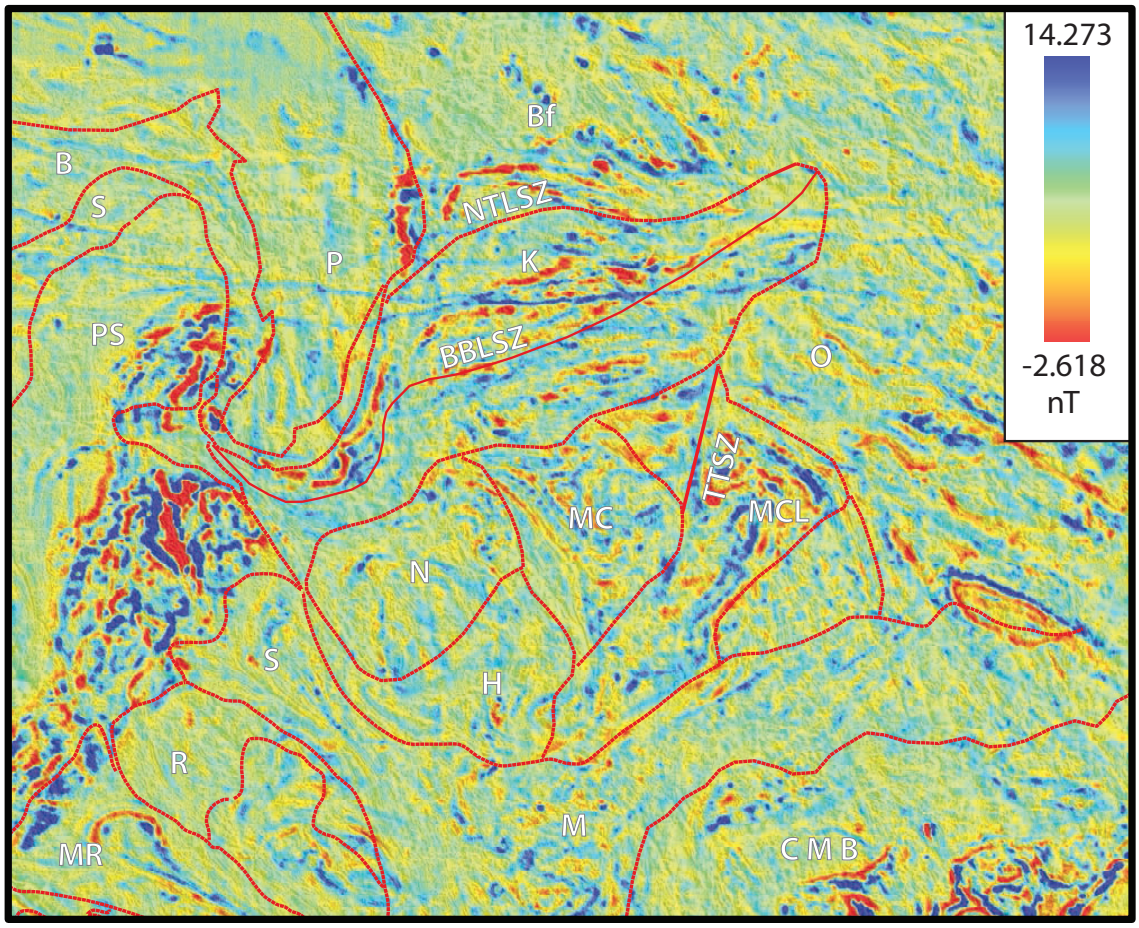


Figure 2.4: Map of the first vertical derivative of the HRAM data for the study area and surrounding lithotectonic domains. Note the strong northeast-trending geophysical lineaments prevalent throughout the Kiosk domain, as opposed to the more chaotic lineament pattern of the surrounding domains. HRAM data from Geological Survey of Canada (2011). Thin red lines represent domain boundaries after Culshaw et al. (1983); Davidson (1984); Culshaw et al. (1988); Davidson and van Breemen (1988); Culshaw et al. (1989, 1990)). For abbreviations see List of abbreviations used.

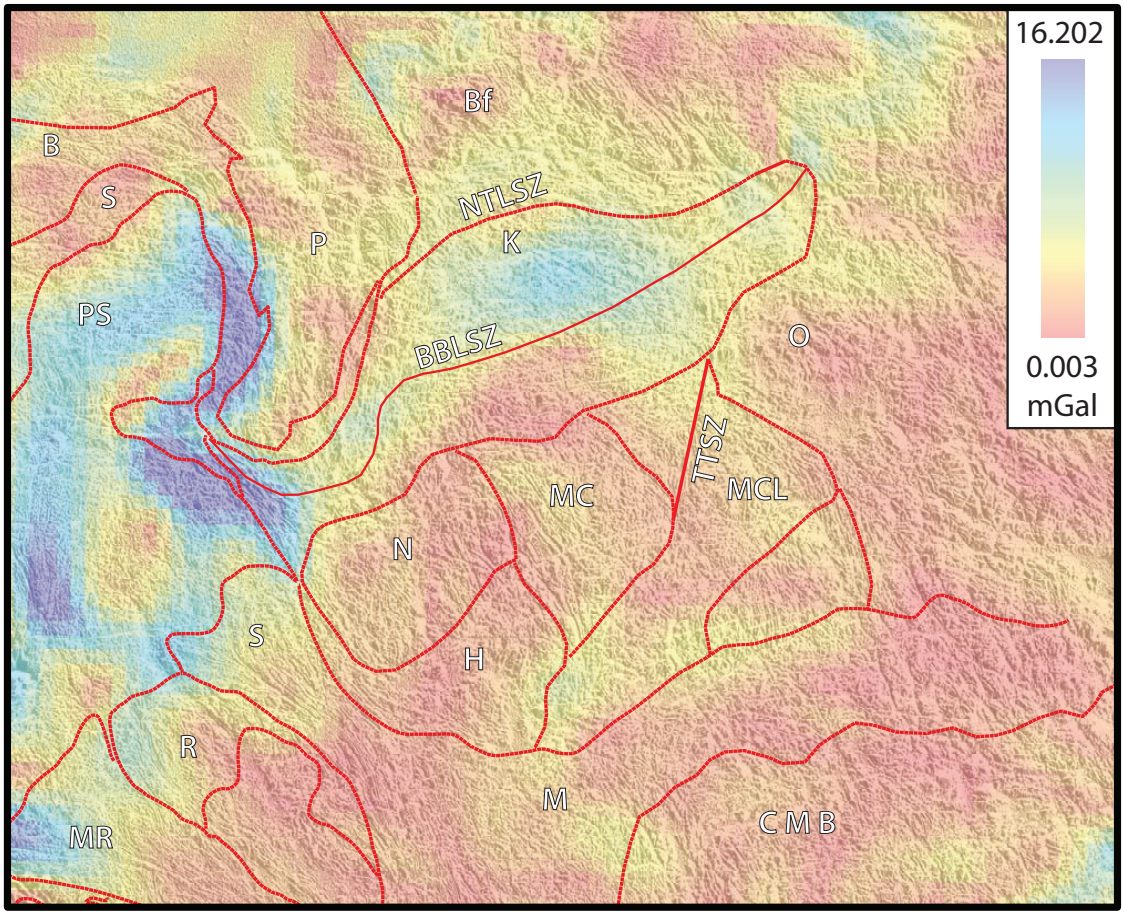


Figure 2.5: Map of the horizontal gradient of the airborne gravity data for the study area and surrounding lithotectonic domains. There is a appreciable difference in the gravitational potential between the northern and southern Kiosk domain. These "belts" of differing gravitational signature are separated by the BBLSZ, as discussed in the text. Note that the Algonquin domain has an overall very uniform gravitational signature, and that signature is similar to that of the southern Kiosk domain. Airborne gravity data from Geological Survey of Canada (2011). Thin red lines represent domain boundaries after Culshaw et al. (1983); Davidson (1984); Culshaw et al. (1988); Davidson and van Breemen (1988); Culshaw et al. (1989, 1990)). For abbreviations see List of abbreviations used.

mafic enclaves or thick mafic dykes where retrogression did not penetrate to the centre of the body granulite-facies assemblages are still preserved. Numerous monzo-granitic to granodioritic meta-plutonic bodies occur mostly in the southern portion of the Kiosk domain (Davidson, 1986c), with one previously unmapped creamy-pink granodioritic amphibole-bearing meta-plutonic body southeast of North Tea Lake that extends to north of Craig Lake (henceforth termed the "Craig Lake pluton," Fig. 2.2). Numerous centimetre- to metre-scale cross-cutting pegmatite dykes are present throughout the Kiosk domain, most commonly associated with shear boundaries.

The dominant lithology in the Kiosk domain is a garnet-amphibole meta-monzonite or meta-quartz-monzonite tectonite that is commonly migmatitic. In highly sheared rocks migmatitic texture has been reworked into a cream-coloured quartz-monzonite straight gneiss with granulite-facies mineral assemblages, composed of fine-grained variable width quartzofeldspathic and mafic bands (Fig. 2.6a and B). The quartzofeldspathic bands vary in colour from cream to creamy-brown to pale-pink on the scale of 1-2m or over tens of metres, making subdivision of this unit in the field exceedingly difficult. Consequently, this rock type has come to represent the whole of the Kiosk domain, often simply classified as a "composite metaplutonic mass" (e.g. Davidson, 1986c). Migmatites with pink to creamy-pink leucosome and dark garnet-rich melanosome are preserved in the interior of the Kiosk domain where they have not been reworked by a high-strain shear zone. These rocks are flattened and well foliated, but not to the same extent as the shear zone equivalents. Migmatites are locally preserved as "rafts" or lenses within high-strain shear zones. Here it is possible to see the original chaotically folded and foliated migmatitic fabric reworked into the northeast-striking shear zone fabric (Fig. 2.7), clearly showing that the migmatitic fabric pre-dates the formation of the shear zone.

Numerous mafic bodies throughout the Kiosk domain range from centimetre-scale mafic layers in orthogneiss, mafic enclaves and lenses, mafic dykes that are several centimetres to over a metre wide and up to ten metres long, to large mafic bodies that are tens of metres wide and upwards of one hundred metres in mappable length. Whilst most of mafic layers are concordant with the host rocks, rare cross-cutting dykes cut

the foliation at low (8-10$^o$) or high (25-33$^o$) angles. Two sampled dykes show various degrees of retrogression to amphibolite-facies mineral assemblages. One preserved relict granulite-facies mineral assemblages with relict orthopyroxene, clinopyroxene, and hastingsite-hornblende. The other is a biotite-free upper-amphibolite-facies assemblage with co-existing pargasitic-hornblende and clinopyroxene (Fig. 2.8). A very large and previously unrecognised coronitic olivine metagabbro that is several tens of metres in width with an unknown strike length was mapped in the hangingwall of the BBLSZ. This is partly amphibolized and intruded by white K-feldspar-rich pegmatites along its margins, but preserves "fresh" rock toward the centre (Fig. 2.9). In their reconnaissance study of the Kiosk domain, Davidson (1986c) focussed largely on the distribution of coronitic olivine metagabbros, and proposed subdividing the Kiosk domain into two informal belts based on the presence of coronitic metagabbro in the "southern Kiosk belt", and its absence in the "north Kiosk belt." This subdivision of the Kiosk domain was not widely used by subsequent authors, and the Kiosk domain is usually discussed as a whole.

## 2.5 The Algonquin domain

The Algonquin domain comprises the structurally highest section of structural level 2 of Culshaw et al. (1997) (Fig. 1.5). Subdomains of the Algonquin domain include the Novar, Huntsville, McCraney, and McLintock (Davidson, 1986c) subdomains (Fig. 2.1). These subdomains comprise strongly foliated, fine grained, granulite- to upper-amphibolite-facies orthogneisses and paragneisses (Culshaw et al., 1983; Davidson, 1986b; Timmermann, 1998), separated by ductile shear zones interpreted to have formed during northwest-directed thrusting or southeast-directed extension (Davidson et al., 1982; Culshaw et al., 1983; Nadeau, 1990). The sense of shear along subdomain boundaries in the southern Algonquin domain remains poorly constrained. However, study of the individual subdomains of the southern Algonquin domain was not the primary aim of this study. For further detailed information of these subdomains, the reader is referred to Nadeau (1990) andTimmermann (1998).

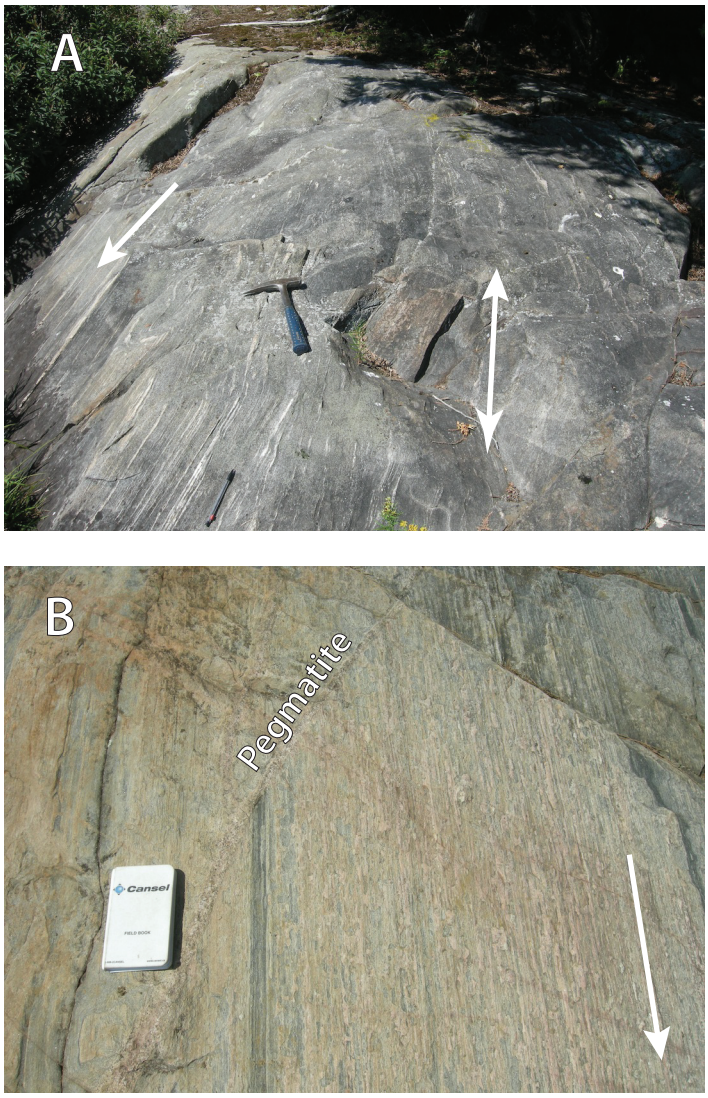


Figure 2.6: Outcrop photos of the representative Kiosk domain orthogneisses. A) Grey meta-quartz-monzodiorite orthogneiss. Double arrow is the strike of foliation, and single arrow is the stretching lineation direction (hammer for scale; UTM x: 0654245, y: 5090487). B) creamy-pink meta-quartz-monzonite straight gneiss. There is a very well developed down-dip lineation (white arrow), and a highly straightened gneissic layering can be seen by the oblique cut of the outcrop through foliation (book for scale; UTM x: 0653719, y: 5089795). Note the outcrop is cut by late-stage granitic pegmatites.

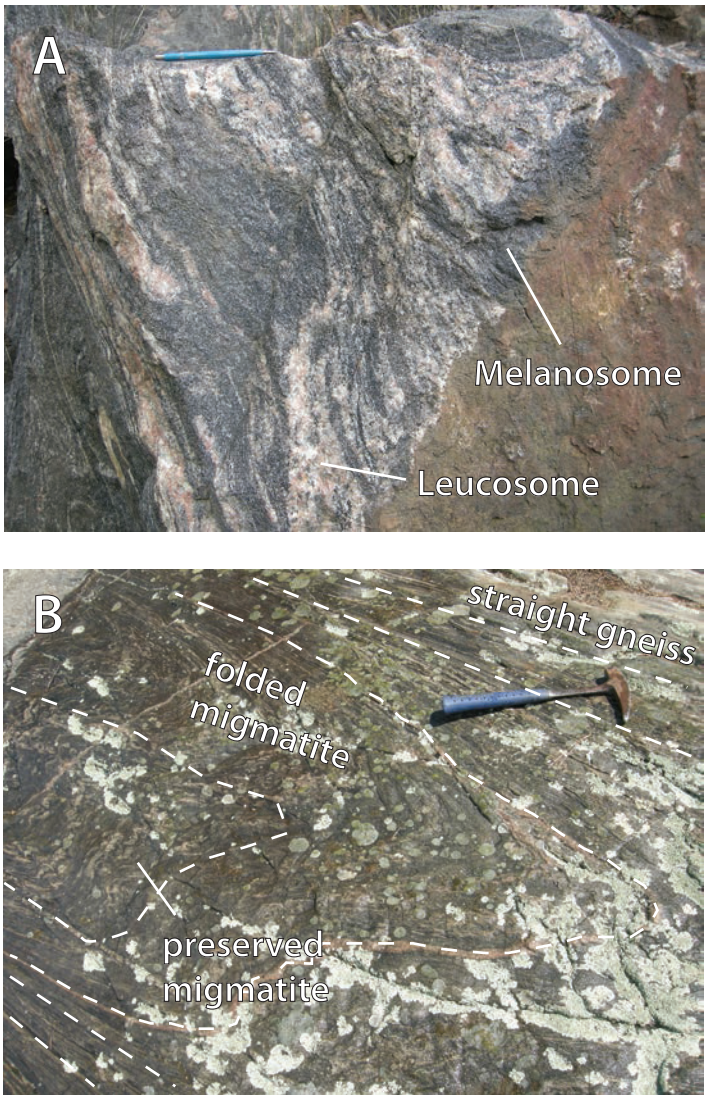


Figure 2.7: Outcrop photos of Kiosk domain migmatites. A) Migmatite from the interior Kiosk domain preserving relatively chaotic migmatitic fabric. Leucosome is K-feldspar-rich and melanosome is plagioclase-garnet-rich (pencil for scale; UTM x: 0625117, y: 5051546) . B) Preserved "raft" of migmatite being reworked parallel to the fabric of the NTLSZ. A central block of preserved migmatite preserves a relatively randomly oriented migmatitic fabric, this is surrounded by a sheath of folded migmatite with a moderately developed foliation, and finally the folded migmatite is completely reworked into straight gneiss, with a strongly developed foliation and down-dip stretching lineation (hammer for scale; UTM x: 0655602, y: 5092871).

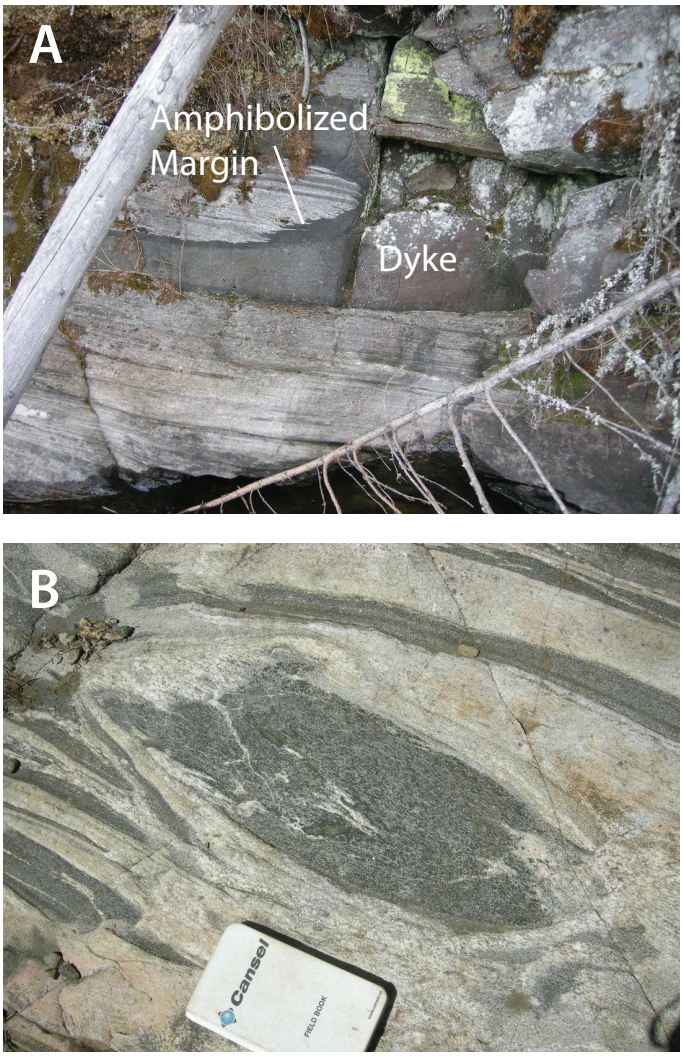


Figure 2.8: Outcrop photos of representative morphologies of mafic bodies in the Kiosk domain. A) Mafic dyke north of the NTLSZ that cross-cuts gneissic foliation (dead tree for scale; UTM x: 0647135, y: 5089126). Note the biotite-amphibole-rich amphibolized margins where the dyke contacts the host orthogneiss. B) Mafic enclave and straightened mafic layers in metatonalite orthogneiss from the interior of the Kiosk domain (book for scale; UTM x: 651141, y: 5069457).

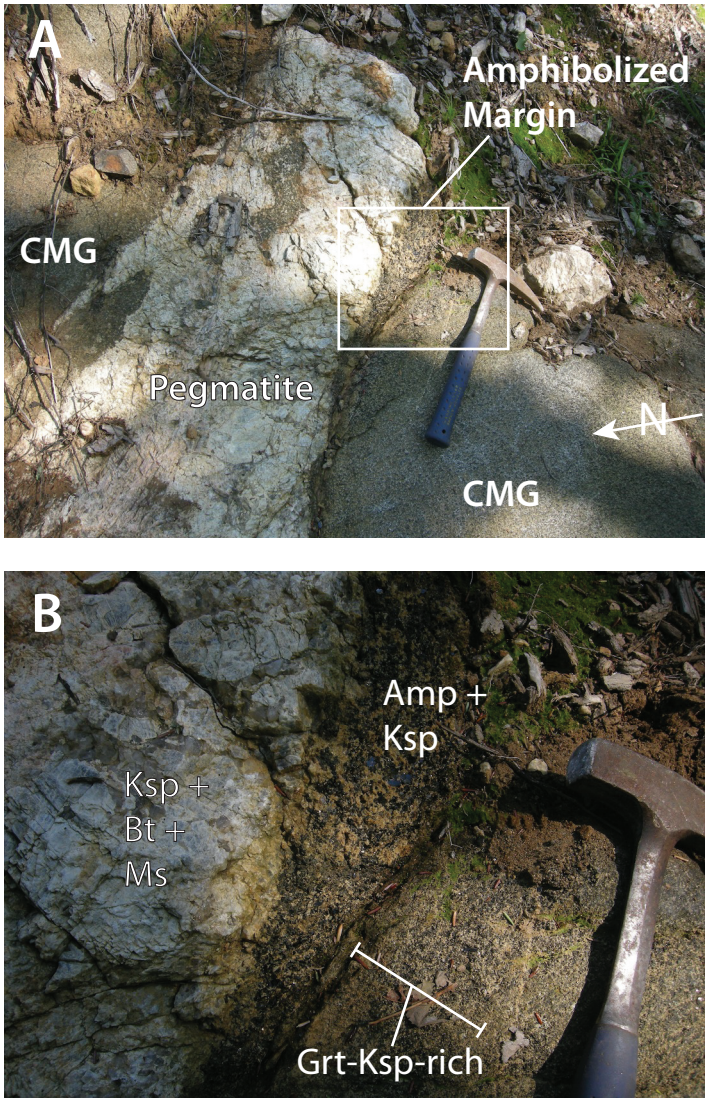


Figure 2.9: Outcrop photos of previously unmapped large coronitic metagabbro from the hangingwall of the BBLSZ. A) Photo of a large K-feldspar-rich pegmatite cutting the coronitic metagabbro, and the amphibolized margin in the contact between these units (white box is field of view of (B), hammer for scale). B) Close up photo of the pegmatite intrusion and amphibolized margin of the coronitic metagabbro. Note the amphibole-K-feldspar-rich amphibolized boundary, and also a layer of garnet-K-feldspar-rich metasomatised coronitic metagabbro (hammer for scale; UTM x: 0651370, y: 5068532).

**The McLintock subdomain** The McLintock subdomain is of particular importance to this study, as a previously unreported geochronology sample is discussed in the following chapters. Timmermann (1998) (Fig. 2.1) noted that the McLintock subdomain comprises dominantly quartzofeldspathic granulites, garnet-rich gneisses and granulites, pink to cream orthogneisses and paragneisses, pelitic to semi-pelitic rocks, pink megacrystic granitoids, and white to grey leucocratic granites (Fig. 2.10). Bounding shear zone rocks were commonly derived from migmatitic orthogneisses and migmatites. She interpreted most of the rocks in the McLintock subdomain as thoroughly retrogressed granulites that now exhibit amphibolite-facies mineral assemblages. Timmermann (1998) documented numerous mafic bodies throughout the McLintock subdomain, especially associated with internal and boundary shear zones. The mafic bodies range up to 10-15m across and include mafic granulites, coronitic metagabbros, and amphibolites that form attenuated bands, disrupted layers, boudins or enclaves. Whilst most of the mafic rocks are concordant, mafic layers rarely cut the foliation at shallow angles (ca. $10^o$). These were interpreted as dykes intruded prior to the latest Grenvillian deformation and metamorphism. Most of the mafic bodies exhibit a granulite-facies mineralogy overprinted by an amphibole-biotite-rich mineral assemblage at their margins, within variably retrogressed granulite-facies host rocks.

## 2.6 Summary

The Kiosk domain comprises late-Paleoproterozoic and Mesoproterozoic orthogneisses and paragneisses that have been pervasively deformed, with a well-developed, northeast-striking, gently southeast-dipping gneissic foliation. Most of the domain is composed of pale-cream to creamy brown-sugar granulite-facies meta-quartz-monzonite that is variably retrogressed. Numerous mafic bodies in the Kiosk domain are reworked parallel to gneissic foliation, but a few dykes exhibit cross cutting relationships. The Bonfield Batholith rocks in the southern Bonfield domain are moderately foliated upper-amphibolite-facies creamy-brown/green orthogneisses that show evidence of only one deformation phase in the field. No new field work in the Algonquin domain was completed in this study, instead existing data from a cross-cutting amphibolite dyke were incorporated into this study (N. Culshaw, *unpub. data*).

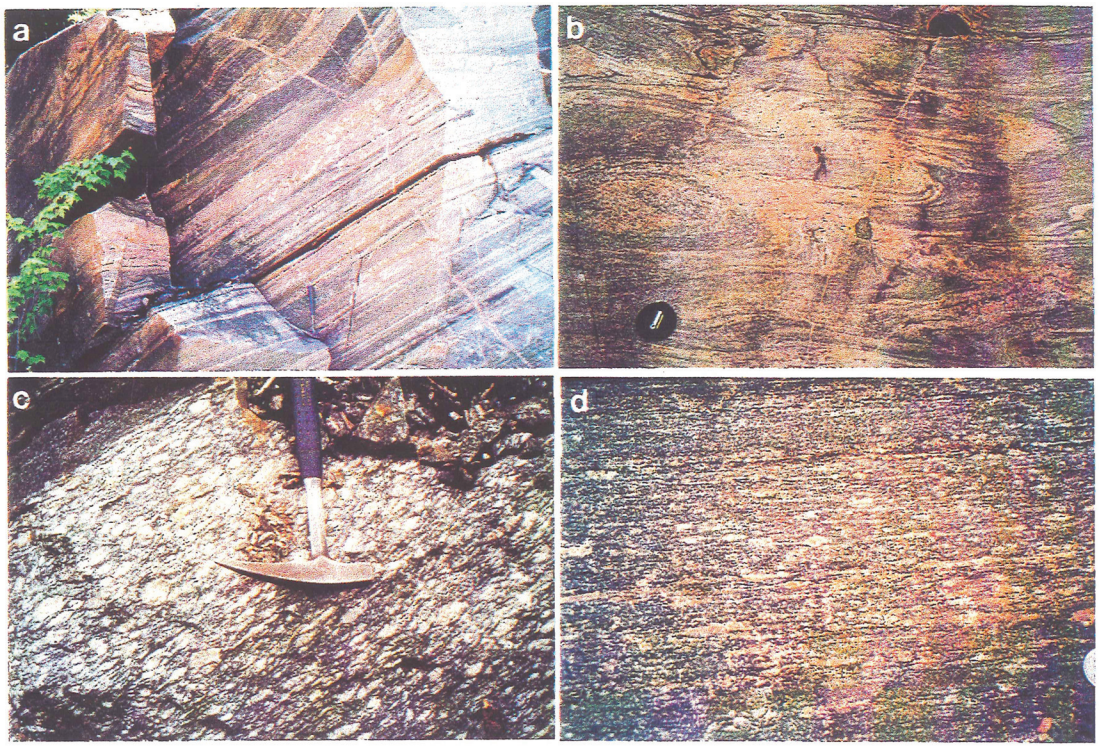


Figure 2.10: Outcrop photos of representative gneisses from the McLintock subdomain from Timmermann (1998). Caption from Timmermann (1998) is as follows: a) Strongly foliated and layered, amphibolite facies migmatitic orthogneiss with isoclinally folded leucosomes and mafic layers, MCL-3 gneiss association. b) Amphibolite facies migmatitic orthogneiss with two generation of leucosomes. c) Megacrystic granitoid with recrystallized feldspar augen. d) Progressive recrystallization and deformation of megacrystic granitoid towards the top of picture.

**Sample selection methodology** Samples collected during field work, and existing samples from previous field seasons (N. Culshaw, *unpub. data*), were selected for analysis in an effort to target the Grenvillian deformation and metamorphic history of major shear zones in the Kiosk domain, and to give a broad understanding of the geochronology of the study area. Samples selected for geochronology were polymetamorphic orthogneisses and paragneisses from inside and in the footwalls of the NTLSZ and the BBLSZ, a mafic enclave from the centre of the Kiosk domain, and a mafic dyke from the northern McLintock subdomain. Samples selected for thermochronology were orthogneisses from the Kiosk domain. These rocks were selected based on petrography of hornblende, optimizing the largest hornblende grains in rocks that contain as little biotite and K-feldspar as possible. Samples chosen for multi-equilibria thermobarometry were based on petrographic criteria: (i) mineral assemblages for which there are established cation exchange and net-transfer reactions; (ii) samples in which several reactions can be calculated; (iii) inferred textural equilibrium of the mineral assemblage; (iv) samples that were used in geochronology; and (v) samples that interpreted to have experienced only Grenvillian metamorphism.

# CHAPTER 3

# ZIRCON GEOCHRONOLOGY

## 3.1 Introduction

Zircon is a widely used chronometer for determination of the ages of igneous and metamorphic events in long-lived polyphase orogens. Aspects of the zircon age, texture, and trace element composition can help shed light on the tectonometamorphic evolution of the Bonfield, Kiosk, and Algonquin domains of the southwest Grenville Province.

The most geologically significant outcome of this analysis is the determination of the age of crystallization and subsequent metamorphic events in the study area. U-Pb dating has shown there is a fundamental difference in the ages of major igneous and metamorphic events of the Kiosk domain orthogneisses, and the gneissic Bonfield Batholith, a component of the Bonfield domain; the former being a polyphase orthogneiss-dominated lithotectonic domain, and the latter being a monocyclic igneous pluton. Zircon dating in this study has also shown that the Kiosk domain and the McLintock subdomain share a common metamorphic history. Linking these dates with textural and trace element chemistry allows a more robust determination of the age and nature of the major tectonic events enjoyed by the Algonquin terrane.

The Central Gneiss Belt has been the focus of geochronology studies for several decades, and the chronology of the major phases of metamorphism and deformation are well documented (e.g. Krogh and Davis, 1969, 1970b; Krogh et al., 1971; van Breemen and Hanmer, 1986; van Breemen et al., 1986; Krogh et al., 1988; van Breemen and Davidson, 1990;

Lumbers et al., 1991; Krogh, 1994; Mezger et al., 1993; Corrigan et al., 1994; Davidson and van Breemen, 1994; Ketchum et al., 1998; Corfu and Easton, 2001; Slagstad, 2003; Slagstad et al., 2004a,c; Marsh et al., 2012). From this work several large-scale tectonic events have been documented that have a direct bearing on the data presented herein: (i) ca. 1750-1600 Ma was a time of crustal formation on the Laurentian margin, that can be correlated with the Granite-Rhyolite Province in the mid-continent (Condie, 1986; Davidson, 1986c; van Breemen and Davidson, 1988; Culshaw et al., 2000; Rivers and Corrigan, 2000); (ii) the Pinwarian orogeny (ca. 1470-1340 Ma), was a time of widespread granulite-grade metamorphism and plutonism in the CGB (Krogh et al., 1996; Rivers, 1997; Wodicka et al., 2004; Slagstad et al., 2004a); (iii) the Elzevirian orogeny (ca. 1245-1220 Ma) is an accretionary orogeny throughout much of the Grenville orogen, and is contemporaneous with generation of bimodal plutonism in the CGB (Moore and Thompson, 1980; Lumbers et al., 1991; Carr et al., 2000; Easton and Ketchum, 2002) and; (iv) the Grenvillian orogeny has been separated into the Shawinigan (ca. 1190-1140 Ma), Ottawan (ca. 1080-1020 Ma), and Rigolet (ca. 1000-980 Ma) orogenic pulses. This was a time of crustal thickening and northwest-directed tectonic transport associated with building of the Grenville Orogen, and later, extensional reactivation of thrust-sense shear zones during orogen-scale extension and exhumation (Rivers et al., 1989; Krogh, 1994; Krogh et al., 1996; Culshaw and Dostal, 1997; Culshaw et al., 1997; Rivers, 1997; Carr et al., 2000; Rivers and Corrigan, 2000; Gower and Krogh, 2002; Hynes and Rivers, 2010).

In this chapter, the U-Pb zircon data from samples analysed in this study (prefixed JF10), as well as two additional samples (prefixed CA; N. Culshaw *unpub. data*) are discussed. Grain-scale analysis locations, U-Pb isotopic data, and trace-element data are given in Appendix A.

## 3.2 Method

Zircons were separated from crushed samples and prepared for analysis at the crystal isolation facilities at Dalhousie University and the University of Maine. Mechanical sample processing to separate the dense crystal fraction was done by standard methods using a jaw crusher, disc mill, Wilfley table, heavy liquid separation (sodium polytungstate and

methylene iodide), and finally magnetic separation. Individual zircon grains were than picked by hand and mounted in epoxy, polished by hand to an even surface, and gold coated for analysis. Electron backscatter (BSE) and cathodoluminescence (CL) images were taken prior to analysis to identify inclusions, imperfections, crystal texture, and compositional and growth zoning patterns. Grains that were heavily fractured or metamict were not chosen for analysis. Radiogenic U-Pb isotope and oxide data, as well as REE and other trace element data, were collected concurrently using the SHRIMP-RG facility at Stanford University (e.g: Mazdab and Wooden (2006)).

The U and Pb isotopic values were corrected for instrument element fractionation using the R33 zircon standard (419$\pm$1 Ma; Black et al. (2004)) and trace elements were calibrated using the MAD zircon standard. Measured concentrations of Pb were also corrected automatically for common lead ($^{204}$Pb) for each measurement, and have a $\leq$1% correction. Output data were processed and plotted using the Squid (Ludwig, 2001) and Isoplot (Ludwig, 2003) programs. Problematic data resulting from poor analyses, or mixing of textural or age domains within the crystal, were omitted from statistical age calculation.

Rare-earth element depletion or enrichment for spot analyses is reported relative to the preferred average Chondrite REE concentrations of Korotev (1996). This REE normalization procedure builds on the normalization procedure of Byonton (1984), and multiplies the average chondrite values of Anders and Grevesse (1989) by a factor of 1.3596. This leads to a Sm normalization factor of 2.0 and maintains consistency with older data sets.

The europium anomaly value Eu/Eu* was calculated from the following relationship:

$$\frac{Eu}{Eu*} = \frac{Eu_m}{Sm_m^{1/2} \cdot Gd_m^{1/2}} \tag{3.1}$$

Similarly, the cerium anomaly value Ce/Ce* was calculated from the following relationship:

$$\frac{Ce}{Ce*} = \frac{Ce_m}{La_m^{1/2} \cdot Pr_m^{1/2}} \tag{3.2}$$

where the subscript *m* in these equations denotes a measured quantity.

## 3.3 Sample description

This section presents outcrop, petrographic, and crystal morphology descriptions of the samples prepared for zircon analysis. Petrography is essential in ascertaining where zircon dominantly occurs in the rock, and what possible phases may have been in chemical equilibrium with zircon. The texture of zircon grains as seen in BSE and CL imagery is a powerful tool to resolve internal zoning and provide insight into crystal growth. Characteristic textures of zircons can help distinguish between igneous crystallization or recrystallization/resorption of the zircon during metamorphism. The reader is directed to Corfu et al. (2003) for a petrographic atlas and exhaustive discussion of zircon texture and morphology. A map showing the location of samples is presented in Figure 3.1.

Unpublished zircon data collected in 2010 by J. Marsh and N. Culshaw from two samples are reported here for the first time, sample CA109 is form the Kiosk domain and sample CA17 is from the McLintock subdomain (N. Culshaw, *unpub. data*). These samples were analysed at the same SHRIMP-RG facility at Stanford University, with the same analytical protocol as other samples from this study.

### *3.3.1 Bonfield Batholith*

Outcrops along the north shore and northeast arm of North Tea Lake comprise part of the Bonfield pluton in the Bonfield domain that was affected by penetrative deformation in the footwall of the NTLSZ. Zircons from one sample of this rock (JF10-48) were extracted and analysed in this study.

In outcrop, this location largely consists of granodioritic orthogneiss with centimetre-scale amphibole-pyroxene-rich ribbons and layers. There is a moderate-to-well developed L-S fabric defining the foliation orientation of 195/35, and a weakly developed stretching

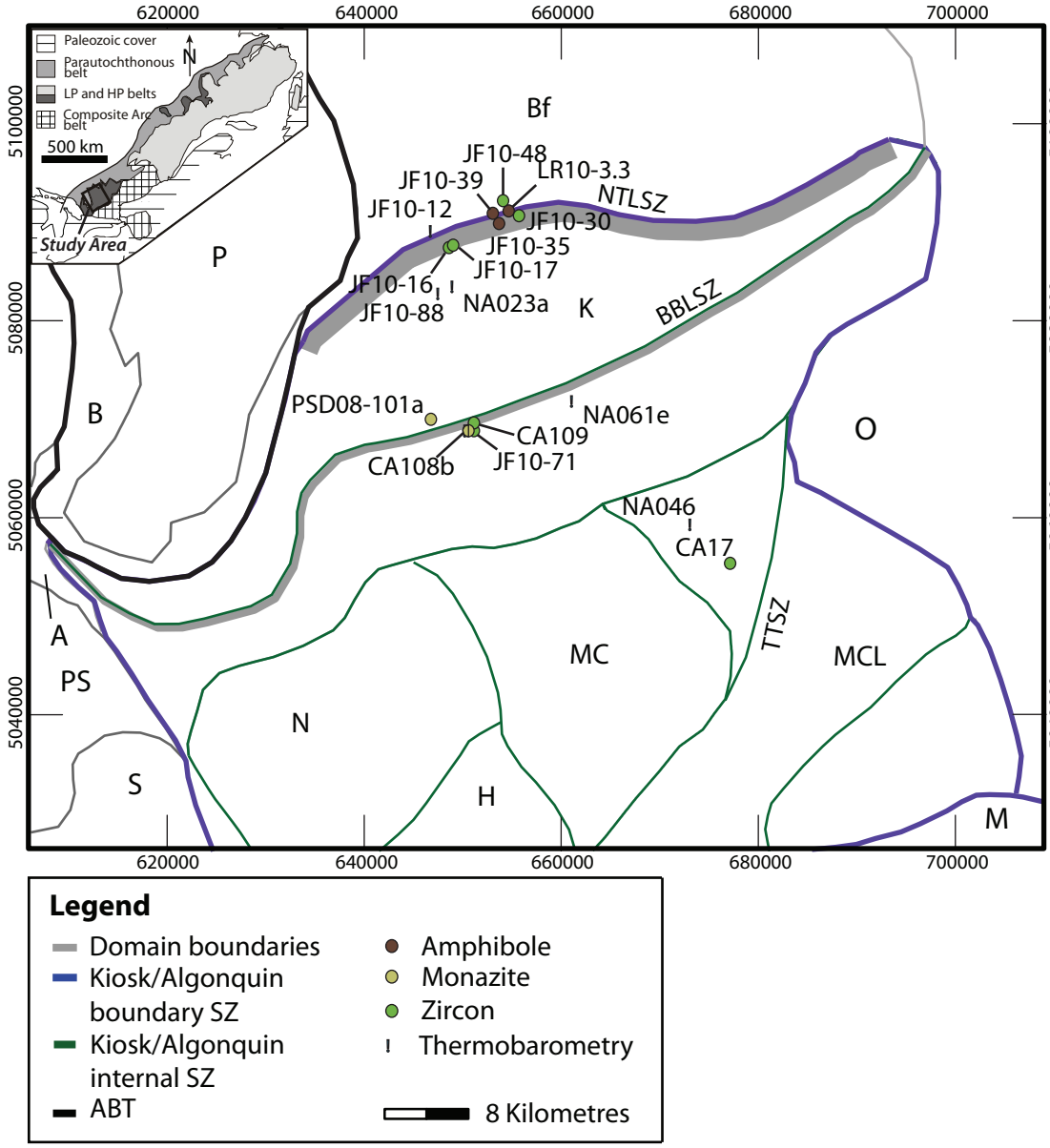


Figure 3.1: Location map of geochronology, thermochronology, and thermobarometry samples evaluated in this study. The boundary shear zones of the Kiosk and Algonquin domains are indicated in blue. Shear zones that internally imbricate the Kiosk and Algonquin domains are indicated in green. The wide deformation zones of the NTLSZ and BBLSZ are indicated schematically by thick grey lines. ABT from Ketchum and Davidson (2000). Domain boundaries after Culshaw et al. (1983); Davidson (1986c). Geology from Ontario Geological Survey (1991) Inset map (modified from Foster, 2005). For abbreviations see List of abbreviations used.

lineation ($L_S$) 150-33 (Fig. 3.2a). The orientation of this fabric is relatively consistent throughout the outcrops visited along North Tea Lake.

This suite of orthogneisses has a very consistent mineralogy in thin-section and is composed of Pl - Ksp - Qtz - Grt - Amp - Opx $\pm$ Bt $\pm$ Ru $\pm$ Ilm. Mafic minerals form discrete compositional bands separated by thick quartz-feldspar-rich bands. The sample shows evidence of recrystallization and annealing in the form of straight grain boundaries between most phases (especially plagioclase, garnet and quartz), triple points, and grain boundary migration in large quartz ribbons (Figs. 3.2b, c). Prismatic zircons large enough to be seen in thin-section are associated with mafic bands (Figs. 3.2d, e), that also contain rare, small, relict orthopyroxene. It is unclear if orthopyroxene is being replaced by amphibole. Where these phases occur together the orthopyroxene grains are small individual grains or grain clusters next to larger amphibole grains, with no obvious reaction texture. Biotite is a minor phase in this rock, forming tips on amphibole grains.

### *3.3.2 Kiosk domain*

Zircons from two lithologies in the Kiosk domain were analysed in this study, from four orthogneiss samples (JF10-16, JF10-17, JF10-30, JF10-71), and one amphibolite sample (CA109). The orthogneiss samples are from the undifferentiated meta-quartz-monzonite orthogneiss that underlies most of the Kiosk domain. These samples share common field relations, mineralogy, and petrographic texture, so sample JF10-30 will be discussed here as representing the four meta-quartz-monzonite orthogneiss samples analysed.

**Kiosk domain orthogneiss** In outcrop and hand-sample scale Kiosk domain orthogneiss has a very well developed foliation defined by compositional banding of felsic and mafic minerals to form straight gneisses and LS tectonites (Fig. 3.3a). Average orientation of the foliation and stretching lineation of sample JF10-30 are 163/35 and 124-35, respectively (*cf.* Fig. 2.3).

The dominant mineralogy of the Kiosk domain gneiss is Pl - Qtz - Ksp - Amp - Grt - Bt $\pm$ Cpx $\pm$ Ilm $\pm$ Ru. Mafic and felsic minerals form thin well-developed compositional bands in thin-section, with small garnet porphyroblasts peppered throughout the

sample. These samples show widespread microstructural evidence of annealing. Quartz and feldspars tend to be relatively large, with little evidence of internal strain, straight crystal terminations, and commonly form triple points. Quartz grains exhibit grain boundary migration textures, subgrain formation, and granoblastic texture (Figs. 3.3b, c). Garnet grains throughout the rock are small and subhedral, and commonly form triple points with quartz and feldspar. A few large quartz grains still preserve internal strain textures (e.g. undulose extinction). Zircons in these samples are large and readily visible in standard transmitted light microscopy. They have a prismatic or acicular crystal habit and are concentrated at the interface of the felsic leucosome with the garnet-rich melanosome (Figs. 3.3d and e), but can be found throughout the sample. Biotite occurs as a minor phase in amphibole-clinopyroxene-rich layers, or replacing amphibole grains (Figs. 3.3b, c).

**Amphibolite enclave** Sample CA109 is an amphibolite enclave cut by K-feldspar-plagioclase-rich leucosome from the central Kiosk domain (Fig. 3.1). Zircons were separated from the amphibolite portion only. The dominant mineralogy of the amphibolite is Amp - Pl - Grt - Fe-Ti Oxide $\pm$ Rtl $\pm$ Bt $\pm$ Qtz. Separating the amphibolite from the leucosome is a Bt + Ksp-rich transition zone (Fig. 3.4). The rock has been recrystallized and annealed, and all phases typically display straight grain boundaries, with triple points between feldspar and quartz in the leucosome, and between amphibole and plagioclase in the amphibolite. In the biotite-rich transition zone, amphibole and biotite occur together, but no obvious replacement texture was observed. Zircon could not be seen in thin-section.

### *3.3.3 McLintock subdomain*

**Amphibolite dyke** Sample CA17 is an amphibolite dyke that cross-cuts the foliation of the host orthogneiss (Figs. 3.1, 3.5a). This dyke cross-cuts foliation outside the TTSZ, and becomes folded within the shear zone. The dyke is a dark, very fine-grained amphibolite with no internal structure visible in hand-sample scale. There is a weak foliation defined by alignment of the long axis of elongate amphibole grains (Fig. 3.5b, c). The mineralogy is is Amp - Pl - Grt - Cpx - Qtz $\pm$ Fe-Ti Oxide $\pm$ Scp. The rock has a very well annealed texture with straight grain boundaries, and triple-points between most

phases in the rock. There are very few signs of earlier, high-strain conditions, and only the largest quartz grains still preserve undulose extinction. Few zircons grains were visible in thin-section (Fig. 3.5c, d).

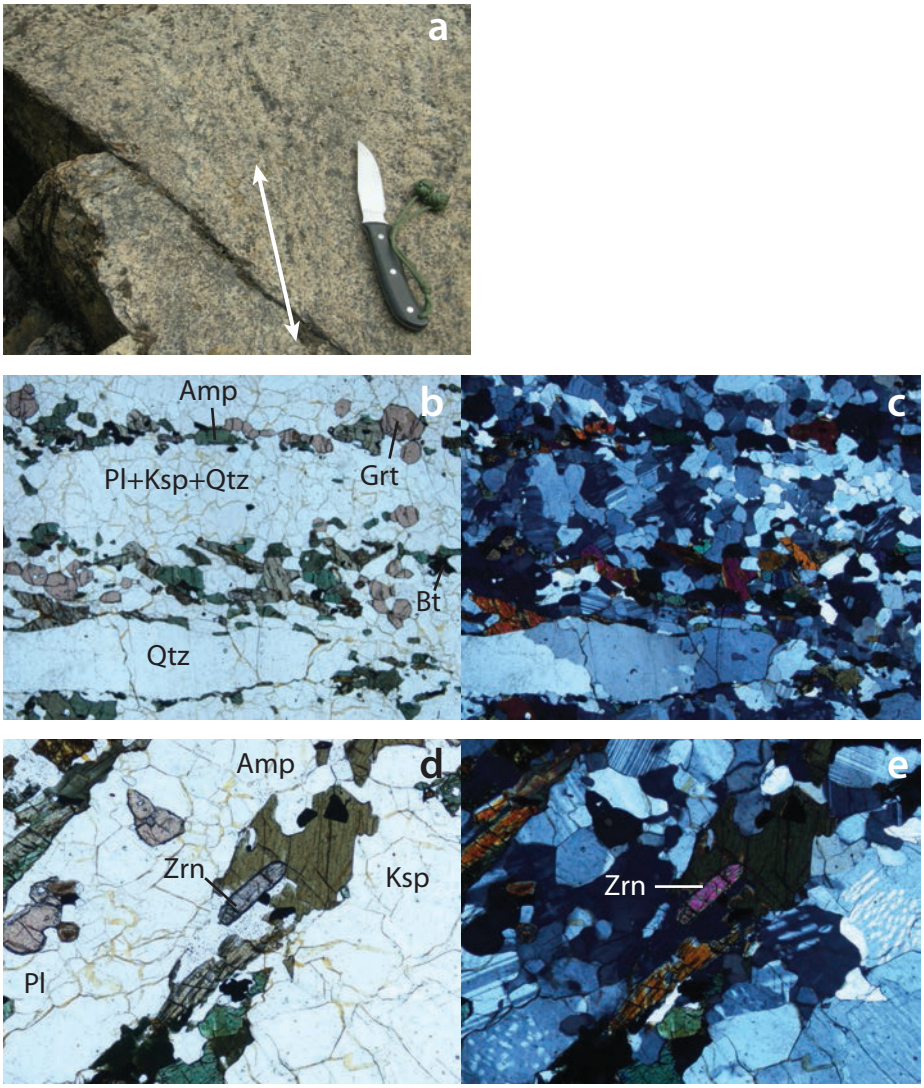


Figure 3.2: Outcrop picture and photomicrographs for sample JF10-48 (UTM x: 0654145, y: 5092096). a) Outcrop picture of the moderately foliated gneissic Bonfield Batholith (white arrow; knife for scale). Photomicrographs showing moderate foliation defined by alignment of mafic minerals and annealed quartz ribbons ( b) PPL, c) XPL; FOV = 6.25 mm). Note the well recrystallized texture, straight grain boundaries and numerous triple points. Zircons visible in thin-section typically occur in, or close to mafic bands ( d) PPL, e) XPL; FOV = 2.5 mm). Large elongate zircons are typically rotated parallel to foliation in this rock suggesting zircon pre-dates formation of foliation.

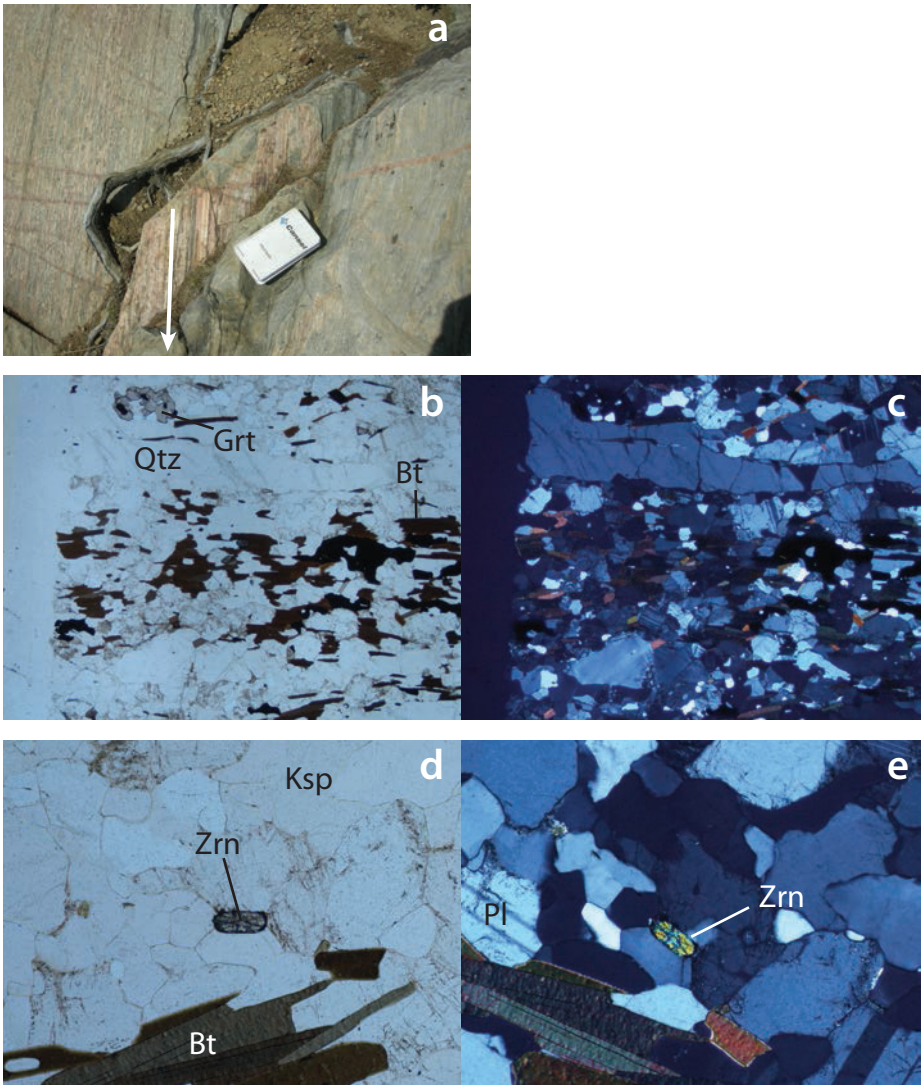


Figure 3.3: Outcrop picture and photomicrographs of typical Kiosk domain meta-quartz-monzonite orthogneiss (sample JF10-30; UTM x: 0655734, y: 5090500). a) Outcrop photo showing very well developed down-dip lineation surface (arrow), and gneissic layering (to the right of photo; notebook for scale). Typical textures of Kiosk domain orthogneiss in thin-section ( b) PPL, c) XPL; FOV = 6.25 mm). Amphibole is variably retrogressed in this rock and, in the case of JF10-30, can be completely replaced by biotite. Note the alignment if elongate biotite and quartz ribbons that define the foliation. Felsic layers have a fine-grained recrystallized texture with straight grain boundaries, relict bulging textures, and annealed quarts grains. Note the large zircon grain ( d) PPL, e) XPL; FOV = 2.5 mm).

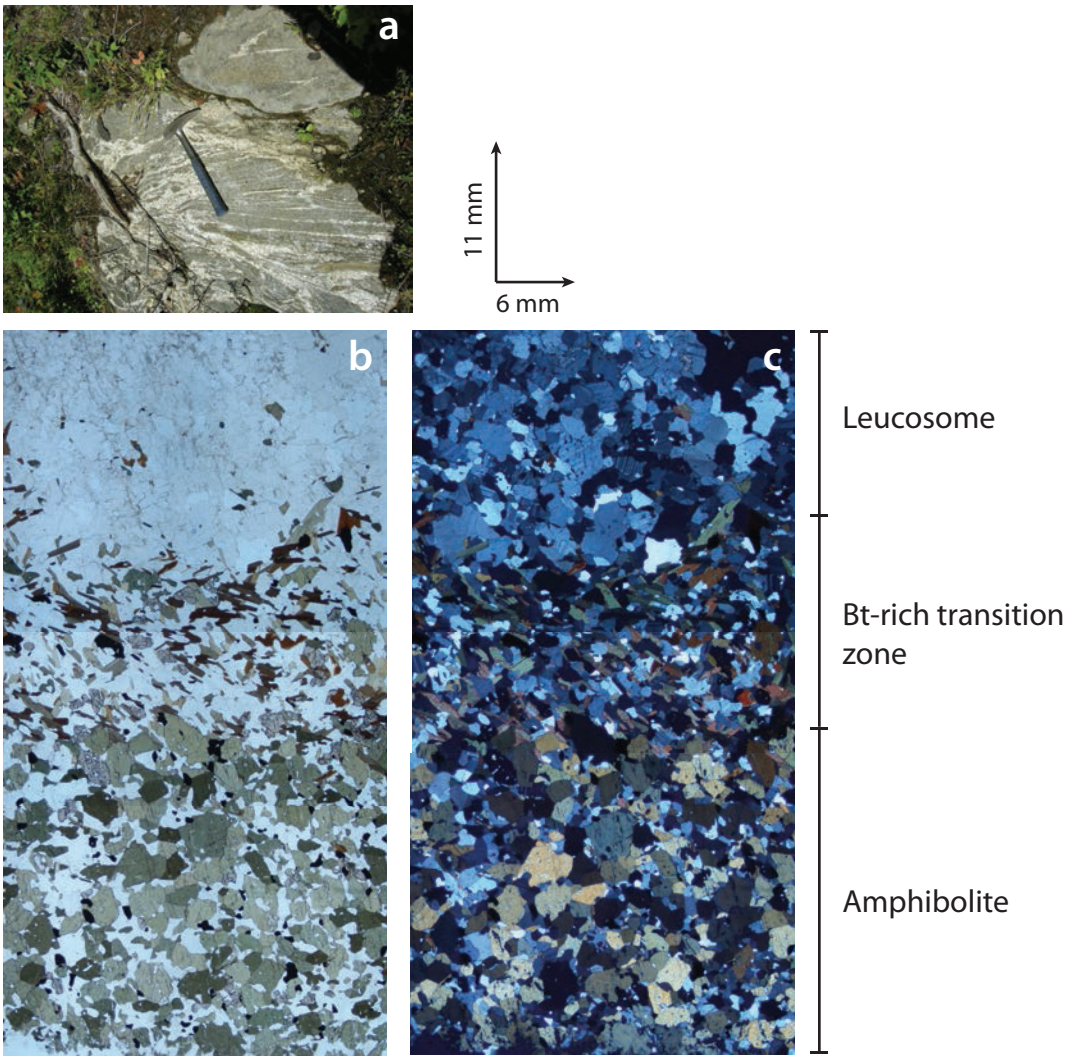


Figure 3.4: Outcrop picture and photomicrographs of Kiosk domain amphibolite enclave sample (sample CA109; UTM x: 651141, y: 5069457). a) Outcrop photo showing a large amphibolite enclave cut by K-feldspar-rich leucosome (hammer for scale). Photomicrographs showing gradational texture from amphibolite to leucosome ( b) PPL, c) XPL; FOV = approximately 6 x 11 mm). Note the biotite-rich transition zone, and infiltration of K-feldspar from the leucosome into the amphibolite.

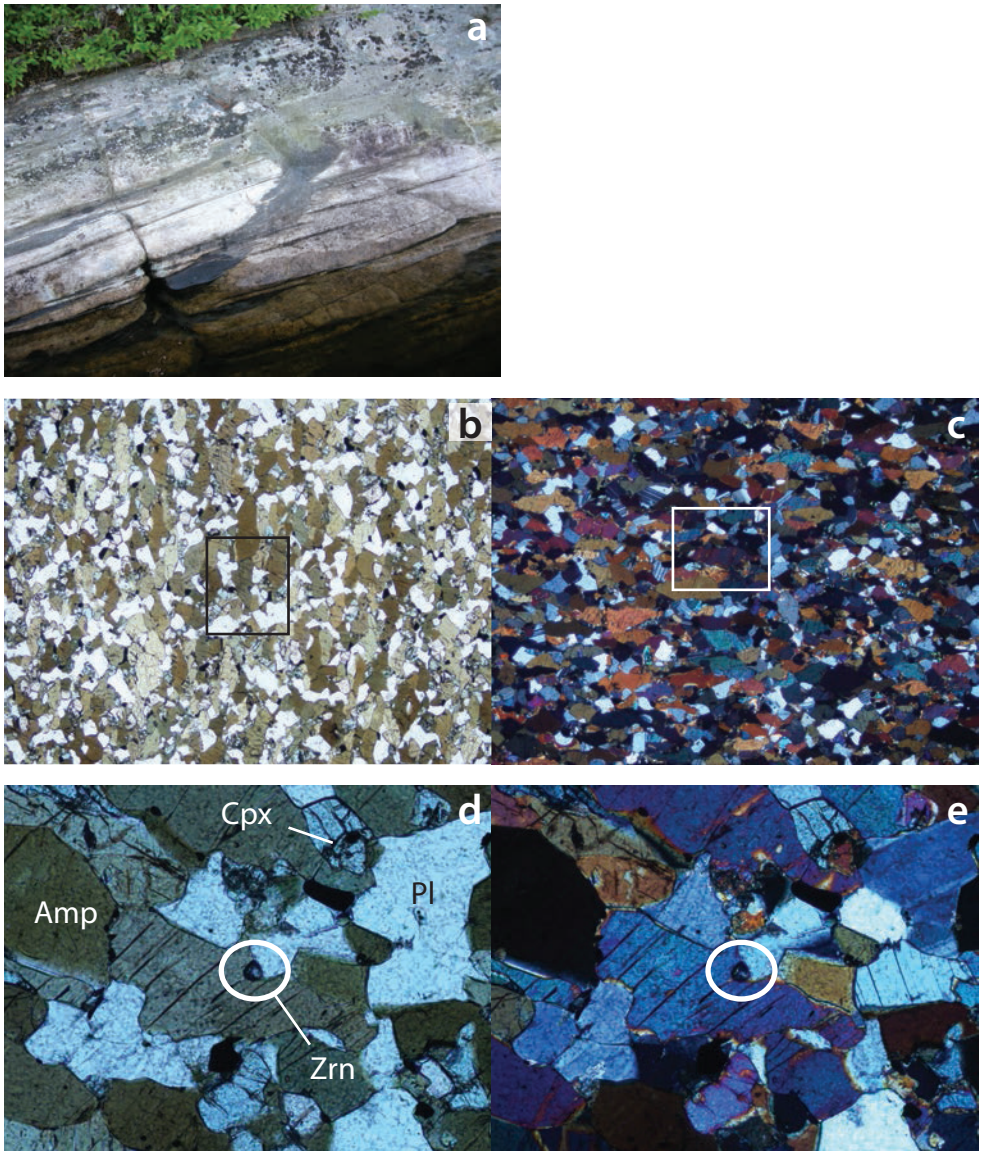


Figure 3.5: Outcrop picture and photomicrographs of McLintock subdomain amphibolite dyke (sample CA17; UTM x: 677193, y: 5055223). a) Outcrop photo showing the cross-cutting relationship of the dyke to the host orthogneiss. In thin-section this rock is dominantly large interlocking amphibole grains ( b) PPL, c) XPL; FOV = 6.25 mm; box shows area of photomicrographs d) and e). Rare zircon grains seen in thin-section are usually ovoid (circle; d) PPL, e) XPL; FOV = 2.5 mm).

## 3.4 Zircon morphology and analytical results

This section presents the crystal morphologies and SHRIMP-RG analytical results for zircons in the Bonfield domain, Kiosk domains, and the McLintock subdomain of the Algonquin domain. Crystal morphologies can provide a useful framework for subdividing the age populations resulting from chemical analyses, as well as provide insight into the growth history of the grain. Another powerful tool to provide insight into zircon petrogenesis are the REE profiles and Th/U ratios. Igneous and metamorphic zircons have characteristic Th/U ratios of approximately 0.5 and 0.07, respectively. These are useful "guidelines" but are not completely diagnostic of metamorphic versus igneous zircon.

**Preferred age** The weighted mean age (henceforth simply "weighted mean") is the preferred statistic for reporting isotopic ages in this study, with the exception of sample CA109, as discussed in section 3.4.2. The advantage of using the weighted mean is that the user can incorporate the internal $2\sigma$ analytical error estimate for the standard analysis with that of the unknown sample, and the calculation is a built-in function in most statistical software packages.

Quadratic summation of mean errors is achieved by the following relationship.

$$\sigma_{Total} = \{\sigma_{Spl}^2 + \sigma_{Std}^2\}^{1/2} \tag{3.3}$$

The Tera-Wasserburg concordia diagram employs the intercept of a statistically best-fit discordant trend line through linearly discordant groups of data to estimate age and error (Wetherill, 1956; Tera and Wasserburg, 1973). This trend line crosses the concordia line forming upper- and lower-intercept age estimations. The Upper-intercept age is defined as the age of crystallization of the zircon. The error calculated from this diagram incorporates the statistical fit error as well as internal $2\sigma$ analytical errors. These two different statistical methodologies produce some variability between the age estimates. The probability density plot is not a rigorous U-Pb age calculation method, but is rather a simple graphical representation of a population of data. Problematic data with unusually large errors, anomalous isotopic concentrations, unusually high Th/U ratios, or reflecting mixing

between zones in the grain have been excluded from the statistical age calculations.

Table 3.1 summarizes upper-intercept ages and weighted mean ages for all analyses. Representative zircon CL images showing internal zoning and textures are presented in Figure 3.6; for CL images of all grains analysed see Appendix A.

Table 3.1: Summary of zircon ages.

| Tera-Wasserburg Upper-Intercept Age | | | | | | | |
|---|---|---|---|---|---|---|---|
| Sample | JF10-48 | JF10-16 | JF10-17 | JF10-30 | JF10-71 | CA109 | CA17 |
| Core | | 1657±16 | | 1654±20 | | | |
| Mantle | | 1461±7 | 1439±25 | 1467±14 | 1460±16 | 1461±8 | 1448±83 |
| Rim | | | | 1009±66 | | | 1027±230 |
| Whole Grain | 1242±49 | | | | | | |

| Weighted Arithmetic Mean Age | | | | | | | |
|---|---|---|---|---|---|---|---|
| Sample | JF10-48 | JF10-16 | JF10-17 | JF10-30 | JF10-71 | CA109 | CA17 |
| Core | | 1642±21 | | 1643±29 | | | |
| Mantle | | 1460±8 | 1435±15 | 1465±11 | 1449±8 | 1454±53 | 1443±46 |
| Rim | | | | 998±44 | | | 1078±28 |
| Whole Grain | 1209±21 | | | | | | |

### *3.4.1 Bonfield domain*

**JF10-48** Separated zircon grains average 0.4 mm in length, are generally elongate, rectangular-prism shaped, and have variable internal morphologies with multiple zone truncations. Most grains contain a variably oscillatory zoned, inherited-looking core surrounded by a mantle of patchy or oscillatory-zoned zircon, and a thin- to moderately-thick rim. Fifteen points were analysed from each of the textural zones within grains. The spots analysed define a single isotopic age population, with ages ranging from 1131±50 Ma to 1258±29 Ma, and a weighted mean age of 1209±21 Ma. The data cluster on the T-W diagram with an upper intercept age of 1242±49 Ma (Fig. 3.7). The uranium concentration in this sample is uniformly low, ranging from 29 to 339 ppm. Low uranium concentration is reflected in the high degree of error in individual analysis spots, and high Th/U ratios. Th/U ratios are relatively uniform, with an average value of 0.44. Rare-earth element profiles for all analysis spots exhibit a strong HREE enrichment and LREE depletion (Fig. 3.8).

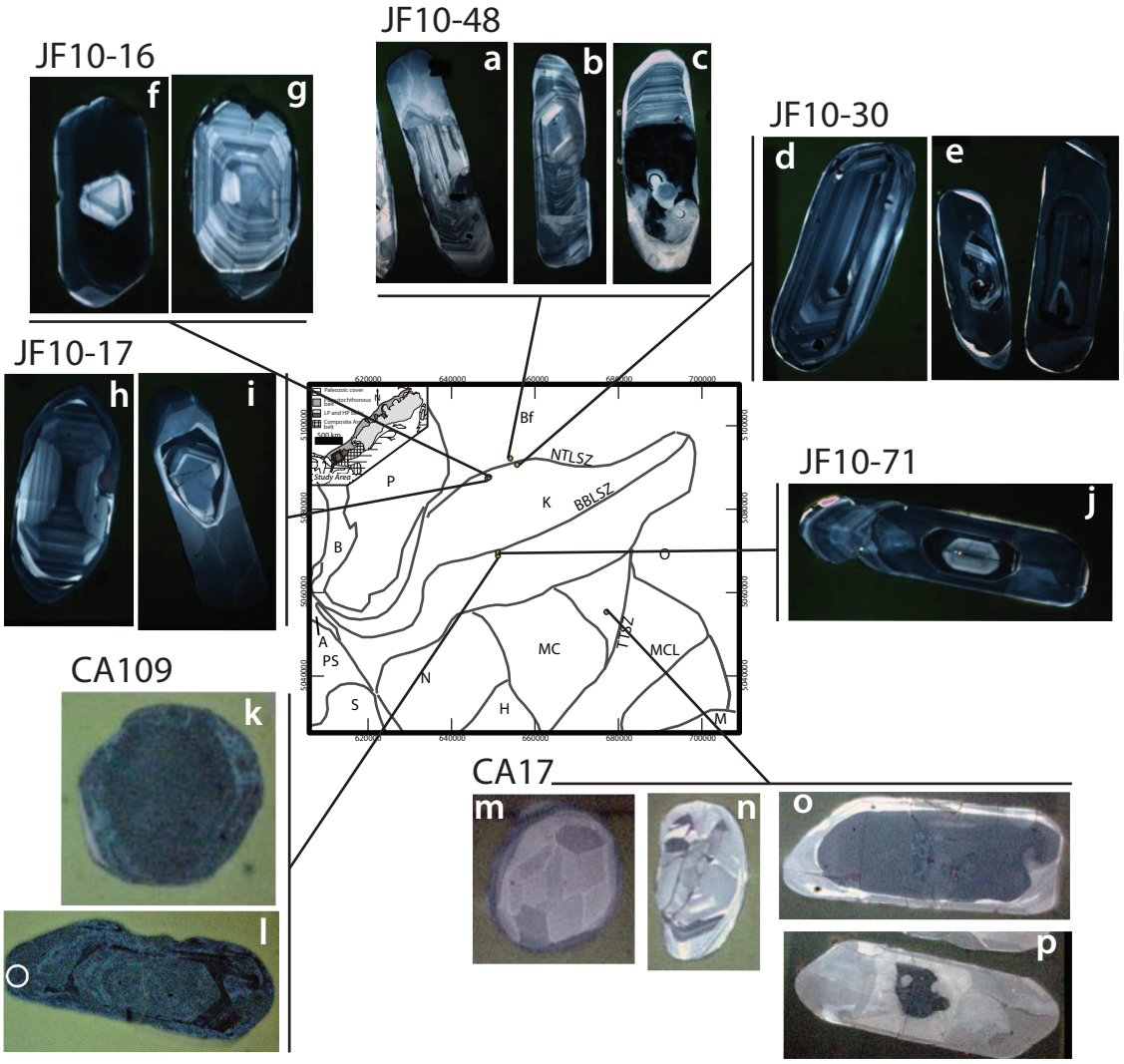


Figure 3.6: Representative CL images of zircons from the study area showing grain morphology. Bonfield domain zircons (JF10-48) have inherited-looking cores, surrounded by a mantle of patchy-zoned zircon. Most zircons from the Kiosk domain (JF10-16, 17, 30, 71, CA109) and elongate grains from the McLintock subdomain (CA17) are texturally equivalent with elongate grains containing xenocrystic cores, thick dark mantles, and a thin bright-to-dark rim. CA109 and CA17 contain ovoid, patchy-zoned, "soccerball" zircons that are surrounded by a rim of variable width.

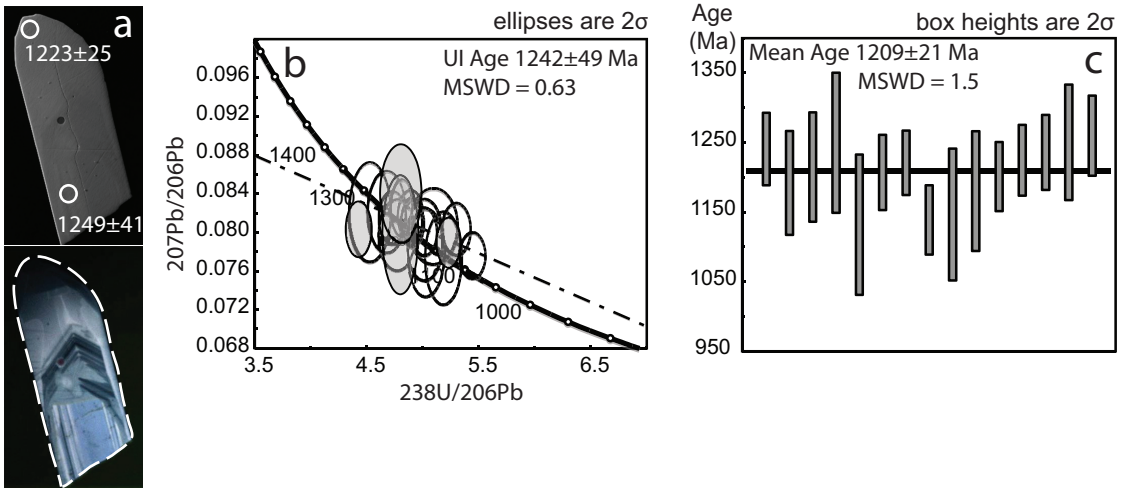


Figure 3.7: Tera-Wasserburg concordia diagram and weighted mean plot for JF10-48. a) Representative BSE (top) and CL (bottom) images of zircons showing spot analysis points. b) Tera-Wasserburg concordia diagram of all data with upper-intercept age of 1242±49 Ma (dashed line). c) Weighted mean plot of all data with weighted mean age of 1209±21 Ma (thick black line). Grey circles in concordia diagrams are excluded data not included in weighted mean plots. Abbreviations are: UI, upper-intercept; MSWD, mean square weighted deviation.

### *3.4.2 Kiosk domain*

**JF10-16** Separated zircon grains average 0.2 mm in length and are generally elongate, rectangular-prism shaped, and have relatively consistent internal morphologies with three distinct textural zones. All grains have inherited-looking cores with well developed oscillatory and rare sector zoning, with thick dark mantles that are weakly oscillatory zoned, and very thin, bright rims. Seven spots were analysed from the mantle, and five spots from the core of grains.

Mantle analysis spots define a single isotopic age population, with ages ranging from 1447±19 Ma to 1478±17 Ma, and a weighted mean age of 1460±8 Ma from these seven spots. A linearly discordant trend is defined by these seven spots with an upper-intercept age of 1461±7 Ma (Fig. 3.9). Th/U ratios for the mantle are uniformly low, with an average of 0.1. Rare-earth element profiles for the mantle are highly variable, with some grains exhibiting LREE enrichment resulting in flat REE profiles. Other mantle grains are LREE depleted and HREE enriched, and exhibit steep REE profiles (Fig. 3.10).

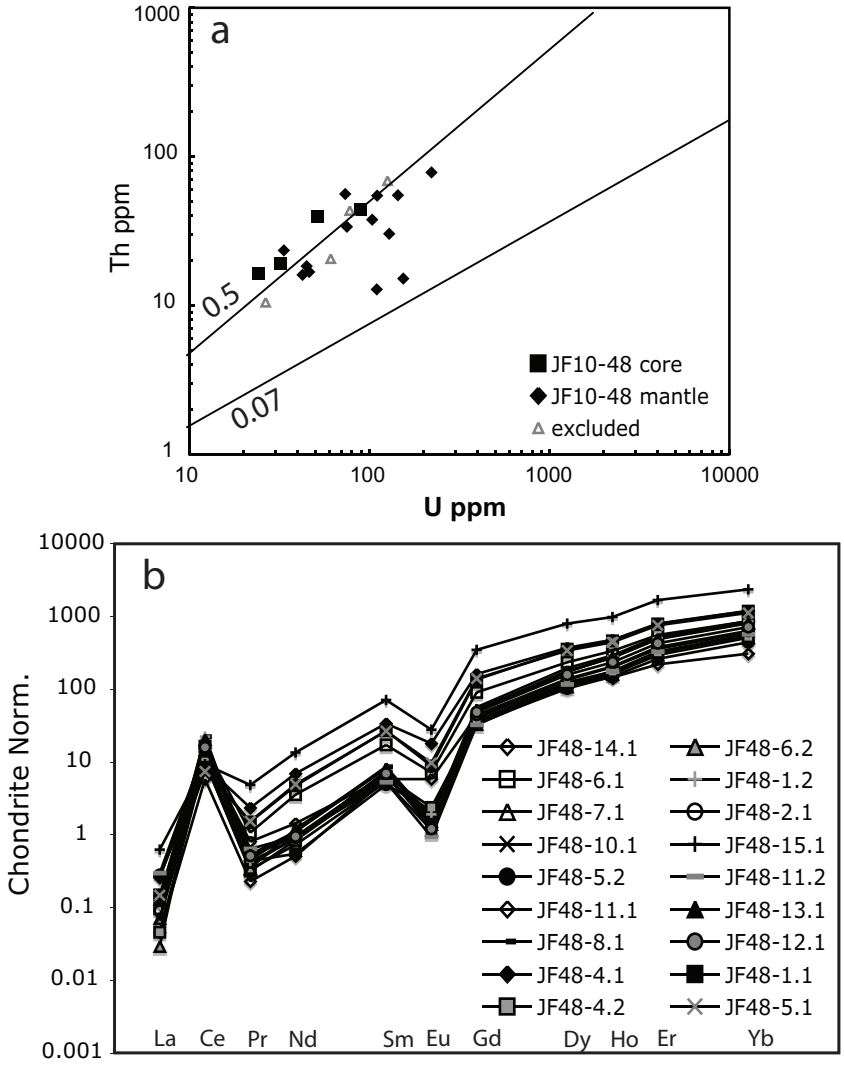


Figure 3.8: Trace element plots for JF10-48. a) Th vs. U plot of all data. Note that most Th/U ratios are tightly clustered on the 0.5 igneous trend line. b) Chondrite normalized REE profiles of all data (chondrite values from Korotev, 1996).

Core analysis spots define a single isotopic age population, with ages ranging from 1632±14 Ma to 1675±17 Ma, and a weighted mean age of 1636±26 Ma from these seven spots. A linearly discordant trend is defined by these five spots with an upper-intercept age of 1657±16 Ma (Fig. 3.9). Th/U ratios for the core are more variable (1-1.8), with an average value of 1.1. Rare-earth element profiles are LREE depleted and HREE enriched, and exhibit steep REE profiles (Fig. 3.10).

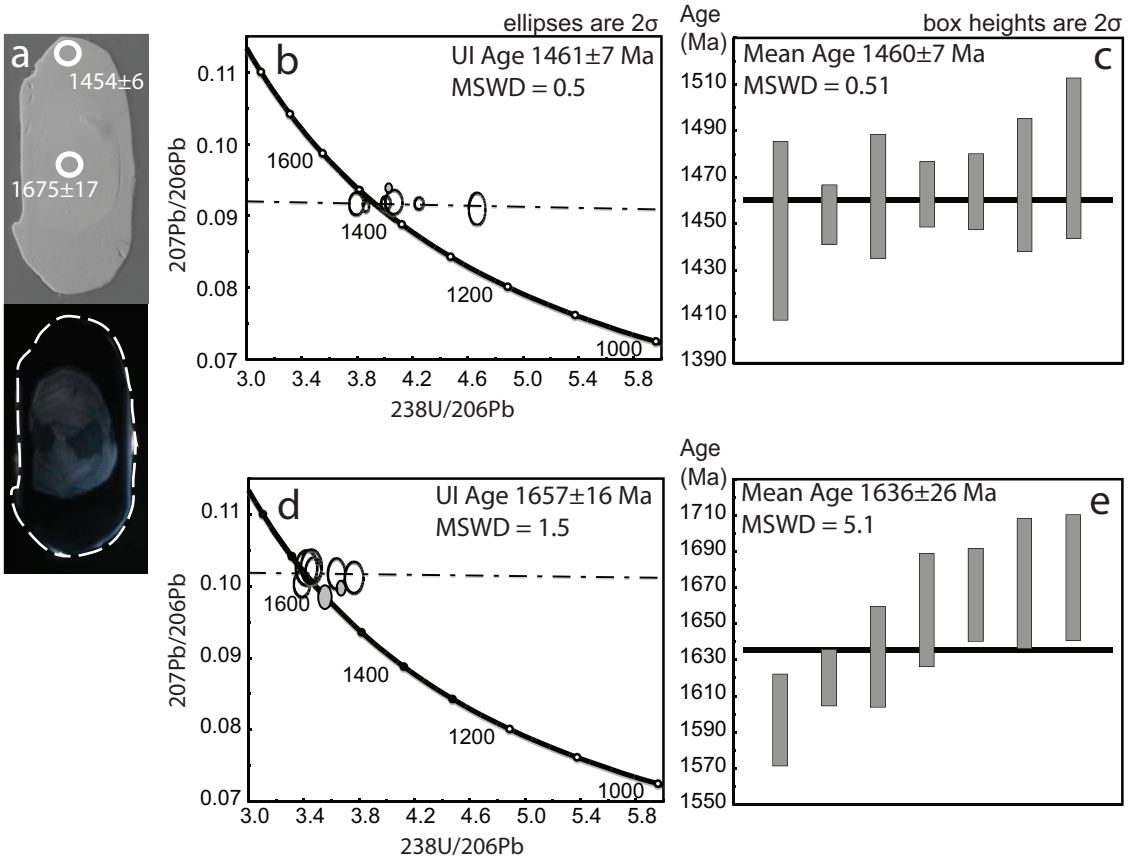


Figure 3.9: Tera-Wasserburg concordia diagram and weighted mean plot for JF10-16. a) Representative BSE (top) and CL (bottom) images of zircons showing spot analysis points. b) Tera-Wasserburg concordia diagram of mantle data with upper-intercept age of 1461±7 Ma (dashed line). c) Weighted mean plot of mantle data with weighted mean age of 1460±60 Ma (thick black line). d) Tera-Wasserburg concordia diagram of core data with upper-intercept age of 1657±17 Ma (dashed line). e) Weighted mean plot of core data with weighted mean age of 1636±26 Ma (thick black line). Grey circles in concordia diagrams are excluded data not included in weighted mean plots. Abbreviations are: UI, upper-intercept; MSWD, mean square weighted deviation.

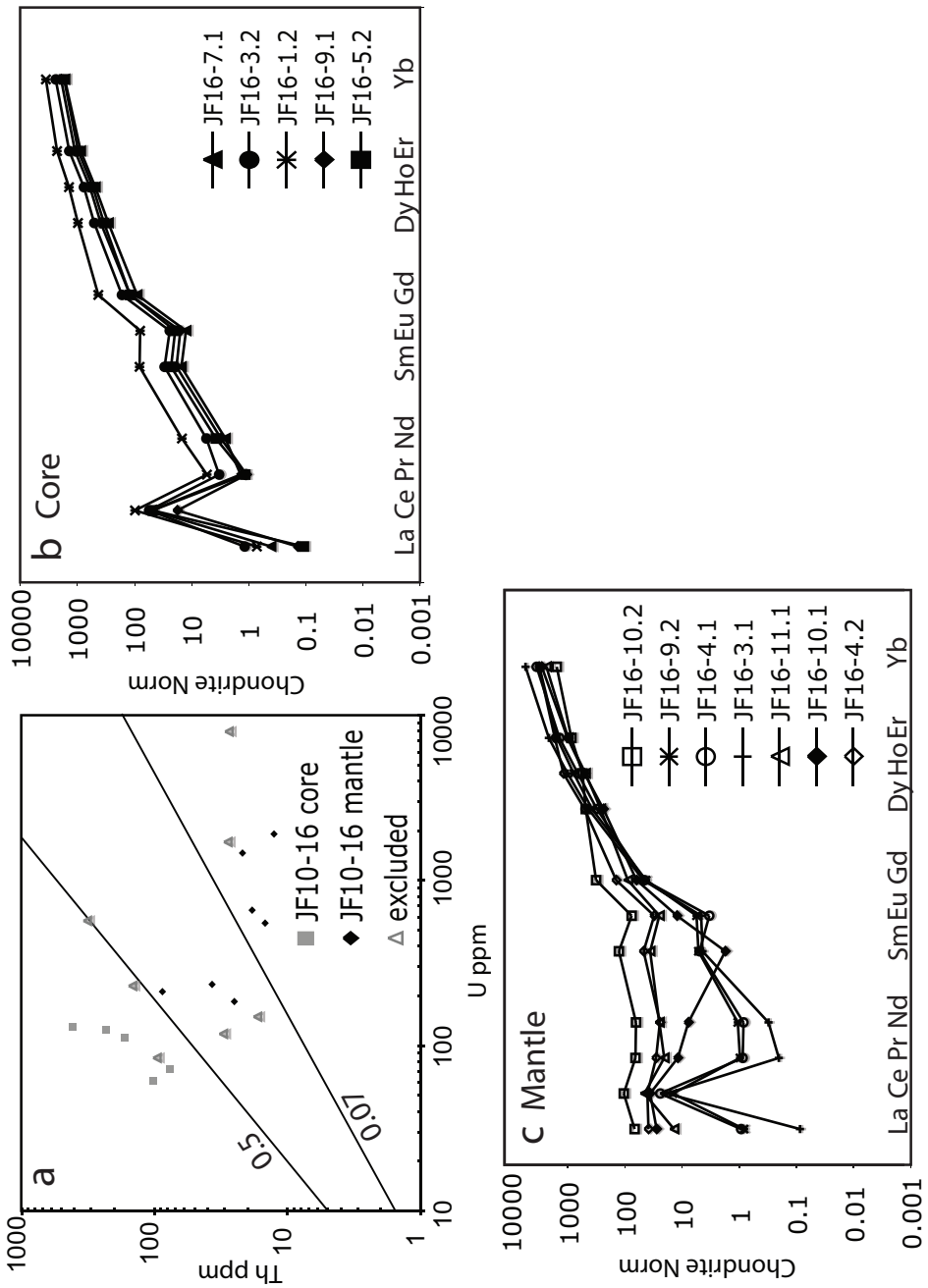


Figure 3.10: Trace element plots for JF10-48. a) Th vs. U plot of all data. Grey triangles represent data excluded from age calculation. b) Chondrite normalized REE profiles of core data and; c) Chondrite normalized REE profiles for mantle data (chondrite values from Korotev, 1996).

**JF10-17** Separated zircon grains average 0.4 mm in length and are generally elongate, tabular shaped, and have similar internal morphologies with three distinct textural zones. All grains have inherited-looking cores with well developed oscillatory and rare sector zoning, with thick dark mantles that are weakly oscillatory zoned, and very thin, bright rims. Six spots were analysed from the mantle. Analysed cores exhibited anomalously high U content and were excluded from the age calculation. Six mantle analysis spots define a single isotopic age population, with ages ranging from 1431±18 Ma to 1445±31 Ma, and a weighted mean age of 1435±15 Ma. A linearly discordant trend is defined by these seven spots with an upper-intercept age of 1439±25 Ma (Fig. 3.11). Th/U ratios from the mantle are relatively uniform with an average of 0.63 rare-earth element profiles are LREE-depleted and HREE-enriched, and exhibit steep REE profiles (Fig. 3.12).

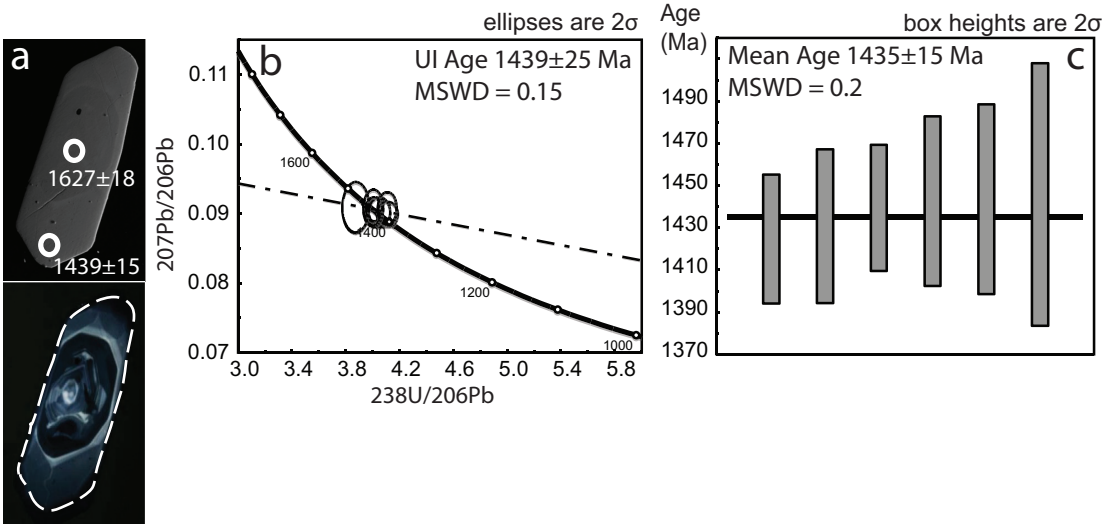


Figure 3.11: Tera-Wasserburg concordia diagram and weighted mean plot for JF10-17. a) Representative BSE (top) and CL (bottom) images of zircons showing spot analysis points. b) Tera-Wasserburg concordia diagram of mantle data with upper-intercept age of 1439±25 Ma (dashed line). c) Weighted mean plot of mantle data with weighted mean age of 1435±15 Ma (thick black line). Grey circles in concordia diagrams are excluded data not included in weighted mean plots. Abbreviations are: UI, upper-intercept; MSWD, mean square weighted deviation.

**JF10-30** Separated zircon grains average 0.4 mm in length and are generally elongate, rectangular-prisms, and have relatively consistent internal morphologies with three

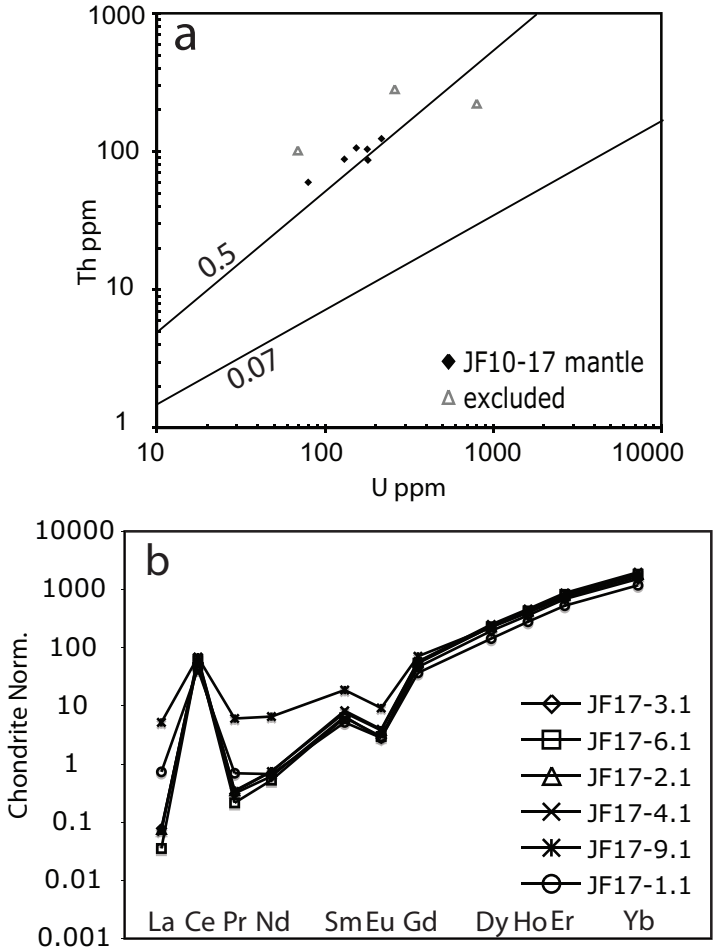


Figure 3.12: Trace element plots for JF10-17. a) Th vs. U plot of all data. Grey triangles represent data excluded from age calculation, and the tight cluster of data near the 0.5 igneous trend line. b) Chondrite normalized REE profiles of core data and; c) Chondrite normalized REE profiles for mantle data (chondrite values from Korotev, 1996).

distinct textural zones. All grains have inherited-looking cores with well developed oscillatory and rare sector zoning, with thick dark mantles that are weakly oscillatory zoned, and very thin, bright rims. Four spots were analysed from grain rims, seven from grain mantles, and three spots from grain cores. This was the only Kiosk domain sample with a sufficiently thick rim zone to permit analysis. Omitted data from the rim zone had large errors resulting from low signal count rate. Due to the thinness of the rims, the technique of "hanging" the beam partially off the sample was used to eliminate contamination with the mantle zone, leading to lower counts as less material is ablated.

Rim analysis spots define a single isotopic age population, with ages ranging from 961±58 Ma to 1014±48 Ma, and a weighted mean age of 998±45 Ma from these four spots. A linearly discordant trend is defined by these four spots with an upper-intercept age of 1009±66 Ma (Fig. 3.13). Th/U ratios for the rim are uniform, with an average of 0.1. Rare-earth element profiles for the rim show little variation, and exhibit a in flat REE profile (Fig. 3.14).

Mantle analysis spots define a single isotopic age population, with ages ranging from 1442±18 Ma to 1492±17 Ma, and a weighted mean age of 1465±11 Ma from these seven spots. A linearly discordant trend is defined by these seven spots with an upper-intercept age of 1467±14 Ma (Fig. 3.13). Th/U ratios for the mantle are variable and range from 0.11 to 0.9, with an average value of 0.7. Rare-earth element profiles exhibit pronounced HREE enrichment are very uniformly steep (Fig. 3.14).

Core analysis spots define a single isotopic age population, with ages ranging from 1636±7 Ma to 1657±13 Ma, and a weighted mean age of 1643±29 Ma from these seven spots. A linearly discordant trend is defined by these three spots with an upper-intercept age of 1654±20 Ma (Fig. 3.9). Th/U ratios for the core are uniform, with an average of 0.6. Rare-earth element profiles with pronounced HREE enrichment are uniformly steep (Fig. 3.10).

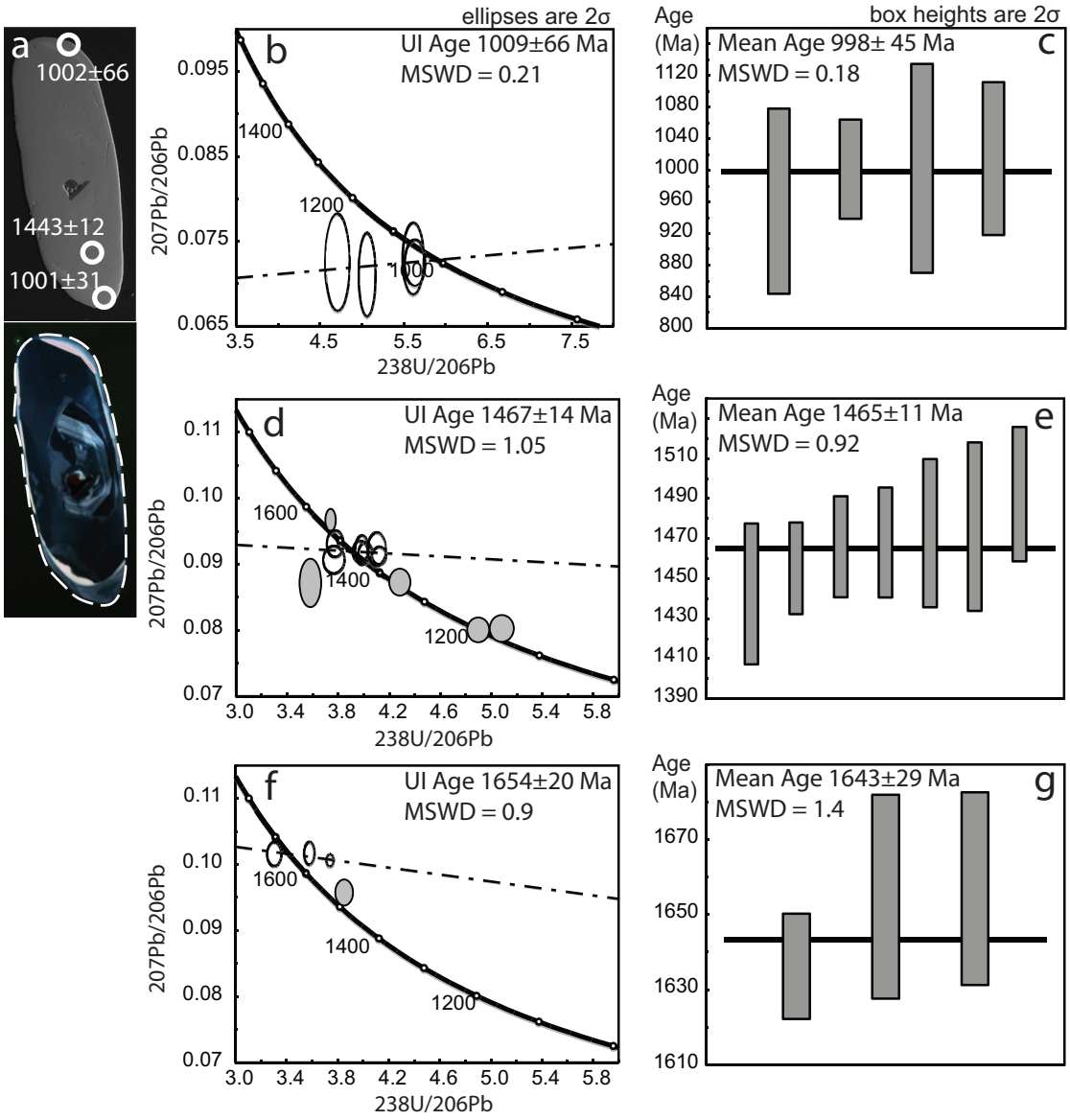


Figure 3.13: Tera-Wasserburg concordia diagram and weighted mean plot for JF10-30. a) Representative BSE (top) and CL (bottom) images of zircons showing spot analysis points. b) Tera-Wasserburg concordia diagram of rim data with upper-intercept age of 1009±66 Ma (dashed line). c) Weighted mean plot of rim data with weighted mean age of 998±44 Ma (thick black line). d) Tera-Wasserburg concordia diagram of mantle data with upper-intercept age of 1467±14 Ma (dashed line). e) Weighted mean plot of mantle data with weighted mean age of 1465±11 Ma (thick black line). f) Tera-Wasserburg concordia diagram of core data with upper-intercept age of 1654±20 Ma (dashed line). g) Weighted mean plot of core data with weighted mean age of 1643±29 Ma (thick black line). Grey circles in concordia diagrams are excluded data not included in weighted mean plots. Abbreviations are: UI, upper-intercept; MSWD, mean square weighted deviation.

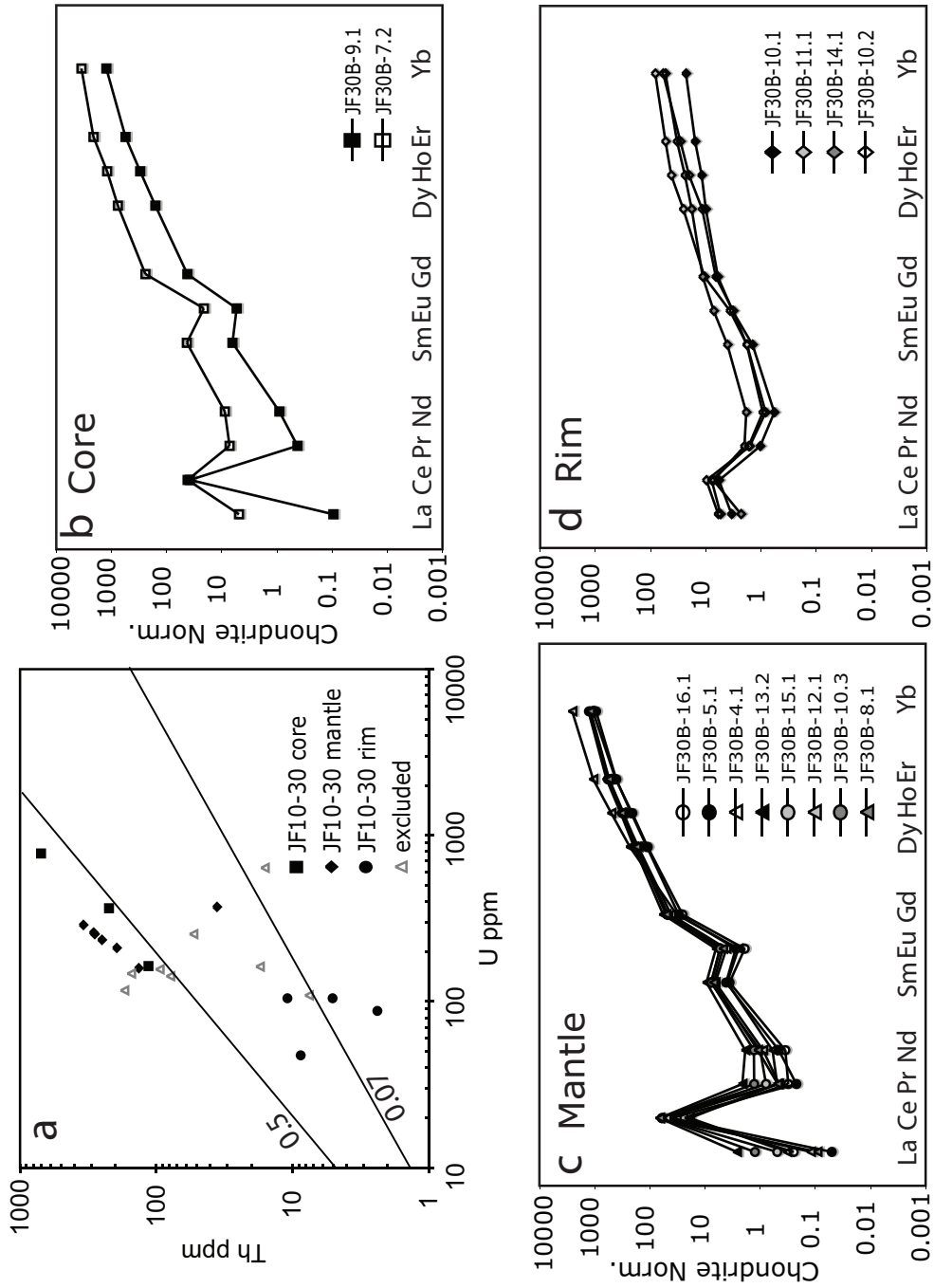


Figure 3.14: Trace element plots for JF10-30. a) Th vs. U plot of all data. Grey triangles represent data excluded from age calculation, and tight cluster of core and mantle data near the 0.5 igneous trend line. b) Chondrite normalized REE profiles of core data; c) Chondrite normalized REE profiles for mantle data and; d) Chondrite normalized REE profiles for rim data (chondrite values from Korotev, 1996).

**JF10-71** Separated zircon grains average 0.25 mm in length and are generally elongate, prismatic with rough edges, and have similar internal morphologies with three distinct textural zones. All grains have inherited-looking cores with well developed oscillatory and rare sector zoning, with thick dark mantles that are weakly oscillatory zoned, and very thin, bright rims. Nine spots were analysed from the mantle. Mantle analysis spots define a single isotopic age population, with ages ranging from 1436±8 Ma to 1468±11 Ma, and a weighted mean age of 1449±8 Ma from these nine spots. A tightly defined linear discordant trend is defined by these nine spots with an upper-intercept age of 1460±16 Ma (Fig. 3.15). Most Th/U ratios for the mantle are variable and range from 0.3 to 0.5, with two outlying points at 0.01 and 0.98. Rare-earth element profiles are overall steep in shape, with variably depleted in LREE, and consistently enriched in HREE (Fig. 3.16).

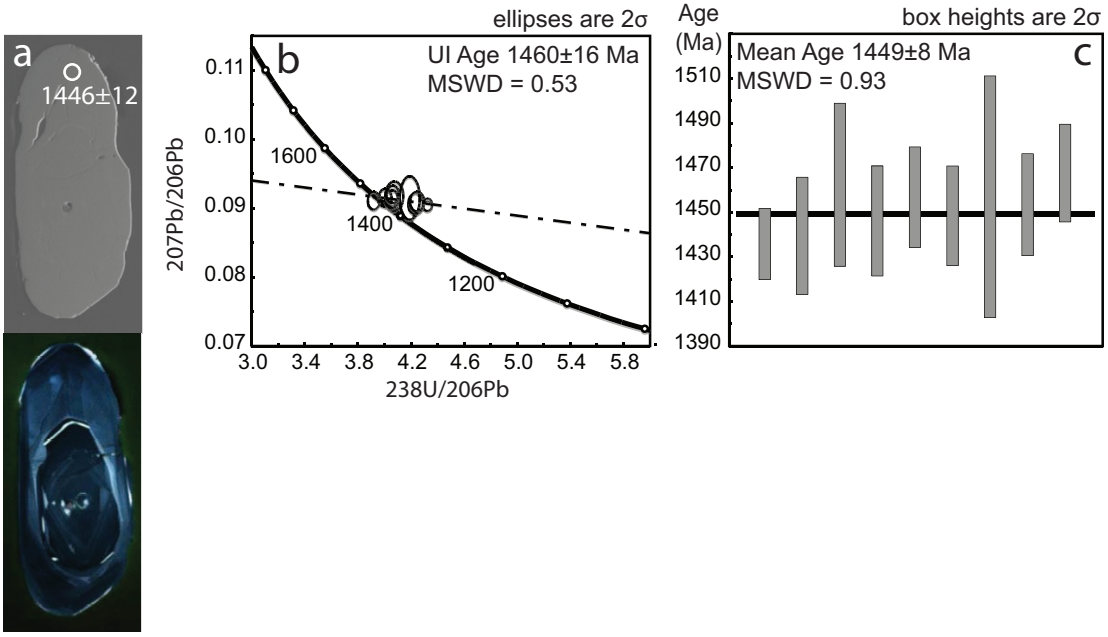


Figure 3.15: Tera-Wasserburg concordia diagram and weighted mean plot for JF10-71. a) Representative BSE (top) and CL (bottom) images of zircons showing spot analysis points. b) Tera-Wasserburg concordia diagram of mantle data with upper-intercept age of 1460±16 Ma (dashed line). c) Weighted mean plot of mantle data with weighted mean age of 1449±8 Ma (thick black line). Grey circles in concordia diagrams are excluded data not included in weighted mean plots. Abbreviations are: UI, upper-intercept; MSWD, mean square weighted deviation.

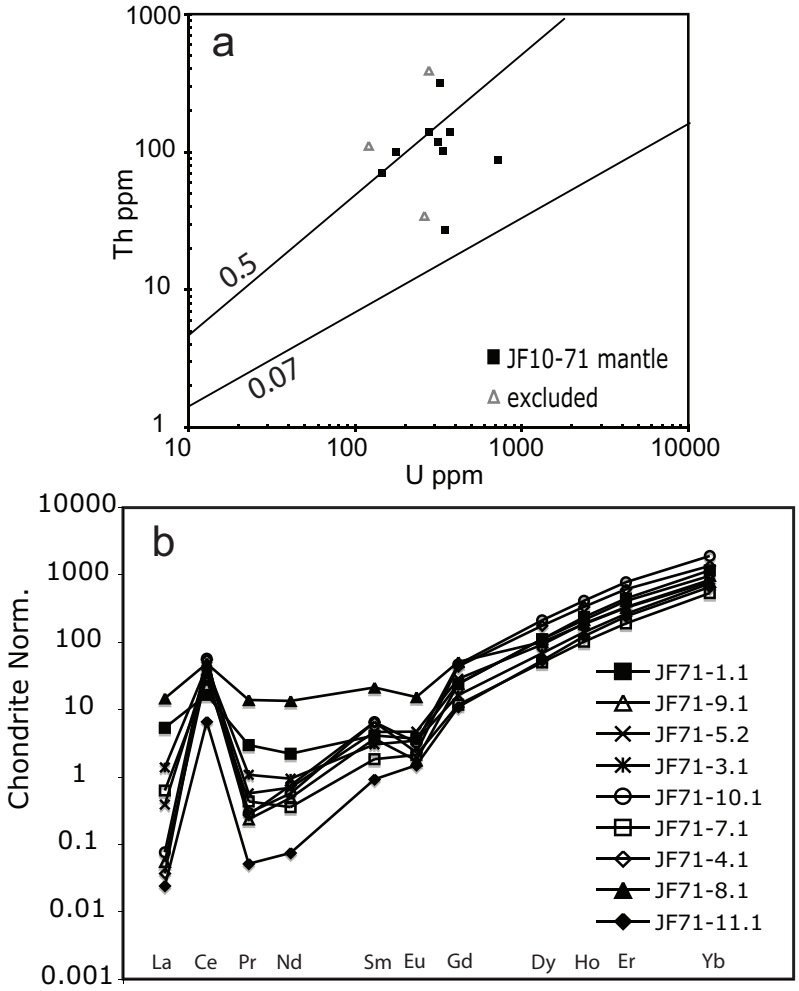


Figure 3.16: Trace element plots for JF10-71. a) Th vs. U plot of all data. Grey triangles represent data excluded from age calculation, and most data clustered near the 0.5 igneous trend line. b) Chondrite normalized REE profiles of mantle data (chondrite values from Korotev, 1996).

**CA109** This is the only amphibolite from the Kiosk domain that was analysed in early reconnaissance work (N. Culshaw, *unpub. data*). Zircon separates show two broad morphologies, (i) grains that are generally elongate, prismatic with rough edges, with multiple internal zones similar to other elongate grains in orthogneiss, and (ii) ovoid grains with rough edges, dark patchy internal zoning surrounded by a lighter rim. Nine spots from the thick inner mantle of grains were analysed. Mantle analysis spots define a single isotopic age population, with ages ranging from 1446±13 Ma to 1461±4 Ma, and a weighted mean age of 1454±53 Ma from these nine spots. A tightly defined linear discordant trend is defined by these nine spots with an upper-intercept age of 1461±8 Ma (Fig. 3.15). The very low error of individual analyses tightly constrains the discordant trend line in the T-W diagram. For this sample, the T-W diagram upper-intercept age is the preferred age. Most Th/U ratios for the mantle are uniformly low with an average value of 0.09.

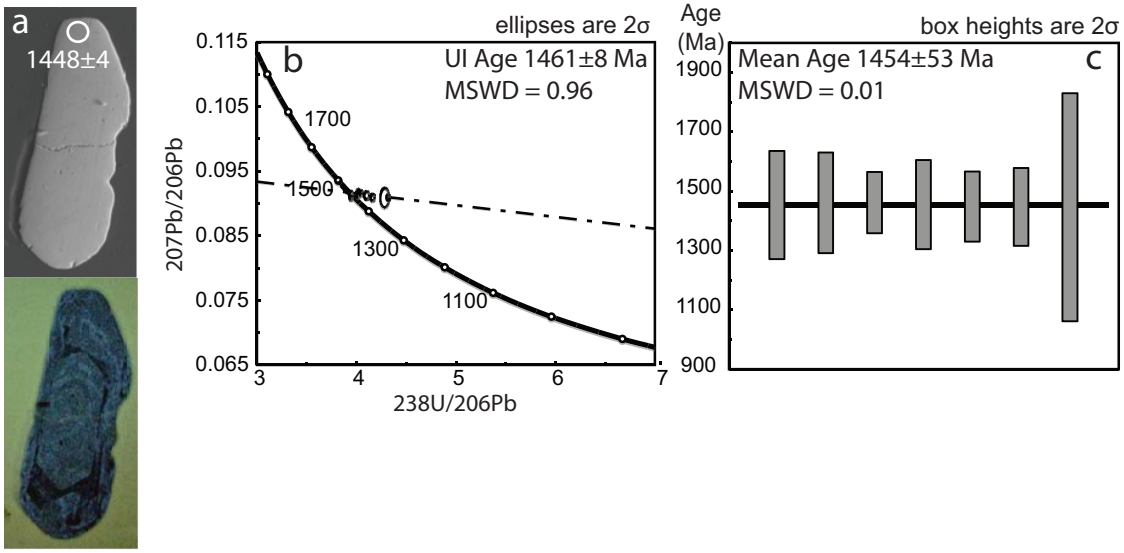


Figure 3.17: Tera-Wasserburg concordia diagram and weighted mean plot for CA109. a) Representative BSE (top) and CL (bottom) images of zircons showing spot analysis points. b) Tera-Wasserburg concordia diagram of mantle data with upper-intercept age of 1461±8 Ma (dashed line). c) Weighted mean plot of mantle data with weighted mean age of 1454±53 Ma (thick black line). Grey circles in concordia diagrams are excluded data not included in weighted mean plots. Abbreviations are: UI, upper-intercept; MSWD, mean square weighted deviation.

### *3.4.3 McLintock subdomain*

**CA17** This cross-cutting dyke from the McLintock subdomain of the Algonquin domain was analysed in reconnaissance work (N. Culshaw, *unpub. data*). Zircon separates show two broad morphologies: (i) grains that are generally elongate, prismatic, with multiple internal zones; and (ii) ovoid ("soccer ball") grains with rough edges and patchy internal zoning surrounded by a lighter rim. Two spots were analysed from the rim, and four from the mantle.

Rim analysis spots define a single isotopic age population, with ages of 1071±17 Ma and 1091±24 Ma, and a weighted mean age of 1078±28 Ma from these two spots. A linearly discordant trend is defined by these two spots with an upper-intercept age of 1027±230 Ma (Fig. 3.18). Two rim analyses points were recognised as non-linearly discordant, and were excluded from age calculation. Consequently, the T-W diagram is based on only two analyses, which introduces a great deal of uncertainly in the statistical fitting of a linearly discordant trend line. Thus, the weighted mean age is taken to be the age of this zone. Th/U ratios for the rim are both low, at 0.04 and 0.12.

Mantle analysis spots define a single isotopic age population, with ages ranging from 1421±11 Ma to 1496±18 Ma, and a weighted mean age of 1443±46 Ma from these four spots. A rough linear discordant trend is defined by these four spots with an upper-intercept age of 1448±83 Ma (Fig. 3.18). Th/U ratios for the mantle are variable and range from 0.06 to 0.9, with an average value of 0.6.

## 3.5 Discussion

### *3.5.1 Zircon morphology*

**Bonfield domain** Zircon grains in the Bonfield domain preserve both igneous crystallization textures and textures indicating later metamorphic or late-magmatic processes. Figures 3.6a through 3.6c CL images of typical zircon textures from the Bonfield pluton gneiss. BSE and CL images of all zircons extracted are presented in Appendix A. All grains are acicular to prismatic, and most are largely intact with few cracks or heavily

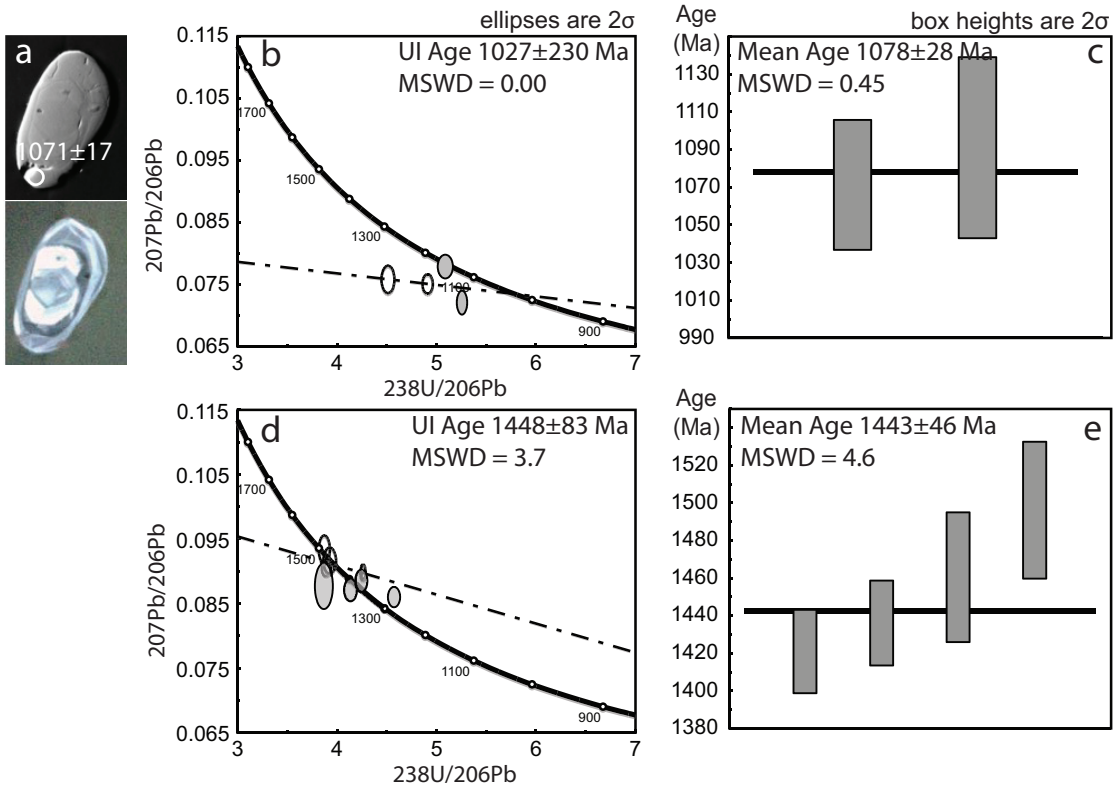


Figure 3.18: Tera-Wasserburg concordia diagram and weighted mean plot for CA17. a) Representative BSE (top) and CL (bottom) images of zircons showing spot analysis points. b) Tera-Wasserburg concordia diagram of rim data with upper-intercept age of 1027±230 Ma (dashed line). c) Weighted mean plot of rim data with weighted mean age of 1078±28 Ma (thick black line). d) Tera-Wasserburg concordia diagram of mantle data with upper-intercept age of 1448±83 Ma (dashed line). e) Weighted mean plot of mantle data with weighted mean age of 1443±46 Ma (thick black line). Grey circles in concordia diagrams are excluded data not included in weighted mean plots. Abbreviations are: UI, upper-intercept; MSWD, mean square weighted deviation.

metamict zones. All grains show euhedral, prismatic cores with well-developed oscillatory zoning typical of igneous growth. A mantle of patchy or oscillatory-zoned zircon generally surrounds these prismatic cores. Surrounding the grains is a bright featureless rim in CL that is highly variable in thickness (Fig. 3.6a though c). Featureless to patchy-zoned mantles, and bright rims are commonly associated with sub-solidus recrystallization of an existing zircon grain, which may or may not have formed in the presence of a melt or late-magmatic fluid during recrystallization. Recrystallization mobilizes some trace elements (e.g. Dy, Gd, Tb and Y) in the crystal structure, depleting them from one area of the grain, creating a bright CL response, and enriching them in another, quenching the CL response (Cesbron et al., 1993; Ohnenstetter et al., 1991; Hanchar and Rudnick, 1995). Trace element mobilization of this type can create discrete dark and light coupled bands, or patchy light and dark zones. Other textural evidence of sub-solidus recrystallization of the zircon grain includes erratic or convoluted zoning patterns (Schaltegger et al., 1999; Corfu et al., 2003).

**Kiosk domain** Textures of Kiosk domain zircons suggest igneous protolith crystallization was followed by at least two major metamorphic events. Figure 3.6d through 3.6p show some examples of CL images of typical zircon grain textures from the Kiosk domain. BSE and CL images of all zircons extracted are presented in Appendix A. The shapes of the zircon overgrowths tend to reflect the shapes of the inherited core. Most large grains are elongate and equant with prismatic xenocrystic cores. All grains show gently rounded edges probably due to sub-solidus resorption of the grain during metamorphism. Small isolated fractures are common in many of the grains.

Zircon grains throughout the Kiosk domain show the same textural pattern in CL images. Inherited cores show well developed prismatic oscillatory and locally sector zoning typical of igneous crystallization. These cores are than surrounded by a thin, black, featureless zone in CL indicative of sub-solidus recrystallization and the local concentration of trace elements in this zone quenching the CL response (Cesbron et al., 1993; Ohnenstetter et al., 1991; Hanchar and Rudnick, 1995). This texture is commonly interpreted to reflect the onset of grain recrystallization and resorption during granulite to upper-amphibolite or granulite facies metamorphism (Schaltegger et al., 1999). This zone is

surrounded by a thick, featureless to weakly oscillatory-zoned mantle that appears dark in CL. These textures have been attributed to the crystallization of new metamorphic zircon in the presence of a melt at upper-amphibolite to granulite facies metamorphism (Corfu et al., 2003). The outermost textural zone is a thin rim characteristic of sub-solidus recrystallization. In the few grains where this rim is sufficiently thick to be well imaged, it consists of a very thin bright CL zone coupled with a dark CL zone. Convoluted zoning indicative of sub-solidus recrystallization is common (Schaltegger et al., 1999; Corfu et al., 2003).

### *3.5.2 Trace-element data*

Distinguishing igneous and metamorphic zircon formed in the presence of a melt is often difficult based solely on trace element data. Recrystallization is not always effective at completely resetting the original igneous trace element signature. Recrystallized zones in metamorphic grains may show so called "ghost zoning," and retain some of their original igneous signature such as steep HREE profiles (Fig. 3.19), and Th/U ratios greater than those in zircon crystallized under metamorphic conditions (Hoskin and Black, 2000; Möller et al., 2003). Chemical equilibrium of zircon with other REE-rich phases such as garnet and monazite can have a large impact on the trace element signatures, for example, depleted HREE concentrations in zircon coexisting with garnet (Nyström and Kriegsman, 2003; Whitehouse, 2003; Corrie and Kohn, 2008; Kelsey et al., 2008). Chemical variation of melts and local disequilibrium effects can also mask the trace element signature (Schaltegger et al., 1999; Hoskin and Shaltegger, 2003). REE concentrations and Th/U ratios can vary significantly even within the same zone in a single grain. Trace element data alone are not sufficient to distinguish metamorphic and igneous formation conditions, and should be used in concert with other textural data.

**Bonfield Batholith** Trace element data from zircons from the Bonfield Batholith show no systematic variation between textural domains, suggesting igneous affinity for all grains. Th/U ratios have a median value of 0.4, characteristic of igneous crystallization, and REE profiles confirm the igneous affinity (Fig. 3.8). The HREE slope is steep, suggesting that zircons did not crystallize in equilibrium with garnet (Rubatto, 2002;

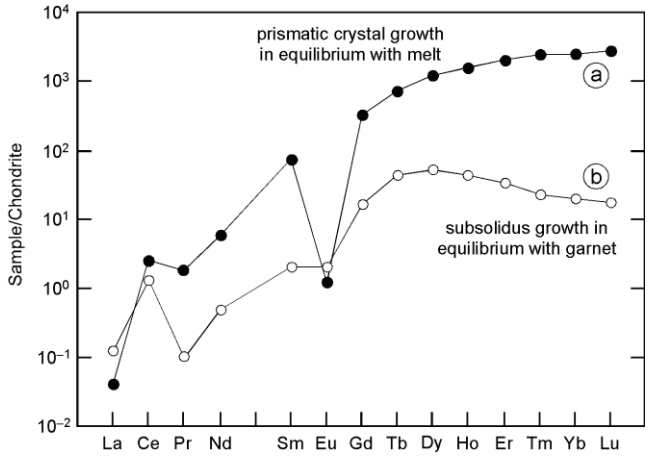


Figure 3.19: Ideal igneous and metamorphic chondrite normalized REE profiles (from Hoskin and Shaltegger, 2003). Note distinct HREE enrichment profile for igneous rocks equilibrated with melt.

Nyström and Kriegsman, 2003). Given that large prismatic zircons tend to be located in the amphibole+garnet-rich layers, it is possible that: (i) zircon was not in equilibrium with garnet at the time of formation; or (ii) garnet was either absent or not present in sufficient modal quantity to affect REE partitioning in zircon. The timing of garnet growth in this rock is unknown, however; neighbouring lithotectonic domains in the southwest Grenville Province experienced regional high-grade metamorphism during Grenvillian orogenesis (ca. 1160-1040 Ma), so it is reasonable to infer that garnet growth in the Bonfield Batholith occurred during the Grenville orogeny.

**Kiosk domain** Zircons from the Kiosk domain have trace element patterns that correlate with distinct textural and age domains. Inherited cores have trace element patterns typical of crustal igneous rocks, whilst the surrounding mantles and rims have trace element patterns that are mixed, or typical of metamorphic rocks.

Cores of zircons in the Kiosk domain orthogneiss have a clear igneous trace element signature. Using sample JF10-30 as an example, the Th/U ratio is $\leq$0.5, and points plot close to or above the igneous trend line (Fig. 3.14a). The REE profiles of these samples are typical of igneous zircon, with steep HREE patterns, large Ce/Ce* values, and

large Eu/Eu* values $\leq 1$ (*cf.* Fig. 3.19 and Appendix A). These data support the conclusion based on the textural characteristics of the grains that these are inherited igneous xenocrysts.

The thick metamorphic mantles of zircon grains in the Kiosk domain orthogneiss have a mixed trace element signature. Th/U ratios in these samples range from 0.01 to 0.9, and span both the igneous and metamorphic fields on the U-Th plot (Figs. 3.10, 3.12, 3.14, 3.16). Most REE profiles in these zircons resemble those for crustal igneous rocks. The analyses show HREE enrichment and LREE depletion relative to chondrite values, Eu/Eu* values $\leq 1$, and positive Ce/Ce* values. Analyses from two samples (JF10-16 and JF10-71) show elevated MREE concentrations, and Eu/Eu* values near 1 (Figs. 3.10c and 3.16b, respectively, and Appendix A). The variability of REE profiles is not systematic, and cannot be conclusively linked to textural domains within the grains.

Rims of zircons in the Kiosk domain orthogneiss have a characteristic metamorphic trace element signature. Data were obtained for only four points in one sample (JF10-30). Though this data set is too limited to describe any systematic variation in this zone, there are clear trends within the data. Th/U ratios are variable, but plot near the metamorphic trend on the Th-U plot (Fig. 3.14a). In addition, the Th/U ratios for these samples are bimodal, with two values at approximately 0.1, and two at approximately 0.07 (Appendix A). These ratios indicate sub-solidus recrystallization of zircon (Hoskin and Black, 2000). This zone is also depleted in HREE, suggesting recrystallization in the presence of garnet. Europium and Ce anomalies in this zone are much less pronounced, with Eu/Eu* and Ce/Ce* values near 1 (Fig. 3.14b and appendix A).

### *3.5.3 Synthesis*

#### *3.5.3.1 Bonfield domain*

Zircon dates from the Bonfield Batholith show that the southern Bonfield domain experienced a single igneous crystallization event at ca. 1240 Ma (Elzevirian-age; Moore and Thompson, 1980). Th/U ratios have a median value of 0.4, which is characteristic of igneous crystallization from a magma. Additionally, the REE profiles have an igneous character, with HREE enrichment and a clear negative Eu anomaly. There is a evidence

for restricted bimodal igneous activity in the Parautochthonous Belt of in the southwest Grenville Province at ca. 1270-1230 Ma hosted in Archean domains (Krogh et al., 1988; Kamo, 1984; Lumbers et al., 1991; Dudas et al., 1994; Davidson and Breemen, 2001; Easton and Ketchum, 2002). Lumbers (1971), Lumbers et al. (1991), and Prevec (1992, 1993) mapped and dated the A-type Mulock Pluton in the Tilden Lake domain to the northwest of the Bonfield domain at $1244^{+4}_{-2}$ Ma, matching the upper-intercept age of the Bonfield Batholith. These ages are coeval with the Fanny Lake and Fall Lake gabbroic intrusions in the Tomiko domain, which are similar in composition to Sudbury-type mafic dykes (ca. 1240-1235 Ma) (Easton and Ketchum, 2002). Magmatism in the Frontenac-Adirondack belt in the CMB was coeval with plutonism in the Parautochthonous Belt, but a genetic linkage between these two locations is not yet known (Easton and Ketchum, 2002). It is interpreted that the Bonfield Batholith is part of this suite of felsic batholiths and associated mafic plutons and dykes in the Parautochthonous Belt.

Although textures of zircons from the Bonfield Batholith appear to be polyphase, with an inherited-looking igneous core and a metamorphic mantle overgrowth, they yield a single igneous crystallization age. Hoskin and Shaltegger (2003) showed that late-stage magmatic fluids can create similar textural effects as metamorphic recrystallization, such as convoluted zoning patterns and thick featureless zones. This rock has been subject to pervasive recrystallization and annealing during high-grade metamorphism. Petrographic evidence of igneous melts or metamorphic fluids has not been preserved. The mechanism that may have given rise to the observed textures of zircon grains is uncertain. It is possible that zircon textural alterations may be the result of: (i) late-stage igneous melt from the final crystallization of the Bonfield batholith; (ii) localized metamorphic fluid interaction during Grenvillian orogenesis that altered the zircon texture, but did not significantly reset the isotopic and trace element signature; or (iii) sub-solidus recrystallization that did not significantly reset the isotopic and trace element signature. The HREE enrichment of the Bonfield Batholith zircons also shows that they did not co-crystallize with an HREE-rich phase like garnet (Rubatto, 2002). Thus, garnet probably formed after the ca. 1240 Ma crystallization of the Bonfield Batholith, likely at high-grade metamorphic conditions during Grenville orogeny. This raises the question of why did new zircon not crystallize during Grenvillian orogenesis? The answer to this question is unclear from the

data presented in this study, and requires further study of the Bonfield Batholith and other lithologies in the Bonfield domain.

### *3.5.3.2 Kiosk and Algonquin domains*

Zircon dates from the Kiosk and Algonquin domains show that these lithotectonic domains have a long-lived, polyphase deformation and metamorphic history. Evidence of the early tectonism at ca. 1640 Ma and ca. 1450 Ma is preserved in the meta-quartz-monzonite orthogneiss and localized amphibolite units (Fig. 3.20). The later stages of Grenvillian evolution during ca. 1080-1000 Ma, however, are recorded in shear zone orthogneisses and cross-cutting mafic dykes.

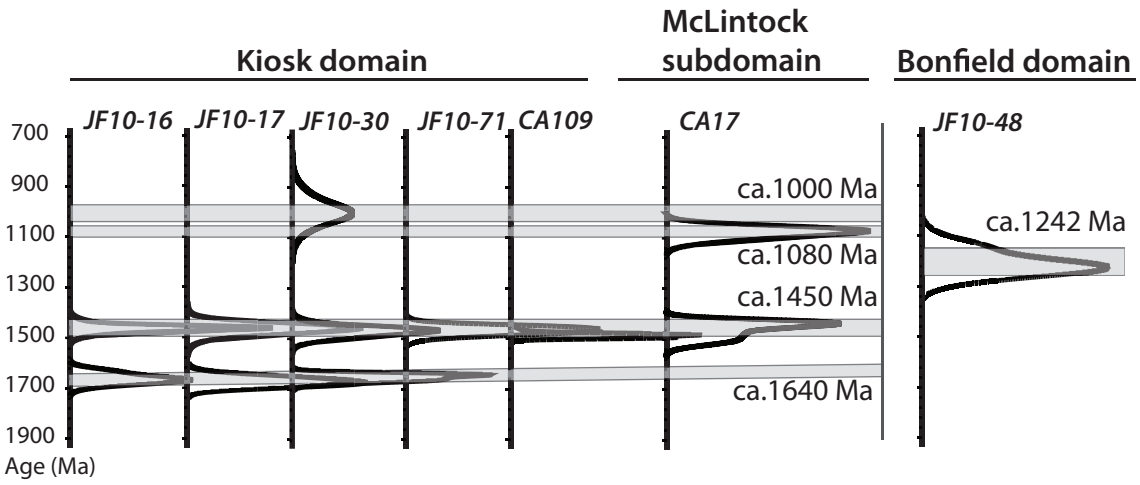


Figure 3.20: Compilation of probability density curves for all data evaluated in this study highlighting trends of ages. Width of grey bar is approximate $2\sigma$ error of weighted mean values. Note that ca. 1000 and ca. 1080 Ma events overlap within error, but are schematically shown as separate.

**Igneous protolith** The oldest population of U-Pb dates from zircon cores indicates that the age of the igneous protolith of the orthogneisses in the Kiosk domain was ca. 1640 Ma. These grains now form the inherited cores in large, equant, polyphase zircons. The cores are prismatic with oscillatory zoning, typical of igneous crystallization. This interpretation is substantiated by trace element data. Th/U ratios of the cores are well above

the common 0.5 value for igneous zircon, and have a median value of 1.0. Furthermore, zircon cores have an HREE enriched profile and a negative Eu anomaly typical of igneous zircon in crustal rocks. The Labradorian orogeny (ca. 1710-1600 Ma) was a time of felsic igneous plutonism on the margin of proto-Laurentia (Krogh and Davis, 1969, 1970b,a, 1971; Krogh et al., 1971; Condie, 1986; Corrigan et al., 1994; Rivers, 1997; Ketchum and Davidson, 2000; Jamieson et al., 2001). Several large granitoid bodies in the Southern and Grenville Provinces crystallized at this time, and were overprinted by later orogenies. The ca. 1640 Ma protolith age is interpreted as belonging to this widespread suite of felsic plutonic rocks.

**High-grade metamorphism and migmatization** The thick mantles of zircons from the Kiosk domain indicates a major metamorphic event at ca. 1450 Ma that was probably responsible for the widespread migmatitic rocks. In the northern boundary shear zone of the Kiosk domain (NTLSZ), leucosomes from preserved migmatite were reworked into the shear zone fabric, demonstrating that leucosome generation pre-dates penetrative deformation in the boundary shear zones (Fig. 2.7). In all zircons from the Kiosk domain the ca. 1450 Ma age zone exhibits the same crystal texture, namely a thin recrystallized zone around the inherited igneous core surrounded by a thick patchy to weakly-oscillatory zoned mantle. Thick metamorphic overgrowths with weak oscillatory zoning patterns require a large volume of melt at high-grade metamorphic conditions to crystallize (Watson and Harrison, 1983; Watson, 1996a,b; Schaltegger et al., 1999; Corfu et al., 2003; Hoskin and Shaltegger, 2003). The ca. 1450 Ma age is consistent with the age of widespread granulite-facies metamorphism and felsic igneous plutonism experienced by the southwestern CGB (Pinwarian orogeny; Davidson, 1986a; van Breemen et al., 1986; Nadeau and van Breemen, 1989; Tuccillo et al., 1992; Haggart et al., 1993; Krogh, 1993; Corrigan et al., 1994; Davidson and van Breemen, 1994; Dudas et al., 1994; Ketchum et al., 1994; Chen et al., 1995; Culshaw and Dostal, 1997; Timmermann et al., 1997; Ketchum et al., 1998; Nadeau and van Breemen, 1998; Slagstad, 2003; Slagstad et al., 2004a,c, 2005). The large melt volumes necessary to grow large metamorphic overgrowths on zircon cores is consistent with the formation of migmatitic rocks in the Kiosk domain at ca. 1460 Ma.

Thick mantles of zircons in the mafic dyke sample in the McLintock subdomain indicates metamorphism at ca. 1450 Ma, coeval with orthogneisses of the Kiosk domain. The zircons that gave this age exhibit the same crystal texture as those from Kiosk domain orthogneisses (*cf.* elongate grains in Fig. 3.7 and Appendix A). These zircons are interpreted as xenocrystic zircons, and are do not constrain the age of metamorphism of the mafic dyke, but rather the host orthogneiss.

**The Grenvillian orogeny** Thin recrystallized outer rims of zircons from the Kiosk and Algonquin domains record two phases of deformation and metamorphism during the Grenville orogeny. Data from small "soccerball" zircons from the cross-cutting dyke (CA109) from the McLintock subdomain indicate a major metamorphic event at ca. 1080 Ma. Zircons from an orthogneiss sample (JF10-30) from the NTLSZ indicate a major metamorphic event at ca. 1000 Ma in the Kiosk domain.

Geochronological studies show that between ca. 1090 Ma and ca. 1040 Ma the entire CGB was undergoing protracted high-grade metamorphism associated with thrust imbrication and thickening of the Grenville Orogen during the Ottawan orogenic pulse (Krogh, 1989; Nadeau and van Breemen, 1989; Rivers et al., 1989; Nadeau, 1990; van Breemen and Davidson, 1990; Tuccillo et al., 1992; Heaman and LeCheminant, 1993; Ketchum et al., 1993; Mezger et al., 1993; Bussy et al., 1995; Ketchum and Krogh, 1997; Rivers, 1997; Timmermann et al., 1997; Ketchum et al., 1998; Timmermann, 1998; Rivers and Corrigan, 2000; Slagstad, 2003; Slagstad et al., 2004c). One sample in this study from the McLintock subdomain recorded an age of 1078±28 Ma (Figs. 3.1 and 3.18). This is interpreted to record Ottawan deformation and high-grade metamorphism.

The young age obtained from the hangingwall of the NTLSZ (998±44 Ma) is more ambiguous due to the large measurement error. This age overlaps within error with Ottawan orogenesis discussed above, and also overlaps with the later Rigolet orogenic pulse at ca. 1010-990 Ma, associated with late-stage metamorphism and extensional deformation in the CGB, and thrust-sense deformation and metamorphism in the GFTZ (Tilton and Grunenfelder, 1968; Krogh, 1989; Rivers et al., 1989; Ketchum et al., 1993; Mezger et al., 1993; Ketchum and Krogh, 1997; Rivers, 1997; Ketchum et al., 1998; Rivers and Corrigan,

2000; Corfu and Easton, 2001). Ratcliffe (2011) conducted a structural and metamorphic study of the narrow North Tea Lake mylonite zone (NTLMZ) that lies within the NTLSZ, and concluded that the NTLMZ is a normal-sense, hangingwall-to-southeast mylonite zone that was active in the late-stage of the Grenville orogeny. It has been demonstrated that early-stage thrust-sense shear zones in the CGB were reactivated as the normal-sense Shawanaga shear zone (e.g. Ketchum et al., 1998). Despite the existence of the normal-sense mylonite zone in the NTLSZ, pervasive recrystallization at high-metamorphic grade have removed any kinematic indicators that would distinguish if the NTLSZ originated as a thrust-sense shear zone that was later reactivated as a normal-sense shear zone. The ambiguity in the age of zircons, the uncertain sense of shear along the NTLSZ, and the precedent for normal-sense reactivation of thrust-sense shear zones in the CGB makes linking this age to a specific tectonic regime problematic. Further work on the kinematics of the NTLSZ is required to address this issue. The only firm conclusion based on this zircon data is that it represents a younger phase of high-grade metamorphism than is recorded in the McLintock subdomain.

## 3.6 Conclusions

1. The Bonfield Batholith of the Bonfield domain crystallized at ca. 1240 Ma and underwent monocyclic deformation to form the Bonfield gneiss during later deformation.

2. The age of the igneous protolith of Kiosk domain orthogneiss is ca. 1640 Ma.

3. Migmatitic orthogneisses and straight gneisses from the Kiosk domain and the McLintock subdomain experienced high-grade metamorphism and migmatization at ca. 1450 Ma.

4. The McLintock subdomain of the Algonquin domain experienced high-grade metamorphism and deformation during the early-stage of the Grenville orogeny at ca. 1080 Ma during thrust-sense crustal thickening of the CGB.

5. The NTLSZ experienced high-grade metamorphism at ca. 1000 Ma.

# CHAPTER 4

# MONAZITE GEOCHRONOLOGY

## 4.1 Introduction

Monazite is the chronometer of choice in paragneisses and metapelitic rocks for providing time constraints on metamorphism and deformation. The U-Pb systematics of monazite have been extensively studied and monazite can provide very robust and accurate age data (e.g. Montel et al., 1996) . When constrained by other data such as petrography, field relations, and thermobarometry these data can provide important constraints on timing of metamorphic events and deformation phases.

U-Pb dating of monazite was carried out at the reconnaissance level in the Kiosk domain in the footwall of the Big Bob Lake Shear Zone. Four grains from differing textural associations in two separate paragneiss units were chosen for study. The goal of study was to: (i) determine what ages were recorded in monazites from the BBLSZ; and (ii) to test monazite as a viable chronometer for study of the Kiosk domain. Monazite analysis has generated robust first-order geochronology data, and shows great potential for further use as a chronometer in the Kiosk domain.

Ages recorded in monazites from the Kiosk domain coincide with Pinwarian and Grenvillian zircon ages of metamorphic events as described in Chapter 3, and in addition have generated evidence of a pre-Grenvillian tectonic episode not recorded in zircon data from the Kiosk or Algonquin domains. The Shawinigan pulse (ca. 1190-1140 Ma) (Rivers,

1997; Corriveau and van Breemen, 2000; Rivers et al., 2002), was a Mesoproterozoic accretionary event that was restricted to the southwest Grenville Province. The Frontenac-Adirondack Belt, the Composite Arc Belt, and the Parry Sound domain, all record evidence of Shawinigan-age tectonism, amalgamation and accretion to Laurentia (Wodicka, 1994; Wodicka et al., 1996; Culshaw et al., 1997; Carr et al., 2000; Corriveau and van Breemen, 2000; Rivers and Corrigan, 2000; Wodicka et al., 2004; Hynes and Rivers, 2010; Marsh et al., 2012). The Shawinigan pulse was also a time of magmatism and metamorphism in the CGB. A widespread suite of coronitic olivine metagabbro intruded many of the allochthonous domains in the CGB at ca. 1170-1150 Ma (Fig. 3.1) (Davidson, 1986c; Davidson and van Breemen, 1988; Heaman and LeCheminant, 1993). Several geochronology studies indicate metamorphism in the southwest CGB recorded in orthogneisses, paragneisses coeval with the crystallization of coronitic olivine metagabbros (van Breemen and Hanmer, 1986; van Breemen et al., 1986; Tuccillo et al., 1992; Mezger et al., 1993; Carr and Berman, 1996, 1997).

## 4.2 Method

Two paragneiss samples were chosen for study based on the mineral assemblage, petrographic fabric, field relations and the presence of monazite in thin-section. Chemical analysis was completed using the JEOL JXA-8200 Superprobe at the Dalhousie University Robert MacKay Electron Microprobe Laboratory. The analytical protocol of monazite follows the procedure of Scherrer et al. (2000) and Pyle et al. (2002) adapted for the instrument configuration by Gagné (2004) and further refined by C. Warren (*unpub. report*, 2006). The analytical procedure differs from the widely used procedure outlined by Williams et al. (2006) in that a double carbon coat is used instead of gold coating to avoid permanent beam damage, and background values of x-ray peak positions were selected by inspection using a linear model instead of a polynomial model (Pyle et al., 2005). For an exhaustive description and explanation of the analytical protocol the reader is directed to Gagné (2004).

Monazite grains were located using back-scatter electron (BSE) imaging followed by a qualitative energy-dispersive scanning EDS to separate monazite from other “bright”

minerals such as apatite. BSE images were then used to make a first order assessment of internal zoning patterns, petrographic setting, and grain morphology. The best candidate grains were than mapped for Y, Pb, Th, and U, and in some cases Ce and Ca, using wavelength-dispersive scanning (WDS) with an average counting time of 50ms/pixel. WDS maps were used to determine chemical domains and zoning patterns in the grain, in particular with respect to Y and Th, which are commonly the best elements for discerning chemical zoning, and also carry petrogenetic information.

Quantitative monazite analysis is a two-phase process, consisting of separate major-element and trace-element analyses. The first phase involves completing quantitative major-element analysis for each distinct chemical or textural zone identified through WDS mapping or BSE imaging. Where possible, multiple points were analysed and the compositions averaged to give a representative major-element composition for that domain. Table 4.1 presents the analytical conditions for major-element analysis at 15kV and 20nA. The second phase of analysis involves quantitative trace-element analysis of the chemical or textural zones. Once the representative major-element composition of a chemical zone is known, that composition is then fixed in the JEOL software and detailed trace-element analysis can be carried out on the elements of interest, Y, Pb, Th, and U. Table 4.2 presents the analytical conditions for trace-element analysis at 15kV and 200nA. Using equation 4.1 with the trace-element concentrations and decay constants, the age ($\tau$) is calculated for each individual analysis.

$$Pb = \frac{Th}{232}\{e^{\lambda^{232}\tau} - 1\}208 + \frac{U}{238.04}0.9928 \times \{e^{\lambda^{238}\tau} - 1\}206 + \frac{U}{238.04}0.0072 \times \{e^{\lambda^{235}\tau} - 1\}207 \quad (4.1)$$

Where Pb, Th, and U are in ppm, and $\lambda^{232}$, $\lambda^{238}$, and $\lambda^{235}$ are the radioactive decay constants of $^{232}$Th, $^{238}$U, and $^{235}$U, respectively.

To obtain statistically robust ages of monazite grains, multiple individual spot-analyses must be carried out for each chemical domain, and weighted mean ages calculated for

each age domain. Individual analyses that are far off the mean, show obvious chemical signs of contamination by an inclusion or mixing of zones were excluded from age calculations. Y is analysed to correct for its interference on Pb, and also because Y content can provide important information on monazite petrogenesis (Pyle et al., 2002). Correction factors were calculated for x-ray peak overlaps, including Y $L\zeta_1 - 2$ and Th $M\zeta_1 - 2$ peaks on Pb $M\alpha$, and Th $M\gamma$ on U $M\beta$ (Scherrer et al., 2000; Pyle et al., 2002; Gagné, 2004; Pyle et al., 2005; Gagné et al., 2009). Correction factors were calculated using the synthetic U- and Pb-free Y-Al-garnet (YAG), and pure $ThO_2$ standards to ensure a robust analysis of the Y and Th peak values. The analytical precision was checked during analysis against the in-house "Monazite53" major-element standard, and the GSC-8153 trace-element consistency standard. It is important here to note that the GSC-8153 standard was not used in calibrations but was used to monitor analytical precision, and in the quadratic error calculations reported with mean arithmetic ages, as discussed in Chapter 3.

A source of analytical variability in trace-element analysis of monazite is the selection of background values for Y, Pb, Th, and U. LREE's, Y, Pb, Th, and U are all significant components of monazite and many have overlapping x-ray peak positions. Since the distribution of x-ray peaks depends on the specific composition of the chemical zone, background positions must be determined for each element in each zone. The resulting x-ray spectra are interpreted by inspection by: (i) fitting the curve to a line of best-fit through the background values; (ii) marking the peak position for the element of interest; and (iii) determining the high- and low-background positions relative to that peak position, while carefully avoiding peak overlap with neighbouring x-ray peaks (Fig. 4.1). Pb was measured on the sensitive PETH crystal in tandem with a sealed Xe counter to minimize curvature in the resulting x-ray spectrum to eliminate most secondary LREE peaks (Gagné, 2004; Jercinovic and Williams, 2005; Pyle et al., 2005; Williams et al., 2006; Gagné et al., 2009). Given the small size of some chemical zones in the monazite grains analysed, an x-ray background scan was not always possible and average grain values were used. This may introduce some analytical uncertainty, and whilst this effect has not been quantified in this study, its effect on the interpretation is thought to be minimal given the large spans of time between monazite crystallization events which are on the order of 10's to 100's of millions of years.

Table 4.1: Instrument analytical conditions for major-element analysis.

| Elements | P | La | Si | Pr | S | Ce | Y | Nd |
|---|---|---|---|---|---|---|---|---|
| Name | P_Mzt | La_Mzt | Si_Mzt | Pr_Mzt | S_Mzt | Ce_Mzt | Y_Mzt | Nd_Mzt |
| X-ray Name | Ka | La | Ka | Lb | Ka | La | La | Lb |
| Order | 1 | 1 | 1 | 1 | 1 | 1 | 1 | 1 |
| Channel | 1 | 2 | 4 | 5 | 1 | 2 | 4 | 5 |
| Crystal | PETJ | LIF | TAP | LIFH | PETJ | LIF | TAP | LIFH |
| Spc.Pos.(mm) | 197.277 | 185.024 | 77.339 | 157.444 | 172.302 | 177.752 | 70.008 | 151.027 |
| Back(+) (mm) | 5 | 3.9 | 5 | 24.2 | 4.8 | 3 | 2.35 | 5.15 |
| Back(-) (mm) | 5 | 5 | 5 | 1.25 | 5 | 3 | 7.45 | 5.9 |
| Peak Seek W. | 1 | 1 | 1 | 1 | 1 | 1 | 1 | 1 |
| Time/Count | Time | Time | Time | Time | Time | Time | Time | Time |
| Mes.Time(sec) | 40 | 40 | 40 | 40 | 40 | 40 | 40 | 40 |
| Bac.Time(sec) | 20 | 20 | 20 | 20 | 20 | 20 | 20 | 20 |
| Mes.Count | 10000 | 10000 | 10000 | 10000 | 10000 | 10000 | 10000 | 10000 |
| Bac.Count | 500 | 500 | 500 | 500 | 500 | 500 | 500 | 500 |
| PHA gain | 16 | 32 | 32 | 32 | 16 | 32 | 16 | 32 |
| High V.(V) | 1730 | 1750 | 1650 | 1750 | 1708 | 1780 | 1724 | 1730 |
| Base L.(V) | 1 | 0.7 | 0.7 | 0.7 | 0.7 | 0.7 | 1 | 1 |
| Window (V) | 5 | 9.3 | 9.3 | 9.3 | 9.3 | 9.3 | 6 | 8 |
| Diff/Int | Diff | Diff | Diff | Diff | Diff | Diff | Diff | Diff |

| Elements | Th | Dy | Sm | U | Gd | Ca | Eu |
|---|---|---|---|---|---|---|---|
| Name | Th_Mzt | Dy_Mzt | Sm_Mzt | U_Mtz | Gd_Mzt | Ca_Mzt | Eu |
| X-ray Name | Ma | La | Lb | Mb | Lb | Ka | La |
| Order | 1 | 1 | 1 | 1 | 1 | 1 | 1 |
| Channel | 1 | 2 | 5 | 1 | 5 | 1 | 5 |
| Crystal | PETJ | LIF | LIFH | PETJ | LIFH | PETJ | LIFH |
| Spc.Pos.(mm) | 132.862 | 132.338 | 139.325 | 119.441 | 128.756 | 108.139 | 147.865 |
| Back(+) (mm) | 3 | 5.5 | 5.8 | 4 | 1.5 | 4.5 | 5 |
| Back(-) (mm) | 3.5 | 3.2 | 11.8 | 3.4 | 1 | 5 | 3.5 |
| Peak Seek W. | 1 | 0 | 0 | 0 | 0 | 1 | 1 |
| Time/Count | Time | Time | Time | Time | Time | Time | Time |
| Mes.Time(sec) | 40 | 40 | 40 | 40 | 40 | 40 | 40 |
| Bac.Time(sec) | 20 | 20 | 20 | 20 | 20 | 20 | 20 |
| Mes.Count | 10000 | 10000 | 10000 | 10000 | 10000 | 10000 | 10000 |
| Bac.Count | 500 | 500 | 500 | 500 | 500 | 500 | 500 |
| PHA gain | 16 | 32 | 32 | 16 | 32 | 16 | 32 |
| High V.(V) | 1682 | 1730 | 1730 | 1690 | 1610 | 1718 | 1750 |
| Base L.(V) | 1 | 0.7 | 1 | 2 | 1 | 0.7 | 0.7 |
| Window (V) | 5 | 9.3 | 8 | 4 | 9 | 9.3 | 9.3 |
| Diff/Int | Diff | Diff | Diff | Int | Diff | Diff | Diff |

## 4.3 Sample description

This section presents outcrop, petrographic, and monazite crystal morphology descriptions for the samples analysed in this study. Petrography and BSE imaging are very

Table 4.2: Instrument analytical conditions for minor-element analysis.

| Elements | Th | U | Y | Pb |
|---|---|---|---|---|
| Name | Th_Mtz | U_Mtz | Y_Mtz | Pb_Mtz |
| X-ray Name | Ma | Mb | La | Ma |
| Order | 1 | 1 | 1 | 1 |
| Channel | 1 | 2 | 4 | 5 |
| Crystal | PETJ | PETJ | TAP | PETH |
| Spc.Pos.(mm | 132.916 | 118.517 | 70.028 | 169.603 |
| Back(+) (mm) | 2 | 2.5 | 2 | 1 |
| Back(-) (mm) | 3 | 4 | 1 | 3 |
| Peak Seek W | 1 | 1 | 1 | 1 |
| Time/Count | Time | Time | Time | Time |
| Mes.Time(sec | 360 | 360 | 360 | 360 |
| Bac.Time(sec | 180 | 180 | 180 | 180 |
| Mes.Count | 10000 | 10000 | 10000 | 10000 |
| Bac.Count | 500 | 500 | 500 | 500 |
| PHA gain | 16 | 64 | 16 | 64 |
| High V.(V) | 1682 | 1716 | 1724 | 1756 |
| Base L.(V) | 1 | 2.5 | 1 | 2.5 |
| Window (V) | 5 | 3 | 6 | 3 |
| Diff/Int | Diff | Diff | Diff | Diff |

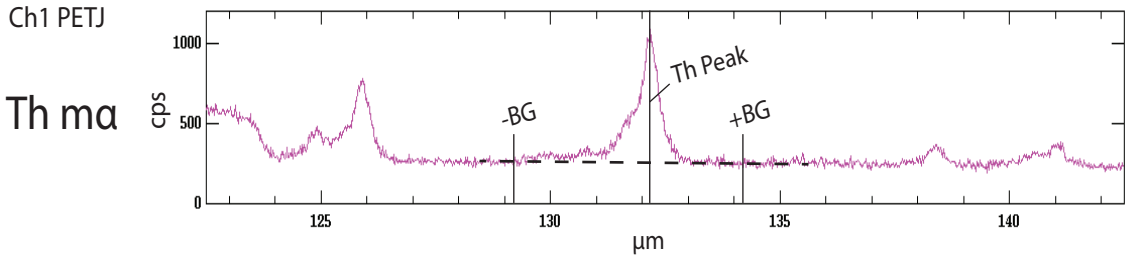


Figure 4.1: Example of background selection procedure for high and low background positions on the Th M$\alpha$ peak from WDS scan of monazite.

useful in ascertaining where monazite is concentrated in the rock, and what phases may have been in chemical communication. The textures of the monazite grain seen in BSE images can help investigate the intra-crystal zoning pattern, provide insight into crystal growth stages, and help target subsequent chemical analyses.

### *4.3.1 CA108b*

Sample CA108b is a K-feldspar-rich sillimanite-bearing paragneiss from the BBLSZ (Fig. 3.1). This rock is intercalated with quartzite and mafic horizons of similar mineralogy but lacking aluminosilicate. This unit and the associated lithologies are well exposed along the side of a logging road in the interior Kiosk domain. In outcrop and hand sample this rock is dominated by thick, pink K-feldspar-rich layers intercalated with dark garnet-rich layers. The rock is streaked with thin layers of white, chalky sillimanite, typically at the interface of the K-feldspar- and garnet-rich layers (Fig. 4.2a). The foliation is defined by the dark garnet-rich layers and dips at 120/23; no stretching lineation was observed in the field.

This rock contains the equilibrium assemblage of Ksp - Qtz - Grt - Pl - Bt ± Ilm ± Sil ± Ap. The compositional layering observed at outcrop-scale is reflected in thin-section, with thick K-feldspar-rich layers and garnet-rich layers on the scale of several millimetres to over a centimetre thick. Garnet occurs throughout the rock, however, it differs texturally between the compositional bands. In garnet-rich bands, garnet grains tend to be much larger and were deformed and elongated parallel to the foliation, whereas in the K-feldspar-rich layers garnets tend to be small and ovoid. Both types of garnets preserve evidence of melting, showing lobate infiltration patterns of K-feldspar or plagioclase along grain boundaries, or concentrated along cracks or pathways toward the centre of the grain (Fig. 4.2b). Monazite grain size is typically below the resolution of optical microscopy, but grains large enough to be seen are associated with apatite and garnet, most commonly along the interface between garnet-rich and K-feldspar-rich layers (Fig. 4.2c). This rock is relatively biotite-poor, with biotite concentrated in garnet-rich layers. The felsic matrix minerals in this rock show evidence of static recrystallization and recovery, such as small polygonal grains, triple points between K-feldspar, plagioclase and quartz, and strain-free quartz.

Back-scatter electron imagery is the best way to image the internal zoning of monazite grains. There are two types of grain morphologies in this rock that are independent of the host compositional layer: (i) large grains (100's of microns) that are complexly chemically zoned (Fig. 4.3a and b); and (ii) small grains (10's of microns) that have simple concentric zoning (Fig. 4.3c and d). In this study one grain of each morphological type was chosen for detailed chemical analysis to test if grain morphology reflects recorded ages. The large monazite grain measures approximately 350x200 microns, and contains five internal zones (Fig. 4.3b). The small monazite grain measures approximately 150x90 microns, and contains three internal zones (Fig. 4.3d). The internal zoning is discussed further in section 4.4.

### *4.3.2 PS08-101a*

Sample PS08-101a, a K-feldspar-biotite sillimanite-bearing paragneiss that lies in the footwall of the BBLSZ, preserves a well developed foliation (Fig. 3.1). In hand-sample, the foliation is defined by K-feldspar and biotite-rich compositional bands. There are a few isolated porphyroclasts of plagioclase and white K-feldspar with pink K-feldspar-biotite mantles. Garnet forms relatively sparse, large rounded grains that are several millimetres across. Aluminosilicate is difficult to see in hand sample; however, sample PS08-101b, a second sample of the same paragneiss unit, contains isolated, wispy layers of white sillimanite (Fig. 4.4a).

This rock contains the assemblage Ksp - Pl - Qtz - Bt - Grt - Sil $\pm$ Ilm $\pm$ Chl $\pm$ Ms. Compositional banding in this sample is on the millimetre scale, and is defined by elongate ribbons of K-feldspar and quartz, and biotite grains display a crystallographic preferred orientation (Fig. 4.4b). Sparsely distributed, rounded garnets and are wrapped by rims of matrix biotite, and some larger garnets have numerous biotite inclusions (Fig. 4.4c). Though the foliation of this rock is well developed (Fig. 4.4b), the garnets are largely undeformed. There are also several large K-feldspar porphyroclasts that average 3-5 mm across. These grains tend to be rimmed by recrystallized zones of K-feldspar and biotite, with matrix biotite wrapping around these grains. This suggests that both large

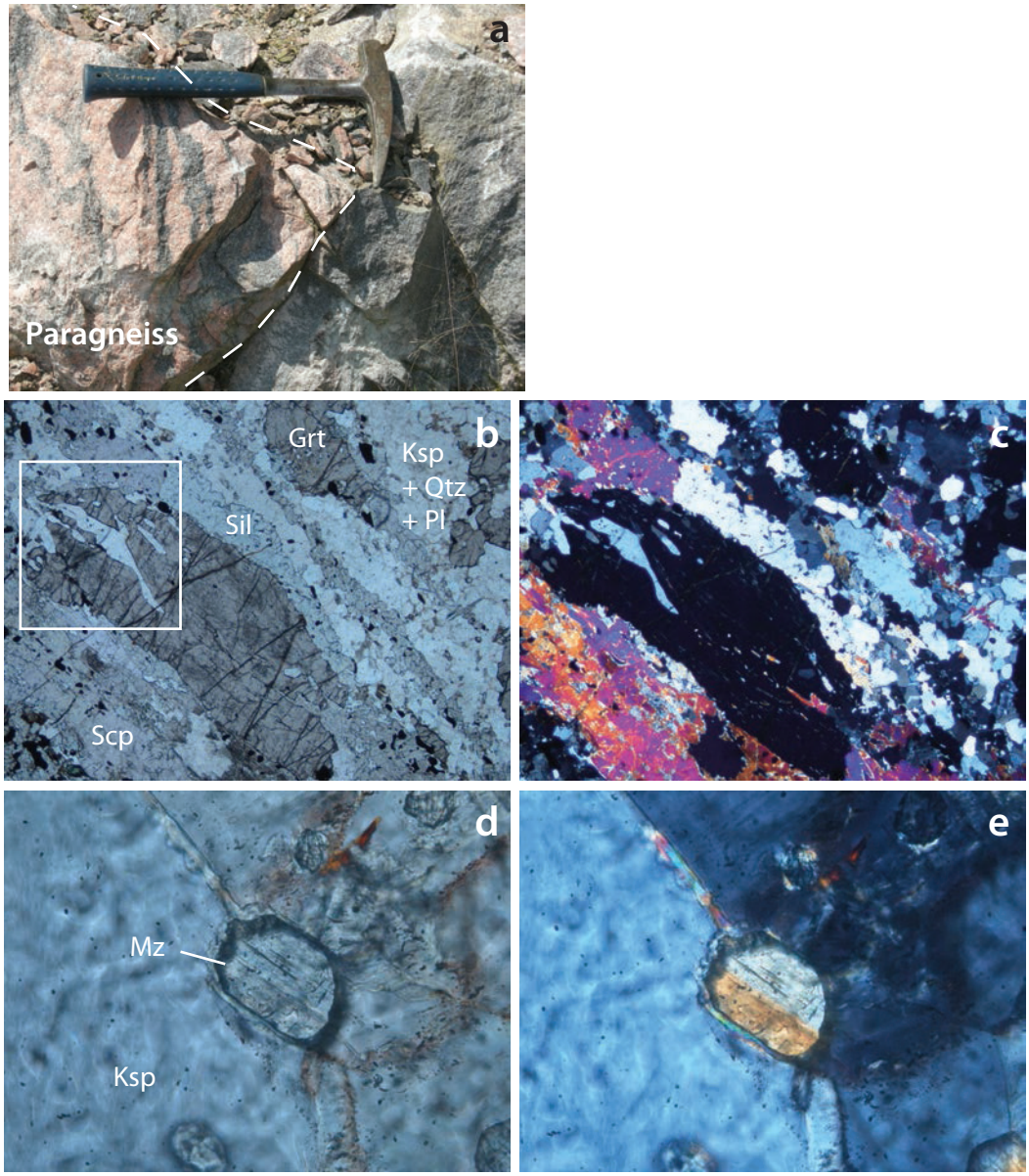


Figure 4.2: Outcrop pictures and photomicrographs for sample CA108b. a) Outcrop picture showing sample location and fabric (UTM x: 650709, y: 5068739). Photomicrographs of garnet-rich layer showing the flattened garnets aligned parallel with the dominant foliation. The flattened garnet grain shows evidence of feldspar melt infiltration (white box). Note the stretched sillimanite grains surrounding the large garnet porphyroclasts ( b) PPL c) XPL; FOV=6.25mm). Photomicrographs of a large monazite grain with the characteristic yellow birefringence colour, and simple twinning. ( d) PPL e) XPL; FOV=0.25mm).

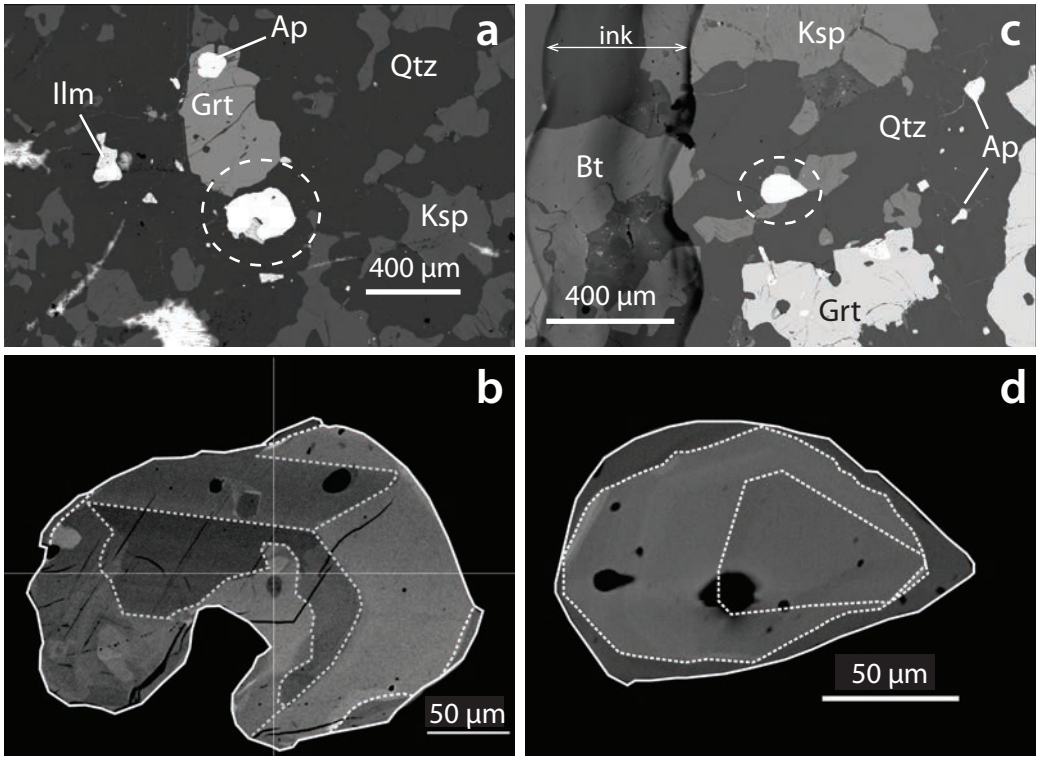


Figure 4.3: BSE images of the two grains analysed in sample CA108b. a) Image of the large monazite grain (dashed circle) showing the relation to surrounding phases. b) Detailed image of the large monazite grain showing the internal zoning pattern. c) Image of the small monazite grain (dashed circle) showing the relation to surrounding phases. d) Detailed image of the small monazite grain showing the internal zoning pattern.

garnet and large Ksp porphyroclasts pre-date the formation of the current biotite-rich fabric. Quartz grains display undulose extinction, and other evidence of recrystallization and recovery includes straight grain boundaries between most phases, especially K-feldspar - plagioclase - quartz - garnet, as well as triple points between these phases, and evidence of quartz grain boundary migration (Fig. 4.4d). Monazite in this rock was too small to be seen in thin-section, however, prior to analysis other phosphate minerals such as apatite, were observed in thin-section, suggesting the possibility that other phosphate phases, namely monazite, may exist in this rock.

Back-scatter electron imagery was the only way to confirm the presence of monazite in this rock. Monazite grains exhibit a common morphology, and tend to be small and irregular with simple zoning patterns. The larger matrix grains are associated with garnet, but in a few instances occur in the deformed Ksp-Qtz ribbons. In this study one grain from the Ksp-Qtz ribbon (Fig. 4.5a and b) and one from the matrix (Fig. 4.5a and b) were chosen for detailed analysis to test if monazites in these different textural domains recorded different chemical compositions or ages.

## 4.4 Monazite chemical zoning and analytical results

The major and trace-element chemical compositions of monazites were studied in detail for the four grains selected for geochronology. High-resolution WDS maps were created to ascertain internal chemical zoning patterns. Quantitative chemical analysis was carried out in each distinct intra-crystal chemical zone using WDS analysis. The major elements analysed in order of increasing atomic number, were Si, P, S, Ca, La, Ce, Pr, Nd, Sm, Eu, Gd, and Dy. The trace elements analysed for U-Th-Pb geochronology were Y, Pb, Th, and U. Individual analysis points were grouped based on chemical and age domains, and weighted mean ages were calculated on zones with multiple analysis points to ensure statistically robust values. Populations of ages were fit to a Gaussian curve in the probability density plot, which itself is not a rigorous age calculation method, but is rather a simple graphical tool for representation of a population of age data. Results for major and minor element analyses are given in Appendix B.

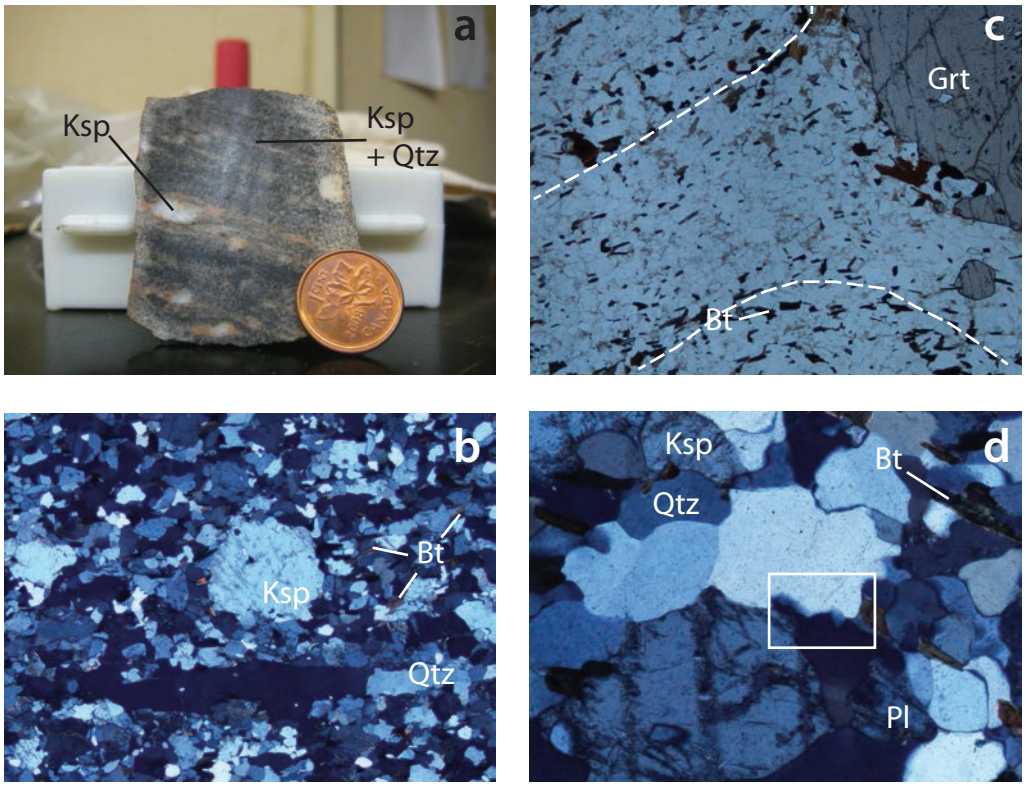


Figure 4.4: Hand-sample pictures and photomicrographs for sample PS08-101a. a) Hand-sample picture showing the well-developed fabric and Ksp porphyroclasts (penny for scale; UTM x: 646836, y: 5069917). b) Photomicrograph showing the flattened the flattened Ksp-Qtz ribbon aligned parallel with the dominant foliation. Also shown is a small Ksp porphyroclast (XPL, FOV=6.25mm). c) Photomicrograph showing the matrix of Ksp + Qtz + Bt wrapping around a large Grt porphyroclast (PPL, FOV=6.25mm). c) Photomicrograph highlighting the straight grain boundaries and triple-points in Qtz and Ksp (centre-left). Also note grain relict boundary migration textures in Qtz (box).

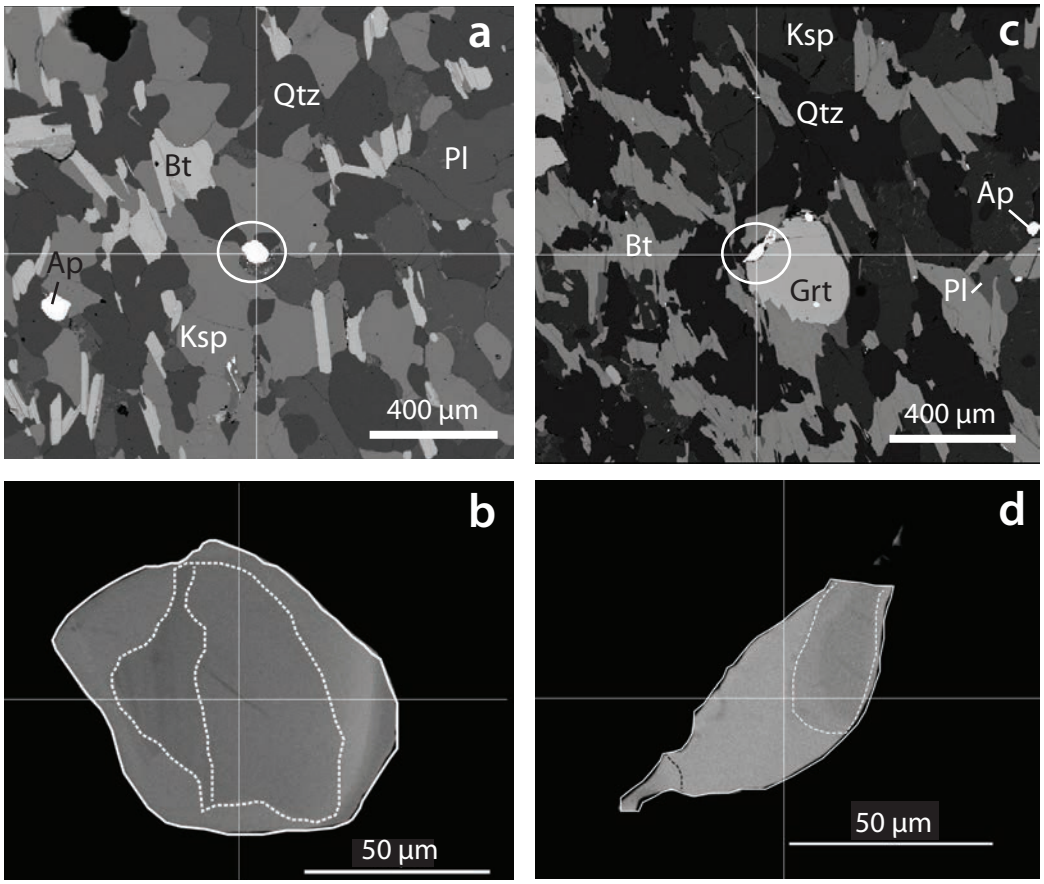


Figure 4.5: BSE images of the two grains analysed in sample PS08-101a. a) Image of the Ksp-Qtz ribbon monazite grain (dashed circle) showing the relation to surrounding phases. b) Detailed image of the Ksp-Qtz ribbon monazite grain showing the internal zoning pattern. c) Image of the matrix monazite grain (dashed circle) showing the relation to surrounding phases. d) Detailed image of the matrix monazite grain showing the internal zoning pattern.

A summary table of weighted mean ages for each zone in each grain analysed is given in Table 4.3.

Table 4.3: Summary table of monazite weighted mean ages.

| Sample | Zone 1 | Zone 2 | Zone 3 | Zone 4 | Zone 5 |
|---|---|---|---|---|---|
| ***CA108b*** | | | | | |
| Large grain | 1485±23 | 1484±26 | 1078±24 | 1473±33 | 1485±17 |
| Small grain | 1464±26 | 1435±24 | 1058±19 | | |
| ***PS08-101a*** | | | | | |
| Ribbon grain | 1158±9 | 1177±10 | 1157±15 | | |
| Matrix grain | 1204±13 | 1170±7 | 1136±8 | | |

### *4.4.1 CA108b*

**Large matrix grain** The larger grain displayed a complex zoning pattern consisting of five distinct chemical zones. The most diagnostic element maps for visualizing intra-crystal chemical zones were Y and Th (Fig. 4.6a through c). Chemical zone 1 has the highest Y concentration and an intermediate Th concentration. Chemical zone 2 has a low concentration of Y relative to zone 1, and the highest concentration of Th in the crystal. Chemical zone 4 falls in the same Y concentration range as zone 2, but with distinctly lower concentrations of Th. Chemical zone 3 forms a very thin and poorly preserved outermost zone. This zone is distinct in its increased Y and decreased Th content that does not follow the crystal sector zoning pattern of the ”core” zones 1, 2, and 4. Chemical zone 5 is a zone of intermediate composition in the lower portion of the grain.

The large monazite grain has a complex zoning pattern consisting of five distinct zones, however; there are only two statistically distinct age domains (Fig. 4.7a and b). The outermost rim zone, only preserved as small tips and thin edges on the grain, yield a weighted mean age of 1078±24 Ma (Fig. 4.7c). The rest of the grain contains no statistically distinct age domains, and is interpreted as a single ”core zone,” with a weighted mean age of 1483±11 Ma (Fig. 4.7d).

**Small matrix grain** The smaller grain has a simple concentric zoning pattern consisting of three distinct chemical zones. As was the case for the large monazite, the most

diagnostic element maps were Y and Th (Fig. 4.6d through f). Chemical zones 1 and 2 show concentric growth zoning, with zone 1 having a low Y and relatively low Th signal, and zone 2 showing a steady increase in Y and Th concentration from the centre of the crystal to the edge of the zone. Zone 3, the outermost rim of the grain, is characterized by a notably higher concentration of Y, and lower concentrations of Th relative to the core of the grain.

The smaller monazite grain has a simple concentric zoning pattern with three distinct zones, however; there are only two statistically distinct age domains (Fig. 4.8a and b). The outermost rim zone has a weighted mean age of 1058±19 Ma (Fig. 4.8c). The inner two chemical zones of this grain are not statistically distinct age domains, and is interpreted as a single "core zone," with a weighted mean age of 1448±18 Ma (Fig. 4.8d).

### *4.4.2 PS08-101a*

**Chemical zoning** The element suite used in WDS mapping of grains from PS08-101a was different from the standard Y, U, Th and Pb suite. At the time of analysis U and Pb were giving problematic results, so the decision was made to use a different element suite. One grain from the matrix was WDS mapped in detail for Y, Pb, Ce, and Ca. A second grain from the matrix was mapped in detail for Y, Pb, Ce, Ca, and Th.

Both grains have similar chemical characteristics despite their different textural relationships in the rock, including variable zoning patterns and three distinct zones in BSE images. The most useful element maps were Y and Ca (Fig. 4.9). Both these grains show a low-Y core, and progressively higher Y concentration with each successive zone. The inverse relationship is true of Ca concentration in these grains, with high-Ca cores changing to low-Ca rims.

**K-feldspar-quartz ribbon grain** Monazite from the Ksp-Qtz-rich ribbon has three texturally and chemically distinct zones, however; there are only two statistically distinct age populations (Fig. 4.10a and b). The weighted mean age for zone 3 is 1178±9 Ma (Fig. 4.10c). The weighted mean ages for zones 1 and 2 combined is 1154±7 Ma (Fig. 4.10d).

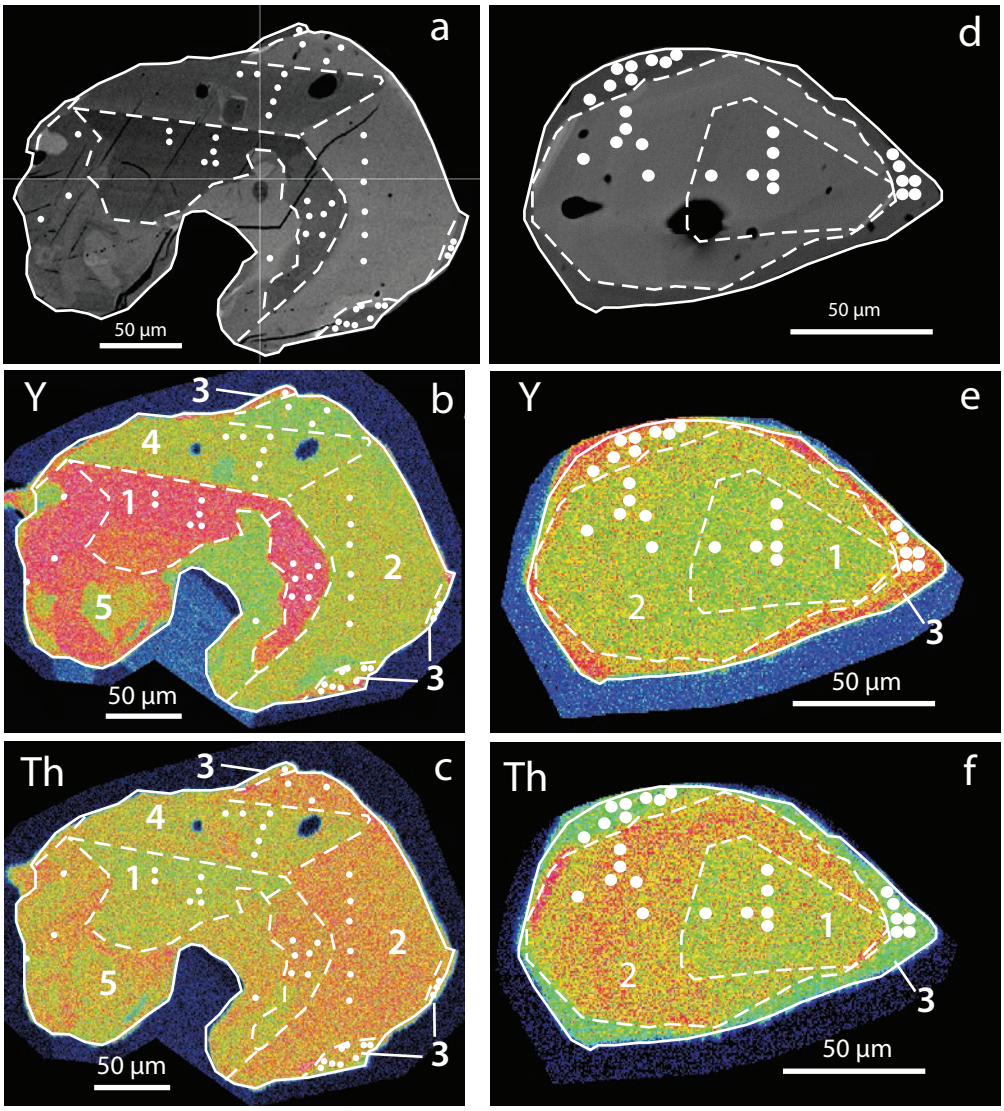


Figure 4.6: WDS chemical maps for two grains analysed in CA108b discussed in text. Circle size is proportional to beam size. a) reference BSE image of large grain showing analysis locations, and internal zone boundaries based on BSE images and chemical zoning. b) Y WDS map of large grain. c) Th map of large grain. d) reference BSE image of small grain showing analysis locations, and internal zone boundaries based on BSE images and chemical zoning. e) Y WDS map of small grain. f) Th map of small grain. Note the dark spot in (d) is a beam damaged zone from prolonged WDS analysis of that location. Colour scales in these maps are schematic, and highlight relative differences in chemical concentration rather than absolute values.

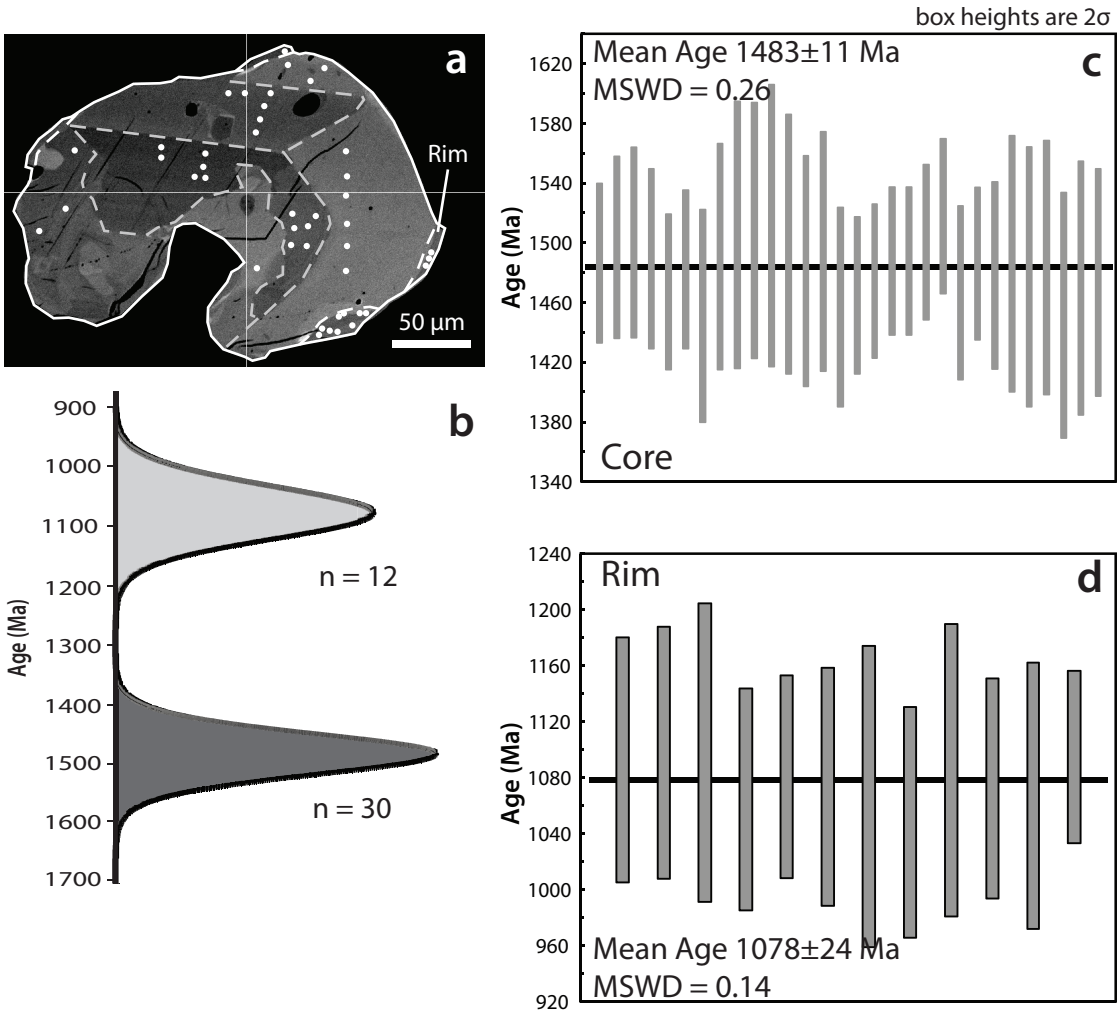


Figure 4.7: Geochronology results for the large grain in sample CA108b. Circle size is proportional to beam diameter, and dashed lines separate chemical zones. a) reference BSE image of large grain showing analysis locations, and internal zone boundaries based on BSE images and chemical maps. Note the small, poorly preserved outer rim zone. b) Probability density curves for age populations in the large monazite grain. c) Weighted mean age of the core zones. d) Weighted mean age of the rim zone.

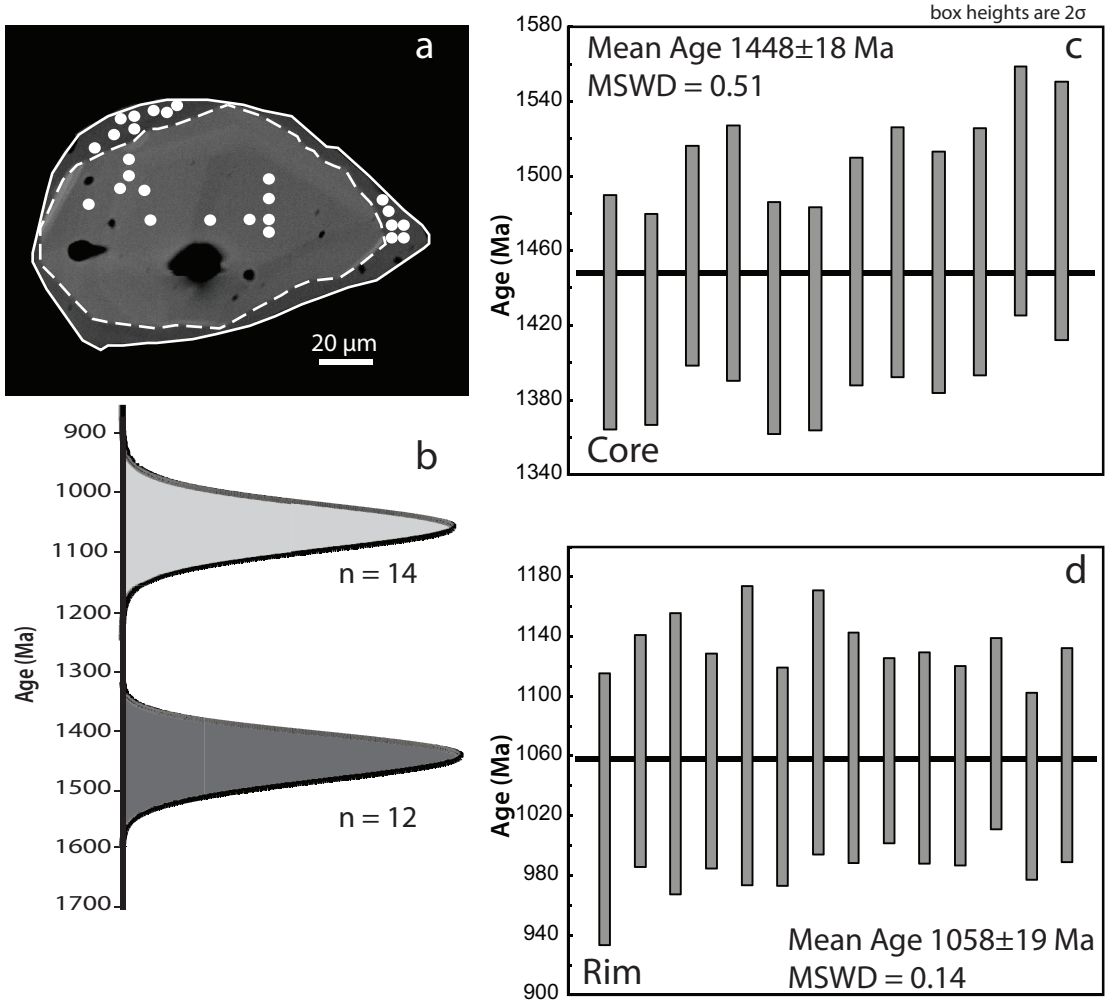


Figure 4.8: Geochronology results for the small grain in sample CA108b. Circle size is proportional to beam diameter, and dashed lines separate chemical zones. a) reference BSE image of large grain showing analysis locations, and internal zone boundaries based on BSE images and chemical maps. b) Probability density curves for age populations in the small monazite grain. c) Weighted mean age of the core zones. d) Weighted mean age of the rim zone.

**Matrix grain** The smaller matrix grain has three distinct textural and chemical zones that correspond to statistically distinct age populations (Fig. 4.11a and b). The weighted mean age for zone 1 is 1204±13 Ma (Fig. 4.11c). The weighted mean age for zone 2 is 1170±7 Ma (Fig. 4.11d). The weighted mean ages for zone 3 is 1136±8 Ma (Fig. 4.11e).

## 4.5 Discussion

The monazite geochronology data produced in this study suggest protracted and episodic phases of monazite crystallization in the Kiosk domain. Episodic monazite crystallization has been observed in many monazite geochronology studies, but the controls on this phenomena are as yet poorly understood (Foster et al., 2002; Foster and Parrish, 2003). The most common approach is to study multiple grains from a given rock to find commonalities in ages, and describe statistically distinct age populations. This monazite geochronology study was carried out at the reconnaissance level to test the feasibility of the method, and does not have the data density required to define the statistical populations of ages of crystallization or re-crystallization events that may be present in the samples analysed. It can, however; provide important first-order data on the major phases of deformation and metamorphism experienced by paragneisses in the Kiosk domain.

### *4.5.1 ca. 1480-1450 Ma ages*

The ca. 1480 Ma and ca. 1450 Ma monazite cores from sample CA108b may represent the initial episodic growth of monazite at high metamorphic grade during the Pinwarian orogeny. Whilst monazite can survive weathering and burial in sedimentary basins, it is likely chemically reactive at low grades of metamorphism in many silica-rich bulk compositions such that detrital monazite is only rarely found in metamorphic rocks (Parrish, 1990; Morton and Hallsworth, 1999). Metamorphic monazite is the dominant replacement mineral of precursor allanite, apatite, pre-existing igneous monazite, and other REE-rich phosphates at amphibolite-grade and higher metamorphic conditions (Smith and Barreiro, 1990; Pan, 1997; Finger et al., 1998; Ayers et al., 1999; Townsend et al., 2000; Foster and Parrish, 2003). Monazite present in the Kiosk domain paragneiss is interpreted to be the result of: (i) growth during prograde metamorphism; or (ii) inherited igneous monazite. As discussed in Chapter 3, ca. 1450 Ma ages recorded in zircon ages and trace-element

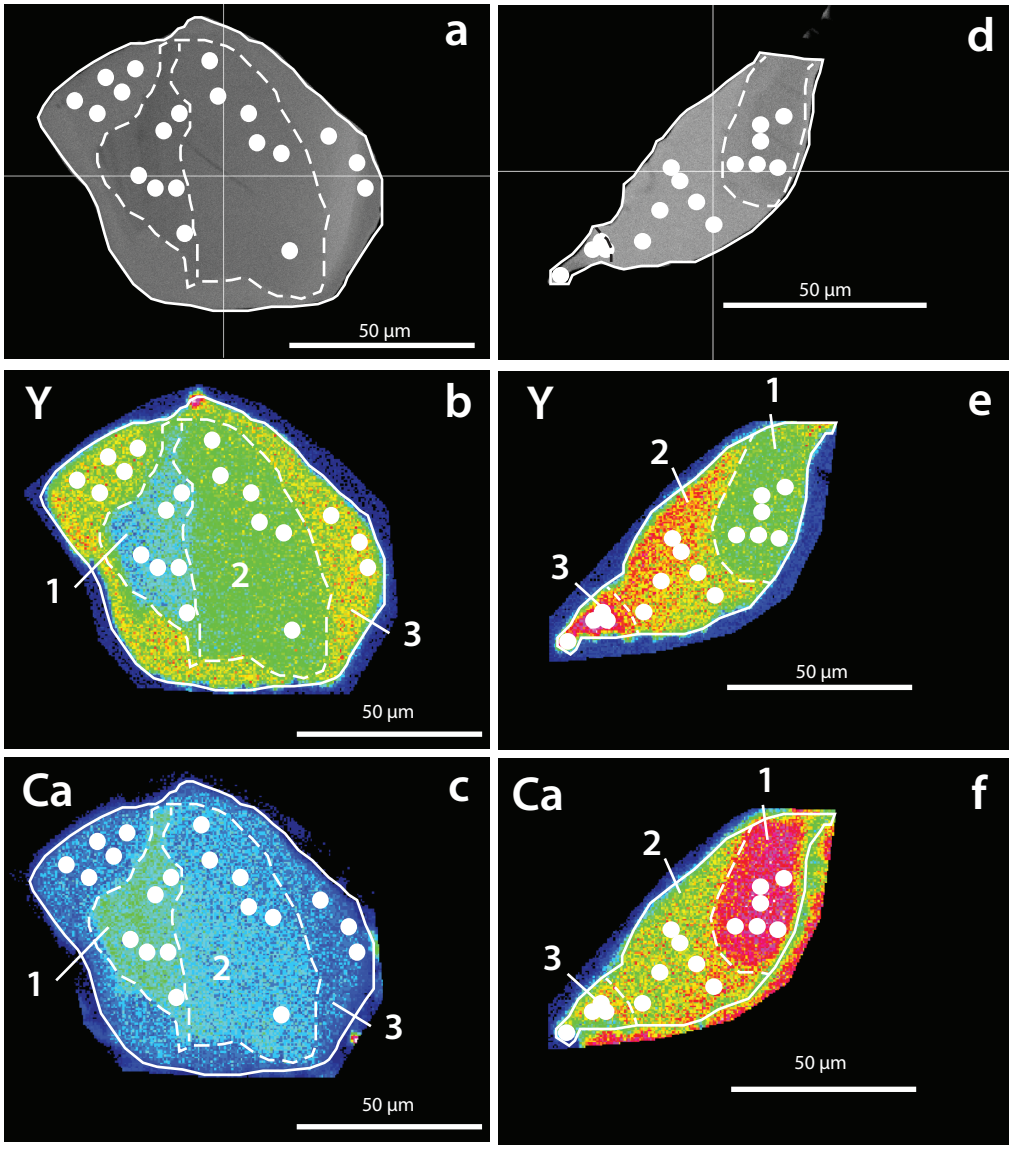


Figure 4.9: WDS chemical maps for two grains analysed in PS08-101a discussed in text. a) reference BSE image of Ksp-Qtz ribbon grain showing analysis locations, and internal zone boundaries based on BSE images and chemical zoning. b) Y WDS map of Ksp-Qtz ribbon grain. c) Ca map of Ksp-Qtz ribbon grain. d) reference BSE image of matrix grain showing analysis locations, and internal zone boundaries based on BSE images and chemical zoning. e) Y WDS map of matrix grain. f) Ca map of matrix grain. Colour scales in these maps are schematic, and highlight relative differences in chemical concentration rather than absolute values.

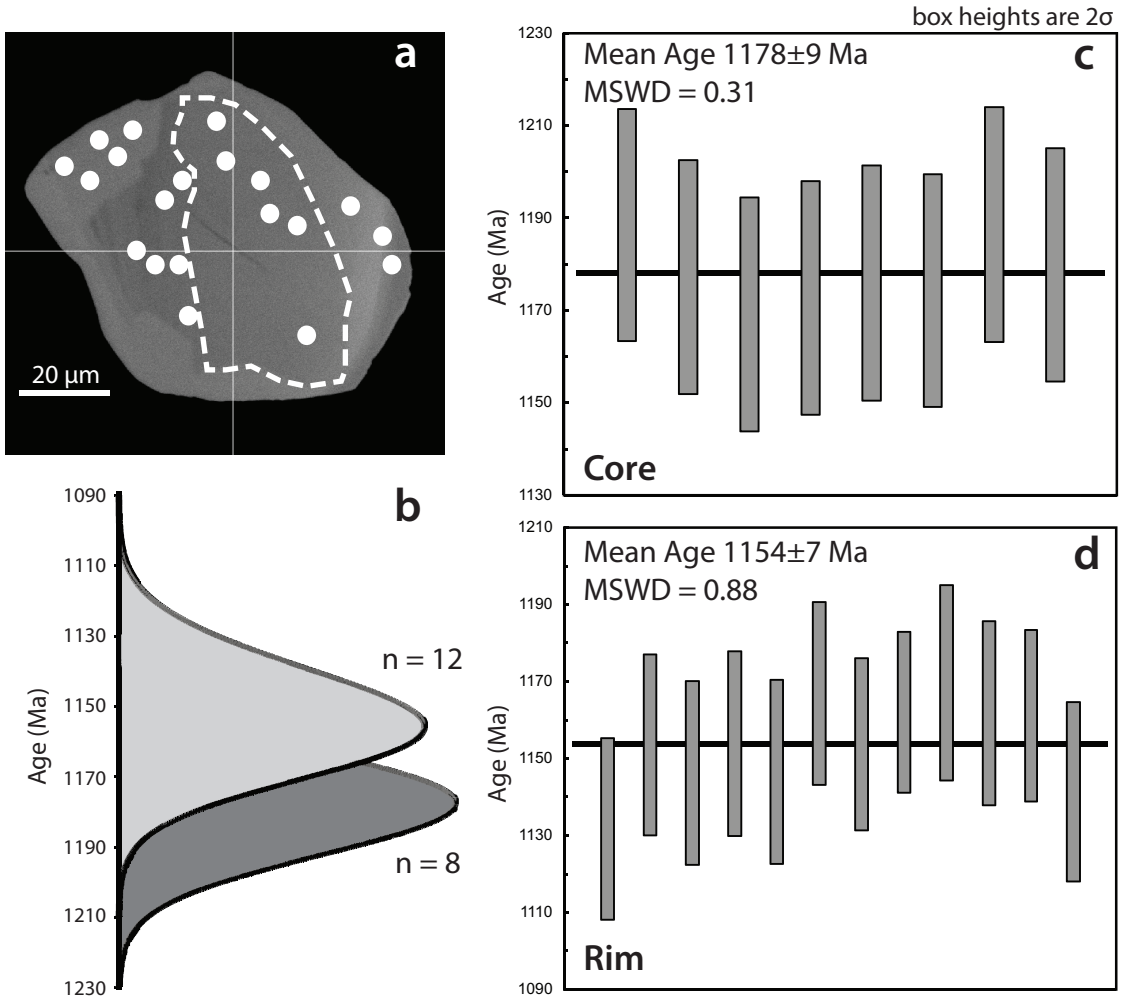


Figure 4.10: Geochronology results for the Ksp-Qtz ribbon grain in sample PS08-101a. a) reference BSE image of Ksp-Qtz ribbon grain showing analysis locations, and internal zone boundaries based on BSE images and chemical zoning. Note here that the "rim" zone refers to chemical zones 1 and 2 that are the same age. b) Probability density curves for age populations in the Ksp-Qtz ribbon monazite grain. c) Weighted mean age of zones 1 and 3. d) Weighted mean age of zone 2.

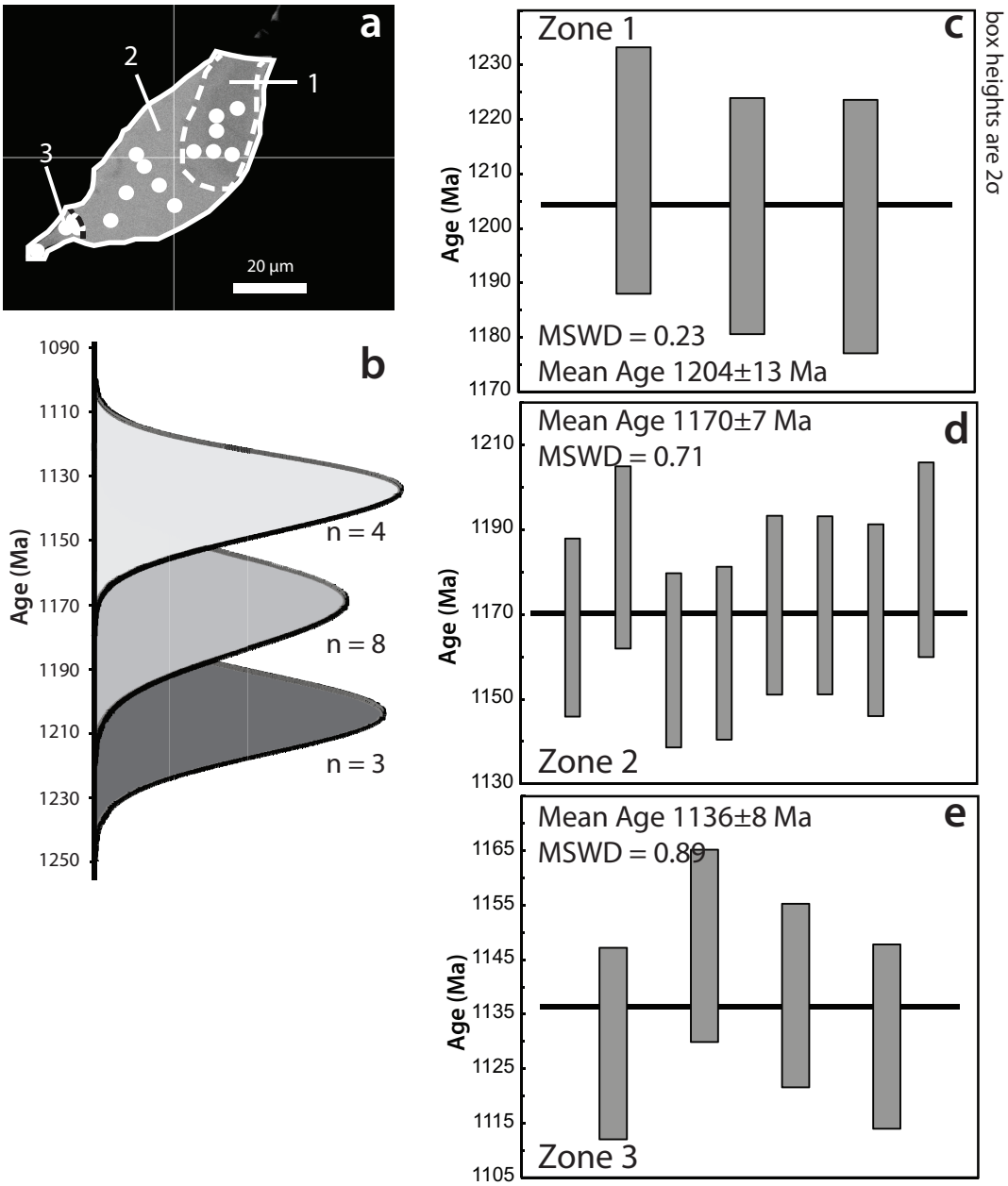


Figure 4.11: Geochronology results for the matrix grain in sample PS08-101a. a) reference BSE image of matrix grain showing analysis locations, and internal zone boundaries based on BSE images and chemical zoning. Note that the age zones here follow the chemical zoning pattern discussed earlier in the text. b) Probability density curves for age populations in the matrix monazite grain. c) Weighted mean age of zone 1. d) Weighted mean age of zone 2. e) Weighted mean age of zone 3.

geochemistry demonstrates that this was a period of widespread high-grade metamorphism and migmatization of the Kiosk domain. Furthermore, ca. 1470-1340 Ma was a time of widespread high-grade metamorphism and plutonism in the southwest CGB (e.g. Davidson, 1986a; van Breemen et al., 1986; Krogh et al., 1992; Krogh, 1993; Tuccillo et al., 1992; Corrigan et al., 1994; Ketchum et al., 1994, 1998). The similarity of these ages suggests that these rocks were affected by the same period of high-grade metamorphism and igneous activity.

### *4.5.2 ca. 1200-1135 Ma ages*

Monazites from sample PS08-101a record a history of protracted and episodic crystallization during the Shawinigan pulse (ca. 1200-1140 Ma; Rivers, 1997; Corriveau and van Breemen, 2000; Rivers et al., 2002). The two grains analysed record five statistically distinct ages from the different chemical zones of the grains, at ca. 1200 Ma, ca. 1180, ca. 1170 Ma, ca. 1150 Ma, and ca 1135 Ma (figs. 4.10 and 4.11). Several geochronology studies in orthogneisses, paragneisses, and pelites in the southwest CGB have shown a protracted tectonic event from ca. 1160-1100 Ma (van Breemen and Hanmer, 1986; van Breemen et al., 1986; Tuccillo et al., 1992; Mezger et al., 1993; Carr and Berman, 1996, 1997). These ages also coincide with widespread emplacement of coronitic metagabbros in the southwestern CGB at ca. 1170±30 to 1152±2 Ma (Davidson, 1986c; Davidson and van Breemen, 1988; Heaman and LeCheminant, 1993; Dudas et al., 1994).

### *4.5.3 ca. 1080-1060 Ma ages*

Rims of grains in sample CA108b from the BBLSZ record monazite crystallization at ca. 1080 and 1060 Ma. As discussed in Chapter 3 many geochronological studies show that at ca. 1080 Ma to ca. 1040 Ma the western CGB was undergoing a protracted episode of high-grade metamorphism associated with thrust imbrication and thickening during the peak of the Ottawan pulse (Davidson and van Breemen, 1988; Nadeau, 1990; van Breemen and Davidson, 1990; Krogh et al., 1992; Tuccillo et al., 1992; Krogh et al., 1993; Mezger et al., 1993; Wodicka, 1994; Bussy et al., 1995; Rivers, 1997; Timmermann et al., 1997; Slagstad, 2003; Slagstad et al., 2009). Furthermore, Davidson and van Breemen (1988) and van Breemen and Davidson (1990) noted metamorphism and reworking of the

suite of coronitic olivine metagabbros in the western CGB during this tectonic episode coeval with the reworking of their host gneisses.

## 4.6 Conclusions

1. The cores of monazites in paragneiss from the BBLSZ (sample CA108b) preserve evidence of a pre-Grenvillian initial monazite crystallization event at ca. 1480-1450 Ma.

2. Monazites in paragneiss from the interior of the Kiosk domain in the footwall of the BBLSZ (sample PS08-101a) record Grenvillian protracted and episodic monazite crystallization at ca. 1200-1135 Ma.

3. The rims of monazites in paragneiss from the BBLSZ (sample CA108b) record Grenvillian monazite crystallization event at ca. 1080-1060 Ma.

# CHAPTER 5

# $^{40}$AR/$^{39}$AR THERMOCHRONOLOGY

## 5.1 Introduction

There have been few $^{40}$Ar/$^{39}$Ar thermochronology studies completed in the Kiosk subdomain. In other locations in the CGB and GFTZ argon cooling ages have provided useful in constraints on exhumation history of lithotectonic domains, and thermal history of shear zones (e.g. Haggart et al., 1993; Reynolds et al., 1995). The purpose of this study was to elucidate the cooling history of the NTLSZ and resolve any thermal break across the northern boundary of the Algonquin domain.

Re-evaluating the amphibole data of Ratcliffe (2011), combined with a new amphibole sample from this study, it can be demonstrated that the NTLSZ cooled through the amphibole $^{40}$Ar closure temperature at ca. 1030 Ma. Amphibole $^{40}$Ar/$^{39}$Ar data from the Powassan domain record a cooling age of ca. 1100 Ma, representing a break in thermal history of ca. 70 Ma from hangingwall to footwall of the Northern Algonquin domain boundary.

A map showing the location of the three amphibole samples evaluated in this study is presented in figure 3.1.

**Summary of relevant amphibole thermochronology data** The study of Cosca et al. (1991) focussed on $^{40}$Ar thermochronology of the Algonquin domain and the western

CGB. They studied amphibole separates from a variety of rock types within the Algonquin domain, separating metamorphic amphibole grains to elucidate the cooling of the CGB through ca. 500°C. Their study revealed a spread of ages ranging from ca. 930 Ma to ca. 1025 Ma, with most rocks cooling through amphibole closure at ca. 1000 Ma (Fig. 5.1). Their northernmost sample *MR86-1A* is particularly interesting in that, though it is not the closest sample geographically, its plateau age of 1025±3 Ma matches almost exactly the plateau age of JF10-35. The authors suggested that cooling was relatively uniform within lithotectonic domains, but variable between domains. These findings are consistent with other studies in the CGB (e.g. Dallmeyer and Sutter, 1980; Cosca et al., 1992; Haggart et al., 1993; Reynolds et al., 1995). Cosca et al. (1991) suggested that the non-systematic variation and spread in the $^{40}$Ar amphibole closure temperatures is related to differential exhumation related to erosion, relative tectonostratigraphic position within the orogen, or late-stage extensional tectonics.

## 5.2 Method

The following criteria were used for selection of samples for hornblende separation and analysis : (i) abundant amphibole in the rock; (ii) minimal inclusions of biotite in large amphibole grains; and (iii) consistent amphibole mineral chemistry. Two samples (JF10-35 and JF10-39) met these criteria and were chosen for analysis.

McDougall and Harrison (1988, 1999) described the principles and method of $^{40}$Ar/$^{39}$Ar dating. Amphibole grains were separated from orthogneiss samples JF10-35 and JF10-39 at the crystal isolation facility at Dalhousie University. The sample processing followed the in-house laboratory protocol for zircon crystal separation outlined in section 3.2. A by-product of separation of zircons is the production of a mafic mineral fraction. Individual amphibole grains were hand-picked to obtain a pure mineral concentrate for analysis. The separated amphibole concentrates were individually wrapped in aluminium foil, then stacked in an aluminium irradiation canister. Interspersed among the samples were five to seven aliquots of the flux monitor, Fish Canyon tuff sanidine, which has an apparent K-Ar age of 28.205±0.046 Ma (Kuiper et al., 2008). The canister was irradiated with fast neutrons in the nuclear reactor at McMaster University in Hamilton, Ontario, Canada.

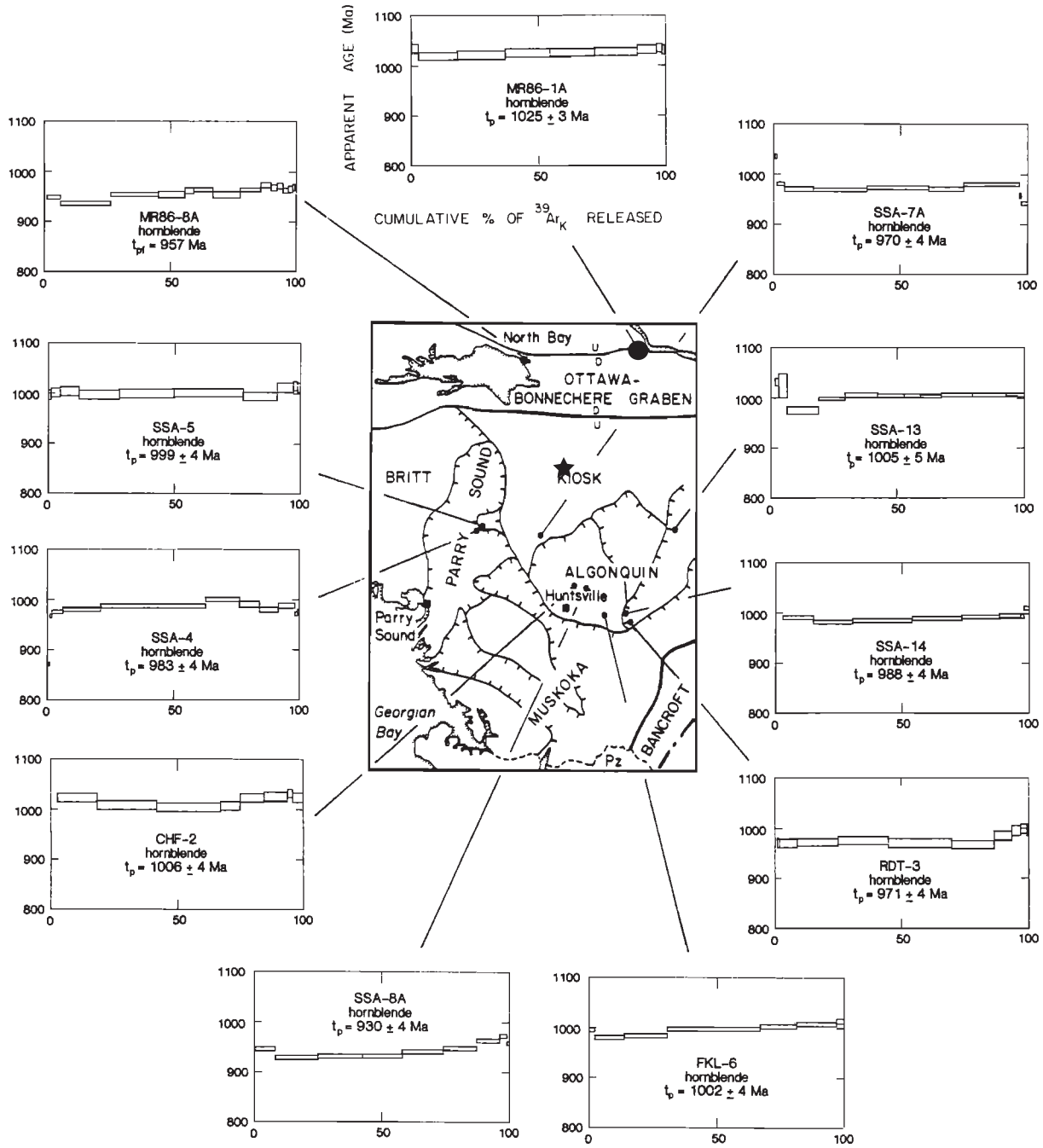


Figure 5.1: Amphibole $^{40}Ar/^{39}Ar$ age spectra reported in Cosca et al. (1991). The location of samples MF86-1A (black circle) and JF10-35 (black star) are indicated (modified from Cosca et al., 1991)

At Dalhousie University, a double-vacuum tantalum resistance furnace was used to carry out the step-heating. Isotopic analyses were made using a VG3600 mass spectrometer using both Faraday and electron multiplier collectors to measure the abundance of $^{39}$Ar for $^{40}$Ar/$^{39}$Ar and $^{36}$Ar/$^{39}$Ar ratios, respectively. Errors are reported at the $2\sigma$ level and include the uncertainty in the irradiation parameter, $J$, but not uncertainty in the assumed age of the flux monitor (*K. Taylor, pers. comm. 2012*).

Amphibole $^{40}$Ar/$^{39}$Ar data were processed and age plots were created using Isoplot (Ludwig, 2003). The definition of "plateau age" follows that of Ludwig (2003), and requires that: (i) three or more contiguous steps comprising more than 60% of the $^{39}$Ar; (ii) the probability-of-fit of the weighted-mean age of the steps is greater than 95%; (iii) the slope of the error-weighted line through the plateau ages is zero at 5% confidence; (iv) the ages of the outermost two steps on either side of the plateau must not be significantly different from the weighted-mean plateau age (at $2\sigma$); and (v) the outermost two steps on either side of the plateau must not have non-zero slopes with the same sign (at $2\sigma$).

Data from sample LR10-3.3 (prefix *LR10* used here to distinguish from *JF10* samples) were re-evaluated using the plateau age definition of this study. For full details of the sample preparation method, the reader is referred to Ratcliffe (2011).

## 5.3 Sample description

This section presents outcrop and petrographic descriptions for samples analysed in this study. For detailed description of sample LR10-3.3, the reader if referred to Ratcliffe (2011). The samples chosen for hornblende thermochronology were selected primarily on the modal abundance of amphibole that is relatively biotite-inclusion-free, and tectonostratigraphic position. One sample from the footwall and one sample from the hangingwall of the NTLSZ were chosen for analysis.

### *5.3.1 JF10-39*

Sample JF10-39 is an orthogneiss that from the northeast shore of North Tea Lake in the Powassan domain (Fig. 3.1). In outcrop, this location largely consists of intermediate

orthogneiss with centimetre-scale hornblende-pyroxene-rich bands. Moderate-to-well developed L-S fabric defines the foliation orientation (160/32), with a weakly developed down-dip stretching lineation that could not be measured confidently in the field. The outcrop is cut by pegmatites that range from 0.5 to >5 cm in width (Fig. 5.2a).

In thin-section this rock has the assemblage Pl - Hbl - Ksp - Qtz - Grt - Bt ± Cpx ± Ilm ± Ru. Mafic minerals form compositional bands and are separated by thick quartz-feldspar-rich bands that range from a few millimetres to several centimetres in width. The sample shows evidence of annealing in the form of straight grain boundaries between most phases, especially plagioclase, amphibole and quartz, and triple points between in all major rock-forming phases (figs. 5.5b and c). Biotite is concentrated in mafic bands, and forms inclusions in large amphibole grains. Biotite also forms tips on large amphibole grains suggesting retrograde replacement of amphibole by biotite.

### *5.3.2 JF10-35*

Sample JF10-35 is a straightened grey orthogneiss from a small island in the southern part of North Tea Lake in the Kiosk subdomain (Fig. 3.1). This rock comprises a fine grained grey matrix with straight, discontinuous, white K-feldspar-rich layers (Fig. 5.3a). The penetrative foliation (108/40) is defined by alignment of mafic minerals and K-feldspar-rich layers. There is a well-developed, roughly-down-dip stretching lineation (121-40).

In thin-section this rock has the assemblage Pl - Hbl - Qtz - Ksp - Bt - Grt - Ilm ± Cpx ± Zrn, and contains a significant abundance of amphibole. The rock has an annealed texture throughout and shows other evidence of recovery such as straight grain boundaries between amphibole, garnet, and feldspar grains, triple points between all rock-forming phases, granoblastic quartz, plagioclase, and K-feldspar, and relict grain-boundary migration textures (Fig. 5.3c). K-feldspar is concentrated in felsic layering, though grains can be found throughout the rock. Biotite occurs in association with amphibole, and often is in contact with larger amphibole grains. These two phases do not show signs of replacement, such as biotite tips on amphibole grains, but appear to be in equilibrium. Extra care was taken to separate only large amphibole grains that had no biotite or K-feldspar inclusions.

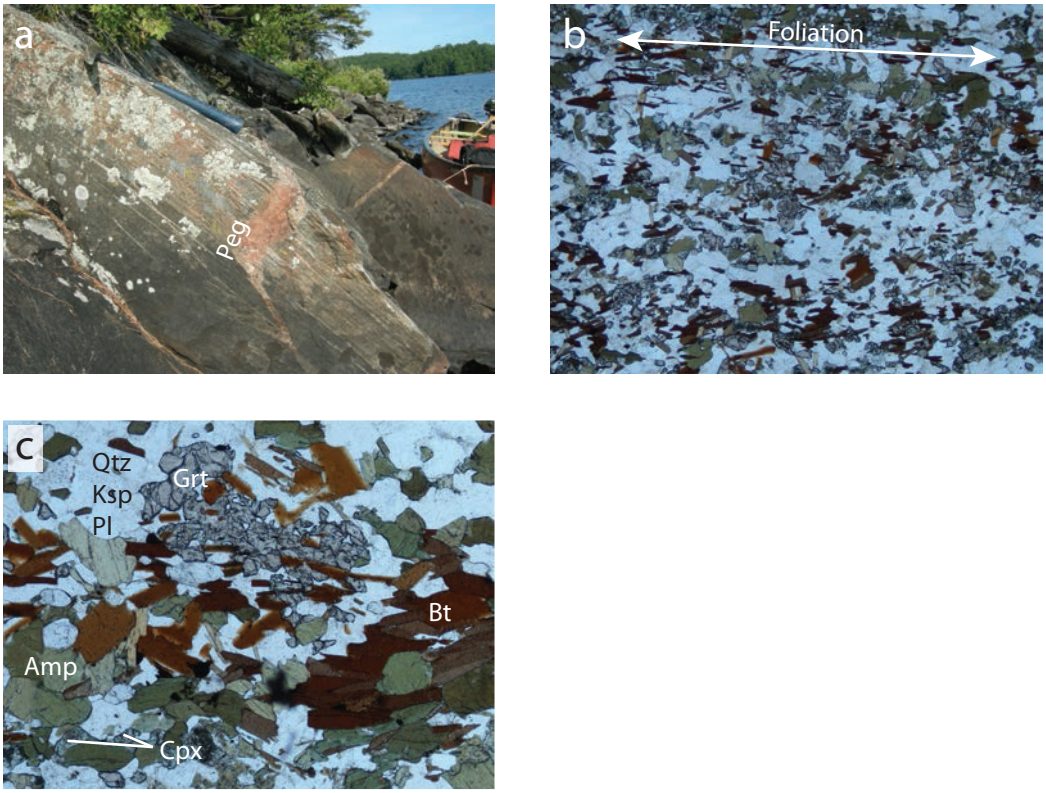


Figure 5.2: Outcrop and photomicrographs of sample JF10-39. a) Outcrop photo showing well developed gneissic layering of K-feldspar-rich layers (photo taken looking northeast, UTM x: 0653099, y: 5090740; hammer for scale). b) Photomicrograph showing the textural association of amphibole and biotite grains (PPL: FOV = 6.25 mm). c) Photomicrograph showing texture of biotite, amphibole, and garnet grain cluster. Some larger amphibole grains have small thin biotite inclusions, and are inter-grown with large biotite aggregates (PPL: FOV = 2.5 mm).

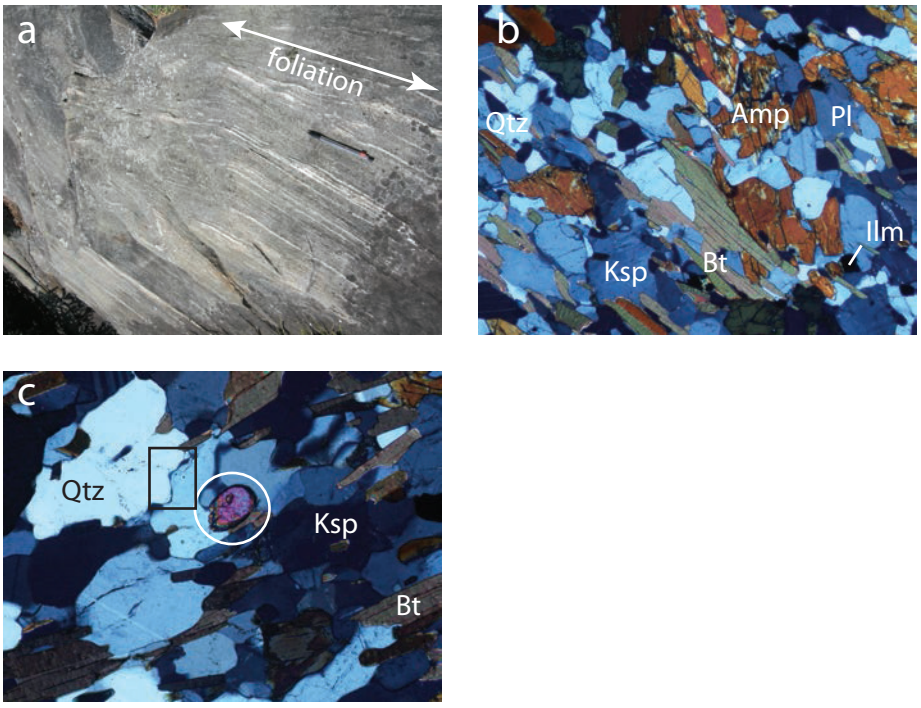


Figure 5.3: Outcrop and photomicrographs of sample JF10-35. a) Outcrop photo showing the dark-grey, amphibole-rich texture of the rock. Note discontinuous K-feldspar-rich layers (arrow defined foliation strike, UTM x: 0653719, y: 5089795; Pencil for scale). b) Photomicrograph showing the textural association of amphibole, biotite, and K-feldspar grains (XPL: FOV = 2.5 mm). c) Photomicrograph of the felsic layer showing relict grain boundary migration textures (black box), the numerous straight grain boundaries and triple-point between phases. Note the large zircon grain (white circle).

## 5.4 Hornblende analytical results

This section presents analytical results for $^{40}Ar/^{39}Ar$ thermochronology. Table 5.1 summarizes the plateau and weighted mean ages of samples evaluated in this study. Table 5.2 presents mean hornblende compositions from EMP analysis. Analysis locations and mineral composition data for samples JF10-35 and JF10-39 are given in Appendix C. For complete composition data for sample LR10-3.3 the reader is directed to Ratcliffe (2011).

Table 5.1: Summary of plateau and weighted mean ages.

| JF10-39 | JF10-35 | LR10-3.3[1] |
|---|---|---|
| Weighted mean age | Plateau age | Weighted mean age |
| 1099±5 Ma | 1029±5 Ma | 1027±5 Ma |

1 Modified from Ratcliffe (2011)

### *5.4.1 JF10-39*

Analysis of potassian-tschermakitic hornblende in sample JF10-39 yields a weighted mean age of 1099±5 Ma (Tables 5.2 and 5.1). The argon age spectrum for sample JF10-39 has a U-shape, and did not define a plateau age. A weighted mean age was calculated using four roughly similar age steps (Fig. 5.4). The Ca/K ratio of 5.7 plots close to the $^{37}Ar/^{39}Ar$ ratio measured during analysis, indicating the measured argon gas was released mostly from hornblende over the steps used in weighted mean age calculation. Detailed argon data are presented in table 5.3.

### *5.4.2 JF10-35*

Analysis of potassian-tschermakitic hornblende in sample JF10-35 yields a plateau age of 1029±5 Ma (Tables 5.2 and 5.1). The steps used in plateau age calculation are indicated in grey in figure 5.5. The Ca/K ratio of 5.1 plots close to the $^{37}Ar/^{39}Ar$ ratio measured during analysis, indicating the measured argon gas was released mostly from hornblende over the steps used in plateau age calculation. Detailed argon data are presented in table 5.4.

### *5.4.3 LR10-3.3*

Analysis of potassian-magnesian-hastingsitic hornblende in sample LR10-3.3 yields a weighted mean age of 1027±5 Ma (Tables 5.2 and 5.1). The argon age spectrum for sample LR10-3.3 has a U-shape, and did not define a plateau age. A weighted mean age was calculated using four roughly similar age steps (Fig. 5.6). The Ca/K ratio of 5.0 plots close to the $^{37}Ar/^{39}Ar$ ratio measured during analysis, indicating the measured argon gas

Table 5.2: Average amphibole compositions.

| Sample | JF10-35 | JF10-39 | LR10-3.3 [1] |
|---|---|---|---|
| Wt. % | | | |
| SiO2 | 41.59 | 42.54 | 40.84 |
| TiO2 | 1.96 | 1.82 | 1.16 |
| Al2O3 | 12.12 | 12.37 | 11.70 |
| FeO | 15.34 | 13.19 | 19.14 |
| MnO | 0.21 | 0.05 | 0.81 |
| MgO | 10.68 | 11.88 | 8.52 |
| CaO | 10.26 | 10.54 | 11.19 |
| Na2O | 1.74 | 1.76 | 1.84 |
| K2O | 1.71 | 1.55 | 1.74 |
| Cr2O3 | 0.00 | 0.00 | 0.05 |
| Total | 95.61 | 95.70 | 97.03 |
| | | | |
| Cations | | | |
| Si | 6.36 | 6.39 | 6.12 |
| Ti | 0.23 | 0.21 | 0.13 |
| Al | 2.18 | 2.19 | 2.09 |
| Fe | 1.96 | 1.66 | 2.49 |
| Mn | 0.03 | 0.01 | 0.11 |
| Mg | 2.43 | 2.66 | 1.96 |
| Ca | 1.68 | 1.70 | 1.86 |
| Na | 0.52 | 0.51 | 0.59 |
| K | 0.33 | 0.30 | 0.37 |
| Total | 15.72 | 15.62 | 15.71 |

Structural Formulae [2,3]

| | |
|---|---|
| JF10-35 | $(Na_{0.17}K_{0.33})(Ca_{1.67}Na_{0.34})(Mg_{2.4}Fe_{1.93}Al_{0.42}Ti_{0.22})(Si_{6.27}Al_{1.73})O_{22}(OH)_2$ |
| JF10-39 | $(Na_{0.19}K_{0.29})(Ca_{1.67}Na_{0.32})(Mg_{2.64}Fe_{1.64}Al_{0.51}Ti_{0.2})(Si_{6.34}Al_{1.66})O_{22}(OH)_2$ |
| LR10-3.3 | $(Na_{0.38}K_{0.34})(Ca_{1.85}Na_{0.17})(Mg_{2.94}Fe_{1.45}Al_{0.36}Ti_{0.13})(Si_{6.25}Al_{1.75})O_{22}(OH)_2$ |

End-members [3]

| | |
|---|---|
| JF10-35 | Potassian-Tschermakitic Hornblende |
| JF10-39 | Potassian-Tschermakitic Hornblende |
| LR10-3.3 | Potassian-Magnesian-Hastingsitic Hornblende |

| | | | |
|---|---|---|---|
| Oxygen pfu. | 23 | 23 | 23 |

1 Modified from Ratcliffe (2011)

1 Structural formulae after Deer et al. (1996)

2 Amphibole cation values and classification using PROBE-AMPH (Tindle and Webb (1994), and references therein)

was released mostly from hornblende over the steps used in weighted mean age calculation. Detailed argon data are presented in table 5.5.

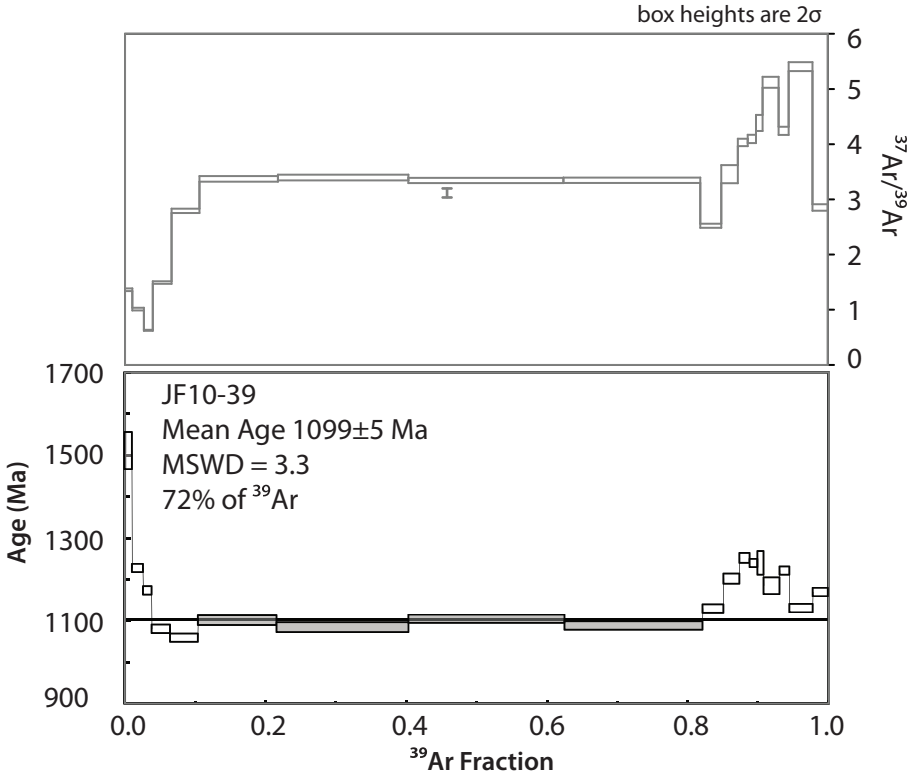


Figure 5.4: Amphibole $^{40}Ar/^{39}Ar$ weighted mean age plot for sample JF10-39. Black boxes are sample age, with steps used in plateau age calculation shaded in grey. Thick black line indicates the weighted mean age. Grey boxes are the corresponding $^{37}Ar/^{39}Ar$ ratios. The average amphibole $^{37}Ar/^{39}Ar$ proxy ratio of Ca/K from EMP analysis is shown by the grey vertical bar (bar height is $2\sigma$).

## 5.5 Discussion

**Amphibole closure temperature** Mark Harrison (1981) suggested a closure temperature of 490-500°C for amphibole in high-grade rocks, and this temperature has since become an accepted value. This value has since been the subject of considerable debate and reinterpretation (c.f. Harrison and Fitzgerald, 1986; Onstott and Peacock, 1987; Gaber et al., 1988; Blanckenburg et al., 1989; Baldwin et al., 1990). Harrison and Fitzgerald (1986) demonstrated the variability of argon closure temperatures in amphibole at

Table 5.3: Amphibole $^{40}Ar/^{39}Ar$ data for sample JF10-39. Analyses used in weighted-mean age calculation are denoted by an asterisk.

| T°C | 37Ar/39Ar | 36Ar/40Ar | 39Ar/40Ar | 39Ar(%) | $\pm 1\sigma$ (Ma) |
|---|---|---|---|---|---|
| 750 | 1.33 | 0.00157 | 0.00099 | 1 | 1506±22 |
| 850 | 0.99 | 0.00023 | 0.00230 | 1.6 | 1229±5 |
| 900 | 0.61 | 0.00014 | 0.00252 | 1.2 | 1176±5 |
| 950 | 1.46 | 0.00005 | 0.00288 | 2.6 | 1085±4 |
| 975 | 2.73 | 0.00004 | 0.00297 | 3.9 | 1063±5 |
| 1000 | 3.3 | 0.00001 | 0.00285 | 11.1 | 1104±6* |
| 1025 | 3.33 | 0.00002 | 0.00290 | 18.5 | 1088±6* |
| 1050 | 3.27 | 0.00002 | 0.00283 | 22 | 1107±4* |
| 1075 | 3.28 | 0.00002 | 0.00289 | 19.4 | 1092±5* |
| 1100 | 2.47 | 0.00001 | 0.00275 | 2.9 | 1132±5 |
| 1125 | 3.39 | 0.00002 | 0.00253 | 2.3 | 1202±6 |
| 1150 | 3.95 | 0.00005 | 0.00238 | 1.4 | 1251±6 |
| 1175 | 4.01 | 0.00007 | 0.00240 | 1.1 | 1238±5 |
| 1200 | 4.33 | 0.00007 | 0.00240 | 0.9 | 1236±17 |
| 1225 | 5.02 | 0.00004 | 0.00257 | 2.2 | 1183±10 |
| 1250 | 4.15 | 0.00006 | 0.00245 | 1.4 | 1221±5 |
| 1300 | 5.92 | 0.00010 | 0.00268 | 3.3 | 1132±5 |
| 1350 | 2.79 | 0.00013 | 0.00254 | 2.1 | 1171±5 |
| | | | | Total Gas Age | 1124±9 |
| J = .002412 | $\pm 2.412e^{-05}$ | | Weighted-mean Age | | 1099±5 |

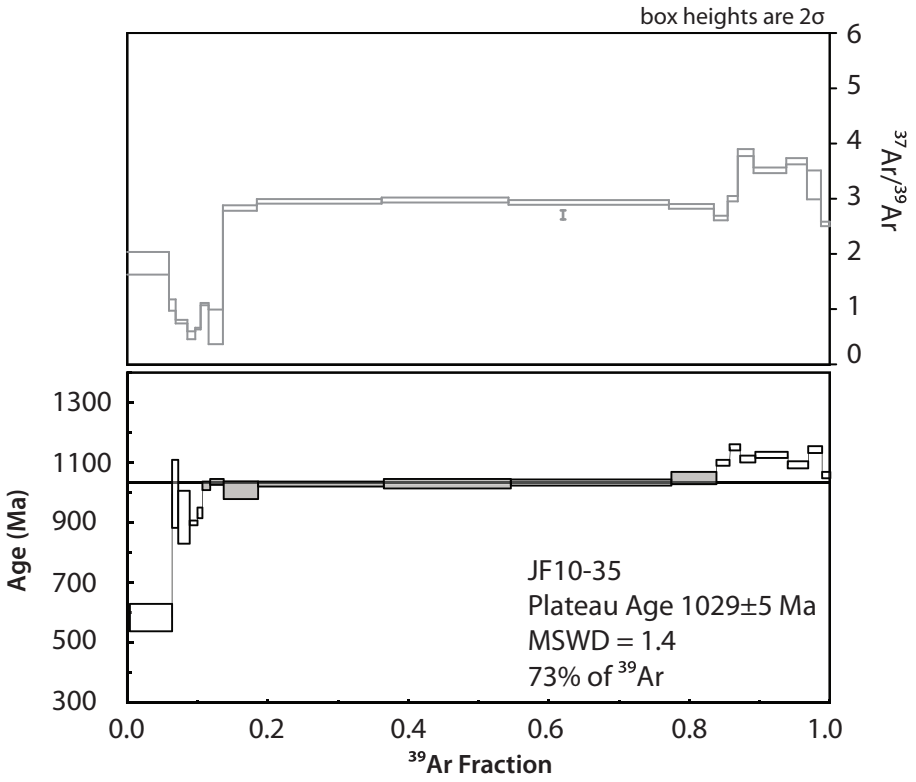


Figure 5.5: Amphibole $^{40}Ar/^{39}Ar$ plateau age plot for sample JF10-35. Black boxes are sample age, with steps used in plateau age calculation shaded in grey. Thick black line indicates the plateau age. Grey boxes are the corresponding $^{37}Ar/^{39}Ar$ ratios. The average amphibole $^{37}Ar/^{39}Ar$ proxy ratio of Ca/K from EMP analysis is shown by the grey vertical bar (bar height is $2\sigma$).

Table 5.4: Amphibole $^{40}Ar/^{39}Ar$ data for sample JF10-35.

| T°C | 37Ar/39Ar | 36Ar/40Ar | 39Ar/40Ar | 39Ar(%) | Age$\pm 1\sigma$ (Ma) |
|---|---|---|---|---|---|
| 650 | 1.77 | 0.00213 | 0.00234 | 5.9 | 582±23 |
| 750 | 1.04 | 0.00174 | 0.00159 | 0.9 | 995±57 |
| 850 | 0.75 | 0.00020 | 0.00342 | 1.6 | 917±4 |
| 900 | 0.51 | 0.00007 | 0.00366 | 1.1 | 898±4 |
| 925 | 0.63 | 0.00007 | 0.00350 | 0.7 | 931±9 |
| 950 | 1.06 | 0.00005 | 0.00312 | 1.1 | 1021±7 |
| 975 | 0.66 | 0.00003 | 0.00308 | 2 | 1035±5 |
| 1000 | 2.73 | 0.00001 | 0.00322 | 4.8 | 1006±15 |
| 1025 | 2.85 | 0.00001 | 0.00314 | 17.7 | 1026±4 |
| 1050 | 2.87 | 0.00001 | 0.00313 | 18 | 1028±8 |
| 1075 | 2.83 | 0.00002 | 0.00311 | 22.8 | 1031±5 |
| 1100 | 2.76 | 0.00002 | 0.00305 | 6.3 | 1045±10 |
| 1125 | 2.56 | 0.00001 | 0.00288 | 1.9 | 1097±5 |
| 1150 | 2.9 | 0.00001 | 0.00270 | 1.4 | 1149±5 |
| 1200 | 3.7 | 0.00004 | 0.00280 | 2.2 | 1109±6 |
| 1250 | 3.39 | 0.00003 | 0.00276 | 4.6 | 1123±5 |
| 1300 | 3.55 | 0.00007 | 0.00285 | 2.9 | 1090±5 |
| 1350 | 3.14 | 0.00007 | 0.00268 | 1.9 | 1141±6 |
| 1400 | 2.46 | 0.00032 | 0.00275 | 1.2 | 1056±5 |
| | | | | Total Gas Age | 1019±9 |
| J = .002412 | ±.000024 | | | Plateau Age | 1029±5 |

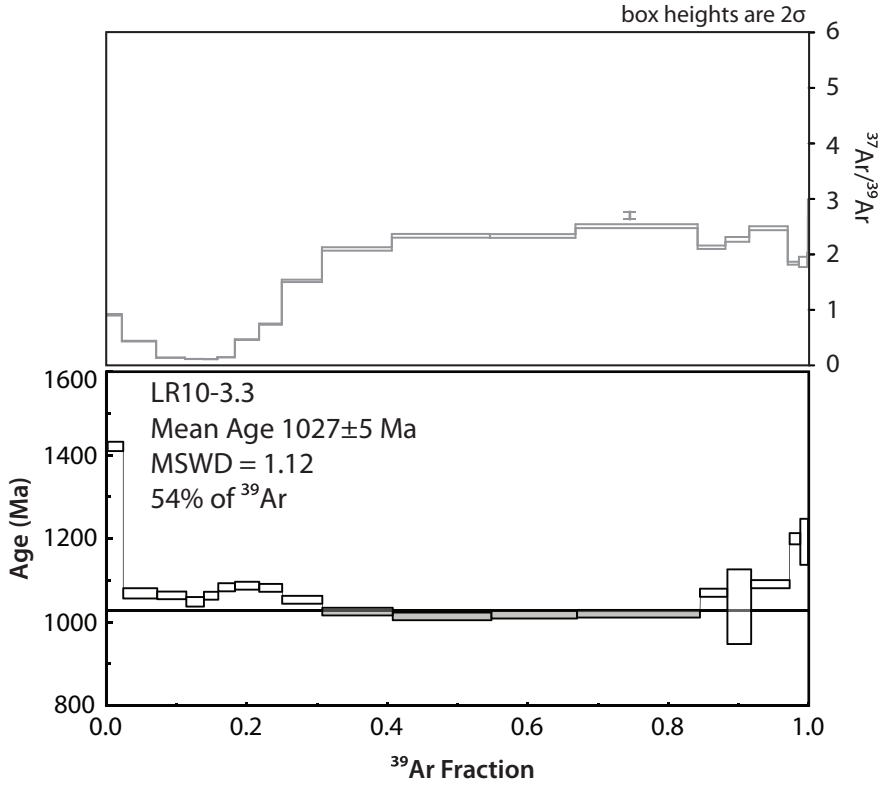


Figure 5.6: Amphibole $^{40}Ar/^{39}Ar$ weighted-mean age plot for sample LR10-3.3. Black boxes are sample age, with steps used in weighted mean age calculation shaded in grey. Thick black line indicates the weighted mean age. Grey boxes are the corresponding $^{37}Ar/^{39}Ar$ ratios. The average amphibole $^{37}Ar/^{39}Ar$ proxy ratio of Ca/K from EMP analysis is shown by the grey vertical bar (bar height is $2\sigma$).

Table 5.5: Amphibole $^{40}Ar/^{39}Ar$ data for sample LR10-3.3. Analyses used in weighted-mean age calculation are denoted by an asterisk.

| T°C | 37Ar/39Ar | 36Ar/40Ar | 39Ar/40Ar | 39Ar(%) | $\pm 1\sigma$ (Ma) |
|---|---|---|---|---|---|
| 600 | 0.91 | 0.00014 | 0.00205 | 2.2 | 1421.8±5.4 |
| 700 | 0.43 | 0.00050 | 0.00269 | 4.8 | 1076±6.1 |
| 750 | 0.13 | 0.00006 | 0.00312 | 4.1 | 1071.1±4.6 |
| 775 | 0.11 | 0.00005 | 0.00319 | 2.5 | 1056±5.6 |
| 800 | 0.11 | 0.00005 | 0.00313 | 2 | 1070.1±4.6 |
| 850 | 0.14 | 0.00006 | 0.00304 | 2.4 | 1090.1±4.8 |
| 900 | 0.46 | 0.00006 | 0.00303 | 3.4 | 1093.8±4.7 |
| 925 | 0.74 | 0.00004 | 0.00306 | 3.2 | 1088.9±4.7 |
| 950 | 1.52 | 0.00002 | 0.00319 | 5.7 | 1060.8±4.6 |
| 975 | 2.09 | 0.00001 | 0.00331 | 9.9 | 1033.2±4.5* |
| 1000 | 2.33 | 0.00001 | 0.00337 | 13.9 | 1021.9±4.5* |
| 1025 | 2.33 | 0.00000 | 0.00335 | 12.1 | 1025.5±4.5* |
| 1050 | 2.5 | 0.00000 | 0.00334 | 17.3 | 1028.1±4.5* |
| 1075 | 2.12 | 0.00001 | 0.00313 | 3.9 | 1077.4±4.8 |
| 1100 | 2.26 | 0.00002 | 0.00326 | 3.3 | 1044.5±44 |
| 1150 | 2.47 | 0.00002 | 0.00305 | 5.4 | 1097.5±4.7 |
| 1200 | 1.84 | 0.00006 | 0.00266 | 1.5 | 1204.5±6.6 |
| 1250 | 1.86 | 0.00025 | 0.00253 | 1.1 | 1197.4±27.2 |
| 1300 | 1.99 | 0.00047 | 0.00087 | 0 | 2286.7±73.8 |
| 1325 | 2.82 | 0.00036 | 0.00087 | 0.1 | 2337.2±107 |
| | | | | Total Gas Age | 1067±9 |
| J = .002571 $\pm 2.571e^{-05}$ | | | | Weighted-mean Age | 1027±5 |

different metamorphic grades, and cautioned against the use of a universal closure temperature for the system. Nonetheless, the accepted 500°C closure temperature may be a good approximation for this study, as this temperature was estimated in a Mesoproterozoic, high-grade metamorphic terrane.

**Polymineralic argon signal** Amphibole age spectra in this study suggest contamination by high-K and high-Ca inclusion degassing in the initial and final stages of analysis. Degassing of non-amphibole inclusions during step-heating often produces discordant amphibole age spectra, which are accompanied by similar variations in the corresponding $^{37}Ar/^{39}Ar$ ratios (Di Vincenzo et al., 2004). It is possible to divide the age spectra of the samples analysed in this study into three domains (Fig. 5.7). Domain 1 is the initial argon gas measured which is very high in $^{39}Ar$, lowering the $^{40}Ar/^{39}Ar$ ratio. This suggests loss of $^{40}Ar$ or contamination by a high-K phase (e.g. biotite) (Rex et al., 1993). Domain 2 is the centre section of the age spectrum and represents the gas released from amphibole (Lee et al., 1991; Lee, 1993). For the samples analysed in this study, the Ca/K ratio from EMP analysis of amphibole plots very near the ratio of the measured $^{37}Ar/^{39}Ar$ gas, indicating that this argon was released by amphibole degassing. Domain 3 has a variable character, with higher $^{40}Ar/^{39}Ar$ ratio values. This indicates contamination by a high-Ca phase (e.g. feldspar) (Parsons et al., 1999; Daszinnies et al., 2009). For the samples analysed in this study, the consistency of $^{40}Ar/^{39}Ar$ ratios, the low atmospheric correction factor, and the close match of $^{37}Ar/^{39}Ar$ values to Ca/K ratio suggest that domain 2 indicates of the age of amphibole cooling through 500°C.

**Cooling of the NTLSZ** $^{40}Ar/^{39}Ar$ data from this study suggest the NTLSZ cooled through amphibole closure temperature at ca. 1030 Ma. Sample JF10-35, an amphibole separate of an orthogneiss in the NTLSZ, yielded a robust plateau age of 1029±5 Ma for the cooling through 500°C, although orthogneiss sample LR10-3.3 (Ratcliffe, 2011) did not yield a plateau age, re-evaluation of the data suggests a weighted mean age of 1027±5 Ma, within error of the 1029±5 Ma plateau age from sample JF10-35. Both spectra are discordant in the initial and final stages possibly reflecting biotite and K-feldspar impurities. Sample LR10-3.3 does not show a clear difference between domain 1 and domain

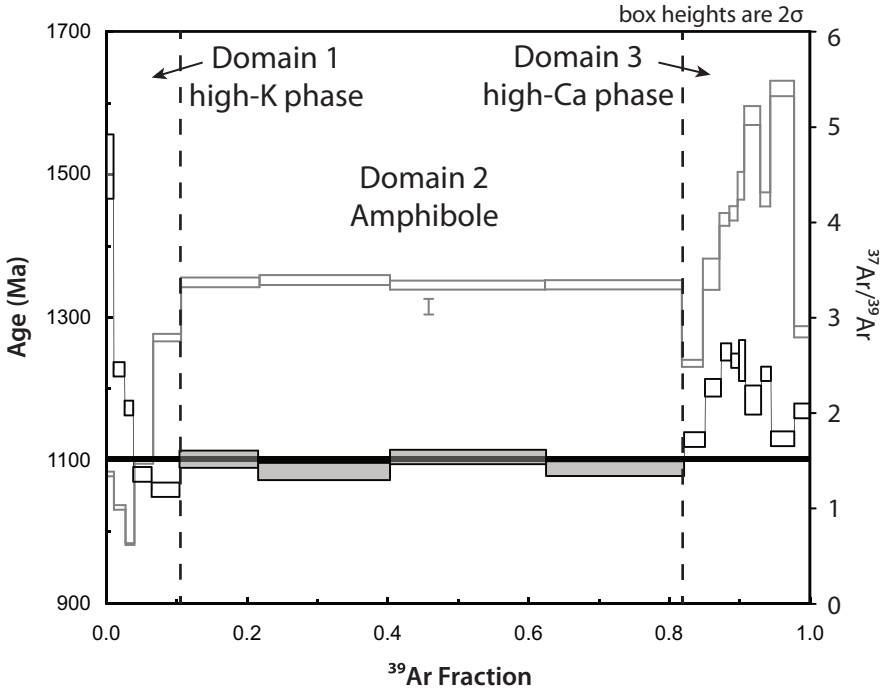


Figure 5.7: Example amphibole $^{40}Ar/^{39}Ar$ age spectra (sample JF10-39) showing the argon degassing domains discussed in text.

2 sections of the argon age spectrum, but nonetheless provides a statistically meaningful weighted-mean age for cooling through amphibole closure. The ca. 1030 Ma ages of these samples are interpreted to the represent the maximum age at which the NTLSZ cooled through amphibole closure at approximately 500°C.

**Cooling of the footwall of the NTLSZ** This study presents the first $^{40}Ar/^{39}Ar$ data from the southern Bonfield Batholith of the Bonfield domain, in the footwall of the NTLSZ. Despite the spatial proximity of this sample to the hangingwall samples (Fig. 3.1), the apparent ages show a ca. 70 Ma difference from hangingwall to footwall with footwall ages older than the hangingwall. As discussed above, the JF10-39 age spectrum is disturbed in the initial and final stages by biotite and K-feldspar impurities, respectively, yet analytical steps related to amphibole out gassing are resolvable. The weighted mean age of 1099±5 Ma is interpreted as the maximum age of cooling of the Bonfield Pluton through amphibole closure at approximately 500°C. This shows that the rocks of the immediate footwall of the NTLSZ were not subject to sufficient reheating during metamorphism and deformation along the NTLSZ to reset the amphibole argon isotopic system during subsequent Grenvillian metamorphic events.

## 5.6 Conclusions

1. The NTLSZ cooled through amphibole closure at approximately 500°C at a maximum of ca. 1030 Ma.

2. The rocks of the southern Bonfield Batholith of the Bonfield domain in the footwall of the NTLSZ cooled through amphibole closure at approximately 500°C at a maximum of ca. 1100 Ma.

# CHAPTER 6

# THERMOBAROMETRY

## 6.1 Introduction

Thermobarometry techniques have been applied successfully to rocks of the western Central Gneiss Belt since the late-1980's. Since that time there has been a considerable body of geobarometry and geothermometry work completed using single- and multi-equilibria approaches (Grant, 1989; Anovitz and Essene, 1990; Jamieson et al., 1992; Tuccillo et al., 1992; Corrigan et al., 1994; Ketchum et al., 1994; Wodicka, 1994; Jamieson et al., 1995; Busch et al., 1996; Timmermann et al., 1997; Timmermann, 1998). These studies focussed largely on the easily accessible domains along the shores of Lake Huron, or along existing right-of-ways. The internal Algonquin domain, however, has been largely unstudied for nearly two decades due to the logistical challenges in access, and the regulations surrounding working in Algonquin Provincial Park.

The purpose of thermobarometry work in this study was to add to the growing database for the Kiosk and Algonquin domains. Classical methods of multi-equilibria thermobarometry were chosen for this study for two reasons: (i) integration with existing historical datasets; (ii) problems with the application of equilibrium-assemblage pseudosections in metabasites; and (iii) evidence that late metasomatism has changed the bulk composition during retrogression. Three new samples collected during field work in 2010 were analysed, and data from three analyses collected by McLeish (2008) were re-evaluated using the methodology of this study. The analytical approach used here has yielded different results for the pressure-temperature conditions of the Kiosk domain and McLintock

subdomain than generated previously.

The samples chosen lie along a northwest-southeast transect through the Kiosk domain and McLintock subdomains and display granulite-facies mineral assemblages. Petrographic evidence and field relations discussed in the following sections suggest that this metamorphism may represent conditions on the retrograde part of the pressure-temperature (P-T) path. Integrating these data with geochronology suggests that rocks of the Kiosk domain and McLintock subdomain re-equilibrated during protracted metamorphism during the Ottawan pulse of the Grenville orogeny at ca. 1080-1060 Ma.

### *6.1.1 Summary of relevant thermobarometry data*

There have been few studies of the thermobarometry of the Algonquin domain, in the western CGB. Most studies were conducted many years ago and focussed largely on the Parry Sound and Britt domains (Grant, 1989; Jamieson et al., 1992; Tuccillo et al., 1992; Corrigan et al., 1994; Ketchum et al., 1994; Wodicka, 1994; Jamieson et al., 1995; Busch et al., 1996; Timmermann et al., 1997; Timmermann, 1998). Anovitz and Essene (1990) complied the existing CGB data to produce a set of regional P-T maps for the whole of the western CGB and northwestern CMB (Fig. 6.1). Though Anovitz and Essene (1990) projected their calculated isobars and isotherms through the Kiosk and Algonquin domains, there were few data available at the time to constrain their maps, a problem that still persists today. Their methodology was tailored to assess pressure and temperature recorded in the matrix mineral assemblage, by avoiding retrograde rims of garnet, using reintegrated analysis of minerals showing exolution (e.g. perthite and ilmenite), and average mineral compositions. A drawback to their study was they did not correlate P-T estimates with age of metamorphism, however, it does provide a good first-order approximation of regional P-T conditions. To calculate pressures and temperatures for specific geothermometers and geobarometers they used the now outdated EQUILI program (*Wall and Essene, unpub*). This software package used mineral thermodynamic data to determine pressure and temperature by reducing Gibbs energy of formation $\Delta G_r(P_2, T_2)$, given a reference pressure and temperature (cf. Perkins et al., 1977). Limitations and uncertainties in this approach result from incomplete thermodynamic data available at the time, mixing of polyphase mineral assemblages, and a poor understanding of the regional geology at

the time of their study. Nonetheless, the regional pattern of isobars and isotherms fits with the current understanding of structural boundaries on a large scale. Their maps show the Kiosk and Algonquin domains to have been affected by pressures of ca. 10 kbar, and temperatures of ca. 750-800°C like most of the CGB. The average pressure-temperature results of the six samples analysed in this study broadly agree with the regional geothermometry and geobarometry framework of Anovitz and Essene (1990).

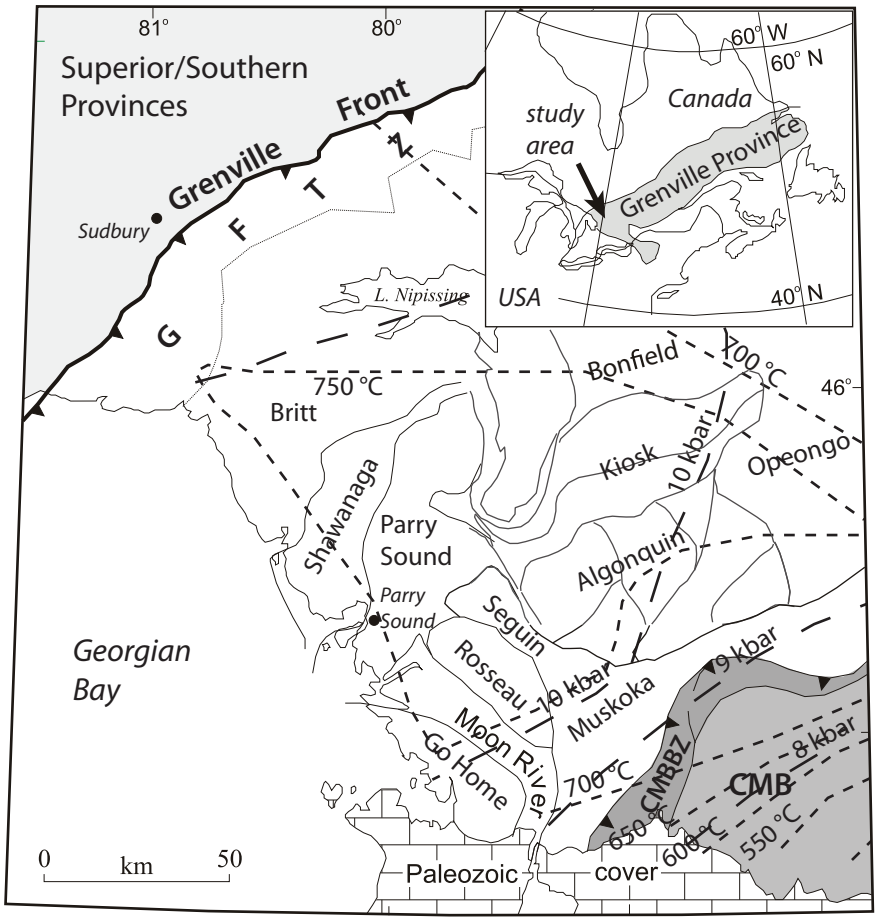


Figure 6.1: Map showing regional isotherms and isobars for the CGB (modified from Anovitz and Essene, 1990; Culshaw et al., 1997).

McLeish (2008) completed a reconnaissance study that included thermobarometry in the Kiosk and Algonquin domains. The goal of his study was to define the peak pressure-temperature conditions using five samples from various lithologies along a transect through

the Kiosk domain and McLintock subdomain. Raw data from three samples were re-evaluated using the methodology of this study, and have produced markedly different pressure estimates (Table 6.1), reflecting the different methods. While both McLeish (2008) and this study used multi-equilibria calculations, McLeish (2008) used the TWEEQU program (Berman, 1991) for pressure-temperature calculations instead of THERMOCALC (Holland and Powell, 1998). The internally-consistent database of Berman (1991) contains fewer thermodynamic data for key minerals than the database of Holland and Powell (1998) (e.g. amphibole). McLeish (2008) omitted quartz from reaction calculation on the basis of quartz causing erroneous equilibria intersections. As discussed in chapter 2, the Kiosk domain orthogneisses typically have a metaquartz-monzonite composition. Save only one outcrop location in the Kiosk domain where the rock is a silica-undersaturated, corundum-bearing orthogneiss, quartz was likely present in excess in the system during metamorphic events in the Kiosk and Algonquin domains. Omission of this phase can affect the net-transfer reactions responsible for calculation of pressures in particular. McLeish (2008) also included $H_2O$ as a phase in excess in pressure-temperature calculations. Nadeau and van Breemen (1998); Timmermann (1998) noted that the Algonquin domain, and likely the Kiosk domain, experienced high-temperature granulite-facies metamorphism at ca. 1450-1425 Ma. It is unlikely that $H_2O$ was in excess when these rocks chemically re-equilibrated during the ca. 1080-1060 Ma Ottawan orogenic phase, given the widespread melting and dehydration of the study area (see discussion in Chapter 3 and Chapter 4). It is likely that the pressure was over-estimated as a result of the methodology chosen by McLeish (2008). This led to the misinterpretation of his results as the peak pressure-temperature conditions, rather than post-peak conditions of the Algonquin domain.

## 6.2 Method

### *6.2.1 Data acquisition*

Six samples were chosen for thermobarometry based on inferred chemical equilibrium between coexisting minerals. Chemical analysis was completed using the JEOL JXA-8200 Superprobe at the Dalhousie University Robert MacKay Electron Microprobe Laboratory. The analytical protocol for major silicate mineral analyses follows the in-house protocol

Table 6.1: Comparison of thermobarometry results for samples from McLeish (2008) that were re-evaluated in this study.

| | McLeish (2008) | | | This Study | | |
|---|---|---|---|---|---|---|
| Sample | Assemblage | T (°C) | P (kbar) | Assemblage | T (°C) | P (kbar) |
| NA023a | Pl-Cpx-Opx Amp-Grt-$H_2O$ | 813±2 | 14.0±0.04 | Pl-Qtz-Cpx Opx-Grt-Amp | 812±102 | 10.6±1.5 |
| NA046 | Pl-Grt-Opx Cpx-Amp-$H_2O$ | 805±17 | 12.4±0.2 | Pl-Qtz-Grt Opx-Cpx-Amp | 722±112 | 8.1±1.7 |
| NA061e | Pl-Grt-Opx Cpx-Amp-$H_2O$ | 823±21 | 14.2±0.3 | Pl-Qtz-Grt Opx-Cpx-Amp | 817±121 | 10.4±1.7 |

developed by R. MacKay (D. MacDonald, *pers. comm.* 2011). Polished thin sections are carbon coated to provide a conductive surface and prevent electrostatic charging of the sample during analysis. Prior to and at regular intervals during analysis, the "KK" amphibole consistency standard is run monitor the performance of the instrument and gauge analytical precision (Jarosewich et al., 1980). This standard also acts at a reference standard for garnet during analysis. As the KK standard is not a garnet, this can introduce background correction errors in the data, and garnet analyses must be corrected post-analysis. An in-house standard, "Garnet12442," is run for use in post-analysis garnet correction.

Prior to quantitative chemical analysis of individual minerals, BSE images of the whole sample area and WDS maps of specific minerals were collected. BSE imagery is a useful tool in determining mineralogy, texture, and qualitative modal abundance of minerals. This can serve as a useful guide to planning which specific grains to analyse, and which grains to map in detail in WDS. WDS maps are powerful tools for determining internal chemical zoning within grains, and assessing retrograde chemical diffusion effects. The most useful minerals to assess chemical zoning are garnet, pyroxene and plagioclase (Spear, 1995; Spear and Kohn, 1996; Pyle and Spear, 1999). The best candidate garnet grains were mapped for Mg, Ca, Mn, and Fe with an average counting time of 40 ms/pixel. High-resolution WDS map of at least one garnet per sample area were collected prior to quantitative analysis of individual minerals.

Major elements included in quantitative analysis were Na, Mg, Fe, Al, Si, K, Ca, Ti, Mn, and Cr. Instrument analytical conditions for silicate mineral major-element analysis are shown in Table 6.2. Quantitative analysis is a two-fold procedure consisting of: (i) line traverses across suspect zoned grains; and (ii) spot analyses of individual grains for each phase of interest. Traverses across suspect zoned minerals such as garnet or plagioclase were used to document the zoning profile of the grain and to characterise each zone. This procedure consists of analysing many closely spaced points across a single grain, and plotting the results of each cation. Once chemical zoning is fully described, individual analyses of each phase of interest are completed. To help reduce analytical error and natural variability of mineral composition the data are pooled and average mineral compositions determined. At least ten individual analyses are collected for each phase of interest in a sample, preferably from different grains in a relatively small area of the sample. This procedure is repeated, if possible, at another location in the same sample. This approach allows the investigation of chemical heterogeneity of specific minerals in the sample, since one criterion for assessing equilibrium if that any given mineral be chemically homogeneous on the scale of investigation. Structural formulae and common end-member proportions were calculated for average mineral compositions for each phase in the equilibrium assemblage. General forms of mineral formulae are after Deer et al. (1996). Cation proportions for amphibole and pyroxene were calculated following the methods of Tindle and Webb (1994) and Sturm (2002), respectively.

**Analysis and data processing** Analysis involved identification of multiple locations in the polished-section that contained all the minerals in the target assemblage. Grains that were not heavily cracked or inclusion-rich were chosen for analysis. Grains that are in contact with other minerals in the assemblage were preferentially analysed (e.g. amphibole in contact with plagioclase, amphibole in contact with biotite, etc.). Analytical preference was given to minerals that undergo ion exchange reactions: (i) Fe⇌Mg exchange reactions, such as garnet-clinopyroxene (e.g. Ravna, 2000), garnet-amphibole (e.g. Graham and Powell, 1984), garnet-biotite (e.g. Ferry and Spear, 1978), garnet-ilmenite (e.g. Pownceby et al., 1987), orthopyroxene-ilmenite (e.g. Docka et al., 1986) and, clinopyroxene-ilmenite (e.g. Docka et al., 1986); (ii) Fe⇌Ca⇌Mg orthopyroxene-clinopyroxene exchange reaction (e.g. Kretz, 1982); and (iii) Na⇌K two-feldspar exchange reaction (e.g.

Table 6.2: Major-element electron-microprobe analytical conditions

| Elements | K | Cr | Na | Si | Mn | Ca |
|---|---|---|---|---|---|---|
| Name | K | Cr | Na_P | Si_Ca | Mn | Ca_Fe |
| X-ray Name | Ka | Ka | Ka | Ka | Ka | Ka |
| Order | 1 | 1 | 1 | 1 | 1 | 1 |
| Channel | 1 | 2 | 3 | 4 | 5 | 1 |
| Crystal | PETJ | PETJ | TAPH | TAP | LIFH | PETJ |
| Spc.Pos.(mm) | 120.251 | 72.592 | 129.601 | 77.343 | 146.601 | 108.099 |
| High BG (mm) | 5 | 5 | 5 | 5.7 | 5 | 5.5 |
| Low BG (mm) | 5 | 4.5 | 5 | 7 | 5 | 5 |
| Peak Seek W. | 1 | 1 | 1 | 1 | 1 | 1 |
| Time/Count | Time | Time | Time | Time | Time | Time |
| Mes.Time(sec) | 20 | 20 | 20 | 20 | 20 | 20 |
| Bac.Time(sec) | 10 | 10 | 10 | 10 | 10 | 10 |
| Mes.Count | 10000 | 10000 | 10000 | 10000 | 10000 | 10000 |
| Bac.Count | 500 | 500 | 500 | 500 | 500 | 500 |
| PHA gain | 64 | 32 | 32 | 32 | 32 | 16 |
| High V.(V) | 1618 | 1780 | 1700 | 1700 | 1745 | 1718 |
| Base L.(V) | 0.7 | 0.7 | 0.7 | 0.7 | 0.7 | 0.7 |
| Window (V) | 9.3 | 7.3 | 9.3 | 9.3 | 9.3 | 9.3 |
| Diff/Int | Diff | Diff | Diff | Diff | Diff | Diff |

| Elements | Ti | Mg | Al | Fe | Ba |
|---|---|---|---|---|---|
| Name | Ti | Mg_K | Al | Fe | Ba |
| X-ray Name | Ka | Ka | Ka | Ka | La |
| Order | 1 | 1 | 1 | 1 | 1 |
| Channel | 2 | 3 | 4 | 5 | 2 |
| Crystal | PETJ | TAPH | TAP | LIFH | PETJ |
| Spc.Pos.(mm) | 87.397 | 107.608 | 90.539 | 135.013 | 88.251 |
| Back(+) (mm) | 5 | 6.2 | 5 | 5 | 5 |
| Back(-) (mm) | 5 | 5.8 | 6 | 6.5 | 6 |
| Peak Seek W. | 1 | 1 | 1 | 1 | 1 |
| Time/Count | Time | Time | Time | Time | Time |
| Mes.Time(sec) | 20 | 20 | 20 | 20 | 1 |
| Bac.Time(sec) | 10 | 10 | 10 | 10 | 1 |
| Mes.Count | 10000 | 10000 | 10000 | 10000 | 10000 |
| Bac.Count | 500 | 500 | 500 | 500 | 500 |
| PHA gain | 32 | 32 | 32 | 32 | 64 |
| High V.(V) | 1790 | 1706 | 1715 | 1760 | 1640 |
| Base L.(V) | 0.7 | 0.7 | 0.7 | 0.7 | 2 |
| Window (V) | 9.3 | 9.3 | 9.3 | 9.3 | 4 |
| Diff/Int | Diff | Diff | Diff | Diff | Diff |

Whitney and Stormer, 1977). Preference was also given to minerals that undergo net-transfer reactions: (i) garnet-plagioclase-hornblende-quartz (e.g. Kohn and Spear, 1989); (ii) garnet-plagioclase-orthopyroxene-quartz (e.g. Powell and Holland, 1988); (iii) garnet-plagioclase-clinopyroxene-quartz (Powell and Holland, 1988); (iv) pyroxene-plagioclase-quartz (e.g. Wood et al., 1980); (v) amphibole-plagioclase (e.g. Spear, 1980, 1981); and (vi) amphibole-plagioclase-clinopyroxene-quartz (Liogys and Jenkins, 2000). Included phases were analysed as analytical time permitted. Typically, the inclusions that were analysed did not significantly vary in composition from matrix minerals. During the course of WDS mapping and EMP mineral analysis, it became evident that the compositions of many commonly zoned metamorphic minerals (e.g. garnet and clinopyroxene) were completely homogeneous. Without preserved zoning to provide evidence of earlier metamorphic stages for use in inclusion thermobarometry, the decision was made to shift primary focus to matrix mineral analysis. The average mineral compositions presented in the following sections reflect the mean of the matrix minerals only.

Data acquired for the the assemblage was reduced and selected for use in *Average P-T* calculations. Data processing involved the use of the *Minitab* statistical software to calculate descriptive statistics of each mineral (e.g. median, mode, arithmetic mean, etc.). Data points that were far off the mean and median values were inspected for textural evidence of a poor analysis location, and the EMP output checked to ensure the analysis had run properly. If no textural or instrument evidence for exclusion could be found the data were included in the population. *Average P-T* calculations were then run for each sample using the mean, median, and specific individual analyses, to qualitatively assess variance arising from using different combinations of mineral compositions. Individual analyses were selected based on chemical criteria (e.g. highest and lowest Ca plagioclase, highest and lowest Mg and Fe in pyroxene and amphibole, highest and lowest $Al^{iv}$ amphibole, highest and lowest K in K-feldspar, highest and lowest Ti biotite and ilmenite, highest and lowest Ca, Fe, Mg, Mn garnet), or from specific textural domains (e.g. garnet and clinopyroxene in contact, two pyroxenes in contact, two feldspars in contact, amphibole and clinopyroxene in contact). The results based on selected analyses did not vary significantly from the results based on the mean or median compositions for all matrix

minerals. Furthermore, given the homogeneous compositions of garnet and clinopyroxene the mineral assemblage was interpreted as compositionally equilibrated so that mean compositions are representative of the entire rock and can be used in P-T calculations. The low standard deviation (2SD) values reflect the homogeneous mineral compositions of the samples, and are typically $< 1$ Oxide Wt% (see data tables in the following sections).

### *6.2.2 Pressure-temperature calculation*

Multi-equilibria thermobarometry calculations were done with the THERMOCALC 3.33 program in *average P-T* mode (Powell and Holland, 1994). In all calculations the internally-consistent mineral thermodynamic dataset of Holland and Powell (1998) was used. The multi-equilibria *average P-T* approach allows the results of this study to be integrated directly with historical datasets in the western CGB.

*Average P-T* calculations are done by calculating all the possible reaction equilibria, and determining their statistically most common intersection point in P-T space. Conditions that must be satisfied are: (i) the minerals are in chemical equilibrium in the rock; and (ii) each component is included in the internally consistent data set. For each reaction in a system with a fixed bulk composition, the thermodynamics for each reaction will be a function of the Gibbs free energy equation such that:

$$\Delta G_{rxn} = \Delta E_{rxn} + P\Delta V_{rxn} - T\Delta S_{rxn} \tag{6.1}$$

Given that,

$$0 = \Delta G_{rxn} + RTlnK \tag{6.2}$$

The equation can be rearranged to become,

$$0 = \frac{\Delta E_{rxn} + P\Delta V_{rxn} - T\Delta S_{rxn}}{-RTlnK} \tag{6.3}$$

where the intensive variables are pressure ($P$) and temperature ($T$), and extensive variables are internal energy ($E$), volume ($V$), and entropy ($S$), and the ideal gas constant

($R$). The equilibrium coefficient ($K$) is primarily a function of the calculated activities of equilibrium minerals (cf. Powell, 1978; Spear, 1995). These activities are calculated at a user-defined reference pressure and temperature using the AX program included with the THERMOCALC 3.33 package. The activities of calculated components were inspected prior to pressure-temperature calculation, and those with very low activities were excluded. For example, in sample CA108b AX will calculate an activity for the garnet end-member spessartine ($Mn_3^{2+}Al_2(SiO_4)_3$), even though MnO is typically $< 1$ Oxide Wt%, and spessartine constitutes $\leq 2\%$ of the end-member composition. In all cases, the result of removing an end-member was qualitatively assessed prior to elimination. Generally, removal of a low-activity end-member reduces the error, but does not significantly affect the result. The software uses the calculated activities for the assemblage components and solves equation 6.3 for P and T. A set of several independent reactions is calculated, and the resulting pressure and temperature intersection values are averaged using a least-squares model to arrive at the average P-T result (Powell and Holland, 1994).

With the instrument uncertainty minimised by pooling the chemical data, the main uncertainties in this method are: (i) the assumption of chemical equilibrium of the mineral assemblage; (ii) the uncertainty of the enthalpy values of mineral components in the internally-consistent data set propagating into the equilibrium coefficient ($K$); and (iii) uncertainty associated with imprecise activity-composition models for minerals (Powell and Holland, 1994). These uncertainties are propagated through equation 6.3 and contribute to the $1\sigma$ standard deviation reported by the software. For a complete explanation of the mathematics of error propagation, the reader is directed to Powell and Holland (1988).

## 6.3 Sample descriptions and analytical results

This section presents sample descriptions and analytical results for the samples evaluated in this study. All electron-microprobe analysis locations and mineral composition data for samples JF10-12, JF10-88, and CA108b are given in Appendix E. For electron-microprobe analysis locations and mineral composition data for samples NA023a, NA046, and NA061e, the reader is directed to McLeish (2008).

High-resolution WDS maps and traverses of garnet were carried to discern any preserved chemical zoning or other systematic compositional variation that could affect analysis of other phases. Chemical zoning of metamorphic minerals such as garnet, clinopyroxene and plagioclase has been used to derive pressure-temperature paths, or path segments resulting from single or multiple stages of metamorphism (e.g. Pattison and Begin, 1994b,a; Alcock, 1996; O'Brien, 1999; Pyle and Spear, 1999; Cooke et al., 2000; Caddick et al., 2010). high temperature conditions persist for an extended period, zoned minerals may become homogenized by diffusion (Tacey et al., 1976; Frost and Chacko, 1989; Spear, 1995; Alcock, 1996). Multiple and protracted high-grade metamorphic episodes experienced by the western CGB are likely to have obliterated any prograde chemical zoning that may have been present in the minerals analysed in this study (Jamieson et al., 1995). Maps obtained from this study show chemical zoning is limited to the outermost rims of garnets in contact with biotite, probably reflecting retrograde Fe-Mg ion exchange (Spear, 1995). This thin retrograde rim zone is visible on high-resolution WDS maps, although the absolute change in concentration of this rim zone is very small relative to the centre of the mapped crystal, and is within the nominal 2% instrument error.

Table 6.3 is a summary of the average pressure-temperature estimates for each sample. Figure 6.6 is a P-T plot of the average pressure-temperature conditions and reactions of each of the six samples.

Table 6.3: Average pressure-temperature results for the six samples evaluated.

| Sample | T (°C) | $1\sigma$ | P (kbar) | $1\sigma$ |
|---|---|---|---|---|
| JF10-12 | 775 | 196 | 10.6 | 2.8 |
| JF10-88 | 807 | 135 | 11.1 | 2.1 |
| NA061e | 817 | 121 | 10.4 | 1.7 |
| NA023a | 812 | 102 | 10.6 | 1.5 |
| NA046 | 722 | 112 | 8.1 | 1.7 |
| CA108b | 717 | 124 | 8.6 | 1.7 |
| | | | | |
| Median | 791 | 123 | 10.5 | 1.7 |

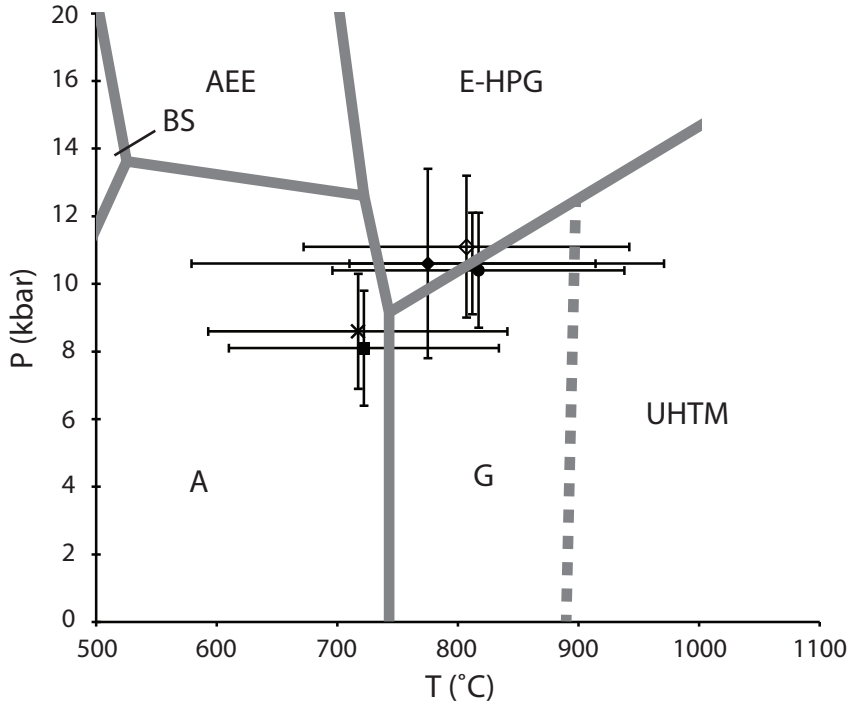


◆ ***JF10-12***
1) Prp + 2Grs + 3Qtztz = 3An + 3Di
2) 3Hed + 3Cats = 2Grs + Alm
3) 2Prp + 4Grs + 3Ts + 12Qtztz = 12An + 3Tr
4) 2Grs + Alm + 3Qtztz = 3An + 3Hed
5) 4Grs + 5Alm + 3Ts + 12Qtztz = 3Prp + 12An + 3Fact
6) 12An + 18Di + 3Parg = 5Prp + 10Grs + 3Ab + 3Tr
7) Ab + Hed + 3Cats + Ts + Geik = 4An + Parg + Ilm

● ***NA061e***
1) Prp + 2Grs + 3Qtztz = 3An + 3Di
2) 2Prp + Grs + 3Qtz = 3An + 3En
3) 2Grs + Alm + 3Qtz = 3An + 3Hed
4) Grs + 2Alm + 3Qtz = 3An + 3Fs
5) 5Prp + 10Grs + 3Fact + 15Qtz = 15An + 15Hed + 3Tr
6) 12An + 18Di + 3Parg = 5Prp + 10Grs + 3Ab + 3Tr

■ ***NA046***
1) Cats + Qtz = An
2) 3Di + 3Cats = Prp + 2Grs
3) 3Cats + 3En = 2Prp + Grs
4) 2Grs + Alm + 3Qtz = 3An + 3Hed
5) 3Cats + 3Fs = Grs + 2Alm
6) 5Prp + 3Fact = 5Alm + 3Tr
7) 12Di + 3Ts = 2Prp + 4Grs + 3Tr
8) 12An + 18Di + 3Parg = 5Prp + 10Grs + 3Ab + 3Tr

◇ ***JF10-88***
1) Prp + 2Grs + 3Qtz = 3An + 3Di
2) 2Prp + Grs + 3Qtz = 3An + 3En
3) Grs + En = 2Di + Cats
4) 3Hed + 3Cats = 2Grs + Alm
5) 3Cats + 3Fs = Grs + 2Alm
6) 5Prp + 10Grs + 3Fact = 15Hed + 15Cats + 3Tr
7) 12An + 18Di + 3Parg = 5Prp + 10Grs + 3Ab + 3Tr

▲ ***NA023a***
1) Cats + Qtz = An
2) 3Di + 3Cats = Prp + 2Grs
3) 3Cats + 3En = 2Prp + Grs
4) 3Hed + 3Cats = 2Grs + Alm
5) 3Cats + 3Fs = Grs + 2Alm
6) 5Prp + 3Fact = 5Alm + 3Tr
7) 4En + Ts = 2Prp + Tr
8) 12An + 18Di + 3Parg = 5Prp + 10Grs + 3Ab + 3Tr
9) 2Prp + 4Grs + 3Fact + 3geik = 12Hed + 3Ts + 3Ilm

× ***CA108b***
1) Grs + 2Sill + Qtz = 3An
2) 3Ilm + Sill + 2Qtz = Alm + 3Ru
3) 4Grs + 3phl + 12Sill = Prp + 3East + 12An
4) 3Alm + 3East + 4Qtz = 2Prp + 3Ann + 4Sill

Figure 6.2: Pressure-temperature plot of the six samples evaluated. Error bars of points are 1$\sigma$. Mineral abbreviations are in Appendix D, other abbreviations are: A, Amphibolite facies; AEE, Amphibole-epidote eclogite facies; BS, Blueschist facies; E-HPG, medium-temperature eclogite - high-pressure granulite metamorphism; G, Granulite facies; GS, Greenschist facies; UHTM, Ultrahigh-temperature metamorphism (facies boundaries from Brown, 2009).

### *6.3.1 JF10-12*

JF10-12 is an amphibolite dyke that cross-cuts the foliation of the host orthogneiss from the NTLSZ (Fig. 3.1). The dyke is a dark, fine-grained amphibolite with no visible internal structure (Fig. 6.3a). A weak foliation is defined by alignment of elongate amphibole grains and garnet and clinopyroxene grain clusters (Fig. 6.3b). The mineral assemblage of this rock is Amp - Grt - Pl - Cpx - Qtz $\pm$ Ilm $\pm$ Ru. Scapolite, present in relatively low modal amounts, and occurs as small irregular grains along grain boundaries or interstitial spaces, suggesting late interaction with a $CO_2$-rich fluid (Fig. 6.3c and d). The rock has a recrystallized texture with straight grain boundaries, triple-points between most minerals in the rock. There are few signs of earlier, high-strain conditions, with only the largest quartz grains still preserving undulose extinction.

This rock yields an average P-T of 775$\pm$196°C and 10.6$\pm$2.8 kbar. Average compositions for the equilibrium assemblage used in thermobarometry are given in Table 6.4. Figure 6.4 shows high-resolution WDS garnet maps (Fig. 6.4b through e) and composition profiles (Fig. 6.4f) for a selected garnet crystal. This garnet shows a nearly flat zoning profile in both WDS maps and in the transect. Only weak depletion in Mg was observed in the outermost few microns of the grain.

### *6.3.2 JF10-88*

JF10-88 is a dyke that cross-cuts the foliation of the host orthogneiss from the interior of the Kiosk domain, on the shore of Craig Lake. (Fig. 3.1). The dyke is a dark, very fine grained amphibolite with no visible foliation on the outcrop or hand-sample scale (Fig. 6.5a). The assemblage is Pl - Amp - Ksp - Grt - Cpx - Opx $\pm$ Bt. Carbonate, present in low modal abundance, suggests late metasomatism by a $CO_2$-rich fluid. A weak foliation is defined by alignment of elongate amphibole grains (Fig. 6.5b and c). The rock has a recrystallized texture with straight grain boundaries and triple-points between most minerals in the rock. Orthopyroxene is replaced by clinopyroxene in some areas of the thin-section, but the two minerals are in textural equilibrium in others. A similar relationship exists between amphibole and biotite. Areas of apparent textural equilibrium were selected for EMP analysis. Biotite is interpreted to be retrograde based on replacement textures of amphibole tips, and lack of biotite inclusions in large amphibole grains.

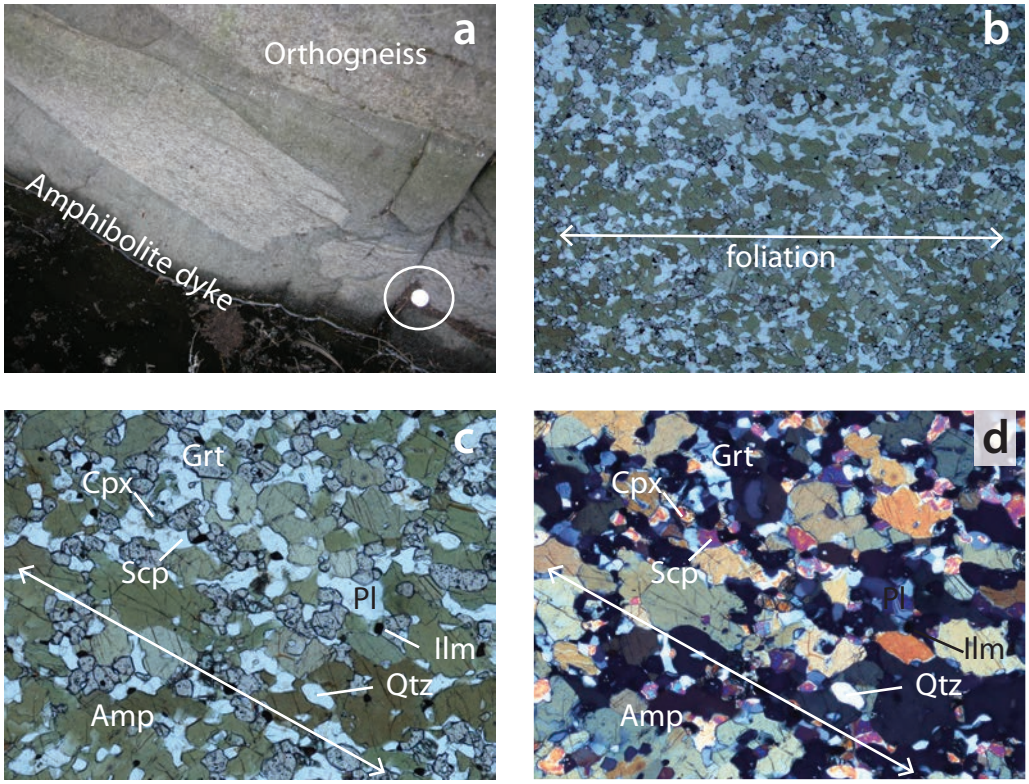


Figure 6.3: Outcrop pictures and photomicrographs for sample JF10-12. a) Outcrop picture of the JF10-12 dyke (quarter for scale; UTM x: 0647135, y: 5089126). b) Photomicrograph showing the fine grain size, and weak foliation (PPL; FOV = 6.25mm). Photomicrographs showing the well equilibrated texture of the dyke. Note the large polygonal amphibole grains, and the numerous straight grain boundaries and triple points between all minerals ( c) PPL; FOV = 2.5mm, d) XPL; FOV = 2.5mm)

Table 6.4: Average mineral compositions for sample JF10-12.

| Mineral | Garnet | 2SD | Plagioclase | 2SD | Amphibole | 2SD | Clinopyroxene | 2SD | Ilmenite | 2SD |
|---|---|---|---|---|---|---|---|---|---|---|
| Wt. % | | | | | | | | | | |
| SiO2 | 38.93 | 0.41 | 54.77 | 0.72 | 42.83 | 0.79 | 51.11 | 0.50 | 0.53 | 1.66 |
| TiO2 | 0.07 | 0.24 | 0.00 | 0.00 | 1.63 | 0.22 | 0.36 | 0.07 | 50.81 | 19.87 |
| Al2O3 | 21.97 | 0.27 | 26.72 | 0.59 | 12.11 | 0.38 | 3.61 | 0.30 | 0.19 | 0.55 |
| FeO | 24.90 | 0.40 | 0.17 | 0.16 | 11.56 | 0.54 | 7.61 | 0.57 | 40.41 | 19.83 |
| MnO | 0.75 | 0.05 | 0.00 | 0.01 | 0.03 | 0.04 | 0.06 | 0.03 | 0.60 | 2.97 |
| MgO | 6.65 | 0.41 | 0.00 | 0.00 | 13.09 | 0.42 | 13.14 | 0.37 | 0.56 | 1.00 |
| CaO | 7.29 | 0.32 | 10.19 | 0.56 | 11.89 | 0.40 | 22.54 | 0.37 | 0.11 | 0.14 |
| Na2O | 0.00 | 0.01 | 6.03 | 0.32 | 1.81 | 0.09 | 0.72 | 0.04 | 0.01 | 0.02 |
| K2O | 0.03 | 0.01 | 0.13 | 0.02 | 1.01 | 0.08 | 0.02 | 0.02 | 0.03 | 0.03 |
| Total | 100.59 | 0.59 | 98.01 | 0.72 | 95.97 | 0.88 | 99.17 | 0.52 | 93.38 | 1.19 |
| | | | | | | | | | | |
| Cations | | | | | | | | | | |
| Si | 3.01 | 0.03 | 2.52 | 0.03 | 6.37 | 0.12 | 1.92 | 0.02 | 0.01 | 0.04 |
| Ti | 0.00 | 0.01 | 0.00 | 0.00 | 0.18 | 0.03 | 0.01 | 0.00 | 1.00 | 0.29 |
| Al | 2.00 | 0.02 | 1.45 | 0.03 | 2.12 | 0.07 | 0.16 | 0.01 | 0.01 | 0.02 |
| Fe 2+ | 1.61 | 0.03 | 0.01 | 0.01 | 1.44 | 0.07 | 0.24 | 0.02 | 0.91 | 0.00 |
| Mn | 0.05 | 0.00 | 0.00 | 0.00 | 0.00 | 0.01 | 0.00 | 0.00 | 0.01 | 0.57 |
| Mg | 0.77 | 0.05 | 0.00 | 0.00 | 2.90 | 0.09 | 0.73 | 0.02 | 0.02 | 0.70 |
| Ca | 0.60 | 0.03 | 0.50 | 0.03 | 1.89 | 0.06 | 0.91 | 0.02 | 0.00 | 0.40 |
| Na | 0.00 | 0.00 | 0.54 | 0.03 | 0.52 | 0.02 | 0.05 | 0.00 | 0.00 | 0.00 |
| K | 0.00 | 0.00 | 0.01 | 0.00 | 0.19 | 0.02 | 0.00 | 0.00 | 0.00 | 0.00 |
| Total | 8.05 | 0.05 | 5.03 | 0.03 | 15.62 | 0.15 | 4.02 | 0.02 | 1.98 | 0.00 |

Structural Formulae [1]

| | |
|---|---|
| Garnet | $(Mg_{0.55}Fe_{1.6}Ca_{0.6})Al_{2.0}(Si_3O_4)$ |
| Plagioclase | $Na_{0.54}Ca_{0.5}Al_{1.45}Si_{2.52}O_8$ |
| Amphibole [2] | $(Na_{0.41}K_{0.19})(Ca_{1.9}Na_{0.11})(Mg_{2.9}Fe_{1.43}Al_{0.48}Ti_{0.18})(Si_{6.37}Al_{1.64})O_{22}(OH)_2$ |
| Clinopyroxene [3] | $(Ca_{0.9}Na_{0.05})(Mg_{0.73}Fe_{0.18}Al_{0.07})(Si_{1.91}Al_{0.09})O_6$ |
| Ilmenite | $Fe_{0.01}Ti_{0.01}O_3$ |

End-members

| | |
|---|---|
| Garnet | $Grs_{20}$ $Alm_{53}$ $Prp_{25}$ $Spss_2$ |
| Plagioclase | $Ab_{52}$ $An_{48}$ |
| Amphibole [2] | Pargasitic Hornblende |
| Clinopyroxene | $Di_{75}$ $Hd_{25}$ |

| Oxygen pfu. | 12 | 8 | 8 | 6 | 3 |
|---|---|---|---|---|---|

1 Structural formulae after Deer et al. (1996)

2 Amphibole cation values and classification using PROBE-AMPH (Tindle and Webb, 1994, and reference therein)

3 Cation values after Sturm (2002)

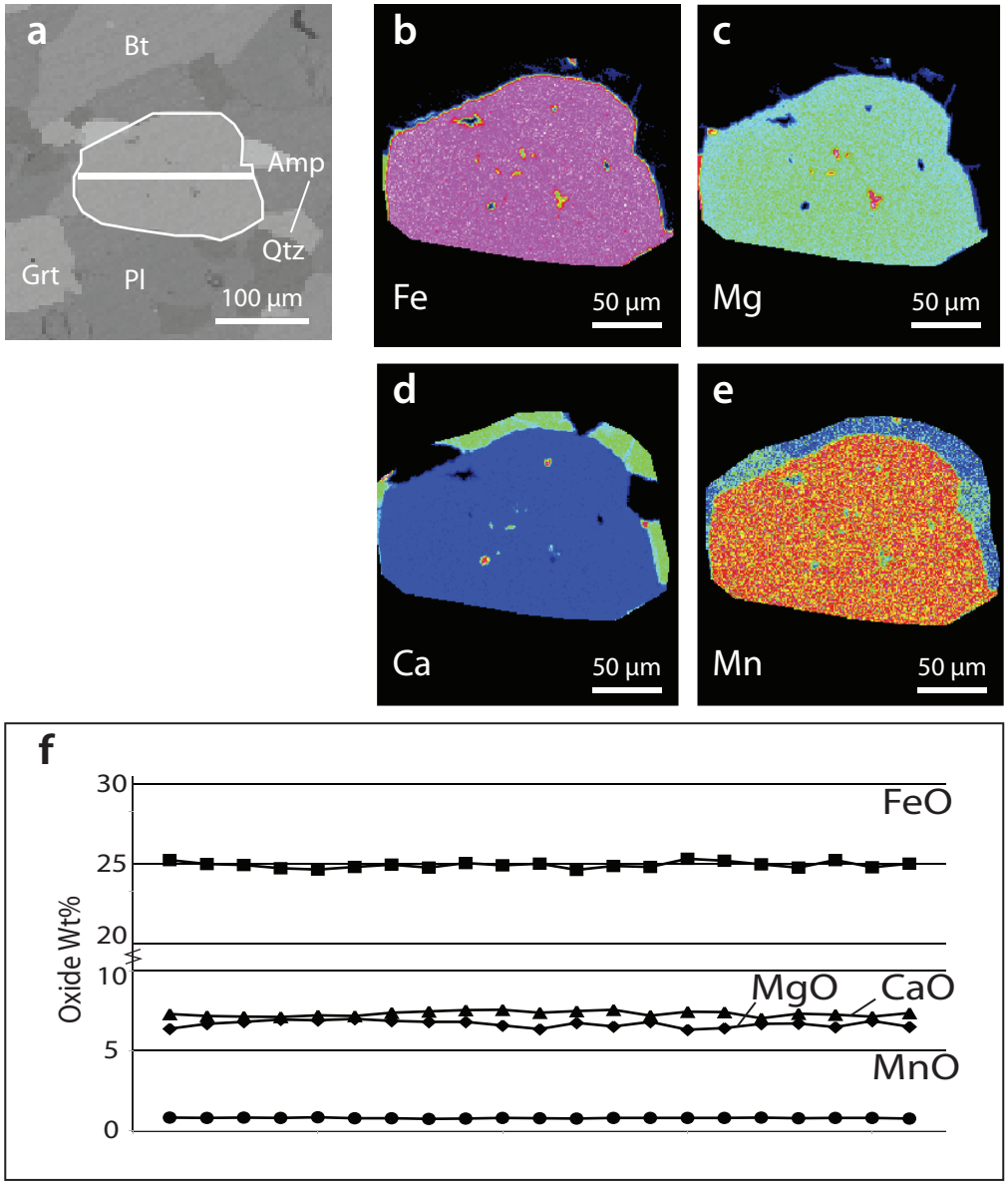


Figure 6.4: High-resolution WDS maps and analytical traverse of a selected garnet in sample JF10-12. Note that WDS maps are cropped close to target garnet grain, and warmer colours in maps represent increased relative concentration. a) BSE image of garnet selected for WDS mapping. The traverse line is indicated by the thick white line. b) Fe M$\alpha$ WDS map of selected garnet. c) Mg M$\alpha$ WDS map of selected garnet. Note the slightly lower concentration along the grain boundary. d) Ca M$\alpha$ WDS map of selected garnet. d) Mn M$\alpha$ WDS map of selected garnet. f) Analytical traverse across the selected garnet.

This rock yields an average P-T of 807±135°C and 11.1±2.1 kbar. Average compositions for the assemblage used in thermobarometry are given in Table 6.5. Figure 6.6 shows high-resolution WDS garnet maps (Fig. 6.6b through e) and analytical profiles (Fig. 6.6f) for a selected garnet crystal. This garnet shows a nearly flat zoning profile in both WDS maps and the analytical profile. Weak depletion in Fe and Mg was resolvable in WDS maps in the outermost 10-15 microns of the grain. This thin zone is resolvable in the WDS maps, but the change in absolute oxide concentration is very small (Fig. 6.6f).

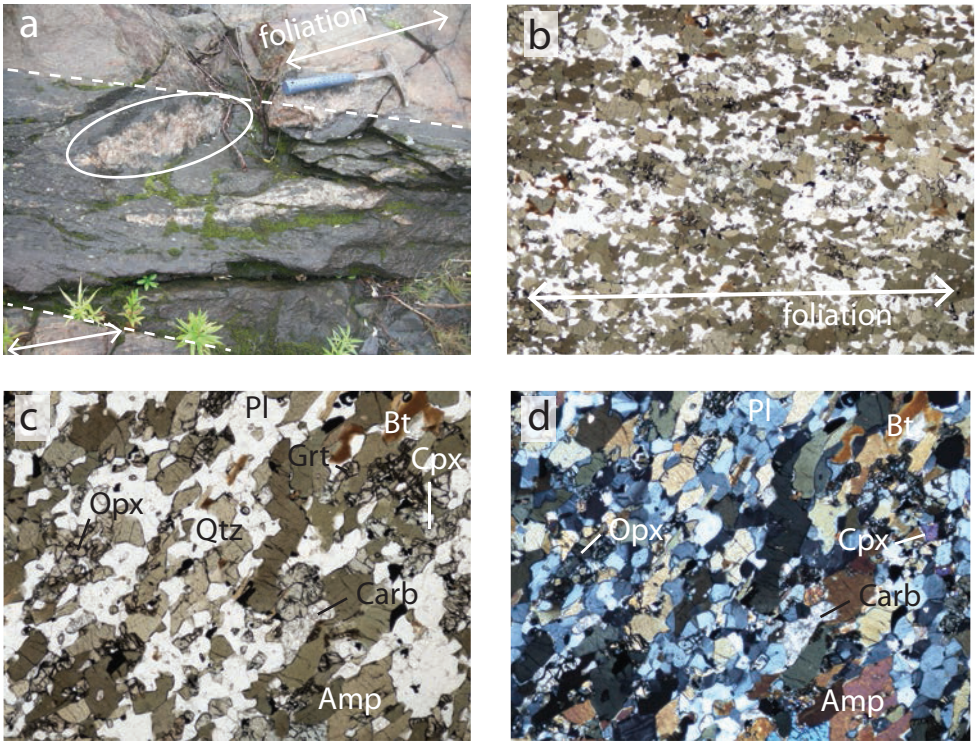


Figure 6.5: Outcrop pictures and photomicrographs for sample JF10-88. a) Outcrop picture of the JF10-88 dyke. Note part of the host orthogneiss mixed with the dyke (white ellipse) (hammer for scale; UTM x: 0649311, y: 5083497). b) Photomicrograph showing the fine grain size, and weak foliation (PPL; FOV = 6.25mm). Photomicrographs showing the very fine grained, equilibrium texture of the dyke. Note the numerous straight grain boundaries and triple points between all minerals ( c) PPL; FOV = 2.5mm, d) XPL; FOV = 2.5mm)

### *6.3.3 CA108b*

Sample CA108b is a well foliated paragneiss from the BBLSZ (Fig. 3.1). Detailed outcrop and petrographic description of this rock are presented in section 4.3.1. This rock

Table 6.5: Average mineral compositions for sample JF10-88.

| Mineral | Garnet | 2SD | Plagioclase | 2SD | K-feldspar | 2SD | Amphibole | 2SD | Orthopyroxene | 2SD | Clinopyroxene | 2SD |
|---|---|---|---|---|---|---|---|---|---|---|---|---|
| Wt. % | | | | | | | | | | | | |
| SiO2 | 38.15 | 0.79 | 59.33 | 0.92 | 59.61 | 2.12 | 42.46 | 1.02 | 51.87 | 0.59 | 52.26 | 0.44 |
| TiO2 | 0.05 | 0.08 | 0.00 | 0.00 | 0.47 | 0.20 | 1.74 | 0.18 | 0.07 | 0.04 | 0.19 | 0.07 |
| Al2O3 | 22.27 | 0.36 | 24.83 | 0.45 | 19.09 | 0.39 | 12.01 | 0.70 | 1.56 | 0.18 | 2.71 | 0.29 |
| FeO | 26.08 | 0.60 | 0.21 | 0.19 | 0.39 | 0.24 | 13.60 | 0.68 | 24.45 | 0.86 | 8.90 | 0.59 |
| MnO | 3.36 | 0.86 | 0.00 | 0.01 | 0.01 | 0.02 | 0.16 | 0.03 | 0.92 | 0.07 | 0.30 | 0.02 |
| MgO | 5.17 | 0.86 | 0.02 | 0.10 | 0.00 | 0.01 | 12.53 | 0.65 | 21.08 | 0.51 | 13.09 | 0.25 |
| CaO | 6.12 | 0.26 | 6.13 | 0.41 | 0.09 | 0.11 | 11.51 | 0.27 | 0.32 | 0.08 | 22.35 | 0.33 |
| Na2O | 0.02 | 0.06 | 8.04 | 0.24 | 0.99 | 0.26 | 1.83 | 0.09 | 0.02 | 0.02 | 0.97 | 0.05 |
| K2O | 0.01 | 0.02 | 0.18 | 0.10 | 13.34 | 0.93 | 1.59 | 0.14 | 0.00 | 0.01 | 0.03 | 0.01 |
| Total | 101.23 | 1.15 | 98.57 | 1.10 | 94.00 | 2.38 | 97.43 | 0.46 | 100.29 | 0.61 | 100.79 | 0.51 |
| | | | | | | | | | | | | |
| Cations | | | | | | | | | | | | |
| Si | 2.95 | 0.06 | 2.70 | 0.04 | 2.94 | 0.10 | 6.36 | 0.15 | 1.94 | 0.02 | 1.93 | 0.02 |
| Ti | 0.00 | 0.00 | 0.00 | 0.00 | 0.02 | 0.01 | 0.20 | 0.02 | 0.00 | 0.00 | 0.01 | 0.00 |
| Al | 2.03 | 0.03 | 1.33 | 0.02 | 1.11 | 0.02 | 2.12 | 0.12 | 0.07 | 0.01 | 0.12 | 0.01 |
| Fe | 1.69 | 0.04 | 0.01 | 0.01 | 0.02 | 0.01 | 1.70 | 0.09 | 0.77 | 0.03 | 0.28 | 0.02 |
| Mn | 0.22 | 0.06 | 0.00 | 0.00 | 0.00 | 0.00 | 0.02 | 0.00 | 0.03 | 0.00 | 0.01 | 0.00 |
| Mg | 0.60 | 0.10 | 0.00 | 0.01 | 0.00 | 0.00 | 2.80 | 0.15 | 1.18 | 0.03 | 0.72 | 0.01 |
| Ca | 0.51 | 0.02 | 0.30 | 0.02 | 0.00 | 0.01 | 1.85 | 0.04 | 0.01 | 0.00 | 0.89 | 0.01 |
| Na | 0.00 | 0.01 | 0.71 | 0.02 | 0.09 | 0.03 | 0.53 | 0.03 | 0.00 | 0.00 | 0.07 | 0.00 |
| K | 0.00 | 0.00 | 0.01 | 0.01 | 0.84 | 0.06 | 0.30 | 0.03 | 0.00 | 0.00 | 0.00 | 0.00 |
| Total | 8.00 | 0.12 | 5.06 | 0.06 | 5.03 | 0.13 | 15.88 | 0.10 | 4.00 | 0.02 | 4.02 | 0.02 |

| Structural Formulae [1] | |
|---|---|
| Garnet | $(Mg_{0.6}Fe_{1.69}Ca_{0.51})Al_{2.0}(Si_{2.9}O_4)$ |
| Plagioclase | $Na_{0.71}Ca_{0.3}Al_{1.33}Si_{2.95}O_8$ |
| K-feldspar | $K_{0.84}Na_{0.09}Al_{1.11}Si_{2.94}O_8$ |
| Amphibole [2] | $(Na_{0.34}K_{0.3})(Ca_{1.89}Na_{0.18})(Mg_{2.76}Fe_{1.68}Al_{0.35}Ti_{0.19})(Si_{6.27}Al_{1.74})O_{22}(OH)_2$ |
| Orthopyroxene [3] | $(Mg_{1.78}Fe_{0.77}Al_{0.01})(Si_{1.94}Al_{0.06})O_6$ |
| Clinopyroxene [3] | $(Ca_{0.88}Na_{0.07})(Mg_{0.72}Fe_{0.1}Al_{0.04})(Si_{1.92}Al_{0.08})O_6$ |

| End-members | |
|---|---|
| Garnet | $Grs_{17}$ $Alm_{56}$ $Prp_{20}$ $Spss_7$ |
| Plagioclase | $Ab_{70}$ $An_{30}$ |
| K-feldspar | $Or_{90}$ $Ab_{10}$ |
| Amphibole [2] | Potassian-Magnesio-Hastingsitic Hornblende |
| Orthopyroxene | $En_{61}$ $Fs_{39}$ |
| Clinopyroxene | $Di_{72}$ $Hd_{28}$ |

| Oxygen pfu. | 12 | 8 | 8 | 23 | 6 | 6 |
|---|---|---|---|---|---|---|

1 Structural formulae after Deer et al. (1996)

2 Amphibole cation values and classification using PROBE-AMPH (Tindle and Webb (1994), and references therein

3 Cation values after Sturm (2002)

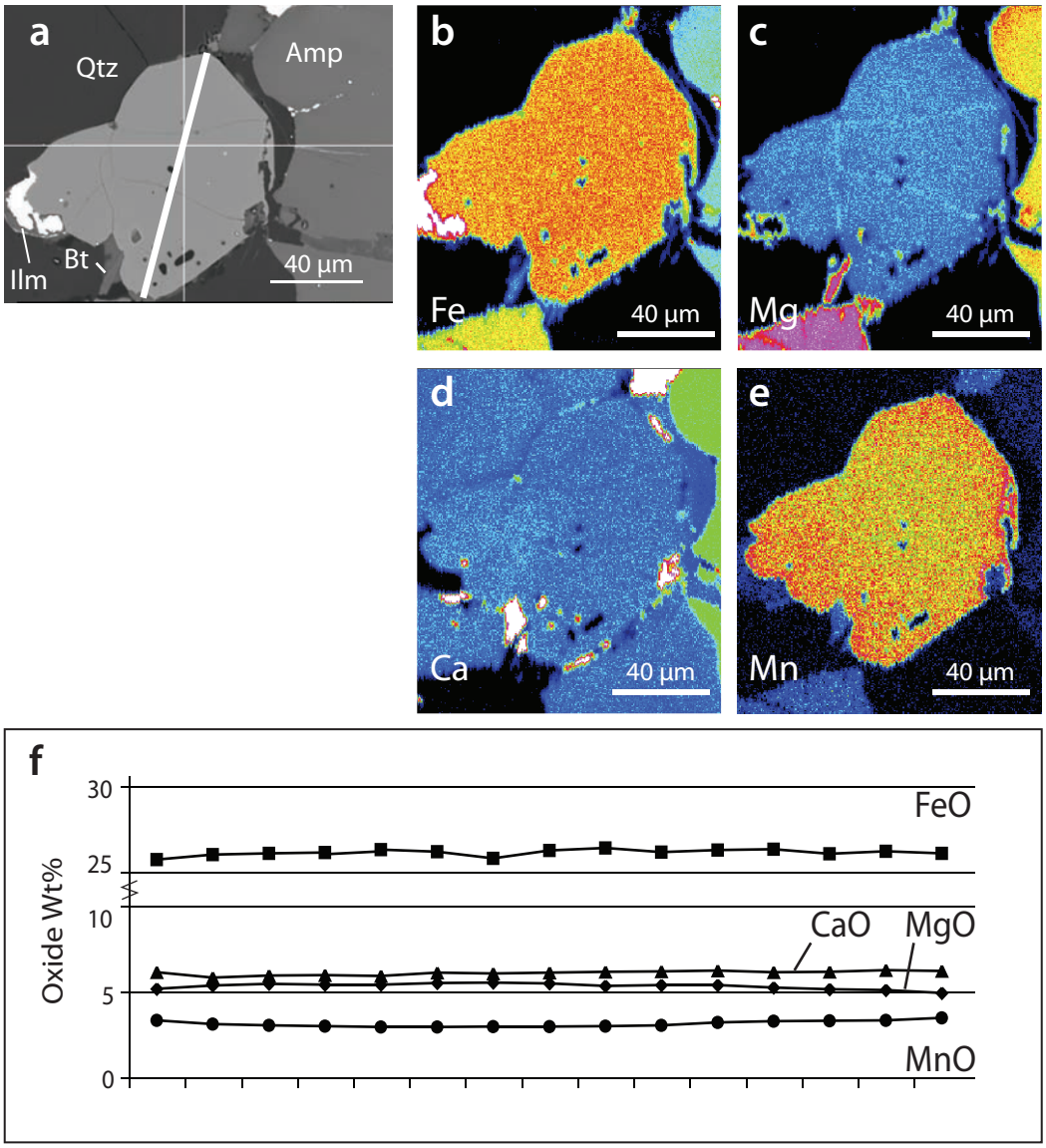


Figure 6.6: High-resolution WDS maps and analytical traverse of a selected garnet in sample JF10-88. High-resolution WDS maps and analytical traverse of a selected garnet in sample JF10-12. Note that WDS maps are cropped close to target garnet grain, and warmer colours in maps represent increased relative concentration. a) BSE image of garnet selected for WDS mapping. The traverse line is indicated by the thick white line. b) Fe M$\alpha$ WDS map of selected garnet. c) Mg M$\alpha$ WDS map of selected garnet. d) Ca M$\alpha$ WDS map of selected garnet. e) Mn M$\alpha$ WDS map of selected garnet. Note the slightly higher concentration along the grain boundary. f) Analytical traverse across the selected garnet.

has the assemblage Ksp - Qtz - Grt - Pl - Ilm - Sil - Bt, and yields an average P-T of 717±124°C and 8.6±1.6 kbar. Average compositions for the minerals used in thermobarometry are given in Table 6.6. Figure 6.7 shows high-resolution WDS garnet maps (Fig. 6.7b through e) and analytical profiles (Fig. 6.7f) for a selected garnet crystal. This garnet shows a nearly flat zoning profile in both WDS and in analytical traverses.

### *6.3.4 Orthogneiss samples*

Electron-microprobe data from three orthogneiss samples from the Kiosk domain and the McLintock subdomain from McLeish (2008) were reprocessed as part of this study. This section presents EMP data and results only. For outcrop and petrographic descriptions of samples NA023a, NA046, and NA061e, the reader is referred to McLeish (2008).

McLeish (2008) analysed mineral assemblages and assessed compositional variation, however; high-resolution WDS maps or analytical traverses were beyond the scope of his study. Due to analytical time constraints, these samples were not re-analysed. Inspection of the EMP data shows that the mineral composition is very consistent in these samples. Standard deviations of EMP data for the rock-forming minerals such as garnet, plagioclase, amphibole and pyroxene are typically $<1$ Wt% oxide, and within the 2% analytical error of average mineral compositions. Thus, it is reasonable to assume that these minerals are not zoned, and that mean mineral compositions can be used for P-T calculations.

**NA023a** Sample NA023a is a well foliated metamonzonite orthogneiss from the interior of the Kiosk domain (Fig. 3.1). This rock has the assemblage Grt - Pl - Amp - Opx - Cpx - Qtz - Ilm, and yields an average P-T of of 812±102°C and 10.6±1.5 kbar. Average compositions for the assemblage used in thermobarometry are given in Table 6.7.

**NA046** Sample NA046 is a well foliated metaquartz-monzonite orthogneiss from the northern McLintock subdomain (Fig. 3.1). This rock has the assemblage Grt - Pl - Amp - Qtz - Opx - Cpx - Ilm, and yields an average P-T of of 722±112°C and 8.1±1.7 kbar. Average compositions for the assemblage used in thermobarometry are given in Table 6.8.

Table 6.6: Average mineral compositions for sample CA108b.

| Mineral | Garnet | 2SD | Plagioclase | 2SD | K-feldspar | 2SD | Biotite | 2SD | Ilmenite | 2SD |
|---|---|---|---|---|---|---|---|---|---|---|
| Wt. % | | | | | | | | | | |
| SiO2 | 37.62 | 0.58 | 62.54 | 0.83 | 64.73 | 0.75 | 36.12 | 0.74 | 0.06 | 0.08 |
| TiO2 | 0.02 | 0.04 | 0.00 | 0.00 | 0.04 | 0.04 | 3.87 | 0.36 | 47.56 | 4.76 |
| Al2O3 | 21.14 | 0.38 | 23.88 | 0.67 | 18.67 | 0.39 | 17.10 | 0.41 | 0.02 | 0.03 |
| FeO | 31.65 | 0.64 | 0.04 | 0.09 | 0.02 | 0.02 | 14.86 | 0.91 | 51.09 | 4.41 |
| MnO | 0.90 | 0.14 | 0.00 | 0.00 | 0.01 | 0.02 | 0.01 | 0.02 | 0.25 | 0.25 |
| MgO | 6.45 | 0.45 | 0.00 | 0.00 | 0.00 | 0.01 | 13.24 | 0.86 | 0.00 | 0.01 |
| CaO | 1.58 | 0.14 | 4.97 | 0.73 | 0.08 | 0.05 | 0.02 | 0.02 | 0.03 | 0.06 |
| Na2O | 0.00 | 0.01 | 9.14 | 0.50 | 1.99 | 2.01 | 0.07 | 0.03 | 0.01 | 0.02 |
| K2O | 0.02 | 0.03 | 0.17 | 0.34 | 13.89 | 2.90 | 9.41 | 0.43 | 0.04 | 0.03 |
| Total | 99.40 | 0.52 | 100.74 | 0.44 | 99.43 | 0.60 | 94.70 | 1.28 | 99.20 | 1.44 |
| | | | | | | | | | | |
| Cations | | | | | | | | | | |
| Si | 2.97 | 0.05 | 2.75 | 0.04 | 2.95 | 0.03 | 2.70 | 0.06 | 0.00 | 0.00 |
| Ti | 0.00 | 0.00 | 0.00 | 0.00 | 0.00 | 0.00 | 0.22 | 0.02 | 0.93 | 0.06 |
| Al | 1.97 | 0.04 | 1.24 | 0.03 | 1.00 | 0.02 | 1.51 | 0.04 | 0.00 | 0.00 |
| Fe 2+ | 2.09 | 0.04 | 0.00 | 0.00 | 0.00 | 0.00 | 0.93 | 0.06 | 1.12 | 0.13 |
| Mn | 0.06 | 0.01 | 0.00 | 0.00 | 0.00 | 0.00 | 0.00 | 0.00 | 0.01 | 0.01 |
| Mg | 0.76 | 0.05 | 0.00 | 0.00 | 0.00 | 0.00 | 1.48 | 0.10 | 0.00 | 0.00 |
| Ca | 0.13 | 0.01 | 0.23 | 0.03 | 0.00 | 0.00 | 0.00 | 0.00 | 0.00 | 0.00 |
| Na | 0.00 | 0.00 | 0.78 | 0.04 | 0.18 | 0.18 | 0.01 | 0.00 | 0.00 | 0.00 |
| K | 0.00 | 0.00 | 0.01 | 0.02 | 0.81 | 0.17 | 0.90 | 0.04 | 0.00 | 0.00 |
| Total | 7.99 | 0.05 | 5.02 | 0.03 | 4.94 | 0.07 | 7.75 | 0.12 | 2.06 | 0.06 |

| Structural Formulae [1] | |
|---|---|
| Garnet | $(Mg_{0.76}Fe_{2.1}Ca_{0.13})Al_2(Si_3O_4)$ |
| Plagioclase | $Na_{078}Ca_{0.23}Al_{1.24}Si_{2.75}O_8$ |
| K-feldspar | $K_{0.81}Na_{0.18}Al_{1.0}Si_{3.0}O_8$ |
| Biotite | $(K_{0.9})(Mg_{1.48}Fe_{0.93}Ti_{0.22})(Si_{2.7}Al_{1.5})O_{10}(OH)_2$ |
| ilmenite | $Fe_{1.12}Ti_{0.93}O_3$ |

| End-members | |
|---|---|
| Garnet | $Grs_4$ $Alm_{69}$ $Prp_{25}$ $Spss_2$ |
| Plagioclase | $Ab_{77}$ $An_{23}$ |
| K-feldspar | $Or_{82}$ $Ab_{18}$ |
| Biotite | $Ann_{39}$ $Phl_{61}$ |

| Oxygen pfu. | 12 | 8 | 8 | 11 | 3 |
|---|---|---|---|---|---|

1 Structural formulae after Deer et al. (1996)

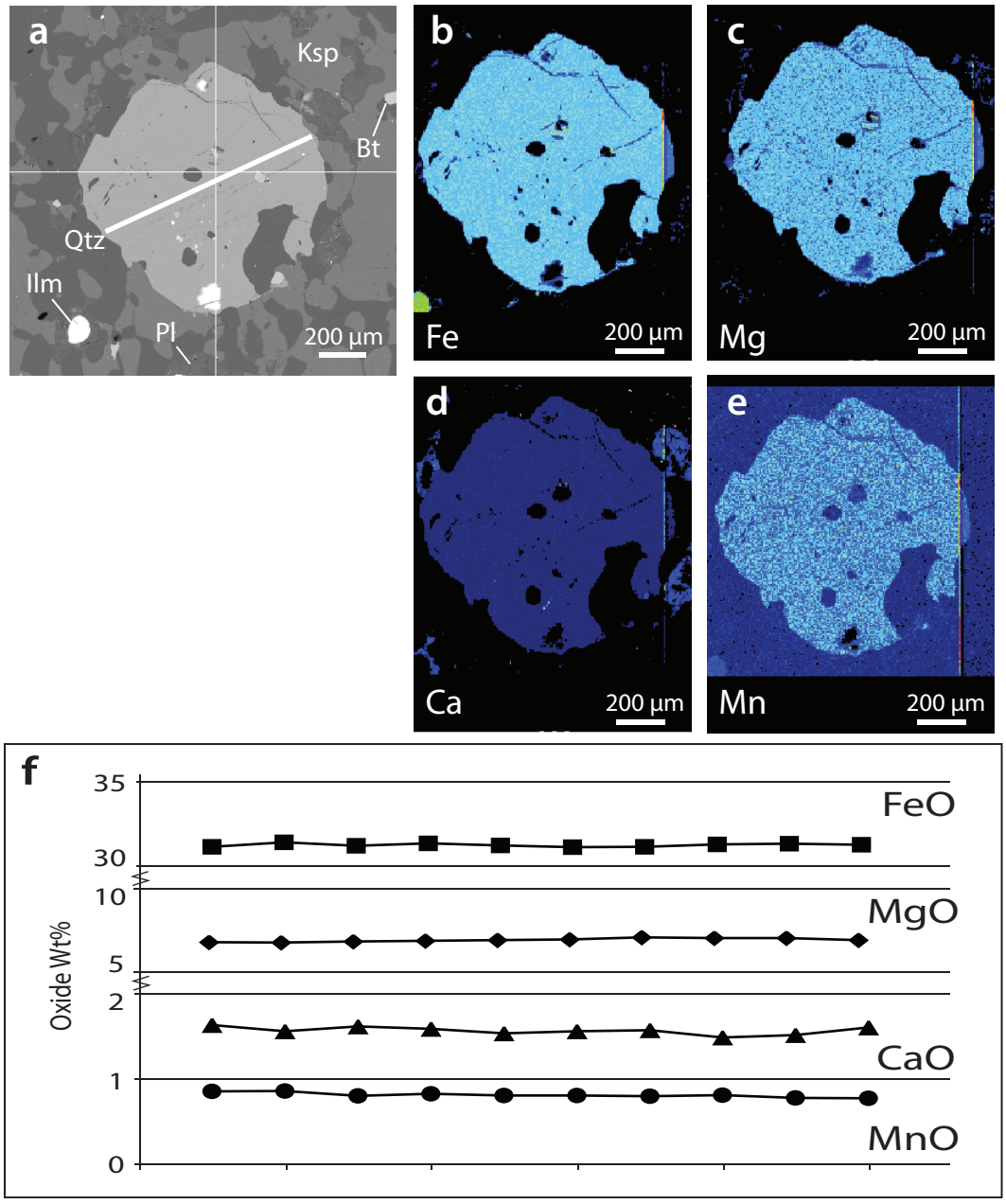


Figure 6.7: High-resolution WDS maps and analytical traverse of a selected garnet in sample CA108b. a) BSE image of garnet selected for WDS mapping. The traverse line is indicated by the thick white line. b) Fe M$\alpha$ WDS map of selected garnet. c) Mg M$\alpha$ WDS map of selected garnet. d) Ca M$\alpha$ WDS map of selected garnet. d) Mn M$\alpha$ WDS map of selected garnet. f) Analytical traverse across the selected garnet. Note the flat zoning profile shown in both the WDS maps and the analytical traverse.

**NA061e** Sample NA061e is a well foliated metamonzonite orthogneiss from the northern McLintock subdomain (Fig. 3.1). This rock has the assemblage Grt - Pl - Amp - Qtz - Opx - Cpx - Ilm, and yields an average P-T of of 817±121°C and 10.4±1.7 kbar. Average compositions for the assemblage used in thermobarometry are given in Table 6.9.

## 6.4 Discussion

### *6.4.1 Interpretation of results*

**Metamorphic conditions** Most samples evaluated in this study exhibit granulite-facies mineral assemblages. Whilst all samples overlap in $1\sigma$ error, there are two closely spaced clusters of data. The upper cluster (JF10-12, JF10-88, NA061e, and NA023a) is composed of Cpx±Opx-bearing granulite-facies mafic dykes and orthogneisses (Fig. 6.2), and has a mean P-T of 803±139°C and 10.7±2 kbar. The similarity of P-T conditions recorded in these units over a large area suggests that they (re)equilibrated during broadly similar regional P-T conditions. The smaller cluster at upper-amphibolite to lower-granulite P-T conditions has a mean P-T of 720±118°C and 8.3±1.7 kbar consists of a sillimanite-bearing granulite-facies paragneiss from the BBLSZ (CA108b), and a Cpx-Opx-bearing granulite-facies orthogneiss from the northern McLintock domain (NA046). Although these rocks a both found in pegmatite-bearing shear zones, they are not spatially or lithologically related. Timmermann (1998) concluded that the P-T conditions of the Algonquin domain are quite variable, and interpreted peak Grenvillian P-T conditions to be granulite-grade at ca. 750-850°C and 10-12 kbar (Fig. 6.8). She attributed lower P-T estimations to represent variable retrograde equilibrium. A similar interpretation is invoked for P-T data in this study, lower-granulite-grade metamorphic conditions could be the result of variable degrees of retrogression, and the peak conditions of Grenvillian metamorphism for the Kiosk domain are similar to the Algonquin domain at ca. 800°C and 10 kbar.

**The polymetamorphic problem** Polymetamorphism in the Kiosk and Algonquin domains creates uncertainty in ascribing the P-T estimates generated to a specific metamorphic event or orogenic phase. For example, Sudbury-type metadiabase dykes that intruded

Table 6.7: Average mineral compositions for sample NA023a (after McLeish, 2008)

| Mineral | Garnet | 2SD | Plagioclase | 2SD | Amphibole | 2SD | Orthopyroxene | 2SD | Clinopyroxene | 2SD | Ilmenite | 2SD |
|---|---|---|---|---|---|---|---|---|---|---|---|---|
| Wt. % | | | | | | | | | | | | |
| SiO2 | 38.05 | 0.28 | 60.38 | 1.19 | 42.31 | 0.86 | 51.99 | 0.43 | 51.85 | 0.95 | 0.08 | 0.04 |
| TiO2 | 0.01 | 0.02 | 0.00 | 0.01 | 2.12 | 0.28 | 0.07 | 0.05 | 0.24 | 0.13 | 46.39 | 5.33 |
| Al2O3 | 21.23 | 0.34 | 26.05 | 0.80 | 12.63 | 0.30 | 1.65 | 0.26 | 3.06 | 1.07 | 0.05 | 0.05 |
| Cr2O3 | 0.00 | 0.01 | 0.00 | 0.01 | 0.03 | 0.07 | 0.01 | 0.02 | 0.03 | 0.07 | 0.23 | 0.03 |
| FeO | 26.71 | 1.00 | 0.43 | 0.48 | 14.39 | 1.03 | 25.23 | 1.18 | 9.39 | 1.09 | 53.58 | 4.88 |
| MnO | 1.25 | 0.09 | 0.01 | 0.03 | 0.07 | 0.05 | 0.32 | 0.03 | 0.16 | 0.06 | 0.35 | 0.11 |
| MgO | 6.14 | 0.48 | 0.03 | 0.17 | 11.92 | 0.77 | 21.39 | 0.86 | 12.90 | 1.03 | 0.06 | 0.03 |
| CaO | 6.77 | 0.79 | 6.78 | 0.86 | 11.91 | 0.25 | 0.36 | 0.04 | 22.61 | 0.66 | 0.11 | 0.07 |
| Na2O | 0.03 | 0.02 | 7.49 | 0.40 | 1.67 | 0.16 | 0.00 | 0.02 | 0.92 | 0.13 | 0.00 | 0.01 |
| K2O | 0.02 | 0.01 | 0.36 | 0.12 | 1.68 | 0.12 | 0.03 | 0.01 | 0.03 | 0.02 | 0.07 | 0.02 |
| Total | 100.20 | 0.63 | 101.53 | 1.30 | 98.74 | 1.04 | 101.06 | 0.85 | 101.21 | 0.87 | 100.91 | 1.29 |
| | | | | | | | | | | | | |
| Cations | | | | | | | | | | | | |
| Si | 2.98 | 0.01 | 2.65 | 0.05 | 6.26 | 0.05 | 1.94 | 0.01 | 1.92 | 0.02 | 0.00 | 0.00 |
| Ti | 0.00 | 0.00 | 0.00 | 0.00 | 0.24 | 0.03 | 0.00 | 0.00 | 0.01 | 0.00 | 0.90 | 0.07 |
| Al | 1.96 | 0.02 | 1.35 | 0.04 | 2.20 | 0.04 | 0.07 | 0.01 | 0.13 | 0.05 | 0.00 | 0.00 |
| Cr | 0.00 | 0.00 | 0.00 | 0.00 | 0.00 | 0.01 | 0.00 | 0.00 | 0.00 | 0.00 | 0.01 | 0.00 |
| Fe | 1.75 | 0.07 | 0.02 | 0.02 | 1.78 | 0.13 | 0.79 | 0.03 | 0.29 | 0.03 | 1.16 | 0.14 |
| Mn | 0.08 | 0.01 | 0.00 | 0.00 | 0.01 | 0.01 | 0.01 | 0.00 | 0.01 | 0.00 | 0.01 | 0.00 |
| Mg | 0.71 | 0.05 | 0.00 | 0.01 | 2.63 | 0.17 | 1.19 | 0.05 | 0.71 | 0.05 | 0.00 | 0.00 |
| Ca | 0.57 | 0.07 | 0.32 | 0.04 | 1.89 | 0.05 | 0.01 | 0.00 | 0.90 | 0.02 | 0.00 | 0.00 |
| Na | 0.00 | 0.00 | 0.64 | 0.03 | 0.48 | 0.05 | 0.00 | 0.00 | 0.07 | 0.01 | 0.00 | 0.00 |
| K | 0.00 | 0.00 | 0.02 | 0.01 | 0.32 | 0.02 | 0.00 | 0.00 | 0.00 | 0.00 | 0.00 | 0.00 |
| Total | 8.05 | 0.01 | 5.00 | 0.01 | 15.80 | 0.07 | 4.02 | 0.01 | 4.04 | 0.01 | 2.09 | 0.07 |

Structural Formulae [1]

| | |
|---|---|
| Garnet | $(Mg_{0.71}Fe_{1.7}Ca_{0.57})Al_{1.96}(Si_{2.9}O_4)$ |
| Plagioclase | $Na_{0.64}Ca_{0.32}Al_{1.41}Si_{2.6}O_8$ |
| Amphibole | $(Na_{0.37}K_{0.32})(Ca_{1.89}Na_{0.11})(Mg_{2.63}Fe_{1.78}Al_{0.46}Ti_{0.24})(Si_{6.26}Al_{1.74})O_{22}(OH)_2$ |
| Orthopyroxene | $(Mg_{1.19}Fe_{0.79})(Si_{1.94}Al_{0.08})O_6$ |
| Clinopyroxene | $(Ca_{0.9}Na_{0.07})(Mg_{0.71}Fe_{0.29}Al_{0.05})(Si_{1.91}Al_{0.08})O_6$ |

End-members

| | |
|---|---|
| Garnet | $Grs_{18}$ $Alm_{56}$ $Prp_{23}$ $Sps_3$ |
| Plagioclase | $Ab_{67}$ $An_{33}$ |
| Amphibole [2] | Potassian-magnesian-hastingsite |
| Orthopyroxene | $En_{60}$ $Fs_{40}$ |
| Clinopyroxene | $Di_{71}$ $Hd_{29}$ |

| Oxygen pfu. | 12 | 8 | 23 | 6 | 6 | 3 |
|---|---|---|---|---|---|---|

1 Structural formulae after Deer et al. (1996)

2 Amphibole cation values and classification using PROBE-AMPH (Tindle and Webb (1994), and references therein)

Table 6.8: Average mineral compositions for sample NA046 (after McLeish, 2008)

| Mineral | Garnet | 2SD | Plagioclase | 2SD | Amphibole | 2SD | Orthopyroxene | 2SD | Clinopyroxene | 2SD | Ilmenite | 2SD |
|---|---|---|---|---|---|---|---|---|---|---|---|---|
| Wt. % | | | | | | | | | | | | |
| SiO2 | 37.60 | 0.78 | 58.68 | 0.72 | 42.31 | 0.51 | 51.97 | 0.73 | 52.07 | 0.58 | 0.07 | 0.04 |
| TiO2 | 0.06 | 0.03 | 0.00 | 0.00 | 2.52 | 0.34 | 0.09 | 0.03 | 0.20 | 0.12 | 52.18 | 2.15 |
| Al2O3 | 21.05 | 0.36 | 27.00 | 0.46 | 12.73 | 0.41 | 0.97 | 0.30 | 2.03 | 0.78 | 0.02 | 0.00 |
| Cr2O3 | 0.04 | 0.03 | 0.00 | 0.00 | 0.04 | 0.04 | 0.04 | 0.03 | 0.01 | 0.02 | 0.20 | 0.04 |
| FeO | 27.98 | 0.56 | 0.14 | 0.31 | 15.82 | 0.91 | 28.02 | 0.40 | 10.43 | 1.27 | 49.10 | 0.27 |
| MnO | 0.97 | 0.06 | 0.00 | 0.00 | 0.06 | 0.04 | 0.29 | 0.07 | 0.13 | 0.06 | 0.33 | 0.04 |
| MgO | 4.95 | 0.37 | 0.00 | 0.01 | 10.41 | 0.80 | 19.41 | 0.29 | 12.67 | 1.21 | 0.62 | 0.25 |
| CaO | 6.99 | 0.31 | 8.10 | 0.23 | 11.97 | 0.28 | 0.45 | 0.05 | 22.85 | 0.89 | 0.06 | 0.01 |
| Na2O | 0.03 | 0.02 | 6.84 | 0.16 | 1.47 | 0.11 | 0.01 | 0.02 | 0.54 | 0.07 | 0.01 | 0.01 |
| K2O | 0.03 | 0.02 | 0.27 | 0.08 | 1.80 | 0.10 | 0.03 | 0.02 | 0.03 | 0.01 | 0.06 | 0.01 |
| Total | 99.71 | 1.12 | 101.03 | 0.82 | 99.14 | 0.50 | 101.27 | 0.70 | 100.96 | 0.73 | 102.66 | 1.59 |
| | | | | | | | | | | | | |
| Cations | | | | | | | | | | | | |
| Si | 2.97 | 0.02 | 2.60 | 0.02 | 6.27 | 0.04 | 1.96 | 0.01 | 1.94 | 0.01 | 0.00 | 0.00 |
| Ti | 0.00 | 0.00 | 0.00 | 0.00 | 0.28 | 0.04 | 0.00 | 0.00 | 0.01 | 0.00 | 0.97 | 0.02 |
| Al | 1.96 | 0.01 | 1.41 | 0.02 | 2.22 | 0.07 | 0.04 | 0.01 | 0.09 | 0.03 | 0.00 | 0.00 |
| Cr | 0.00 | 0.00 | 0.00 | 0.00 | 0.00 | 0.00 | 0.00 | 0.00 | 0.00 | 0.00 | 0.00 | 0.00 |
| Fe | 1.85 | 0.06 | 0.01 | 0.01 | 1.96 | 0.12 | 0.88 | 0.02 | 0.33 | 0.04 | 1.02 | 0.03 |
| Mn | 0.07 | 0.00 | 0.00 | 0.00 | 0.01 | 0.00 | 0.01 | 0.00 | 0.00 | 0.00 | 0.01 | 0.00 |
| Mg | 0.58 | 0.04 | 0.00 | 0.00 | 2.30 | 0.17 | 1.09 | 0.02 | 0.70 | 0.07 | 0.02 | 0.01 |
| Ca | 0.59 | 0.02 | 0.38 | 0.01 | 1.90 | 0.04 | 0.02 | 0.00 | 0.91 | 0.03 | 0.00 | 0.00 |
| Na | 0.00 | 0.00 | 0.59 | 0.02 | 0.42 | 0.03 | 0.00 | 0.00 | 0.04 | 0.01 | 0.00 | 0.00 |
| K | 0.00 | 0.00 | 0.02 | 0.00 | 0.34 | 0.02 | 0.00 | 0.00 | 0.00 | 0.00 | 0.00 | 0.00 |
| Total | 8.04 | 0.02 | 5.00 | 0.01 | 15.72 | 0.04 | 4.01 | 0.01 | 4.03 | 0.01 | 2.03 | 0.02 |

Structural Formulae [1]

| | |
|---|---|
| Garnet | $(Mg_{0.58}\ Fe_{1.85}\ Ca_{0.59})Al_{1.96}Si_{2.97}O_4)$ |
| Plagioclase | $Na_{0.59}Ca_{0.38}Al_{1.41}Si_{2.6}0O_8$ |
| Amphibole | $(Na_{0.42}K_{0.34})Ca_{1.9}(Mg_{2.3}Fe_{1.96}Al_{0.48}Ti_{0.28})(Si_{6.27}Al_{1.73})O_{22}(OH)_2$ |
| Orthopyroxene | $(Mg_{1.09}Fe_{0.88})(Si_{1.96}Al_{0.04})O_6$ |
| Clinopyroxene | $(Ca_{0.9}Na_{0.04})(Mg_{0.71}Fe_{0.33}Al_{0.03})(Si_{1.94}Al_{0.06})O_6$ |
| Biotite | $(K_{0.92})(Mg_{1.36}Fe_{1.09}Ti_{0.34})(Si_{2.73}Al_{1.3})O_{10}(OH)_2$ |

End-members

| | |
|---|---|
| Garnet | $Grs_{19}\ Alm_{60}\ Prp_{19}\ Spss_{\ 2}$ |
| Plagioclase | $Ab_{60}\ An_{40}$ |
| Amphibole [2] | Titanian-potassian-ferroan-pargasite |
| Orthopyroxene | $En_{55}\ Fs_{45}$ |
| Clinopyroxene | $Di_{68}\ Hd_{32}$ |
| Biotite | $Phl_{55}\ Ann_{45}$ |

| Oxygen pfu. | 12 | 8 | 23 | 6 | 6 | 3 |
|---|---|---|---|---|---|---|

1 Structural formulae after Deer et al. (1996)

2 Amphibole cation values and classification using PROBE-AMPH (Tindle and Webb (1994), and references therein)

Table 6.9: Average mineral compositions for sample NA061e (after McLeish, 2008)

| Mineral | Garnet | 2SD | Plagioclase | 2SD | Amphibole | 2SD | Orthopyroxene | 2SD | Clinopyroxene | 2SD |
|---|---|---|---|---|---|---|---|---|---|---|
| Wt. % | | | | | | | | | | |
| SiO2 | 38.11 | 0.49 | 58.09 | 2.12 | 42.08 | 1.14 | 52.36 | 1.43 | 52.07 | 1.20 |
| TiO2 | 0.05 | 0.03 | 0.00 | 0.01 | 2.51 | 0.61 | 0.07 | 0.06 | 0.24 | 0.17 |
| Al2O3 | 21.33 | 0.40 | 26.73 | 0.76 | 13.28 | 0.70 | 1.60 | 0.36 | 3.08 | 1.50 |
| Cr2O3 | 0.01 | 0.02 | 0.00 | 0.01 | 0.03 | 0.05 | 0.03 | 0.05 | 0.01 | 0.05 |
| FeO | 24.37 | 1.35 | 0.23 | 0.36 | 12.01 | 0.88 | 22.71 | 1.14 | 8.07 | 1.03 |
| MnO | 0.90 | 0.05 | 0.00 | 0.01 | 0.05 | 0.03 | 0.27 | 0.06 | 0.13 | 0.04 |
| MgO | 7.65 | 0.57 | 0.03 | 0.25 | 12.55 | 0.93 | 22.59 | 0.98 | 13.63 | 0.99 |
| CaO | 7.02 | 1.42 | 7.80 | 0.68 | 12.06 | 0.21 | 0.45 | 0.16 | 22.63 | 1.06 |
| Na2O | 0.02 | 0.02 | 6.86 | 0.32 | 1.71 | 0.10 | 0.01 | 0.02 | 0.73 | 0.15 |
| K2O | 0.03 | 0.02 | 0.36 | 0.13 | 1.85 | 0.31 | 0.02 | 0.02 | 0.02 | 0.02 |
| Total | 99.49 | 0.72 | 100.09 | 2.13 | 98.15 | 1.27 | 100.11 | 1.55 | 100.61 | 0.99 |
| | | | | | | | | | | |
| Cations | | | | | | | | | | |
| Si | 2.97 | 0.02 | 2.60 | 0.04 | 6.20 | 0.10 | 1.95 | 0.02 | 1.93 | 0.03 |
| Ti | 0.00 | 0.00 | 0.00 | 0.00 | 0.28 | 0.07 | 0.00 | 0.00 | 0.01 | 0.00 |
| Al | 1.96 | 0.03 | 1.41 | 0.05 | 2.31 | 0.11 | 0.07 | 0.02 | 0.13 | 0.07 |
| Cr | 0.00 | 0.00 | 0.00 | 0.00 | 0.00 | 0.01 | 0.00 | 0.00 | 0.00 | 0.00 |
| Fe | 1.59 | 0.09 | 0.01 | 0.01 | 1.48 | 0.12 | 0.71 | 0.04 | 0.25 | 0.03 |
| Mn | 0.06 | 0.00 | 0.00 | 0.00 | 0.01 | 0.00 | 0.01 | 0.00 | 0.00 | 0.00 |
| Mg | 0.89 | 0.06 | 0.00 | 0.02 | 2.76 | 0.19 | 1.25 | 0.05 | 0.75 | 0.06 |
| Ca | 0.59 | 0.12 | 0.37 | 0.03 | 1.91 | 0.05 | 0.02 | 0.01 | 0.90 | 0.04 |
| Na | 0.00 | 0.00 | 0.59 | 0.03 | 0.49 | 0.03 | 0.00 | 0.00 | 0.05 | 0.01 |
| K | 0.00 | 0.00 | 0.02 | 0.01 | 0.35 | 0.06 | 0.00 | 0.00 | 0.00 | 0.00 |
| Total | 8.05 | 0.02 | 5.01 | 0.02 | 15.78 | 0.07 | 4.01 | 0.02 | 4.03 | 0.01 |

Structural Formulae [1]

| | |
|---|---|
| Garnet | $(Mg_{0.89}Fe_{1.59}Ca_{0.59})Al_{1.96}(Si_{2.97}O_4)$ |
| Plagioclase | $Na_{0.59}Ca_{0.37}Al_{1.41}Si_{2.6}0O_8$ |
| Amphibole [2] | $(Na_{0.40}K_{0.35})(Ca_{1.9}(Na_{0.09})(Mg_{2.76}Fe_{1.48}Al_{0.51}Ti_{0.28})(Si_{6.2}Al_{1.8})O_{22}(OH)_2$ |
| Orthopyroxene | $(Mg_{1.25}Fe_{0.71}Al_{0.02})(Si_{1.96}Al_{0.05})O_6$ |
| Clinopyroxene | $(Ca_{0.9}Na_{0.05})(Mg_{0.75}Fe_{0.25}Al_{0.06})(Si_{1.93}Al_{0.07})O_6$ |
| Biotite | $(K_{0.92})(Mg_{1.69}Fe_{1.79}Ti_{0.22})(Si_{2.73}Al_{1.3})O_{10}(OH)_2$ |

End-members

| | |
|---|---|
| Garnet | $Grs_{19}$ $Alm_{51}$ $Prp_{28}$ $Sps_2$ |
| Plagioclase | $Ab_{61}$ $An_{39}$ |
| Amphibole 2 | Titanian-potassian-ferroan-pargasite |
| Orthopyroxene | $En_{64}$ $Fs_{36}$ |
| Clinopyroxene | $Di_{75}$ $Hd_{25}$ |
| Biotite | $Phl_{68}$ $Ann_{32}$ |

| Oxygen pfu. | 12 | 8 | 23 | 6 | 3 |
|---|---|---|---|---|---|

1 Structural formulae after Deer et al. (1996)

2 Amphibole cation values and classification using PROBE-AMPH (Tindle and Webb (1994), and references therein)

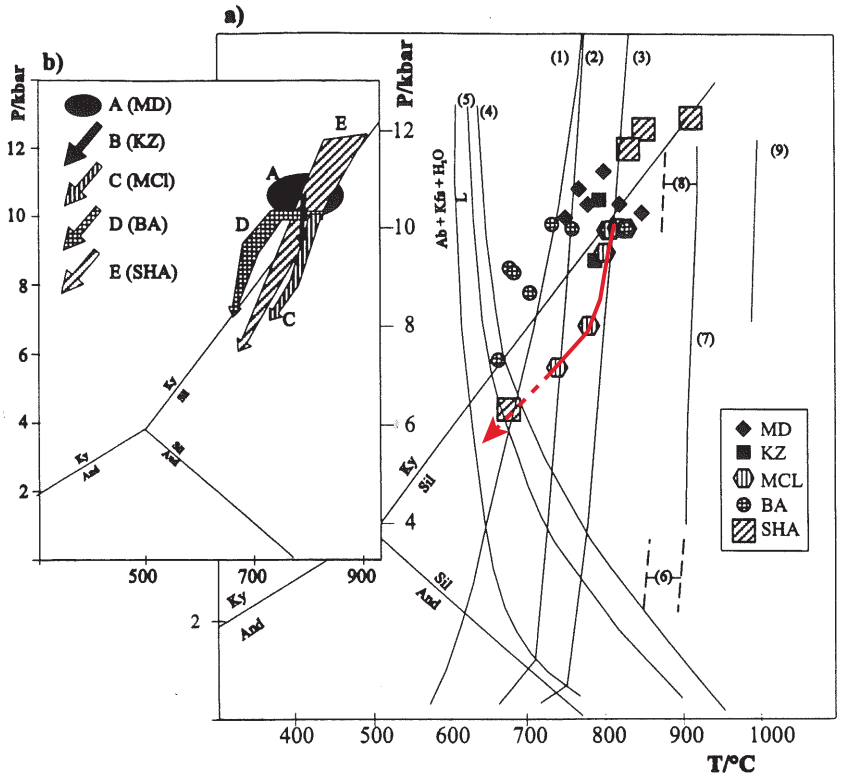


Figure 6.8: Summary of thermobarometry and P-T paths for the Algonquin domain. PT data (a) and PT paths (b) for the southern Algonquin domain. Note the estimations for the McLintock subdomain cluster at ca. 800°C at 10 kbar, and follow a general retrograde P-T path to ca. 750°C at 7 kbar (red line). Reaction lines relevant to the McLintock subdomain are (3) Bt + Pl + Qtz $\rightarrow$ Opx + Ksp + liquid (Clemens et al., 1981); (2) Bt + $Al_2SiO_3$ + Pl + Qtz $\rightarrow$ Grt + Ksp + liquid (Le Breton and Thompson, 1988). Abbreviations are: BA, Birkendale assemblage; KZ, Kagawama zone; MCL, McLintock subdomain; MD, Muskoka domain; SHA, Southern Huntsville assemblage (modified from Timmermann, 1998).

many areas of the southwest Grenville Province at ca. 1240 Ma have been used to monitor Grenvillian P-T conditions. The dykes near the Grenville Front have been metamorphosed at conditions approaching granulite-facies (>700°C and >8.0 kbar) (e.g. Jamieson et al., 1995; Bethune and Davidson, 1997). In areas in or near the GFTZ these dykes experienced only Grenvillian metamorphism, thus the metamorphic overprint is easier to recognise and link to tectonic episodes. In the polymetamorphic allochthonous domains of the CGB, however, successive high-grade metamorphic events have altered and homogenized the bulk compositions of many minerals. In the study area, where textural or geochemical evidence linking a particular mineral composition to a geochronometer is lacking, age constraints provided by geochronology can only be thought of as the maximum age of (re)equilibration.

**Linking thermobarometry and geochronology** Sample CA108b provides a link between thermobarometry and geochronology results. As discussed in Chapter 4, monazite U-Pb dating provides important timing constraints of monazite crystallization associated with metamorphism in the Kiosk domain, and records two major events at ca. 1480-1450 Ma and 1080-1060 Ma. Though the exact P-T conditions of monazite crystallization in this sample have not been investigated, amphibolite-granulite facies assemblages are consistent with monazite stability (Foster and Parrish, 2003). It is unlikely that the 8.6±1.7 kbar and 717±124 °C P-T estimate from CA108b corresponds to the ca. 1480 Ma event. Along strike from sample CA108b, sample NA061e is intercalated with a unit that preserves relict corundum (McLeish, 2008). The preservation of relict corundum suggests an older, very-high-temperature metamorphic event (Graham et al., 2008). The ca. 1480-1450 Ma event is coeval with high-temperature granulite-facies metamorphism and plutonism in the CGB, and migmatization and initial growth of monazite in the Kiosk domain (e.g. Nadeau, 1990; Timmermann, 1998; Slagstad et al., 2004b). Pervasive recrystallization of Kiosk domain rocks occurred sometime after this high-grade metamorphic event. Monazite data have shown that the Kiosk domain experienced high-grade metamorphism at ca. 1200-1130 Ma during the Shawinigan pulse, and again at ca. 1080-1060 Ma during the Ottawan pulse of the Grenville orogeny, thus ca. 1200 Ma is the upper-limit of recrystallization and (re)equilibration of the Kiosk domain.

## 6.5 Conclusions

1. The Kiosk domain records granulite-facies metamorphism at approximately 10.5±1.7 kbar and 791±123 °C.

2. Kiosk domain mineral assemblages last equilibrated at granulite-grade sometime after ca. 1200 Ma.

# CHAPTER 7

# DISCUSSION AND CONCLUSIONS

This chapter is intended to synthesize data discussed in previous chapters into a timeline of tectonic development of the Kiosk domain, with reference to the underlying Bonfield domain and overlying McLintock subdomain, to place the Kiosk domain in a broader tectonic framework, and to propose topics for further research.

## 7.1 Tectonic history of the study area

This section discusses the key aspects to be considered in the development of the study area. These are: (i) ca. 1655 Ma igneous protolith zircon ages of the Kiosk domain; (ii) ca. 1480-1450 Ma zircon and monazite ages of metamorphism of the Kiosk and Algonquin domains; (iii) ca. 1240 Ma igneous zircon crystallization age of the Bonfield Batholith in the Bonfield domain; (iv) ca. 1200-1130 Ma monazite age from the Kiosk domain; (v) ca. 1080-1060 Ma Grenvillian (Ottawan pulse) zircon and monazite ages of metamorphism in the Kiosk and Algonquin domains; (vi) possible ca. 1000 Ma Grenvillian (Rigolet pulse) zircon age of metamorphism along the NTLSZ; (vii) internal structural and lithological boundary within the Kiosk domain; (viii) pervasive structural grain preserved in the Kiosk and Algonquin domains; (ix) lithological and geochronological similarities of the Bonfield domain with the Tilden Lake and Tomiko domains in the Parautochthonous Belt; (x) lithological and geochronological similarities of the Kiosk domain with the Britt and Algonquin domains.

Figure 7.1 presents a conceptual interpretation of the tectonic history for the study area in the southwest Grenville Province. Specific stages are discussed in the following sections.

### *7.1.1 Pre-Grenvillian development*

#### *7.1.1.1 ca. 1655 Ma*

The oldest population of U-Pb dates from zircon cores indicates that the age of igneous protolith crystallization of the orthogneisses in the Kiosk domain was ca. 1655 Ma. This age is coeval with the the Labradorian orogeny in the eastern Grenville Province. Major additions of crust along the margin of Laurentia involved ”Andean”-style, calc-alkaline magmatic arcs and coeval backarc magmatism between ca. >1700-1600 and 1470-1340 Ma (e.g. Rivers, 1997; Ketchum and Davidson, 2000; Jamieson et al., 2001). Detailed studies of metaplutonic rocks in the CGB of the southwestern Grenville Province have demonstrated that protoliths can be locally variable, and include rocks with an extensional intra-arc magmatic affinity (Culshaw and Dostal, 1997, 2002; Slagstad, 2003). The geochemistry of the orthogneisses of the Kiosk domain has not been studied, and their petrogenetic affinity is not yet constrained, however, given the spatial relation to other magmatic arc-related igneous rocks (e.g. the intra-arc granitic metaplutonic rocks of the Muskoka domain; Slagstad et al. (2004c)), a magmatic arc setting can be inferred.

#### *7.1.1.2 ca. 1460 Ma*

Zircon and monazite data suggest that the Kiosk domain experienced high-grade metamorphism and migmatization during the Pinwarian orogeny (ca. 1480 to 1450 Ma) coeval with widespread plutonism in the southwest Grenville Province. Thick metamorphic mantles on zircons throughout the Kiosk domain, and monazite cores from the BBLSZ, consistently exhibit metamorphic ages in the ca. 1480 to 1450 Ma range, with most zircon ages at ca. 1460 Ma. Inherited xenocrystic zircons from the host orthogneiss incorporated into a dyke in the northern McLintock subdomain are texturally similar to those in the Kiosk domain and have equivalent ages. Granulite-facies metamorphism and igneous plutonic ages in the Algonquin domain at ca. 1450-1425 Ma are well constrained (Nadeau and van Breemen, 1998; Timmermann, 1998). The broad coincidence of the age of high-grade metamorphism in both the Algonquin and Kiosk domains, coupled with

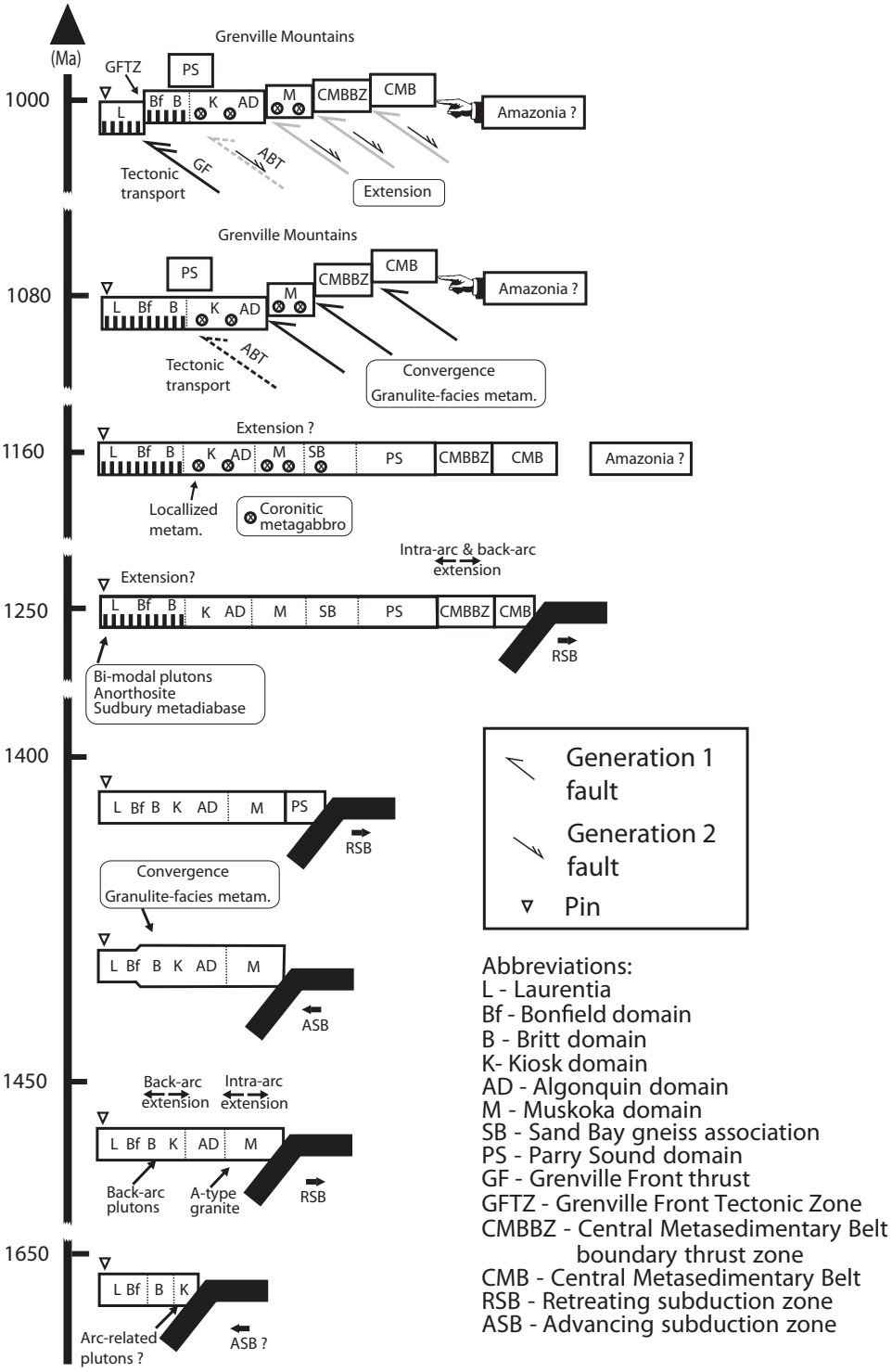


Figure 7.1: Conceptual tectonic model of the development of the study area in the southwest Grenville Province discussed in the text. The stages depicted are only those that pertain to the Kiosk domain that have been identified in this study (modified from Slagstad, 2003).

widespread migmatization and plutonism in the Algonquin domain, suggests these domains were closely related at the time of high-grade metamorphism. Furthermore, studies in the Britt and Muskoka domains have also revealed the presence of equivalent igneous plutonic bodies and metamorphism. Geochemistry of these units suggest the Pinwarian orogeny was a phase of backarc and intra-arc related plutonism and high-grade metamorphism in the CGB (e.g. van Breemen and Davidson, 1988; Ketchum et al., 1994; Slagstad et al., 2004a, 2009). This study shows that equivalent ages exist in the Kiosk domain gneisses, where they represent the widespread migmatization of igneous protoliths. Granitoid meta-plutonic bodies in the Kiosk domain have not been studied, and their age and affinity remain uncertain. The magmatic setting invoked for the surrounding lithotectonic domains can also be inferred to be responsible for high-grade metamorphism, migmatization, and potentially plutonism in the Kiosk domain reflected in Pinwarian ages.

#### *7.1.1.3 ca. 1240 Ma*

Zircons from the southern Bonfield Batholith show that igneous crystallization in the southern Bonfield domain occurred at ca. 1240 Ma. This corresponds to an Elzevirian-aged bimodal suite of igneous rocks that crystallized far inboard of the Laurentian margin in the Tilden Lake and Tomiko domains, and the emplacement of the Sudbury metadiabase dyke swarm (e.g. Moore and Thompson, 1980; Bethune and Davidson, 1988; Dudas et al., 1994). Zircon crystal morphology and trace-element geochemistry suggest that this is the age of igneous crystallization, rather than metamorphism. This suggests an important linkage of the Bonfield Batholith to the age-equivalent A-Type Mulock Pluton in the Tilden Lake domain to the northwest of the Bonfield domain, which crystallized at $1244^{+4}_{-2}$ Ma, and other intrusions to the northwest of the study area in the Tomiko domain (*cf.* Fig. 1.7; (Lumbers et al., 1991; Davidson and Breemen, 2001; Easton and Ketchum, 2002) ). Bimodal igneous bodies of this suite intruded a variety of host rocks in the Parautochthonous Belt, such as Archean gneisses in the case of the Mulock Pluton, and Mesoproterozoic orthogneisses of the Nepewassi domain in the case of the Powassan Batholith. Equivalent crystallization ages of these metaplutonic units call into question the interpretation of the Bonfield domain as part of the Allochthonous Belt. Instead the geochronological data strongly suggest that the Bonfield domain was closely associated with the Parautochthonous domains of the Laurentian margin at ca. 1240 Ma.

### *7.1.2 Grenvillian orogeny*

#### *7.1.2.1 ca. 1200-1130 Ma*

Monazites from the interior Kiosk domain preserve Grenvillian ages (ca. 1200-1135 Ma), apparently recording the Shawinigan orogenic pulse (1190-1140 Ma; Rivers, 1997; Rivers and Corrigan, 2000). These ages are under-represented in paragneisses in the CGB (e.g. Carr and Berman, 1996, 1997), and are most commonly associated with the crystallization of coronitic olivine metagabbros in the CGB at ca. 1170-1150 Ma (e.g. Davidson, 1986c), and the Parry Sound domain klippe (e.g. van Breemen et al., 1986; Wodicka, 1994; Wodicka et al., 1996). The paragneiss unit that preserves these ages lies along strike from a linear trend of coronitic olivine metagabbro bodies (Fig. 2.1). Equivalent ages have not been recorded previously from Kiosk or Algonquin domain orthogneisses or paragneisses, and may record metamorphism related to emplacement of voluminous coronitic olivine metagabbros, or deformation associated with the assembly of the Parry Sound domain, for reasons previously discussed.

#### *7.1.2.2 ca. 1080-1060 Ma*

Ottawan ages from the Kiosk domain and McLintock subdomain are compatible with the ages of widespread high-grade metamorphism of the CGB during the Ottawan orogenic pulse (ca. 1090-1040; Krogh, 1989; Bussy et al., 1995; Rivers, 1997; Rivers and Corrigan, 2000; Rivers et al., 2002; Slagstad et al., 2004c). Metamorphic zircon from a dyke in the McLintock subdomain give an age of metamorphism of ca. 1080 Ma, and monazite from an internal shear zone in the Kiosk domain give an age of metamorphism at ca. 1080-1060 Ma. Monazite data from a paragneiss in the BBLSZ may record the age of metamorphism associated with deformation of the Kiosk domain. Zircon ages from the McLintock subdomain are interpreted to represent initial metamorphism of the amphibolite dyke during Ottawan metamorphism. The coincidence of the monazite age with a comparable zircon age from the McLintock subdomain shows that the Kiosk and Algonquin domains experienced the same orogen-scale high-grade tectonic episode during the Ottawan orogenic pulse.

#### *7.1.2.3 ca. 1000 Ma*

Imprecise zircon ages from the NTLSZ of the Kiosk domain suggest the possibility of metamorphism during the Rigolet orogenic pulse (ca. 1005-980 Ma; Rivers, 1997; Rivers

and Corrigan, 2000)). However, within error, the 998±44 Ma age overlaps with monazite and zircon ages from the BBLSZ and McLintock subdomain, as well as ca. 1030-1075 Ma ages of deformation and granulite-facies metamorphism in the Algonquin domain (van Breemen and Hanmer, 1986; Nadeau and van Breemen, 1989; Nadeau, 1990; Heaman and LeCheminant, 1993; Timmermann et al., 1997; Timmermann, 1998). Alternatively, this age may represent normal-sense reactivation of the NTLSZ at ca. 1000 Ma, akin to the normal-sense reactivation of the Shawanaga shear zone at ca. 1020-990 Ma (Ketchum et al., 1998). In the absence of independent kinematic information to demonstrate the sense of shear along the NTLSZ, assigning this zircons recrystallization age to a particular tectonic regime is not yet possible.

**Cooling of the NTLSZ** Reconnaissance-level investigation of the thermal history of the NTLSZ has shown a thermal break of ca. 70 Ma from the shear zone to the footwall. $^{40}Ar/^{39}Ar$ thermochronology of hornblende from the NTLSZ suggests cooling through approximately 500°C at ca. 1030 Ma, and the footwall of the NTLSZ at ca. 1100 Ma. Equivalent hornblende cooling ages in the GFTZ date exhumation and cooling during cratonward tectonic transport of the Grenville Orogen (Cosca et al., 1991; Haggart et al., 1993; Reynolds et al., 1995). In contrast, hornblende cooling ages from the southwest Kiosk domain and the Algonquin domain are ca. 1005-930 Ma Cosca et al. (1991). This study lacks the data density required to confidently place the northern Kiosk domain into a regional framework of exhumation and cooling.

Figure 7.2 summarises the major tectonic events and important lithologies of the Algonquin, Kiosk and Bonfield domains with nearby lithotectonic domains in the CGB.

## 7.2 Regional implications

**Affinity of the Kiosk domain** The most important regional implication of this thesis is the tectonic affinity of the Kiosk and Algonquin domains with the Britt domain, as indicated by the ca. 1640 Ma age of igneous protolith of Kiosk domain gneisses. Corrigan et al. (1994) dated the Key Harbour leucogranite in the Britt domain at ca. 1685 Ma; this was migmatized and intruded by granitoid rocks at ca. 1450 Ma. The Britt domain also

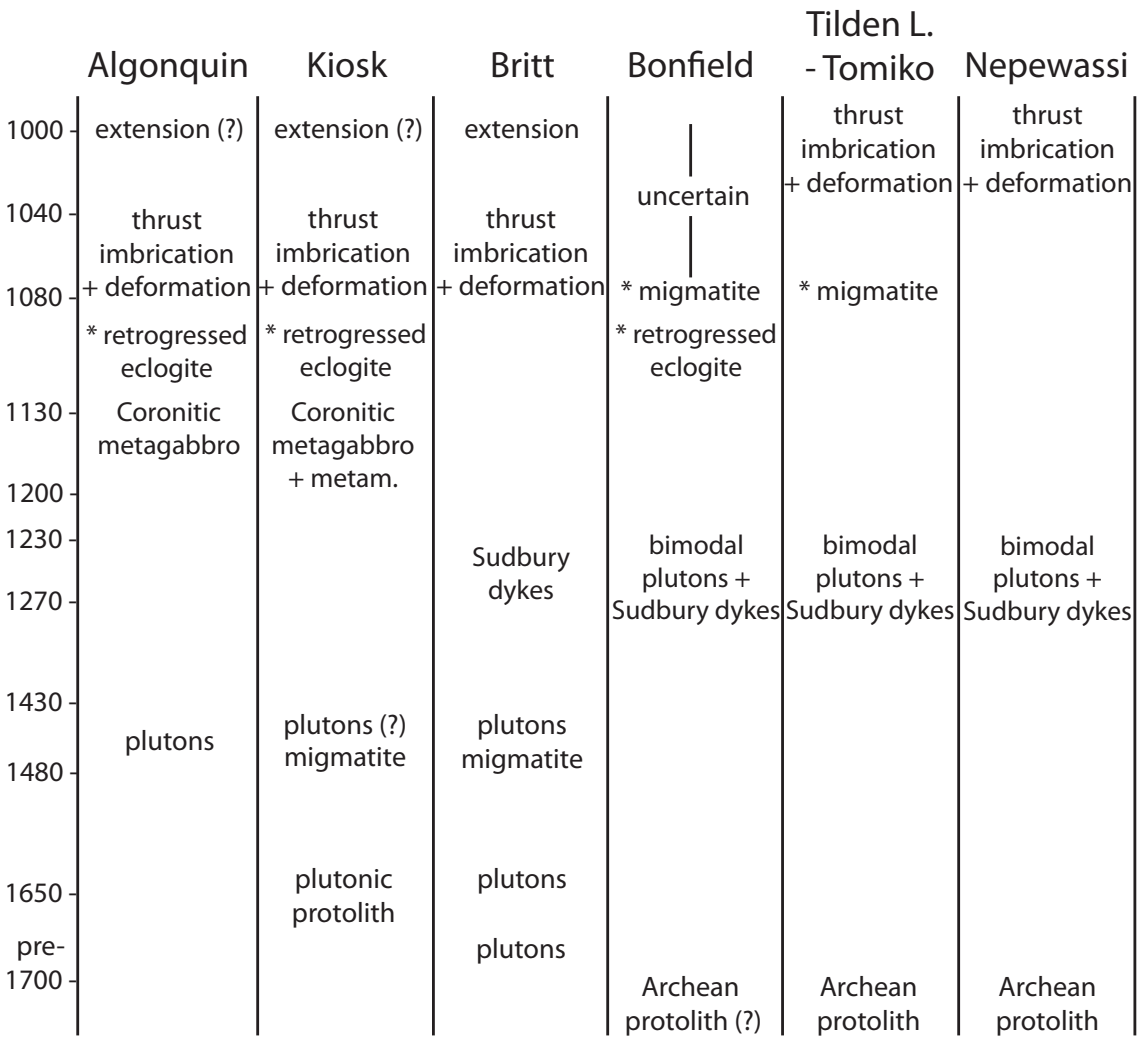


Figure 7.2: Summary of major tectonic events and lithologies for select domains in the CGB. Note the broad similarities in the tectonic events of the Bonfield domain with those of the Tilden Lake, Tomiko, and Nepewassi domains in the Parautochthonous Belt, and between the Algonquin and Kiosk domains with those of the Britt domain. Asterisk denotes uncertain timing.

exhibits an Ottawan metamorphic history at ca. 1080-1060 Ma, based on monazite and titanite, similar to the Kiosk and Algonquin domains (Tuccillo et al., 1992). This suggests that all three domains experienced a common Ottawan history. The cross-cutting relationships in the Britt domain are analogous to the Kiosk domain, which was migmatized and potentially intruded by felsic granitoids at ca. 1450 Ma. These field relations are distinct from the overlying Algonquin domain which exhibits plutonic ages of ca. 1450 Ma (e.g. Nadeau and van Breemen, 1998), but may lack ca. 1640 Ma rocks. Nadeau and van Breemen (1998) did not date the country rock to ca. 1450 Ma plutons, so the possibility of equivalent ca. 1640 Ma granitoid rocks similar to those in the Kiosk domain cannot be discounted. Based on these data, Kiosk has clear affinities with Britt; however, a linkage with the Algonquin domain is not yet confirmed pre-ca. 1450 Ma.

**The Kiosk domain and the foreland fold-and-thrust model** Geochronology of the Kiosk and Bonfield domains in the study area has shed light on the structural position of these lithotectonic domains relative to the ABT, within the framework of the thrust tectonics model for the southwestern Grenville Province. The criteria for the position of the ABT are: (i) parautochthonous rocks in the footwall have pre-Grenvillian and Grenvillian histories that can be correlated with less deformed and metamorphosed precursor rocks in the foreland; and (ii) allochthonous polycyclic rocks exhibit pre-Grenvillian and Grenvillian deformation and metamorphism, but have no direct linkage with rocks in the parautochthon (Rivers et al., 1989). Ketchum and Davidson (2000) further refined the criteria for the ABT in the southwest Grenville Province to include the presence of retrogressed eclogitic rocks and coronitic olivine metagabbro in the hangingwall, the absence of these rocks in the footwall, and Sudbury-type diabase dykes in the footwall. These criteria place the ABT along the northern boundary of the Bonfield domain near Lake Nipissing (Fig. 1.7). This suggests that both the Kiosk and Bonfield domains are allochthonous, however; this study has demonstrated that the Bonfield Batholith is coeval with other plutonic bodies in a bimodal suite of rock in the Nepewassi, Tilden Lake, and Tomiko domains in the Parautochthonous Belt. Furthermore, the Kiosk domain and the parautochthonous Britt domain appear to have a common tectonic history. This suggests that the boundary shear zone of the Bonfield and Kiosk domains (NTLSZ), or possibly

the interior Kiosk domain shear zone (BBLSZ), represents the ABT. The NTLSZ separates granulite-facies polycyclic rocks which record pre-Grenvillian metamorphism in the northern Kiosk domain from upper-amphibolite-facies monocyclic rocks in the southern Bonfield domain. Within the Kiosk domain the BBLSZ coincides with the position of the ABT of Dickin and McNutt (2003) based on Nd isotope mapping, separating 2000-1800 Ma model ages in the southern Kiosk domain, from 1600-1400 Ma model ages in the northern Kiosk domain. This suggests that the northern Kiosk domain and Bonfield domain are part of the Parautochthonous Belt. However, this arrangement would violate the lithological constraints of Ketchum and Davidson (2000), who noted retrogressed eclogite rocks and coronitic metagabbros along the northern boundary of the Bonfield domain (Fig. 1.7; *cf.* section 1.1.3). These contradictory data further complicate the location of a fundamental boundary of the fold-and-thrust model of the southwestern Grenville Province, and may call into question the validity of a single through-going ABT in this area.

The existence of multiple shear zones in the southwest Grenville Province that satisfy the definition of the ABT, according to Ketchum and Davidson (2000), may suggest that in the study area the ABT itself is an imbricated shear zone. A forward-stepping imbricate-fan thrust geometry could account for the apparent multiple positions of the ABT. The ABT may have been the internal Kiosk domain shear zone (BBLSZ) (cf. Dickin and McNutt, 2003) prior to propagating forward into the foreland, possibly at the NTLSZ, or to its postulated map position (cf. Ketchum and Davidson, 2000) (Fig. 1.7 and 7.3). In this conceptual model the BBLSZ as an "early ABT" would satisfy the lithological constraints of coronitic olivine metagabbro in the southern Kiosk domain, the apparent parautochthonous character of the Bonfield domain, and the ABT position inferred from Nd isotope mapping. It would also allow the current map position of the ABT to represent the "late ABT," satisfying the lithological criteria of coronitic olivine metagabbros and retrogressed eclogitic rocks near North Bay. These expressions of the ABT would require a larger detachment surface at depth that would represent a basal detachment of the Allochthonous Polycyclic Belt.

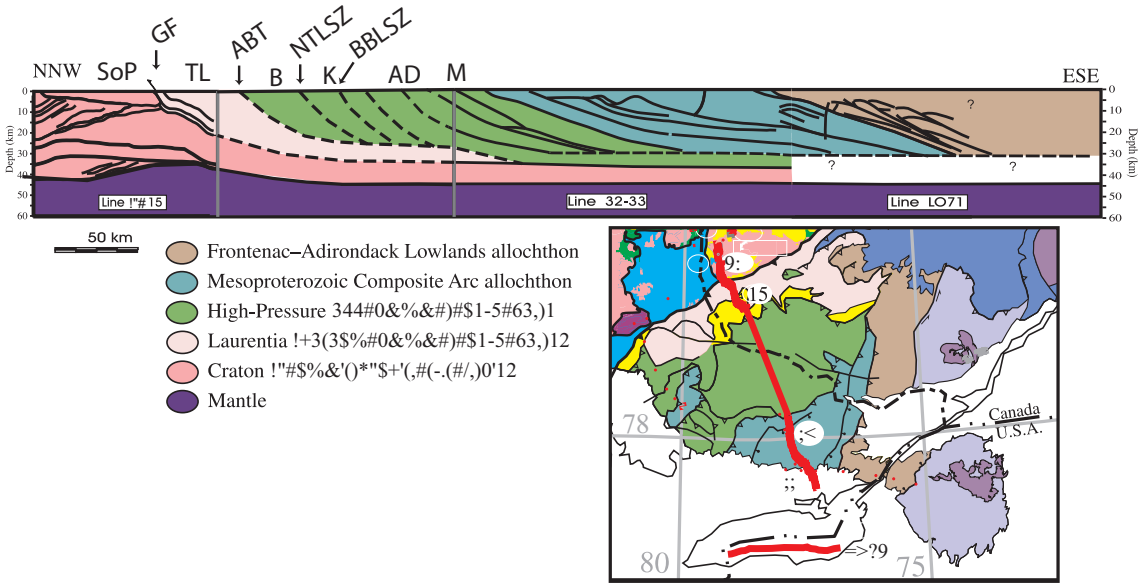


Figure 7.3: Structural cross-section through the study area. Inset map indicates the location of the cross-section (red line) with seismic lines indicated (white circles). The Bonfield domain shown schematically with the allochthonous high-pressure domains above the ABT. The NTLSZ and BBLSZ are indicated schematically, and form an imbricate-fan geometry splaying from the main ABT basal detachment. Inset map and seismic interpretations of lines 15, 16, 32, 33, and LO71 are modified from Ludden and Hynes (2000). Abbreviations after List of abbreviations used.

**The Kiosk domain and the heterogeneous-flow model** Lower-crustal heterogeneous flow, based on numerical models for the southwest Grenville Province, may provide a framework for interpreting of the distinctive lithological characteristics and structural position of the Kiosk domain (Jamieson et al., 2007, 2010). The *stop-convergence* numerical model of Jamieson et al. (2010) is particularly useful for interpreting the generation of the first-order crustal structure of the CGB. In this model, the mid- and lower-Laurentian crust is simplified and subdivided into blocks representing a range of crustal types, from very strong Archean cratonic crust, to weak juvenile crust, to very weak peri-cratonic crust, blow a uniform melt-weakened crust of granitoid rocks (yellow in Fig. 7.4). Lower crustal blocks in this model go though an early phase of thickening with relatively little tectonic transport prior to the formation of the mid-crustal flow zone at ca. 60 My-emt, after which melt-weakened lower crust is partially exhumed and ductile thrust nappes (purple and blue blocks in Fig. 7.4a) begin to progressively overthrust the competent lower crustal indentor. When convergence stops at 87 My-emt, gravity-driven tectonic transport of ductile thrust nappes continues to propagate the orogen cratonward for ca. 15-30 My-emt (Fig. 7.4b). The final model structure is similar to the crustal structure of the Lithoprobe transect along Georgian Bay, as inferred from seismic and geologic data (White et al., 2000) (Fig. 7.4c and d). This model predicts the position of the allochthonous thrust sheets (e.g. Shawanaga domain and Parry Sound domain), relative thickness and distribution of lithotectonic domains, distribution of melt weakened crust (e.g Muskoka domain), and shallow to gently dipping structures near the orogenic core (e.g. Algonquin domain), as well as extensional reactivation of thrust-sense shear zones (e.g. Shawanaga shear zone). These criteria were used to conclude that the model is geologically reasonable.

An interesting feature of these models pertains directly to the formation of the Kiosk and Algonquin domains. Despite a fundamental difference in the age and origin of the lithologies that make up the Kiosk and Algonquin domains, they share a common Grenvillian tectonic history. Furthermore, the Kiosk domain has historically been thought of as a large, thick, competent block of granitoid crust (e.g. Davidson, 1986c). Results from field work and geochronology in this study have shown that a major shear zone in the

centre of the Kiosk domain likely imbricates the granitoid orthogneisses of the Kiosk domain, thereby thickening the entire granitoid crust, analogous to the imbrication of the Algonquin domain over the Kiosk domain. The model structure in Figure 7.4 (red box) shows that the yellow granitoid weak-mid crust that occupies the position of the Algonquin and Kiosk domains is thickened during early convergence, and remains a relatively short-travelled, thick block of granitoid crust, relative to other lithotectonic domains in the model. Although the Kiosk domain represents a "strong block", rather than the partially melted, weak-mid crust in the equivalent model position, the model results are still useful for making first-order comparisons to other modelled areas in the CGB. In light of this model, the Algonquin and Kiosk domains can be thought of as linked, "not-so-far"-travelled domains. This interpretation is supported by the common of tectonic histories of the Kiosk and Algonquin domains, and the similarities in the tectonic histories of the Kiosk domain and the parautochthonous Britt domain discussed in previous sections.

This raises the question of why the structural grain, namely the straight, northeast-striking, gently southeast-dipping foliation, was preserved in the Kiosk domain? The answer to this might be found in the older protolith ages of Kiosk domain orthogneisses. These rocks were subject to widespread high-temperature granulite-facies metamorphism at ca. 1460 Ma coeval with equivalent metamorphism and juvenile crust formation in the Algonquin and Muskoka domains (e.g. Timmermann, 1998; Slagstad, 2003; Slagstad et al., 2004a; McLeish, 2008). Melt weakening of crustal blocks is a key factor controlling the final model structure of the numerical models (Jamieson et al., 2007, 2010). This study has shown that the ca. 1460 Ma tectonic episode was responsible for migmatization of the Kiosk domain, and that there are very few textures suggesting large volumes of new melt formed, or significant $H_2O$+$CO_2$-rich fluid infiltration during pervasive recrystallization of migmatites during subsequent tectonic episodes. The fluid budget of the Kiosk domain may have been largely depleted during ca. 1460 Ma high-grade metamorphism and the effects of fluid weakening during Grenvillian orogenesis may have been limited (Gerbi et al., 2010). This would limit the effect of ductile flow, and allow the preservation of an early orogen-parallel, shallow-dipping structural grain related to northwest-directed tectonic transport in a mid-crustal flow regime.

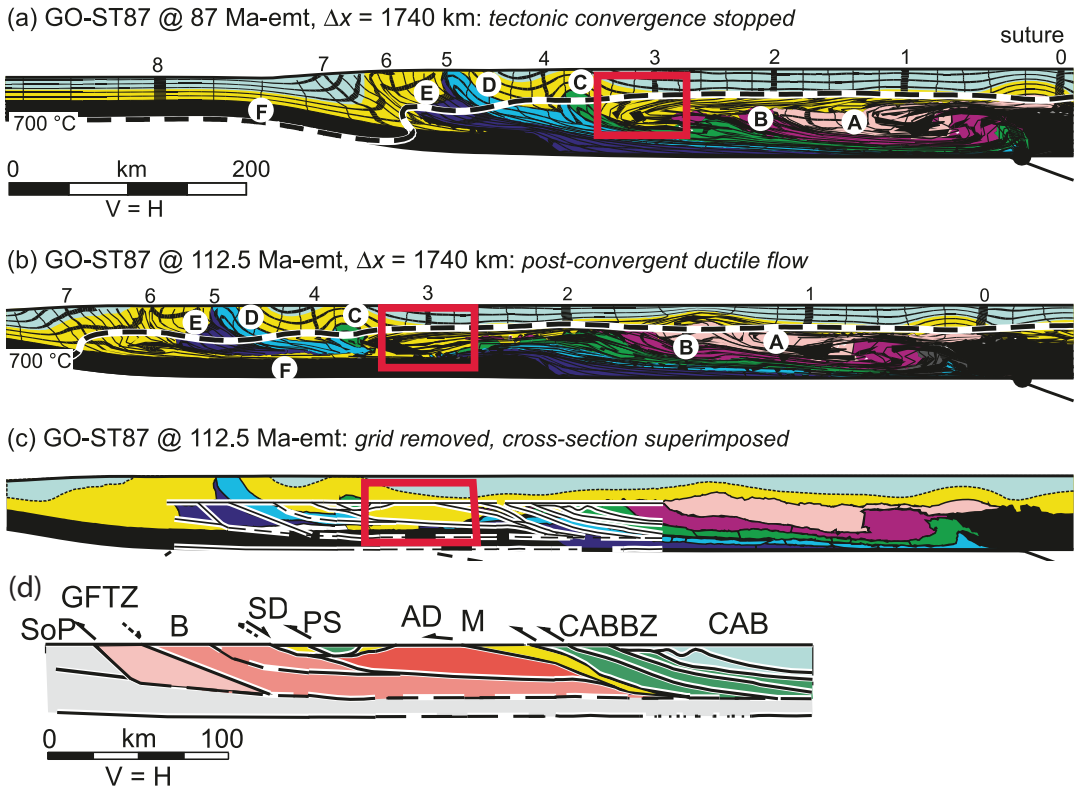


Figure 7.4: Selected results from the GO-ST87 numerical model of the southwest Grenville Province discussed in text. Red box indicated the approximate structural level of the Kiosk and Algonquin domain. a) model structure at cessation of convergence at 87 My-emt. b) crustal structure after 25.5 My-emt of gravity driven tectonic transport. c) The equivalent time-step as (b) but with the geophysically derived crustal cross-section superimposed. d) Seismic crustal structure of the Georgian Bay transect. Note that there is ca. 200 km of additional gravity driven tectonic transport after the cessation of forward convergence. Abbreviations in List of abbreviations used (modified from Jamieson et al., 2010).

## 7.3 Future work

- Further geochronological and major- and trace-element geochemical data are needed from the metaplutonic bodies in the Kiosk domain to ascertain the petrogenetic affinity, to study the linkage between the metaplutonic rocks and widespread migmatization, and test the proposed petrogenetic link between the Kiosk and Britt domains.

- Further geochronology and geochemistry of Bonfield domains metaplutonic rocks and host orthogneisses is needed in order to strengthen the proposed interpretation of petrogenetic relation of the Bonfield Batholith to other ca. 1270-1235 Ma igneous bodies.

- Further monazite geochronology and trace-element geochemistry of paragneisses and metaplutonic bodies of the Kiosk domain would be useful to further constrain the Kiosk domain in a regional tectonic framework.

- Further thermochronological study is needed, using multiple thermochronometers along a wider transect through the Bonfield, Kiosk, and Algonquin domains to constrain the cooling history of the area.

## 7.4 Conclusions

1. The BBLSZ is a previously unmapped, through-going shear zone in the Kiosk domain.

2. The age of the igneous protolith of Kiosk domain orthogneiss is ca. 1660 Ma.

3. Migmatitic orthogneisses and straight gneisses from the Kiosk domain experienced granulite-facies metamorphism and migmatization at ca. 1480-1450 Ma.

4. The Bonfield Batholith of the Bonfield domain crystallized at ca. 1240 Ma.

5. Monazites in paragneiss from the interior of the Kiosk domain in the footwall of the BBLSZ (sample PS08-101a) record pre-Grenvillian protracted and episodic monazite crystallization at ca. 1200-1135 Ma.

6. The McLintock subdomain of the Algonquin domain experienced high-grade metamorphism and deformation during the Ottawan phase of the Grenville orogeny at ca. 1080-1060 Ma.

7. The NTLSZ cooled through amphibole closure at ca. 1030 Ma, and the footwall rocks of the Bonfield Batholith cooled through amphibole closure at ca. 1100 Ma, representing a thermal break of ca. 70 Ma.

8. The Kiosk domain experienced penetrative metamorphism at granulite-facies conditions at approximately 10.5±1.7 kbar and 791±123°C, probably during the Ottawan phase of the Grenville orogeny.

9. The Kiosk, Algonquin and Britt domains share a common history of tectonic development, which suggests the Kiosk and Algonquin domains are part of the Parautochthonous Belt.

# APPENDIX A

# ZIRCON ANALYTICAL DATA

Appendix A presents SHRIMP-RG analytical data of zircons analysed in this study. This appendix is subdivided into three sections. *Section 1* presents annotated CL and BSE images of zircons. *Section 2* presents U-Pb isotopic data. *Section 3* presents trace-element data collected during U-Pb isotopic analyses.

## Section 1: CL and BSE Imagery

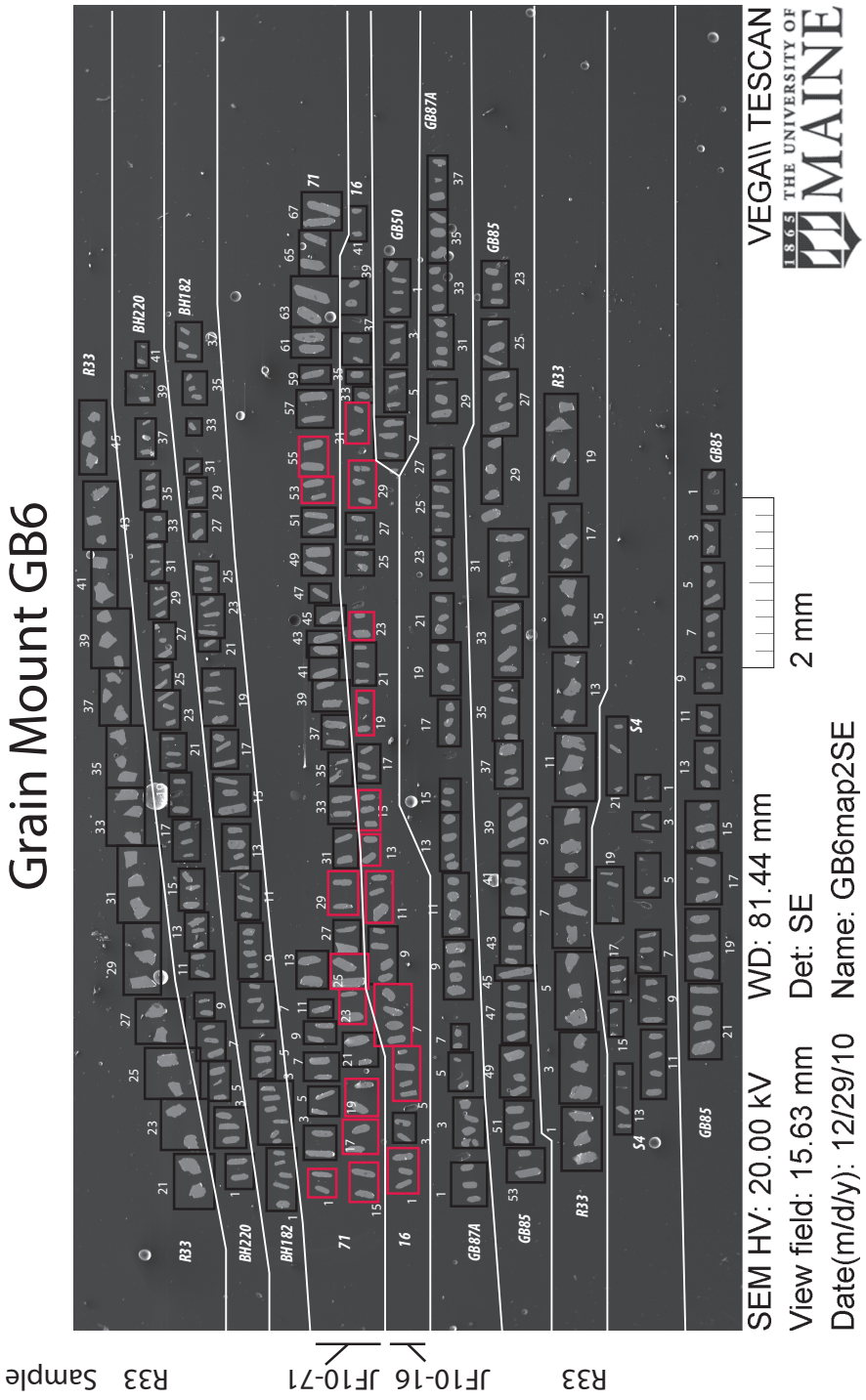


Figure A.1: Grain Mount (GB6). Numbered boxes correspond to close up CL and BSE images, red boxes are those in the following sections.

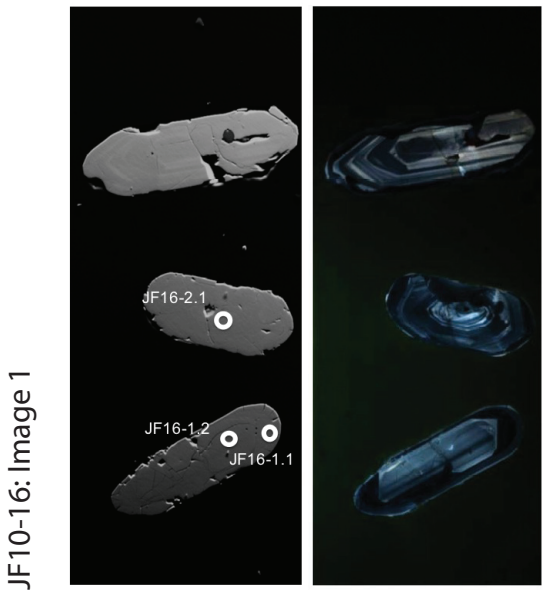
JF10-16: Image 1
JF16-2.1
JF16-1.2
JF16-1.1

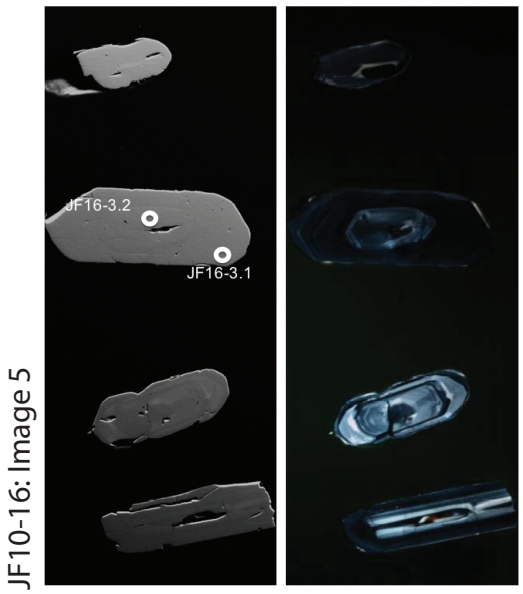
JF10-16: Image 5
JF16-3.2
JF16-3.1

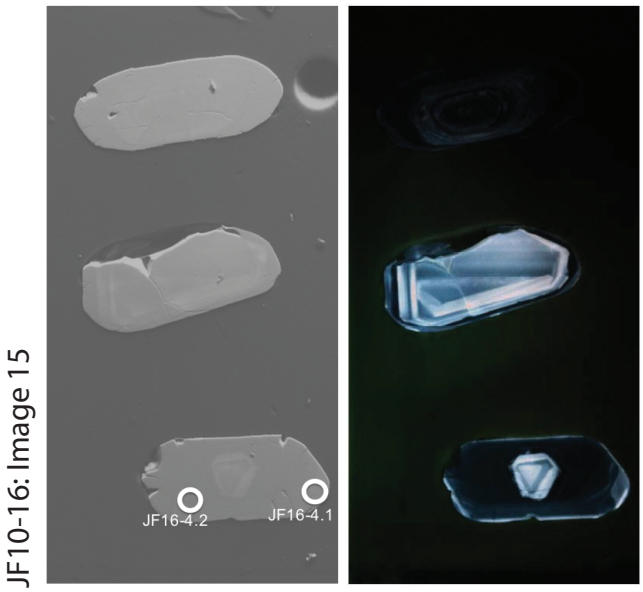
JF10-16: Image 15
JF16-4.2
JF16-4.1

JF10-16: Image 23

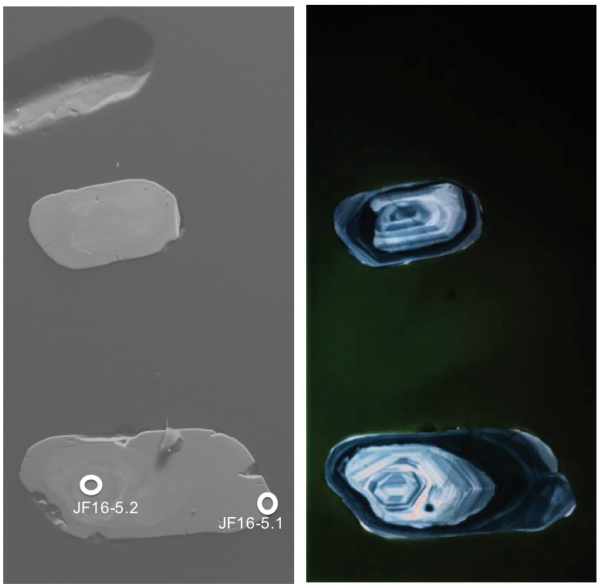


JF10-16: Image 31

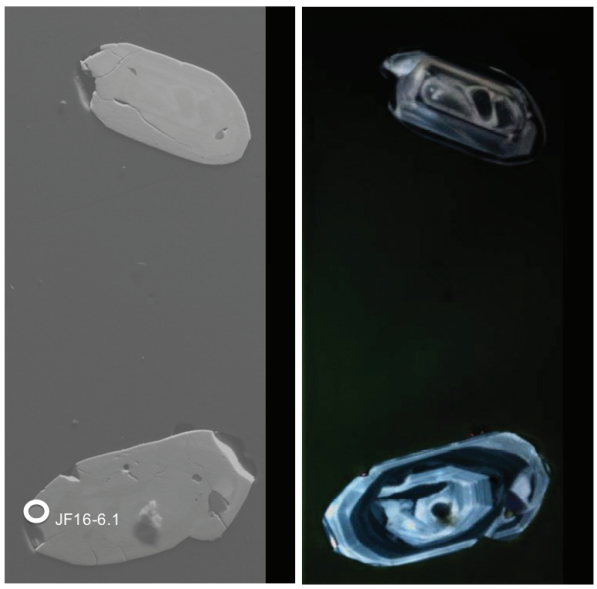

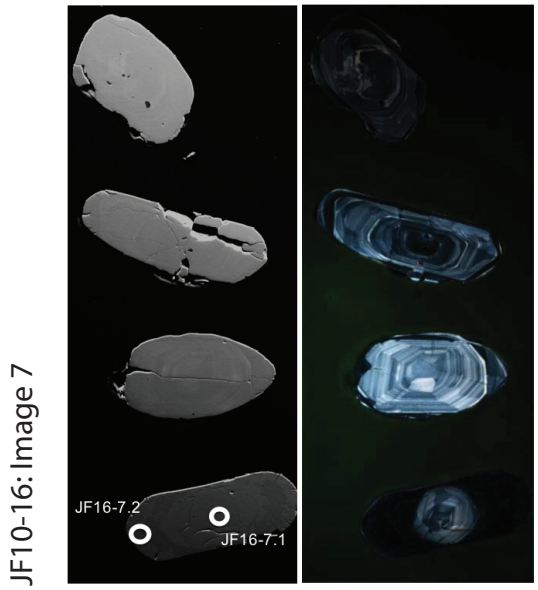


JF10-16: Image 7


JF10-16: Image 11

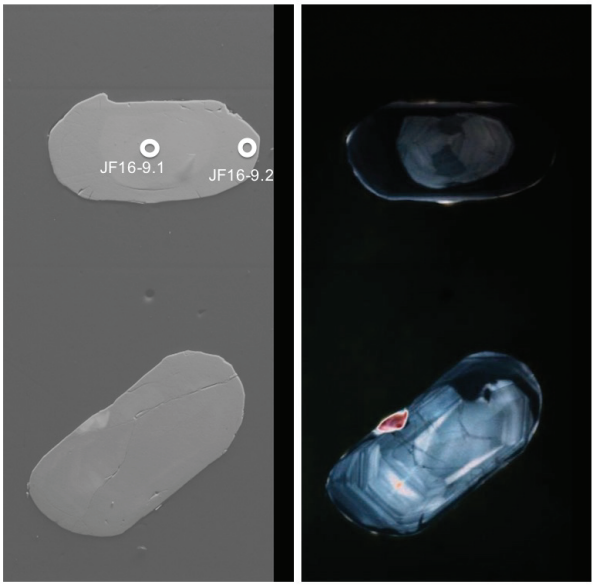


JF10-16: Image 13

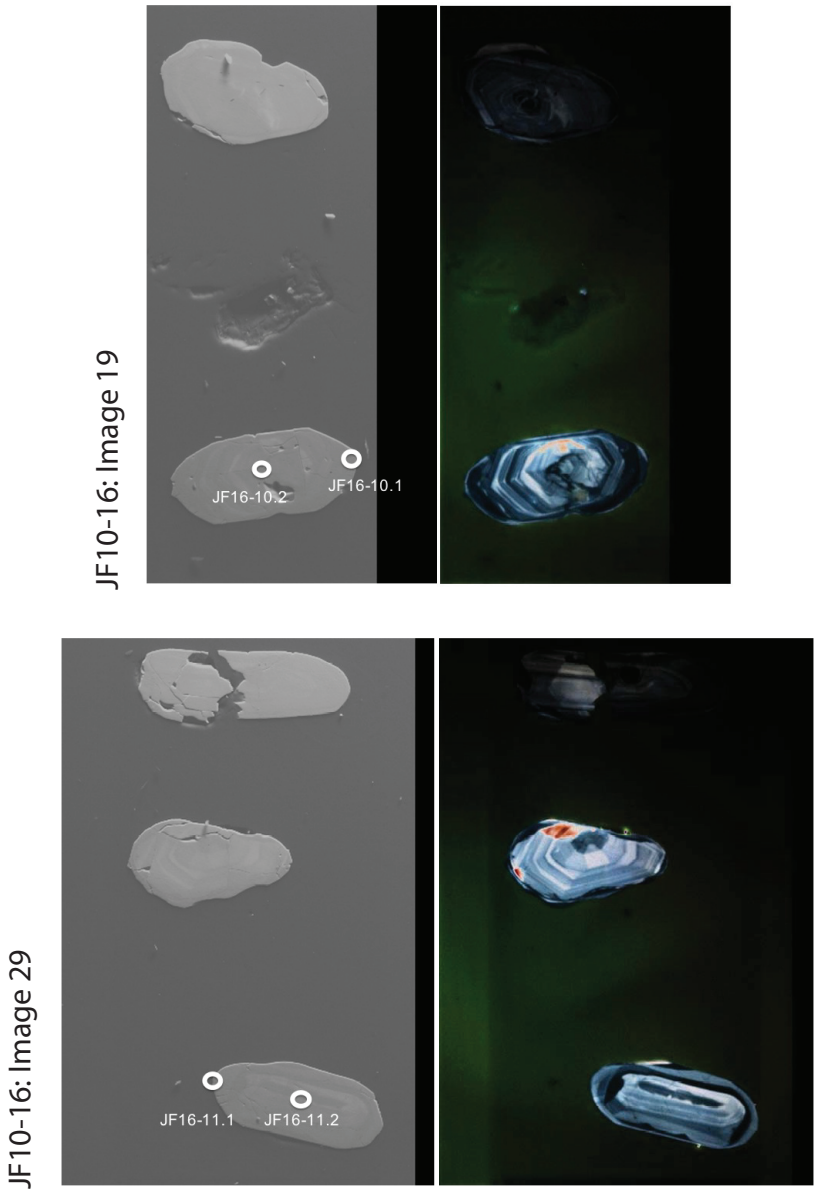
JF10-16: Image 19
JF16-10.2
JF16-10.1
JF10-16: Image 29
JF16-11.1
JF16-11.2

JF10-71: Image 1

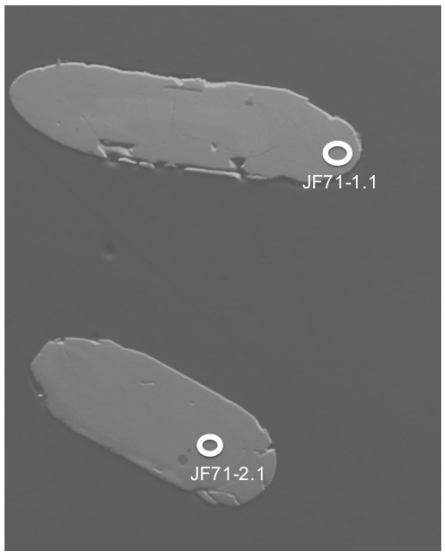


JF10-71: Image 15

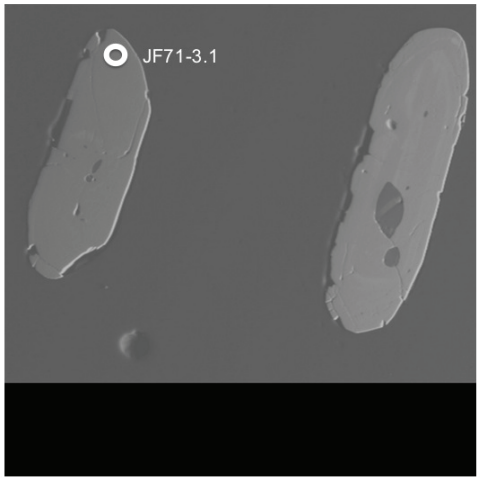


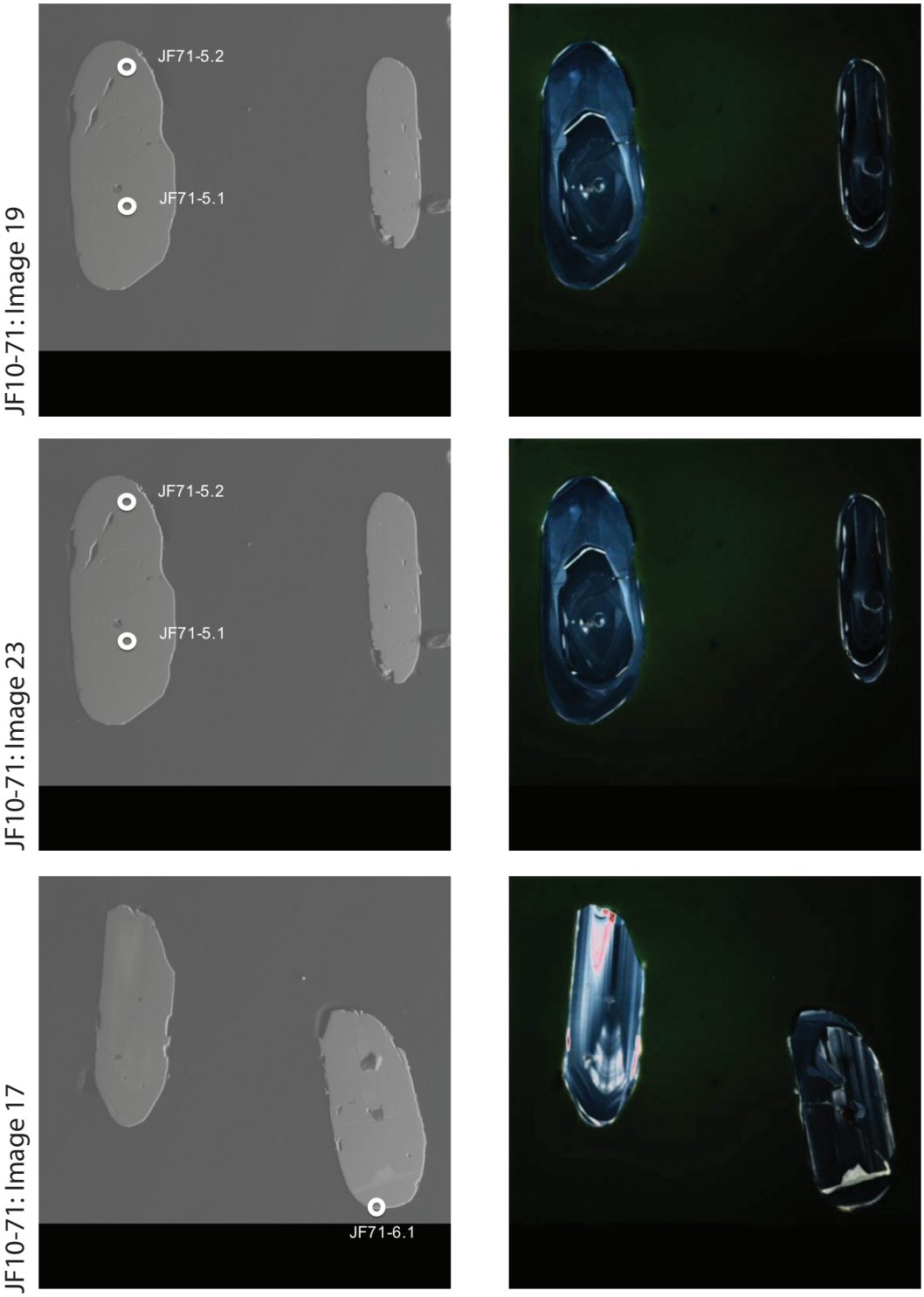
JF10-71: Image 19
JF71-5.2
JF71-5.1
JF10-71: Image 23
JF71-5.2
JF71-5.1
JF10-71: Image 17
JF71-6.1

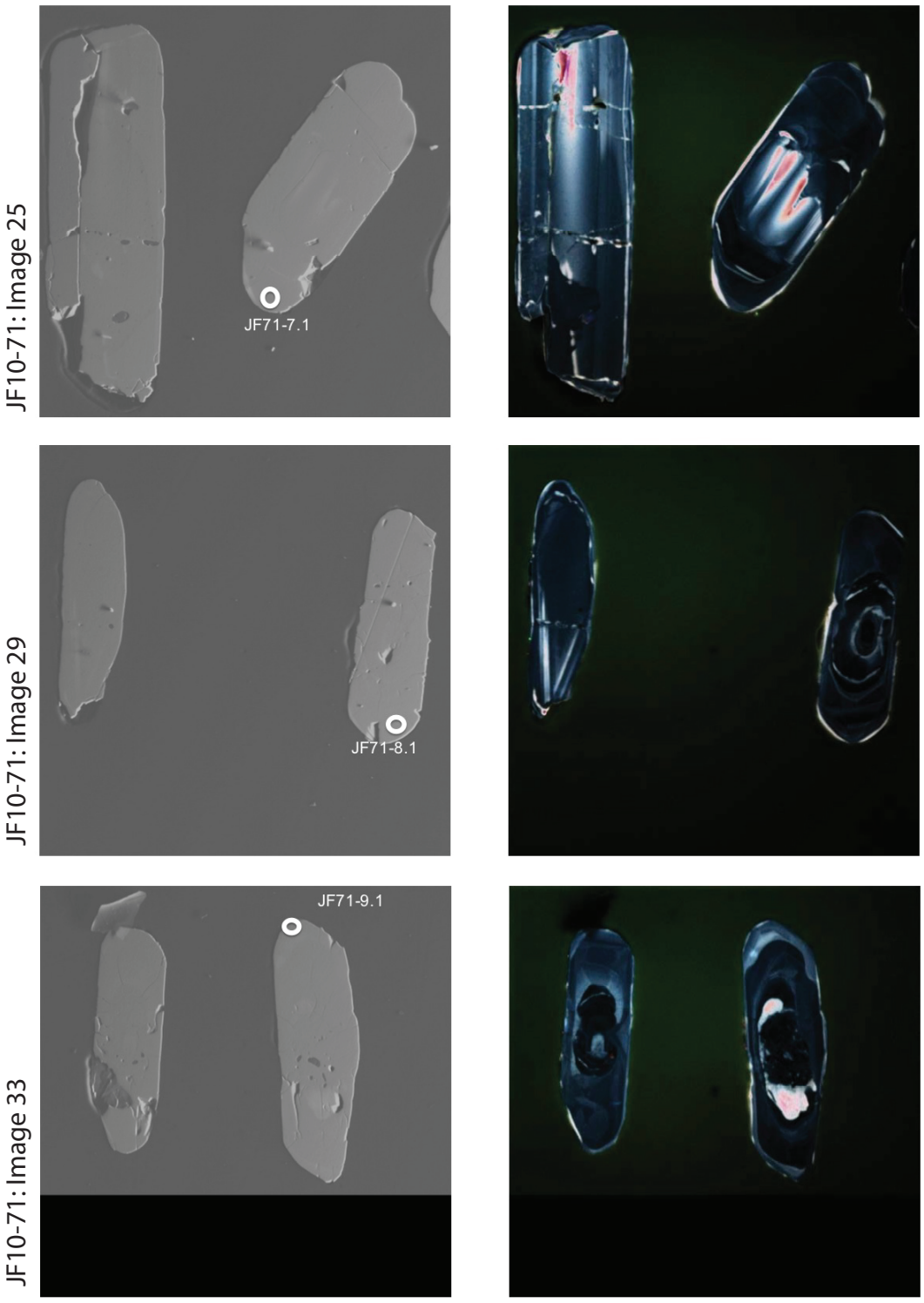
JF10-71: Image 25
JF71-7.1
JF10-71: Image 29
JF71-8.1
JF10-71: Image 33
JF71-9.1

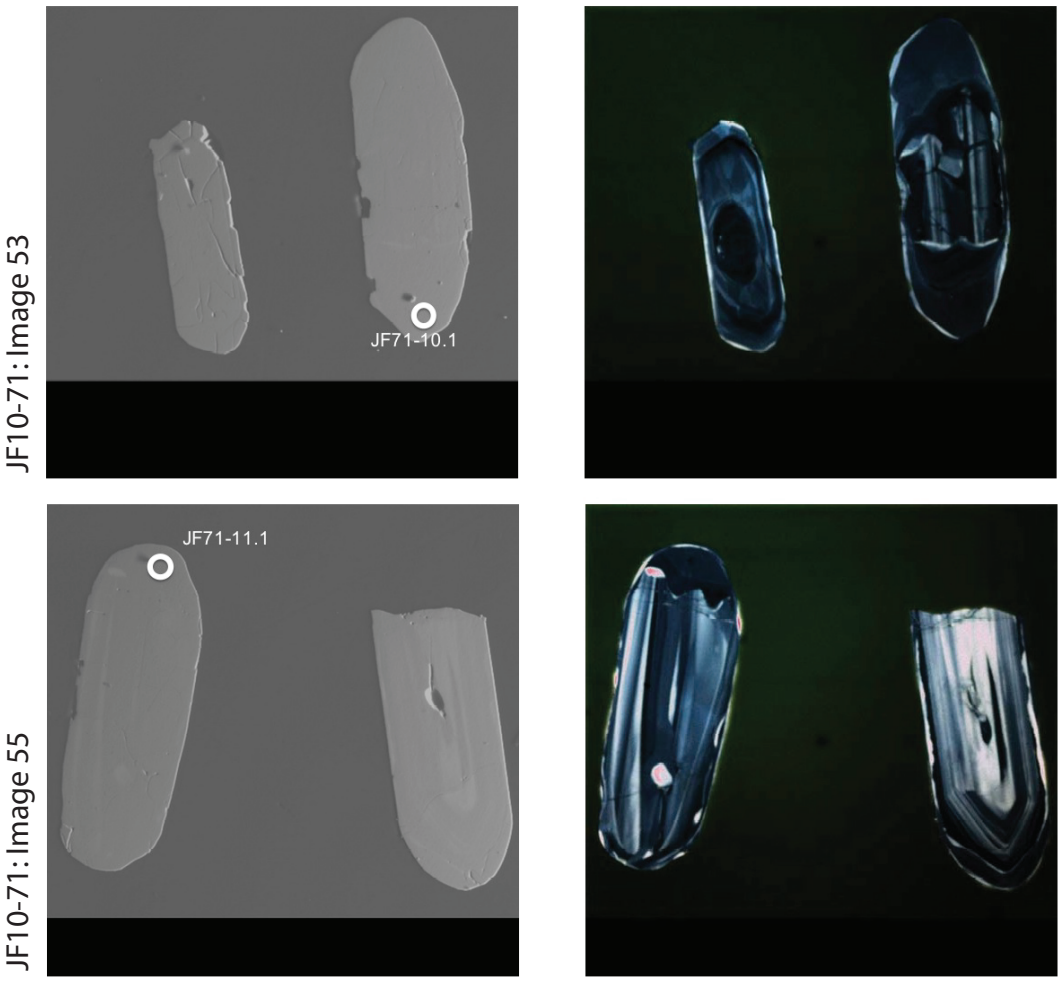
JF10-71: Image 53
JF71-10.1
JF10-71: Image 55
JF71-11.1

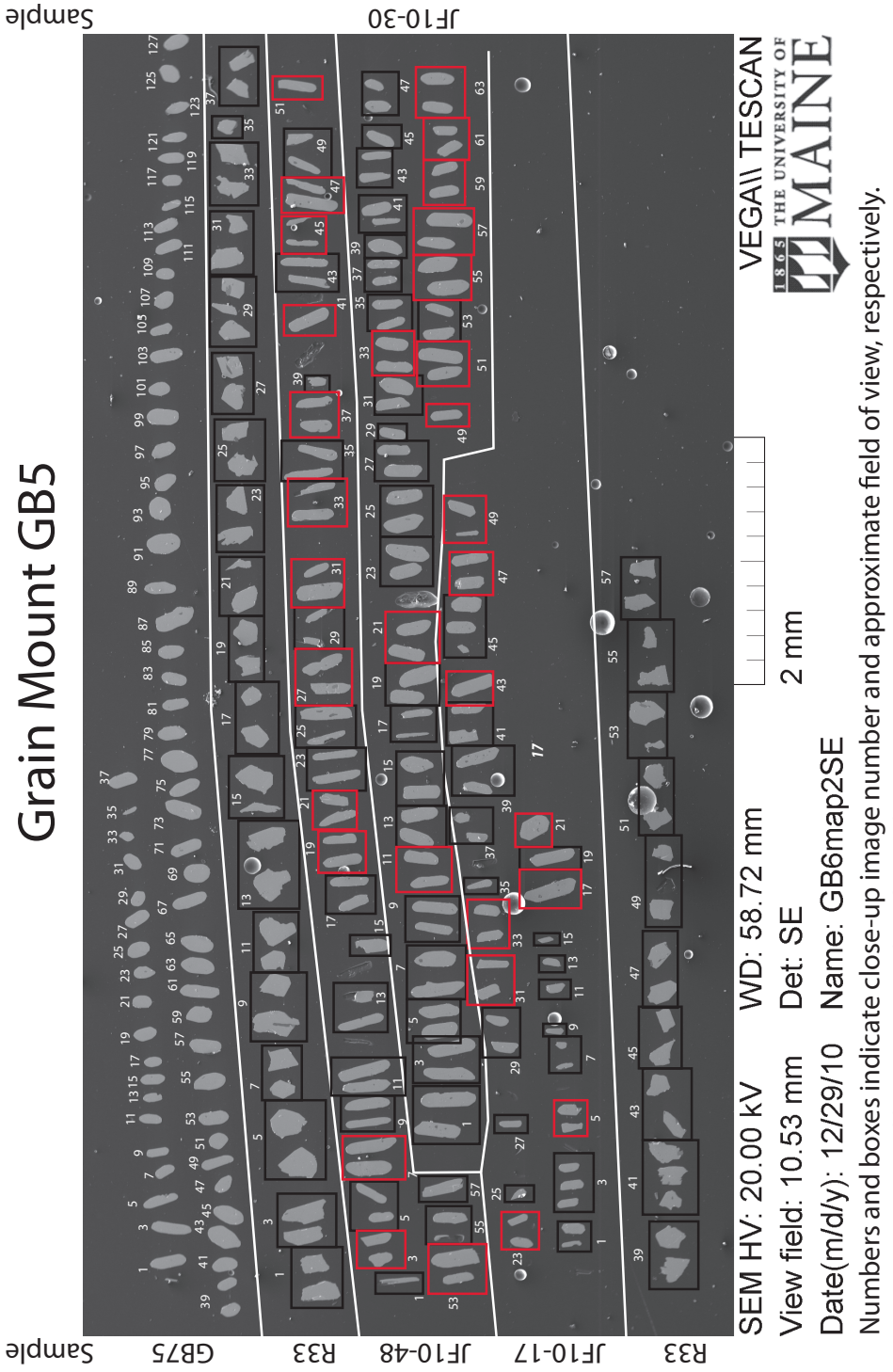


Figure A.2: Grain Mount (GB5). Numbered boxes correspond to close up CL and BSE images, red boxes are those in the following sections.

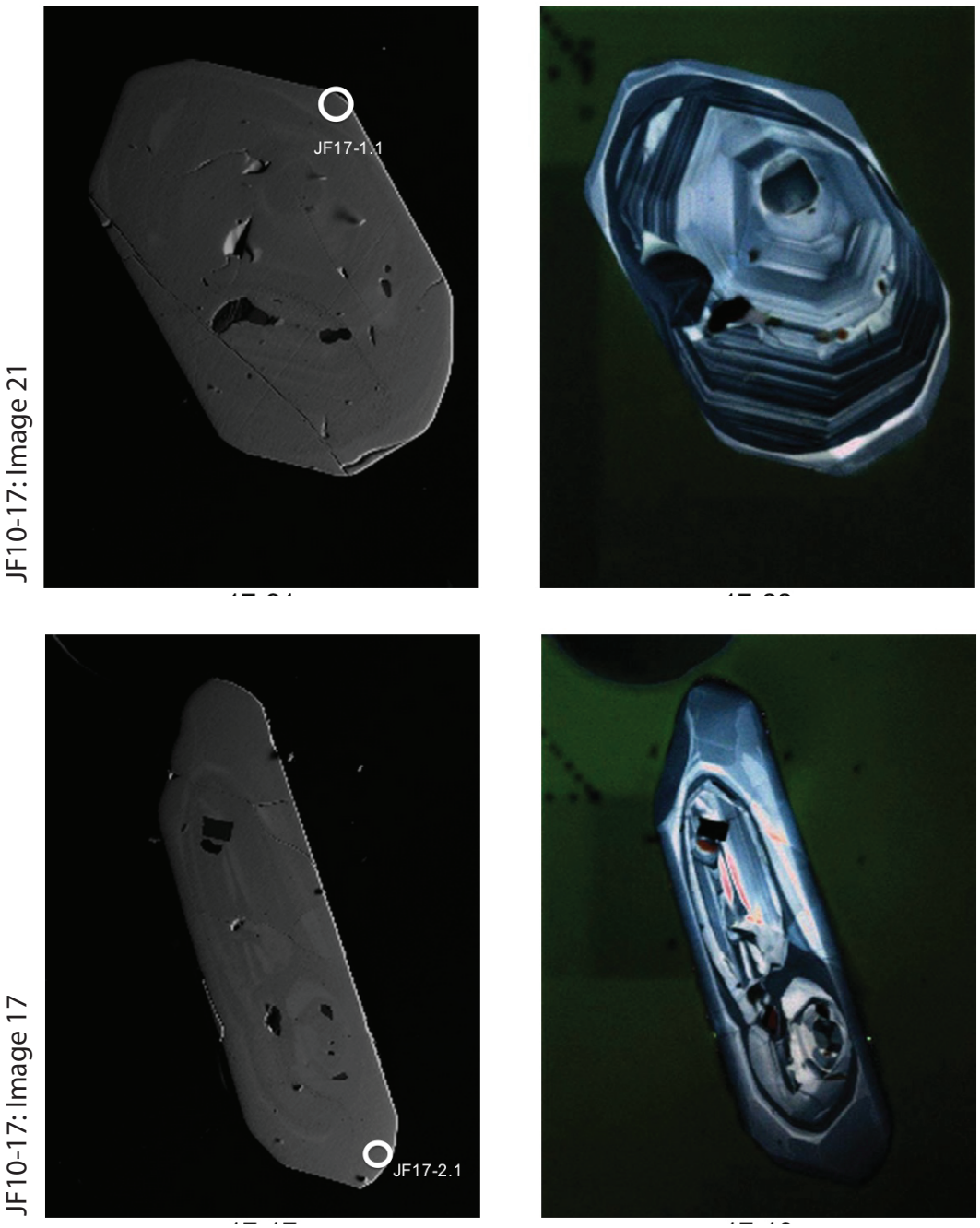
JF10-17: Image 21
JF17-1.1
JF10-17: Image 17
JF17-2.1

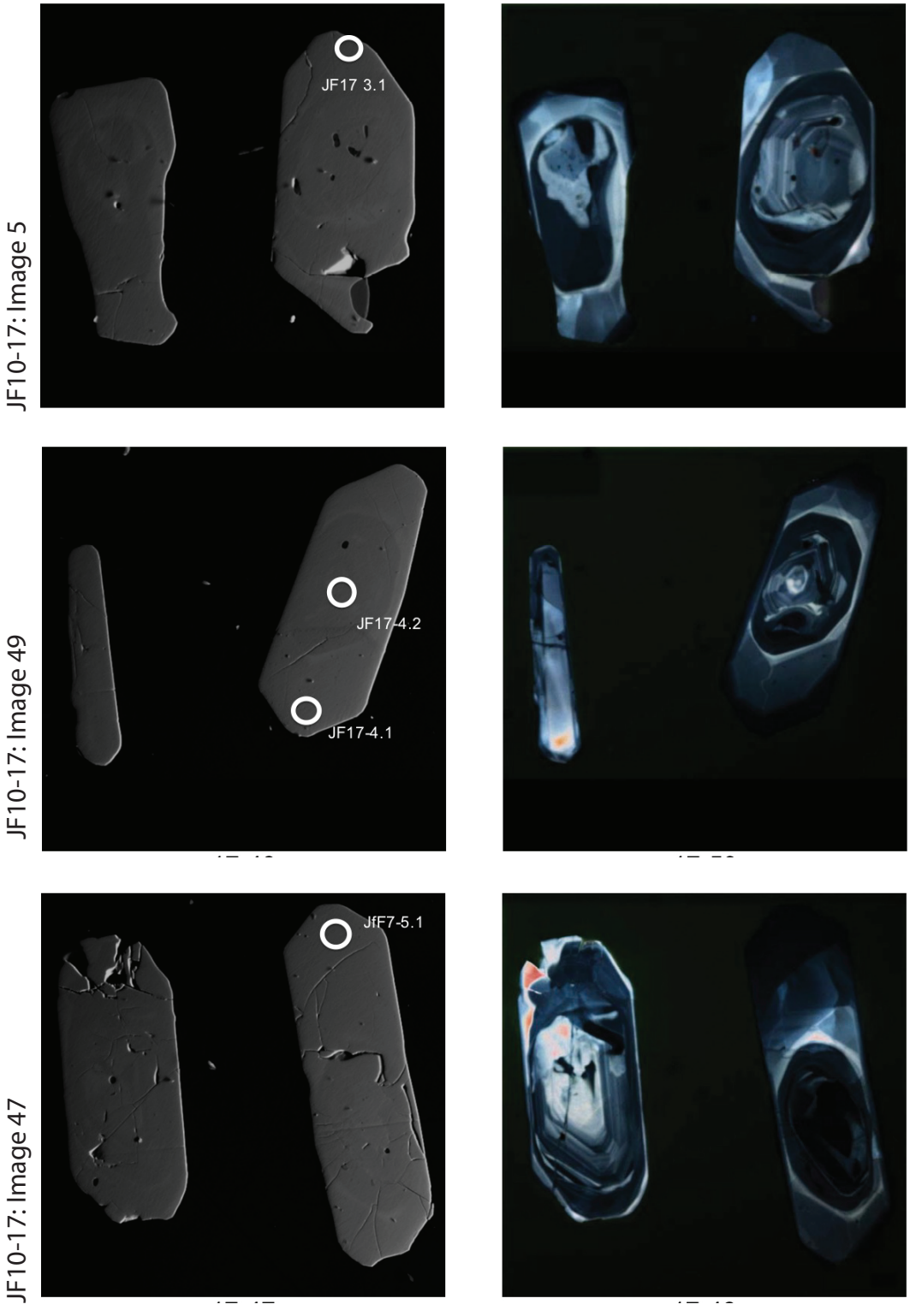
JF10-17: Image 5
JF17 3.1
JF10-17: Image 49
JF17-4.2
JF17-4.1
JF10-17: Image 47
JfF7-5.1

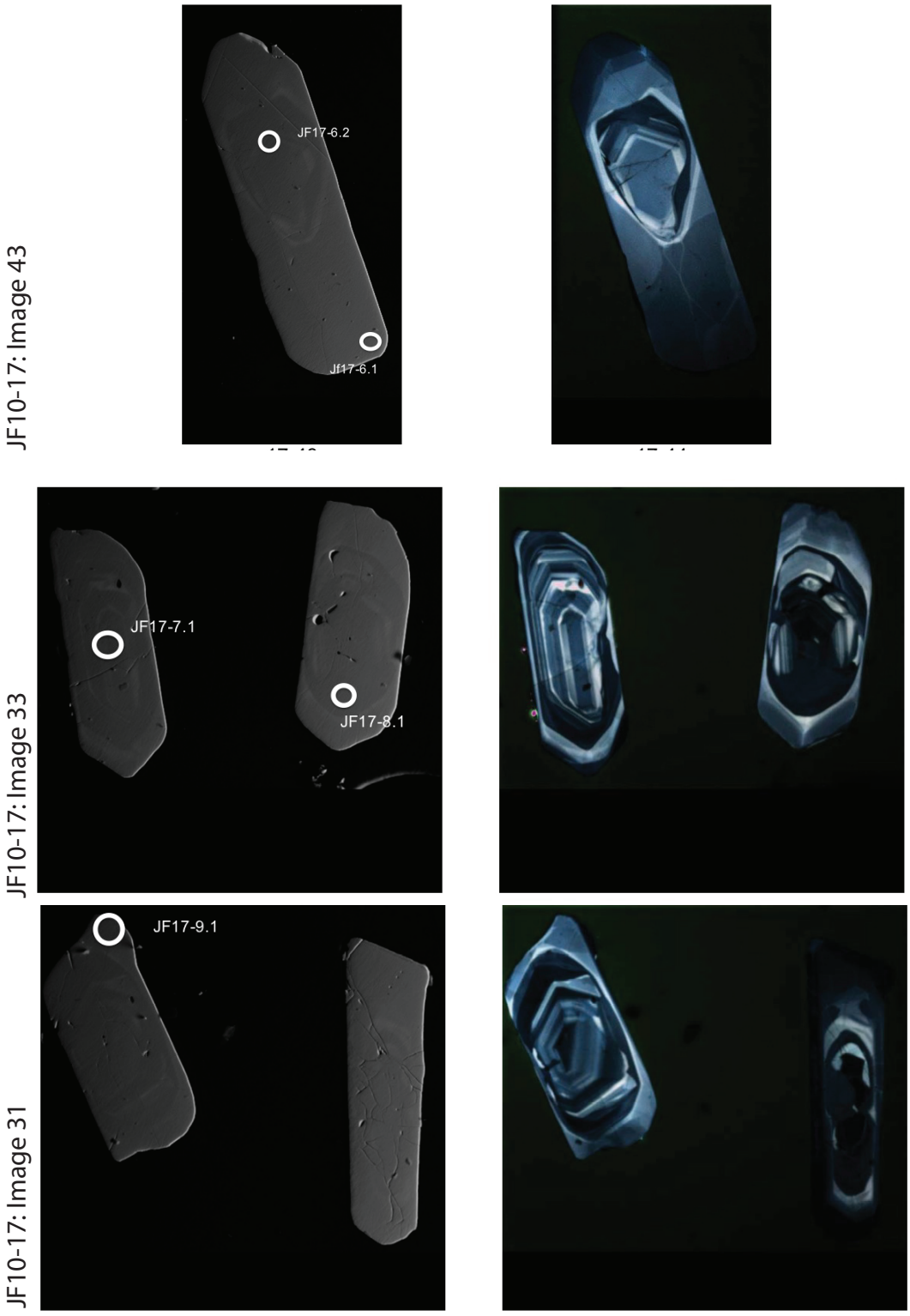
JF10-17: Image 43
JF17-6.2
JF17-6.1
JF10-17: Image 33
JF17-7.1
JF17-8.1
JF10-17: Image 31
JF17-9.1

JF10-17: Image 23

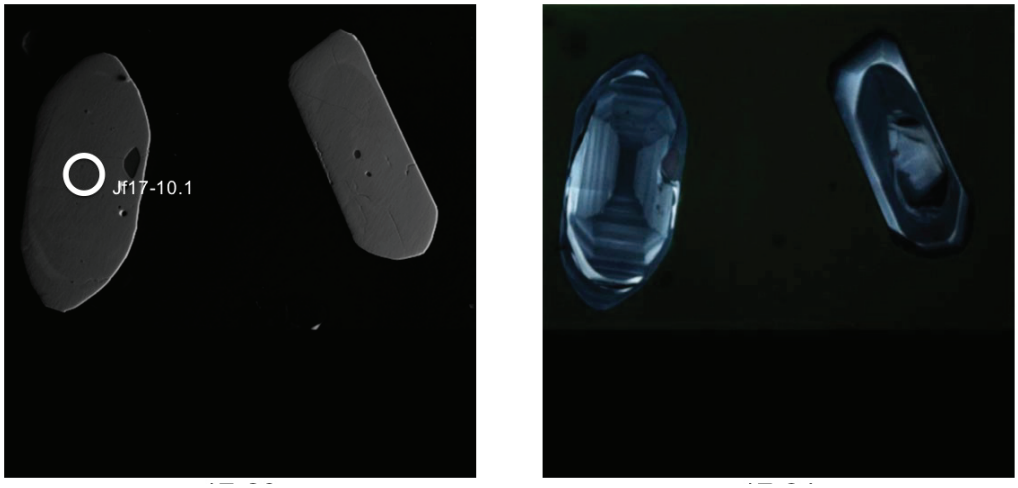

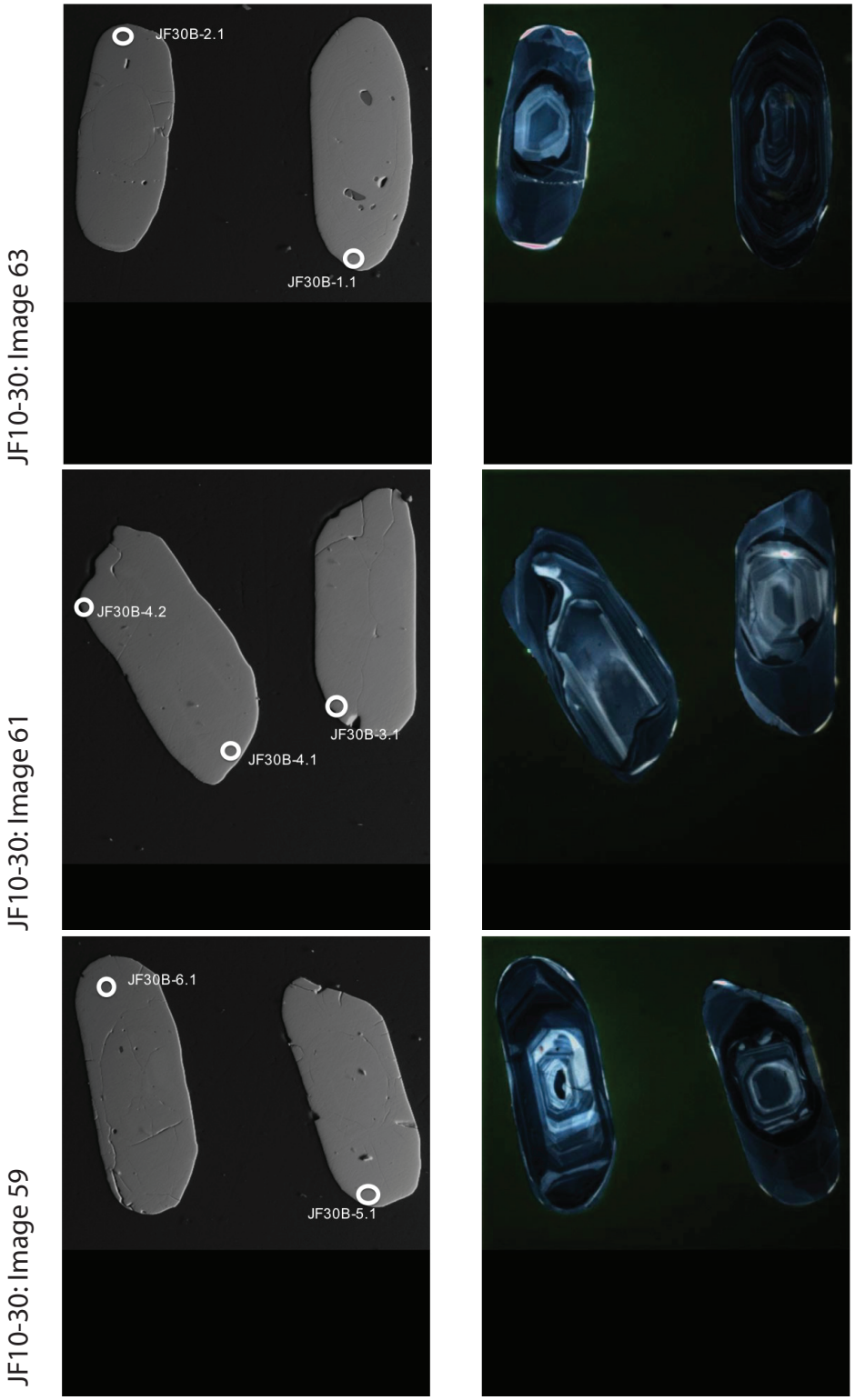
JF10-30: Image 63
JF30B-2.1
JF30B-1.1
JF10-30: Image 61
JF30B-4.2
JF30B-3.1
JF30B-4.1
JF10-30: Image 59
JF30B-6.1
JF30B-5.1

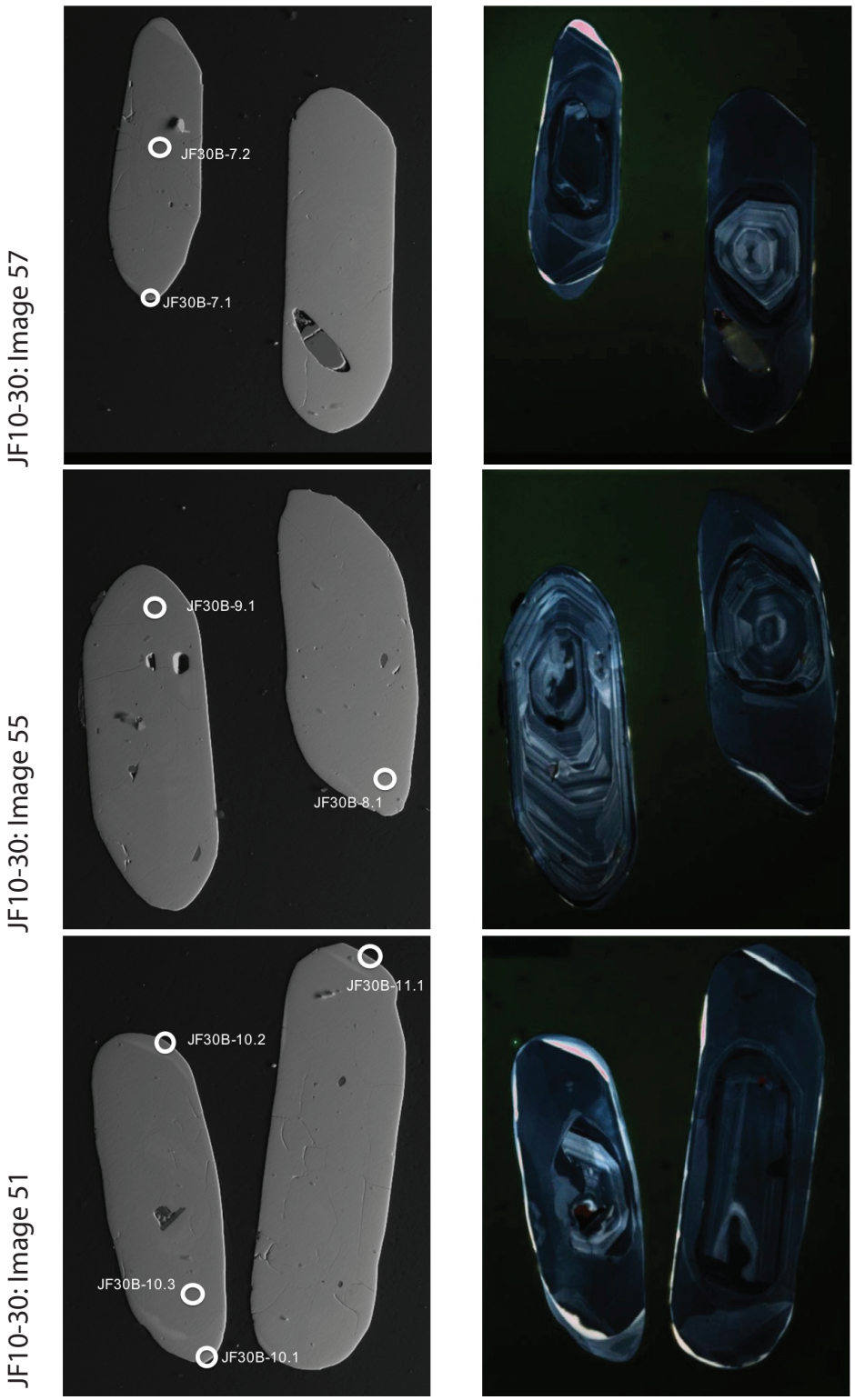
JF10-30: Image 57
JF30B-7.2
JF30B-7.1
JF10-30: Image 55
JF30B-9.1
JF30B-8.1
JF10-30: Image 51
JF30B-11.1
JF30B-10.2
JF30B-10.3
JF30B-10.1

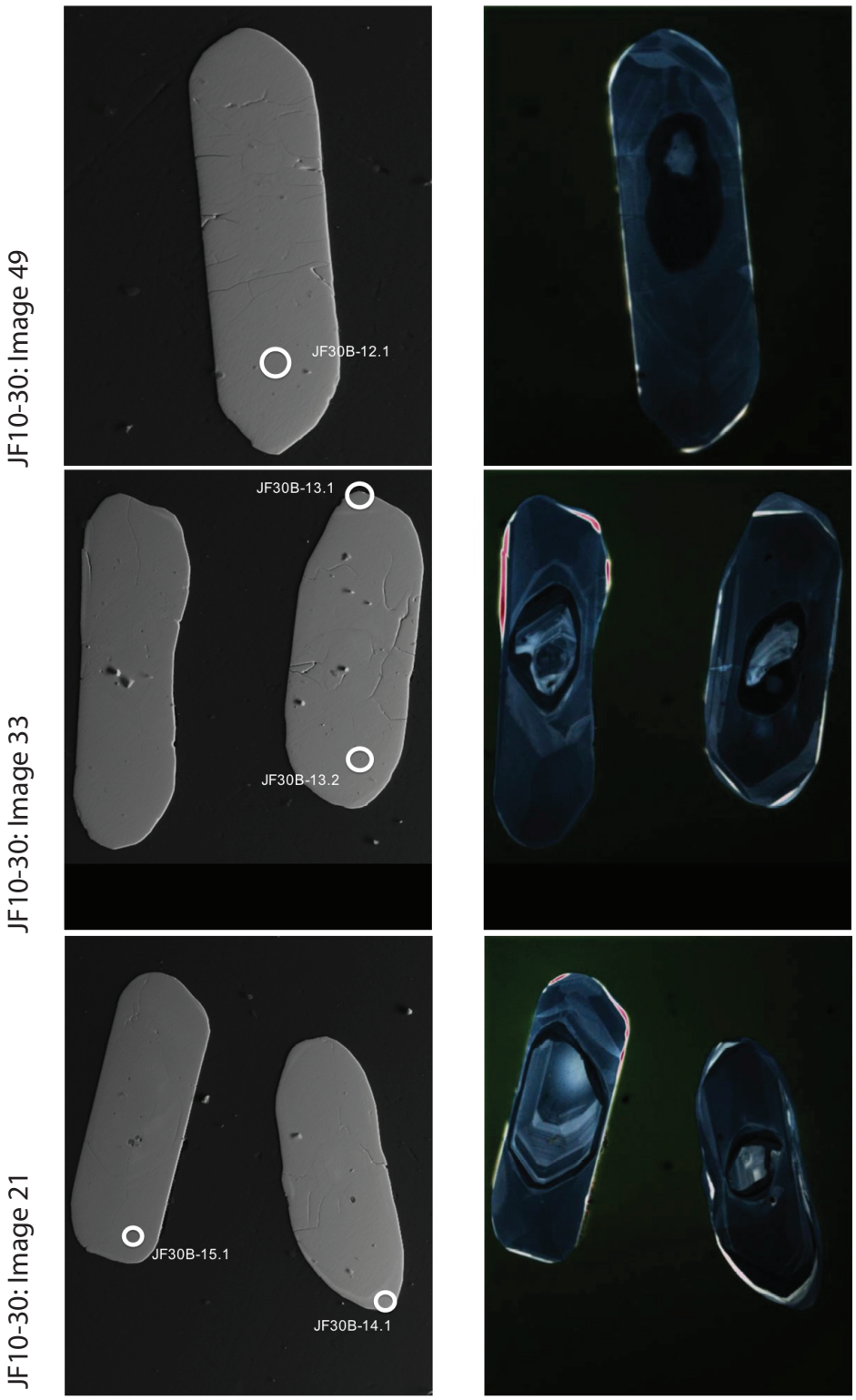
JF10-30: Image 49
JF30B-12.1
JF10-30: Image 33
JF30B-13.1
JF30B-13.2
JF10-30: Image 21
JF30B-15.1
JF30B-14.1

JF10-30: Image 11


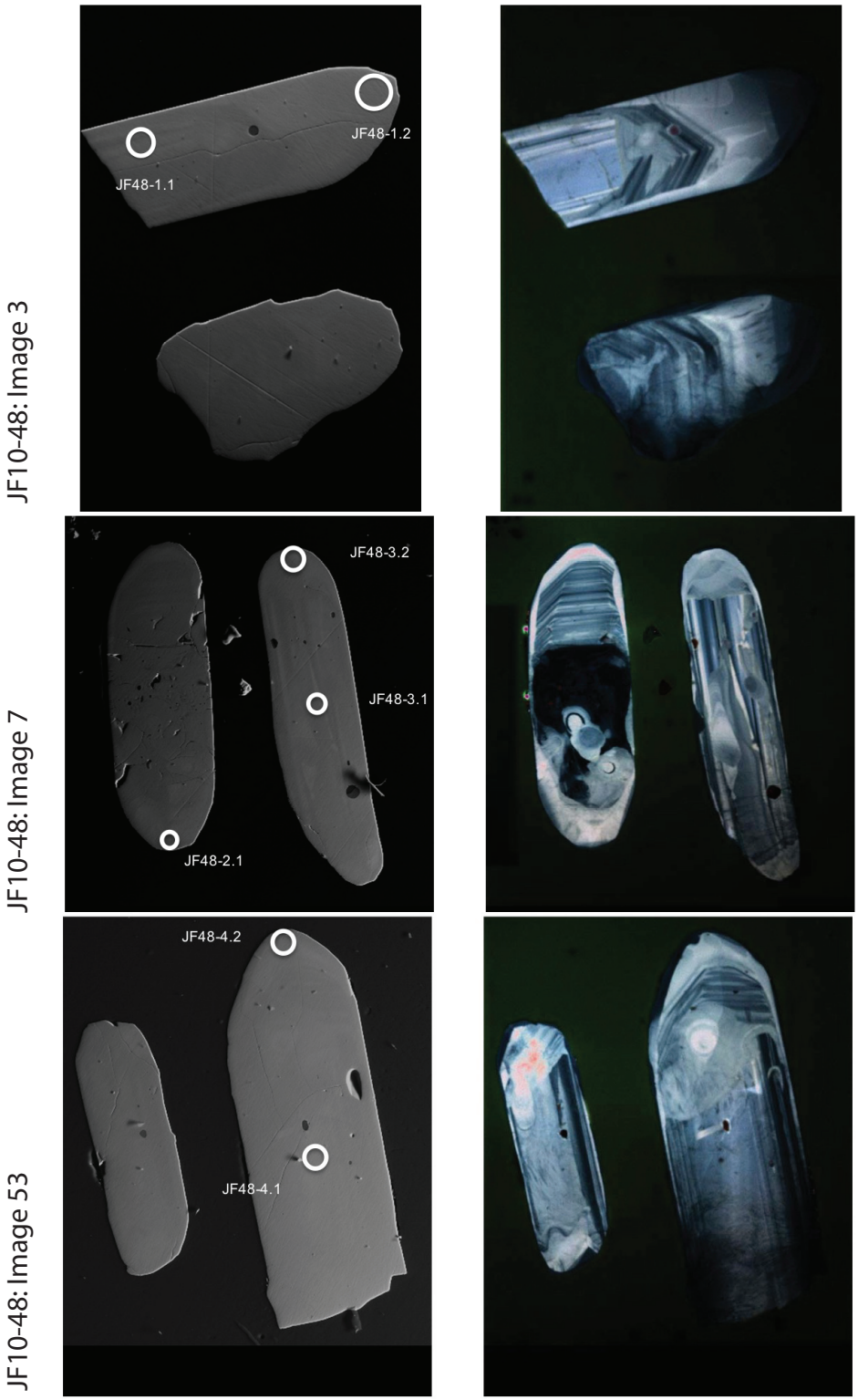
JF10-48: Image 3
JF48-1.1
JF48-1.2
JF10-48: Image 7
JF48-3.2
JF48-3.1
JF48-2.1
JF10-48: Image 53
JF48-4.2
JF48-4.1

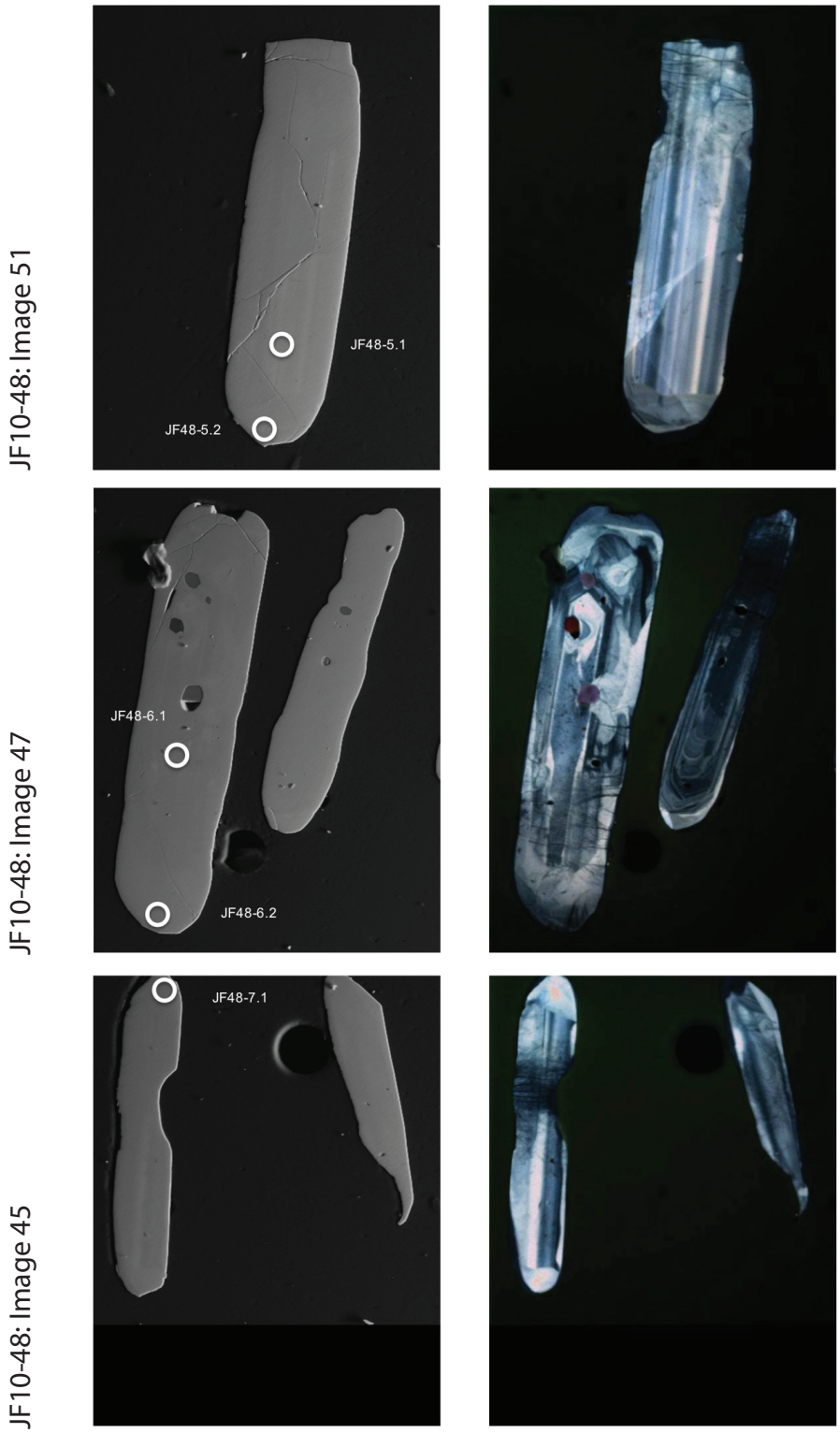
JF10-48: Image 51
JF48-5.1
JF48-5.2
JF10-48: Image 47
JF48-6.1
JF48-6.2
JF10-48: Image 45
JF48-7.1

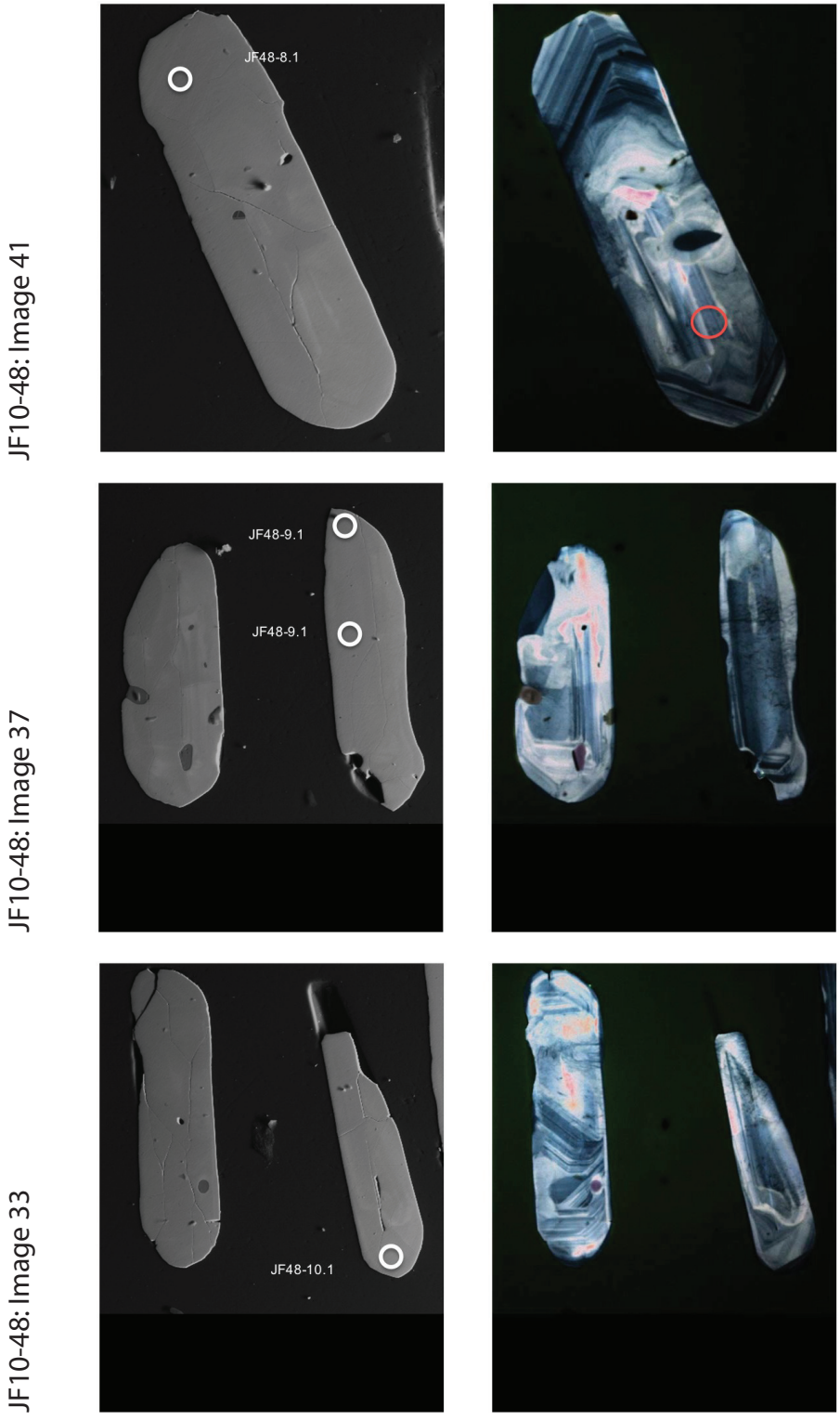
JF10-48: Image 41
JF10-48: Image 37
JF10-48: Image 33
JF48-8.1
JF48-9.1
JF48-9.1
JF48-10.1

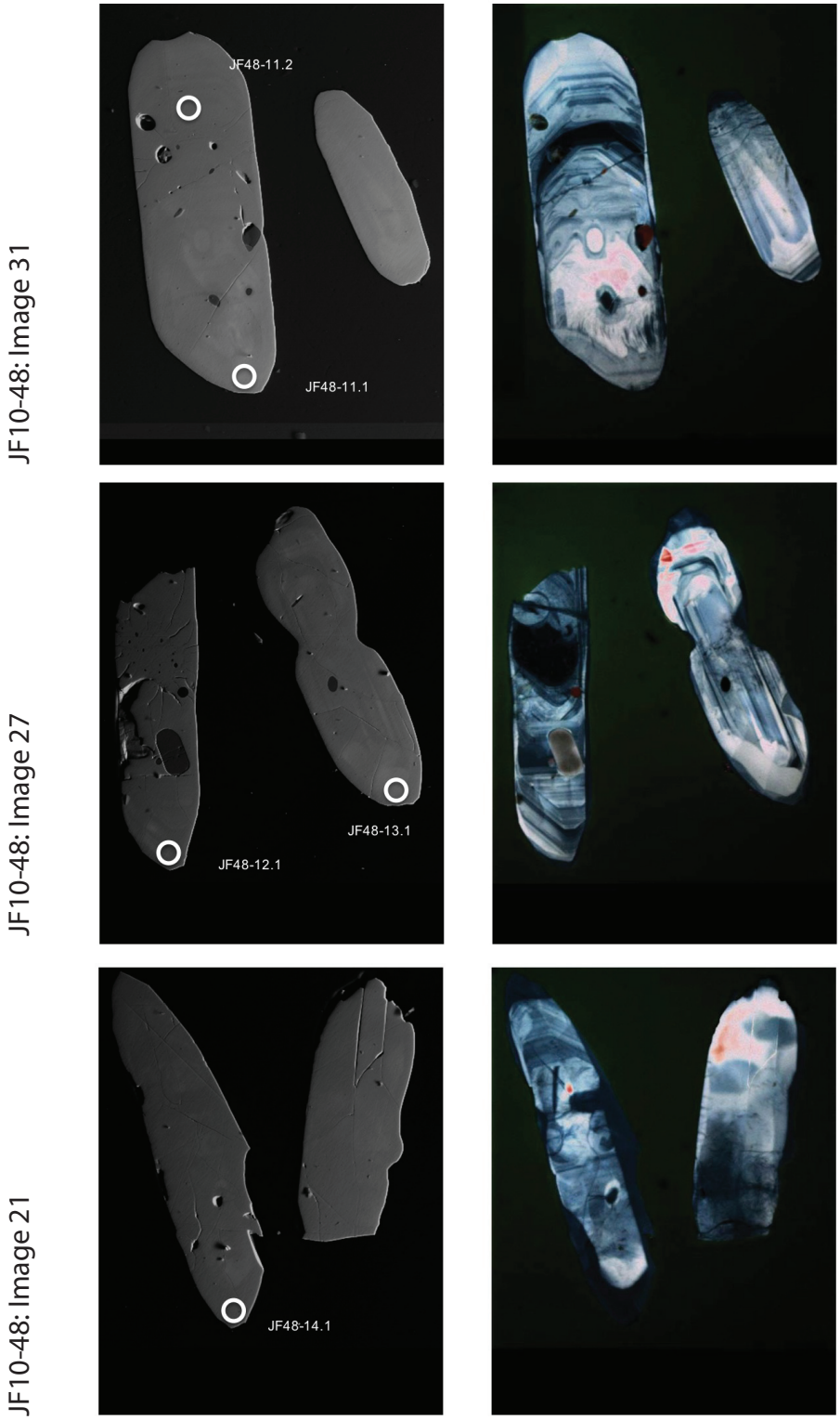
JF10-48: Image 31
JF48-11.2
JF48-11.1
JF10-48: Image 27
JF48-13.1
JF48-12.1
JF10-48: Image 21
JF48-14.1

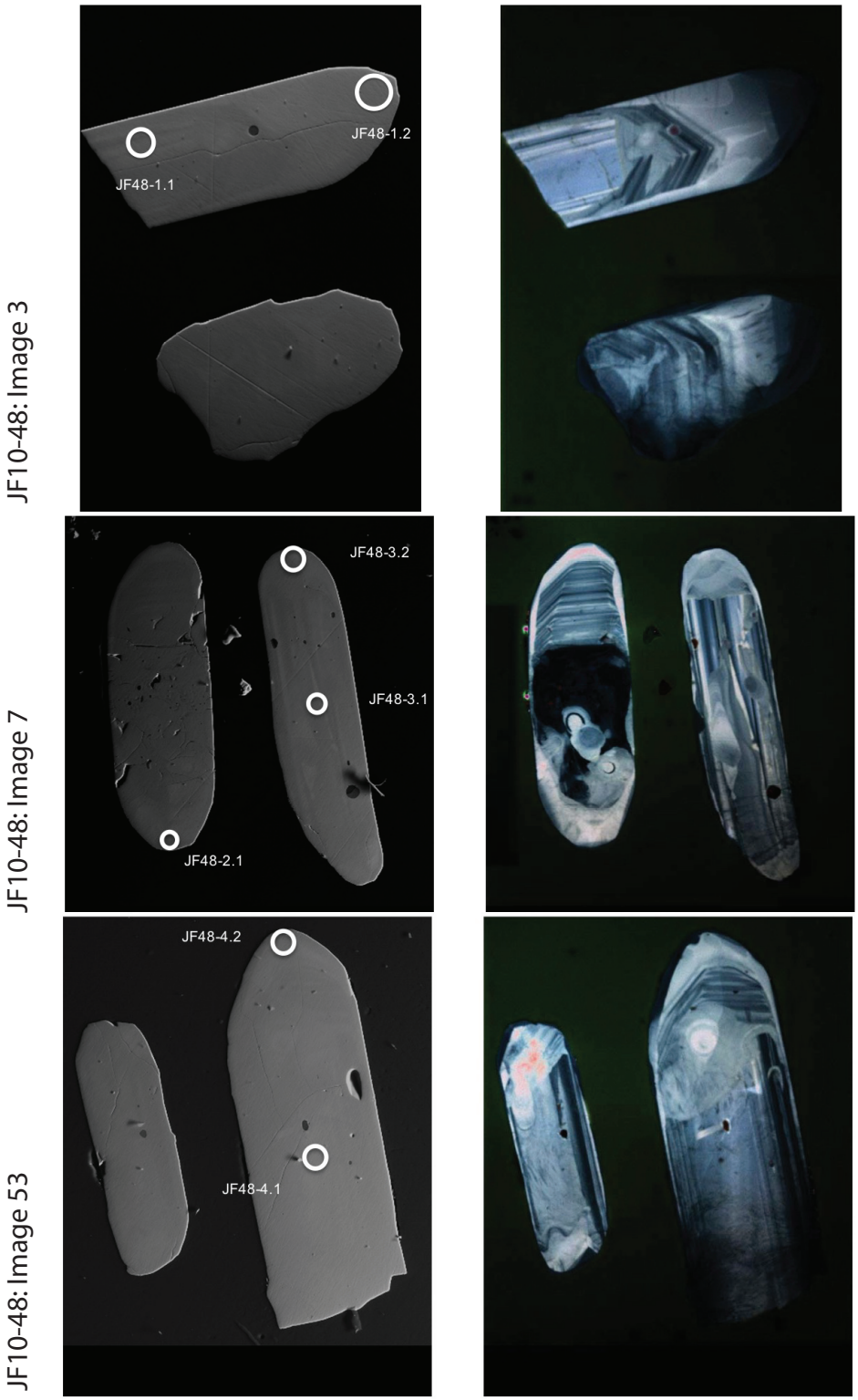
JF10-48: Image 3
JF48-1.1
JF48-1.2
JF10-48: Image 7
JF48-3.2
JF48-3.1
JF48-2.1
JF10-48: Image 53
JF48-4.2
JF48-4.1

# Section 2: Zircon U-Pb Isotopic Data

Table A.1: Table of Zircon U-Pb Analytical Data

| Spot # | U (ppm) | Th (ppm) | Th/U | % $^{206}$Pb | $^{204}$Pb/$^{206}$Pb | $^{204}$Pb corrected | | | | $^{207}$Pb/$^{206}$Pb | ±1s |
|---|---|---|---|---|---|---|---|---|---|---|---|
| | | | | | | $^{206}$Pb/$^{238}$U | err (%) | $^{207}$Pb/$^{206}$Pb | err (%) | Age (Ma) | |
| **JF10-16** | | | | | | | | | | | |
| *Mantle* | | | | | | | | | | | |
| JF16-3.1 | 647 | 23 | 0.04 | 0.02 | 121.5E-7 | 0.2496 | 0.4 | 0.0918 | 0.4 | 1464 | 8 |
| JF16-4.1 | 226 | 30 | 0.13 | 0.03 | 185.1E-7 | 0.2460 | 0.6 | 0.0920 | 0.8 | 1467 | 14 |
| JF16-4.2 | 1070 | 21 | 0.02 | 0.02 | 113.4E-7 | 0.2355 | 0.3 | 0.0918 | 0.4 | 1463 | 7 |
| JF16-9.2 | 1561 | 17 | 0.01 | 0.01 | 333.3E-8 | 0.2588 | 0.2 | 0.0914 | 0.3 | 1454 | 6 |
| JF16-11.1 | 272 | 41 | 0.15 | 0.06 | 355.3E-7 | 0.2635 | 0.6 | 0.0917 | 0.7 | 1462 | 13 |
| JF16-10.1 | 636 | 20 | 0.03 | 0.15 | 936.0E-7 | 0.3743 | 0.5 | 0.0925 | 0.9 | 1478 | 17 |
| JF16-10.2 | 261 | 86 | 0.33 | 0.06 | 380.3E-7 | 0.2144 | 0.5 | 0.0910 | 1.0 | 1447 | 19 |
| *Core* | | | | | | | | | | | |
| JF16-1.2 | 170 | 305 | 1.80 | 0.05 | 316.3E-7 | 0.2751 | 0.7 | 0.1018 | 0.8 | 1657 | 16 |
| JF16-3.2 | 159 | 186 | 1.17 | 0.02 | 114.5E-7 | 0.2883 | 0.7 | 0.1023 | 0.7 | 1666 | 13 |
| JF16-5.2 | 88 | 93 | 1.06 | 0.00 | 100.0E-34 | 0.2925 | 0.9 | 0.1026 | 1.0 | 1672 | 18 |
| JF16-7.1 | 148 | 143 | 0.97 | 0.00 | 100.0E-34 | 0.2953 | 0.7 | 0.1004 | 0.7 | 1632 | 14 |
| JF16-9.1 | 102 | 75 | 0.73 | 0.03 | 214.9E-7 | 0.2895 | 0.9 | 0.1028 | 0.9 | 1675 | 17 |
| *Omitted from calculation* | | | | | | | | | | | |
| JF16-1.1 | 1445 | 33 | 0.02 | 0.01 | 497.1E-8 | 0.2482 | 0.2 | 0.0941 | 0.3 | 1510 | 5 |
| JF16-2.1 | 273 | 129 | 0.47 | 0.07 | 441.9E-7 | 0.2816 | 0.5 | 0.0986 | 0.7 | 1597 | 13 |
| JF16-5.1 | 201 | 22 | 0.11 | 0.34 | 204.9E-6 | 0.2631 | 0.7 | 0.0871 | 1.3 | 1363 | 25 |
| JF16-6.1 | 170 | 36 | 0.21 | 0.14 | 858.3E-7 | 0.2818 | 0.8 | 0.0859 | 1.6 | 1337 | 30 |
| JF16-7.2 | 5239 | 32 | 0.01 | 0.24 | 143.7E-6 | 0.1624 | 0.2 | 0.0869 | 0.4 | 1359 | 9 |
| JF16-8.1 | 580 | 248 | 0.43 | 0.03 | 202.4E-7 | 0.2724 | 0.4 | 0.0998 | 0.4 | 1620 | 8 |
| JF16-11.2 | 122 | 92 | 0.75 | 0.09 | 545.5E-7 | 0.2659 | 0.7 | 0.1013 | 0.9 | 1648 | 16 |
| **JF10-17** | | | | | | | | | | | |
| *Mantle* | | | | | | | | | | | |
| JF17-1.1 | 81 | 61 | 0.75 | 0.24 | 145.9E-6 | 0.2581 | 1.0 | 0.0909 | 1.6 | 1445 | 31 |
| JF17-2.1 | 153 | 107 | 0.70 | 0.00 | 100.0E-34 | 0.2497 | 0.7 | 0.0908 | 1.2 | 1443 | 22 |
| JF17-3.1 | 130 | 89 | 0.68 | 0.00 | 100.0E-34 | 0.2468 | 0.8 | 0.0902 | 1.0 | 1431 | 18 |
| JF17-4.1 | 215 | 125 | 0.58 | 0.06 | 363.7E-7 | 0.2492 | 0.6 | 0.0906 | 0.8 | 1439 | 15 |
| JF17-6.1 | 177 | 105 | 0.59 | 0.00 | 100.0E-34 | 0.2434 | 0.8 | 0.0900 | 0.8 | 1424 | 15 |
| JF17-9.1 | 185 | 88 | 0.47 | 0.11 | 678.9E-7 | 0.2434 | 0.7 | 0.0908 | 1.0 | 1442 | 20 |
| *Omitted from calculation* | | | | | | | | | | | |
| JF17-4.2 | 92 | 96 | 1.04 | 0.00 | 100.0E-34 | 0.2673 | 0.9 | 0.1002 | 1.0 | 1627 | 18 |
| JF17-5.1 | 787 | 222 | 0.28 | 0.01 | 330.9E-8 | 0.2504 | 0.3 | 0.0922 | 0.4 | 1472 | 8 |
| JF17-6.2 | 69 | 104 | 1.50 | -0.07 | 000.0E-2 | 0.2812 | 1.2 | 0.1040 | 1.1 | 1696 | 21 |
| JF17-7.1 | 234 | 560 | 2.39 | 0.13 | 808.4E-7 | 0.2824 | 0.6 | 0.1016 | 0.7 | 1654 | 14 |
| JF17-8.1 | 119 | 184 | 1.54 | 0.00 | 100.0E-34 | 0.2981 | 0.8 | 0.1007 | 0.9 | 1637 | 16 |
| JF17-10.1 | 253 | 281 | 1.11 | 0.06 | 351.6E-7 | 0.2945 | 0.6 | 0.0995 | 0.7 | 1616 | 12 |
| **JF10-30** | | | | | | | | | | | |
| *Rim* | | | | | | | | | | | |
| JF30B-10.1 | 118 | 7 | 0.06 | 0.09 | 555.9E-7 | 0.1776 | 0.9 | 0.0725 | 1.5 | 1001 | 31 |
| JF30B-10.2 | 66 | 12 | 0.18 | 0.52 | 307.5E-6 | 0.2124 | 1.3 | 0.0726 | 3.2 | 1002 | 66 |
| JF30B-11.1 | 125 | 14 | 0.11 | 0.46 | 266.5E-6 | 0.1976 | 0.8 | 0.0711 | 2.8 | 961 | 58 |
| JF30B-14.1 | 101 | 4 | 0.04 | 0.33 | 194.1E-6 | 0.1783 | 0.9 | 0.0730 | 2.4 | 1014 | 48 |

| Spot # | U (ppm) | Th (ppm) | Th/U | % $^{206}$Pb | $^{204}$Pb/$^{206}$Pb | $^{204}$Pb corrected | | | | $^{207}$Pb/$^{206}$Pb | ±1s |
|---|---|---|---|---|---|---|---|---|---|---|---|
| | | | | | | $^{206}$Pb/$^{238}$U | err (%) | $^{207}$Pb/$^{206}$Pb | err (%) | Age (Ma) | |
| *Mantle* | | | | | | | | | | | |
| JF30B-4.1 | 335 | 37 | 0.11 | 0.03 | 156.7E-7 | 0.2428 | 0.6 | 0.0914 | 0.6 | 1355 | 27 |
| JF30B-5.1 | 162 | 111 | 0.68 | 0.03 | 185.1E-7 | 0.2655 | 0.9 | 0.0908 | 0.9 | 1445 | 20 |
| JF30B-8.1 | 249 | 211 | 0.85 | 0.02 | 118.1E-7 | 0.2648 | 0.7 | 0.0932 | 0.9 | 1475 | 22 |
| JF30B-10.3 | 243 | 206 | 0.85 | 0.02 | 950.6E-8 | 0.2510 | 0.5 | 0.0922 | 1.0 | 1443 | 12 |
| JF30B-12.1 | 205 | 151 | 0.74 | 0.00 | 100.0E-34 | 0.2439 | 0.7 | 0.0924 | 1.1 | 1375 | 15 |
| JF30B-13.2 | 269 | 241 | 0.90 | 0.04 | 264.7E-7 | 0.2493 | 0.5 | 0.0919 | 0.7 | 1432 | 12 |
| JF30B-15.1 | 228 | 187 | 0.82 | 0.02 | 120.1E-7 | 0.2518 | 0.6 | 0.0920 | 0.7 | 1441 | 14 |
| *Core* | | | | | | | | | | | |
| JF30B-6.1 | 327 | 166 | 0.51 | 0.11 | 690.1E-7 | 0.2796 | 0.5 | 0.1018 | 0.7 | 1389 | 16 |
| JF30B-7.2 | 616 | 437 | 0.71 | 0.03 | 182.8E-7 | 0.2675 | 0.3 | 0.1007 | 0.4 | 1495 | 8 |
| JF30B-9.1 | 169 | 97 | 0.57 | 0.03 | 185.7E-7 | 0.3027 | 0.7 | 0.1017 | 0.7 | 1675 | 20 |
| | | | | | | | | | | | |
| *Omitted from calculation* | | | | | | | | | | | |
| JF30B-1.1 | 518 | 19 | 0.04 | 0.03 | 168.2E-7 | 0.2669 | 0.4 | 0.0968 | 0.7 | 1563 | 14 |
| JF30B-2.1 | 134 | 138 | 1.03 | 0.40 | 245.4E-6 | 0.2785 | 1.0 | 0.0873 | 1.7 | 1368 | 33 |
| JF30B-3.1 | 146 | 71 | 0.49 | 0.03 | 186.2E-7 | 0.2333 | 0.8 | 0.0875 | 1.0 | 1371 | 18 |
| JF30B-4.2 | 240 | 51 | 0.21 | 0.00 | 100.0E-34 | 0.2041 | 0.7 | 0.0803 | 0.9 | 1204 | 19 |
| JF30B-7.1 | 165 | 20 | 0.12 | 0.00 | 100.0E-34 | 0.1967 | 0.8 | 0.0805 | 1.0 | 1209 | 20 |
| JF30B-13.1 | 129 | 10 | 0.08 | 1.47 | 848.7E-6 | 0.2165 | 1.0 | 0.0666 | 4.3 | 827 | 90 |
| JF30B-16.2 | 154 | 124 | 0.81 | 0.03 | 165.3E-7 | 0.2593 | 0.7 | 0.0959 | 0.8 | 1545 | 16 |
| | | | | | | | | | | | |
| **JF10-48** | | | | | | | | | | | |
| JF48-1.1 | 38 | 24 | 0.65 | 0.13 | 758.1E-7 | 0.2139 | 1.5 | 0.0821 | 2.1 | 1249 | 41 |
| JF48-1.2 | 183 | 67 | 0.36 | 0.00 | 100.0E-34 | 0.2041 | 0.8 | 0.0811 | 1.3 | 1223 | 25 |
| JF48-2.1 | 49 | 18 | 0.37 | 0.22 | 131.7E-6 | 0.1993 | 1.3 | 0.0793 | 2.2 | 1179 | 43 |
| JF48-4.1 | 37 | 21 | 0.57 | 0.00 | 100.0E-34 | 0.1962 | 1.7 | 0.0807 | 2.0 | 1214 | 39 |
| JF48-4.2 | 102 | 15 | 0.14 | 0.00 | 100.0E-34 | 0.1887 | 1.0 | 0.0804 | 1.4 | 1206 | 27 |
| JF48-5.1 | 29 | 18 | 0.62 | 0.23 | 140.6E-6 | 0.2209 | 1.7 | 0.0821 | 2.6 | 1248 | 50 |
| JF48-6.2 | 97 | 37 | 0.38 | 0.00 | 100.0E-34 | 0.2039 | 0.9 | 0.0809 | 1.2 | 1220 | 23 |
| JF48-7.1 | 46 | 18 | 0.39 | 0.00 | 100.0E-34 | 0.1989 | 1.3 | 0.0780 | 2.4 | 1146 | 47 |
| JF48-8.1 | 102 | 49 | 0.48 | 0.05 | 292.8E-7 | 0.1993 | 0.9 | 0.0801 | 1.3 | 1200 | 25 |
| JF48-10.1 | 114 | 30 | 0.26 | 0.00 | 100.0E-34 | 0.1837 | 0.9 | 0.0777 | 1.2 | 1138 | 25 |
| JF48-11.1 | 49 | 20 | 0.41 | 0.35 | 208.0E-6 | 0.1929 | 1.3 | 0.0774 | 2.5 | 1131 | 50 |
| JF48-11.2 | 86 | 42 | 0.49 | 0.06 | 333.1E-7 | 0.2045 | 1.0 | 0.0817 | 1.3 | 1239 | 26 |
| JF48-12.1 | 73 | 33 | 0.45 | 0.00 | 100.0E-34 | 0.2116 | 1.1 | 0.0815 | 1.4 | 1235 | 27 |
| JF48-13.1 | 130 | 50 | 0.39 | 0.04 | 270.0E-7 | 0.2079 | 0.8 | 0.0825 | 1.5 | 1258 | 29 |
| JF48-15.1 | 54 | 38 | 0.70 | 0.18 | 106.9E-6 | 0.2097 | 1.4 | 0.0798 | 1.9 | 1191 | 37 |
| | | | | | | | | | | | |
| *Omitted from calculations* | | | | | | | | | | | |
| JF48-3.1 | 62 | 22 | 0.35 | 0.23 | 135.0E-6 | 0.2081 | 1.3 | 0.0800 | 3.1 | 1196 | 61 |
| JF48-3.2 | 31 | 12 | 0.40 | 0.00 | 100.0E-34 | 0.2079 | 1.6 | 0.0842 | 2.4 | 1297 | 47 |
| JF48-5.2 | 134 | 17 | 0.13 | 0.04 | 246.2E-7 | 0.1964 | 0.9 | 0.0773 | 1.2 | 1130 | 25 |
| JF48-6.1 | 74 | 51 | 0.69 | 0.12 | 734.9E-7 | 0.1973 | 1.1 | 0.0763 | 1.8 | 1102 | 35 |
| JF48-9.1 | 76 | 41 | 0.54 | 0.06 | 387.8E-7 | 0.2254 | 1.1 | 0.0805 | 1.4 | 1210 | 28 |
| JF48-9.2 | 114 | 59 | 0.52 | 0.04 | 259.1E-7 | 0.1910 | 0.8 | 0.0792 | 1.3 | 1176 | 26 |
| JF48-14.1 | 339 | 7 | 0.02 | 0.03 | 147.4E-7 | 0.1777 | 0.5 | 0.0745 | 0.7 | 1054 | 15 |
| | | | | | | | | | | | |
| **JF10-71** | | | | | | | | | | | |
| *Mantle* | | | | | | | | | | | |
| JF71-1.1 | 706 | 86 | 0.12 | 0.01 | 421.2E-8 | 0.2313 | 0.3 | 0.0905 | 0.4 | 1436 | 8 |
| JF71-3.1 | 270 | 138 | 0.51 | 0.03 | 196.3E-7 | 0.2361 | 0.5 | 0.0907 | 0.7 | 1440 | 13 |
| JF71-4.1 | 174 | 99 | 0.57 | 0.00 | 100.0E-34 | 0.2455 | 0.7 | 0.0918 | 1.0 | 1462 | 18 |
| JF71-5.2 | 322 | 317 | 0.98 | 0.04 | 229.6E-7 | 0.2356 | 0.5 | 0.0910 | 0.6 | 1446 | 12 |
| JF71-7.1 | 306 | 117 | 0.38 | 0.00 | 100.0E-34 | 0.2497 | 0.5 | 0.0915 | 0.6 | 1457 | 11 |
| JF71-8.1 | 357 | 136 | 0.38 | 0.04 | 244.1E-7 | 0.2551 | 0.5 | 0.0911 | 0.6 | 1449 | 11 |
| JF71-9.1 | 146 | 71 | 0.48 | 0.00 | 100.0E-34 | 0.2387 | 0.7 | 0.0915 | 1.4 | 1457 | 27 |

| Spot # | U (ppm) | Th (ppm) | Th/U | % $^{206}$Pb | $^{204}$Pb/$^{206}$Pb | $^{204}$Pb corrected | | | | $^{207}$Pb/$^{206}$Pb | ±1s |
|---|---|---|---|---|---|---|---|---|---|---|---|
| | | | | | | $^{206}$Pb/$^{238}$U | err (%) | $^{207}$Pb/$^{206}$Pb | err (%) | Age (Ma) | |
| JF71-10.1 | 326 | 100 | 0.31 | 0.02 | 127.2E-7 | 0.2466 | 0.5 | 0.0913 | 0.6 | 1453 | 11 |
| JF71-11.1 | 339 | 27 | 0.08 | 0.00 | 100.0E-34 | 0.2462 | 0.5 | 0.0920 | 0.6 | 1468 | 11 |
| *Omitted from calculation* | | | | | | | | | | | |
| JF71-2.1 | 119 | 109 | 0.92 | 0.04 | 222.3E-7 | 0.2647 | 0.8 | 0.0995 | 0.9 | 1615 | 18 |
| JF71-5.1 | 271 | 385 | 1.42 | 0.07 | 431.7E-7 | 0.2707 | 0.5 | 0.0959 | 0.7 | 1546 | 14 |
| JF71-6.1 | 256 | 34 | 0.13 | 0.10 | 624.1E-7 | 0.2468 | 0.6 | 0.0884 | 0.9 | 1391 | 16 |
| **CA17** | | | | | | | | | | | |
| *Rim* | | | | | | | | | | | |
| CA17-8 | 287 | 12 | 0.04 | 0.13 | 791.0E-7 | 0.2037 | 0.4 | 0.0751 | 0.9 | 1071 | 17 |
| CA17-12 | 175 | 21 | 0.12 | 0.21 | 122.2E-6 | 0.2217 | 0.6 | 0.0758 | 1.2 | 1091 | 24 |
| *Mantle* | | | | | | | | | | | |
| CA17-2 | 150 | 111 | 0.74 | 0.02 | 109.7E-7 | 0.2584 | 0.6 | 0.0934 | 1.0 | 1496 | 18 |
| CA17-4 | 968 | 55 | 0.06 | 0.04 | 233.0E-7 | 0.2347 | 0.3 | 0.0898 | 0.6 | 1421 | 11 |
| CA17-5 | 230 | 214 | 0.93 | 0.02 | 153.2E-7 | 0.2569 | 0.5 | 0.0905 | 0.6 | 1436 | 11 |
| CA17-7 | 105 | 75 | 0.71 | 0.08 | 475.7E-7 | 0.2548 | 0.7 | 0.0917 | 0.9 | 1460 | 17 |
| *Omitted from calculation* | | | | | | | | | | | |
| CA17-1 | 128 | 81 | 0.63 | 0.04 | 266.4E-7 | 0.2413 | 0.6 | 0.0873 | 0.8 | 1366 | 16 |
| CA17-3 | 163 | 104 | 0.63 | 0.03 | 207.0E-7 | 0.2184 | 0.6 | 0.0862 | 0.7 | 1342 | 14 |
| CA17-6 | 143 | 102 | 0.71 | -0.04 | -272.7E-7 | 0.2352 | 0.6 | 0.0886 | 0.8 | 1396 | 15 |
| CA17-9 | 149 | 21 | 0.14 | 0.00 | 100.0E-34 | 0.1964 | 0.6 | 0.0781 | 1.0 | 1149 | 20 |
| CA17-10 | 646 | 2 | 0.00 | 0.25 | 148.7E-6 | 0.1900 | 0.4 | 0.0723 | 1.1 | 995 | 22 |
| CA17-11 | 54 | 40 | 0.74 | 0.25 | 151.7E-6 | 0.2579 | 0.9 | 0.0878 | 1.6 | 1379 | 32 |
| **CA109** | | | | | | | | | | | |
| *Mantle* | | | | | | | | | | | |
| 109-2 | 2447 | 155 | 0.06 | 0.00 | 100.0E-34 | 0.2535 | 0.2 | 0.0913 | 0.3 | 1453 | 6 |
| 109-3 | 2053 | 128 | 0.06 | 0.01 | 403.4E-8 | 0.2489 | 0.2 | 0.0917 | 0.3 | 1460 | 6 |
| 109-5 | 3779 | 61 | 0.02 | 0.00 | 100.0E-34 | 0.2472 | 0.2 | 0.0917 | 0.2 | 1461 | 4 |
| 109-6 | 1953 | 243 | 0.12 | 0.00 | 100.0E-34 | 0.2438 | 0.3 | 0.0914 | 0.3 | 1454 | 5 |
| 109-8 | 3762 | 415 | 0.11 | 0.04 | 268.2E-7 | 0.2316 | 0.2 | 0.0911 | 0.2 | 1448 | 4 |
| 109-9 | 2510 | 270 | 0.11 | 0.04 | 218.5E-7 | 0.2404 | 0.2 | 0.0910 | 0.2 | 1447 | 5 |
| 109-10 | 511 | 68 | 0.13 | 0.05 | 325.6E-7 | 0.2336 | 0.4 | 0.0910 | 0.7 | 1446 | 13 |
| *Omitted from calculation* | | | | | | | | | | | |
| 109-1 | 759 | 31 | 0.04 | 0.06 | 396.7E-7 | 0.2246 | 0.3 | 0.0884 | 0.7 | 1392 | 14 |
| 109-4 | 185 | 143 | 0.78 | 0.00 | 100.0E-34 | 0.2741 | 0.7 | 0.1013 | 0.7 | 1648 | 14 |
| 109-7 | 97 | 46 | 0.47 | 0.05 | 327.5E-7 | 0.2483 | 1.0 | 0.0972 | 1.2 | 1572 | 22 |

# Section 3: Zircon Trace Element Data

Table A.2: Table of Zircon Trace-Element Analytical Data

| Sample | Y | La | Ce | Nd | Sm | Eu | Gd | Dy | Er | Yb | Hf | Ce/Ce* | Eu/Eu* |
|---|---|---|---|---|---|---|---|---|---|---|---|---|---|
| **JF10-16** | | | | | | | | | | | | | |
| *Mantle* | | | | | | | | | | | | | |
| JF16-3.1 | 2100.01 | 0.03 | 15.04 | 0.19 | 0.87 | 0.35 | 12.53 | 141.35 | 454.99 | 1190.97 | 13844.62 | 141 | 0.32 |
| JF16-4.1 | 1384.26 | 0.29 | 19.52 | 0.51 | 0.97 | 0.25 | 12.00 | 100.34 | 299.22 | 766.04 | 12501.29 | 27 | 0.22 |
| JF16-4.2 | 2480.87 | 12.14 | 32.74 | 14.88 | 9.28 | 2.32 | 37.61 | 164.50 | 357.79 | 691.00 | 13514.15 | 1 | 0.38 |
| JF16-9.2 | 1640.33 | 0.26 | 11.63 | 0.64 | 1.02 | 0.42 | 11.29 | 123.12 | 328.90 | 686.09 | 14185.88 | 16 | 0.37 |
| JF16-10.1 | 1065.14 | 8.79 | 29.25 | 4.71 | 0.35 | 0.92 | 16.42 | 77.19 | 215.71 | 621.53 | 9516.46 | 2 | 1.17 |
| JF16-10.2 | 1156.29 | 21.24 | 84.70 | 38.70 | 25.21 | 5.70 | 84.36 | 157.20 | 183.95 | 338.60 | 8782.80 | 2 | 0.38 |
| JF16-11.1 | 1023.52 | 4.33 | 36.82 | 15.07 | 7.13 | 1.87 | 23.42 | 86.16 | 209.96 | 517.84 | 12287.61 | 3 | 0.44 |
| *Core* | | | | | | | | | | | | | |
| JF16-1.2 | 2961.22 | 0.23 | 80.21 | 9.07 | 16.24 | 6.03 | 114.83 | 319.70 | 489.58 | 779.18 | 7761.79 | 50 | 0.42 |
| JF16-3.2 | 1614.92 | 0.37 | 45.36 | 3.37 | 5.93 | 1.84 | 44.29 | 166.56 | 297.75 | 526.79 | 9370.22 | 28 | 0.35 |
| JF16-5.2 | 1129.94 | 0.03 | 39.31 | 2.32 | 4.54 | 1.47 | 31.89 | 112.41 | 207.30 | 373.54 | 9084.29 | 136 | 0.37 |
| JF16-7.1 | 1028.23 | 0.13 | 41.08 | 1.57 | 3.00 | 0.96 | 23.85 | 94.39 | 188.05 | 363.48 | 8883.69 | 67 | 0.34 |
| JF16-9.1 | 1270.27 | 0.04 | 14.60 | 1.88 | 3.65 | 1.20 | 31.87 | 128.53 | 236.63 | 423.26 | 8613.24 | 46 | 0.34 |
| | | | | | | | | | | | | | |
| *Omitted* | | | | | | | | | | | | | |
| JF16-1.1 | 1227.99 | 2.80 | 23.11 | 6.28 | 4.15 | 1.48 | 17.02 | 90.70 | 260.91 | 747.79 | #REF! | #REF! | #REF! |
| JF16-2.1 | 1453.50 | 1.21 | 46.43 | 2.23 | 2.97 | 0.93 | 22.74 | 121.09 | 279.78 | 609.19 | #REF! | #REF! | #REF! |
| JF16-5.1 | 1086.50 | 1.95 | 20.62 | 1.68 | 1.42 | 0.37 | 10.46 | 75.85 | 226.86 | 594.67 | #REF! | #REF! | #REF! |
| JF16-6.1 | 1500.52 | 5.33 | 26.18 | 5.10 | 3.96 | 1.02 | 25.70 | 124.82 | 284.58 | 566.29 | #REF! | #REF! | #REF! |
| JF16-7.2 | 5311.78 | 17.58 | 205.08 | 81.63 | 63.17 | 25.54 | 283.14 | 663.28 | 809.04 | 1922.56 | #REF! | #REF! | #REF! |
| JF16-8.1 | 1151.42 | 5.85 | 52.77 | 11.02 | 8.71 | 1.97 | 37.68 | 118.12 | 211.17 | 448.07 | #REF! | #REF! | #REF! |
| JF16-11.2 | 1292.86 | 2.20 | 21.33 | 9.07 | 7.94 | 2.03 | 42.49 | 133.07 | 228.69 | 382.73 | #REF! | #REF! | #REF! |
| | | | | | | | | | | | | | |
| **JF10-17** | | | | | | | | | | | | | |
| *Mantle* | | | | | | | | | | | | | |
| JF17-1.1 | 592.49 | 0.23 | 34.85 | 0.41 | 1.04 | 0.21 | 9.88 | 47.14 | 114.29 | 262.11 | 11308.49 | 60 | 0.20 |
| JF17-2.1 | 910.63 | 0.02 | 53.06 | 0.46 | 1.53 | 0.29 | 15.24 | 75.51 | 173.37 | 400.00 | 12655.76 | 399 | 0.18 |
| JF17-3.1 | 765.57 | 0.03 | 45.54 | 0.38 | 1.31 | 0.21 | 12.34 | 64.57 | 147.99 | 337.48 | 12160.17 | 356 | 0.16 |
| JF17-4.1 | 979.01 | 0.02 | 56.12 | 0.46 | 1.64 | 0.30 | 15.50 | 82.89 | 188.21 | 438.17 | 13258.61 | 446 | 0.18 |
| JF17-6.1 | 909.83 | 0.01 | 51.58 | 0.33 | 1.25 | 0.23 | 14.46 | 75.54 | 177.64 | 406.70 | 13108.66 | 723 | 0.16 |
| JF17-9.1 | 852.62 | 1.66 | 56.62 | 4.04 | 3.72 | 0.70 | 18.94 | 74.00 | 159.01 | 367.23 | 11882.65 | 12 | 0.25 |
| *Core* | | | | | | | | | | | | | |
| JF17-4.2 | 1229.00 | 0.06 | 57.92 | 2.66 | 4.43 | 1.73 | 32.42 | 116.38 | 225.03 | 443.69 | 8110.10 | 136 | 0.44 |
| JF17-7.1 | 3076.21 | 1.44 | 319.39 | 7.40 | 14.07 | 6.55 | 109.47 | 339.54 | 534.55 | 864.68 | 8344.57 | 62 | 0.51 |
| JF17-8.1 | 3383.90 | 0.08 | 125.93 | 8.21 | 14.29 | 7.07 | 101.75 | 352.44 | 611.57 | 1057.48 | 9260.91 | 160 | 0.56 |
| | | | | | | | | | | | | | |
| *Omitted* | | | | | | | | | | | | | |
| JF17-5.1 | 1351.43 | 0.03 | 65.19 | 0.43 | 1.73 | 0.25 | 18.52 | 104.80 | 266.43 | 697.63 | 18165.86 | 437 | 0.13 |
| JF17-6.2 | 1703.97 | 0.18 | 47.72 | 5.51 | 7.95 | 3.20 | 56.03 | 179.85 | 303.32 | 508.68 | 7910.31 | 41 | 0.46 |
| JF17-10.1 | 2509.35 | 1.07 | 78.90 | 6.51 | 10.32 | 1.02 | 72.19 | 256.56 | 446.82 | 777.64 | 10504.93 | 20 | 0.11 |
| | | | | | | | | | | | | | |
| **JF10-30** | | | | | | | | | | | | | |
| *Rim* | | | | | | | | | | | | | |
| JF30-10.1 | 25.14 | 1.09 | 4.69 | 0.35 | 0.28 | 0.25 | 1.61 | 3.26 | 3.35 | 5.05 | 9390.84 | 3 | 1.11 |
| JF30-10.2 | 42.35 | 1.71 | 6.39 | 0.57 | 0.36 | 0.24 | 1.75 | 3.82 | 6.20 | 13.07 | 7476.14 | 3 | 0.93 |
| JF30-11.1 | 89.10 | 1.89 | 7.92 | 0.51 | 0.36 | 0.28 | 2.80 | 8.43 | 11.62 | 18.19 | 7453.88 | 3 | 0.83 |
| JF30-14.1 | 50.70 | 0.73 | 5.95 | 1.13 | 0.81 | 0.54 | 3.02 | 5.94 | 7.14 | 11.87 | 9347.15 | 3 | 1.06 |
| *Mantle* | | | | | | | | | | | | | |
| JF30-4.1 | 1061.98 | 0.10 | 15.34 | 0.37 | 0.79 | 0.19 | 8.67 | 75.88 | 229.90 | 562.92 | 12201.19 | 47 | 0.22 |
| JF30-5.1 | 462.82 | 0.02 | 32.93 | 0.28 | 0.82 | 0.21 | 7.96 | 36.99 | 87.19 | 209.04 | 12462.36 | 381 | 0.25 |
| JF30-8.1 | 690.36 | 0.03 | 53.71 | 0.68 | 1.39 | 0.36 | 13.55 | 57.66 | 120.24 | 268.76 | 11982.49 | 312 | 0.25 |
| JF30-10.3 | 634.76 | 0.40 | 49.51 | 0.80 | 1.52 | 0.41 | 12.38 | 56.89 | 117.17 | 260.71 | 10409.20 | 48 | 0.29 |
| JF30-12.1 | 643.47 | 0.04 | 40.68 | 0.54 | 1.29 | 0.31 | 10.97 | 53.35 | 120.85 | 281.93 | 11465.25 | 212 | 0.25 |
| JF30-13.2 | 711.06 | 0.84 | 54.54 | 1.15 | 1.87 | 0.48 | 15.31 | 63.21 | 130.62 | 286.22 | 10970.36 | 28 | 0.27 |
| JF30-15.1 | 676.84 | 0.16 | 48.92 | 0.61 | 1.55 | 0.40 | 12.91 | 57.56 | 124.50 | 280.00 | 11300.98 | 96 | 0.27 |

| Sample | Y | La | Ce | Nd | Sm | Eu | Gd | Dy | Er | Yb | Hf | Ce/Ce* | Eu/Eu* |
|---|---|---|---|---|---|---|---|---|---|---|---|---|---|
| *Core* | | | | | | | | | | | | | |
| JF30-6.1 | 1120.38 | 17.23 | 89.87 | 46.45 | 34.25 | 6.46 | 102.88 | 134.86 | 189.05 | 358.79 | 9884.35 | 2 | 0.33 |
| JF30-7.2 | 2523.84 | 1.55 | 34.30 | 5.42 | 8.58 | 1.61 | 64.93 | 253.20 | 454.68 | 773.33 | 7424.38 | 7 | 0.21 |
| JF30-9.1 | 638.45 | 0.03 | 31.03 | 0.56 | 1.28 | 0.41 | 11.27 | 52.94 | 120.29 | 273.88 | 10501.36 | 189 | 0.33 |
| | | | | | | | | | | | | | |
| *Omitted* | | | | | | | | | | | | | |
| JF30-1.1 | 901.60 | 1.55 | 18.95 | 5.94 | 4.47 | 1.45 | 17.30 | 74.90 | 191.45 | 574.70 | 13099.09 | 4 | 0.50 |
| JF30-2.1 | 287.97 | 204.60 | 561.70 | 82.52 | 2.11 | 2.99 | 22.64 | 25.26 | 52.56 | 126.87 | 9673.61 | 2 | 1.32 |
| JF30-3.1 | 297.98 | 0.02 | 20.99 | 0.24 | 0.61 | 0.28 | 5.58 | 26.46 | 58.59 | 138.71 | 12017.44 | 243 | 0.46 |
| JF30-4.2 | 455.38 | 0.02 | 11.54 | 0.14 | 0.53 | 0.22 | 8.28 | 41.92 | 82.21 | 158.06 | 14369.54 | 161 | 0.32 |
| JF30-7.1 | 184.17 | 0.03 | 6.76 | 0.06 | 0.23 | 0.19 | 2.76 | 16.15 | 34.11 | 73.81 | 12176.36 | 82 | 0.74 |
| JF30-13.1 | 71.95 | 7.21 | 16.76 | 2.21 | 0.19 | 0.57 | 3.40 | 7.16 | 10.01 | 15.93 | 9580.53 | 2 | 2.17 |
| JF30-16.1 | 442.14 | 0.08 | 19.29 | 0.21 | 0.72 | 0.14 | 6.81 | 35.96 | 89.93 | 237.06 | 12377.20 | 85 | 0.20 |
| JF30-16.2 | 914.84 | 0.06 | 44.16 | 1.14 | 2.53 | 0.81 | 21.25 | 85.02 | 167.77 | 329.73 | 9498.99 | 139 | 0.34 |
| | | | | | | | | | | | | | |
| **JF10-48** | | | | | | | | | | | | | |
| JF48-1.1 | 976.16 | 0.05 | 6.90 | 2.89 | 5.35 | 0.67 | 36.35 | 116.76 | 170.81 | 262.28 | 8169.50 | 18 | 0.15 |
| JF48-1.2 | 586.75 | 0.03 | 18.25 | 0.53 | 1.49 | 0.14 | 12.92 | 57.04 | 108.59 | 190.71 | 10554.82 | 104 | 0.10 |
| JF48-2.1 | 437.72 | 0.03 | 8.78 | 0.55 | 1.29 | 0.11 | 11.83 | 45.76 | 82.03 | 140.15 | 8994.30 | 55 | 0.08 |
| JF48-4.1 | 1015.83 | 0.09 | 7.31 | 4.24 | 6.78 | 1.36 | 42.98 | 122.26 | 172.69 | 264.16 | 7397.00 | 11 | 0.24 |
| JF48-4.2 | 369.62 | 0.01 | 8.33 | 0.51 | 1.26 | 0.18 | 9.68 | 40.98 | 69.42 | 116.93 | 10253.03 | 85 | 0.16 |
| JF48-5.1 | 937.51 | 0.05 | 6.04 | 3.03 | 5.34 | 0.74 | 37.28 | 112.64 | 163.39 | 247.88 | 8273.29 | 16 | 0.16 |
| JF48-5.2 | 317.75 | 0.09 | 8.73 | 0.33 | 0.97 | 0.16 | 9.19 | 33.80 | 56.54 | 97.31 | 9692.13 | 30 | 0.17 |
| JF48-6.1 | 709.99 | 0.03 | 13.47 | 2.19 | 3.42 | 0.55 | 24.12 | 77.30 | 119.75 | 191.26 | 8827.97 | 51 | 0.18 |
| JF48-6.2 | 573.10 | 0.01 | 15.37 | 0.74 | 1.62 | 0.12 | 13.49 | 59.10 | 105.16 | 178.71 | 10054.49 | 187 | 0.08 |
| JF48-7.1 | 341.03 | 0.02 | 8.27 | 0.45 | 1.06 | 0.09 | 8.71 | 35.59 | 64.06 | 113.21 | 8940.68 | 66 | 0.09 |
| JF48-8.1 | 619.09 | 0.02 | 18.21 | 0.69 | 1.73 | 0.12 | 15.15 | 63.99 | 114.41 | 189.56 | 9519.92 | 122 | 0.07 |
| JF48-10.1 | 426.00 | 0.02 | 9.98 | 0.56 | 1.17 | 0.15 | 10.50 | 44.26 | 77.67 | 134.21 | 9423.53 | 74 | 0.13 |
| JF48-11.1 | 361.96 | 0.08 | 10.29 | 0.88 | 1.23 | 0.11 | 9.73 | 38.14 | 65.86 | 116.64 | 8651.03 | 28 | 0.10 |
| JF48-11.2 | 373.57 | 0.09 | 12.54 | 0.58 | 1.05 | 0.07 | 8.68 | 38.35 | 70.81 | 125.84 | 9728.94 | 35 | 0.07 |
| JF48-12.1 | 497.30 | 0.05 | 13.03 | 0.58 | 1.38 | 0.09 | 12.97 | 52.30 | 92.08 | 157.46 | 9304.53 | 58 | 0.07 |
| JF48-13.1 | 583.79 | 0.04 | 16.74 | 0.67 | 1.63 | 0.11 | 14.13 | 57.32 | 106.23 | 181.27 | 10776.83 | 78 | 0.07 |
| JF48-14.1 | 307.73 | 0.01 | 4.74 | 0.31 | 1.16 | 0.44 | 11.61 | 38.85 | 47.60 | 67.82 | 10416.13 | 57 | 0.36 |
| JF48-15.1 | 2091.37 | 0.20 | 7.64 | 8.26 | 14.16 | 2.10 | 93.14 | 263.44 | 362.09 | 520.00 | 7486.40 | 5 | 0.18 |
| | | | | | | | | | | | | | |
| *Omitted* | | | | | | | | | | | | | |
| JF48-3.1 | 324.11 | 0.03 | 9.96 | 0.34 | 0.92 | 0.08 | 7.92 | 32.22 | 60.24 | 108.09 | 9643.12 | 80 | 0.09 |
| JF48-3.2 | 314.16 | 0.02 | 6.40 | 0.44 | 1.03 | 0.08 | 8.16 | 33.32 | 60.03 | 105.47 | 7959.38 | 50 | 0.09 |
| JF48-9.1 | 609.52 | 0.02 | 15.25 | 0.80 | 1.98 | 0.11 | 15.88 | 63.19 | 114.68 | 192.37 | 9900.29 | 103 | 0.06 |
| JF48-9.2 | 1709.64 | 0.09 | 15.55 | 5.58 | 9.96 | 1.04 | 67.93 | 204.17 | 290.06 | 418.11 | 7869.21 | 21 | 0.12 |
| | | | | | | | | | | | | | |
| **JF10-71** | | | | | | | | | | | | | |
| *Mantle* | | | | | | | | | | | | | |
| JF71-1.1 | 503.75 | 1.71 | 13.56 | 1.37 | 0.83 | 0.28 | 6.48 | 36.90 | 96.68 | 259.19 | 11949.81 | 4 | 0.37 |
| JF71-3.1 | 301.88 | 0.44 | 35.48 | 0.58 | 0.61 | 0.27 | 4.39 | 22.69 | 56.93 | 165.36 | 10277.60 | 35 | 0.49 |
| JF71-4.1 | 714.15 | 0.01 | 45.19 | 0.46 | 1.31 | 0.18 | 11.73 | 58.19 | 132.87 | 302.12 | 12594.96 | 546 | 0.14 |
| JF71-5.2 | 401.70 | 0.12 | 32.53 | 0.43 | 0.93 | 0.36 | 7.65 | 30.62 | 71.80 | 186.78 | 9790.16 | 84 | 0.41 |
| JF71-7.1 | 216.32 | 0.20 | 22.76 | 0.22 | 0.37 | 0.16 | 3.15 | 16.57 | 41.32 | 118.98 | 10414.35 | 53 | 0.45 |
| JF71-8.1 | 392.91 | 4.69 | 39.69 | 8.28 | 4.25 | 1.16 | 13.69 | 33.36 | 70.32 | 173.95 | 11525.67 | 3 | 0.46 |
| JF71-9.1 | 457.56 | 0.02 | 29.10 | 0.30 | 0.74 | 0.13 | 6.44 | 36.60 | 88.34 | 214.58 | 11898.25 | 312 | 0.19 |
| JF71-10.1 | 878.17 | 0.02 | 46.86 | 0.35 | 1.31 | 0.25 | 12.60 | 70.01 | 168.28 | 424.09 | 13170.90 | 384 | 0.18 |
| JF71-11.1 | 260.99 | 0.01 | 5.43 | 0.05 | 0.19 | 0.11 | 2.92 | 17.68 | 52.09 | 147.05 | 13130.23 | 188 | 0.47 |
| | | | | | | | | | | | | | |
| *Omitted* | | | | | | | | | | | | | |
| JF71-2.1 | 922.39 | 0.04 | 69.24 | 1.32 | 2.81 | 1.13 | 23.80 | 91.14 | 168.15 | 302.43 | 9438.06 | 247 | 0.42 |
| JF71-5.1 | 1435.16 | 0.07 | 52.84 | 1.42 | 2.51 | 1.77 | 27.89 | 122.54 | 251.51 | 524.17 | 7531.26 | 137 | 0.64 |
| JF71-6.1 | 230.63 | 4.01 | 15.87 | 1.35 | 0.13 | 0.27 | 3.99 | 17.30 | 43.30 | 111.05 | 10194.30 | 3 | 1.12 |

# APPENDIX B

# MONAZITE ANALYTICAL DATA

Appendix B presents major- and trace-element electron microprobe data of monzaites analysed in this study.

Table B.1: Monazite major-element data

| No. | Comment | SiO2 | P2O5 | SO3 | CaO | Y2O3 | La2O3 | Ce2O3 | Pr2O3 | Nd2O3 | Sm2O3 | Eu2O3 | Gd2O3 | Dy2O3 | ThO2 | UO2 | Total |
|---|---|---|---|---|---|---|---|---|---|---|---|---|---|---|---|---|---|
| PSD08 - 101a Ksp-Qtz Ribbon Grain | | | | | | | | | | | | | | | | | |
| 69 | 101a_MZ8_1_1 | 0.142 | 28.437 | 1.244 | 1.629 | 0.752 | 12.731 | 27.078 | 2.771 | 13.025 | 2.313 | 0.977 | 1.408 | 0.387 | 2.346 | 0.464 | 95.704 |
| 70 | 101a_MZ8_1_2 | 0.168 | 29.094 | 1.188 | 1.629 | 0.635 | 12.731 | 27.498 | 2.82 | 13.446 | 2.253 | 0.995 | 1.378 | 0.248 | 2.154 | 0.349 | 96.586 |
| 71 | 101a_MZ8_1_3 | 0.165 | 28.93 | 1.146 | 1.686 | 0.843 | 12.822 | 26.923 | 2.898 | 13.256 | 2.378 | 1.11 | 1.487 | 0.243 | 2.149 | 0.387 | 96.423 |
| 72 | 101a_MZ8_2_4 | 0.125 | 29.318 | 0.584 | 1.124 | 1.794 | 12.334 | 26.036 | 2.829 | 12.835 | 2.475 | 1.089 | 1.965 | 0.629 | 2.147 | 0.505 | 95.789 |
| 73 | 101a_MZ8_2_5 | 0.115 | 29.673 | 0.518 | 0.99 | 2.039 | 12.368 | 26.801 | 2.933 | 13.329 | 2.473 | 0.961 | 2.126 | 0.813 | 2.244 | 0.428 | 97.811 |
| 74 | 101a_MZ8_2_6 | 0.162 | 29.574 | 0.449 | 0.964 | 2.12 | 11.883 | 26.23 | 2.732 | 13.351 | 2.582 | 1.003 | 1.88 | 0.678 | 2.348 | 0.377 | 96.333 |
| 75 | 101a_MZ8_2_7 | 0.160 | 29.695 | 0.51 | 1.012 | 2.243 | 12.086 | 25.639 | 2.874 | 13.218 | 2.592 | 1.15 | 2.226 | 0.856 | 2.293 | 0.365 | 96.919 |
| 76 | 101a_MZ8_3_8 | 0.163 | 29.357 | 0.727 | 1.14 | 1.66 | 12.713 | 26.878 | 2.789 | 13.084 | 2.486 | 1.12 | 1.904 | 0.581 | 1.998 | 0.36 | 96.96 |
| 77 | 101a_MZ8_3_9 | 0.119 | 29.491 | 0.84 | 1.249 | 1.62 | 12.626 | 26.723 | 2.846 | 13.085 | 2.437 | 1.158 | 1.867 | 0.5 | 2.128 | 0.419 | 97.108 |
| 78 | 101a_MZ8_3_10 | 0.135 | 29.238 | 0.818 | 1.247 | 1.583 | 12.627 | 26.659 | 2.823 | 13.331 | 2.487 | 1.122 | 1.897 | 0.56 | 1.96 | 0.423 | 96.91 |
| PSD08 - 101a Matrix Grain | | | | | | | | | | | | | | | | | |
| 79 | 101a_MZ19_1_1 | 0.137 | 29.029 | 0.96 | 1.414 | 0.836 | 12.533 | 27.193 | 2.813 | 13.629 | 2.507 | 1.077 | 1.672 | 0.305 | 2.073 | 0.46 | 96.638 |
| 80 | 101a_MZ19_1_2 | 0.152 | 29.001 | 0.92 | 1.437 | 0.894 | 12.614 | 28.32 | 2.898 | 14.225 | 2.464 | 1.17 | 1.612 | 0.367 | 2.157 | 0.572 | 98.803 |
| 81 | 101a_MZ19_1_3 | 0.183 | 28.893 | 1.013 | 1.488 | 0.842 | 12.705 | 27.234 | 2.955 | 13.069 | 2.415 | 1.095 | 1.404 | 0.147 | 2.009 | 0.497 | 95.949 |
| 82 | 101a_MZ19_2_4 | 0.220 | 29.436 | 0.477 | 0.88 | 1.603 | 11.829 | 26.359 | 2.784 | 13.731 | 2.746 | 1.189 | 2.337 | 0.628 | 1.639 | 0.637 | 96.495 |
| 83 | 101a_MZ19_2_5 | 0.147 | 29.258 | 0.465 | 0.928 | 1.833 | 11.933 | 25.956 | 2.799 | 13.384 | 2.773 | 1.18 | 2.457 | 0.677 | 1.742 | 0.639 | 96.171 |
| 84 | 101a_MZ19_2_6 | 0.120 | 29.152 | 0.458 | 0.9 | 1.477 | 12.34 | 26.489 | 2.788 | 13.713 | 2.747 | 1.131 | 1.917 | 0.539 | 1.5 | 0.638 | 95.909 |
| 85 | 101a_MZ19_3_7 | 0.243 | 29.329 | 0.625 | 0.994 | 2.86 | 12.037 | 25.28 | 2.796 | 12.733 | 2.92 | 1.289 | 2.373 | 0.94 | 1.197 | 0.44 | 96.056 |
| CA108b Large Grain | | | | | | | | | | | | | | | | | |
| 45 | CA108b1_MZ14_7 | 0.185 | 29.503 | 0.02 | 0.734 | 0.668 | 13.979 | 28.14 | 2.915 | 13.003 | 2.222 | 1.004 | 1.438 | 0.417 | 3.045 | 0.179 | 97.452 |
| 47 | CA108b1_MZ14_9 | 0.198 | 29.421 | - | 0.735 | 0.72 | 13.656 | 28.327 | 2.928 | 12.95 | 2.241 | 0.895 | 1.342 | 0.248 | 2.999 | 0.079 | 96.739 |
| 46 | CA108b1_MZ14_8 | 0.201 | 29.561 | 0.02 | 0.769 | 0.786 | 14.088 | 28.826 | 2.89 | 12.686 | 1.947 | 0.903 | 1.305 | 0.337 | 3.046 | 0.173 | 97.538 |
| 40 | CA108b1_MZ14_2 | 0.499 | 28.154 | 0.052 | 0.597 | 0.212 | 13.035 | 28.595 | 3.016 | 14.134 | 2.173 | 0.844 | 1.201 | 0.133 | 3.649 | 0.095 | 96.389 |
| 41 | CA108b1_MZ14_3 | 0.527 | 28.778 | 0.013 | 0.655 | 0.187 | 12.79 | 28.585 | 2.952 | 13.95 | 2.322 | 0.881 | 1.145 | 0.128 | 3.933 | 0.166 | 97.012 |
| 39 | CA108b1_MZ14_1 | 0.542 | 28.049 | - | 0.556 | 0.215 | 13.188 | 28.685 | 3.168 | 13.962 | 2.283 | 0.728 | 0.988 | 0.139 | 4.093 | 0.159 | 96.755 |
| 49 | CA108b1_MZ14_11 | 0.533 | 29.294 | 0.052 | 0.625 | 0.526 | 14.539 | 27.813 | 2.846 | 12.792 | 2.249 | 0.878 | 1.395 | 0.21 | 3.814 | 0.092 | 97.658 |
| 44 | CA108b1_MZ14_6 | 0.424 | 29.393 | 0.001 | 0.57 | 0.213 | 14.29 | 29.013 | 2.965 | 13.396 | 2.026 | 0.841 | 1.142 | 0.151 | 3.172 | 0.131 | 97.728 |
| 42 | CA108b1_MZ14_4 | 0.448 | 28.981 | 0.038 | 0.575 | 0.106 | 14.018 | 29.602 | 2.936 | 13.67 | 2.019 | 0.893 | 1.18 | 0.18 | 3.171 | 0.134 | 97.951 |
| 43 | CA108b1_MZ14_5 | 0.458 | 28.635 | 0.012 | 0.571 | 0.176 | 13.601 | 29.154 | 3.235 | 13.523 | 2.146 | 0.83 | 1.17 | 0.2 | 3.493 | 0.05 | 97.254 |
| 54 | CA108b1_MZ14_16 | 0.253 | 29.694 | 0.021 | 0.915 | 0.808 | 13.092 | 27.758 | 2.996 | 13.395 | 2.404 | 0.967 | 1.681 | 0.404 | 4.062 | 0.304 | 98.754 |
| 55 | CA108b1_MZ14_17 | 0.282 | 29.221 | - | 0.884 | 0.701 | 12.906 | 28.152 | 2.944 | 12.912 | 2.35 | 0.898 | 1.485 | 0.347 | 4.156 | 0.154 | 97.392 |
| 56 | CA108b1_MZ14_18 | 0.244 | 29.256 | 0.011 | 0.905 | 0.846 | 13.001 | 26.866 | 2.968 | 13.275 | 2.321 | 0.821 | 1.567 | 0.372 | 4.135 | 0.214 | 96.802 |
| CA108b Small Grain | | | | | | | | | | | | | | | | | |
| 57 | CA108b1_MZ21_1 | 0.872 | 28.199 | - | 0.56 | 0.02 | 12.179 | 28.22 | 2.94 | 14.025 | 2.12 | 0.821 | 0.703 | 0.056 | 5.156 | 0.03 | 95.901 |
| 58 | CA108b1_MZ21_2 | 0.888 | 28.153 | - | 0.57 | 0.005 | 12.702 | 28.6 | 3.062 | 14.217 | 2.071 | 0.944 | 0.948 | 0.041 | 5.129 | 0.233 | 97.563 |
| 59 | CA108b1_MZ21_3 | 0.851 | 28.072 | - | 0.555 | 0.106 | 12.577 | 28.417 | 2.915 | 14.255 | 2.011 | 0.931 | 0.878 | 0.081 | 5.127 | 0.083 | 96.859 |
| 60 | CA108b1_MZ21_4 | 1.057 | 27.502 | 0.017 | 0.549 | 0.112 | 12.806 | 28.437 | 3.038 | 13.697 | 1.909 | 0.876 | 0.893 | 0.121 | 6.022 | 0.225 | 97.261 |
| 61 | CA108b1_MZ21_5 | 1.078 | 27.671 | - | 0.585 | 0.062 | 12.496 | 28.197 | 3.07 | 13.755 | 1.958 | 0.874 | 0.914 | 0.12 | 5.96 | 0.237 | 96.977 |
| 62 | CA108b1_MZ21_6 | 1.001 | 27.839 | 0.029 | 0.617 | 0.083 | 12.674 | 27.918 | 3.302 | 14.162 | 2.012 | 0.874 | 0.901 | 0.101 | 5.955 | 0.16 | 97.628 |
| 64 | CA108b1_MZ21_8 | 0.425 | 28.411 | 0.056 | 0.665 | 0.345 | 15.252 | 28.117 | 2.653 | 11.943 | 2.083 | 0.971 | 1.262 | 0.108 | 3.842 | 0.136 | 96.269 |

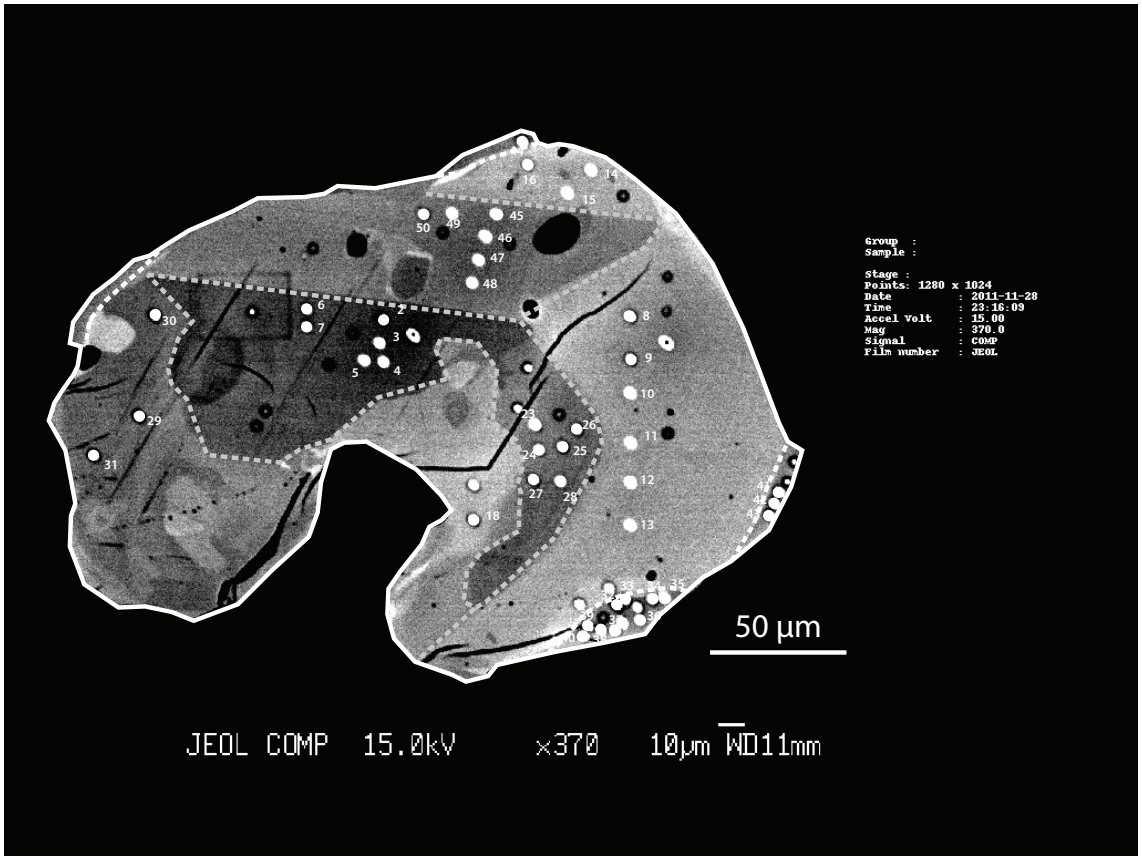


Figure B.1: CA108b large matrix monazite grain trace-element analyses locations.

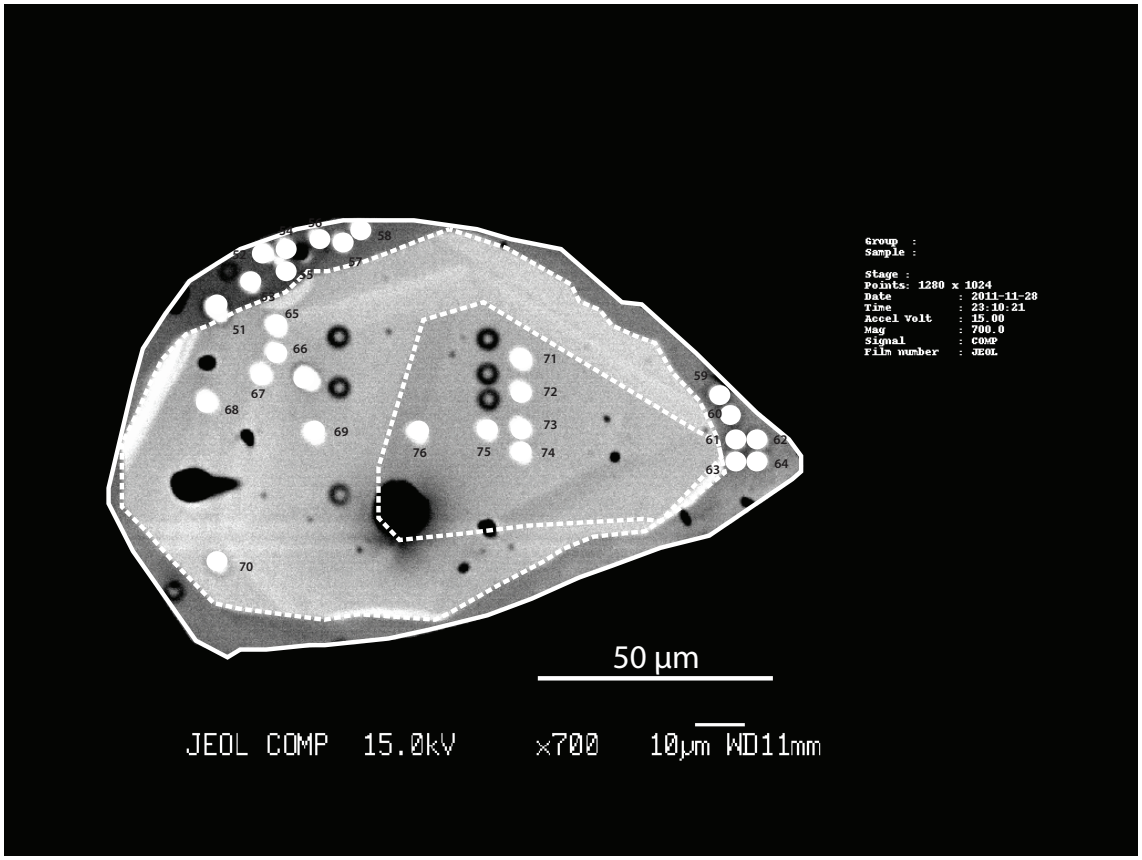


Figure B.2: CA108b small matrix monazite grain trace-element analyses locations.

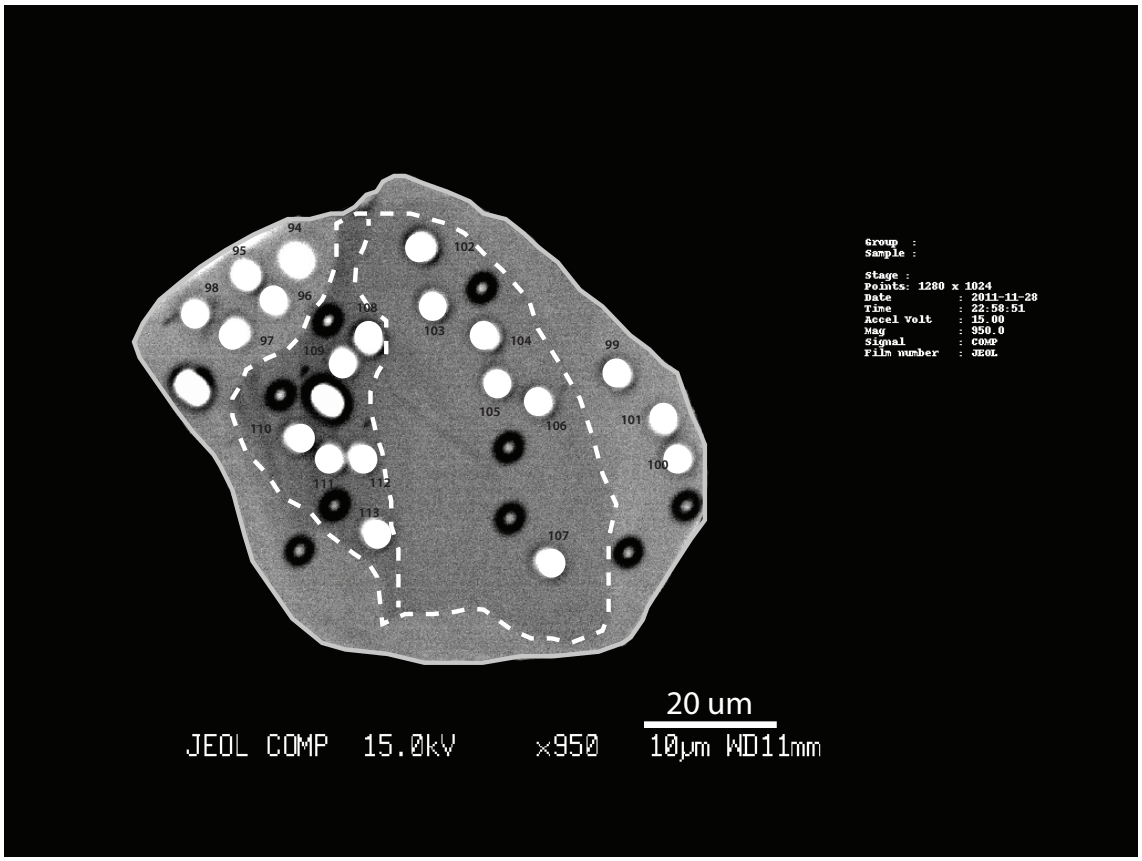


Figure B.3: PS08-101a K-feldspar-quartz ribbon monazite grain trace-element analyses locations.

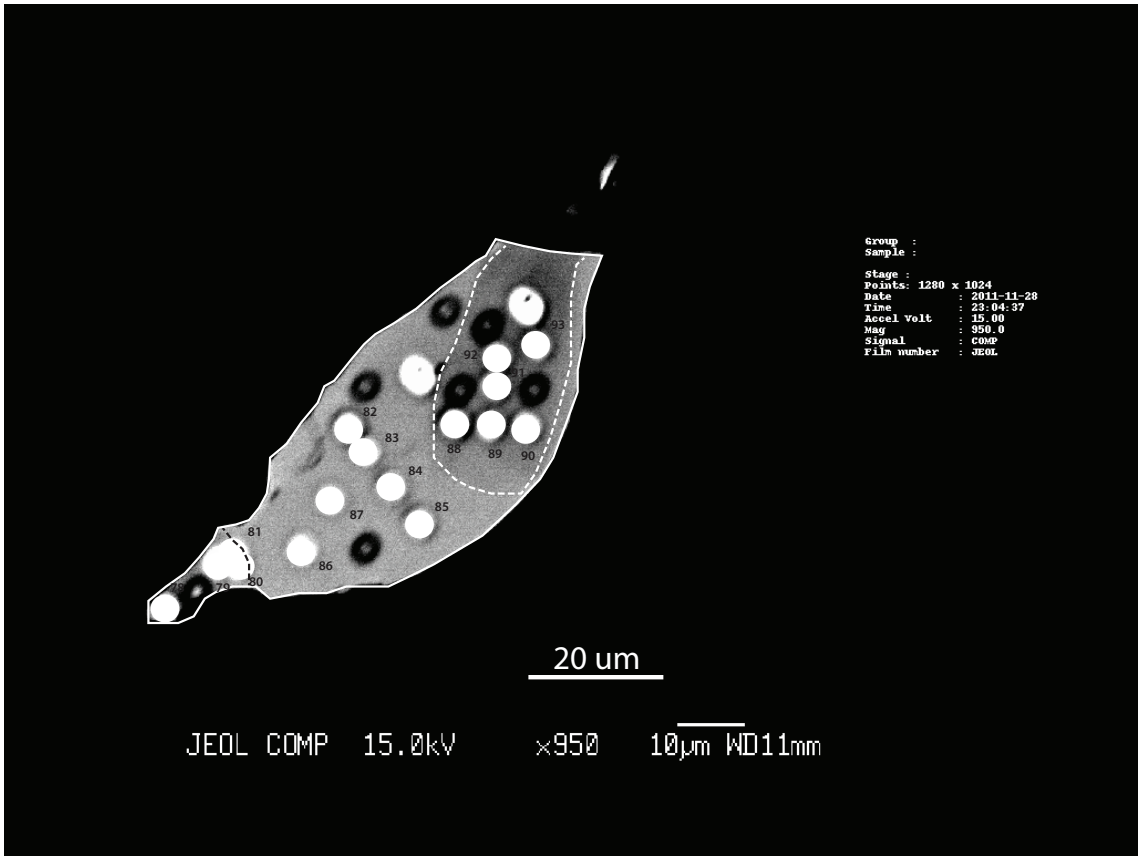


Figure B.4: PS08-101a matrix monazite grain trace-element analyses locations.

Table B.2: Monazite trace-element data and analytical results

| | | Analysis (Wt% Oxide) | | | | Analysis (ppm) | | | | | | |
|---|---|---|---|---|---|---|---|---|---|---|---|---|
| **No.** | **Grain/zone** | **Th** | **U** | **Y** | **Pb** | **Th** | **U** | **Y** | **Pb** | **Age (Ma)** | **± 2σ (Ma)** | **SD 2σ (%)** |
| **CA108b large monazite** | | | | | | | | | | | | |
| *Core* | | | | | | | | | | | | |
| 2 | 108bMz14_1_1 | 2.698 | 0.125 | 0.614 | 0.215 | 26980 | 1250 | 6140 | 2150 | 1486 | 53 | 4 |
| 3 | 108bMz14_1_2 | 2.735 | 0.104 | 0.573 | 0.214 | 27350 | 1040 | 5730 | 2140 | 1496 | 61 | 4 |
| 4 | 108bMz14_1_3 | 2.869 | 0.097 | 0.591 | 0.222 | 28690 | 970 | 5910 | 2220 | 1500 | 64 | 4 |
| 5 | 108bMz14_1_4 | 2.854 | 0.104 | 0.589 | 0.221 | 28540 | 1040 | 5890 | 2210 | 1489 | 60 | 4 |
| 6 | 108bMz14_1_5 | 2.738 | 0.126 | 0.617 | 0.215 | 27380 | 1260 | 6170 | 2150 | 1467 | 52 | 4 |
| 7 | 108bMz14_1_6 | 2.722 | 0.125 | 0.615 | 0.216 | 27220 | 1250 | 6150 | 2160 | 1482 | 53 | 4 |
| 8 | 108bMz14_2_7 | 3.604 | 0.074 | 0.215 | 0.258 | 36040 | 740 | 2150 | 2580 | 1451 | 71 | 5 |
| 9 | 108bMz14_2_8 | 3.628 | 0.07 | 0.21 | 0.266 | 36280 | 700 | 2100 | 2660 | 1490 | 75 | 5 |
| 10 | 108bMz14_2_9 | 3.646 | 0.054 | 0.189 | 0.266 | 36460 | 540 | 1890 | 2660 | 1505 | 89 | 6 |
| 11 | 108bMz14_2_10 | 3.696 | 0.058 | 0.169 | 0.271 | 36960 | 580 | 1690 | 2710 | 1508 | 85 | 6 |
| 12 | 108bMz14_2_11 | 3.615 | 0.05 | 0.184 | 0.264 | 36150 | 500 | 1840 | 2640 | 1511 | 94 | 6 |
| 13 | 108bMz14_2_12 | 3.579 | 0.057 | 0.19 | 0.261 | 35790 | 570 | 1900 | 2610 | 1499 | 86 | 6 |
| 14 | 108bMz14_2_13 | 3.533 | 0.067 | 0.089 | 0.257 | 35330 | 670 | 890 | 2570 | 1481 | 77 | 5 |
| 15 | 108bMz14_2_14 | 3.567 | 0.064 | 0.091 | 0.261 | 35670 | 640 | 910 | 2610 | 1494 | 80 | 5 |
| 16 | 108bMz14_2_15 | 3.638 | 0.081 | 0.105 | 0.263 | 36380 | 810 | 1050 | 2630 | 1457 | 66 | 5 |
| 23 | 108bMz14_5_22 | 3.636 | 0.117 | 0.626 | 0.273 | 36360 | 1170 | 6260 | 2730 | 1464 | 52 | 4 |
| 24 | 108bMz14_5_23 | 3.76 | 0.12 | 0.638 | 0.284 | 37600 | 1200 | 6380 | 2840 | 1474 | 51 | 3 |
| 25 | 108bMz14_5_24 | 3.612 | 0.13 | 0.607 | 0.279 | 36120 | 1300 | 6070 | 2790 | 1487 | 49 | 3 |
| 26 | 108bMz14_5_25 | 3.506 | 0.131 | 0.621 | 0.272 | 35060 | 1310 | 6210 | 2720 | 1487 | 49 | 3 |
| 27 | 108bMz14_5_26 | 3.659 | 0.123 | 0.671 | 0.283 | 36590 | 1230 | 6710 | 2830 | 1500 | 52 | 3 |
| 28 | 108bMz14_5_27 | 3.509 | 0.127 | 0.671 | 0.277 | 35090 | 1270 | 6710 | 2770 | 1517 | 52 | 3 |
| 29 | 108bMz14_5_28 | 3.736 | 0.1 | 0.628 | 0.276 | 37360 | 1000 | 6280 | 2760 | 1466 | 58 | 4 |
| 30 | 108bMz14_5_29 | 3.306 | 0.127 | 0.652 | 0.257 | 33060 | 1270 | 6520 | 2570 | 1486 | 51 | 3 |
| 31 | 108bMz14_5_30 | 3.371 | 0.094 | 0.605 | 0.252 | 33710 | 940 | 6050 | 2520 | 1478 | 62 | 4 |
| 45 | 108bMz14_4_44 | 2.982 | 0.062 | 0.147 | 0.219 | 29820 | 620 | 1470 | 2190 | 1485 | 85 | 6 |
| 46 | 108bMz14_4_45 | 2.891 | 0.06 | 0.168 | 0.211 | 28910 | 600 | 1680 | 2110 | 1477 | 87 | 6 |
| 47 | 108bMz14_4_46 | 2.805 | 0.064 | 0.181 | 0.207 | 28050 | 640 | 1810 | 2070 | 1483 | 85 | 6 |
| 48 | 108bMz14_4_47 | 2.871 | 0.065 | 0.187 | 0.207 | 28710 | 650 | 1870 | 2070 | 1451 | 82 | 6 |
| 49 | 108bMz14_4_48 | 2.945 | 0.062 | 0.153 | 0.214 | 29450 | 620 | 1530 | 2140 | 1469 | 84 | 6 |
| 50 | 108bMz14_4_49 | 2.986 | 0.073 | 0.176 | 0.22 | 29860 | 730 | 1760 | 2200 | 1473 | 76 | 5 |
| *Rim* | | | | | | | | | | | | |
| 32 | 108bMz14_3_31 | 3.687 | 0.032 | 0.122 | 0.189 | 36870 | 320 | 1220 | 1890 | 1092 | 87 | 8 |
| 33 | 108bMz14_3_32 | 3.756 | 0.03 | 0.1 | 0.193 | 37560 | 300 | 1000 | 1930 | 1097 | 90 | 8 |
| 34 | 108bMz14_3_33 | 3.296 | 0.024 | 0.203 | 0.169 | 32960 | 240 | 2030 | 1690 | 1097 | 106 | 10 |
| 36 | 108bMz14_3_35 | 3.268 | 0.04 | 0.242 | 0.165 | 32680 | 400 | 2420 | 1650 | 1064 | 79 | 7 |
| 37 | 108bMz14_3_36 | 3.27 | 0.048 | 0.288 | 0.169 | 32700 | 480 | 2880 | 1690 | 1080 | 72 | 7 |
| 38 | 108bMz14_3_37 | 3.293 | 0.036 | 0.232 | 0.167 | 32930 | 360 | 2320 | 1670 | 1073 | 85 | 8 |
| 39 | 108bMz14_3_38 | 3.303 | 0.022 | 0.176 | 0.164 | 33030 | 220 | 1760 | 1640 | 1066 | 107 | 10 |
| 40 | 108bMz14_3_39 | 3.228 | 0.037 | 0.241 | 0.16 | 32280 | 370 | 2410 | 1600 | 1048 | 82 | 8 |
| 41 | 108bMz14_3_40 | 3.441 | 0.023 | 0.191 | 0.174 | 34410 | 230 | 1910 | 1740 | 1085 | 104 | 10 |
| 42 | 108bMz14_3_41 | 3.492 | 0.039 | 0.196 | 0.177 | 34920 | 390 | 1960 | 1770 | 1072 | 78 | 7 |
| 43 | 108bMz14_3_42 | 3.321 | 0.028 | 0.192 | 0.166 | 33210 | 280 | 1920 | 1660 | 1067 | 95 | 9 |
| 44 | 108bMz14_3_43 | 3.273 | 0.063 | 0.361 | 0.174 | 32730 | 630 | 3610 | 1740 | 1094 | 61 | 6 |
| **CA108b small monazite** | | | | | | | | | | | | |
| *Core* | | | | | | | | | | | | |
| 65 | 108bMz21_2_15 | 5.426 | 0.074 | 0.141 | 0.373 | 54260 | 740 | 1410 | 3730 | 1427 | 63 | 4 |
| 66 | 108bMz21_2_16 | 5.583 | 0.086 | 0.155 | 0.385 | 55830 | 860 | 1550 | 3850 | 1423 | 56 | 4 |
| 67 | 108bMz21_2_17 | 5.659 | 0.083 | 0.151 | 0.399 | 56590 | 830 | 1510 | 3990 | 1457 | 59 | 4 |
| 68 | 108bMz21_2_18 | 5.125 | 0.068 | 0.14 | 0.36 | 51250 | 680 | 1400 | 3600 | 1458 | 68 | 5 |
| 69 | 108bMz21_2_19 | 5.187 | 0.076 | 0.104 | 0.357 | 51870 | 760 | 1040 | 3570 | 1424 | 62 | 4 |
| 70 | 108bMz21_2_20 | 5.232 | 0.081 | 0.16 | 0.361 | 52320 | 810 | 1600 | 3610 | 1423 | 60 | 4 |
| 71 | 108bMz21_1_21 | 4.547 | 0.085 | 0.082 | 0.323 | 45470 | 850 | 820 | 3230 | 1449 | 61 | 4 |
| 72 | 108bMz21_1_22 | 4.562 | 0.075 | 0.086 | 0.324 | 45620 | 750 | 860 | 3240 | 1459 | 67 | 5 |
| 73 | 108bMz21_1_23 | 4.622 | 0.077 | 0.088 | 0.326 | 46220 | 770 | 880 | 3260 | 1448 | 64 | 4 |
| 74 | 108bMz21_1_24 | 4.621 | 0.075 | 0.081 | 0.328 | 46210 | 750 | 810 | 3280 | 1459 | 66 | 5 |
| 75 | 108bMz21_1_25 | 4.586 | 0.078 | 0.089 | 0.334 | 45860 | 780 | 890 | 3340 | 1492 | 66 | 4 |
| 76 | 108bMz21_1_26 | 4.3 | 0.074 | 0.084 | 0.311 | 43000 | 740 | 840 | 3110 | 1481 | 69 | 5 |
| *Rim* | | | | | | | | | | | | |
| 51 | 108bMz21_3_1 | 3.292 | 0.029 | 0.3 | 0.158 | 32920 | 290 | 3000 | 1580 | 1024 | 91 | 9 |
| 52 | 108bMz21_3_2 | 3.351 | 0.041 | 0.403 | 0.169 | 33510 | 410 | 4030 | 1690 | 1063 | 78 | 7 |
| 53 | 108bMz21_3_3 | 3.443 | 0.028 | 0.272 | 0.171 | 34430 | 280 | 2720 | 1710 | 1061 | 94 | 9 |
| 54 | 108bMz21_3_4 | 3.419 | 0.046 | 0.382 | 0.172 | 34190 | 460 | 3820 | 1720 | 1056 | 72 | 7 |

Table B.3: Monazite trace-element data and analytical results (continued)

| | | Analysis (Wt% Oxide) | | | | Analysis (ppm) | | | | | | |
|---|---|---|---|---|---|---|---|---|---|---|---|---|
| No. | Grain/zone | Th | U | Y | Pb | Th | U | Y | Pb | Age (Ma) | ± 2σ (Ma) | SD 2σ (%) |
| 55 | 108bMz21_3_5 | 3.474 | 0.025 | 0.269 | 0.174 | 34740 | 250 | 2690 | 1740 | 1073 | 100 | 9 |
| 56 | 108bMz21_3_6 | 3.487 | 0.043 | 0.361 | 0.173 | 34870 | 430 | 3610 | 1730 | 1046 | 73 | 7 |
| 57 | 108bMz21_3_7 | 3.937 | 0.029 | 0.171 | 0.199 | 39370 | 290 | 1710 | 1990 | 1082 | 88 | 8 |
| 58 | 108bMz21_3_8 | 3.619 | 0.039 | 0.278 | 0.182 | 36190 | 390 | 2780 | 1820 | 1065 | 77 | 7 |
| 59 | 108bMz21_3_9 | 3.774 | 0.056 | 0.346 | 0.192 | 37740 | 560 | 3460 | 1920 | 1063 | 62 | 6 |
| 60 | 108bMz21_3_10 | 3.748 | 0.045 | 0.345 | 0.188 | 37480 | 450 | 3450 | 1880 | 1058 | 70 | 7 |
| 61 | 108bMz21_3_11 | 3.687 | 0.05 | 0.353 | 0.185 | 36870 | 500 | 3530 | 1850 | 1053 | 66 | 6 |
| 62 | 108bMz21_3_12 | 3.612 | 0.055 | 0.386 | 0.186 | 36120 | 550 | 3860 | 1860 | 1074 | 64 | 6 |
| 63 | 108bMz21_3_13 | 3.705 | 0.054 | 0.344 | 0.184 | 37050 | 540 | 3440 | 1840 | 1039 | 62 | 6 |
| 64 | 108bMz21_3_14 | 3.595 | 0.045 | 0.341 | 0.181 | 35950 | 450 | 3410 | 1810 | 1060 | 71 | 7 |
| **PSD08-101a matrix monazite** | | | | | | | | | | | | |
| 78 | 101aMz19_3_2 | 1.861 | 0.626 | 2.416 | 0.207 | 18610 | 6260 | 24160 | 2070 | 1130 | 18 | 2 |
| 79 | 101aMz19_3_3 | 1.965 | 0.626 | 2.269 | 0.216 | 19650 | 6260 | 22690 | 2160 | 1147 | 18 | 2 |
| 80 | 101aMz19_3_4 | 1.94 | 0.705 | 1.995 | 0.227 | 19400 | 7050 | 19950 | 2270 | 1138 | 17 | 1 |
| 81 | 101aMz19_3_5 | 1.869 | 0.701 | 1.808 | 0.221 | 18690 | 7010 | 18080 | 2210 | 1131 | 17 | 1 |
| 82 | 101aMz19_2_6 | 1.363 | 0.518 | 1.4 | 0.168 | 13630 | 5180 | 14000 | 1680 | 1167 | 21 | 2 |
| 83 | 101aMz19_2_7 | 1.338 | 0.506 | 1.289 | 0.167 | 13380 | 5060 | 12890 | 1670 | 1183 | 21 | 2 |
| 84 | 101aMz19_2_8 | 1.475 | 0.525 | 1.115 | 0.174 | 14750 | 5250 | 11150 | 1740 | 1159 | 20 | 2 |
| 85 | 101aMz19_2_9 | 1.635 | 0.51 | 1.07 | 0.18 | 16350 | 5100 | 10700 | 1800 | 1161 | 20 | 2 |
| 86 | 101aMz19_2_10 | 1.351 | 0.517 | 1.326 | 0.168 | 13510 | 5170 | 13260 | 1680 | 1172 | 21 | 2 |
| 87 | 101aMz19_2_11 | 1.349 | 0.523 | 1.332 | 0.169 | 13490 | 5230 | 13320 | 1690 | 1172 | 21 | 2 |
| 88 | 101aMz19_1_12 | 1.949 | 0.407 | 0.712 | 0.186 | 19490 | 4070 | 7120 | 1860 | 1210 | 23 | 2 |
| 89 | 101aMz19_1_13 | 1.922 | 0.443 | 0.734 | 0.19 | 19220 | 4430 | 7340 | 1900 | 1202 | 22 | 2 |
| 90 | 101aMz19_1_14 | 1.781 | 0.396 | 0.717 | 0.173 | 17810 | 3960 | 7170 | 1730 | 1200 | 23 | 2 |
| 92 | 101aMz19_1_16 | 1.759 | 0.402 | 0.719 | 0.168 | 17590 | 4020 | 7190 | 1680 | 1168 | 23 | 2 |
| 93 | 101aMz19_1_17 | 1.762 | 0.4 | 0.714 | 0.17 | 17620 | 4000 | 7140 | 1700 | 1183 | 23 | 2 |
| **PSD08-101a Ksp-Qtz ribbon monazite** | | | | | | | | | | | | |
| 94 | 101aMz8_2_1 | 1.912 | 0.339 | 1.496 | 0.159 | 19120 | 3390 | 14960 | 1590 | 1132 | 23 | 2 |
| 95 | 101aMz8_2_2 | 1.907 | 0.35 | 1.599 | 0.164 | 19070 | 3500 | 15990 | 1640 | 1153 | 23 | 2 |
| 96 | 101aMz8_2_3 | 1.886 | 0.34 | 1.531 | 0.16 | 18860 | 3400 | 15310 | 1600 | 1146 | 24 | 2 |
| 97 | 101aMz8_2_4 | 1.894 | 0.337 | 1.594 | 0.161 | 18940 | 3370 | 15940 | 1610 | 1154 | 24 | 2 |
| 98 | 101aMz8_2_5 | 1.847 | 0.34 | 1.604 | 0.158 | 18470 | 3400 | 16040 | 1580 | 1146 | 24 | 2 |
| 99 | 101aMz8_2_6 | 1.987 | 0.343 | 1.71 | 0.169 | 19870 | 3430 | 17100 | 1690 | 1167 | 24 | 2 |
| 100 | 101aMz8_2_7 | 1.953 | 0.319 | 1.762 | 0.166 | 19530 | 3190 | 17620 | 1660 | 1188 | 25 | 2 |
| 101 | 101aMz8_2_8 | 1.963 | 0.309 | 1.745 | 0.163 | 19630 | 3090 | 17450 | 1630 | 1177 | 25 | 2 |
| 102 | 101aMz8_3_9 | 1.753 | 0.322 | 1.317 | 0.153 | 17530 | 3220 | 13170 | 1530 | 1169 | 25 | 2 |
| 103 | 101aMz8_3_10 | 1.781 | 0.322 | 1.319 | 0.155 | 17810 | 3220 | 13190 | 1550 | 1173 | 25 | 2 |
| 104 | 101aMz8_3_11 | 1.805 | 0.318 | 1.3 | 0.156 | 18050 | 3180 | 13000 | 1560 | 1176 | 25 | 2 |
| 105 | 101aMz8_3_12 | 1.814 | 0.322 | 1.274 | 0.157 | 18140 | 3220 | 12740 | 1570 | 1174 | 25 | 2 |
| 106 | 101aMz8_3_13 | 1.803 | 0.325 | 1.269 | 0.159 | 18030 | 3250 | 12690 | 1590 | 1188 | 25 | 2 |
| 107 | 101aMz8_3_14 | 1.789 | 0.325 | 1.218 | 0.157 | 17890 | 3250 | 12180 | 1570 | 1180 | 25 | 2 |
| 108 | 101aMz8_1_15 | 1.891 | 0.393 | 0.709 | 0.171 | 18910 | 3930 | 7090 | 1710 | 1153 | 22 | 2 |
| 109 | 101aMz8_1_16 | 1.787 | 0.465 | 0.758 | 0.18 | 17870 | 4650 | 7580 | 1800 | 1162 | 21 | 2 |
| 110 | 101aMz8_1_17 | 1.962 | 0.31 | 0.548 | 0.162 | 19620 | 3100 | 5480 | 1620 | 1169 | 25 | 2 |
| 111 | 101aMz8_1_18 | 1.971 | 0.341 | 0.62 | 0.167 | 19710 | 3410 | 6200 | 1670 | 1162 | 24 | 2 |
| 112 | 101aMz8_1_19 | 1.86 | 0.401 | 0.713 | 0.172 | 18600 | 4010 | 7130 | 1720 | 1161 | 22 | 2 |
| 113 | 101aMz8_1_20 | 1.89 | 0.354 | 0.855 | 0.162 | 18900 | 3540 | 8550 | 1620 | 1141 | 23 | 2 |
| **GSC-5183** | | | | | | | | | | | | |
| s1 | GSC_8153_4 | 6.218 | 0.309 | 0.369 | 0.175 | 62180 | 3090 | 3690 | 1750 | 538 | 11 | 2 |
| s2 | GSC_8153_5 | 6.263 | 0.313 | 0.37 | 0.17 | 62630 | 3130 | 3700 | 1700 | 519 | 11 | 2 |
| s3 | GSC_8153_6 | 6.307 | 0.315 | 0.372 | 0.174 | 63070 | 3150 | 3720 | 1740 | 528 | 11 | 2 |
| s4 | GSC_8153_7 | 6.268 | 0.308 | 0.372 | 0.172 | 62680 | 3080 | 3720 | 1720 | 526 | 11 | 2 |
| s5 | GSC_8153_8 | 6.292 | 0.311 | 0.365 | 0.17 | 62920 | 3110 | 3650 | 1700 | 518 | 11 | 2 |
| s6 | GSC_8153_9 | 6.277 | 0.3 | 0.365 | 0.178 | 62770 | 3000 | 3650 | 1780 | 545 | 11 | 2 |
| s7 | GSC_8153_10 | 6.312 | 0.306 | 0.358 | 0.174 | 63120 | 3060 | 3580 | 1740 | 529 | 11 | 2 |
| s8 | GSC_8153_11 | 6.318 | 0.308 | 0.362 | 0.174 | 63180 | 3080 | 3620 | 1740 | 528 | 11 | 2 |
| s9 | GSC_8153_12 | 6.349 | 0.311 | 0.36 | 0.174 | 63490 | 3110 | 3600 | 1740 | 526 | 11 | 2 |
| s10 | GSC_8153_13 | 6.329 | 0.308 | 0.368 | 0.17 | 63290 | 3080 | 3680 | 1700 | 516 | 11 | 2 |
| s11 | GSC_8153_14 | 6.344 | 0.308 | 0.357 | 0.173 | 63440 | 3080 | 3570 | 1730 | 524 | 11 | 2 |
| s12 | GSC_8153_15 | 6.335 | 0.304 | 0.353 | 0.175 | 63350 | 3040 | 3530 | 1750 | 531 | 11 | 2 |

# APPENDIX C

# THERMOCHRONOLOGY HORNBLENDE ANALYTICAL DATA

Appendix C presents major-element electron-microprobe mineral composition data for hornblende thermochronology samples (JF10-35 and JF10-39) analysed in this study. Ten hornblende grains were analysed in each sample, evenly distributed throughout the polished section, to obtain representative mineral compositions.

Table C.1: JF10-35 amphibole analyses

| Analysis No. | 39 | 40 | 41 | 42 | 43 | 44 | 45 | 46 | 47 | 48 | 49 |
|---|---|---|---|---|---|---|---|---|---|---|---|
| Wt. % | | | | | | | | | | | |
| SiO2 | 41.74 | 41.35 | 41.38 | 41.81 | 41.49 | 41.64 | 41.55 | 41.75 | 41.52 | 41.67 | 41.63 |
| TiO2 | 1.94 | 1.89 | 1.91 | 2.00 | 1.95 | 2.02 | 2.03 | 1.95 | 1.88 | 1.98 | 1.97 |
| Al2O3 | 11.91 | 12.13 | 11.93 | 12.11 | 12.24 | 12.26 | 12.23 | 12.13 | 12.30 | 12.12 | 11.96 |
| FeO | 15.26 | 15.35 | 15.33 | 15.32 | 15.45 | 15.88 | 15.43 | 15.44 | 15.09 | 15.18 | 15.00 |
| MnO | 0.22 | 0.23 | 0.24 | 0.19 | 0.22 | 0.24 | 0.18 | 0.21 | 0.19 | 0.17 | 0.21 |
| MgO | 10.80 | 10.67 | 10.68 | 10.80 | 10.64 | 10.56 | 10.55 | 10.55 | 10.79 | 10.71 | 10.68 |
| CaO | 10.39 | 10.12 | 10.25 | 10.44 | 10.14 | 10.15 | 10.30 | 10.28 | 10.21 | 10.32 | 10.29 |
| Na2O | 1.73 | 1.78 | 1.74 | 1.70 | 1.78 | 1.83 | 1.80 | 1.77 | 1.75 | 1.67 | 1.59 |
| K2O | 1.73 | 1.69 | 1.69 | 1.70 | 1.77 | 1.68 | 1.75 | 1.69 | 1.75 | 1.70 | 1.72 |
| Total | 95.73 | 95.21 | 95.16 | 96.08 | 95.67 | 96.24 | 95.83 | 95.76 | 95.46 | 95.52 | 95.09 |
| | | | | | | | | | | | |
| Cations | | | | | | | | | | | |
| Si | 6.38 | 6.32 | 6.33 | 6.39 | 6.34 | 6.37 | 6.35 | 6.38 | 6.35 | 6.37 | 6.37 |
| Ti | 0.22 | 0.22 | 0.22 | 0.23 | 0.22 | 0.23 | 0.23 | 0.22 | 0.22 | 0.23 | 0.23 |
| Al | 2.15 | 2.19 | 2.15 | 2.18 | 2.21 | 2.21 | 2.20 | 2.19 | 2.22 | 2.18 | 2.15 |
| Fe | 1.95 | 1.96 | 1.96 | 1.96 | 1.98 | 2.03 | 1.97 | 1.97 | 1.93 | 1.94 | 1.92 |
| Mn | 0.03 | 0.03 | 0.03 | 0.02 | 0.03 | 0.03 | 0.02 | 0.03 | 0.02 | 0.02 | 0.03 |
| Mg | 2.46 | 2.43 | 2.43 | 2.46 | 2.42 | 2.41 | 2.41 | 2.40 | 2.46 | 2.44 | 2.43 |
| Ca | 1.70 | 1.66 | 1.68 | 1.71 | 1.66 | 1.66 | 1.69 | 1.68 | 1.67 | 1.69 | 1.69 |
| Na | 0.51 | 0.53 | 0.51 | 0.50 | 0.53 | 0.54 | 0.53 | 0.53 | 0.52 | 0.49 | 0.47 |
| K | 0.34 | 0.33 | 0.33 | 0.33 | 0.34 | 0.33 | 0.34 | 0.33 | 0.34 | 0.33 | 0.34 |
| Total | 15.75 | 15.67 | 15.65 | 15.80 | 15.74 | 15.81 | 15.76 | 15.74 | 15.72 | 15.71 | 15.62 |
| | | | | | | | | | | | |
| End-members | | | | | | | | | | | |
| Parg | 23 | 24 | 23 | 23 | 24 | 25 | 24 | 24 | 24 | 23 | 22 |
| Ts | 77 | 76 | 77 | 77 | 76 | 75 | 76 | 76 | 76 | 77 | 78 |
| | | | | | | | | | | | |
| Oxygen pfu. | 23 | | | | | | | | | | |

Table C.2: JF10-39 amphibole analyses

| Analysis No. | 19 | 20 | 21 | 22 | 23 | 24 | 25 | 26 | 27 | 28 |
|---|---|---|---|---|---|---|---|---|---|---|
| Wt. % | | | | | | | | | | |
| SiO2 | 42.738 | 42.596 | 42.353 | 42.388 | 42.983 | 42.34 | 42.733 | 42.451 | 42.425 | 42.37 |
| TiO2 | 1.88 | 1.694 | 1.765 | 1.823 | 1.737 | 1.819 | 2.014 | 1.91 | 1.712 | 1.84 |
| Al2O3 | 12.36 | 12.539 | 12.41 | 12.457 | 11.934 | 12.263 | 12.68 | 12.562 | 12.084 | 12.443 |
| FeO | 13.343 | 13.322 | 13.287 | 13.303 | 13.308 | 12.965 | 12.857 | 12.794 | 13.426 | 13.262 |
| MnO | 0.053 | 0.045 | 0.069 | 0.053 | 0.045 | 0.035 | 0.046 | 0.032 | 0.067 | 0.056 |
| MgO | 11.776 | 11.795 | 11.793 | 11.888 | 12.124 | 11.855 | 11.948 | 11.955 | 11.822 | 11.834 |
| CaO | 10.61 | 10.587 | 10.562 | 10.567 | 10.64 | 10.443 | 10.608 | 10.454 | 10.52 | 10.378 |
| Na2O | 1.789 | 1.78 | 1.752 | 1.789 | 1.654 | 1.726 | 1.732 | 1.743 | 1.778 | 1.821 |
| K2O | 1.662 | 1.41 | 1.561 | 1.584 | 1.43 | 1.537 | 1.628 | 1.653 | 1.486 | 1.504 |
| Total | 96.211 | 95.768 | 95.557 | 95.900 | 95.885 | 95.015 | 96.289 | 95.560 | 95.349 | 95.508 |
| | | | | | | | | | | |
| Cations | | | | | | | | | | |
| Si | 6.421 | 6.400 | 6.364 | 6.369 | 6.458 | 6.362 | 6.421 | 6.378 | 6.374 | 6.366 |
| Ti | 0.213 | 0.191 | 0.200 | 0.206 | 0.196 | 0.206 | 0.228 | 0.216 | 0.194 | 0.208 |
| Al | 2.189 | 2.220 | 2.198 | 2.206 | 2.113 | 2.172 | 2.245 | 2.224 | 2.140 | 2.203 |
| Fe | 1.677 | 1.674 | 1.670 | 1.672 | 1.672 | 1.629 | 1.616 | 1.608 | 1.687 | 1.666 |
| Mn | 0.007 | 0.006 | 0.009 | 0.007 | 0.006 | 0.004 | 0.006 | 0.004 | 0.009 | 0.007 |
| Mg | 2.638 | 2.642 | 2.642 | 2.663 | 2.716 | 2.655 | 2.676 | 2.678 | 2.648 | 2.651 |
| Ca | 1.708 | 1.704 | 1.700 | 1.701 | 1.713 | 1.681 | 1.708 | 1.683 | 1.694 | 1.671 |
| Na | 0.521 | 0.519 | 0.510 | 0.521 | 0.482 | 0.503 | 0.505 | 0.508 | 0.518 | 0.530 |
| K | 0.319 | 0.270 | 0.299 | 0.304 | 0.274 | 0.295 | 0.312 | 0.317 | 0.285 | 0.288 |
| Total | 15.692 | 15.627 | 15.591 | 15.648 | 15.630 | 15.506 | 15.716 | 15.616 | 15.548 | 15.591 |
| | | | | | | | | | | |
| End-members | | | | | | | | | | |
| Parg | 23 | 23 | 23 | 23 | 22 | 23 | 23 | 23 | 23 | 24 |
| Ts | 77 | 77 | 77 | 77 | 78 | 77 | 77 | 77 | 77 | 76 |
| | | | | | | | | | | |
| Oxygen pfu. | 23 | | | | | | | | | |

# APPENDIX D

# MINERAL ABBREVIATIONS USED

| | |
|---|---|
| Amp | amphibole |
| Ab | albite |
| Act | actinolite |
| Alm | almandine |
| And | andalusite |
| Ann | annite |
| An | anorthite |
| Ap | apatite |
| Bt | biotite |
| Cats | calcic-tschermakite |
| Cam | clinoamphibole |
| Cpx | clinopyroxene |
| Carb | carbonate |
| Chl | chlorite |
| Cen | clinoenstatite |
| Cfs | clinoferrosilite |
| Crn | corundum |
| Di | diopside |
| East | eastonite |
| En | enstatite (ortho) |
| Fact | ferroactinolite |
| Fs | ferrosilite (ortho) |
| Geik | geikielite |
| Grt | garnet |
| Grs | grossular |
| Hed | hedenbergite |
| Hs | hastingsite |
| Hem | hematite |
| Hbl | hornblende |
| Ilm | ilmenite |
| Ksp | K-feldspar |
| Ky | kyanite |
| Mgts | magnesian-tschermakite |
| Mnz | monazite |
| Opx | orthopyroxene |
| Or | orthoclase |
| Parg | paragonite |
| Phl | phlogopite |
| Prp | pyrope |
| Pnt | pyrophanite |
| Qtz | quartz |
| Ru | rutile |
| Sil | silimanite |
| Spss | spessertine |
| Tr | tremolite |
| Ts | tschermakite |
| Zrn | zircon |

Kretz (mostly after 1983)

# APPENDIX E

# THERMOBAROMETRY ANALYTICAL DATA

Appendix D presents scanning electron images showing analysis locations, and corresponding major-element electron-microprobe data analysed in this study.

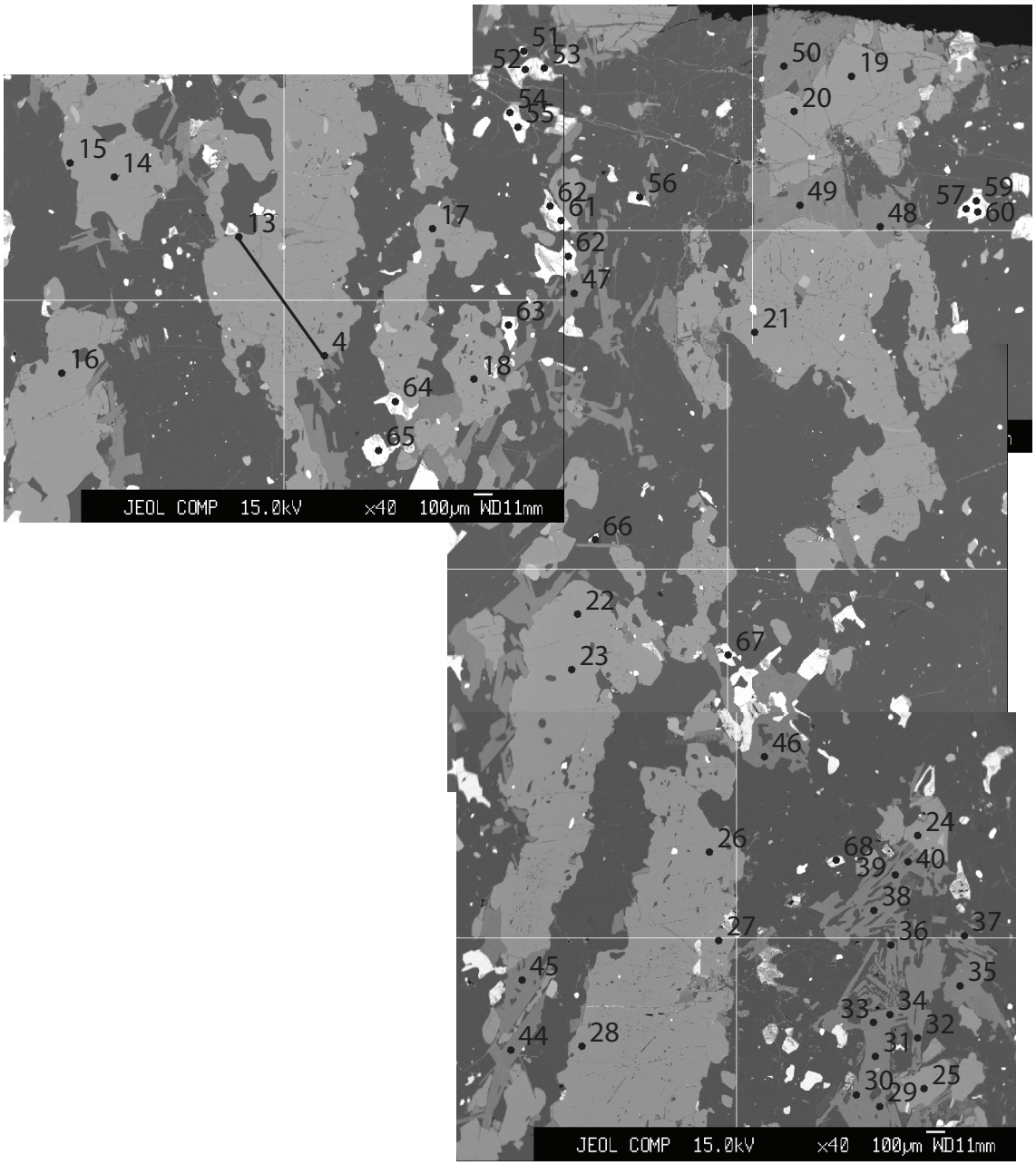


Figure E.1: CA108b analysis locations (i)

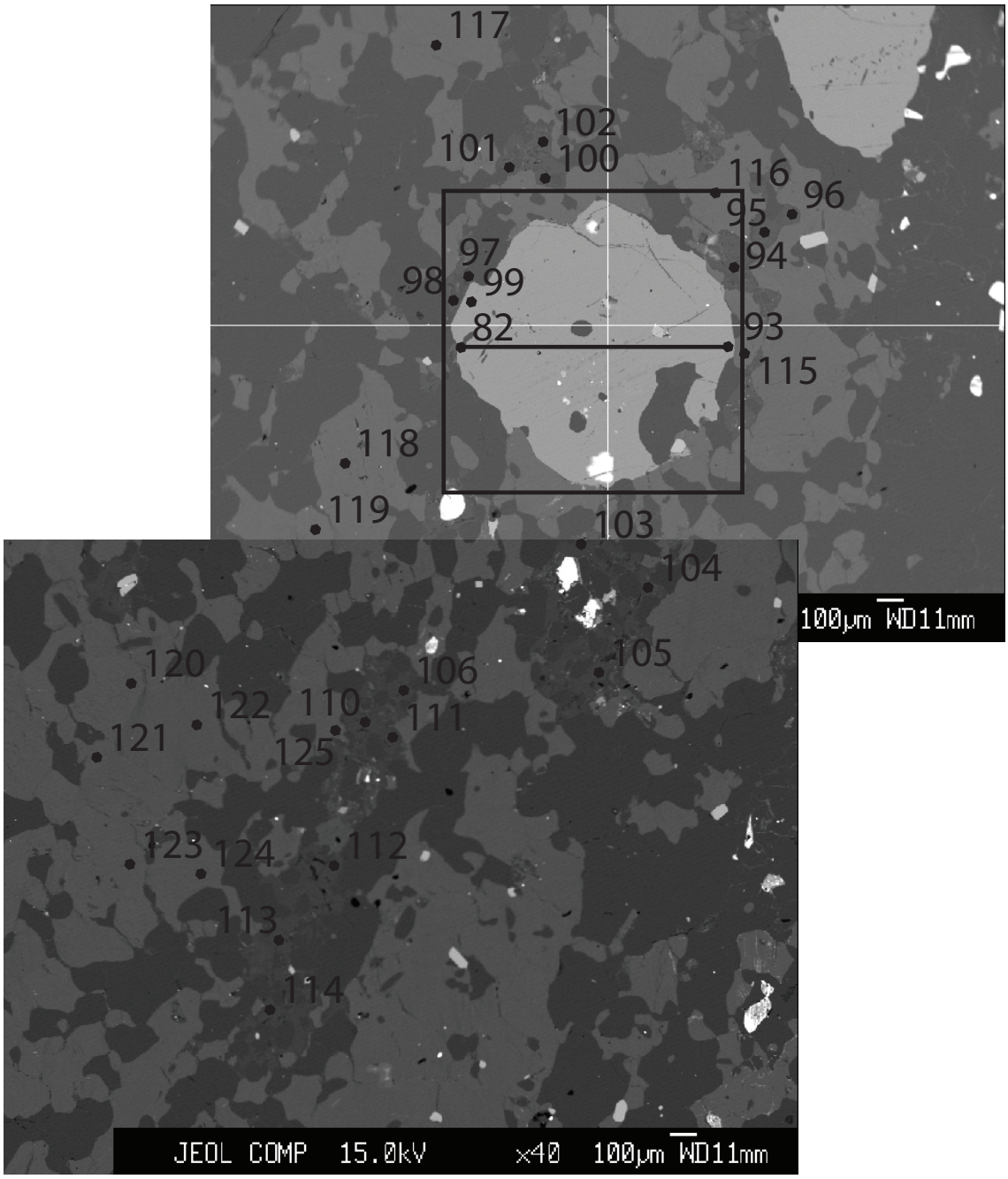


Figure E.2: CA108b analysis locations (ii). Box indicates limits of garnet WDS map.

Table E.1: CA108b biotite analyses

| Analysis No. | 29 | 30 | 31 | 32 | 33 | 34 | 35 | 36 | 37 | 38 | 39 | 40 | 44 | 45 | 46 | 48 | 49 | 50 |
|---|---|---|---|---|---|---|---|---|---|---|---|---|---|---|---|---|---|---|
| Wt. % | | | | | | | | | | | | | | | | | | |
| SiO2 | 36.01 | 35.77 | 35.63 | 35.89 | 36.67 | 36.50 | 36.56 | 36.26 | 35.67 | 35.82 | 35.67 | 35.61 | 36.11 | 36.37 | 36.47 | 36.11 | 36.51 | 36.52 |
| TiO2 | 4.04 | 3.90 | 3.66 | 3.88 | 3.67 | 3.81 | 4.15 | 4.08 | 4.19 | 3.96 | 3.83 | 3.85 | 3.68 | 3.81 | 3.69 | 3.67 | 3.75 | 4.12 |
| Al2O3 | 17.06 | 17.13 | 17.18 | 17.37 | 17.41 | 17.32 | 17.15 | 17.02 | 17.04 | 17.27 | 17.25 | 17.29 | 16.83 | 16.90 | 17.15 | 16.79 | 16.75 | 16.86 |
| FeO | 15.46 | 14.94 | 15.79 | 14.82 | 14.18 | 14.36 | 15.14 | 15.09 | 14.88 | 14.91 | 14.70 | 14.94 | 14.83 | 14.52 | 13.95 | 14.51 | 15.19 | 15.30 |
| MnO | 0.00 | 0.00 | 0.01 | 0.01 | 0.00 | 0.00 | 0.00 | 0.01 | 0.00 | 0.05 | 0.01 | 0.02 | 0.01 | 0.03 | 0.02 | 0.01 | 0.01 | 0.01 |
| MgO | 13.10 | 13.01 | 13.24 | 13.17 | 13.65 | 13.48 | 13.03 | 12.87 | 12.45 | 12.86 | 12.82 | 12.88 | 13.73 | 13.80 | 14.14 | 13.53 | 13.55 | 12.98 |
| CaO | 0.00 | 0.00 | 0.01 | 0.02 | 0.01 | 0.02 | 0.03 | 0.02 | 0.01 | 0.03 | 0.03 | 0.02 | 0.02 | 0.02 | 0.00 | 0.03 | 0.01 | 0.01 |
| Na2O | 0.06 | 0.05 | 0.09 | 0.06 | 0.07 | 0.06 | 0.06 | 0.07 | 0.07 | 0.07 | 0.08 | 0.09 | 0.08 | 0.07 | 0.06 | 0.08 | 0.12 | 0.08 |
| K2O | 9.61 | 9.53 | 8.93 | 9.36 | 9.69 | 9.60 | 9.63 | 9.46 | 9.29 | 9.33 | 9.36 | 9.06 | 9.10 | 9.52 | 9.67 | 9.39 | 9.43 | 9.41 |
| Total | 95.34 | 94.34 | 94.54 | 94.57 | 95.35 | 95.15 | 95.75 | 94.87 | 93.59 | 94.27 | 93.75 | 93.77 | 94.39 | 95.03 | 95.13 | 94.12 | 95.32 | 95.30 |
| | | | | | | | | | | | | | | | | | | |
| Cations | | | | | | | | | | | | | | | | | | |
| Si | 2.70 | 2.68 | 2.67 | 2.69 | 2.75 | 2.73 | 2.74 | 2.71 | 2.67 | 2.68 | 2.67 | 2.67 | 2.70 | 2.72 | 2.73 | 2.70 | 2.73 | 2.73 |
| Ti | 0.23 | 0.22 | 0.21 | 0.22 | 0.21 | 0.21 | 0.23 | 0.23 | 0.24 | 0.22 | 0.22 | 0.22 | 0.21 | 0.21 | 0.21 | 0.21 | 0.21 | 0.23 |
| Al | 1.51 | 1.51 | 1.52 | 1.53 | 1.54 | 1.53 | 1.51 | 1.50 | 1.50 | 1.52 | 1.52 | 1.53 | 1.48 | 1.49 | 1.51 | 1.48 | 1.48 | 1.49 |
| Fe | 0.97 | 0.94 | 0.99 | 0.93 | 0.89 | 0.90 | 0.95 | 0.95 | 0.93 | 0.93 | 0.92 | 0.94 | 0.93 | 0.91 | 0.87 | 0.91 | 0.95 | 0.96 |
| Mn | 0.00 | 0.00 | 0.00 | 0.00 | 0.00 | 0.00 | 0.00 | 0.00 | 0.00 | 0.00 | 0.00 | 0.00 | 0.00 | 0.00 | 0.00 | 0.00 | 0.00 | 0.00 |
| Mg | 1.46 | 1.45 | 1.48 | 1.47 | 1.52 | 1.50 | 1.45 | 1.44 | 1.39 | 1.44 | 1.43 | 1.44 | 1.53 | 1.54 | 1.58 | 1.51 | 1.51 | 1.45 |
| Ca | 0.00 | 0.00 | 0.00 | 0.00 | 0.00 | 0.00 | 0.00 | 0.00 | 0.00 | 0.00 | 0.00 | 0.00 | 0.00 | 0.00 | 0.00 | 0.00 | 0.00 | 0.00 |
| Na | 0.01 | 0.01 | 0.01 | 0.01 | 0.01 | 0.01 | 0.01 | 0.01 | 0.01 | 0.01 | 0.01 | 0.01 | 0.01 | 0.01 | 0.01 | 0.01 | 0.02 | 0.01 |
| K | 0.92 | 0.91 | 0.85 | 0.89 | 0.93 | 0.92 | 0.92 | 0.90 | 0.89 | 0.89 | 0.89 | 0.87 | 0.87 | 0.91 | 0.92 | 0.90 | 0.90 | 0.90 |
| Total | 7.79 | 7.72 | 7.72 | 7.74 | 7.84 | 7.81 | 7.82 | 7.74 | 7.63 | 7.70 | 7.67 | 7.66 | 7.74 | 7.80 | 7.84 | 7.72 | 7.81 | 7.77 |
| | | | | | | | | | | | | | | | | | | |
| End-members | | | | | | | | | | | | | | | | | | |
| Ann | 40 | 39 | 40 | 39 | 37 | 37 | 39 | 40 | 40 | 39 | 39 | 39 | 38 | 37 | 36 | 38 | 39 | 40 |
| Phl | 60 | 61 | 60 | 61 | 63 | 63 | 61 | 60 | 60 | 61 | 61 | 61 | 62 | 63 | 64 | 62 | 61 | 60 |
| | | | | | | | | | | | | | | | | | | |
| Oxygen pfu. | 11 | | | | | | | | | | | | | | | | | |

Table E.2: CA108b garnet analyses

| Analysis No. | 4 | 5 | 6 | 7 | 8 | 9 | 10 | 11 | 12 | 13 | 14 | 15 | 16 | 17 | 18 | 19 | 20 |
|---|---|---|---|---|---|---|---|---|---|---|---|---|---|---|---|---|---|
| Wt. % | | | | | | | | | | | | | | | | | |
| SiO2 | 37.65 | 37.46 | 37.75 | 37.65 | 37.64 | 37.52 | 37.39 | 37.18 | 37.15 | 37.51 | 37.65 | 36.86 | 37.45 | 36.97 | 37.45 | 36.96 | 37.45 |
| TiO2 | 0.00 | 0.06 | 0.01 | 0.03 | 0.04 | 0.01 | 0.04 | 0.04 | 0.03 | 0.05 | 0.05 | 0.05 | 0.04 | 0.05 | 0.04 | 0.04 | 0.05 |
| Al2O3 | 21.29 | 21.49 | 21.24 | 21.44 | 21.27 | 21.45 | 21.29 | 21.19 | 21.29 | 21.40 | 21.34 | 21.38 | 21.19 | 21.31 | 21.40 | 21.29 | 21.28 |
| FeO | 31.30 | 31.24 | 31.33 | 32.24 | 31.42 | 31.77 | 32.15 | 31.91 | 31.74 | 31.51 | 31.51 | 31.78 | 32.36 | 32.73 | 31.57 | 32.30 | 31.70 |
| MnO | 0.78 | 0.78 | 0.85 | 0.82 | 0.88 | 0.86 | 0.92 | 0.89 | 0.81 | 0.79 | 0.81 | 0.82 | 0.83 | 0.85 | 0.82 | 0.85 | 0.80 |
| MgO | 7.03 | 6.90 | 6.75 | 6.36 | 6.64 | 6.54 | 6.27 | 6.46 | 6.68 | 6.80 | 6.74 | 6.80 | 6.14 | 5.98 | 6.74 | 6.40 | 6.75 |
| CaO | 1.52 | 1.60 | 1.58 | 1.64 | 1.54 | 1.71 | 1.60 | 1.49 | 1.41 | 1.45 | 1.69 | 1.39 | 1.59 | 1.63 | 1.63 | 1.64 | 1.53 |
| Na2O | 0.00 | 0.00 | 0.00 | 0.00 | 0.00 | 0.00 | 0.00 | 0.00 | 0.00 | 0.00 | 0.00 | 0.00 | 0.00 | 0.00 | 0.00 | 0.00 | 0.00 |
| K2O | 0.04 | 0.04 | 0.04 | 0.03 | 0.03 | 0.05 | 0.03 | 0.04 | 0.03 | 0.05 | 0.03 | 0.04 | 0.03 | 0.04 | 0.04 | 0.05 | 0.03 |
| Total | 99.60 | 99.57 | 99.55 | 100.23 | 99.47 | 99.92 | 99.69 | 99.19 | 99.14 | 99.55 | 99.83 | 99.12 | 99.62 | 99.54 | 99.70 | 99.52 | 99.59 |
| | | | | | | | | | | | | | | | | | |
| Cations | | | | | | | | | | | | | | | | | |
| Si | 2.97 | 2.96 | 2.98 | 2.97 | 2.97 | 2.96 | 2.95 | 2.94 | 2.93 | 2.96 | 2.97 | 2.91 | 2.96 | 2.92 | 2.96 | 2.92 | 2.96 |
| Ti | 0.00 | 0.00 | 0.00 | 0.00 | 0.00 | 0.00 | 0.00 | 0.00 | 0.00 | 0.00 | 0.00 | 0.00 | 0.00 | 0.00 | 0.00 | 0.00 | 0.00 |
| Al | 1.98 | 2.00 | 1.98 | 2.00 | 1.98 | 2.00 | 1.98 | 1.97 | 1.98 | 1.99 | 1.99 | 1.99 | 1.97 | 1.98 | 1.99 | 1.98 | 1.98 |
| Fe | 2.07 | 2.06 | 2.07 | 2.13 | 2.08 | 2.10 | 2.12 | 2.11 | 2.10 | 2.08 | 2.08 | 2.10 | 2.14 | 2.16 | 2.09 | 2.13 | 2.09 |
| Mn | 0.05 | 0.05 | 0.06 | 0.06 | 0.06 | 0.06 | 0.06 | 0.06 | 0.05 | 0.05 | 0.05 | 0.05 | 0.06 | 0.06 | 0.06 | 0.06 | 0.05 |
| Mg | 0.83 | 0.81 | 0.79 | 0.75 | 0.78 | 0.77 | 0.74 | 0.76 | 0.79 | 0.80 | 0.79 | 0.80 | 0.72 | 0.70 | 0.79 | 0.75 | 0.80 |
| Ca | 0.13 | 0.14 | 0.13 | 0.14 | 0.13 | 0.15 | 0.14 | 0.13 | 0.12 | 0.12 | 0.14 | 0.12 | 0.13 | 0.14 | 0.14 | 0.14 | 0.13 |
| Na | 0.00 | 0.00 | 0.00 | 0.00 | 0.00 | 0.00 | 0.00 | 0.00 | 0.00 | 0.00 | 0.00 | 0.00 | 0.00 | 0.00 | 0.00 | 0.00 | 0.00 |
| K | 0.00 | 0.00 | 0.00 | 0.00 | 0.00 | 0.01 | 0.00 | 0.00 | 0.00 | 0.00 | 0.00 | 0.00 | 0.00 | 0.00 | 0.00 | 0.00 | 0.00 |
| Total | 8.04 | 8.03 | 8.02 | 8.05 | 8.01 | 8.04 | 8.00 | 7.97 | 7.98 | 8.02 | 8.04 | 7.98 | 7.99 | 7.97 | 8.03 | 7.99 | 8.02 |
| | | | | | | | | | | | | | | | | | |
| End-members | | | | | | | | | | | | | | | | | |
| Grs | 4 | 4 | 4 | 5 | 4 | 5 | 4 | 4 | 4 | 4 | 5 | 4 | 4 | 4 | 5 | 4 | 4 |
| Alm | 67 | 67 | 68 | 69 | 68 | 68 | 69 | 69 | 69 | 68 | 68 | 68 | 70 | 71 | 68 | 69 | 68 |
| Prp | 27 | 27 | 26 | 24 | 26 | 25 | 24 | 25 | 26 | 26 | 26 | 26 | 24 | 23 | 26 | 24 | 26 |
| Sps | 2 | 2 | 2 | 2 | 2 | 2 | 2 | 2 | 2 | 2 | 2 | 2 | 2 | 2 | 2 | 2 | 2 |
| | | | | | | | | | | | | | | | | | |
| Oxygen pfu. | 12 | | | | | | | | | | | | | | | | |

Table E.3: CA108b garnet analyses (continued)

| Analysis No. | 21 | 22 | 23 | 24 | 25 | 26 | 27 | 28 | 82 | 83 | 84 | 85 | 86 | 87 | 88 | 89 | 90 |
|---|---|---|---|---|---|---|---|---|---|---|---|---|---|---|---|---|---|
| Wt. % | | | | | | | | | | | | | | | | | |
| SiO2 | 37.98 | 37.56 | 37.81 | 37.75 | 37.74 | 37.80 | 37.81 | 37.94 | 37.86 | 37.59 | 37.85 | 37.86 | 37.88 | 37.80 | 37.81 | 37.94 | 37.86 |
| TiO2 | 0.01 | 0.02 | 0.00 | 0.03 | 0.01 | 0.00 | 0.00 | 0.04 | 0.05 | 0.02 | 0.00 | 0.01 | 0.00 | 0.00 | 0.00 | 0.04 | 0.05 |
| Al2O3 | 21.03 | 21.08 | 20.89 | 21.06 | 20.92 | 21.09 | 20.96 | 20.89 | 20.98 | 21.06 | 20.99 | 20.86 | 21.07 | 21.09 | 20.96 | 20.89 | 20.98 |
| FeO | 31.47 | 31.65 | 31.51 | 31.56 | 31.60 | 31.60 | 31.31 | 31.62 | 31.47 | 31.62 | 31.45 | 31.52 | 31.54 | 31.60 | 31.31 | 31.62 | 31.47 |
| MnO | 0.97 | 0.99 | 0.93 | 0.95 | 0.96 | 0.98 | 0.93 | 0.93 | 1.00 | 0.96 | 0.96 | 0.96 | 0.93 | 0.98 | 0.93 | 0.93 | 1.00 |
| MgO | 6.35 | 6.33 | 6.41 | 6.33 | 6.38 | 6.27 | 6.40 | 6.33 | 6.30 | 6.37 | 6.32 | 6.30 | 6.40 | 6.27 | 6.40 | 6.33 | 6.30 |
| CaO | 1.54 | 1.64 | 1.61 | 1.62 | 1.56 | 1.67 | 1.57 | 1.63 | 1.60 | 1.59 | 1.54 | 1.65 | 1.53 | 1.67 | 1.57 | 1.63 | 1.60 |
| Na2O | 0.01 | 0.02 | 0.00 | 0.01 | 0.01 | 0.00 | 0.00 | 0.02 | 0.01 | 0.01 | 0.02 | 0.00 | 0.01 | 0.00 | 0.00 | 0.02 | 0.01 |
| K2O | 0.00 | 0.01 | 0.01 | 0.02 | 0.00 | 0.01 | 0.01 | 0.02 | 0.02 | 0.02 | 0.02 | 0.02 | 0.02 | 0.01 | 0.01 | 0.02 | 0.02 |
| Total | 99.36 | 99.30 | 99.17 | 99.32 | 99.18 | 99.40 | 98.99 | 99.42 | 99.28 | 99.23 | 99.14 | 99.18 | 99.37 | 99.40 | 98.99 | 99.42 | 99.28 |
| | | | | | | | | | | | | | | | | | |
| Cations | | | | | | | | | | | | | | | | | |
| Si | 3.00 | 2.97 | 2.99 | 2.98 | 2.98 | 2.99 | 2.99 | 3.00 | 2.99 | 2.97 | 2.99 | 2.99 | 2.99 | 2.99 | 2.99 | 3.00 | 2.99 |
| Ti | 0.00 | 0.00 | 0.00 | 0.00 | 0.00 | 0.00 | 0.00 | 0.00 | 0.00 | 0.00 | 0.00 | 0.00 | 0.00 | 0.00 | 0.00 | 0.00 | 0.00 |
| Al | 1.96 | 1.96 | 1.95 | 1.96 | 1.95 | 1.96 | 1.95 | 1.95 | 1.95 | 1.96 | 1.95 | 1.94 | 1.96 | 1.96 | 1.95 | 1.95 | 1.95 |
| Fe | 2.08 | 2.09 | 2.08 | 2.09 | 2.09 | 2.09 | 2.07 | 2.09 | 2.08 | 2.09 | 2.08 | 2.08 | 2.08 | 2.09 | 2.07 | 2.09 | 2.08 |
| Mn | 0.06 | 0.07 | 0.06 | 0.06 | 0.06 | 0.07 | 0.06 | 0.06 | 0.07 | 0.06 | 0.06 | 0.06 | 0.06 | 0.07 | 0.06 | 0.06 | 0.07 |
| Mg | 0.75 | 0.75 | 0.75 | 0.75 | 0.75 | 0.74 | 0.75 | 0.75 | 0.74 | 0.75 | 0.74 | 0.74 | 0.75 | 0.74 | 0.75 | 0.75 | 0.74 |
| Ca | 0.13 | 0.14 | 0.14 | 0.14 | 0.13 | 0.14 | 0.13 | 0.14 | 0.14 | 0.13 | 0.13 | 0.14 | 0.13 | 0.14 | 0.13 | 0.14 | 0.14 |
| Na | 0.00 | 0.00 | 0.00 | 0.00 | 0.00 | 0.00 | 0.00 | 0.00 | 0.00 | 0.00 | 0.00 | 0.00 | 0.00 | 0.00 | 0.00 | 0.00 | 0.00 |
| K | 0.00 | 0.00 | 0.00 | 0.00 | 0.00 | 0.00 | 0.00 | 0.00 | 0.00 | 0.00 | 0.00 | 0.00 | 0.00 | 0.00 | 0.00 | 0.00 | 0.00 |
| Total | 7.98 | 7.98 | 7.97 | 7.98 | 7.97 | 7.98 | 7.96 | 7.98 | 7.97 | 7.97 | 7.97 | 7.97 | 7.99 | 7.98 | 7.96 | 7.98 | 7.97 |
| | | | | | | | | | | | | | | | | | |
| End-members | | | | | | | | | | | | | | | | | |
| Grs | 4 | 5 | 4 | 5 | 4 | 5 | 4 | 5 | 4 | 4 | 4 | 5 | 4 | 5 | 4 | 5 | 4 |
| Alm | 69 | 69 | 69 | 69 | 69 | 69 | 69 | 69 | 69 | 69 | 69 | 69 | 69 | 69 | 69 | 69 | 69 |
| Prp | 25 | 25 | 25 | 25 | 25 | 24 | 25 | 25 | 25 | 25 | 25 | 24 | 25 | 24 | 25 | 25 | 25 |
| Sps | 2 | 2 | 2 | 2 | 2 | 2 | 2 | 2 | 2 | 2 | 2 | 2 | 2 | 2 | 2 | 2 | 2 |

Table E.4: CA108b garnet analyses (continued)

| Analysis No. | 91 | 92 | 93 | 99 |
|---|---|---|---|---|
| Wt. % | | | | |
| SiO2 | 37.59 | 37.85 | 37.86 | 37.88 |
| TiO2 | 0.02 | 0.00 | 0.01 | 0.00 |
| Al2O3 | 21.06 | 20.99 | 20.86 | 21.07 |
| FeO | 31.62 | 31.45 | 31.52 | 31.54 |
| MnO | 0.96 | 0.96 | 0.96 | 0.93 |
| MgO | 6.37 | 6.32 | 6.30 | 6.40 |
| CaO | 1.59 | 1.54 | 1.65 | 1.53 |
| Na2O | 0.01 | 0.02 | 0.00 | 0.01 |
| K2O | 0.02 | 0.02 | 0.02 | 0.02 |
| Total | 99.23 | 99.14 | 99.18 | 99.37 |
| | | | | |
| Cations | | | | |
| Si | 2.97 | 2.99 | 2.99 | 2.99 |
| Ti | 0.00 | 0.00 | 0.00 | 0.00 |
| Al | 1.96 | 1.95 | 1.94 | 1.96 |
| Fe | 2.09 | 2.08 | 2.08 | 2.08 |
| Mn | 0.06 | 0.06 | 0.06 | 0.06 |
| Mg | 0.75 | 0.74 | 0.74 | 0.75 |
| Ca | 0.13 | 0.13 | 0.14 | 0.13 |
| Na | 0.00 | 0.00 | 0.00 | 0.00 |
| K | 0.00 | 0.00 | 0.00 | 0.00 |
| Total | 7.97 | 7.97 | 7.97 | 7.99 |
| | | | | |
| End-members | | | | |
| Grs | 4 | 4 | 5 | 4 |
| Alm | 69 | 69 | 69 | 69 |
| Prp | 25 | 25 | 24 | 25 |
| Sps | 2 | 2 | 2 | 2 |

Table E.5: CA108b ilmenite analyses

| Analysis No. | 51 | 52 | 57 | 59 | 60 | 61 | 62 | 63 | 64 | 65 | 66 | 68 |
|---|---|---|---|---|---|---|---|---|---|---|---|---|
| Wt. % | | | | | | | | | | | | |
| SiO2 | 0.11 | 0.12 | 0.10 | 0.10 | 0.10 | 0.04 | 0.03 | 0.06 | 0.02 | 0.03 | 0.03 | 0.04 |
| TiO2 | 51.03 | 47.66 | 46.37 | 49.64 | 47.72 | 48.81 | 47.23 | 47.68 | 50.47 | 46.73 | 45.09 | 42.32 |
| Al2O3 | 0.02 | 0.01 | 0.03 | 0.04 | 0.04 | 0.04 | 0.03 | 0.00 | 0.00 | 0.01 | 0.01 | 0.01 |
| FeO | 46.86 | 49.45 | 52.67 | 50.11 | 51.16 | 50.30 | 51.44 | 51.46 | 49.20 | 51.67 | 53.23 | 55.58 |
| MnO | 0.48 | 0.49 | 0.28 | 0.32 | 0.31 | 0.19 | 0.16 | 0.13 | 0.13 | 0.16 | 0.14 | 0.22 |
| MgO | 0.02 | 0.01 | 0.00 | 0.01 | 0.00 | 0.00 | 0.00 | 0.01 | 0.00 | 0.00 | 0.00 | 0.00 |
| CaO | 0.07 | 0.06 | 0.07 | 0.08 | 0.06 | 0.02 | 0.00 | 0.02 | 0.01 | 0.00 | 0.00 | 0.01 |
| Na2O | 0.03 | 0.02 | 0.02 | 0.02 | 0.00 | 0.00 | 0.00 | 0.00 | 0.00 | 0.00 | 0.00 | 0.00 |
| K2O | 0.05 | 0.05 | 0.06 | 0.06 | 0.06 | 0.02 | 0.04 | 0.03 | 0.03 | 0.02 | 0.03 | 0.03 |
| Total | 98.90 | 97.85 | 99.60 | 100.36 | 99.45 | 99.40 | 98.94 | 99.38 | 99.86 | 98.62 | 98.54 | 98.21 |
| | | | | | | | | | | | | |
| Cations | | | | | | | | | | | | |
| Si | 0.00 | 0.00 | 0.00 | 0.00 | 0.00 | 0.00 | 0.00 | 0.00 | 0.00 | 0.00 | 0.00 | 0.00 |
| Ti | 0.98 | 0.94 | 0.91 | 0.95 | 0.93 | 0.95 | 0.93 | 0.93 | 0.97 | 0.93 | 0.90 | 0.86 |
| Al | 0.00 | 0.00 | 0.00 | 0.00 | 0.00 | 0.00 | 0.00 | 0.00 | 0.00 | 0.00 | 0.00 | 0.00 |
| Fe2+ | 1.00 | 1.09 | 1.15 | 1.07 | 1.11 | 1.09 | 1.13 | 1.12 | 1.05 | 1.14 | 1.19 | 1.26 |
| Mn | 0.01 | 0.01 | 0.01 | 0.01 | 0.01 | 0.00 | 0.00 | 0.00 | 0.00 | 0.00 | 0.00 | 0.01 |
| Mg | 0.00 | 0.00 | 0.00 | 0.00 | 0.00 | 0.00 | 0.00 | 0.00 | 0.00 | 0.00 | 0.00 | 0.00 |
| Ca | 0.00 | 0.00 | 0.00 | 0.00 | 0.00 | 0.00 | 0.00 | 0.00 | 0.00 | 0.00 | 0.00 | 0.00 |
| Na | 0.00 | 0.00 | 0.00 | 0.00 | 0.00 | 0.00 | 0.00 | 0.00 | 0.00 | 0.00 | 0.00 | 0.00 |
| K | 0.00 | 0.00 | 0.00 | 0.00 | 0.00 | 0.00 | 0.00 | 0.00 | 0.00 | 0.00 | 0.00 | 0.00 |
| Total | 2.01 | 2.05 | 2.08 | 2.04 | 2.06 | 2.05 | 2.07 | 2.06 | 2.03 | 2.07 | 2.09 | 2.13 |
| | | | | | | | | | | | | |
| End-members | | | | | | | | | | | | |
| Ilm | 49 | 46 | 44 | 47 | 46 | 47 | 45 | 45 | 48 | 45 | 43 | 41 |
| Hem | 51 | 54 | 56 | 53 | 54 | 53 | 55 | 55 | 52 | 55 | 57 | 59 |
| | | | | | | | | | | | | |
| Oxygen pfu. | 3 | | | | | | | | | | | |

Table E.6: CA108b biotite analyses

| Analysis No. | 122 | 120 | 119 | 116 | 121 | 124 | 115 | 118 | 125 | 123 |
|---|---|---|---|---|---|---|---|---|---|---|
| Wt. % | | | | | | | | | | |
| SiO2 | 65.42 | 65.07 | 65.16 | 64.87 | 64.40 | 64.59 | 64.49 | 64.46 | 64.34 | 64.51 |
| TiO2 | 0.05 | 0.04 | 0.04 | 0.01 | 0.05 | 0.07 | 0.08 | 0.03 | 0.02 | 0.03 |
| Al2O3 | 19.04 | 18.77 | 18.96 | 18.49 | 18.53 | 18.66 | 18.56 | 18.66 | 18.46 | 18.60 |
| FeO | 0.00 | 0.01 | 0.02 | 0.02 | 0.02 | 0.03 | 0.01 | 0.01 | 0.01 | 0.03 |
| MnO | 0.00 | 0.00 | 0.00 | 0.00 | 0.00 | 0.00 | 0.01 | 0.02 | 0.02 | 0.02 |
| MgO | 0.00 | 0.00 | 0.00 | 0.01 | 0.01 | 0.00 | 0.01 | 0.00 | 0.01 | 0.00 |
| CaO | 0.13 | 0.12 | 0.10 | 0.06 | 0.07 | 0.08 | 0.07 | 0.05 | 0.08 | 0.08 |
| Na2O | 3.79 | 3.32 | 2.99 | 2.04 | 1.48 | 1.44 | 1.31 | 1.20 | 1.16 | 1.16 |
| K2O | 11.17 | 11.86 | 12.86 | 13.63 | 14.72 | 14.49 | 15.02 | 15.06 | 15.08 | 14.98 |
| Total | 99.60 | 99.19 | 100.14 | 99.13 | 99.28 | 99.35 | 99.56 | 99.48 | 99.17 | 99.41 |
| | | | | | | | | | | |
| Cations | | | | | | | | | | |
| Si | 2.98 | 2.97 | 2.97 | 2.96 | 2.94 | 2.94 | 2.94 | 2.94 | 2.93 | 2.94 |
| Ti | 0.00 | 0.00 | 0.00 | 0.00 | 0.00 | 0.00 | 0.00 | 0.00 | 0.00 | 0.00 |
| Al | 1.02 | 1.01 | 1.02 | 0.99 | 1.00 | 1.00 | 1.00 | 1.00 | 0.99 | 1.00 |
| Fe | 0.00 | 0.00 | 0.00 | 0.00 | 0.00 | 0.00 | 0.00 | 0.00 | 0.00 | 0.00 |
| Mn | 0.00 | 0.00 | 0.00 | 0.00 | 0.00 | 0.00 | 0.00 | 0.00 | 0.00 | 0.00 |
| Mg | 0.00 | 0.00 | 0.00 | 0.00 | 0.00 | 0.00 | 0.00 | 0.00 | 0.00 | 0.00 |
| Ca | 0.01 | 0.01 | 0.00 | 0.00 | 0.00 | 0.00 | 0.00 | 0.00 | 0.00 | 0.00 |
| Na | 0.33 | 0.29 | 0.26 | 0.18 | 0.13 | 0.13 | 0.12 | 0.11 | 0.10 | 0.10 |
| K | 0.65 | 0.69 | 0.75 | 0.79 | 0.86 | 0.84 | 0.87 | 0.88 | 0.88 | 0.87 |
| Total | 5.00 | 4.97 | 5.01 | 4.93 | 4.92 | 4.92 | 4.93 | 4.93 | 4.91 | 4.92 |
| | | | | | | | | | | |
| End-members | | | | | | | | | | |
| Or | 66 | 70 | 74 | 81 | 87 | 87 | 88 | 89 | 90 | 90 |
| Ab | 34 | 30 | 26 | 19 | 13 | 13 | 12 | 11 | 10 | 10 |
| An | 2 | 2 | 2 | 2 | 3 | 3 | 3 | 2 | 4 | 4 |
| | | | | | | | | | | |
| Oxygen pfu. | 8 | | | | | | | | | |

Table E.7: CA108b plagioclase analyses

| Analysis No. | 102.000 | 100 | 101 | 111 | 97 | 95 | 106 | 110 | 112 | 96 | 103 | 105 | 113 | 114 |
|---|---|---|---|---|---|---|---|---|---|---|---|---|---|---|
| Wt. % | | | | | | | | | | | | | | |
| SiO2 | 63.41 | 63.18 | 62.88 | 62.99 | 62.23 | 62.27 | 62.66 | 62.29 | 62.43 | 62.27 | 62.05 | 62.41 | 62.15 | 62.36 |
| TiO2 | 0.00 | 0.00 | 0.00 | 0.00 | 0.00 | 0.00 | 0.00 | 0.00 | 0.00 | 0.00 | 0.00 | 0.00 | 0.00 | 0.00 |
| Al2O3 | 23.20 | 23.69 | 23.56 | 23.57 | 23.92 | 23.86 | 23.91 | 24.05 | 24.08 | 23.89 | 24.02 | 24.01 | 23.89 | 24.68 |
| FeO | 0.00 | 0.01 | 0.00 | 0.02 | 0.16 | 0.00 | 0.01 | 0.02 | 0.04 | 0.00 | 0.11 | 0.04 | 0.05 | 0.05 |
| MnO | 0.00 | 0.00 | 0.00 | 0.00 | 0.00 | 0.00 | 0.00 | 0.00 | 0.00 | 0.00 | 0.00 | 0.00 | 0.00 | 0.00 |
| MgO | 0.00 | 0.00 | 0.00 | 0.00 | 0.00 | 0.00 | 0.00 | 0.00 | 0.00 | 0.00 | 0.00 | 0.00 | 0.00 | 0.00 |
| CaO | 4.31 | 4.85 | 4.78 | 4.82 | 5.12 | 5.21 | 5.13 | 5.25 | 5.01 | 5.08 | 5.31 | 5.25 | 5.32 | 4.13 |
| Na2O | 9.54 | 9.37 | 9.33 | 9.30 | 9.25 | 9.19 | 9.14 | 9.12 | 9.10 | 9.08 | 9.07 | 9.02 | 8.98 | 8.45 |
| K2O | 0.11 | 0.14 | 0.13 | 0.15 | 0.11 | 0.10 | 0.10 | 0.10 | 0.24 | 0.12 | 0.12 | 0.09 | 0.13 | 0.74 |
| Total | 100.57 | 101.23 | 100.68 | 100.85 | 100.80 | 100.64 | 100.96 | 100.83 | 100.89 | 100.44 | 100.67 | 100.83 | 100.52 | 100.42 |
| | | | | | | | | | | | | | | |
| Cations | | | | | | | | | | | | | | |
| Si | 2.79 | 2.78 | 2.77 | 2.77 | 2.74 | 2.74 | 2.76 | 2.74 | 2.75 | 2.74 | 2.73 | 2.75 | 2.74 | 2.74 |
| Ti | 0.00 | 0.00 | 0.00 | 0.00 | 0.00 | 0.00 | 0.00 | 0.00 | 0.00 | 0.00 | 0.00 | 0.00 | 0.00 | 0.00 |
| Al | 1.20 | 1.23 | 1.22 | 1.22 | 1.24 | 1.24 | 1.24 | 1.25 | 1.25 | 1.24 | 1.25 | 1.25 | 1.24 | 1.28 |
| Fe | 0.00 | 0.00 | 0.00 | 0.00 | 0.01 | 0.00 | 0.00 | 0.00 | 0.00 | 0.00 | 0.00 | 0.00 | 0.00 | 0.00 |
| Mn | 0.00 | 0.00 | 0.00 | 0.00 | 0.00 | 0.00 | 0.00 | 0.00 | 0.00 | 0.00 | 0.00 | 0.00 | 0.00 | 0.00 |
| Mg | 0.00 | 0.00 | 0.00 | 0.00 | 0.00 | 0.00 | 0.00 | 0.00 | 0.00 | 0.00 | 0.00 | 0.00 | 0.00 | 0.00 |
| Ca | 0.20 | 0.23 | 0.23 | 0.23 | 0.24 | 0.25 | 0.24 | 0.25 | 0.24 | 0.24 | 0.25 | 0.25 | 0.25 | 0.19 |
| Na | 0.81 | 0.80 | 0.80 | 0.79 | 0.79 | 0.78 | 0.78 | 0.78 | 0.78 | 0.77 | 0.77 | 0.77 | 0.77 | 0.72 |
| K | 0.01 | 0.01 | 0.01 | 0.01 | 0.01 | 0.01 | 0.01 | 0.01 | 0.01 | 0.01 | 0.01 | 0.01 | 0.01 | 0.04 |
| Total | 5.02 | 5.05 | 5.02 | 5.03 | 5.02 | 5.01 | 5.03 | 5.02 | 5.02 | 5.00 | 5.01 | 5.02 | 5.00 | 4.98 |
| | | | | | | | | | | | | | | |
| End-members | | | | | | | | | | | | | | |
| Or | 1 | 1 | 1 | 1 | 1 | 1 | 1 | 1 | 2 | 1 | 1 | 1 | 1 | 5 |
| Ab | 80 | 78 | 78 | 78 | 77 | 76 | 76 | 76 | 77 | 76 | 76 | 76 | 75 | 79 |
| An | 20 | 22 | 22 | 22 | 23 | 24 | 24 | 24 | 23 | 24 | 24 | 24 | 25 | 21 |
| | | | | | | | | | | | | | | |
| Oxygen pfu. | 8 | | | | | | | | | | | | | |

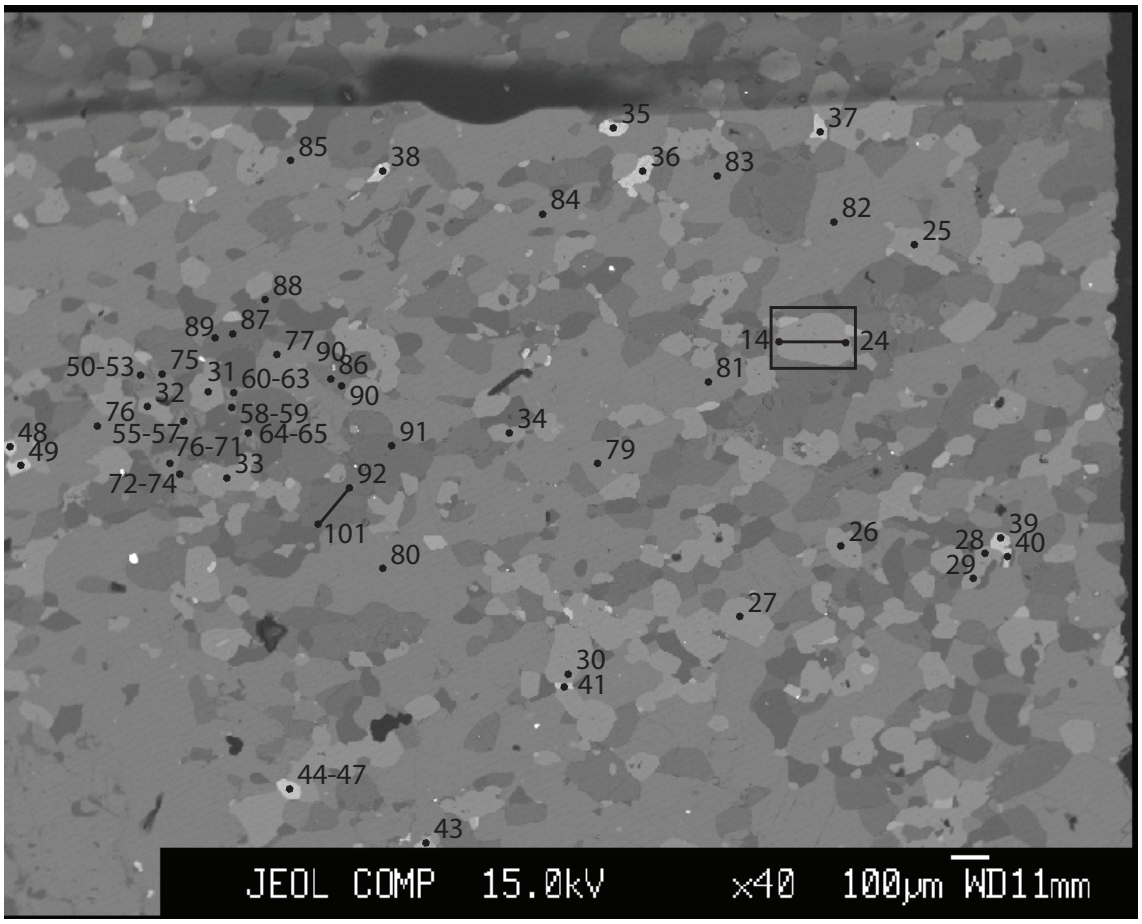


Figure E.3: JF10-12 analysis locations. Box indicates limits of garnet WDS map.

Table E.8: JF10-12 amphibole analyses

| Analysis No. | 75 | 76 | 77 | 79 | 80 | 81 | 82 | 83 | 84 | 85 |
|---|---|---|---|---|---|---|---|---|---|---|
| Wt. % | | | | | | | | | | |
| SiO2 | 43.51 | 43.32 | 42.37 | 42.98 | 43.04 | 42.77 | 42.73 | 42.79 | 42.52 | 42.28 |
| TiO2 | 1.40 | 1.57 | 1.70 | 1.78 | 1.66 | 1.62 | 1.70 | 1.53 | 1.74 | 1.65 |
| Al2O3 | 12.36 | 12.07 | 12.43 | 12.08 | 12.13 | 12.15 | 12.12 | 11.76 | 11.97 | 11.98 |
| FeO | 11.25 | 11.14 | 11.92 | 11.94 | 11.77 | 11.57 | 11.72 | 11.50 | 11.41 | 11.41 |
| MnO | 0.00 | 0.01 | 0.00 | 0.01 | 0.06 | 0.03 | 0.03 | 0.04 | 0.06 | 0.04 |
| MgO | 13.21 | 13.49 | 12.93 | 12.89 | 13.05 | 13.08 | 12.95 | 13.39 | 12.90 | 13.02 |
| CaO | 11.58 | 11.92 | 11.49 | 11.94 | 12.03 | 11.88 | 11.97 | 11.95 | 11.96 | 12.13 |
| Na2O | 1.75 | 1.83 | 1.76 | 1.80 | 1.89 | 1.84 | 1.78 | 1.83 | 1.83 | 1.82 |
| K2O | 0.92 | 1.01 | 0.98 | 1.03 | 1.05 | 1.02 | 1.05 | 0.99 | 1.03 | 1.06 |
| Total | 95.97 | 96.38 | 95.58 | 96.45 | 96.68 | 95.96 | 96.05 | 95.78 | 95.42 | 95.39 |
| | | | | | | | | | | |
| Cations | | | | | | | | | | |
| Si | 6.47 | 6.44 | 6.30 | 6.39 | 6.40 | 6.36 | 6.35 | 6.36 | 6.32 | 6.28 |
| Ti | 0.16 | 0.18 | 0.19 | 0.20 | 0.19 | 0.18 | 0.19 | 0.17 | 0.19 | 0.18 |
| Al | 2.16 | 2.11 | 2.18 | 2.12 | 2.13 | 2.13 | 2.12 | 2.06 | 2.10 | 2.10 |
| Fe | 1.40 | 1.38 | 1.48 | 1.48 | 1.46 | 1.44 | 1.46 | 1.43 | 1.42 | 1.42 |
| Mn | 0.00 | 0.00 | 0.00 | 0.00 | 0.01 | 0.00 | 0.00 | 0.01 | 0.01 | 0.00 |
| Mg | 2.93 | 2.99 | 2.86 | 2.86 | 2.89 | 2.90 | 2.87 | 2.97 | 2.86 | 2.88 |
| Ca | 1.84 | 1.90 | 1.83 | 1.90 | 1.92 | 1.89 | 1.91 | 1.90 | 1.90 | 1.93 |
| Na | 0.50 | 0.53 | 0.51 | 0.52 | 0.54 | 0.53 | 0.51 | 0.53 | 0.53 | 0.52 |
| K | 0.17 | 0.19 | 0.19 | 0.20 | 0.20 | 0.19 | 0.20 | 0.19 | 0.19 | 0.20 |
| Total | 15.63 | 15.72 | 15.53 | 15.66 | 15.73 | 15.62 | 15.61 | 15.61 | 15.52 | 15.53 |
| | | | | | | | | | | |
| End-members | | | | | | | | | | |
| Parg | 21 | 22 | 22 | 21 | 22 | 22 | 21 | 22 | 22 | 21 |
| Ts | 79 | 78 | 78 | 79 | 78 | 78 | 79 | 78 | 78 | 79 |
| | | | | | | | | | | |
| Oxygen pfu. | 23 | | | | | | | | | |

Table E.9: JF10-12 clinopyroxene analyses

| Analysis No. | 50 | 51 | 52 | 53 | 54 | 55 | 56 | 57 | 58 | 59 | 60 | 61 | 62 | 63 | 64 | 65 | 66 |
|---|---|---|---|---|---|---|---|---|---|---|---|---|---|---|---|---|---|
| Wt. % | | | | | | | | | | | | | | | | | |
| SiO2 | 51.34 | 51.14 | 50.97 | 50.76 | 51.20 | 51.17 | 51.08 | 51.11 | 51.20 | 51.46 | 51.31 | 51.60 | 51.33 | 51.58 | 51.10 | 51.07 | 51.14 |
| TiO2 | 0.35 | 0.40 | 0.37 | 0.33 | 0.46 | 0.42 | 0.35 | 0.38 | 0.36 | 0.37 | 0.32 | 0.33 | 0.33 | 0.40 | 0.35 | 0.35 | 0.35 |
| Al2O3 | 3.28 | 3.48 | 3.72 | 3.73 | 3.73 | 3.74 | 3.68 | 3.65 | 3.73 | 3.81 | 3.58 | 3.29 | 3.43 | 3.46 | 3.65 | 3.63 | 3.58 |
| FeO | 6.97 | 7.46 | 7.90 | 7.84 | 7.68 | 7.86 | 7.62 | 7.52 | 7.80 | 7.45 | 7.48 | 7.17 | 7.11 | 7.21 | 7.61 | 7.55 | 7.67 |
| MnO | 0.04 | 0.02 | 0.06 | 0.07 | 0.05 | 0.04 | 0.06 | 0.06 | 0.05 | 0.06 | 0.07 | 0.05 | 0.04 | 0.07 | 0.05 | 0.06 | 0.08 |
| MgO | 13.56 | 13.31 | 12.95 | 12.99 | 13.12 | 12.92 | 13.15 | 13.25 | 12.99 | 13.01 | 13.17 | 13.50 | 13.30 | 13.33 | 12.92 | 13.10 | 13.23 |
| CaO | 22.65 | 22.52 | 22.46 | 22.49 | 22.52 | 22.44 | 22.59 | 22.44 | 22.46 | 22.26 | 22.43 | 22.74 | 22.64 | 22.67 | 22.16 | 22.39 | 22.59 |
| Na2O | 0.69 | 0.72 | 0.75 | 0.71 | 0.73 | 0.77 | 0.72 | 0.72 | 0.72 | 0.73 | 0.69 | 0.68 | 0.72 | 0.69 | 0.71 | 0.72 | 0.74 |
| K2O | 0.04 | 0.03 | 0.03 | 0.04 | 0.02 | 0.03 | 0.02 | 0.03 | 0.03 | 0.02 | 0.02 | 0.02 | 0.04 | 0.02 | 0.03 | 0.02 | 0.02 |
| Total | 98.91 | 99.08 | 99.20 | 98.94 | 99.51 | 99.38 | 99.26 | 99.16 | 99.33 | 99.17 | 99.07 | 99.38 | 98.94 | 99.43 | 98.57 | 98.89 | 99.39 |
| | | | | | | | | | | | | | | | | | |
| Cations | | | | | | | | | | | | | | | | | |
| Si | 1.92 | 1.92 | 1.91 | 1.90 | 1.92 | 1.92 | 1.92 | 1.92 | 1.92 | 1.93 | 1.92 | 1.93 | 1.92 | 1.93 | 1.92 | 1.91 | 1.92 |
| Ti | 0.01 | 0.01 | 0.01 | 0.01 | 0.01 | 0.01 | 0.01 | 0.01 | 0.01 | 0.01 | 0.01 | 0.01 | 0.01 | 0.01 | 0.01 | 0.01 | 0.01 |
| Al | 0.14 | 0.15 | 0.16 | 0.16 | 0.16 | 0.17 | 0.16 | 0.16 | 0.16 | 0.17 | 0.16 | 0.15 | 0.15 | 0.15 | 0.16 | 0.16 | 0.16 |
| Fe | 0.22 | 0.23 | 0.25 | 0.25 | 0.24 | 0.25 | 0.24 | 0.24 | 0.24 | 0.23 | 0.23 | 0.22 | 0.22 | 0.23 | 0.24 | 0.24 | 0.24 |
| Mn | 0.00 | 0.00 | 0.00 | 0.00 | 0.00 | 0.00 | 0.00 | 0.00 | 0.00 | 0.00 | 0.00 | 0.00 | 0.00 | 0.00 | 0.00 | 0.00 | 0.00 |
| Mg | 0.76 | 0.74 | 0.72 | 0.73 | 0.73 | 0.72 | 0.73 | 0.74 | 0.73 | 0.73 | 0.74 | 0.75 | 0.74 | 0.75 | 0.72 | 0.73 | 0.74 |
| Ca | 0.91 | 0.90 | 0.90 | 0.90 | 0.90 | 0.90 | 0.91 | 0.90 | 0.90 | 0.89 | 0.90 | 0.91 | 0.91 | 0.91 | 0.89 | 0.90 | 0.91 |
| Na | 0.05 | 0.05 | 0.05 | 0.05 | 0.05 | 0.06 | 0.05 | 0.05 | 0.05 | 0.05 | 0.05 | 0.05 | 0.05 | 0.05 | 0.05 | 0.05 | 0.05 |
| K | 0.00 | 0.00 | 0.00 | 0.00 | 0.00 | 0.00 | 0.00 | 0.00 | 0.00 | 0.00 | 0.00 | 0.00 | 0.00 | 0.00 | 0.00 | 0.00 | 0.00 |
| Total | 4.02 | 4.02 | 4.02 | 4.01 | 4.03 | 4.02 | 4.02 | 4.02 | 4.02 | 4.02 | 4.02 | 4.03 | 4.02 | 4.03 | 3.99 | 4.01 | 4.03 |
| | | | | | | | | | | | | | | | | | |
| End-members | | | | | | | | | | | | | | | | | |
| Di | 78 | 76 | 74 | 75 | 75 | 75 | 75 | 76 | 75 | 76 | 76 | 77 | 77 | 77 | 75 | 76 | 75 |
| Hd | 22 | 24 | 26 | 25 | 25 | 25 | 25 | 24 | 25 | 24 | 24 | 23 | 23 | 23 | 25 | 24 | 25 |
| | | | | | | | | | | | | | | | | | |
| Oxygen pfu. | 6 | | | | | | | | | | | | | | | | |

Table E.10: JF10-12 clinopyroxene analyses (continued)

| Analysis No. | 67 | 68 | 69 | 70 | 72 | 73 | 74 |
|---|---|---|---|---|---|---|---|
| Wt. % | | | | | | | |
| SiO2 | 50.60 | 50.94 | 50.80 | 50.81 | 50.99 | 50.87 | 51.18 |
| TiO2 | 0.34 | 0.34 | 0.34 | 0.40 | 0.37 | 0.41 | 0.29 |
| Al2O3 | 3.76 | 3.65 | 3.68 | 3.68 | 3.63 | 3.69 | 3.36 |
| FeO | 7.88 | 7.96 | 7.86 | 7.80 | 7.90 | 7.94 | 7.42 |
| MnO | 0.08 | 0.06 | 0.08 | 0.08 | 0.08 | 0.05 | 0.03 |
| MgO | 13.11 | 13.04 | 12.97 | 12.93 | 13.04 | 12.99 | 13.39 |
| CaO | 22.24 | 22.71 | 22.53 | 22.55 | 22.81 | 22.71 | 22.98 |
| Na2O | 0.74 | 0.71 | 0.73 | 0.70 | 0.70 | 0.74 | 0.71 |
| K2O | 0.02 | 0.03 | 0.01 | 0.01 | 0.01 | 0.03 | 0.03 |
| Total | 98.76 | 99.44 | 98.99 | 98.96 | 99.53 | 99.44 | 99.39 |
| | | | | | | | |
| Cations | | | | | | | |
| Si | 1.90 | 1.91 | 1.90 | 1.91 | 1.91 | 1.91 | 1.92 |
| Ti | 0.01 | 0.01 | 0.01 | 0.01 | 0.01 | 0.01 | 0.01 |
| Al | 0.17 | 0.16 | 0.16 | 0.16 | 0.16 | 0.16 | 0.15 |
| Fe | 0.25 | 0.25 | 0.25 | 0.24 | 0.25 | 0.25 | 0.23 |
| Mn | 0.00 | 0.00 | 0.00 | 0.00 | 0.00 | 0.00 | 0.00 |
| Mg | 0.73 | 0.73 | 0.72 | 0.72 | 0.73 | 0.73 | 0.75 |
| Ca | 0.89 | 0.91 | 0.91 | 0.91 | 0.92 | 0.91 | 0.92 |
| Na | 0.05 | 0.05 | 0.05 | 0.05 | 0.05 | 0.05 | 0.05 |
| K | 0.00 | 0.00 | 0.00 | 0.00 | 0.00 | 0.00 | 0.00 |
| Total | 4.00 | 4.03 | 4.01 | 4.01 | 4.03 | 4.03 | 4.03 |
| | | | | | | | |
| End-members | | | | | | | |
| Di | 75 | 74 | 75 | 75 | 75 | 74 | 76 |
| Hd | 25 | 26 | 25 | 25 | 25 | 26 | 24 |

Table E.11: JF10-12 garnet analyses

| Analysis No. | 14 | 15 | 16 | 17 | 18 | 19 | 20 | 21 | 22 | 23 | 24 | 25 | 26 | 27 | 28 | 29 | 30 |
|---|---|---|---|---|---|---|---|---|---|---|---|---|---|---|---|---|---|
| Wt. % | | | | | | | | | | | | | | | | | |
| SiO2 | 38.70 | 38.67 | 38.64 | 38.79 | 38.93 | 39.10 | 39.05 | 38.87 | 38.67 | 39.01 | 38.85 | 38.82 | 38.73 | 39.24 | 38.80 | 38.92 | 39.07 |
| TiO2 | 0.06 | 0.03 | 0.04 | 0.08 | 0.03 | 0.05 | 0.03 | 0.03 | 0.08 | 0.21 | 0.55 | 0.03 | 0.03 | 0.02 | 0.12 | 0.04 | 0.03 |
| Al2O3 | 21.85 | 21.73 | 21.90 | 21.99 | 22.08 | 22.03 | 22.05 | 21.84 | 21.68 | 21.92 | 22.03 | 22.00 | 21.99 | 22.19 | 21.77 | 22.07 | 22.14 |
| FeO | 25.22 | 24.97 | 24.89 | 24.69 | 24.61 | 24.77 | 24.93 | 24.73 | 25.02 | 24.88 | 24.98 | 24.58 | 24.83 | 24.77 | 25.30 | 25.16 | 24.95 |
| MnO | 0.77 | 0.75 | 0.77 | 0.76 | 0.79 | 0.74 | 0.74 | 0.69 | 0.73 | 0.75 | 0.73 | 0.71 | 0.77 | 0.75 | 0.76 | 0.75 | 0.78 |
| MgO | 6.36 | 6.65 | 6.79 | 6.93 | 6.89 | 6.96 | 6.85 | 6.78 | 6.78 | 6.57 | 6.32 | 6.72 | 6.50 | 6.78 | 6.30 | 6.39 | 6.66 |
| CaO | 7.28 | 7.16 | 7.10 | 7.10 | 7.20 | 7.15 | 7.35 | 7.45 | 7.52 | 7.54 | 7.37 | 7.47 | 7.54 | 7.17 | 7.41 | 7.39 | 7.01 |
| Na2O | 0.00 | 0.00 | 0.00 | 0.00 | 0.00 | 0.00 | 0.00 | 0.00 | 0.00 | 0.00 | 0.00 | 0.00 | 0.01 | 0.01 | 0.01 | 0.00 | 0.00 |
| K2O | 0.03 | 0.03 | 0.02 | 0.03 | 0.02 | 0.03 | 0.02 | 0.03 | 0.03 | 0.03 | 0.03 | 0.02 | 0.03 | 0.03 | 0.03 | 0.04 | 0.03 |
| Total | 100.27 | 99.99 | 100.15 | 100.36 | 100.55 | 100.83 | 101.00 | 100.41 | 100.52 | 100.91 | 100.85 | 100.35 | 100.42 | 100.94 | 100.49 | 100.75 | 100.66 |
| | | | | | | | | | | | | | | | | | |
| Cations | | | | | | | | | | | | | | | | | |
| Si | 2.99 | 2.99 | 2.99 | 3.00 | 3.01 | 3.02 | 3.02 | 3.01 | 2.99 | 3.02 | 3.00 | 3.00 | 2.99 | 3.03 | 3.00 | 3.01 | 3.02 |
| Ti | 0.00 | 0.00 | 0.00 | 0.00 | 0.00 | 0.00 | 0.00 | 0.00 | 0.00 | 0.01 | 0.03 | 0.00 | 0.00 | 0.00 | 0.01 | 0.00 | 0.00 |
| Al | 1.99 | 1.98 | 2.00 | 2.00 | 2.01 | 2.01 | 2.01 | 1.99 | 1.98 | 2.00 | 2.01 | 2.01 | 2.00 | 2.02 | 1.98 | 2.01 | 2.02 |
| Fe | 1.63 | 1.61 | 1.61 | 1.60 | 1.59 | 1.60 | 1.61 | 1.60 | 1.62 | 1.61 | 1.62 | 1.59 | 1.61 | 1.60 | 1.64 | 1.63 | 1.61 |
| Mn | 0.05 | 0.05 | 0.05 | 0.05 | 0.05 | 0.05 | 0.05 | 0.05 | 0.05 | 0.05 | 0.05 | 0.05 | 0.05 | 0.05 | 0.05 | 0.05 | 0.05 |
| Mg | 0.73 | 0.77 | 0.78 | 0.80 | 0.79 | 0.80 | 0.79 | 0.78 | 0.78 | 0.76 | 0.73 | 0.77 | 0.75 | 0.78 | 0.73 | 0.74 | 0.77 |
| Ca | 0.60 | 0.59 | 0.59 | 0.59 | 0.60 | 0.59 | 0.61 | 0.62 | 0.62 | 0.62 | 0.61 | 0.62 | 0.62 | 0.59 | 0.61 | 0.61 | 0.58 |
| Na | 0.00 | 0.00 | 0.00 | 0.00 | 0.00 | 0.00 | 0.00 | 0.00 | 0.00 | 0.00 | 0.00 | 0.00 | 0.00 | 0.00 | 0.00 | 0.00 | 0.00 |
| K | 0.00 | 0.00 | 0.00 | 0.00 | 0.00 | 0.00 | 0.00 | 0.00 | 0.00 | 0.00 | 0.00 | 0.00 | 0.00 | 0.00 | 0.00 | 0.00 | 0.00 |
| Total | 8.01 | 8.00 | 8.02 | 8.04 | 8.06 | 8.08 | 8.09 | 8.04 | 8.05 | 8.07 | 8.05 | 8.04 | 8.04 | 8.09 | 8.02 | 8.05 | 8.06 |
| | | | | | | | | | | | | | | | | | |
| End-members | | | | | | | | | | | | | | | | | |
| Grs | 20 | 20 | 19 | 19 | 20 | 19 | 20 | 20 | 20 | 21 | 20 | 20 | 21 | 20 | 20 | 20 | 19 |
| Alm | 54 | 53 | 53 | 53 | 52 | 53 | 53 | 53 | 53 | 53 | 54 | 52 | 53 | 53 | 54 | 54 | 54 |
| Prp | 24 | 25 | 26 | 26 | 26 | 26 | 26 | 26 | 25 | 25 | 24 | 26 | 25 | 26 | 24 | 24 | 25 |
| Sps | 2 | 2 | 2 | 2 | 2 | 2 | 2 | 1 | 2 | 2 | 2 | 2 | 2 | 2 | 2 | 2 | 2 |
| | | | | | | | | | | | | | | | | | |
| Oxygen pfu. | 12 | | | | | | | | | | | | | | | | |

Table E.12: JF10-12 garnet analyses (continued)

| Analysis No. | 31 | 32 | 33 | 34 |
|---|---|---|---|---|
| Wt. % | | | | |
| SiO2 | 38.94 | 39.07 | 39.29 | 39.32 |
| TiO2 | 0.01 | 0.02 | 0.05 | 0.00 |
| Al2O3 | 21.89 | 22.02 | 22.10 | 22.01 |
| FeO | 24.74 | 25.20 | 24.76 | 24.98 |
| MnO | 0.74 | 0.76 | 0.76 | 0.72 |
| MgO | 6.68 | 6.46 | 6.85 | 6.49 |
| CaO | 7.30 | 7.24 | 7.11 | 7.33 |
| Na2O | 0.00 | 0.00 | 0.00 | 0.00 |
| K2O | 0.02 | 0.03 | 0.02 | 0.03 |
| Total | 100.32 | 100.79 | 100.94 | 100.87 |
| | | | | |
| Cations | | | | |
| Si | 3.01 | 3.02 | 3.04 | 3.04 |
| Ti | 0.00 | 0.00 | 0.00 | 0.00 |
| Al | 2.00 | 2.01 | 2.01 | 2.01 |
| Fe | 1.60 | 1.63 | 1.60 | 1.62 |
| Mn | 0.05 | 0.05 | 0.05 | 0.05 |
| Mg | 0.77 | 0.75 | 0.79 | 0.75 |
| Ca | 0.60 | 0.60 | 0.59 | 0.61 |
| Na | 0.00 | 0.00 | 0.00 | 0.00 |
| K | 0.00 | 0.00 | 0.00 | 0.00 |
| Total | 8.03 | 8.06 | 8.09 | 8.07 |
| | | | | |
| End-members | | | | |
| Grs | 20 | 20 | 19 | 20 |
| Alm | 53 | 54 | 53 | 54 |
| Prp | 25 | 25 | 26 | 25 |
| Sps | 2 | 2 | 2 | 2 |

Table E.13: JF10-12 ilmenite analyses

| Analysis No. | 35 | 36 | 37 | 39 | 41 | 43 | 44 | 45 | 47 | 48 | 49 |
|---|---|---|---|---|---|---|---|---|---|---|---|
| Wt. % | | | | | | | | | | | |
| SiO2 | 0.30 | 1.33 | 0.10 | 2.56 | 0.11 | 0.03 | 0.05 | 0.05 | 1.27 | 0.03 | 0.03 |
| TiO2 | 30.08 | 58.61 | 47.66 | 46.61 | 53.93 | 55.63 | 55.39 | 42.11 | 47.79 | 52.21 | 68.94 |
| Al2O3 | 0.14 | 0.41 | 0.04 | 0.79 | 0.02 | 0.01 | 0.03 | 0.01 | 0.58 | 0.01 | 0.03 |
| Cr2O3 | 0.28 | 0.17 | 0.17 | 0.18 | 0.20 | 0.11 | 0.00 | 0.08 | 0.08 | 0.07 | 0.01 |
| FeO | 61.99 | 29.57 | 43.50 | 36.43 | 38.65 | 37.64 | 37.72 | 50.68 | 42.34 | 41.28 | 24.73 |
| MnO | 0.88 | 0.37 | 0.11 | 5.00 | 0.11 | 0.00 | 0.00 | 0.06 | 0.09 | 0.00 | 0.00 |
| MgO | 0.15 | 1.59 | 0.73 | 1.15 | 0.22 | 0.03 | 0.44 | 0.79 | 0.81 | 0.12 | 0.13 |
| CaO | 0.12 | 0.19 | 0.12 | 0.19 | 0.24 | 0.04 | 0.03 | 0.04 | 0.09 | 0.07 | 0.14 |
| Na2O | 0.00 | 0.01 | 0.02 | 0.00 | 0.00 | 0.00 | 0.02 | 0.00 | 0.03 | 0.00 | 0.01 |
| K2O | 0.05 | 0.05 | 0.06 | 0.04 | 0.04 | 0.02 | 0.02 | 0.02 | 0.02 | 0.03 | 0.02 |
| Total | 94.00 | 92.31 | 92.51 | 92.95 | 93.51 | 93.52 | 93.68 | 93.83 | 93.08 | 93.83 | 94.03 |
| | | | | | | | | | | | |
| Cations | | | | | | | | | | | |
| Si | 0.01 | 0.03 | 0.00 | 0.07 | 0.00 | 0.00 | 0.00 | 0.00 | 0.03 | 0.00 | 0.00 |
| Ti | 0.68 | 1.11 | 0.98 | 0.93 | 1.06 | 1.09 | 1.08 | 0.89 | 0.96 | 1.04 | 1.25 |
| Al | 0.00 | 0.01 | 0.00 | 0.02 | 0.00 | 0.00 | 0.00 | 0.00 | 0.02 | 0.00 | 0.00 |
| Cr | 0.01 | 0.00 | 0.00 | 0.00 | 0.00 | 0.00 | 0.00 | 0.00 | 0.00 | 0.00 | 0.00 |
| Fe2+ | 1.56 | 0.62 | 0.99 | 0.81 | 0.85 | 0.82 | 0.82 | 1.19 | 0.95 | 0.91 | 0.50 |
| Mn | 0.02 | 0.01 | 0.00 | 0.11 | 0.00 | 0.00 | 0.00 | 0.00 | 0.00 | 0.00 | 0.00 |
| Mg | 0.01 | 0.06 | 0.03 | 0.05 | 0.01 | 0.00 | 0.02 | 0.03 | 0.03 | 0.00 | 0.00 |
| Ca | 0.00 | 0.01 | 0.00 | 0.01 | 0.01 | 0.00 | 0.00 | 0.00 | 0.00 | 0.00 | 0.00 |
| Na | 0.00 | 0.00 | 0.00 | 0.00 | 0.00 | 0.00 | 0.00 | 0.00 | 0.00 | 0.00 | 0.00 |
| K | 0.00 | 0.00 | 0.00 | 0.00 | 0.00 | 0.00 | 0.00 | 0.00 | 0.00 | 0.00 | 0.00 |
| Total | 2.30 | 1.85 | 2.02 | 1.99 | 1.93 | 1.91 | 1.92 | 2.11 | 2.00 | 1.96 | 1.75 |
| | | | | | | | | | | | |
| End-members | | | | | | | | | | | |
| Ilm | 30 | 64 | 50 | 54 | 56 | 57 | 57 | 43 | 50 | 53 | 71 |
| Hem | 70 | 36 | 50 | 46 | 44 | 43 | 43 | 57 | 50 | 47 | 29 |
| | | | | | | | | | | | |
| Oxygen pfu. | 3 | | | | | | | | | | |

Table E.14: JF10-12 plagioclase analyses

| Analysis No. | 86 | 87 | 88 | 89 | 90 | 91 | 92 | 93 | 94 | 97 | 98 | 99 | 101 |
|---|---|---|---|---|---|---|---|---|---|---|---|---|---|
| Wt. % | | | | | | | | | | | | | |
| SiO2 | 54.92 | 54.90 | 54.18 | 55.07 | 54.44 | 54.88 | 54.99 | 55.05 | 54.22 | 55.05 | 54.35 | 55.28 | 54.69 |
| TiO2 | 0.00 | 0.00 | 0.00 | 0.00 | 0.00 | 0.00 | 0.00 | 0.00 | 0.00 | 0.00 | 0.00 | 0.00 | 0.00 |
| Al2O3 | 26.46 | 26.79 | 27.14 | 26.71 | 26.35 | 26.73 | 26.27 | 26.80 | 27.25 | 26.46 | 26.88 | 26.57 | 26.96 |
| FeO | 0.11 | 0.23 | 0.11 | 0.13 | 0.13 | 0.35 | 0.16 | 0.21 | 0.29 | 0.11 | 0.08 | 0.19 | 0.13 |
| MnO | 0.00 | 0.00 | 0.00 | 0.00 | 0.00 | 0.01 | 0.00 | 0.00 | 0.00 | 0.00 | 0.01 | 0.01 | 0.00 |
| MgO | 0.00 | 0.00 | 0.00 | 0.00 | 0.00 | 0.00 | 0.01 | 0.00 | 0.00 | 0.00 | 0.00 | 0.00 | 0.00 |
| CaO | 10.21 | 10.30 | 10.45 | 10.14 | 10.07 | 10.09 | 9.71 | 10.08 | 10.65 | 9.90 | 10.50 | 9.86 | 10.46 |
| Na2O | 6.12 | 5.97 | 5.80 | 6.09 | 6.06 | 6.13 | 6.30 | 6.07 | 5.73 | 6.18 | 5.89 | 6.12 | 5.93 |
| K2O | 0.13 | 0.12 | 0.14 | 0.14 | 0.13 | 0.12 | 0.13 | 0.14 | 0.12 | 0.14 | 0.13 | 0.14 | 0.15 |
| Total | 97.95 | 98.32 | 97.82 | 98.28 | 97.19 | 98.30 | 97.56 | 98.36 | 98.26 | 97.84 | 97.83 | 98.17 | 98.32 |
| | | | | | | | | | | | | | |
| Cations | | | | | | | | | | | | | |
| Si | 2.53 | 2.53 | 2.50 | 2.54 | 2.51 | 2.53 | 2.53 | 2.54 | 2.50 | 2.54 | 2.50 | 2.55 | 2.52 |
| Ti | 0.00 | 0.00 | 0.00 | 0.00 | 0.00 | 0.00 | 0.00 | 0.00 | 0.00 | 0.00 | 0.00 | 0.00 | 0.00 |
| Al | 1.44 | 1.45 | 1.47 | 1.45 | 1.43 | 1.45 | 1.43 | 1.45 | 1.48 | 1.44 | 1.46 | 1.44 | 1.46 |
| Fe | 0.00 | 0.01 | 0.00 | 0.01 | 0.00 | 0.01 | 0.01 | 0.01 | 0.01 | 0.00 | 0.00 | 0.01 | 0.01 |
| Mn | 0.00 | 0.00 | 0.00 | 0.00 | 0.00 | 0.00 | 0.00 | 0.00 | 0.00 | 0.00 | 0.00 | 0.00 | 0.00 |
| Mg | 0.00 | 0.00 | 0.00 | 0.00 | 0.00 | 0.00 | 0.00 | 0.00 | 0.00 | 0.00 | 0.00 | 0.00 | 0.00 |
| Ca | 0.50 | 0.51 | 0.52 | 0.50 | 0.50 | 0.50 | 0.48 | 0.50 | 0.53 | 0.49 | 0.52 | 0.49 | 0.52 |
| Na | 0.55 | 0.53 | 0.52 | 0.54 | 0.54 | 0.55 | 0.56 | 0.54 | 0.51 | 0.55 | 0.53 | 0.55 | 0.53 |
| K | 0.01 | 0.01 | 0.01 | 0.01 | 0.01 | 0.01 | 0.01 | 0.01 | 0.01 | 0.01 | 0.01 | 0.01 | 0.01 |
| Total | 5.03 | 5.04 | 5.02 | 5.05 | 4.99 | 5.05 | 5.02 | 5.05 | 5.03 | 5.03 | 5.02 | 5.04 | 5.04 |
| | | | | | | | | | | | | | |
| End-members | | | | | | | | | | | | | |
| Ab | 52 | 51 | 50 | 52 | 52 | 52 | 54 | 52 | 49 | 53 | 50 | 53 | 51 |
| An | 48 | 49 | 50 | 48 | 48 | 48 | 46 | 48 | 51 | 47 | 50 | 47 | 49 |
| | | | | | | | | | | | | | |
| Oxygen pfu. | 8 | | | | | | | | | | | | |

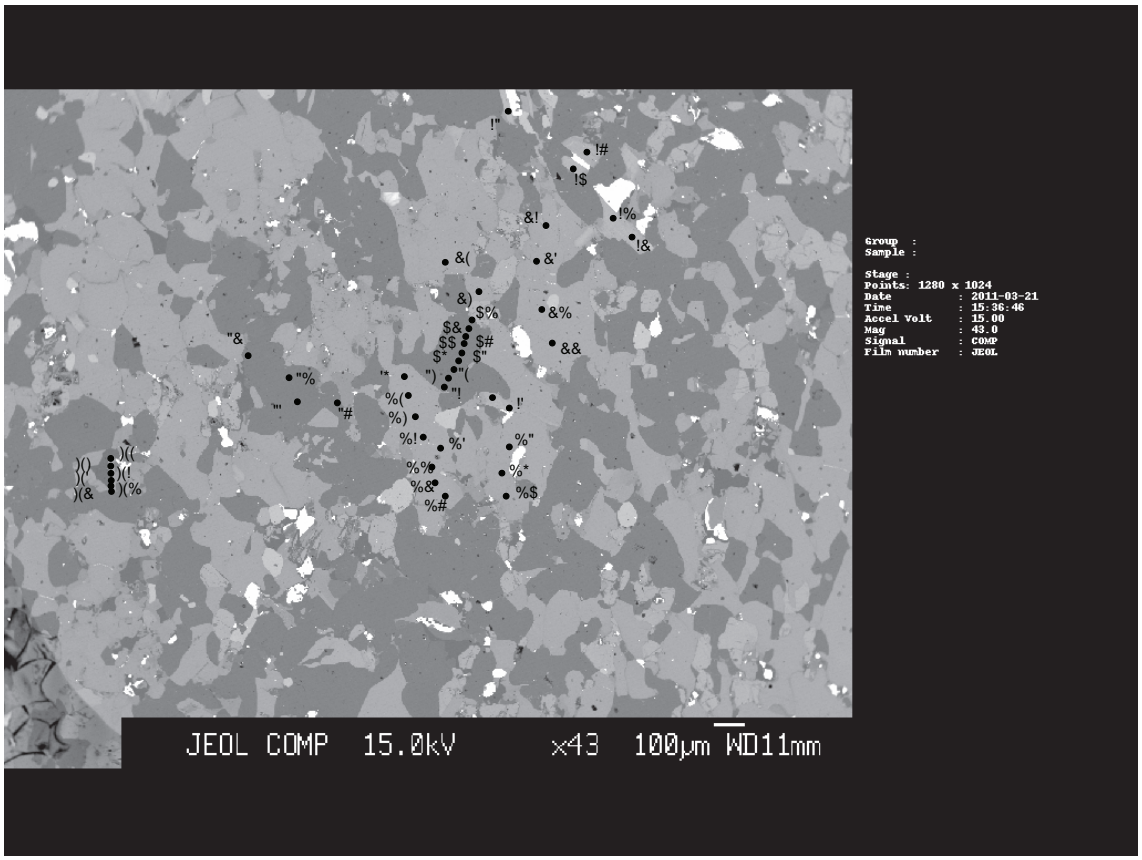


Figure E.4: JF10-88 analysis locations (i)

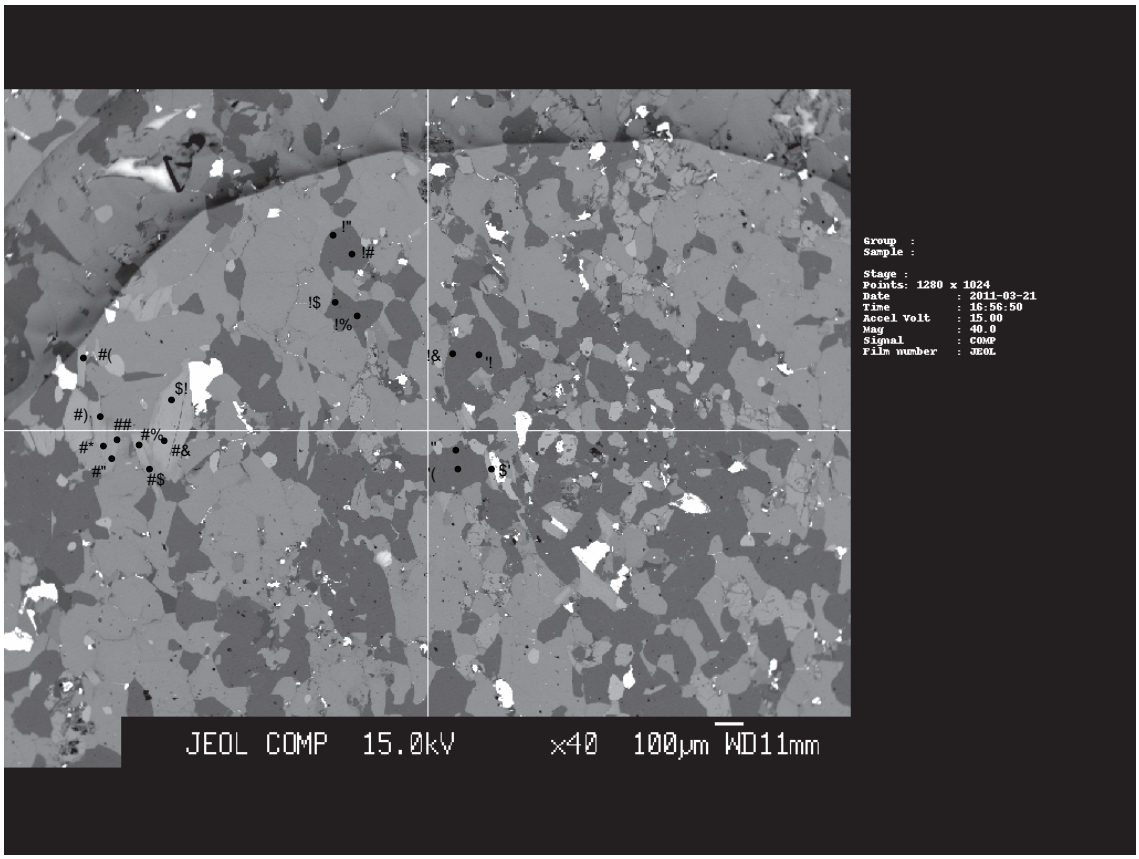


Figure E.5: JF10-88 analysis locations (ii)

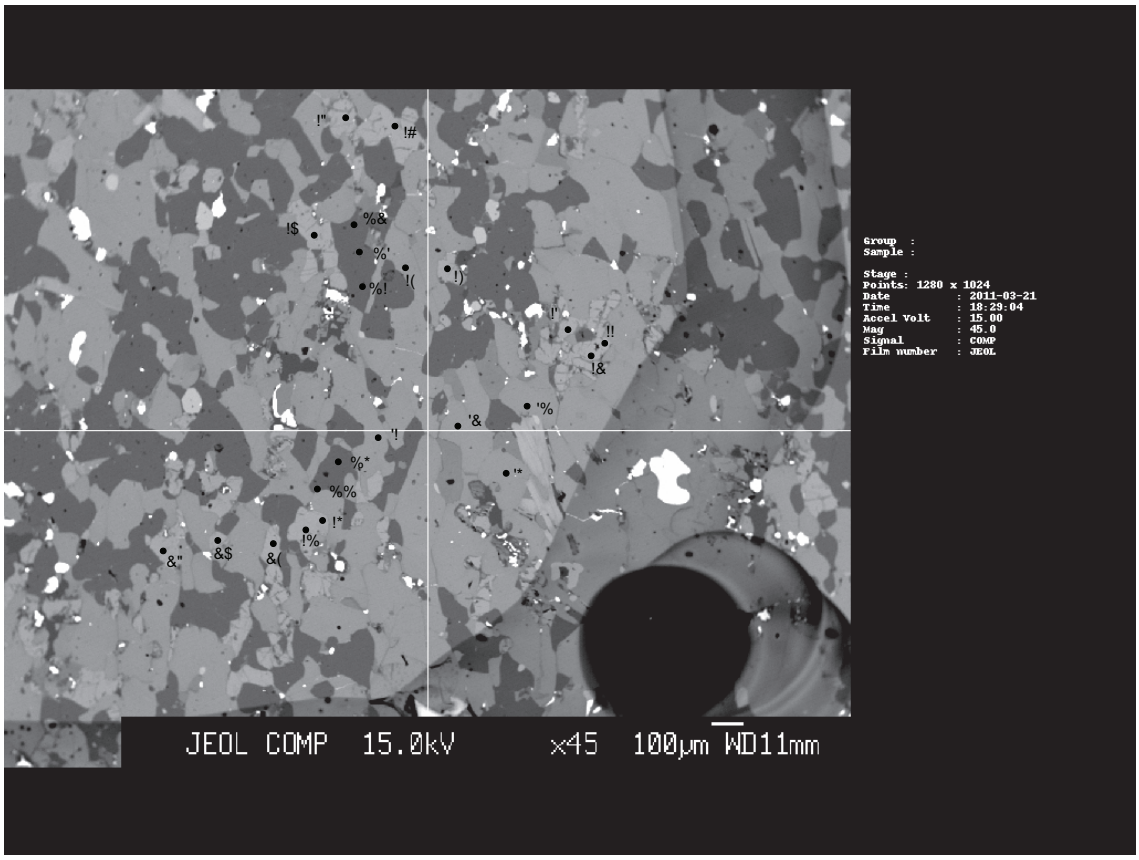


Figure E.6: JF10-88 analysis locations (iii)

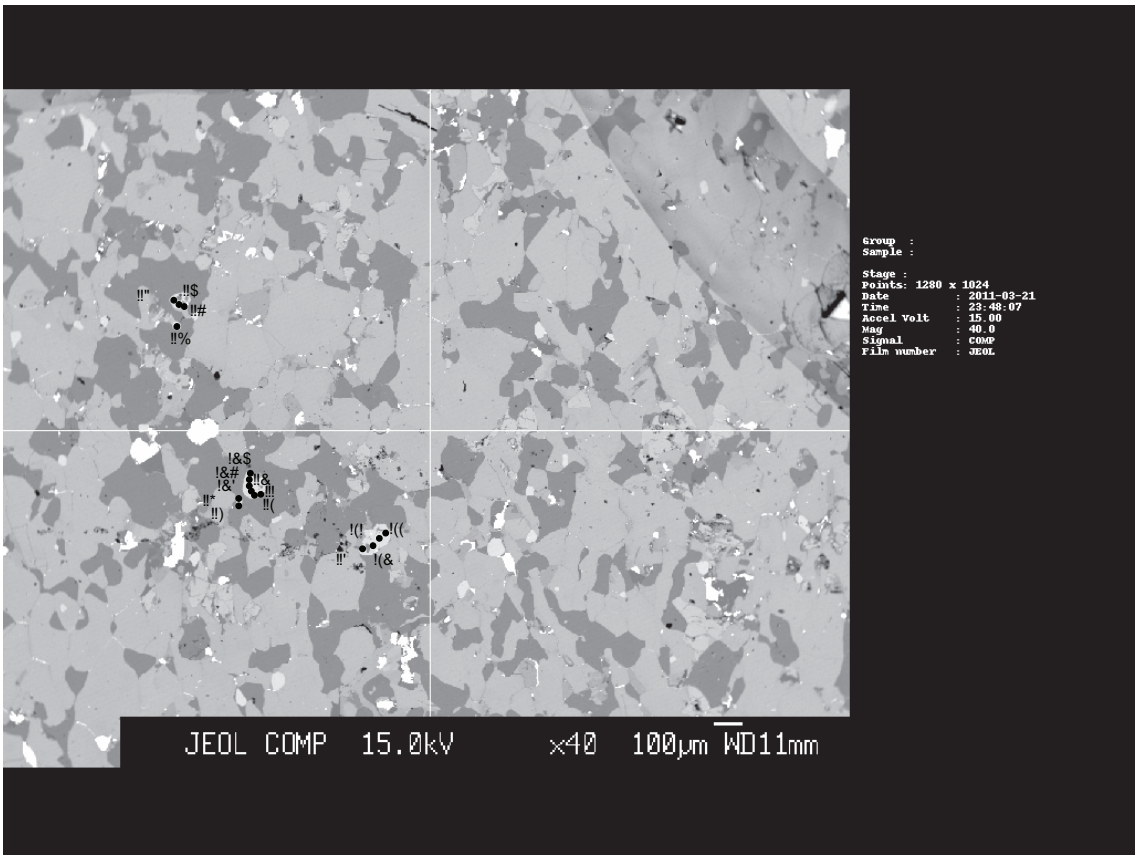


Figure E.7: JF10-88 analysis locations (iv)

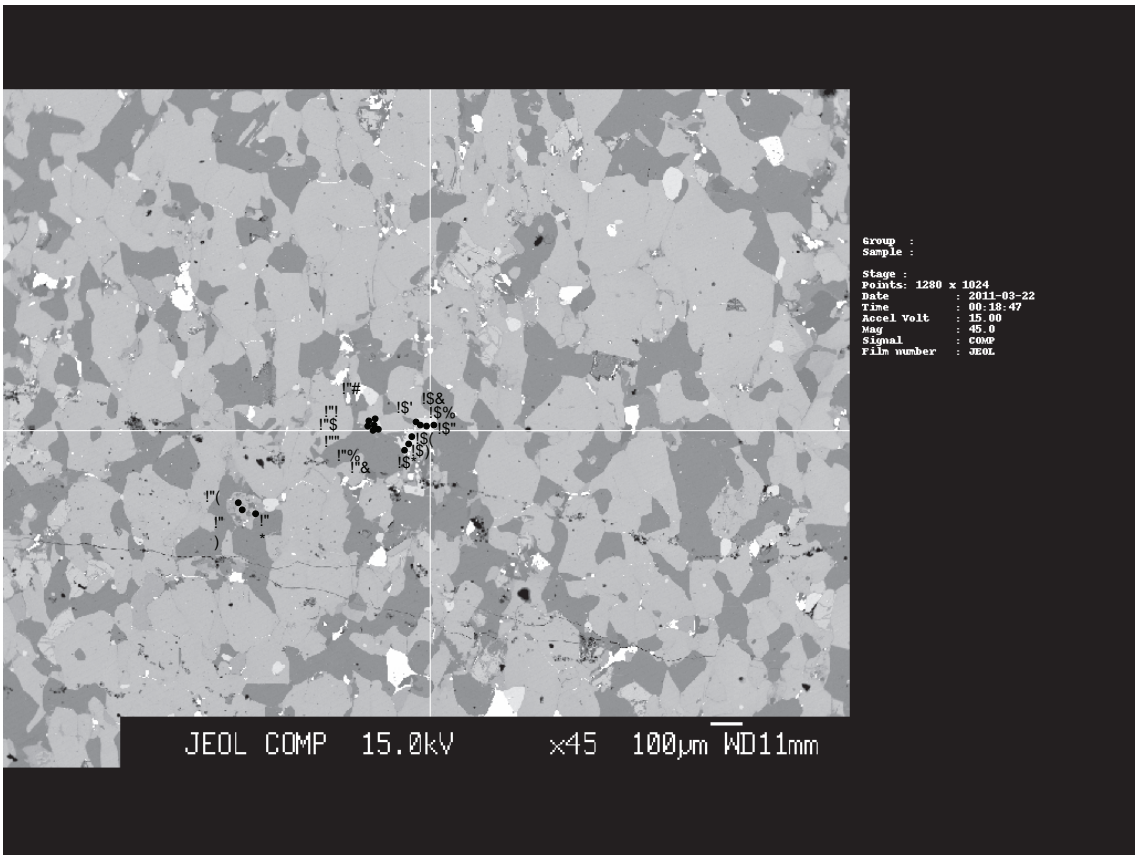


Figure E.8: JF10-88 analysis locations (v)

Table E.15: JF10-88 amphibole analyses

| Analysis No. | 39 | 40 | 41 | 42 | 43 | 45 | 46 | 48 | 50 | 51 | 52 | 53 | 54 | 57 | 58 | 59 | 60 |
|---|---|---|---|---|---|---|---|---|---|---|---|---|---|---|---|---|---|
| Wt. % | | | | | | | | | | | | | | | | | |
| SiO2 | 42.11 | 42.43 | 42.40 | 42.95 | 41.19 | 42.36 | 42.24 | 42.44 | 42.86 | 42.40 | 41.57 | 43.07 | 42.84 | 42.49 | 42.63 | 42.57 | 43.25 |
| TiO2 | 1.81 | 1.75 | 1.67 | 1.66 | 1.91 | 1.78 | 1.93 | 1.74 | 1.63 | 1.73 | 1.71 | 1.66 | 1.67 | 1.80 | 1.70 | 1.75 | 1.60 |
| Al2O3 | 12.05 | 12.01 | 11.92 | 11.67 | 12.92 | 12.18 | 12.03 | 11.90 | 11.73 | 11.93 | 12.74 | 11.81 | 11.64 | 11.74 | 12.09 | 12.13 | 11.70 |
| FeO | 13.65 | 13.59 | 13.95 | 13.65 | 14.25 | 13.79 | 13.94 | 13.30 | 13.68 | 13.33 | 13.83 | 13.01 | 13.44 | 13.90 | 13.54 | 13.47 | 12.93 |
| MnO | 0.15 | 0.16 | 0.18 | 0.14 | 0.14 | 0.17 | 0.19 | 0.18 | 0.16 | 0.15 | 0.13 | 0.15 | 0.13 | 0.16 | 0.18 | 0.15 | 0.15 |
| MgO | 12.38 | 12.42 | 12.56 | 12.65 | 11.66 | 12.41 | 12.27 | 12.84 | 12.59 | 12.60 | 12.25 | 13.14 | 12.83 | 12.38 | 12.51 | 12.53 | 12.89 |
| CaO | 11.62 | 11.46 | 11.58 | 11.56 | 11.60 | 11.69 | 11.53 | 11.29 | 11.20 | 11.55 | 11.59 | 11.54 | 11.59 | 11.42 | 11.53 | 11.34 | 11.66 |
| Na2O | 1.84 | 1.82 | 1.78 | 1.73 | 1.89 | 1.77 | 1.88 | 1.89 | 1.81 | 1.78 | 1.80 | 1.86 | 1.87 | 1.81 | 1.85 | 1.88 | 1.84 |
| K2O | 1.63 | 1.55 | 1.53 | 1.56 | 1.74 | 1.62 | 1.60 | 1.57 | 1.51 | 1.60 | 1.75 | 1.59 | 1.53 | 1.55 | 1.56 | 1.63 | 1.52 |
| Total | 97.25 | 97.19 | 97.56 | 97.58 | 97.30 | 97.77 | 97.62 | 97.14 | 97.17 | 97.07 | 97.36 | 97.84 | 97.53 | 97.25 | 97.59 | 97.46 | 97.55 |
| | | | | | | | | | | | | | | | | | |
| Cations | | | | | | | | | | | | | | | | | |
| Si | 6.31 | 6.36 | 6.35 | 6.43 | 6.17 | 6.35 | 6.33 | 6.36 | 6.42 | 6.35 | 6.23 | 6.45 | 6.42 | 6.37 | 6.39 | 6.38 | 6.48 |
| Ti | 0.20 | 0.20 | 0.19 | 0.19 | 0.22 | 0.20 | 0.22 | 0.20 | 0.18 | 0.19 | 0.19 | 0.19 | 0.19 | 0.20 | 0.19 | 0.20 | 0.18 |
| Al | 2.13 | 2.12 | 2.10 | 2.06 | 2.28 | 2.15 | 2.12 | 2.10 | 2.07 | 2.11 | 2.25 | 2.09 | 2.06 | 2.07 | 2.14 | 2.14 | 2.07 |
| Fe | 1.71 | 1.70 | 1.75 | 1.71 | 1.78 | 1.73 | 1.75 | 1.67 | 1.71 | 1.67 | 1.73 | 1.63 | 1.68 | 1.74 | 1.70 | 1.69 | 1.62 |
| Mn | 0.02 | 0.02 | 0.02 | 0.02 | 0.02 | 0.02 | 0.02 | 0.02 | 0.02 | 0.02 | 0.02 | 0.02 | 0.02 | 0.02 | 0.02 | 0.02 | 0.02 |
| Mg | 2.77 | 2.77 | 2.81 | 2.83 | 2.60 | 2.77 | 2.74 | 2.87 | 2.81 | 2.81 | 2.73 | 2.94 | 2.87 | 2.77 | 2.79 | 2.80 | 2.88 |
| Ca | 1.87 | 1.84 | 1.86 | 1.86 | 1.86 | 1.88 | 1.85 | 1.81 | 1.80 | 1.85 | 1.86 | 1.85 | 1.86 | 1.83 | 1.85 | 1.82 | 1.87 |
| Na | 0.53 | 0.53 | 0.52 | 0.50 | 0.55 | 0.51 | 0.55 | 0.55 | 0.53 | 0.52 | 0.52 | 0.54 | 0.54 | 0.53 | 0.54 | 0.55 | 0.53 |
| K | 0.31 | 0.30 | 0.29 | 0.30 | 0.33 | 0.31 | 0.30 | 0.30 | 0.29 | 0.31 | 0.33 | 0.30 | 0.29 | 0.30 | 0.30 | 0.31 | 0.29 |
| Total | 15.85 | 15.84 | 15.89 | 15.89 | 15.82 | 15.92 | 15.88 | 15.87 | 15.83 | 15.83 | 15.87 | 16.01 | 15.92 | 15.82 | 15.91 | 15.90 | 15.94 |
| | | | | | | | | | | | | | | | | | |
| End-members | | | | | | | | | | | | | | | | | |
| Parg | 22 | 22 | 22 | 21 | 23 | 21 | 23 | 23 | 23 | 22 | 22 | 23 | 23 | 22 | 23 | 23 | 22 |
| Ts | 78 | 78 | 78 | 79 | 77 | 79 | 77 | 77 | 77 | 78 | 78 | 77 | 77 | 78 | 77 | 77 | 78 |
| | | | | | | | | | | | | | | | | | |
| Oxygen pfu. | 23 | | | | | | | | | | | | | | | | |

Table E.16: JF10-88 amphibole analyses

| Analysis No. | 12 | 13 | 14 | 15 | 16 | 19 | 20 | 21 | 22 | 23 |
|---|---|---|---|---|---|---|---|---|---|---|
| Wt. % | | | | | | | | | | |
| SiO2 | 52.16 | 52.10 | 52.12 | 51.96 | 52.02 | 52.62 | 52.49 | 52.33 | 52.34 | 52.42 |
| TiO2 | 0.22 | 0.22 | 0.20 | 0.18 | 0.22 | 0.14 | 0.15 | 0.16 | 0.22 | 0.14 |
| Al2O3 | 2.88 | 2.86 | 2.77 | 2.78 | 2.79 | 2.52 | 2.44 | 2.71 | 2.74 | 2.60 |
| FeO | 9.17 | 9.10 | 9.34 | 9.01 | 9.13 | 8.58 | 8.55 | 8.70 | 8.85 | 8.53 |
| MnO | 0.31 | 0.30 | 0.31 | 0.28 | 0.30 | 0.28 | 0.29 | 0.32 | 0.30 | 0.29 |
| MgO | 13.15 | 12.95 | 12.98 | 13.01 | 13.03 | 13.24 | 13.34 | 13.05 | 13.06 | 13.15 |
| CaO | 22.43 | 22.35 | 22.11 | 22.17 | 22.29 | 22.57 | 22.61 | 22.32 | 22.20 | 22.42 |
| Na2O | 0.96 | 1.00 | 0.98 | 0.95 | 0.99 | 0.93 | 0.94 | 0.97 | 0.99 | 1.01 |
| K2O | 0.03 | 0.04 | 0.03 | 0.03 | 0.04 | 0.03 | 0.04 | 0.03 | 0.03 | 0.02 |
| Total | 101.31 | 100.92 | 100.82 | 100.36 | 100.80 | 100.91 | 100.85 | 100.59 | 100.71 | 100.58 |
| | | | | | | | | | | |
| Cations | | | | | | | | | | |
| Si | 1.93 | 1.93 | 1.93 | 1.92 | 1.92 | 1.95 | 1.94 | 1.94 | 1.94 | 1.94 |
| Ti | 0.01 | 0.01 | 0.01 | 0.00 | 0.01 | 0.00 | 0.00 | 0.00 | 0.01 | 0.00 |
| Al | 0.13 | 0.12 | 0.12 | 0.12 | 0.12 | 0.11 | 0.11 | 0.12 | 0.12 | 0.11 |
| Fe | 0.28 | 0.28 | 0.29 | 0.28 | 0.28 | 0.27 | 0.26 | 0.27 | 0.27 | 0.26 |
| Mn | 0.01 | 0.01 | 0.01 | 0.01 | 0.01 | 0.01 | 0.01 | 0.01 | 0.01 | 0.01 |
| Mg | 0.72 | 0.71 | 0.72 | 0.72 | 0.72 | 0.73 | 0.74 | 0.72 | 0.72 | 0.72 |
| Ca | 0.89 | 0.89 | 0.88 | 0.88 | 0.88 | 0.89 | 0.90 | 0.88 | 0.88 | 0.89 |
| Na | 0.07 | 0.07 | 0.07 | 0.07 | 0.07 | 0.07 | 0.07 | 0.07 | 0.07 | 0.07 |
| K | 0.00 | 0.00 | 0.00 | 0.00 | 0.00 | 0.00 | 0.00 | 0.00 | 0.00 | 0.00 |
| Total | 4.04 | 4.02 | 4.01 | 4.00 | 4.02 | 4.03 | 4.03 | 4.01 | 4.02 | 4.01 |
| | | | | | | | | | | |
| End-members | | | | | | | | | | |
| Di | 72 | 72 | 71 | 72 | 72 | 73 | 74 | 73 | 72 | 73 |
| Hd | 28 | 28 | 29 | 28 | 28 | 27 | 26 | 27 | 28 | 27 |

Oxygen pfu. 6

Table E.17: JF10-88 biotite analyses

| Analysis No. | 23 | 24 | 25 | 27 | 28 | 29 | 30 | 31 | 32 | 33 | 34 | 35 | 36 | 37 |
|---|---|---|---|---|---|---|---|---|---|---|---|---|---|---|
| Wt. % | | | | | | | | | | | | | | |
| SiO2 | 36.09 | 35.40 | 35.74 | 35.63 | 35.67 | 35.92 | 35.78 | 35.46 | 36.04 | 35.78 | 35.03 | 35.72 | 35.38 | 35.47 |
| TiO2 | 5.76 | 4.95 | 5.15 | 4.70 | 5.16 | 5.53 | 5.72 | 5.66 | 5.43 | 5.25 | 5.38 | 5.37 | 5.42 | 5.33 |
| Al2O3 | 14.16 | 14.29 | 14.19 | 14.29 | 14.46 | 14.29 | 14.37 | 14.47 | 14.18 | 14.41 | 14.23 | 14.06 | 14.07 | 14.27 |
| FeO | 13.33 | 11.95 | 11.84 | 11.73 | 12.86 | 13.32 | 13.33 | 13.36 | 13.15 | 12.88 | 13.23 | 12.96 | 12.91 | 13.08 |
| MnO | 0.06 | 0.04 | 0.05 | 0.05 | 0.04 | 0.06 | 0.06 | 0.06 | 0.08 | 0.07 | 0.05 | 0.07 | 0.06 | 0.04 |
| MgO | 15.19 | 15.89 | 16.06 | 16.22 | 15.15 | 14.85 | 14.79 | 14.52 | 15.09 | 15.06 | 14.95 | 15.01 | 14.89 | 14.86 |
| CaO | 0.07 | 0.03 | 0.05 | 0.04 | 0.05 | 0.02 | 0.02 | 0.06 | 0.03 | 0.04 | 0.04 | 0.01 | 0.08 | 0.05 |
| Na2O | 0.09 | 0.06 | 0.05 | 0.03 | 0.04 | 0.06 | 0.06 | 0.06 | 0.05 | 0.06 | 0.21 | 0.05 | 0.05 | 0.04 |
| K2O | 8.12 | 7.92 | 7.87 | 8.26 | 8.60 | 8.64 | 8.52 | 8.18 | 8.70 | 8.43 | 8.07 | 8.40 | 8.03 | 8.47 |
| Total | 92.86 | 90.52 | 91.01 | 90.96 | 92.04 | 92.69 | 92.64 | 91.83 | 92.75 | 91.98 | 91.20 | 91.65 | 90.89 | 91.61 |
| | | | | | | | | | | | | | | |
| Cations | | | | | | | | | | | | | | |
| Si | 2.74 | 2.68 | 2.71 | 2.70 | 2.71 | 2.72 | 2.71 | 2.69 | 2.73 | 2.71 | 2.66 | 2.71 | 2.68 | 2.69 |
| Ti | 0.33 | 0.28 | 0.29 | 0.27 | 0.29 | 0.32 | 0.33 | 0.32 | 0.31 | 0.30 | 0.31 | 0.31 | 0.31 | 0.30 |
| Al | 1.27 | 1.28 | 1.27 | 1.28 | 1.29 | 1.28 | 1.28 | 1.29 | 1.27 | 1.29 | 1.27 | 1.26 | 1.26 | 1.28 |
| Fe | 0.85 | 0.76 | 0.75 | 0.74 | 0.82 | 0.84 | 0.85 | 0.85 | 0.83 | 0.82 | 0.84 | 0.82 | 0.82 | 0.83 |
| Mn | 0.00 | 0.00 | 0.00 | 0.00 | 0.00 | 0.00 | 0.00 | 0.00 | 0.01 | 0.00 | 0.00 | 0.00 | 0.00 | 0.00 |
| Mg | 1.72 | 1.80 | 1.82 | 1.83 | 1.71 | 1.68 | 1.67 | 1.64 | 1.71 | 1.70 | 1.69 | 1.70 | 1.68 | 1.68 |
| Ca | 0.01 | 0.00 | 0.00 | 0.00 | 0.00 | 0.00 | 0.00 | 0.01 | 0.00 | 0.00 | 0.00 | 0.00 | 0.01 | 0.00 |
| Na | 0.01 | 0.01 | 0.01 | 0.00 | 0.01 | 0.01 | 0.01 | 0.01 | 0.01 | 0.01 | 0.03 | 0.01 | 0.01 | 0.01 |
| K | 0.79 | 0.77 | 0.76 | 0.80 | 0.83 | 0.84 | 0.82 | 0.79 | 0.84 | 0.82 | 0.78 | 0.81 | 0.78 | 0.82 |
| Total | 7.70 | 7.58 | 7.62 | 7.64 | 7.67 | 7.69 | 7.68 | 7.60 | 7.71 | 7.65 | 7.58 | 7.62 | 7.55 | 7.61 |
| | | | | | | | | | | | | | | |
| End-members | | | | | | | | | | | | | | |
| Ann | 33 | 30 | 29 | 29 | 32 | 33 | 34 | 34 | 33 | 32 | 33 | 33 | 33 | 33 |
| Phl | 67 | 70 | 71 | 71 | 68 | 67 | 66 | 66 | 67 | 68 | 67 | 67 | 67 | 67 |
| | | | | | | | | | | | | | | |
| Oxygen pfu. | 11 | | | | | | | | | | | | | |

Table E.18: JF10-88 garnet analyses

| Analysis No. | 8 | 9 | 10 | 11 | 12 | 13 | 14 | 15 | 16 | 17 | 18 | 19 | 20 | 21 | 22 | 107 | 108 |
|---|---|---|---|---|---|---|---|---|---|---|---|---|---|---|---|---|---|
| Wt. % | | | | | | | | | | | | | | | | | |
| SiO2 | 38.49 | 38.46 | 38.28 | 38.38 | 38.72 | 38.65 | 38.47 | 38.58 | 38.69 | 38.54 | 38.57 | 38.72 | 38.60 | 38.55 | 38.44 | 37.72 | 37.83 |
| TiO2 | 0.01 | 0.00 | 0.02 | 0.01 | 0.01 | 0.00 | 0.02 | 0.01 | 0.00 | 0.00 | 0.00 | 0.00 | 0.01 | 0.02 | 0.00 | 0.08 | 0.08 |
| Al2O3 | 22.30 | 22.46 | 22.42 | 22.48 | 22.36 | 22.52 | 22.48 | 22.47 | 22.21 | 22.56 | 22.17 | 22.57 | 22.63 | 22.39 | 22.46 | 22.32 | 22.19 |
| FeO | 25.66 | 25.95 | 26.02 | 26.07 | 26.25 | 26.13 | 25.74 | 26.20 | 26.34 | 26.09 | 26.21 | 26.26 | 26.00 | 26.14 | 26.02 | 25.80 | 25.85 |
| MnO | 3.37 | 3.16 | 3.08 | 3.03 | 2.98 | 2.99 | 3.01 | 3.00 | 3.04 | 3.08 | 3.26 | 3.32 | 3.36 | 3.38 | 3.51 | 3.44 | 3.33 |
| MgO | 5.21 | 5.41 | 5.49 | 5.44 | 5.44 | 5.54 | 5.57 | 5.53 | 5.37 | 5.43 | 5.42 | 5.28 | 5.18 | 5.13 | 4.96 | 5.14 | 5.18 |
| CaO | 6.16 | 5.85 | 5.96 | 6.00 | 5.96 | 6.15 | 6.09 | 6.13 | 6.19 | 6.22 | 6.26 | 6.18 | 6.20 | 6.30 | 6.24 | 6.02 | 6.18 |
| Na2O | 0.00 | 0.16 | 0.12 | 0.10 | 0.01 | 0.01 | 0.01 | 0.00 | 0.00 | 0.00 | 0.00 | 0.00 | 0.01 | 0.00 | 0.01 | 0.01 | 0.01 |
| K2O | 0.00 | 0.00 | 0.00 | 0.00 | 0.00 | 0.00 | 0.00 | 0.00 | 0.00 | 0.01 | 0.00 | 0.00 | 0.00 | 0.00 | 0.00 | 0.00 | 0.00 |
| Total | 101.20 | 101.44 | 101.39 | 101.51 | 101.72 | 101.98 | 101.38 | 101.92 | 101.85 | 101.93 | 101.90 | 102.33 | 101.98 | 101.91 | 101.64 | 100.54 | 100.64 |
| | | | | | | | | | | | | | | | | | |
| Cations | | | | | | | | | | | | | | | | | |
| Si | 2.98 | 2.98 | 2.96 | 2.97 | 3.00 | 2.99 | 2.98 | 2.98 | 2.99 | 2.98 | 2.98 | 3.00 | 2.99 | 2.98 | 2.97 | 2.92 | 2.93 |
| Ti | 0.00 | 0.00 | 0.00 | 0.00 | 0.00 | 0.00 | 0.00 | 0.00 | 0.00 | 0.00 | 0.00 | 0.00 | 0.00 | 0.00 | 0.00 | 0.00 | 0.00 |
| Al | 2.03 | 2.05 | 2.04 | 2.05 | 2.04 | 2.05 | 2.05 | 2.05 | 2.03 | 2.06 | 2.02 | 2.06 | 2.06 | 2.04 | 2.05 | 2.04 | 2.02 |
| Fe | 1.66 | 1.68 | 1.68 | 1.69 | 1.70 | 1.69 | 1.67 | 1.70 | 1.70 | 1.69 | 1.70 | 1.70 | 1.68 | 1.69 | 1.68 | 1.67 | 1.67 |
| Mn | 0.22 | 0.21 | 0.20 | 0.20 | 0.20 | 0.20 | 0.20 | 0.20 | 0.20 | 0.20 | 0.21 | 0.22 | 0.22 | 0.22 | 0.23 | 0.23 | 0.22 |
| Mg | 0.60 | 0.62 | 0.63 | 0.63 | 0.63 | 0.64 | 0.64 | 0.64 | 0.62 | 0.63 | 0.63 | 0.61 | 0.60 | 0.59 | 0.57 | 0.59 | 0.60 |
| Ca | 0.51 | 0.48 | 0.49 | 0.50 | 0.49 | 0.51 | 0.50 | 0.51 | 0.51 | 0.52 | 0.52 | 0.51 | 0.51 | 0.52 | 0.52 | 0.50 | 0.51 |
| Na | 0.00 | 0.02 | 0.02 | 0.01 | 0.00 | 0.00 | 0.00 | 0.00 | 0.00 | 0.00 | 0.00 | 0.00 | 0.00 | 0.00 | 0.00 | 0.00 | 0.00 |
| K | 0.00 | 0.00 | 0.00 | 0.00 | 0.00 | 0.00 | 0.00 | 0.00 | 0.00 | 0.00 | 0.00 | 0.00 | 0.00 | 0.00 | 0.00 | 0.00 | 0.00 |
| Total | 8.01 | 8.04 | 8.04 | 8.04 | 8.05 | 8.08 | 8.04 | 8.07 | 8.06 | 8.07 | 8.06 | 8.09 | 8.07 | 8.05 | 8.03 | 7.95 | 7.96 |
| | | | | | | | | | | | | | | | | | |
| End-members | | | | | | | | | | | | | | | | | |
| Grs | 17 | 16 | 16 | 17 | 16 | 17 | 17 | 17 | 17 | 17 | 17 | 17 | 17 | 17 | 17 | 17 | 17 |
| Alm | 55 | 56 | 56 | 56 | 56 | 56 | 55 | 56 | 56 | 56 | 56 | 56 | 56 | 56 | 56 | 56 | 56 |
| Prp | 20 | 21 | 21 | 21 | 21 | 21 | 21 | 21 | 20 | 21 | 20 | 20 | 20 | 20 | 19 | 20 | 20 |
| Sps | 7 | 7 | 7 | 7 | 6 | 6 | 7 | 6 | 7 | 7 | 7 | 7 | 7 | 7 | 8 | 8 | 7 |
| | | | | | | | | | | | | | | | | | |
| Oxygen pfu. | 12 | | | | | | | | | | | | | | | | |

Table E.19: JF10-88 garnet analyses (continued)

| Analysis No. | 109 | 110 | 111 | 112 | 113 | 114 | 115 | 116 | 117 | 118 | 119 | 120 | 121 | 122 | 123 | 124 | 125 |
|---|---|---|---|---|---|---|---|---|---|---|---|---|---|---|---|---|---|
| Wt. % | | | | | | | | | | | | | | | | | |
| SiO2 | 37.51 | 37.85 | 37.63 | 37.89 | 37.45 | 37.50 | 38.07 | 38.17 | 38.22 | 38.29 | 37.63 | 37.63 | 37.78 | 37.86 | 38.17 | 37.93 | 38.18 |
| TiO2 | 0.05 | 0.09 | 0.09 | 0.09 | 0.06 | 0.09 | 0.07 | 0.04 | 0.09 | 0.04 | 0.09 | 0.11 | 0.08 | 0.10 | 0.05 | 0.07 | 0.10 |
| Al2O3 | 22.32 | 22.24 | 22.24 | 22.33 | 21.90 | 22.10 | 22.08 | 22.47 | 22.10 | 22.10 | 22.21 | 22.11 | 22.27 | 22.22 | 22.20 | 22.26 | 22.28 |
| FeO | 25.89 | 26.34 | 25.86 | 25.93 | 25.59 | 25.58 | 25.90 | 25.84 | 25.95 | 25.99 | 25.74 | 26.54 | 26.68 | 26.25 | 25.99 | 26.37 | 26.24 |
| MnO | 3.28 | 3.18 | 3.21 | 3.28 | 3.72 | 3.69 | 3.48 | 3.44 | 3.31 | 3.40 | 3.50 | 3.13 | 3.20 | 3.36 | 3.10 | 3.19 | 3.23 |
| MgO | 5.41 | 5.34 | 5.34 | 5.35 | 4.92 | 5.00 | 4.98 | 5.23 | 5.30 | 5.22 | 5.05 | 5.32 | 5.25 | 4.96 | 5.31 | 5.28 | 5.16 |
| CaO | 6.09 | 5.89 | 6.07 | 6.12 | 6.19 | 6.31 | 6.28 | 6.05 | 6.03 | 6.28 | 5.99 | 6.01 | 6.09 | 6.26 | 6.05 | 6.06 | 6.04 |
| Na2O | 0.01 | 0.01 | 0.03 | 0.02 | 0.02 | 0.03 | 0.00 | 0.01 | 0.00 | 0.00 | 0.00 | 0.02 | 0.01 | 0.00 | 0.00 | 0.00 | 0.00 |
| K2O | 0.00 | 0.01 | 0.01 | 0.00 | 0.01 | 0.01 | 0.03 | 0.01 | 0.00 | 0.02 | 0.02 | 0.02 | 0.02 | 0.00 | 0.01 | 0.01 | 0.01 |
| Total | 100.56 | 100.95 | 100.49 | 101.02 | 99.87 | 100.31 | 100.89 | 101.25 | 101.00 | 101.34 | 100.23 | 100.89 | 101.37 | 101.01 | 100.89 | 101.17 | 101.23 |
| | | | | | | | | | | | | | | | | | |
| Cations | | | | | | | | | | | | | | | | | |
| Si | 2.90 | 2.93 | 2.91 | 2.93 | 2.90 | 2.90 | 2.95 | 2.95 | 2.96 | 2.96 | 2.91 | 2.91 | 2.92 | 2.93 | 2.95 | 2.93 | 2.95 |
| Ti | 0.00 | 0.01 | 0.01 | 0.01 | 0.00 | 0.01 | 0.00 | 0.00 | 0.01 | 0.00 | 0.01 | 0.01 | 0.00 | 0.01 | 0.00 | 0.00 | 0.01 |
| Al | 2.04 | 2.03 | 2.03 | 2.04 | 2.00 | 2.02 | 2.01 | 2.05 | 2.02 | 2.01 | 2.03 | 2.02 | 2.03 | 2.03 | 2.02 | 2.03 | 2.03 |
| Fe | 1.68 | 1.70 | 1.67 | 1.68 | 1.66 | 1.66 | 1.68 | 1.67 | 1.68 | 1.68 | 1.67 | 1.72 | 1.73 | 1.70 | 1.68 | 1.71 | 1.70 |
| Mn | 0.21 | 0.21 | 0.21 | 0.22 | 0.24 | 0.24 | 0.23 | 0.23 | 0.22 | 0.22 | 0.23 | 0.21 | 0.21 | 0.22 | 0.20 | 0.21 | 0.21 |
| Mg | 0.62 | 0.62 | 0.62 | 0.62 | 0.57 | 0.58 | 0.57 | 0.60 | 0.61 | 0.60 | 0.58 | 0.61 | 0.61 | 0.57 | 0.61 | 0.61 | 0.59 |
| Ca | 0.51 | 0.49 | 0.50 | 0.51 | 0.51 | 0.52 | 0.52 | 0.50 | 0.50 | 0.52 | 0.50 | 0.50 | 0.50 | 0.52 | 0.50 | 0.50 | 0.50 |
| Na | 0.00 | 0.00 | 0.00 | 0.00 | 0.00 | 0.00 | 0.00 | 0.00 | 0.00 | 0.00 | 0.00 | 0.00 | 0.00 | 0.00 | 0.00 | 0.00 | 0.00 |
| K | 0.00 | 0.00 | 0.00 | 0.00 | 0.00 | 0.00 | 0.00 | 0.00 | 0.00 | 0.00 | 0.00 | 0.00 | 0.00 | 0.00 | 0.00 | 0.00 | 0.00 |
| Total | 7.96 | 7.98 | 7.95 | 7.99 | 7.88 | 7.92 | 7.96 | 8.01 | 7.99 | 8.01 | 7.92 | 7.97 | 8.01 | 7.97 | 7.98 | 8.00 | 8.00 |
| | | | | | | | | | | | | | | | | | |
| End-members | | | | | | | | | | | | | | | | | |
| Grs | 17 | 16 | 17 | 17 | 17 | 17 | 17 | 17 | 17 | 17 | 17 | 16 | 17 | 17 | 17 | 17 | 17 |
| Alm | 55 | 56 | 56 | 56 | 56 | 55 | 56 | 56 | 56 | 56 | 56 | 57 | 57 | 56 | 56 | 56 | 57 |
| Prp | 21 | 20 | 21 | 20 | 19 | 19 | 19 | 20 | 20 | 20 | 20 | 20 | 20 | 19 | 20 | 20 | 20 |
| Sps | 7 | 7 | 7 | 7 | 8 | 8 | 8 | 8 | 7 | 7 | 8 | 7 | 7 | 7 | 7 | 7 | 7 |

Table E.20: JF10-88 garnet analyses (continued)

| Analysis No. | 126 | 127 | 128 | 129 | 130 | 131 | 132 | 133 | 134 | 135 |
|---|---|---|---|---|---|---|---|---|---|---|
| Wt. % | | | | | | | | | | |
| SiO2 | 38.42 | 38.51 | 38.41 | 38.46 | 38.31 | 38.11 | 37.78 | 38.11 | 37.78 | 37.32 |
| TiO2 | 0.09 | 0.08 | 0.07 | 0.06 | 0.06 | 0.09 | 0.10 | 0.08 | 0.00 | 0.03 |
| Al2O3 | 22.34 | 22.22 | 22.19 | 22.31 | 21.91 | 22.09 | 22.29 | 22.18 | 22.02 | 21.83 |
| FeO | 26.52 | 26.34 | 26.47 | 25.71 | 25.68 | 25.81 | 25.83 | 26.13 | 26.66 | 26.77 |
| MnO | 3.51 | 3.27 | 3.17 | 3.29 | 3.76 | 3.64 | 3.58 | 3.42 | 3.53 | 5.83 |
| MgO | 4.98 | 5.23 | 5.39 | 5.33 | 4.95 | 5.09 | 5.14 | 5.00 | 4.42 | 2.75 |
| CaO | 6.27 | 6.18 | 6.00 | 6.10 | 6.50 | 6.30 | 6.11 | 6.05 | 5.98 | 6.00 |
| Na2O | 0.01 | 0.01 | 0.00 | 0.02 | 0.01 | 0.01 | 0.00 | 0.02 | 0.01 | 0.01 |
| K2O | 0.03 | 0.01 | 0.02 | 0.01 | 0.05 | 0.04 | 0.02 | 0.01 | 0.00 | 0.01 |
| Total | 102.18 | 101.84 | 101.71 | 101.28 | 101.24 | 101.19 | 100.87 | 101.01 | 100.39 | 100.57 |
| | | | | | | | | | | |
| Cations | | | | | | | | | | |
| Si | 2.97 | 2.98 | 2.97 | 2.98 | 2.96 | 2.95 | 2.92 | 2.95 | 2.92 | 2.89 |
| Ti | 0.01 | 0.00 | 0.00 | 0.00 | 0.00 | 0.01 | 0.01 | 0.00 | 0.00 | 0.00 |
| Al | 2.04 | 2.03 | 2.02 | 2.03 | 2.00 | 2.01 | 2.03 | 2.02 | 2.01 | 1.99 |
| Fe | 1.72 | 1.70 | 1.71 | 1.66 | 1.66 | 1.67 | 1.67 | 1.69 | 1.72 | 1.73 |
| Mn | 0.23 | 0.21 | 0.21 | 0.22 | 0.25 | 0.24 | 0.23 | 0.22 | 0.23 | 0.38 |
| Mg | 0.57 | 0.60 | 0.62 | 0.61 | 0.57 | 0.59 | 0.59 | 0.58 | 0.51 | 0.32 |
| Ca | 0.52 | 0.51 | 0.50 | 0.51 | 0.54 | 0.52 | 0.51 | 0.50 | 0.50 | 0.50 |
| Na | 0.00 | 0.00 | 0.00 | 0.00 | 0.00 | 0.00 | 0.00 | 0.00 | 0.00 | 0.00 |
| K | 0.00 | 0.00 | 0.00 | 0.00 | 0.01 | 0.00 | 0.00 | 0.00 | 0.00 | 0.00 |
| Total | 8.06 | 8.05 | 8.04 | 8.02 | 7.99 | 7.99 | 7.97 | 7.97 | 7.89 | 7.81 |
| | | | | | | | | | | |
| End-members | | | | | | | | | | |
| Grs | 17 | 17 | 16 | 17 | 18 | 17 | 17 | 17 | 17 | 17 |
| Alm | 56 | 56 | 56 | 55 | 55 | 55 | 56 | 56 | 58 | 59 |
| Prp | 19 | 20 | 20 | 20 | 19 | 19 | 20 | 19 | 17 | 11 |
| Sps | 8 | 7 | 7 | 7 | 8 | 8 | 8 | 7 | 8 | 13 |

Table E.21: JF10-88 K-feldspar analyses

| Analysis No. | 17 | 18 | 24 | 25 | 26 |
|---|---|---|---|---|---|
| Wt. % | | | | | |
| SiO2 | 58.99 | 58.92 | 61.48 | 59.31 | 59.36 |
| TiO2 | 0.54 | 0.49 | 0.30 | 0.53 | 0.50 |
| Al2O3 | 19.07 | 19.25 | 18.76 | 19.14 | 19.21 |
| FeO | 0.26 | 0.45 | 0.27 | 0.47 | 0.52 |
| MnO | 0.01 | 0.00 | 0.00 | 0.01 | 0.03 |
| MgO | 0.00 | 0.00 | 0.00 | 0.01 | 0.01 |
| CaO | 0.07 | 0.07 | 0.20 | 0.07 | 0.07 |
| Na2O | 0.82 | 1.02 | 0.89 | 1.12 | 1.09 |
| K2O | 13.30 | 13.07 | 14.14 | 13.15 | 13.03 |
| Total | 93.05 | 93.26 | 96.03 | 93.82 | 93.82 |
| | | | | | |
| Cations | | | | | |
| Si | 2.91 | 2.91 | 3.03 | 2.93 | 2.93 |
| Ti | 0.02 | 0.02 | 0.01 | 0.02 | 0.02 |
| Al | 1.11 | 1.12 | 1.09 | 1.11 | 1.12 |
| Fe | 0.01 | 0.02 | 0.01 | 0.02 | 0.02 |
| Mn | 0.00 | 0.00 | 0.00 | 0.00 | 0.00 |
| Mg | 0.00 | 0.00 | 0.00 | 0.00 | 0.00 |
| Ca | 0.00 | 0.00 | 0.01 | 0.00 | 0.00 |
| Na | 0.08 | 0.10 | 0.09 | 0.11 | 0.10 |
| K | 0.84 | 0.82 | 0.89 | 0.83 | 0.82 |
| Total | 4.97 | 4.99 | 5.13 | 5.02 | 5.02 |
| | | | | | |
| End-members | | | | | |
| Or | 91 | 89 | 91 | 89 | 89 |
| Ab | 9 | 11 | 9 | 11 | 11 |
| | | | | | |
| Oxygen pfu. | 8 | | | | |

Table E.22: JF10-88 orthopyroxene analyses

| Analysis No. | 61 | 62 | 63 | 64 | 65 | 66 | 67 | 68 | 69 | 70 | 71 | 72 |
|---|---|---|---|---|---|---|---|---|---|---|---|---|
| Wt. % | | | | | | | | | | | | |
| SiO2 | 52.22 | 52.28 | 52.06 | 52.10 | 52.12 | 51.90 | 51.71 | 51.42 | 51.57 | 51.45 | 51.72 | 51.91 |
| TiO2 | 0.05 | 0.08 | 0.04 | 0.10 | 0.08 | 0.07 | 0.07 | 0.08 | 0.05 | 0.10 | 0.08 | 0.07 |
| Al2O3 | 1.54 | 1.31 | 1.60 | 1.58 | 1.49 | 1.55 | 1.64 | 1.67 | 1.56 | 1.62 | 1.55 | 1.55 |
| FeO | 23.72 | 24.21 | 24.45 | 24.11 | 24.82 | 25.08 | 24.94 | 24.22 | 24.47 | 25.01 | 24.21 | 24.12 |
| MnO | 0.90 | 0.89 | 0.83 | 0.98 | 0.93 | 0.94 | 0.90 | 0.91 | 0.94 | 0.92 | 0.91 | 0.94 |
| MgO | 21.44 | 20.96 | 21.01 | 21.35 | 21.06 | 20.74 | 20.68 | 21.05 | 21.11 | 20.88 | 21.22 | 21.46 |
| CaO | 0.37 | 0.38 | 0.31 | 0.36 | 0.34 | 0.33 | 0.31 | 0.36 | 0.28 | 0.29 | 0.26 | 0.29 |
| Na2O | 0.03 | 0.05 | 0.01 | 0.02 | 0.01 | 0.03 | 0.03 | 0.04 | 0.02 | 0.02 | 0.01 | 0.02 |
| K2O | 0.00 | 0.00 | 0.00 | 0.00 | 0.00 | 0.00 | 0.00 | 0.01 | 0.00 | 0.00 | 0.01 | 0.00 |
| Total | 100.27 | 100.17 | 100.31 | 100.60 | 100.86 | 100.65 | 100.27 | 99.77 | 99.99 | 100.28 | 99.97 | 100.35 |
| | | | | | | | | | | | | |
| Cations | | | | | | | | | | | | |
| Si | 1.96 | 1.96 | 1.95 | 1.95 | 1.95 | 1.94 | 1.94 | 1.93 | 1.93 | 1.93 | 1.94 | 1.94 |
| Ti | 0.00 | 0.00 | 0.00 | 0.00 | 0.00 | 0.00 | 0.00 | 0.00 | 0.00 | 0.00 | 0.00 | 0.00 |
| Al | 0.07 | 0.06 | 0.07 | 0.07 | 0.07 | 0.07 | 0.07 | 0.07 | 0.07 | 0.07 | 0.07 | 0.07 |
| Fe | 0.74 | 0.76 | 0.77 | 0.76 | 0.78 | 0.79 | 0.78 | 0.76 | 0.77 | 0.78 | 0.76 | 0.76 |
| Mn | 0.03 | 0.03 | 0.03 | 0.03 | 0.03 | 0.03 | 0.03 | 0.03 | 0.03 | 0.03 | 0.03 | 0.03 |
| Mg | 1.20 | 1.17 | 1.17 | 1.19 | 1.18 | 1.16 | 1.15 | 1.18 | 1.18 | 1.17 | 1.18 | 1.20 |
| Ca | 0.01 | 0.02 | 0.01 | 0.01 | 0.01 | 0.01 | 0.01 | 0.01 | 0.01 | 0.01 | 0.01 | 0.01 |
| Na | 0.00 | 0.00 | 0.00 | 0.00 | 0.00 | 0.00 | 0.00 | 0.00 | 0.00 | 0.00 | 0.00 | 0.00 |
| K | 0.00 | 0.00 | 0.00 | 0.00 | 0.00 | 0.00 | 0.00 | 0.00 | 0.00 | 0.00 | 0.00 | 0.00 |
| Total | 4.01 | 3.99 | 4.00 | 4.02 | 4.02 | 4.00 | 3.99 | 3.98 | 3.99 | 3.99 | 3.99 | 4.01 |
| | | | | | | | | | | | | |
| End-members | | | | | | | | | | | | |
| En | 62 | 61 | 61 | 61 | 60 | 60 | 60 | 61 | 61 | 60 | 61 | 61 |
| Fs | 38 | 39 | 39 | 39 | 40 | 40 | 40 | 39 | 39 | 40 | 39 | 39 |
| | | | | | | | | | | | | |
| Oxygen pfu. | 6 | | | | | | | | | | | |

Table E.23: JF10-88 plagioclase analyses

| Analysis No. | 74 | 76 | 77 | 80 | 82 | 84 | 85 | 86 | 87 | 88 | 89 | 90 | 91 | 92 | 93 | 94 |
|---|---|---|---|---|---|---|---|---|---|---|---|---|---|---|---|---|
| Wt. % | | | | | | | | | | | | | | | | |
| SiO2 | 58.47 | 59.26 | 59.15 | 58.97 | 58.77 | 58.92 | 59.04 | 59.12 | 59.65 | 59.83 | 59.78 | 59.39 | 59.51 | 59.66 | 60.32 | 59.40 |
| TiO2 | 0.00 | 0.00 | 0.00 | 0.00 | 0.00 | 0.00 | 0.00 | 0.00 | 0.00 | 0.00 | 0.00 | 0.00 | 0.00 | 0.00 | 0.00 | 0.00 |
| Al2O3 | 24.81 | 24.69 | 24.71 | 24.62 | 24.60 | 24.77 | 24.65 | 24.65 | 25.13 | 25.09 | 24.91 | 24.58 | 25.03 | 25.14 | 24.65 | 25.22 |
| FeO | 0.23 | 0.09 | 0.14 | 0.13 | 0.31 | 0.08 | 0.20 | 0.12 | 0.14 | 0.32 | 0.20 | 0.43 | 0.19 | 0.28 | 0.17 | 0.29 |
| MnO | 0.01 | 0.02 | 0.00 | 0.00 | 0.00 | 0.00 | 0.00 | 0.01 | 0.00 | 0.01 | 0.00 | 0.00 | 0.00 | 0.00 | 0.00 | 0.00 |
| MgO | 0.00 | 0.00 | 0.00 | 0.00 | 0.00 | 0.00 | 0.00 | 0.00 | 0.00 | 0.00 | 0.06 | 0.19 | 0.00 | 0.00 | 0.00 | 0.00 |
| CaO | 6.36 | 6.14 | 5.99 | 6.07 | 6.03 | 6.18 | 6.26 | 5.89 | 6.15 | 6.14 | 6.12 | 5.95 | 6.28 | 6.41 | 5.63 | 6.43 |
| Na2O | 7.94 | 8.07 | 8.14 | 8.10 | 8.03 | 7.99 | 7.94 | 8.15 | 7.90 | 8.01 | 7.91 | 8.15 | 8.04 | 7.97 | 8.35 | 7.93 |
| K2O | 0.18 | 0.20 | 0.21 | 0.17 | 0.29 | 0.18 | 0.18 | 0.19 | 0.20 | 0.17 | 0.18 | 0.09 | 0.22 | 0.08 | 0.15 | 0.21 |
| Total | 98.01 | 98.46 | 98.35 | 98.06 | 98.04 | 98.12 | 98.28 | 98.13 | 99.17 | 99.57 | 99.16 | 98.79 | 99.27 | | | |
| | | | | | | | | | | | | | | | | |
| Cations | | | | | | | | | | | | | | | | |
| Si | 2.66 | 2.70 | 2.69 | 2.69 | 2.68 | 2.68 | 2.69 | 2.69 | 2.72 | 2.73 | 2.72 | 2.71 | 2.71 | 2.72 | 2.75 | 2.71 |
| Ti | 0.00 | 0.00 | 0.00 | 0.00 | 0.00 | 0.00 | 0.00 | 0.00 | 0.00 | 0.00 | 0.00 | 0.00 | 0.00 | 0.00 | 0.00 | 0.00 |
| Al | 1.33 | 1.33 | 1.33 | 1.32 | 1.32 | 1.33 | 1.32 | 1.32 | 1.35 | 1.35 | 1.34 | 1.32 | 1.34 | 1.35 | 1.32 | 1.35 |
| Fe | 0.01 | 0.00 | 0.01 | 0.01 | 0.01 | 0.00 | 0.01 | 0.00 | 0.01 | 0.01 | 0.01 | 0.02 | 0.01 | 0.01 | 0.01 | 0.01 |
| Mn | 0.00 | 0.00 | 0.00 | 0.00 | 0.00 | 0.00 | 0.00 | 0.00 | 0.00 | 0.00 | 0.00 | 0.00 | 0.00 | 0.00 | 0.00 | 0.00 |
| Mg | 0.00 | 0.00 | 0.00 | 0.00 | 0.00 | 0.00 | 0.00 | 0.00 | 0.00 | 0.00 | 0.00 | 0.01 | 0.00 | 0.00 | 0.00 | 0.00 |
| Ca | 0.31 | 0.30 | 0.29 | 0.30 | 0.29 | 0.30 | 0.31 | 0.29 | 0.30 | 0.30 | 0.30 | 0.29 | 0.31 | 0.31 | 0.27 | 0.31 |
| Na | 0.70 | 0.71 | 0.72 | 0.72 | 0.71 | 0.71 | 0.70 | 0.72 | 0.70 | 0.71 | 0.70 | 0.72 | 0.71 | 0.70 | 0.74 | 0.70 |
| K | 0.01 | 0.01 | 0.01 | 0.01 | 0.02 | 0.01 | 0.01 | 0.01 | 0.01 | 0.01 | 0.01 | 0.01 | 0.01 | 0.00 | 0.01 | 0.01 |
| Total | 5.03 | 5.05 | 5.05 | 5.03 | 5.03 | 5.03 | 5.04 | 5.04 | 5.08 | 5.10 | 5.08 | 5.07 | 5.09 | 5.10 | 5.10 | 5.10 |
| | | | | | | | | | | | | | | | | |
| End-members | | | | | | | | | | | | | | | | |
| Ab | 69 | 70 | 71 | 71 | 71 | 70 | 70 | 71 | 70 | 70 | 70 | 71 | 70 | 69 | 73 | 69 |
| An | 31 | 30 | 29 | 29 | 29 | 30 | 30 | 29 | 30 | 30 | 30 | 29 | 30 | 31 | 27 | 31 |
| | | | | | | | | | | | | | | | | |
| Oxygen pfu. | 8 | | | | | | | | | | | | | | | |

# REFERENCES


Alcock, J. 1996. Effect of grossular on garnet-biotite, FeMg exchange reactions: evidence from garnet with mixed growth and diffusion zoning. Contributions to Mineralogy and Petrology, **124**(2): 209–215.

Anders, E. and Grevesse, N. 1989. Abundances of the elements: Meteoritic and solar. Geochimica et Cosmochimica Acta, **53**(1): 197–214.

Anovitz, L.M. and Essene, E.J. 1990. Thermobarometry and Pressure-Temperature Paths in the Grenville Province of Ontario. Journal of Petrology, **31**(1): 197–241.

Ayers, J.C., Miller, C., Gorisch, B., and Millman, J. 1999. Textural development of monazite during high-grade metamorphism: Hydrothermal growth kinetics, with implications for U,Th-Pb geochronology. American Mineralogist, **84**(11-12): 1766–1780.

Baldwin, S.L., Harrison, T.M., and Gerald, J.D.F. 1990. Diffusion of 40Ar in metamorphic hornblende. Contributions to Mineralogy and Petrology, **105**(6): 691–703.

Beaumont, C., Jamieson, R.a., Nguyen, M.H., and Lee, B. 2001. Himalayan tectonics explained by extrusion of a low-viscosity crustal channel coupled to focused surface denudation. Nature, **414**: 738–742.

Beaumont, C., Jamieson, R.A., Nguyen, M.H., and Medvedev, S. 2004. Crustal channel flows: 1. Numerical models with applications to the tectonics of the Himalayan-Tibetan orogen. J. Geophys. Res., **109**(B6): B06406.

Beaumont, C., Nguyen, M.H., Jamieson, R.A., and Ellis, S. 2006. Crustal flow modes in large hot orogens. Geological Society, London, Special Publications, **268**(1): 91–145.

Berman, R.G. 1991. Thermobarometry using Multi-equilibrium Calculations: A New Technuque, with Petrological Applications. Canadian Mineralogist, **29**: 833–855.

Bethune, K.M. and Davidson, A. 1988. Diabase dykes and the Grenville Front southwest of Sudbury, Ontario. Current Research, Part A, **88-1C**: 151–159.

Bethune, K.R. and Davidson, A. 1997. Metamorphism of the Sudbury Diabase Dyke Swarm: From Protolith to Two-Pyroxene Garnet-Coronite. Canadian Mineralogist, **35**(1996481): 1,191–12.

Black, L.P., Kamo, S.L., Allen, C.M., David, D.W., Aleinikoff, J.N., Valley, J.W., Mundil, R., Campbell, I.H., Korsch, R.J., Williams, I.S., and Foundoulis, C. 2004. Improved 206Pb/238U microprobe geochronology by the monitoring of a trace-element- related matrix effect; SHRIMP, ID TIMS, ELA-ICP-MS and oxygen isotope documentation for a series of zircon standards. Chemical Geology, **205**: 115–140.

Blanckenburg, F., Villa, I.M., Baur, H., Morteani, G., and Steiger, R.H. 1989. Time calibration of a PT-path from the Western Tauern Window, Eastern Alps: the problem of closure temperatures. Contributions to Mineralogy and Petrology, **101**(1): 1–11.

Borg, S.G. and DePaolo, D.J. 1994. Laurentia, Australia, and Antarctica as a Late Proterozoic supercontinent: Constraints from isotopic mapping. Geology, **22**(4): 307–310.

Brown, M. 2009. Metamorphic patterns in orogenic systems and the geological record. In Accretionary Orogens in Space and Time, edited by P.A. Cawood and A. Kröner, The Geological Society, Special Publications vol. 318, pp. 37–74.

Busch, J.P., Essene, E.J., and van der Pluijm, B.A. 1996. Evolution of deep-crustal normal faults: constraints from thermobarometry in the Grenville Orogen, Ontario, Canada. Tectonophysics, **265**(1â2): 83–100.

Bussy, F., Krogh, T.E., Klemens, W.P., and Schwerdtner, W.M. 1995. Tectonic and metamorphic events in the westernmost Grenville Province, central Ontario: new results from high-precision UPb zircon geochronology. Canadian Journal of Earth Sciences, **32**(5): 660–671.

Byonton, W.V. 1984. Geochemistry of the rare earth elements: meteorite studies. In Rare Earth Element Geochemistry, Elsevier, pp. 193–216.

Caddick, M.J., Konopásek, J., and Thompson, A.B. 2010. Preservation of Garnet Growth Zoning and the Duration of Prograde Metamorphism. Journal of Petrology, **51**(11): 2327–2347.

Carr, S.D. and Berman, R.G. 1996. Metamorphic history of the Central Metasedimentary Belt boundary thrust zone and adjacent footwall rocks in the Algonquin domain (Central Gneiss Belt); Bancroft-Whitney-Barrys Bay area, Ontario Grenville. In Abitibi-Grenville Lithoprobe, Atelier 96, Abstracts, p. 8.

Carr, S.D. and Berman, R.G. 1997. Metamorphic history of the Bancroft-Barry's Bay area, Ontario. In Geological Association of Canada, Abstract Volume, v. 22, p. A23.

Carr, S.D., Easton, R.M., Jamieson, R.A., and Culshaw, N.G. 2000. Geologic transect across the Grenville orogen of Ontario and New York. Canadian Journal of Earth Sciences, **37**(2-3): 193–216.

Carr, S.D. and Simony, P.S. 2006. Ductile thrusting versus channel flow in the southeastern Canadian Cordillera: evolution of a coherent crystalline thrust sheet. Geological Society, London, Special Publications, **268**(1): 561–587.

Cesbron, F., Ohnenstetter, D., Blanc, P., Rouer, O., and Sichere, M.C. 1993. Incorporation de terres rres dans les zircons de synthse: etude par cathodoluminescence. Comptes rendus de l'Académie des sciences. Série 2, **316**(9): 2131–1238.

Chen, Y.D., Krogh, T.E., and Lumbers, S.B. 1995. Neoarchean trondhjemitic and tonalitic orthogneiss identified within the northern Grenville Province in Ontario by precise U-Pb dating and petrologic studies. Precambrian Research, **72**: 263–281.

Clemens, J.D., Wall, V.J., Sciences, E., and Victoria, C. 1981. Origin and Crystallization of some Peraluminour (S-Type) Granitic Magmas. The Canadian Mineralogist, **19**: 111–131.

Condie, C.K. 1986. Geochemistry and Tectonic Setting of Early Proterozoic supracrustal Rocks in the Southwestern United States. Journal of Geology, **94**: 845–864.

Cooke, OBrien, and Carswell. 2000. Garnet zoning and the identification of equilibrium mineral compositions in high-pressuretemperature granulites from the Moldanubian Zone, Austria. Journal of Metamorphic Geology, **18**(5): 551–569.

Corfu, F. and Easton, R.M. 2001. U-Pb evidence for polymetamorphic history of Huronian rocks in the Grenville Front Tectonic Zone east of Sudbury, Ontario. Chemical Geology, **172**: 149–171.

Corfu, F., Hanchar, J.M., and Hoskin, P.W.O. 2003. 16 Atlas of Zircon Textures. In Zircon, edited by J.M. Hanchar and P.W.O. Hoskin, The Mineralogical Society of America, Washington, DC, chapter 16, pp. 469–495. Volume 53 edition.

Corrie, S.L. and Kohn, M.J. 2008. Trace-element distributions in silicates during prograde metamorphic reactions: implications for monazite formation. Journal of Metamorphic Geology, **26**(4): 451–464.

Corrigan, D. 1995. Mesoproterozoic evolution of the south- central Grenville orogen: structural, metamorphic and geo- chronologic constraints from the Mauricie transect. Ph.D Thesis, Carlton University, Ottawa.

Corrigan, D., Culshaw, N.G., and Mortensen, J.K. 1994. Pre-Grenvillian evolution and Grenvillian overprinting of the Parautochthonous Belt in Key Harbour, Ontario: UPb and field constraints. Canadian Journal of Earth Sciences, **31**(3): 583–596.

Corriveau, L. and van Breemen, O. 2000. Docking of the Central Metasedimentary Belt to Laurentia in geon 12 : evidence from the 1 . 17 1 . 16 Ga Chevreuil intrusive suite and host gneisses , Quebec 1. Canadian Journal of Earth Sciences, **37**: 253–269.

Cosca, M.A., Essene, E.J., Kunk, M.J., and Sutter, J.F. 1992. Differential unroofing within the central metasedimentary Belt of the Grenville Orogen: constraints from 40Ar/39Ar thermochronology. Contributions to Mineralogy and Petrology, **110**(2): 211–225.

Cosca, M.A., Sutter, J.F., and Essene, E.J. 1991. Cooling and inferred uplift/erosion history of the Grenville Orogen, Ontario: Constraints from 40Ar/39Ar thermochronology. Tectonics, **10**(5): 959–977.

Culshaw, N. and Dostal, J. 2002. Amphibolites of the Shawanaga domain, Central Gneiss Belt, Grenville Province, Ontario: tectonic setting and implications for relations between the Central Gneiss Belt and Midcontinental USA. Precambrian Research, **113**(12): 65–85.

Culshaw, N.G., Beaumont, C., and Jamieson, R.A. 2006. The orogenic superstructure-infrastructure concept: Revisited, quantified, and revived. Geology, **34**(9): 733–736.

Culshaw, N.G., Check, G., Corrigan, D., Drage, J., Gower, R., Haggart, M.J., Wallace, P., and Wodicka, N. 1989. Georgian Bay geological synthesis: Dillon to Twelve Mile Bay, Grenville Province of Ontario. Current Research, Part C, **89-1C**: 157–163.

Culshaw, N.G., Corrigan, D., Drage, J., and Wallace, P. 1988. Georgian Bay geological synthesis: Key Harbour to Dillon, Grenville Province of Ontario. Current Research, Part C, **88-1C**: 129–133.

Culshaw, N.G., Corrigan, D., Ketchum, J.W.F., and Wallace, P. 1990. Georgian Bay geological synthesis: Twelve Mile Bay to Port Severn, Grenville Province of Ontario. Current Research, Part C, **90-1C**: 107–112.

Culshaw, N.G., Davidson, A., and Nadeau, L. 1983. Structural subdivisions of the Grenville Province in the Parry Sound-Algonquin region, Ontario. Current Research, Part B, **83-1B**: 243–252.

Culshaw, N.G. and Dostal, J. 1997. Sand Bay gneiss association, Grenville Province, Ontario: a Grenvillian rift- (and -drift) assemblage stranded in the Central Gneiss Belt? Precambrian Research, **85**(1-2): 97–113.

Culshaw, N.G., Jamieson, R.A., Ketchum, J.W.F., Wodicka, N., Corrigan, D., and Reynolds, P.H. 1997. Transect across the northwestern Grenville orogen, Georgian Bay, Ontario: Polystage convergence and extensionin the lower orogenic crust. Tectonics, **16**(6): 966–982.

Culshaw, N.G., Ketchum, J.W.F., Wodicka, N., and Wallace, P. 1994. Deep crustal ductile extension following thrusting in the southwestern Grenville Province, Ontario. Canadian Journal of Earth Sciences, **31**: 160–175.

Culshaw, N.G., Reynolds, P., and Bogutyn, P. 2000. The Humboldt Bay high strain zone, Onaman-Tashota greenstone belt, Wabigoon subprovince: a preliminary report. In Western Superior Transect, Lithoprode Report #77, pp. 29–37.

Dallmeyer, R.D. and Sutter, J.F. 1980. Acquisitional chronology of remnant magnetization along the ”grenville Polar Path”: evidence from 39Ar/40Ar ages of hornblende and biotite from the Whitestone diorite, Ontario. Journal of Geophysical Research, **85**: 3177–3186.

Daszinnies, M.C., Jacobs, J., Wartho, J.A., and Grantham, G.H. 2009. Post Pan-African thermo-tectonic evolution of the north Mozambican basement and its implication for

the Gondwana rifting. Inferences from 40Ar/39Ar hornblende, biotite and titanite fission-track dating. Geological Society, London, Special Publications, **324**(1): 261–286.

Davidson, A. 1984. Identification of ductile shear zones in the southwestern Grenville Province of the Canadian Shield. In Precambrian Tectonics Illustrated, edited by E. Greiling, Schweizerbart'sche Verlagsbuchhandlung, Stuttgart, pp. 263–279.

Davidson, A. 1986a. Grenville Front Relationships Near Killarney, Ontario. In The Grenville Province, edited by J.M. Moore, A. Davidson, and A.J. Baer, Geological Association of Canada Special Paper 31, pp. 107–117.

Davidson, A. 1986b. New Interpretations in the Southwestern Grenville Province. In The Grenville Province, edited by J.M. Moore, A. Davidson, and A.J. Baer, Geological Association of Canada Special Paper 31, pp. 61–74.

Davidson, A. 1986c. New Interpretations in the Southwestern Grenville Province. In The Grenville Province, edited by J.M. Moore, A. Davidson, and A.J. Baer, Geological Association of Canada Special Paper 31, pp. 61–74.

Davidson, A. 1996. Geology of the Grenville Province. Geological Survey of Canada, Open File 3346, Scale 1:2,000,000.

Davidson, A. 1998. An overview of the Grenville Province Geology, Canadian Shield. In Provinces and Precambrian fossils in North America, edited by M.R. St-Onge, Geological Survey of Canada No. 7, chapter 3, pp. 205–217.

Davidson, A. and Breemen, O.V. 2001. Mid-Mesoproterozoic granitoid rocks in the North Bay area, Grenville Province, Ontario. Current Research, **2001-F8**: 1–21.

Davidson, A., Culshaw, N.G., and Nadeau, L. 1982. A tectono-metamorphic framework for part of the Grenville Province, Parry Sound Region, Ontario. Current Research, Part A, **82-1A**: 175–190.

Davidson, A. and Morgan, W.C. 1981. Preliminary notes on the geology east of Georgian Bay, Grenville Structural Province, Ontario. Current Research, Part A, **81-1A**: 291–298.

Davidson, A. and van Breemen, O. 1988. Baddeleyite-zircon relationships in coronitic metagabbro, Grenville Province, Ontario: implications for geochronology. Contributions to Mineralogy and Petrology, **100**(3): 291–299.

Davidson, A. and van Breemen, O. 1994. U-Pb ages of granites near the Grenville Front. Radiogenic Age and Isotopic Studies: Report 8, **94-F**: 107–144.

Deer, W.A., Howie, R.A., and Zussman, J. 1996. An Introduction to the Rock Forming Minerals. Longman, London, UK, 2nd edition.

Di Vincenzo, G., Carosi, R., and Palmeri, R. 2004. The Relationship between Tectonometamorphic Evolution and Argon Isotope Records in White Mica: Constraints from in situ 40Ar39Ar Laser Analysis of the Variscan Basement of Sardinia. Journal of Petrology, **45**(5): 1013–1043.

Dickin, A.P. and McNutt, R.H. 2003. An application of Nd isotope mapping in structural geology: delineating an allochthonous Grenvillian terrane at North Bay, Ontario. Geological Magazine, **140**(5): 539–548.

Docka, J.A., Berg, J.H., and Kelwin, K.W. 1986. Geothermometry in the Kiglapait Aureole: Part II. Evaluation of Exchange Thermometry in a Well-Constrained Thermal Setting. Journal of Petrology, **27**(3): 605–626.

Dudas, F.O., Davidson, A., and Bethune, K.M. 1994. Age of the Sudbury diabase dykes and their metamorphism in the Grenville Province, Ontario. Current Research, **1994-F**: 97–106.

Easton, R.M. 1992. The Grenville Province. In The Geology of Ontario, Ontario Geological Survey Special Volume 4, chapter 19, pp. 713–904.

Easton, R.M. and Ketchum, J.W.F. 2002. Evidence for a major Mesoproterozoic magmatic province within the Western Grenvile Province near North Bay, Ontario. In 2002 Geological Sociaety of America Annual Meeting. Geological Society of America, Denver, Colorado, pp. Paper No. 106–2.

Ferry, J.M. and Spear, F.S. 1978. Experimental calibration of the partitioning of Fe and Mg between biotite and garnet. Contributions to Mineralogy and Petrology, **66**(2): 113–117.

Finger, F., Broska, I., Roberts, M.P., and Schermaier, A. 1998. Replacement of primary monazite by apatiteallaniteepidote coronas in an amphibolite facies granite gneiss from the eastern Alps. American Mineralogist, **83**: 248–258.

Foster, G., Gibson, H.D., Parrish, R., Horstwood, M., Fraser, J., and Tindle, A. 2002. Textural, chemical and isotopic insights into the nature and behaviour of metamorphic monazite. Chemical Geology, **191**(1â3): 183–207.

Foster, G. and Parrish, R.R. 2003. Metamorphic monazite and the generation of P-T-t paths. Geochronology: Linking the Isotopic Record with Petrology and Textures, **220**(1): 25–47.

Foster, J.G.J. 2005. Mid-Crustal Structure and Petrology of a Ductile, High-Grade, Back-Thrust Belt, Manicouagan Reservoir Area, Grenville Province of Southeastern Quebec. B.Sc (Hons.) Thesis, Memorial University of Newfoundland.

Frost, B.R. and Chacko, T. 1989. The Granulite Uncertainty Principle: Limitations on Thermobarometry in Granulites. The Journal of Geology, **97**(4): 435–450.

Gaber, L.J., Foland, K.A., and Corbató, C.E. 1988. On the significance of argon release from biotite and amphibole during 40Ar/39Ar vacuum heating. Geochimica et Cosmochimica Acta, **52**(10): 2457–2465.

Gagné, S. 2004. Textural, Chemical and Age variation in Monazites of the Paleoproterozoic Lonstaff Bluff Formation, Central Baffin Island, Nunavut. M.Sc Thesis, Dalhousie University, Halifax, Nova Scotia.

Gagné, S., Jamieson, R.A., MacKay, R., Wodicka, N., and Corrigan, D. 2009. Texture, Composition, and Age variations in the monazite from the Lower Amphibolite to the Granulite facies, Longstaff Bluff Formation, Baffin Island, Canada. Canadian Journal of Earth Sciences, **47**: 847–869.

Geological Survey of Canada. 2011. Canadian Aeromagnetic Database. Airborne Geophysics Section; GSC-NRC, Ottawa, Ontario.

Gerbi, C., Culshaw, N., and Marsh, J. 2010. Magnitude of weakening during crustal-scale shear zone development. Journal of Structural Geology, **32**(1): 107–117.

Godin, L., Grujic, D., Law, R.D., and Searle, M.P. 2006. Channel flow, ductile extrusion and exhumation in continental collision zones: an introduction. Geological Society, London, Special Publications, **268**(1): 1–23.

Gower, C.F. and Krogh, T.E. 2002. A UÄìPb geochronological review of the Proterozoic history of the eastern Grenville Province. Canadian Journal of Earth Sciences, **39**(5): 795–829.

Gower, C.F., Rivers, T., and Ryan, A.B. 1990. Mid-Proterozoic Laurentia-Baltica. Geological Association of Canada Special Paper 38.

Graham, C.M. and Powell, R. 1984. A garnethornblende geothermometer: calibration, testing, and application to the Pelona Schist, Southern California. Journal of Metamorphic Geology, **2**(1): 13–31.

Graham, I., Sutherland, L., Zaw, K., Nechaev, V., and Khanchuk, A. 2008. Advances in our understanding of the gem corundum deposits of the West Pacific continental margins intraplate basaltic fields. Ore Geology Reviews, **34**(12): 200–215.

Grant, S.M. 1987. The petrology and structural relations of metagabbros, southwestern Grenville Province, Canada. Ph.D Thesis, University of Leicester, UK.

Grant, S.M. 1988. Diffusion models for corona formation in metagabbros from the Western Grenville Province, Canada. Contributions to Mineralogy and Petrology, **98**(1): 49–63.

Grant, S.M. 1989. Tectonic implications from sapphirine-bearing lithologies, south-west Grenville Province, Canada. Journal of Metamorphic Geology, **7**(6): 583–598.

Haggart, M.J., Jamieson, R.A., Reynolds, P.H., Krogh, T.E., Beaumont, C., and Culshaw, N.G. 1993. Last Gasp of the Grenville Orogeny: Thermochronology of the Grenville Front Tectonic Zone near Killarney, Ontario. The Journal of Geology, **101**(5): 575–589.

Hanchar, J.M. and Rudnick, R.L. 1995. Revealing hidden structures: The application of cathodoluminescence and back-scattered electron imaging to dating zircons from lower crustal xenoliths. Lithos, **36**(34): 289–303.

Hanmer, S. and McEachern, S. 1992. Kinematical and rheological evolution of a crustal-scale ductile thrust zone, Central Metasedimentary Belt, Grenville orogen, Ontario. Canadian Journal of Earth Sciences, **29**(8): 1779–1790.

Harrison, T. and Fitzgerald, J.D. 1986. Exsolution in hornblende and its consequences for 40Ar39Ar age spectra and closure temperature. Geochimica et Cosmochimica Acta, **50**(2): 247–253.

Heaman, L.M. and LeCheminant, A.N. 1993. Paragenesis and U-Pb systematics of baddeleyite (ZrO2). Chemical Geology, **110**(1-3): 95–126.

Hodges, K.V. 2006. A synthesis of the Channel Flow-Extrusion hypothesis as developed for the Himalayan-Tibetan orogenic system. Geological Society, London, Special Publications, **268**(1): 71–90.

Hoffman, P.F. 1988. United Plates of America, The Birth of a Craton: Early Proterozoic Assembly and Growth of Laurentia. Annual Review of Earth and Planetary Sciences, **16**(1): 543–603.

Hoffman, P.F. 1989. Precambrian Geology and Tectonic History of North America. In The Geology of North America - An Overview, edited by A.W. Bally and A.R. Palmer, Geological Society of America vol. A, pp. 447–512.

Hoffman, P.F. 1991. Did the Breakout of Laurentia Turn Gondwanaland Inside-Out? Science, **252**(5011): 1409–1412.

Holland, T.J.B. and Powell, R. 1998. An internally consistent thermodynamic data set for phases of petrological interest. Journal of Metamorphic Geology, **16**(3): 309–343.

Hoskin, P.W.O. and Black, L.P. 2000. Metamorphic zircon formation by solid-state recrystallization of protolith igneous zircon. Journal of Metamorphic Geology, **18**: 423–439.

Hoskin, P.W.O. and Shaltegger, U. 2003. The Composition of Zircon and Igneous and Metamorphic Petrogenesis. In Zircon, edited by J.M. Hanchar and P.W.O. Hoskin, The Mineralogical Society of America, Washington, DC, chapter 2, pp. 27–62. Volume 53 edition.

Hynes, A. and Rivers, T. 2010. Protracted continental collisionÄî evidence from the Grenville OrogenThis article is one of a series of papers published in this Special Issue

on the theme Lithoprobe Äî parameters, processes, and the evolution of a continent. Canadian Journal of Earth Sciences, **47**(5): 591–620.

Indares, A. 1997. Garnet-kyanite clinopyroxenites and garnet-kyanite restites from the Manicouagan imbricate zone; a case of high-P - high-T metamorphism in the Grenville Province. The Canadian Mineralogist, **35**(5): 1161–1171.

Indares, A. and Rivers, T. 1995. Textures , metamorphic reactions and thermobarometry of eclogitized metagabbros : a Proterozoic example. European Journal of Mineralogy, **7**: 43–56.

Jamieson, R.A., Beaumont, C., Medvedev, S., and Nguyen, M.H. 2004. Crustal channel flows: 2. Numerical models with implications for metamorphism in the Himalayan-Tibetan orogen. J. Geophys. Res., **109**(B6): B06407.

Jamieson, R.A., Beaumont, C., Nguyen, M.H., and Culshaw, N.G. 2007. Synconvergent ductile flow in variable-strength continental crust: Numerical models with application to the western Grenville orogen. Tectonics, **26**(5): TC5005.

Jamieson, R.A., Beaumont, C., Warren, C.J., and Nguyen, M.H. 2010. The Grenville Orogen explained? Applications and limitations of integrating numerical models with geological and geophysical dataThis article is one of a series of papers published in this Special Issue on the theme Lithoprobe Äî parameters, processes, a. Canadian Journal of Earth Sciences, **47**(4): 517–539.

Jamieson, R.A., Culshaw, N.G., and Corrigan, D. 1995. North-west propagation of the Grenville orogen: Grenvillian structure and metamorphism near Key Harbour, Georgian Bay, Ontario, Canada*. Journal of Metamorphic Geology, **13**(2): 185–207.

Jamieson, R.A., Culshaw, N.G., Wodicka, N., Corrigan, D., and Ketchum, J.W.F. 1992. Timing and tectonic setting of Grenvillian metamorphism - constraints from a transect along Georgian Bay, Ontario. Journal of Metamorphic Geology, **10**(3): 321–332.

Jamieson, R.A., Williams, M.L., Jercinovic, M.J., and Timmermann, H. 2001. Chemical Age zoning in monazite from polycyclic paragneiss, Central Gneiss Belt, Grenville Orogen, Ontario. In Program with Abstracts 26. Geological Association of Canada -Mineralogical Association of Canada, p. 72.

Jarosewich, E., Nelen, J.A., and Norberg, J.A. 1980. Reference Samples for Electron Microprobe Analysis*. Geostandards Newsletter, **4**(1): 43–47.

Jercinovic, M.J. and Williams, M.L. 2005. Analytical perils (and progress) in electron microprobe trace element analysis applied to geochronology: Background acquisition, interferences, and beam irradiation effects. American Mineralogist, **90**(4): 526–546.

Kamo, S.L. 1984. The petrology, chemistry, and U-Pb age date of a Sudbury Dyke. B.Sc Thesis, University of Toronto, Ontario.

Kelsey, D.E., Clark, C., and Hand, M. 2008. Thermobarometric modelling of zircon and monazite growth in melt-bearing systems: examples using model metapelitic and metapsammitic granulites. Journal of Metamorphic Geology, **26**(2): 199–212.

Ketchum, J.W.F. 1994. Extensional Shear Zones and Lithotectonic Domains in the Southwest Grenville Orogen: Structure, Metamorphism, and U-Pb Geochronology of the Central Gneiss Belt near Pointe-au-Baril, Ontario. Ph.D Thesis, Dalhousie University, Halifax.

Ketchum, J.W.F., Culshaw, N.G., Heaman, L.M., and Krogh, T.E. 1993. U-Pb constraints on the late orogenic extensional and shear history of the Central Britt shear zone, an allochton-parautochthon boundary in the Central Gneiss Belt, Ontario. In Lithoprobe Abitibi-Grenville Project Report No. 33, pp. 161–164.

Ketchum, J.W.F. and Davidson, A. 2000. Crustal architecture and tectonic assembly of the Central Gneiss Belt, southwestern Grenville Province, Canada: a new interpretation. Canadian Journal of Earth Sciences, **37**(2-3): 217–234.

Ketchum, J.W.F., Heaman, L.M., Krogh, T.E., Culshaw, N.G., and Jamieson, R.A. 1998. Timing and thermal infleuence of late orogenic extension in the lower crust: a U-Pb geochronological study from the southwest Grenville orogen, Canada. Precambrian Research, **89**: 25–45.

Ketchum, J.W.F., Jamieson, R.A., Heaman, L.M., Culshaw, N.G., and Krogh, T.E. 1994. 1.45 Ga granulites in the southwestern Grenville Province: geologic setting, P-T conditions, and U-Pb geochronology. Geology, **22**: 215–218.

Ketchum, J.W.F. and Krogh, T.E. 1997. U-Pb constraints on high-pressure metamorphism in the Central Gneiss Belt, southwestern Grenville orogen. Geological Association of Canada, Abstract Volume, **22**: A78.

Kohn, M.J. and Spear, F.S. 1989. Empirical calibration of geobarometers for the assemblage garnet + plagioclase + quartz. American Mineralogist, **74**(1-2): 77–84.

Korotev, R.L. 1996. A Self-Consistent Compliation of Elimental Concentration Data for 93 Geochemical Reference Samples. Geostandards Newsletter, **20**(2): 217–245.

Kretz, R. 1982. Transfer and exchange equilibria in a portion of the pyroxene quadrilateral as deduced from natural and experimental data. Geochimica et Cosmochimica Acta, **46**(3): 411–421.

Kretz, R. 1983. Symbole for Rock-Forming Minerals. American Mineralogist, **68**(1-2): 277–279.

Krogh, T.E. 1989. Provenance and metamorphic ages in the Grenville (NW). In Lithoprobe Abitibi-Grenville Project Workshop, pp. 5–7.

Krogh, T.E. 1993. High precision U-Pb ages for granulite metamorphism and deformation in the Archean Kapuskasing structural zone, Ontario: implications for structure and development of the lower crust. Earth and Planetary Science Letters, **119**: 1–18.

Krogh, T.E. 1994. Precise U-Pb ages for Grenvillian and pre-Grenvillian thristing of Proterozoic and Archean metamorhphic assemblages in the Grenville Front Tectonic Zone. Tectonics, **13**: 963–982.

Krogh, T.E., Chen, Y.D., Culshaw, N.G., and Ketchum, J.W.F. 1992. New Terrane identification within the Grenville Province. In Lithoprobe Abitibi-Grenville Transect: Workshop IV.

Krogh, T.E., Corfu, F., Davis, D.W., Dunning, G.R., Heaman, L.M., Kamo, S.L., Machado, N., Greenough, J.D., and Nakamura, E. 1988. Precise U-Pb isotopic ages of diabase dykess and mafic to ultramafic rocks using trace amounts of baddeleyite and zircon. In Mafic Dyke Swarms, edited by H.C. Hallf and W.F. Fahrig, Geological Association of Canada Special Paper 34, pp. 147–152.

Krogh, T.E., Culshaw, N.G., and Ketchum, J.W.F. 1993. Multiple ages of deformation and metamorphism in the Parry Sound-Pointe-au-Baril area. In Lithoprobe Abitibi-Grenville Project, volume Report no., p. 39.

Krogh, T.E. and Davis, G.L. 1969. Old isotopic ages in the northwestern Grenville Province, Ontario. In Geological Association of Canada Special Paper 5, Geological Association of Canada, pp. 189–192.

Krogh, T.E. and Davis, G.L. 1970a. Isotopic ages along the Grenville Province of Ontario. In Carnegie Institution of Washington, Yearbook 68, pp. 309–313.

Krogh, T.E. and Davis, G.L. 1970b. Metamorphism 1700+100 m.y. and 800+100 m.y. ago in the northwest part of the Grenville Province of Ontario. In Carnegie Institution of Washington, Yearbook 68, pp. 309–313.

Krogh, T.E. and Davis, G.L. 1971. Paragneiss studies in the Georgian Bay area - 90 km southeast of the Grenville Front. In Carnegie Institution of Washington, Yearbook 69, pp. 339–341.

Krogh, T.E., Davis, G.L., and Frarey, M.J. 1971. Isotopic ages along the Grenville Front in the Bell Lake area, SW of Sudbury Ontario. In Carnegie Institution of Washington, Yearbook 69, pp. 337–339.

Krogh, T.E., Gower, C.F., and Wardle, R.J. 1996. Pre-Labradorian Crust and later Labradorian, Pinwarian and Grenvillian metamorphism in the Mealy Mountains terrane, Grenville Province, eastern Labrador. In Program and Abstracts, edited by C.F. Gower. Proterozoic Evolution in the North Atlantic Realm, COPENA-ECSOOT-IBTA confenrence, pp. 106–107.

Kuiper, K.F., Deino, A., Hilgen, F.J., Krijgsman, W., Renne, P.R., and Wijbrans, J.R. 2008. Synchronizing Rock Clocks of Earth History. Science, **320**(5875): 500–504.

Le Breton, N. and Thompson, A.B. 1988. Fluid-absent (dehydration) melting of biotite in metapelites in the early stages of crustal anatexis. Contributions to Mineralogy and Petrology, **99**(2): 226–237.

Lee, J.K.W. 1993. The argon release mechanisms of hornblende in vacuo. Chemical Geology, **106**(12): 133–170.

Lee, J.K.W., Onstott, T.C., Cashman, K.V., Cumbest, R.J., and Johnson, D. 1991. Incremental heating of hornblende in vacuo: Implications for 40Ar/39Ar geochronology and the interpretation of thermal histories. Geology, **19**(9): 872–876.

Liogys and Jenkins. 2000. Hornblende geothermometry of amphibolite layers of the Popple Hill gneiss, north-west Adirondack Lowlands, New York, USA. Journal of Metamorphic Geology, **18**(5): 513–530.

Ludden, J. and Hynes, A. 2000. The Lithoprobe Abitibi-Grenville transect: two billion years of crust formation and recycling in the Precambrian Shield of Canada. Canadian Journal of Earth Sciences, **37**(2-3): 459–476.

Ludwig, K.R. 2001. Squid: Special Publication No.2. Berkley, CA.

Ludwig, K.R. 2003. Isoplot: Special Publication No.4. Berkley, CA.

Lumbers, S.B. 1971. Geology of the North Bay area Districts of Nipissing and Parry Sound. Technical report, Department of Mines and Northern Affairs, Toronto.

Lumbers, S.B. 1975. Geology of the Burwsh area, Districts of Nippissing, Parry Sound, and Sudbury. Technical report, Ministry of natural Resources, Division of Mines, Toronto.

Lumbers, S.B., Wu, T.W., Heaman, L.M., Vertolli, V.M., and MacRae, N.D. 1991. Petrology and age of the A-type Mulock granite batholith, northern Grenville Province, Ontario. Precambrian Research, **53**(34): 199–231.

Mark Harrison, T. 1981. Diffusion of 40Ar in hornblende. Contributions to Mineralogy and Petrology, **78**(3): 324–331.

Marsh, J.H., Gerbi, C.C., Culshaw, N.G., Johnson, S.E., Wooden, J.L., and Clark, C. 2012. Using zircon U-Pb ages and trace element chemistry to constrain the timing of metamorphic events, pegmatite dike emplacement, and shearing in the southern Parry Sound domain, Grenville Province, Canada. Precambrian Research, **192-195**: 142–165.

Mazdab, F.K. and Wooden, J.L. 2006. Trace element analysis in zircon by ion microprobe (SHRIMP-RG): Technique and applications. Geochimica et Cosmochimica Acta, **70**(18, Supplement): A405.

McDougall, I. and Harrison, T.M. 1988. Geochronology and thermochronology by the 40Ar/39Ar method. Oxford University Press, New York, 1st edition.

McDougall, I. and Harrison, T.M. 1999. Geochronology and thermochronology by the 40Ar/39Ar method. Oxford University Press, New York, 2nd edition.

McLeish, D.F. 2008. Geology, Petrology, and Metamorphic History of Western Algonquin Park: Implications for the Tectonic Evolution of the Western Grenville Orogen. B.Sc (Hons.) Thesis, Dalhousie Uninversity, Halifax, Nova Scotia.

McLelland, J., Daly, J., and McLelland, J.M. 1996. The Grenville Orogenic Cycle (ca. 1350-1000 Ma): an Adirondack perspective. Tectonophysics, **265**(12): 1–28.

McMenamin, M.A.S. and McMenamin, D.L.S. 1990. The emergence of animals: The Cambrian Breakthrough. Columbia University Press, New York.

Mezger, K., Essene, E.J., Pluijm, B.A., and Halliday, A.N. 1993. U-Pb geochronology of the Grenville Orogen of Ontario and New York: constraints on ancient crustal tectonics. Contributions to Mineralogy and Petrology, **114**(1): 13–26.

Möller, A., OBrien, P.J., Kennedy, A., and Kröner, A. 2003. Linking growth episodes of zircon and metamorphic textures to zircon chemistry: an example from the ultrahigh-temperature granulites of Rogaland (SW Norway). Geological Society, London, Special Publications, **220**(1): 65–81.

Montel, J.M., Foret, S., Veschambre, M.A., Nicollet, C., and Provost, A. 1996. Electron microprobe dating of monazite. Chemical Geology, **131**(1-4): 37–53.

Moore, J.M. and Thompson, P.H. 1980. The Flinton Group: a late Precambrian metasedimentary succession in the Grenville Province of eastern Ontario. Canadian Journal of Earth Sciences, **17**(12): 1685–1707.

Moores, E.M. 1991. Southwest U.S.-East Antarctic (SWEAT) connection: A hypothesis. Geology, **19**(5): 425–428.

Morton, A.C. and Hallsworth, C.R. 1999. Processes controlling the composition of heavy mineral assemblages in sandstones. Sedimentary Geology, **124**: 3–29.

Nadeau, L. 1990. Tectonic, thermal and magmatic evolution of the Central Gneiss Belt, Huntsville region, southwestern Grenville orogen. PhD Thesis, Carlton University, Ottawa, Ontario.

Nadeau, L. and Hanmer, S. 1992. Deep-crustal break-back stacking and slow exhumation of the continental footwall beneath a thrusted marginal basin, Grenville orogen, Canada. Tectonophysics, **210**(34): 215–233.

Nadeau, L. and van Breemen, O. 1989. U-Pb geochronology and structural evolution of the Central Gneiss Belt, Huntsville region, southwestern Grenville Province. In Geological Association of Canada, Program with Abstracts. p. A52.

Nadeau, L. and van Breemen, O. 1998. Plutonic ages and tectonic setting of the Algonquin and Muskoka allochthons, Central Gneiss Belt, Grenville Province, Ontario. Canadian Journal of Earth Sciences, **35**(12): 1423–1438.

Nyström, A.I. and Kriegsman, L.M. 2003. Prograde and retrograde reactions, garnet zoning patterns, and accessory phase behaviour in SW Finland migmatites, with implications for geochronology. Geological Society, London, Special Publications, **220**(1): 213–230.

O'Brien, P.J. 1999. Asymmetric zoning profiles in garnet from HP-HT granulite and implications for volume and grain-boundary diffusion. Mineralogical Magazine, **63**(2): 227–238.

Ohnenstetter, D., Watkinson, D.H., and Dahl, R. 1991. Zoned hollingworthite from the Two Duck Lake Intrusion, Coldwell Complex, Ontario. American Mineralogist, **76**(9-10): 1694–1700.

Onstott, T.C. and Peacock, M.W. 1987. Argon retentivity of hornblendes: A field experiment in a slowly cooled metamorphic terrane. Geochimica et Cosmochimica Acta, **51**(11): 2891–2903.

Ontario Geological Survey. 1991. Bedrock Geology of Ontario, Southern Sheet. Ontario Geological Survey Map:2544, Scale 1:1,000,000.

Pan, Y.M. 1997. Zircon- and monazite-forming metamorphic reactions at Manitouwadge, Ontario. Canadian Mineralogist, **35**(Part 1): 105–118.

Parrish, R.R. 1990. UPb dating of monazite and its application to geological problems. Canadian Journal of Earth Sciences, **27**(11): 1431–1450.

Parsons, I., Brown, W.L., and Smith, J.V. 1999. 40Ar/39Ar thermochronology using alkali feldspars: real thermal history or mathematical mirage of microtexture? Contributions to Mineralogy and Petrology, **136**(1): 92–110.

Pattison, D.R.M. and Begin, N.J. 1994a. Hierarchy of closure temperatures in granulites and the importance of an intergranular exchange medium ( melt ?) in controlling maximum Fe-Mg exchange temperatures. Mineralogical Magazine, **58**: 694–695.

Pattison, D.R.M. and Begin, N.J. 1994b. Zoning patterns in orthopyroxene and garnet in granulites: implications for geothermometry. Journal of Metamorphic Geology, **12**(4): 387–410.

Perkins, D., Essene, E.J., Westrum, E.F., and Wall, V.J. 1977. Application of new thermodynamic data to grossular phase relations. Contributions to Mineralogy and Petrology, **64**(2): 137–147.

Platt, J.R. 1986. Dynamics of orogenic wedges and the uplift of high-pressure metamorphic rocks. Geological Society of America Bulletin, **97**: 1037–1053.

Powell, R. 1978. Equilibrium Thermodynamics in Petrology: An Introduction. Harper & Row, London, UK.

Powell, R. and Holland, T.J.B. 1988. An internally consistent dataset with uncertainties and correlations: 3. Applications to geobarometry, worked examples and a computer program. Journal of Metamorphic Geology, **6**(2): 173–204.

Powell, R. and Holland, T.J.B. 1994. Optimal geothermometry and geobarometry. American Mineralogist, **79**(1): 120–133.

Pownceby, M.I., Wall, V.J., and O'Neill, H.S.C. 1987. Fe-Mn partitioning between garnet and ilmenite: experimental calibration and applications. Contributions to Mineralogy and Petrology, **97**(1): 116–126.

Prevec, S.A. 1992. U-Pb age constraints on Early Proterozoic mafic magmatism from the southern Superior and western Grenville provinces, Ontario. Radiogenic Age and Isotopic Studies, Report 6, pp. 97–106.

Prevec, S.A. 1993. An isotopic, geochemical and petrographic investigation of the genesis of early Proterozoic mafic intrusions and associated volcanics near Sudbury, Ontario. Ph.D Thesis, University of Alberta, Edmonton, Alberta.

Pyle, J.M. and Spear, F.S. 1999. Yttrium zoning in garnet : Coupling of major and accessory phases during metamorphic reactions. Geological Materials Research, **1**(6): 1–49.

Pyle, J.M., Spear, F.S., and Wark, D.A. 2002. Electron Microprobe Analysis of REE in Apatite, Monazite and Xenotime: Protocols and Pitfalls. Reviews in Mineralogy and Geochemistry, **48**(1): 337–362.

Pyle, J.M., Spear, F.S., Wark, D.A., Daniel, C.G., and Storm, L.C. 2005. Contributions to precision and accuracy of monazite microprobe ages. American Mineralogist, **90**(4): 547–577.

Ratcliffe, L. 2011. Structural, Geochronological, and Metamorphic Investigation of the North Tea Lake Mylonite Zone: A Late Extensional Feature within the Central Gneiss Belt, Grenville Province, Algonquin Park, Ontario. B.Sc (Hons.) Thesis, Dalhousie University, Halifax, Nova Scotia.

Ravna, K. 2000. The garnetclinopyroxene Fe2+Mg geothermometer: an updated calibration. Journal of Metamorphic Geology, **18**(2): 211–219.

Rex, D.C., Guise, P.G., and Wartho, J.A. 1993. Disturbed 40Ar/39Ar spectra from hornblendes: Thermal loss or contamination. Chemical Geology, **103**(14): 271–281.

Reynolds, P.H., Culshaw, N.G., Jamieson, R.A., Grant, S.L., and McKenzie, K.J. 1995. 40Ar/39Ar traverse Grenville Front Tectonic Zone to Britt Domain, Grenville Province, Ontario, Canada*. Journal of Metamorphic Geology, **13**(2): 209–221.

Rivers, T. 1983a. Progressive metamorphism of pelitic and quartzofeldspathic rocks in the Grenville Province of western Labrador tectonic implications of bathozone 6 assemblages. Canadian Journal of Earth Sciences, **20**: 1791–1804.

Rivers, T. 1983b. The northern margin of the Grenville Province in western Labrador anatomy of an ancient orogenic front. Precambrian Research, **22**: 41–37.

Rivers, T. 1994. Tectonic model for the eastern Grenville Province: A Himalayan analogue. Lithoprobe A-G, **41**: 103–106.

Rivers, T. 1997. Lithotectonic elements of the Grenville Province: review and tectonic implications. Precambrian Research, **86**(3-4): 117–154.

Rivers, T. and Corrigan, D. 2000. Convergent margin on southeastern Laurentia during the Mesoproterozoic: tectonic implications. Canadian Journal of Earth Sciences, **37**: 359–383.

Rivers, T., Ketchum, J., Indares, A., and Hynes, A. 2002. The High Pressure belt in the Grenville Province: architecture, timing, and exhumation. Canadian Journal of Earth Sciences, **39**(5): 867–893.

Rivers, T., Martignole, J., Gower, C.F., and Davidson, A. 1989. New tectonic divisions of the Grenville Province, Southeast Canadian Shield. Tectonics, **8**(1): 63–84.

Rubatto, D. 2002. Zircon trace element geochemistry: partitioning with garnet and the link between U-Pb ages and metamorphism. Chemical Geology, **184**(1-2): 123–138.

Schaltegger, U., Fanning, C.M., Günther, D., Maurin, J.C., Schulmann, K., and Gebauer, D. 1999. Growth, annealing and recrystallization of zircon and preservation of monazite in high-grade metamorphism: conventional and in-situ U-Pb isotope, cathodoluminescence and microchemical evidence. Contributions to Mineralogy and Petrology, **134**(2): 186–201.

Scherrer, N.C., Engi, M., Gnos, E., Jakob, V., and Liechti, A. 2000. Monazite analysis ; from sample preparation to microprobe age dating and REE quantification. Schweizer Mineralogische und Petrographische Mitteilungen, **80**: 93–105.

Slagstad, T. 2003. Muskoka and Shawanaga domains, Central Gneiss Belt, Grenville Province, Ontario: Geochemical and geochronological constraints on pre-Grenvillian and Grenvillian geological evolution. Ph.D Thesis, Dalhousie University, Halifax, Nova Scotia.

Slagstad, T., Culshaw, N.G., Daly, J.S., and Jamieson, R.A. 2009. Western Grenville Province holds key to midcontinental Granite-Rhyolite Province enigma. Terra Nova, **21**(3): 181–187.

Slagstad, T., Culshaw, N.G., Jamieson, R.A., and Ketchum, J.W.F. 2004a. Early Mesoproterozoic tectonic history of the southwestern Grenville Province, Ontario: Constraints

from geochemistry and geochronology of high-grade gneisses. In Proterozoic tectonic evolution of the Grenville orogen in North America, edited by R. Tollo, L. Corriveau, J. McLelland, and M. Bartholomew, Geological Society of America, Boulder, Colorado, volume Memoir 197, pp. 209–241.

Slagstad, T., Culshaw, N.G., Jamieson, R.A., and Ketchum, J.W.F. 2004b. Early Mesoproterozoic tectonic history of the southwestern Grenville Province, Ontario: Constraints from geochemistry and geochronology of high-grade gneisses.

Slagstad, T., Hamilton, M.A., Jamieson, R.A., and Culshaw, N.G. 2004c. Timing and duration of melting in the mid orogenic crust: Constraints from U-Pb (SHRIMP) data, Muskoka and Shawanaga domains, Grenville Province, Ontario. Canadian Journal of Earth Sciences, **41**(11): 1339–1365.

Slagstad, T., Jamieson, R.A., and Culshaw, N.G. 2005. Formation, Crystallization, and Migration of Melt in the Mid-orogenic Crust: Muskoka Domain Migmatites, Grenville Province, Ontario. Journal of Petrology, **46**(5): 893–919.

Smith, H.A. and Barreiro, B. 1990. Monazite U-Pb dating of staurolite grade metamorphism in pelitic schists. Contributions to Mineralogy and Petrology, **105**: 602–515.

Spear, F.S. 1980. NaSiCaAl exchange equilibrium between plagioclase and amphibole. Contributions to Mineralogy and Petrology, **72**(1): 33–41.

Spear, F.S. 1981. An experimental study of hornblende stability and compositional variability in amphibolite. American Journal of Science, **281**(6): 697–734.

Spear, F.S. 1995. Metamorphic Phase Equilibria and Pressure-Temperature-Time Paths. Mineralogical Society of America, Washington, DC, 2nd edition.

Spear, F.S. and Kohn, M.J. 1996. Trace element zoning in garnet as a monitor of crustal melting. Geology, **24**(12): 1099–1102.

St-Onge, M.R., Searle, M.P., and Wodicka, N. 2006. Trans-Hudson Orogen of North America and Himalaya-Karakoram-Tibetan Orogen of Asia: Structural and thermal characteristics of the lower and upper plates. Tectonics, **25**(4): TC4006.

Sturm, R. 2002. PX-NOMan interactive spreadsheet program for the computation of pyroxene analyses derived from the electron microprobe. Computers & Geosciences, **28**(4): 473–483.

Tacey, R.J., Robinson, P., and Thompson, A.B. 1976. Garnet composition and zoning in the determination of temperature and pressure of metamorphism, central Massachusetts. American Mineralogist, **61**: 762–775.

Tera, F. and Wasserburg, G.J. 1973. A response to a comment on U-Pb systematics in lunar basalts. Earth and Planetary Science Letters, **19**: 213–217.

Tilton, G.R. and Grunenfelder, M.H. 1968. Sphene: uranium-lead ages. Science, **159**: 1458–1461.

Timmermann, H. 1998. Geology, Metamorphism, and U-Pb Geochronology of the Central Gneiss Belt between Huntsville and Haliburton, Southwestern Grenville Province, Ontario. Ph.D Thesis, Dalhousie University, Halifax, Nova Scotia.

Timmermann, H., Parrish, R.R., Jamieson, R.A., and Culshaw, N.G. 1997. Time of metamorphism beneath the Central Metasedimentary Belt boundary thrust zone, Grenville Orogen, Ontario: accretion at 1080Ma? Canadian Journal of Earth Sciences, **34**(7): 1023–1029.

Tindle, A.G. and Webb, P.C. 1994. Probe-AMPH–A spreadsheet program to classify microprobe-derived amphibole analyses. Computers & Geosciences, **20**(7-8): 1201–1228.

Tohver, E., Teixeira, W., van der Pluijm, B., Geraldes, M.C., Bettencourt, J.S., and Rizzotto, G. 2006. Restored transect across the exhumed Grenville orogen of Laurentia and Amazonia, with implications for crustal architecture. Geology, **34**(8): 669–672.

Tollo, R.P., Aleinikoff, J.N., Borduas, E.A., Hackley, P.C., and Fanning, C.M. 2004. Petrologic and geochronologic evolution of the Grenville orogen, northern Blue Ridge Province, Virginia. Geological Society of America Memoirs, **197**: 647–677.

Townsend, K.J., Miller, F.C., D'Andrea, J.L., Ayers, J.C., Harrison, T.M., and Coath, C.D. 2000. Low temperature replacement of monazite in the Ireteba granite, Southern Nevada: geochronological implications. Chemical Geology, **172**: 95–112.

Tuccillo, M.E., Mezger, K., Essene, E.J., and van der Pluijm, B.A. 1992. Thermobarometry, Geochronology and the Interpretation of PTt Data in the Britt Domain, Ontario Grenville Orogen, Canada. Journal of Petrology, **33**(6): 1225–1259.

van Breemen, O. and Davidson, A. 1988. Northeast extension of Proterozoic terranes of mid-continental North America. Geological Society of America Bulletin, **100**(5): 630–638.

van Breemen, O. and Davidson, A. 1990. U-Pb zircon and baddeleyite ages from the Central Gneiss Belt, Ontario. Radiogenic Age and Isotopic Studies: Report 3, **89-2**: 85–92.

van Breemen, O., Davidson, A., Loveridge, W.D., and Sullivan, R.W. 1986. U-Pb Zircon Geochronology of Grenville Tectonites, Granulites and Igneous Precursors, Parry Sound, Ontario.

van Breemen, O. and Hanmer, S. 1986. U-Pb zircon ages of granites and syenites in the Central Metasedimentary Belt, Grenville Province, Ontario. Current Research, Part B, **86-1B**: 775–784.

van Gool, J.A.M. 1992. The Grenville Front foreland fold-and-thrust belt in southwestern Labrador: Mid-crustal structural and metamorphic configuration of a Proterozoic orogenic thrust wedge. Ph.D, Memorial University of Newfoundland, St. John's.

Watson, E.B. 1996a. Dissolution, growth and survival of zircons during crustal fusion: Kinetic principles, geological models and implications for isotopic inheritance. Transactions of the Royal Society of Edinburgh, **87**: 43–56.

Watson, E.B. 1996b. Surface enrichment and trace-element uptake during crystal growth. Geochimica et Cosmochimica Acta, **60**: 5013–5020.

Watson, E.B. and Harrison, T.M. 1983. Zircon Saturation Revisited: Temperature and Composition effects in a Variety of Crustal Magama Types. Earth and Planetary Science Letters, **64**: 295–304.

Weil, A.B., Van der Voo, R., Mac Niocaill, C., and Meert, J.G. 1998. The Proterozoic supercontinent Rodinia: paleomagnetically derived reconstructions for 1100 to 800 Ma. Earth and Planetary Science Letters, **154**(14): 13–24.

Wetherill, G.S. 1956. An interpretation of the Rhodesia and Witwatersrand age patterns. Geochimica et Cosmochimica Acta, **9**: 290–292.

White, D.J., Forsyth, D., Asudeh, I., Carr, S.D., Wu, H., Easton, R.M., and Mereu, R.F. 2000. A seismic-based cross-section of the Grenville Orogen in southern Ontario and western Quebec. Canadian Journal of Earth Sciences, **37**(2-3): 183–192.

Whitehouse, M.J. 2003. Rare earth elements in zircon: a review of applications and case studies from the Outer Hebridean Lewisian Complex, NW Scotland. Geological Society, London, Special Publications, **220**(1): 49–64.

Whitney, J.A. and Stormer, J.C. 1977. Two-feldspar geothermometry, geobarometry in mesozonal granitic intrusions: Three examples from the Piedmont of Georgia. Contributions to Mineralogy and Petrology, **63**(1): 51–64.

Williams, P.F., Jiang, D., and Lin, S. 2006. Interpretation of deformation fabrics of infrastructure zone rocks in the context of channel flow and other tectonic models. Geological Society, London, Special Publications, **268**(1): 221–235.

Wilson, M.E. 1918. The subprovincial limitations of pre-Cambrian nomenclature in the St. Lawrence basin. Journal of Geology, **26**: 325–333.

Wodicka, N. 1994. Middle Proterozoic evolution of the Parry Sound domain, southwestern Grenville Orogen, Ontario: structural, metamorphic, U/Pb, and 40Ar/39Ar constraints. Ph.D Thesis, Dalhousie University, Halifax, Nova Scotia.

Wodicka, N., Corriveau, L., and Stern, R.A. 2004. SHRIMP U-Pb zircon geochronology of the Bondy gneiss complex: Evidence for circa 1.39 Ga arc magmatism and polyphase Grenvillian metamorphism in the Central Metasedimentary Belt, Grenville Province, Québec . Geological Society of America Memoirs, **197**: 243–266.

Wodicka, N., Parrish, R.R., and Jamieson, R.A. 1996. The Parry Sound Domain a far-travelled allochthon? new evidence from U-Pb zircon geochronology. Canadian Journal of Earth Sciences, **33**: 1087–1104.

Wood, B.J., Holland, T.J.B., Newton, R.C., and Kleppa, O.J. 1980. Thermochemistry of jadeite diopside pyroxenes. Geochimica et Cosmochimica Acta, **44**(9): 1363–1371.

Wynne-Edwards, H.R. 1972. The Grenville Province. In Variations in tectonic styles in Canada, Geological Association of Canada Special Paper 11, pp. 263–334.